Suvranu De · Wonmuk Hwang
Ellen Kuhl *Editors*

# Multiscale Modeling in Biomechanics and Mechanobiology

Springer

# Multiscale Modeling in Biomechanics and Mechanobiology

Suvranu De · Wonmuk Hwang
Ellen Kuhl
Editors

# Multiscale Modeling in Biomechanics and Mechanobiology

Springer

*Editors*
Suvranu De
Department of Mechanical, Aerospace, and Nuclear Engineering
Rensselaer Polytechnic Institute
Troy, NY
USA

Wonmuk Hwang
Department of Biomedical Engineering
Texas A&M University
College Station, TX
USA

Ellen Kuhl
Departments of Mechanical Engineering, Bioengineering and Cardiothoracic Surgery
Stanford University
Stanford, CA
USA

ISBN 978-1-4471-6598-9 ISBN 978-1-4471-6599-6 (eBook)
DOI 10.1007/978-1-4471-6599-6

Library of Congress Control Number: 2014951146

Springer London Heidelberg New York Dordrecht



Printed on acid-free paper

Springer is part of Springer Science+Business Media (www.springer.com)

# Preface

Biological systems are arguably the most complex subjects in scientific research, especially regarding the enormous range of length and time scales involved. At the molecular level, structures and dynamics involving biomolecules are highly sophisticated and stochastic. At the cellular level, numerous molecular components, many of which are unidentified, interact and organize in space and time, from which nonequilibrium physiological processes emerge at the tissue and organ levels, and beyond. While vast knowledge is accumulating for any given biological system, establishing quantitative relations between systems defined at different scales requires an integrative approach such as Multiscale Modeling (MSM).

This book is intended as a field manual for MSM methods that link at least two scales. Given the extreme diversity of the topic, the best way to learn MSM is via system-specific case studies. A quick approach toward developing a multiscale model would be to link the scales phenomenologically. Here, however, we suggest a more holistic approach, where real physical and structural information is passed across the scales. This information is becoming increasingly available via rapid advances in imaging and other measurement techniques. Furthermore, physical modeling is inevitable when considering mechanical phenomena in biology, as forces are intrinsically coupled to spatial variables in any physical process.

Among the many possible topics of MSM, our focus is on biomechanics and mechanobiology. The two terms are subtly different, yet closely correlated: Biomechanics is the study of biological systems by means of mechanical tools. It is thus often associated with the "passive" nature of a biological system including strain, stress, and stiffness. Mechanobiology is the study of the role of mechanical forces in modulating biological systems. It is associated with the "active" response of a living system including mechanoreception, signal transduction, and target activation. For a complete understanding of living systems, we have to understand both aspects equally.

The organization of this book naturally follows the biological hierarchy. At the molecular level, we focus on linking discrete and continuum descriptions of biofilaments, molecular motors, and biofilament assemblies. At the cellular level, major topics are the emergence of motile behavior, filament network-to-continuum

transition, and transport phenomena. At the organ level, we review specific organ systems including tendons and ligaments, arteries, and heart valves. Through these case studies, we hope that the reader will develop "numerical instincts" to advance methods and tools and to generalize MSM to other living systems.

We would like to extend our thanks to all contributing authors whose expert contributions made this monograph possible. We would also like to thank the U.S. Interagency Modeling and Analysis Group (IMAG), in particular, Dr. Grace Peng at the National Institutes of Health, interaction with whom and the IMAG activities were one of the catalyzing factors for conceiving this edited volume. Finally, we wish to express our deepest gratitude to Ms. Gabriella Anderson and her colleagues at Springer, who provided us with the encouragement and technical assistance essential to the success of this project.

Suvranu De
Wonmuk Hwang
Ellen Kuhl

# Contents

**Part III Multiscale Modeling Around the Organ Level**

# Part I
# Multiscale Modeling Around the Molecular Level

# Chapter 1
# Proteins: Ssp DnaE Intein

**Albert K. Dearden and Saroj K. Nayak**

**Abstract** During the twentieth century, there have been many rapid advances in scientific understanding about the natural world. Of these advances, our understanding of molecular biology has taken great leaps, starting with the first description of the DNA double helix as described in a scientific article in April of 1953. Since then, vast numbers of research articles have been written all in an effort to better understand our world from a molecular standpoint. However, despite this large effort, specific details about the mechanics of molecular interactions at the atomistic scale remain elusive. One method to illuminate details of these interactions is through the use of quantum mechanical computer simulations based on basic physical principles. Through the use of computational models, new insights into the mechanistic behavior of protein interactions at an atomic scale can be discovered, furthering our understanding of biological systems.

Since their discovery in 1987 [1–3], inteins have been found to exist in all domains of life. They have proven useful for many biotechnology applications as well as have been found in various forms of cancer and infections like tuberculosis. Thus, the ability to control the functions of inteins would be beneficial over a wide range of areas.s However, although it is generally understood that for protein splicing to take place, in which an intein must first self-cleave off the flanking N and C extein polypeptides, a detailed understanding of the mechanics of this process is still not understood. In this aspect, computational simulations with foundations in basic physical principles allow for new insights into biological problems faced today. Using Density Functional Theory (DFT) [4, 5], a greater understanding of biological systems is made possible through investigations into the specific interactions within these systems.

In the context of this work, the Synechocystis sp. Strain PCC6803 DnaE intein was examined by Belfort et al. [6]. In their experiment, their goal was to obtain control

A.K. Dearden (✉)
Department of Physics, Applied Physics, and Astronomy,
Rensselaer Polytechnic Institute, Troy, NY 12180, USA
e-mail: dearda@rpi.edu

S.K. Nayak
School of Basic Sciences, Indian Institute of Technology, Bhubaneswar, India



S. De et al. (eds.), *Multiscale Modeling in Biomechanics and Mechanobiology*, DOI 10.1007/978-1-4471-6599-6_1

over the intein splicing process without mutating catalytic residues. For the DnaE intein, there exist two nucleophilic cysteine residues, the Cys1 at the N-terminus and Cys+1 at the C-terminus, that are used in splicing. At the N-terminus, Cys1 initiates splicing by attacking the backbone amide bond of the N-extein residue at the -1 position, termed the N-S acyl shift. Traditionally, the splicing processes at the N and C-termini are independent of one another in terms of which end first splices. However, the DnaE intein is unique in that the N-terminus has always been observed to splice before the C-terminus. As such, by mutating the residue at the -3 position to a cysteine, the entire intein splicing process was halted at the N-terminus junction through an engineered disulfide bond between Cys1 and Cys-3that created a disulfide loop with a CXXC motif, which in this case is a loop of cysteine, proline, glycine, and cysteine (CPGC). This process revealed for the first time the structure of the intein precursor. Upon examination of the crystal structure, an unusual geometry conformation in the dihedral angles of Gly-1 was discovered. Until this time, the presence of dihedral angles of glycine in a forbidden region of the Ramachandran [7] plot had never before been seen in a CXXC loop motif. Thus, our task is to answer three questions:

- What is the cause of the distorted angles?
- Is the source of the unusual dihedral angles a result of the engineered disulfide loop?
- What effect does this distortion at Gly-1 have on the intein splicing process?

To answer these questions, quantum mechanical simulations, using DFT as implemented in the Gaussian 03 code [8], performed over systems of various sizes combined with mutational data obtained through experiment were carried out.

In order to obtain an accurate quantitative description of protein complexes, systems ranging from hundreds of atoms that span over a nanometer in length to small configurations in which only a few amino acids were examined over the course of this study. This poses a difficult task due to the fact that in traditional DFT calculations, the time a single calculation takes is on the order of $N^3$ where N is the number of atoms in a system. Thus performing calculations on systems containing hundreds of atoms, as required by calculations on biological systems, quickly becomes exceedingly expensive. To overcome this obstacle, we take advantage of the fact that the majority of the biological complex is present only to serve as structural support in the calculations. Interactions such as bond breaking and forming or charge transfers that occur far away from the region in which is being examined do not appreciably affect the region of interest. As such, multiscale methods can be employed to help reduce the computational cost of these large systems using a method known as the mixed Quantum Mechanics and Molecular Mechanics, or QM/MM, method [9, 10]. This method combines the accuracy of fully quantum mechanical DFT with the efficiency of lower level molecular mechanicscalculations. Furthermore, this method has been employed successfully in past cases to solve similar problems [11, 12], and is becoming an important tool in biophysical investigations.

While using the QM/MM method allows for practical calculations on large-scale systems, there are a number of challenges that must first be faced. To start, we must be

sure we have an accurate description of the physical system. Ordinarily, molecular structures that will be studied using DFT come from PDB files obtained through crystallography. During the process by which a biological system is crystalized, many water molecules that are present in vivo are removed. It is very important that these molecules exist in DFT calculations because many biological processes depend on the presence of water. Thus, one must ensure that these water molecules are replaced so that the system is accurately described. Additionally, there will be hydrogen atoms missing from amines. The crystal structure must be carefully examined to find amines that are missing necessary hydrogen atoms.

Another challenge that must be met when using DFT on biological systems is that the mixed QM/MM system has been appropriately chosen. Enough of the local area of interest must be included in the high level QM region in order to properly model the properties of the system. To determine whether enough has been included within the QM region, a DFT calculation must be performed on the entire system to be used as a control for selecting the different regions for QM/MM. Despite computational cost, this is a necessary function since if not enough is included in full QM, the resulting calculations from QM/MM will be inaccurate. On the other hand, it is possible to include too much in the QM region and therefore computational resources are wasted on what could have been in the lower level MM region. Thus, by performing a calculation on the entire system in full DFT, a proper point of reference can be established for the construction of the QM/MM system. Even though this initial procedure is computationally difficult, the resulting QM/MM system is not only accurate for what will be studied, but much faster as well. Armed with these tools, we can set out to answer our first two posed questions; (i) Is the source of the unusual dihedral angles a result of the engineered disulfide loop? and (ii) If the distortion at Gly-1 is not due to the engineered loop, what then is the cause?

To answer our first question, we must first obtain our accurate QM/MM system. Since the majority of the protein complex is unrelated to our study, we took the CPGC loop and an extending 10 Å radius outward as our computational system from the PDB crystal structure published prior to this work [6]. The resulting system contained 289 atoms, of which the CPGC loop was placed in full QM while the remaining structure was within the MM regime after our preliminary calculations were performed. Furthermore, the nearby threonine, Thr69, which is a highly conserved residue appearing more than 90 % of the time in this position with the next most common being serine at roughly 4 %, was also placed in full QM as it was hypothesized that the hydrogen bonding interactions between Thr69 and Gly-1 are the source of the unusual conformation. For the QM part of the calculations, we used the Becke hybrid functional B3LYP [13–15] with the 6−31 G(d, p) [16–25] basis set, and for the MM part we used the AMBER force field [26]. We performed a geometry optimization using our QM/MM system and obtained $(\phi, \psi)$ values of $(-123.19°, 77.81°)$ which compare well with the full DFT calculated values $(-134.18°, 74.72°)$, indicating a successful construction of our QM/MM system.

Now confident with our model system, we began a mutagenesis study involving the mutation of Thr69 to other amino acids to verify if the hypothesis was correct. Our study involved mutating Thr69 to the amino acids serine, alanine, valine, cysteine,

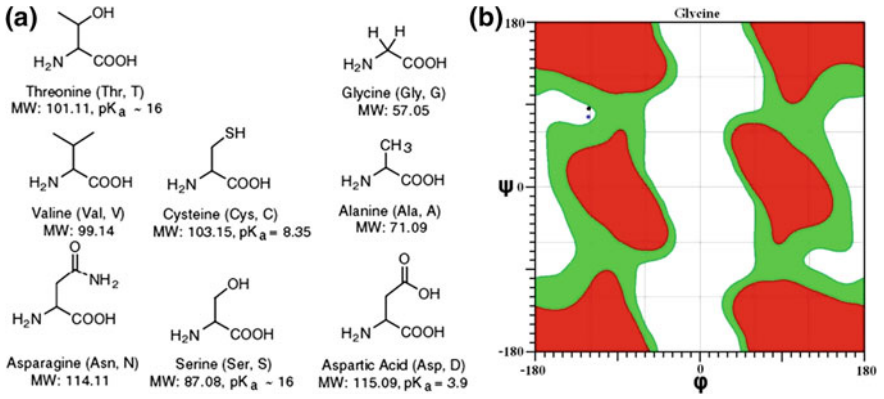


**Fig. 1.1** (*Color online*) **a** Schematic of amino acids used in mutagenesis calculations. Threonine is given as a reference. **b** Figure of the Ramachandran plot of the Gly-1 dihedral angles from experiment (*black dot*) and the QM/MM calculation (*blue dot*). Plot transitions from white, which is the non-allowed region, to *red*, which is the allowed region

glycine, asparagine, and aspartic acid, whose structures can be seen in Fig. 1.1a. Upon mutation of Thr69 to amino acids that are lacking the side chain hydroxyl group, such as to alanine or T69A, we find that the resulting Gly-1 dihedral angles are all within the allowed region of the Ramachandran plot. Examining the structures, it can be seen that serine and threonine are very similar in structure, the only difference being serine is missing the methyl group on the side chain, indicating the possibility that serine might be able to produce the same effect as threonine. As such, upon mutating threonine to serine, resulting system was able to provide both allowed and non-allowed dihedral angles in Gly-1 depending on the initial orientation of serine before the geometry optimization. Starting from the optimized system with threonine, mutating to serine, and then running an additional geometry optimization, serine is able to provide non-allowed dihedral angles in Gly-1. However, by starting with the original crystal structure, mutating Thr69 to Ser69, and then performing the geometry optimization, the resulting dihedral angles are within the allowed region of the Ramachandran plot. As with all DFT calculations, to discern which configuration of the same system is the ground state, we must examine the total energies. Interestingly, there was no energy difference between the allowed and non-allowed configurations, indicating that both structures are equally possible. Upon examination of the individual structures, it was found that the hydroxyl group was closest to Gly-1 when the calculation resulted in non-allowed dihedral angles, and further away when the calculation resulted in allowed dihedral angles. This is a possible reason as to why serine is not as conserved in this position as threonine.

To examine the possibility that threonine could also produce allowed dihedral angles in Gly-1 in the same manner as serine, we mutated serine, in the case where serine provided allowed dihedral angles, back to threonine. Upon completion of a geometry optimization, we found that threonine indeed did provide allowed dihedral

**Table 1.1** Results of the mutagenesis calculations

| | $\phi$ | $\psi$ | Region |
|---|---|---|---|
| Exp. | −121.03 | 87.31 | NA |
| Thr DFT | −134.18 | 74.72 | NA |
| Thr QM/MM | −123.19 | 77.81 | NA |
| S69T | −124.61 | 52.95 | A |
| Gly | −99.37 | 54.37 | A |
| Ala | −119.64 | 50.68 | A |
| Ser | −124.64 | 53.03 | A |
| T69S | −129.55 | 72.01 | NA |
| Val | −116.86 | 51.94 | A |
| Cys | −119.68 | 52.42 | A |
| Asn | −139.97 | 49.72 | A |
| Asp(+) | −117.56 | 51.89 | A |

S69T and T69S refer to the threonine starting from serine and serine starting from threonine calculations, respectively

angles, however comparing the energy of this system to when threonine provided non-allowed dihedral angles, there was a large energy difference. Indeed, the case with threonine providing non-allowed dihedral angles is more stable thanthe allowed case by 0.5 eV, indicating that despite Gly-1 being in an unfavorable conformation, the presence of threonine stabilizes the non-allowed conformation and is indeed the lowest energy state. The results of our mutagenesis calculations can be found in Table 1.1.

As a result of the mutagenesis calculations, and the fact that with Thr69 present the system is much more stable with the non-allowed dihedral angles, we can conclude that the reason for the distortion at the Gly-1 position is due to the nearby threonine. Due to threonine forming a hydrogen bond with glycine through the hydroxyl group on the side chain of threonine, a distortion occurs. Furthermore, serine is also able to facilitate this hydrogen bond under certain conditions. The fact that serine is able to provide both allowed and non-allowed dihedral angles in Gly-1 implies that serine would cause a slowing of the intein splicing process. Conversely, if Thr69 is mutated to an amino acid such as alanine, or T69A, which lacks the side chain hydroxyl group, the distortion at Gly-1 vanishes. Experimentally, this was verified later with a T69A mutation that produced a Gly-1 conformation that fell within the allowed region of the Ramachandran plot. This structure was then compared with disulfide loops consisting of the CPGC motif within other structures and they were found to be similar [27–31]. With this, we have successfully answered the question as to the source of the non-allowed dihedral angles in Gly-1.

In order to address the second question of if the engineered disulfide loop is the cause of the distortion at Gly-1, we examined just the CPGC loop outside of the protein context. Cutting the loop out from the larger system, and adding hydrogen to facilitate now dangling bonds, we performed three calculations to address this

question. Using DFT without any mixed methods, we performed a geometry optimization on the CPGC loop without any imposed constraints. We found the resulting dihedral angles of Gly-1 to be (−105.07°, 22.20°) which are well within the allowed region of the Ramachandran plot. Furthermore, by examining the disulfide bond, we found a bond length of 2.09 Å. Comparing this value with the disulfide bond lengths from the QM/MM systems in which there were the non-allowed angles with threonine and the allowed angles with serine, which were 2.07 Å, we can conclude that there is no strain imposed by either conformation of Gly-1. With the structure of the lone CPGC loop returning to allowed angles within the Ramachandran plot and the lack of strain on the disulfide bond, we can conclude that the distortion at Gly-1 is not a result of the engineered bond.

Now that we know the source of the distortion in Gly-1 is due to the nearby threonine, and that mutation to amino acids that lack the side chain hydroxyl group alleviates the strain, we focus our attention to what effect this distortion has upon the intein splicing process. Specifically, we examined the N-S acyl shift at the N-terminus intein/extein junction. Since threonine appears in this position more than 90 % of the time in nature, there must be some benefit that the distortion at Gly-1 induced by Thr69 has in the splicing process and thus it was hypothesized that the reaction barrier for the N-S acyl shift would be reduced in the case where threonine was present. In order to carry out this part of the investigation, it was required that we eliminate the disulfide bond in the CPGC loop as this was the means by which splicing was halted. For our model system, we used full QM DFT on a reduced structure obtained from QM/MM calculations. The system consisted of the catalytic Cys1, Gly-1, and Pro-2 bound together as in the original model system, as well as the nearby amino acid in which we wanted to investigate. We examined the effects that Thr69 would have on the splicing region as well as the effects the T69A mutation would have for comparison. Due to the fact that the system was reduced, the affecting nearby amino acids, either Thr69 or Ala69, were held at a fixed distance from the catalytic region of the CPGC loop using distances obtained from the QM/MM calculations. Furthermore, we held the dihedral angles of Gly-1 constant in two different orientations for our calculations. All dihedral angles used were obtained from the original QM/MM calculations, where for the case of threonine we took the allowed angles from the S69T calculation and the non-allowed angles were from the original Thr69 calculation. For alanine, the allowed angles were from the original QM/MM calculation, however since alanine was never able to provide a non-allowed configuration in Gly-1, we decided to use the non-allowed angles obtained from threonine. For each configuration of angles, two calculations were required, one for the reactant and then one for the transition state, totaling eight calculations. Each system was fully optimized with the constraints mentioned earlier. Although other possible schemes for proton transfer have been proposed [32], for the transition state calculations,we considered the conserved method of proton transfer [33] similar to the mechanism proposed by Anraku and Satow [34]. We feel this is a reasonable choice because of the proximity of the carbonyl group on Gly-1 and the sulfhydryl of Cys1. An image of the model system can be found in Fig. 1.2.

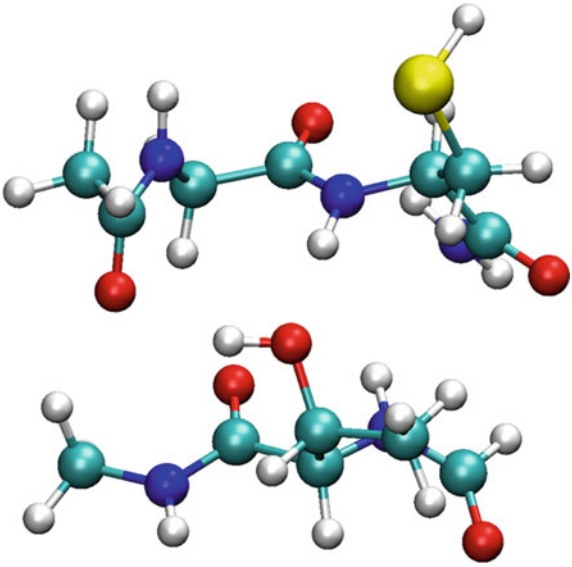

**Fig. 1.2** Representation of the reaction barrier system

Now that we have designated our model system, we used the Synchronous Transit and Quasi-Newton [35, 36] technique which was then refined with the Berny algorithm for the transition state calculations. Single-point energy calculations were used to confirm the existence of a single negative frequency, indicating that a transition state had been achieved. At this point, we must take into consideration the fact that standard DFT calculations are, by their nature, performed in vacuum at zero temperature. While this method has been successfully able to accurately predict structures and energies of bulk structures in computational physics, and while biological structures are generally well described, the energetics of these biological systems are not so well described. To overcome this obstacle, we must include solvent effects into our calculations. There are generally two ways in which solvent effects can be included in DFT calculations, either by an explicit contribution from solvent molecules or an implicit description using dielectric fields. Using explicit solvent molecules proves to be quite challenging in many aspects. First, the precise position and orientation of the solvent molecules are unknown. During the crystallography process, many important solvent molecules are removed and thus the lengthy process of performing calculations while slowly adding solvent molecules to the system to find an equilibrium state must be done. For systems of sufficient size, this method quickly becomes unviable. The second and most limiting obstacle of using explicit solvent molecules is computational cost. For a system containing even a relatively small amount of atoms, a large number of solvent molecules must be added. In turn, these molecules contain multiple atoms themselves. Thus, while the initial system may only contain a few atoms, the number of atoms added to the calculation quickly becomes excessive to the point that the calculation becomes too costly for even the most powerful computers to perform in a reasonable amount of time.

The other method that may be used to add solvent effects to DFT calculations is through an implicit solvent method. In this method, the solvent effects are simulated through dielectric fields rather than explicit solvent molecules. Using an implicit solvent method is advantageous due to the fact it side steps the necessity for a large number of solvent molecules as well as a description of their orientation within the system and instead, the solvent environment is determined by the value of the dielectric constant. However, although the computational cost is not as extreme as including large numbers of solvent molecules, the calculations are still relatively expensive and more time than standard DFT calculations is required to perform them. For our system in question, we used the Polarized Continuum Model (PCM) [37] to simulate the presence of water as would be in experiment. This method encloses the system in a block of dielectric material, where withinspheres are carved out with a radius dependent on the type of atom being enclosed. Care must also be taken with solvent calculations in that the accuracy must be increased beyond default parameters to ensure proper values are obtained. Our calculations were performed first in vacuum ($\varepsilon = 1$) and geometries obtained were used in single point calculations involving solvents. We believe this is an acceptable method to help curb computational cost since tests showed that the energy difference between the solvent single point calculations using the vacuum optimized geometries and geometries obtained through optimizations in solvent were negligible. Furthermore, two solvents were considered. Initially, we performed calculations in full water solvent ($\varepsilon = 78.3553$), however after a literature search, we found that the dielectric constant within biological systems is generally less than that of the external solvent experimentally [38, 39]. Instead, when water is the solvent used in experiment, the dielectric constant is generally between $\varepsilon = 4 - 15$ in the interior part of the system. As such, we performed calculations with dielectric constant $\varepsilon = 10$. Our results for the reaction barrier study can be found in Table 1.2.

Examining the table, our values show that the non-allowed conformation provides a lower barrier and thus reaction rate when threonine is present. However, in the case of alanine, the allowed conformation would provide a lower reaction rate than the non-allowed. Comparing between threonine and alanine, our results suggest that alanine should greatly slow the reaction rate of the N-S acyl shift and although our results represent an upper bound due to the lack of thermal dependence in our calculations,

**Table 1.2** Values obtained from the reaction barrier calculations

| | $\phi$ | $\psi$ | Region | Barrier (eV) | Charge (e) | |
|---|---|---|---|---|---|---|
| | | | | | $S_{Cys}$ | $O_{Gly}$ |
| Thr | −124.61 | 52.95 | A | 0.6 | −0.37 | −0.65 |
| | −123.19 | 77.81 | NA | 1.5 | −0.26 | −0.67 |
| Ala | −119.64 | 50.68 | A | 1.1 | −0.65 | −0.67 |
| | −123.19 | 77.81 | NA | 2.1 | −0.77 | −0.68 |

$S_{Cys}$ and $O_{Gly}$ are the sulfur on the catalytic cysteine and oxygen of the carbonyl group on glycine, respectively

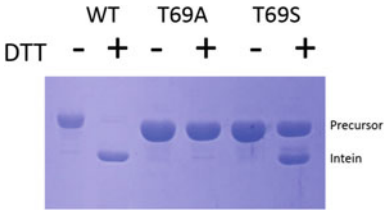


**Fig. 1.3** Gel of WT, T69A, and T69S mutations. WT corresponds to the native wild type intein without mutations, while T69A and T69S correspond to mutations of threonine to alanine and serine, respectively

we believe this provides an estimate in the reduction of the reaction barrier due to threonine. To examine the cause behind the difference in energy barriers, we examine the charges on the sulfur of the catalytic cysteine and the carbonyl oxygen on the glycine. We used the Natural Population Analysis (NPA) [40] scheme to obtain the atomic charges for the system. We see that with the presence of the threonine nearby, the sulfur charge on the catalytic cysteine is reduced from that of the system containing alanine. Furthermore, we believe that the solvent is causing a charge screening effect between the sulfur and oxygen. Thus, the screening effect combined with the reduced atomic charges on the sulfur allow for an easier transition of the sulfur to bond with the carbon during the N-S acyl shift, which is represented by a lower reaction barrier. This conclusion is supported by experimental results shown in Fig. 1.3, which show that upon mutation of threonine to alanine, the splicing reaction is halted. Furthermore, when threonine is mutated to serine, the reaction does not proceed as quickly as with the wild type threonine, however it is not completely halted like in the case of alanine. This lends further support to the conclusion that the hydroxyl side chain bonding with the glycine at the -1 position is affecting the intein splicing process.

In conclusion, we have used multiscale modeling to investigate the DnaE intein that was trapped in its precursor state that had previously never before been observed. Using a mixed QM/MM method to incorporate the accuracy of fully quantum mechanical density functional theory combined with inexpensive molecular mechanics methods for large structures, we were able to reliably investigate the source of a distortion found at Gly-1. We determined that the source is due to a hydrogen bonding interaction between Gly-1 and the nearby Thr69. Furthermore, we were able to computationally predict the structure of the system when threonine was mutated to alanine, which was then later verified by experiment. By investigating the effects of threonine and alanine on the catalytic region between Cys1 and Gly-1, we found that threonine serves to enhance the reaction rate by lowering the reaction barrier of the N-S acyl shift. We have also shown that when alanine is present in place of threonine, the reaction barrier is far greater and splicing ceases. This study not only provides a greater insight into the fundamental understanding of protein splicing, but also could possibly have implications in reactions that require isolation of precursor structures.Although still a relatively new method of investigation, multiscale modeling may help open the door to new and larger studies theoretically that will help further our knowledge of experiments.

## References


1. Hirata, R., et al. 1990, J. Biol. Chem., Vol. 265, p. 6726.
2. Zimniak, L., et al. 1988, J. Biol. Chem., Vol. 263, p. 9102.
3. Bowman, E. J. 1988, J. Biol. Chem, Vol. 263, p. 13994.
4. Kohn, W. and Sham, L. J. 1965, Phys. Rev., Vol. 140, p. 1133.
5. Hohenberg, P. and Kohn, W. 1964, Phys. Rev., Vol. 136, p. 864.
6. Callahan, B. P., et al. 2011, Nat. Struct. Mol. Biol., Vol. 18, p. 630.
7. Ramachandran, G. N., Ramakrishnan, C. and Sasisekharan, V. 1963, J. Mol. Bio., Vol. 7, p. 95.
8. Gaussian 03, Revision C.02, M. J. Frisch, G. W. Trucks, H. B. Schlegel, G. E. Scuseria, M. A. Robb, J. R. Cheeseman, J. A. Montgomery, Jr., T. Vreven, K. N. Kudin, J. C. Burant, J. M. Millam, S. S. Iyengar, J. Tomasi, V. Barone, B. Mennucci, M. Cossi, G.
9. Maseras, F. and Morokuma, K. 1995, J. Comp. Chem., Vol. 16, p. 1170.
10. Senn, H. M. and Thiel, W. 2009, Angew. Chem. Int. Ed., Vol. 48, p. 1198.
11. Shemella, P., et al. 3, 2007, Biophysical Journal, Vol. 92, pp. 847–853.
12. Dearden, A. K., et al. 5, 2013, Protein Science, Vol. 22, pp. 557–563.
13. Raghavachari, K. 2000, Theor. Chem. Acc., Vol. 103, p. 361.
14. Miehlich, B., et al. 1989, Chem. Phys. Lett., Vol. 157, p. 200.
15. Lee, C. T., Yang, W. T. and Parr, R. G. 1988, Phys. Rev. B, Vol. 37, p. 785.
16. Rassolov, V. A., et al. 2001, J. Comp. Chem., Vol. 22, p. 976.
17. Rassolov, V. A., et al. 1998, J. Chem. Phys., Vol. 109, p. 1223.
18. Blaudeau, J. P., et al. 1997, J. Chem. Phys., Vol. 107, p. 5016.
19. Binning, R. C. and Curtiss, L. A. 1990, J. Comp. Chem., Vol. 11, p. 1206.
20. Francl, M. M., et al. 1982, J. Chem. Phys., Vol. 77, p. 3654.
21. Gordon, M. S. 1980, Chem. Phys. Lett., Vol. 76, p. 163.
22. Harihara, P. C. and Pople, J. A. 1974, Mol. Phys., Vol. 27, p. 209.
23. Harihara, P. C. and Pople, J. A. 1973, Theor. Chim. Acta, Vol. 28, p. 213.
24. Hehre, W. J., Ditchfie, R. and Pople, J. A. 1972, J. Chem. Phys., Vol. 56, p. 2257.
25. Ditchfie, R., Hehre, W. J. and Pople, J. A. 1971, J. Chem. Phys., Vol. 54, p. 724.
26. Cornell, W. D., et al. 1995, J. Am. Chem. Soc., Vol. 117, p. 5179.
27. Xu, Q., et al. 1999, Cell, Vol. 98, p. 651.
28. Poland, B., Xu, M. Q. and Quiocho, F. A. 2000, J. Biol. Chem., Vol. 275, p. 16408.
29. Romanelli, A., et al. 2004, Proc. Natl. Acad. Sci. USA, Vol. 101, p. 6397.
30. Johansson, D. G. A., et al. 2009, J. Am. Chem. Soc., Vol. 131, p. 9475.
31. Klabunde, T., et al. 1998, Nat. Struct. Biol., Vol. 5, p. 31.
32. Paulus, H. 1998, Chem. Rev., Vol. 27, p. 375.
33. Blomberg, M. R. A. and Siegbahn, P. E. M. 2006, Biochim. Biophys. Acta, Vol. 1757, p. 969.
34. Anraku, Y. and Satow, Y. 2009, Proc. Jpn. Acad. Ser. B, Vol. 85, p. 409.
35. Peng, C. and Schlegel, H. B. 1993, Isr. J. Chem., Vol. 33, p. 449.
36. Peng, C., et al. 1996, J. Comput. Chem., Vol. 17, p. 49.
37. Miertus, S., Scrocco, E. and Tomasi, J. 1981, J. Chem. Phys., Vol. 55, p. 117.
38. Schutz, C. N. and Warshel, A. 2001, Proteins, Vol. 44, p. 400.
39. Jordanides, X. J., et al. 1999, J. Phys. Chem. B, Vol. 103, p. 7995.
40. Reed, A. E., Weinstock, R. B. and Weinhold, F. 1985, J. Chem. Phys., Vol. 83, p. 735.

# Chapter 2
# Protein Crystals: Molecular to Continuum Level Models Based on Crystal Plasticity Theory

**Suvranu De and Amir Reza Zamiri**

## 2.1 Background

Biological materials are extremely well organized in a hierarchical structure from the molecular building blocks at their first level of organization up to the tissue and organ levels with fascinating nonuniform (anisotropic) properties. Nature utilizes hierarchical structures in an intriguing way to self-assemble biomaterials based on molecular building blocks such as amino acids, nucleic acids, polysaccharides, and lipids that are organized into efficient multifunctional structures and systems ranging from the nanoscopic to the macroscopic length scales [1, 2]. The most basic properties and functions of the biomaterials are defined at the very first level of organization. Therefore, it is imperative to incorporate information from the finer scale biological processes, which often govern processes at the coarser scale, to measure the properties and analyze the functions of biological systems.

Proteins are the primary building blocks of biological materials, and are necessary for providing key functions to biological systems, ranging from structural elements to transmitting information between cells, and biological catalysis [1], in particular under mechanical stimulation. Protein materials in a biological system are made up of self-assembled functional protein molecules that are composed of polypeptide sequence of 20 different amino acids, which allows it to fold up into a specific three-dimensional shape, or conformation [1, 2]. This variety in the amino acids leads to a range of different properties in charge, hydrophobicity, interactions, chemical reactivity, and functionality.

The biological function of protein material in the biological systems is connected to the structural deformations whose mechanical actions are coupled to the chemical events that are associated with the conformational changes [1]. While excellent understanding has been gained on the biological function of proteins at the molecular

S. De (✉) · A.R. Zamiri
Department of Mechanical, Aerospace and Nuclear Engineering,
Rensselaer Polytechnic Institute, 110 8th Street, Troy, NY 12180, USA
e-mail: des@rpi.edu



S. De et al. (eds.), *Multiscale Modeling in Biomechanics and Mechanobiology*, DOI 10.1007/978-1-4471-6599-6_2

scale, how molecular properties, and range of material scales and hierarchies contribute to the biological function that leads to the unique properties of the specific protein material at the mesoscale, which spans from nanometers to micrometers on length scale and nanoseconds to microseconds on timescale, and what role they play in the physiological and pathological phenomena, remains an active frontier of research. This type of bottom-up hierarchical approach toward understanding behavior of protein material holds great potential for fundamental contributions to biology and medicine as well as for the synthesis of self-assembled engineered materials.

The hierarchical structure of protein in the form of self-assembled three-dimensional molecular crystals enables dissipation of mechanical energy through crystallographic slip, that is sliding of molecules against each other, and, hence, delays the catastrophic failure. For example, the staggered arrangement of protein molecules into fibrils plays a key part in increasing the toughness of various collagen materials such as bone [3–5]. The plastic deformation may also induce refolding of protein into a new three-dimensional folded structure. This unfolding may occur locally and involve only certain domains of the protein that may lead to deformation hotspots. Protein folding is critical to biological functions, and misfolding lead to diseases and disorders such as Alzheimer's disease, Parkinson's disease, Type II diabetes, and several types of cancer [6, 7]. Hence, it may be of interest to relate the response of deformation of distinct domain of the protein to their biological function. This may also be used to advance our understanding of diseases and potentially lead to development of new therapeutic drugs. Further, an improved understanding of how the deformation mechanisms at the multiple scales contributes to the mechanical stability of the protein material in diseases could bring about new strategies for the treatment through selective breakdown of foreign material deposits in diseased tissues in case of Alzheimer's disease, Parkinson's disease, and Type II diabetes [8–11]. Also, detailed understanding of mechanical stability, adhesion properties of the protein crystals due to change in amino acid sequence and solvent effects may help to contribute to advance the understand the molecular origin of sickle cell anemia, or Alzheimer's disease. Aside from therapeutics, it may also help in the development of biomimetic materials and devices for a range of engineering and medical applications including regenerative medicine, electronic materials, biotechnology, nanotechnology, and drug delivery.

However, the mechanical properties and stability of many protein materials under different conditions has not been extensively studied. A little is known about their molecular deformation mechanisms, and influence of the nanoscale processes on the mechanical properties. Therefore, further research is needed to explore the fundamental design principles for the development of such materials with optimal functionality and stability. Goal is to understand the relationship between fine scale primary structure and processes and macroscale response of the protein molecular crystals.

In this chapter, we study the bulk mechanical properties of the of protein crystal such that it accounts for the properties of the molecular crystal along with the phenomena occurring at the lower scale. Like most crystalline solids, the mechanical properties of protein materials are strongly influenced by defects such as dislocations through slip-induced plastic deformation [12], which is captured using

continuum-based crystal plasticity model. We apply this model to investigate the temperature- and humidity-dependent mechanical response of tetragonal lysozyme crystals.

## 2.2 Multiscale Modeling Challenges

A large number of computational methods for modeling protein materials at disparate length- and time-scale have been employed. At the bottom, *ab initio* quantum mechanical simulations can be used to develop potential fields for molecular dynamic (MD) simulations. These coarse-graining approaches are able to reach timescale of the order of 100 ns and length scale of 10 nm [13]. Nonetheless, the computational prediction of the three-dimensional folded structure of proteins directly from the amino acid sequence is still beyond current computational capabilities [14]. Likewise, many questions of practical importance involve system sizes and timescales that significantly exceed what can be treated in classical atomistic simulations.

Larger length scales and timescales can be reached using the results of the classical MD calculation to create parameters for a new simulation capable of exploring length- and time-scales of greater orders of magnitude. These hierarchies of simulation techniques, integrated through multiscale methods are based on the concept of informing coarser scales from finer scales, enabling one to establish direct links between chemical structure and larger scales. The process of systematic coarse graining requires transformation of detailed models to simplified descriptions with less degrees of freedom, effectively averages over some chosen properties of lower scale entities to form larger basic units.

The hierarchical coarse-graining approach seems to be capable of simulating any material regardless of complexity on length scales. However, there is no unique way to perform coarse graining. Besides, purely atomistic-based simulations are computationally expensive and typically limited to very small systems of the order of billions of particles that may be simulated over very short timescales of less than a microsecond. Hence, they are incapable of accounting for defects such as dislocations [15] and other microstrcutural effects in any realistic way, which are assumed to play a fundamental role in determining material properties or functional stability of protein crystals.

Continuum modeling represents a discrete system as a continuous body or fluid, and provides the starting point for multiscale modeling. For example, a continuous system with appropriate material properties and characteristics represents the discrete nanostructures involved with the protein folding process [16]. When the material properties and constitutive relations are developed using data gathered from higher accuracy models of lower scale, the resulting continuum models are hierarchical multiscale model. Continuum models like coarse-grain models greatly reduce the degrees of freedom required modeling the protein of interest. However, the major challenge in the development of continuum multiscale model is to develop a constitutive law and

continuum-level equations of a biological system, whose parameters are computed from finer scale models of the system.

## 2.3 Methods

A continuum slip theory-based micromechanical constitutive model has been developed to predict the mechanical behavior of the protein molecular crystals, in which crystallographic slip is the predominant deformation mechanism [17]. We now introduce the basic terminology that is necessary to develop a single crystal plasticity model.

Let $\mathbf{m}^{\alpha}$ bea unit normal to the slip-plane and $\mathbf{s}^{\alpha}$ a unit vector denoting the slip-direction of a typical slip-system $\alpha$ in the crystal coordinate system. Then, the slip-system $\alpha$ can be represented by an orientation matrix

$$\mathbf{I}^{\alpha} = \mathbf{s}^{\alpha} \otimes \mathbf{m}^{\alpha} \tag{2.1}$$

with symmetric and antisymmetric parts defined as

$$\mathbf{P}^{\alpha} = \frac{1}{2}\left(\mathbf{I}^{\alpha} + \mathbf{I}^{\alpha T}\right) \tag{2.2}$$

$$\mathbf{w}^{\alpha} = \frac{1}{2}\left(\mathbf{I}^{\alpha} - \mathbf{I}^{\alpha T}\right) \tag{2.3}$$

which defines the plastic rate of deformation $\mathbf{D}^{p}$ and spin rate $\mathbf{\Omega}^{p}$ as

$$\mathbf{D}^{p} = \sum_{\alpha=1}^{N} \dot{\gamma}^{\alpha} \mathbf{P}^{\alpha} \tag{2.4}$$

$$\mathbf{\Omega}^{p} = \sum_{\alpha=1}^{N} \dot{\gamma}^{\alpha} \mathbf{w}^{\alpha} \tag{2.5}$$

where $N$ is the number of slip systems in the crystal and $\dot{\gamma}^{\alpha}$ is the shear slip-rate.

We now derive the specific form of plastic slip-rate based on dislocation dynamics models. The average velocities of dislocations on a slip-plane $\alpha$ may be expressed as

$$\bar{v}^{\alpha} = v_0^{\alpha} f_p\left(\tau^{\alpha}, \boldsymbol{\chi}\right) \tag{2.6}$$

where $v_0^{\alpha}$ is the limiting velocity, $f_p$ is a probability function, $\tau^{\alpha}$ is the resolved shear stress on slip system $\alpha$, and $\boldsymbol{\chi}$ is a vector containing state variables such

as temperature. It has been shown that for most materials the probability function satisfies a power type expression

$$f_p\left(\tau^\alpha, \boldsymbol{\chi}\right) = \lambda \mathrm{sgn}(\tau^\alpha)\left(\frac{\tau^\alpha}{\tau_y^\alpha}\right)^{2n-1} \tag{2.7}$$

where $\lambda$ and $n$ are material constants and $\tau_y^\alpha$ is the critical resolved shear stress of the slip-system $\alpha$. The rate of shear strain on a slip-system $\alpha$ is

$$\dot{\gamma}^\alpha = \varphi^\alpha \rho^\alpha b^\alpha \bar{v}^\alpha \tag{2.8}$$

where $\varphi^\alpha$ is a material parameter, $\rho^\alpha$ is the dislocation density, and $b^\alpha$ is the Burgers vector. Combining Eqs. (2.6)–(2.8) one obtains:

$$\dot{\gamma}^\alpha = \lambda \mathrm{sgn}(\tau^\alpha)\left(\frac{\tau^\alpha}{\tau_y^\alpha}\right)^{2n-1} \tag{2.9}$$

where the resolved shear stress $\tau^\alpha$ on the slip-system can be related to the Cauchy stress tensor $\boldsymbol{\sigma}$ in the fixed coordinate system as:

$$\tau^\alpha = \boldsymbol{\sigma} : \mathbf{P}^{\boldsymbol{\alpha}} \tag{2.10}$$

Using Eq. (2.9), the overall accumulated slip $\bar{\gamma}$ in a the crystal can be obtained by

$$\bar{\gamma} = \sum_{\alpha=1}^{N} \int_0^t \left|\dot{\gamma}^\alpha\right| dt \tag{2.11}$$

The accumulated slip $\bar{\gamma}$ can be used as a good measure for evaluation of the deformation propensity of a crystal having specific orientation with respect to the external load.

According to the normality rule in plasticity, a yield function $f(\sigma, \chi)$ could be defined such that

$$\mathbf{D}^P = \lambda \frac{\partial f(\boldsymbol{\sigma}, \boldsymbol{\chi})}{\partial \boldsymbol{\sigma}} \tag{2.12}$$

where $\lambda$ is a positive parameter which depends on the type of dislocation barriers. Comparing Eqs. (2.4) and (2.5) and solving the differential Equation (2.12), a yield surface for protein crystals can be defined as:

$$f(\boldsymbol{\sigma}, \boldsymbol{\chi}) = \frac{1}{2n}\left(\sum_{\alpha=1}^{N}\left|\frac{\boldsymbol{\sigma} : \mathbf{P}^\alpha}{\tau_y^\alpha}\right|^{2n} - 1\right) \tag{2.13}$$

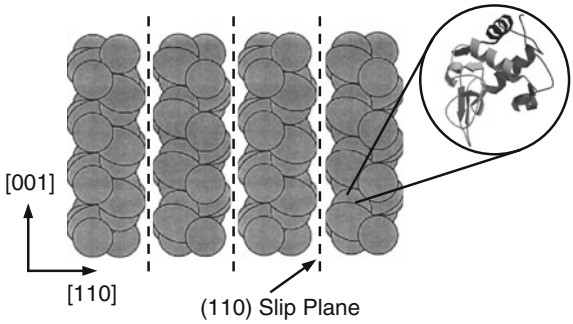


**Fig. 2.1** A 3D crystallized structure of a tetragonal lysozyme crystal (protein molecule is from PDB code: 133L [18])

Substituting Eqs. (2.9) and (2.10) into Eqs. (2.4) and (2.5) leads to the following expressions for plastic rate of the deformation and spin:

$$\mathbf{D}^p = \lambda \sum_{\alpha=1}^{N} \frac{\operatorname{sgn}(\tau^\alpha)}{\tau_y^\alpha} \left| \frac{\tau^\alpha}{\tau_y^\alpha} \right|^{2n-1} \mathbf{P}^\alpha \tag{2.14}$$

$$\mathbf{\Omega}^p = \lambda \sum_{\alpha=1}^{N} \frac{\operatorname{sgn}(\tau^\alpha)}{\tau_y^\alpha} \left| \frac{\tau^\alpha}{\tau_y^\alpha} \right|^{2n-1} \mathbf{w}^\alpha \tag{2.15}$$

The effects of the temperature, water molecules, and other environmental effects on the deformation behavior of protein crystalsare considered through their influence on the critical resolved shear stress $\tau_y^\alpha$.

## 2.4 Results

We present a particularly interesting application of the protein model in modeling the effects of deformation mechanisms, temperature, and amounts of intracrystalline water on the stability and mechanical behavior of tetragonal lysozyme crystals. Lysozyme is a well-studied enzyme, which is found in egg white, tear, saliva, mucus, and other body fluids. The main role of these enzymes is to lyse cell walls of gram positive bacteria. Lysozyme can be easily self-assembled into different crystal structures including orthorhombic, tetragonal, and monoclinic. Its well-known and stable crystal structure makes it a good choice for our study. Figure 2.1 shows a self-assembled structure of a tetragonal lysozyme protein crystal. The tetragonal lysozyme crystal belongs to the $P4_32_12$ space group with lattice constants of $a = b = 7.91$ nm, $c = 3.79$ nm, and $Z = 8$ [12]. In these molecular crystals there are specific molecular planes such as (110) which have the greatest separation and therefore, may glide on each other under external loads, see Fig. 2.2. The plastic deformation in the lysozyme protein crystals at the microscale has been established due to crystalline slip [12].

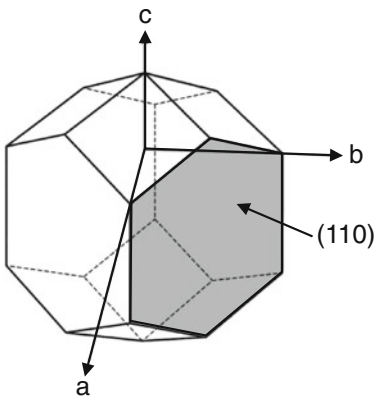


**Fig. 2.2** A tetragonal lysozyme single crystal

The indentation and compression analysis of three-dimensional crystallized form of the tetragonal lysozyme protein crystals reveal that they are relatively fragile and soft materials and their mechanical properties are highly sensitive to both environmental conditions and the type of the protein molecule [19], and size dependent [12, 19]. The compression testing of crystal leads to nonlinear elastic deformation leading to fracture, whereas, during microindentation, the microcrystals exhibit elastic-plastic deformation. The temperature and amount of intracrystalline water have significant effects on the elastic and plastic properties of the crystals. At lower temperature and water content, the crystal is more brittle while it is more ductile at higher temperature and humidity [12].

The elastic constants of tetragonal lysozyme crystal are highly sensitive to both temperature and humidity [20–24]. The Young's modulus of lysozyme crystal decreases with increasing temperature according to the following relationship [20]:

$$\Delta E = -C_T E_\circ \Delta T \tag{2.16}$$

where $\Delta E$ and $\Delta T$ are increments in the Young's modulus and temperature, respectively, $E_\circ$ is the Young's modulus at 300 K and $C_T$ is a constant equal to $2 \times 10^{-3} \mathrm{K}^{-1}$ for lysozyme crystals [20]. The Young's modulus increases with increasing amount of the intracrystalline water molecules [21, 22] as

$$\Delta E = C_w E_\circ \Delta t \tag{2.17}$$

where $\Delta t$ is the evaporation time and $C_w$ is a constant whose value depends on environmental parameters such as temperature. For natural evaporation of water from lysozyme crystal surface at room temperature, $C_w$ was calculated to be 0.0396 (1/min) [17].

The plastic flow in the lysozyme crystals is induced by the dislocation glide along the preferred slip-systems [25]. The tetragonal lysozyme crystal has two sets of slip

systems [20], a primary {110}<001> system and a secondary {110}<110> system. Depending on the crystal orientation and environmental conditions, the primary slip-systems {110}<001> get activated first followed by the secondary slip systems at higher stresses. We perform computer simulations of microindentation experiments of lysozyme single crystals. The critical resolved shear stresses (CRSS) for these slip systems is then characterized from experimental data as a function of temperature and intracrystalline water molecule [17].

### 2.4.1 *Temperature Dependence of Plastic Deformation of Lysozyme Crystals*

We first examine the temperature-dependent plastic deformation of the tetragonal lysozyme molecular crystals. Figure 2.3 shows the temperature dependency of the CRSS of tetragonal lysozyme crystals. At normal rates of deformation, thermal fluctuations provide the energy to carry the dislocations over the lattice potential barriers [26, 27]. Hence, the dislocations at higher temperatures have a higher probability of overcoming lattice potential barriers due to higher thermal fluctuations. This leads to decrease in the CRSS for activation of the slip systems with increasing temperature, as shown in Fig. 2.3. At lower temperatures, the CRSS of the {110}<001> slip system is much less than that of the {110}<110> slip system, therefore, the former can be more easily activated. However, at higher temperatures the CRSS of both slip-systems are small and, hence, both can easily get activated. At temperatures below room temperature, the deformation in lysozyme crystals is primarily elastic, whereas, at higher temperatures it is elastic-plastic. Therefore, at lower temperatures, the variation of CRSS is primarily due to the temperature dependence of the elastic constant. However, at higher temperatures, both the elastic constant and dislocation mechanisms are affected by temperature, which results in a higher drop in CRSS with increasing temperature.

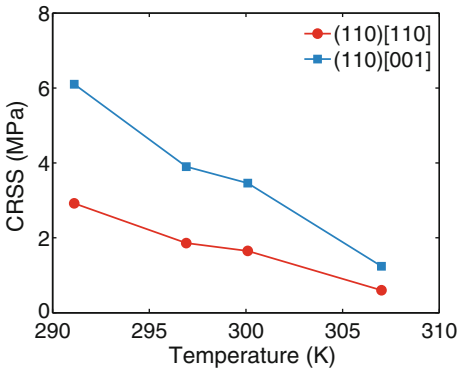


**Fig. 2.3** The effect of temperature on critical resolved shear stresses of the tetragonal lysozyme crystal

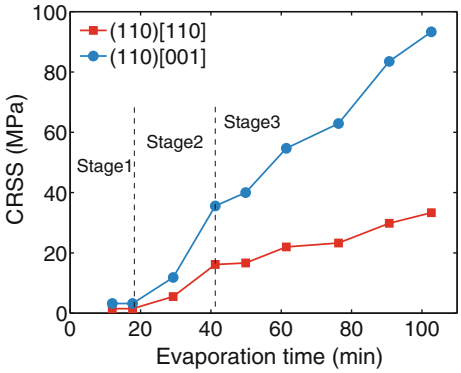


**Fig. 2.4** The effect of the amount of intracrystalline water molecule on critical resolved shear stresses of slip systems in tetragonal lysozyme crystal

### *2.4.2 Effect of Humidity on the Plastic Deformation of Lysozyme Crystals*

We next study the humidity-dependence of the plastic deformation of the tetragonal lysozyme molecular crystals. Protein crystals in biological systems are usually in a fluid environment and, therefore, have a significant amount of intercrystalline water. In Fig. 2.4, we see that the CRSS for both slip systems increase with evaporation time, that is, with the decreasing amount of intracrystalline water. The decrease in the amount of intracrystalline water leads to an increase in elastic constants and a decrease in the lattice parameters[38]. This increases the self energy of the dislocations significantly and hinders their nucleation and activation, thereby increasing the CRSS of the slip systems.

The decrease in CRSS with increasing temperature may also be related to the water molecules, see Fig. 2.4. Two types of intracrystalline water may be present in the lattice, the mobile water, which can easily traverse through the crystal, and bounded water, which is more strongly bound to the molecules [20, 22]. The mobile water has a high diffusion coefficient at higher temperatures [26] and, therefore, has little interaction with dislocations. However, at lower temperatures, it may interact with dislocations and thereby affect dislocation creation and motion in the lattice [20].

### *2.4.3 Anisotropic Plastic Yielding of Lysozyme Crystals*

Figure 2.5, shows two-dimensional plots of the yield function, as given in Eq. (2.13), for three different crystal orientations of tetragonal lysozyme crystals at 285 and 307 K. From the yield surface plot in the Fig. 2.5, it is evident that the tetragonal lysozyme crystal is highly anisotropic and the shape of its yield surface changes with both temperature and crystal orientation. As discussed in the previous sections, at higher temperatures both {110}<110> and {110}<001> slip systems are activate during the deformation, therefore, the material is softer while at low temperature

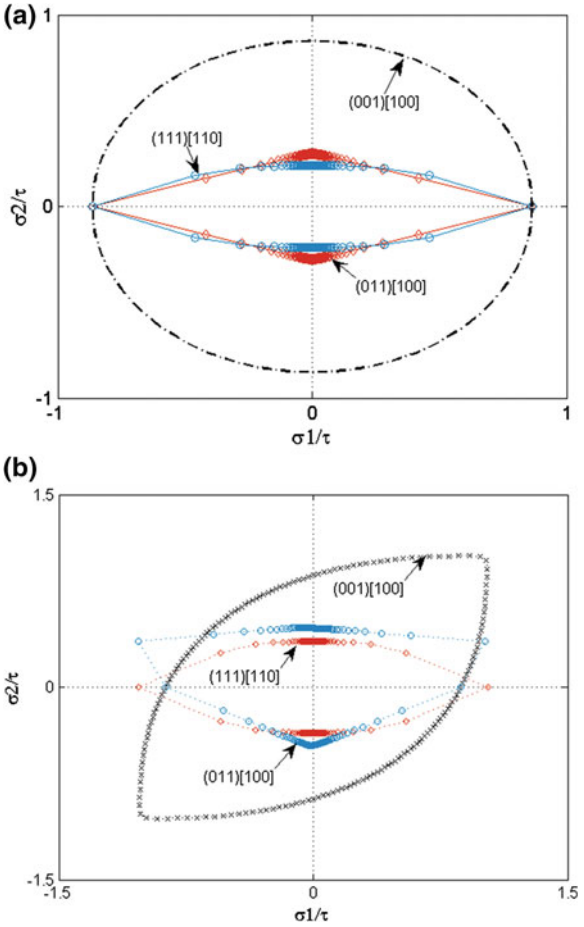


**Fig. 2.5** The yield surface of the tetragonal lysozyme crystals for three different crystallographic orientations of (001)[100], (011)[100], and (111)[110] at two temperature of **a** 285 K and **b** 307 K

only the {110}<001> slip system can get activated and, hence, materials is more rigid. At room temperature, for the lysozyme crystals that have high amount of intracrystalline water both {110}<110> and {110}<001> slip systems are getting activated, however, at the lower amounts of intracrystalline water only {110}<001> slip system is getting activated (Figs. 2.6, 2.7 and 2.8).

## 2.5 Discussion and Future Work

In this work, we analyze the mechanical properties and deformation behavior of three-dimensional crystallized proteins such as tetragonal lysozyme crystal using continuum-slip theory based on micromechanical model that accounts for the

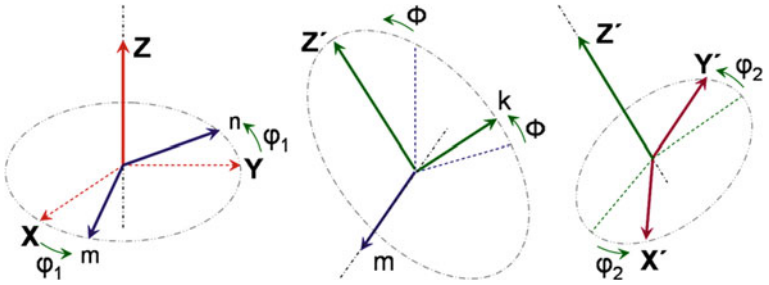


**Fig. 2.6** Orientation of a crystal (X', Y', Z') with respect to the fixed coordinate system (X, Y, Z) based on Bunge Euler angles [28]

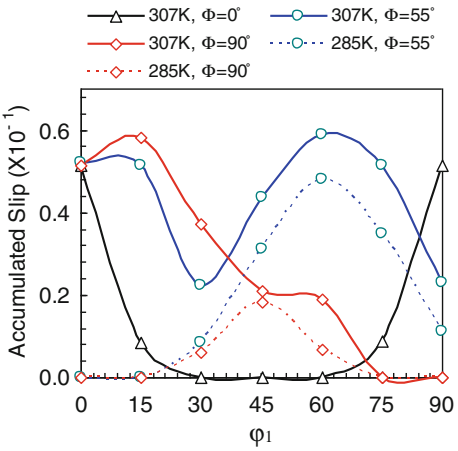


**Fig. 2.7** The orientation-dependent accumulated slip $\bar{\gamma}$ obtained for 3D lysozyme crystals loaded up to 0.01 strain at two different temperatures of 285 K and 307 K and Euler angle $\phi = 0°$, 55°, and 90°. In all these analyses, Euler angles $\varphi_2 = 0°$

molecular and crystal properties, and defects such as dislocations through slip-induced plastic deformation. The results of our investigation show that the propensity to plastic deformation for all slips systems increases with increasing temperature and the quantity of intracrystalline water molecules. Further analysis of the deformation along different crystallographic directions shows that the mechanical properties of the lysozyme crystals are highly anisotropic and the degree of anisotropy is a function of temperature and intracrystalline water molecules. We also observe that at higher temperatures the crystals are very ductile while they are more rigid at lower temperatures. These observations may provide valuable information regarding design of the structures, devices and systems using three-dimensional crystallized protein materials. The analysis present here could be easily extended to explore the mechanical behavior of the any three-dimensional self-assembled protein crystal under different loading conditions. However, further work is necessary, especially in experimental characterization of protein crystals, to develop sophisticated models for post yield behavior, hardening, damage, and softening under different environmental conditions.

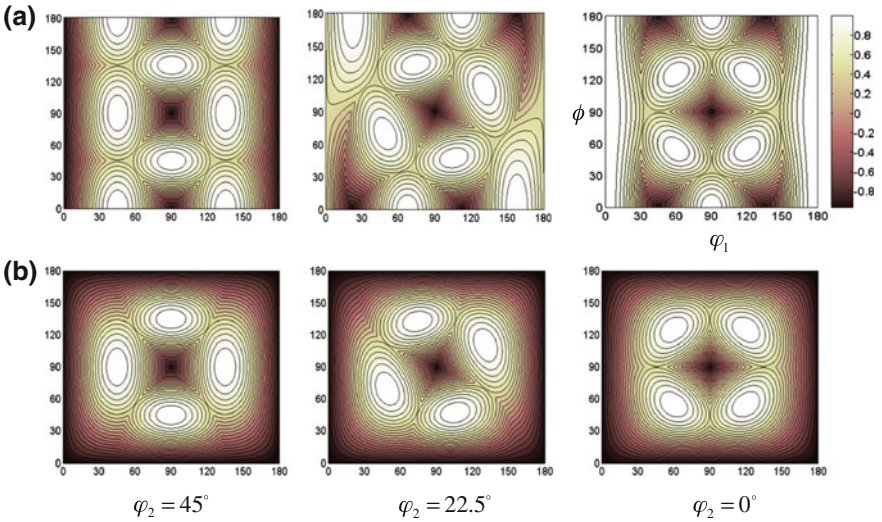


**Fig. 2.8** The deformation distribution maps of the 3D assembled lysozyme crystal at two different temperatures of **a** 307 K and **b** 285 K, and for different values of $\varphi_2$. For all orientations the uniaxial compression is along the $X$-axis of the lab coordinate system with compression up to 1 % strain. At any $\varphi_2$ section, the maps show the crystal orientations that have the highest and the lowest values of the yield function (Eq. (2.13)) and, therefore, the greatest tendency for plastic deformation and elastic deformation, respectively

Many challenges associated with the characterization of protein crystals including stability, remain an open field of research. The functionality and stability of protein molecules are largely dependent on the environmental working conditions such as temperature, pH and the surrounding fluid. However, the mechanical stability of protein crystals under different conditions has not been extensively studies. Therefore, further research is needed to explore the fundamental design principles for the development of such materials with optimal functionality and stability.

## References

1. Alberts, B., Johnson, A., Lewis, J., Raff, M., Roberts, K., & Walter, P. (2002). *Molecular Biology of the Cell*. New York, Taylor & Francis.
2. Fratzl, P., & Weinkamer, R. (2007). Nature's hierarchical materials. *Prog. Mater. Sci.* **52**, 1263–1334.
3. Gupta, H.S., et al. (2006). Cooperative deformation of mineral and collagen in bone at the nanoscale. *Proc. Natl Acad. Sci. USA* **103**, 17741–17746.
4. Gupta, H.S., et al. (2007). Evidence for an elementary process in bone plasticity with an activation enthalpy of 1 eV. *J. R. Soc. Interf.* **4**, 277–282.
5. Buehler, M.J. (2006). Nature designs tough collagen: Explaining the nanostructure of collagen fibrils. *Proc. Natl Acad. Sci. USA* **103**, 12285–12290.
6. Chan, Hue, & SunDill, K.A. (1993). The protein folding problem. *Phys. Today* **46**( 2), 24.

7. Chiti, F., & Dobson, C.M. (2006). Protein misfolding, functional amyloid, and human disease. *Annu. Rev. Biochem.* **75**, 333–366.
8. Mesquida, P., Riener, C.K., MacPhee, C.E., & McKendry, R.A. (2007). Morphology and mechanical stability of amyloid-like peptide fibrils. *J. Mater. Sci. Mater. Med.* **18**, 1325–1331.
9. Iconomidou, V.A., & Hamodrakas, S.J. (2008). Natural protective amyloids. *Curr. Protein Pept. Sci.* **9**, 291–309.
10. Hardy, J., & Selkoe, D.J. (2002). Medicine: The amyloid hypothesis of Alzheimer'sdisease. Progress and problems on the road to therapeutics. *Science* **297**, 353–356.
11. Selkoe, D.J. (2001). Alzheimer's disease: Genes, proteins, and therapy. *Physiol. Rev.* **81**, 741–766.
12. Tachibana, M., Kobayashi, Y., Shimazu, T., Ataka, M., & Kojima, K. (1999). Growth and mechanical properties of lysozyme crystals. *J. Crystal Growth* **198**, 661–664.
13. Niemela, P.S., Ollila, S., Hyvonen, M.T., Karttunen, M., & Vattulainen, I. (2007). *PLoSComput. Biol.* **3**, 0304.
14. Snow, C.D., Sorin, E.J., Rhee, Y.M., & Pande, V.S. (2005). How well can simulation predict protein folding kinetics and thermodynamics? *Annu. Rev. Biophys. Biomol. Struct.* **34**, 43–69.
15. Cormier, J., Rickman, J. M., Delph, T.J. (2001). Stress calculation in atomistic simulations of perfect and imperfect solids. *J. Appl. Phys.* **89**, 99.
16. Odegard, G.M., Gates, T.S., Nicholson, L.M., & Wise, K.E. (2002). Equivalent- continuum modeling of nano-structured materials. *Comp. Sci. Technol.* **62**14, 1869–1880.
17. Zamiri, A., & De, S. (2009). Modeling the mechanical response of tetragonal lysozyme crystals. *Langmuir* **26**(6), 4251–4257.
18. Harata, K., Muraki, M., & Jigami, Y. (1993). Role of Arg115 in the catalytic action of human lysozyme: X-ray structure of His115 and Glu115 mutants. *J. Mol. Biol.* **233**(3), 524–535.
19. Tait, S., White, E.T., & Litster, J.D. (2008). Mechanical characterization of protein crystals. *Part. Part. Syst. Character.* **25**(3), 266–276.
20. Koizumi, H., Tachibana, M., Kawamoto, H., & Kojima†, K. (2004). Temperature dependence of microhardness of tetragonal hen-egg-white lysozyme single crystals. *Philos. Mag.* **84**(28), 2961–2968.
21. Koizumi, H., Tachibana, M., & Kojima, K. (2006). Observation of all the components of elastic constants using tetragonal hen egg-white lysozyme crystals dehydrated at 42% relative humidity. *Phys. Rev. E* **73**(4), 041910.
22. Koizumi, H., Kawamoto, H., Tachibana, M., & Kojima, K. (2008). Effect of intracrystalline water on micro-Vickers hardness in tetragonal hen egg-white lysozyme single crystals. *J. Phys. D: Appl. Phys.* **41**(7), 074019.
23. Koizumi, H., Tachibana, M., & Kojima, K. (2009). Elastic constants in tetragonal hen egg-white lysozyme crystals containing large amount of water. *Phys. Rev. E* **79**(6), 061917.
24. Alvarado-Contreras, J., Polak, M.A., & Penlidis, A. (2007). Micromechanical approach to modeling damage in crystalline polyethylene. *Poly. Eng. Sci.* **47**(4), 410–420.
25. Tachibana, M., Koizumi, H., & Kojima, K. (2004). Effect of intracrystalline water on longitudinal sound velocity in tetragonal hen-egg-white lysozyme crystals. *Phys. Rev. E* **69**(5), 051921.
26. Granato, A.V., Lucke, K., Schlipf, J., & Teutonico, L.J. (1964). Entropy factors for thermally activated unpinning of dislocations. *J. Appl. Phys.* **35**(9), 2732–2745.
27. Kocks, U.F., Argon, A.S., Ashby, M.F. (1975). Thermodynamics and Kinetics of Slip. In Chalmers, B., Christian, J.W., Massalski, T.B. (Eds.). *Progress in Materials Science.* New York, Pergamon.
28. Bunge, H.-J. (1982). *Texture Analysis in Materials Science: Mathematical Methods.* London, Butterworths.

# Chapter 3
# Molecular Motors: Cooperative Phenomena of Multiple Molecular Motors

**Stefan Klumpp, Corina Keller, Florian Berger and Reinhard Lipowsky**

**Abstract** Transport of various types of cargoes in cells is based on molecular motors moving along the cytoskeleton. Often, these motors work in teams rather than as isolated molecules. This chapter discusses analytical and computational approaches to study the cooperation of multiple molecular motors theoretically. In particular, we focus on stochastic methods on various levels of coarse-graining and discuss how the parameters in a mesoscopic theoretical description can be determined by averaging of the underlying microscopic processes. These methods are applied toward understanding the effects of elastic coupling in a motor pair and in the cooperation of several motors pulling a bead. In addition, we review how coupling can have different effects on different motor species.

## 3.1 Background

Long-distance transport in cells is powered by molecular motors of the kinesin, myosin, and dynein superfamilies that move along microtubules or actin filaments [41, 64, 81]. Representatives of each superfamily have been characterized biochemically, structurally, and biophysically in some detail. In particular, the development of single-molecule techniques has greatly expanded our knowledge about the dynamics of these motors and provided a detailed picture of the stepping of the motors and the forces they exert [19, 42, 70, 82, 86, 89, 97]. These experimental efforts have been complemented by theoretical investigations studying relatively coarse-grained stochastic descriptions of one or several chemomechanical working cycles of specific molecular motors [12, 29, 44, 61]. In addition, molecular dynamics and Brownian dynamics simulations, using both detailed empirical force fields as well as structure-based (Gō-type) approaches, have been used to address the mechanical details of the motors' molecular motion, see, e.g., [33, 43, 45].

S. Klumpp (✉) · C. Keller · F. Berger · R. Lipowsky
Max Planck Institute of Colloids and Interfaces, Science Park Golm,
14424 Potsdam, Germany
e-mail: klumpp@mpikg.mpg.de



S. De et al. (eds.), *Multiscale Modeling in Biomechanics and Mechanobiology*, DOI 10.1007/978-1-4471-6599-6_3

In cells, these motors often work in small teams rather than as single molecules [9, 34]. Therefore in recent years, the cooperation of motors and the dynamics of motor complexes have moved to center stage, in experimental [5, 22, 34] as well as theoretical studies [9, 51]. In contrast to earlier work on motor cooperation [46], which mostly dealt with large numbers of motors, as in the contraction of muscle, which is based on the cooperation of billions of myosin molecules [40], the recent studies focus on defined complexes of small numbers of motors, starting with motor pairs up to complexes of 7 motors. These numbers are typical for transport in cells, as indicated by electron microscopy and as deduced from *in vivo* force and velocity measurements [34].

Specifically, the recent development of synthetic complexes linking a defined number of motors [1, 25, 30, 66, 79, 96] enables the detailed quantitative characterization of the dynamical behavior of coupled motors using the techniques originally developed for single motor molecules. Previous quantitative characterizations of coupled motors [5, 90] have remained somewhat limited by the fact that only the average number of motors rather than their actual number could be prescribed. These synthetic complexes link motors via a DNA linker [30, 66, 79], a quantum dot [1], an antibody [96], or via a DNA origami scaffold [25]. In particular, the latter method allows to control the numbers and types of motors as well as their geometric arrangement.

In this chapter, we discuss the analytical and computational treatment of cooperative molecular motors and motor complexes consisting of a small number of motors coupled with elastic linkers. We review three approaches describing such systems at different levels of detail, with different theoretical scopes and invoking different computational costs. The three approaches start with different descriptions of single motor molecules, specifically (i) as a random walker on a chemomechanical network of motor conformations, (ii) as a stochastic stepper with force-dependent rates, and (iii) as a molecule moving in three spatial dimensions subject to geometric constraints such as binding to a bead, but with a rather coarse-grained description of its internal degrees of freedom. In all three cases, we consider two or more such motors coupled via some elastic element, which may correspond to the flexible stalk or tail of the motor, a linker molecule, or the common cargo of the coupled molecular motors.

### *3.1.1 Length and Time Scales of Molecular Motor Motility*

The movements of individual motor molecules as well as of motor complexes involve motion on a wide range of length scales, which we illustrate here for the best studied motor, dimeric kinesin-1 (conventional kinesin). The movement of kinesin-1 (as well as of other cytoskeletal motors) is powered by the hydrolysis of adenosine triphosphate (ATP) to adenosine diphosphate (ADP). The kinesin-1 dimer has two heads, each of which contains an ATP binding site and can bind to a microtubule. The hydrolysis reaction involves conformational rearrangements in the ATP binding pocket that occur on a length scale of $\lesssim$1 nm. These small movements lead

to allosteric conformational changes in other parts of the same head of the motor, including the microtubule binding site. They also affect the other head, possibly via the generation and release of strain between the two heads [35, 45, 76, 99]. This process is believed to involve the docking of a flexible structure called the neck linker to the leading head [76] and ultimately leads to large-scale motion of the rear head, the actual step of the motor.

That step, which brings the rear head of the motor in front of the leading head in a hand-over-hand fashion [100], is quite long, 16 nm for kinesin (and even 72 nm for myosin-V). The corresponding movements of the motor's center of mass is 8 nm (or 36 nm, respectively). Typically a single motor performs tens or even hundreds such steps while bound to the filament along which it walks, so that overall the motion of a motor bound to a filament proceeds over distances of $\sim 1\,\mu$m. This distance, which is called the run length and which is still quite small on the scale of the cell, is further increased by the cooperation of motors: Complexes with several motors can remain attached to a filament as long as at least one motor is bound to the filament, thus giving unbound motors a chance to rebind while the complex is still attached to the filament [51]. In addition to enhancing the overall run length of motors, motor cooperation also has an impact on the smaller length scales. In particular, the elastic coupling of the motors results in forces between the motors that can affect stepping, binding to the microtubule, and, via the motors' chemomechanical coupling, even their chemical rates of nucleotide binding and hydrolysis.

The corresponding timescales also range over several orders of magnitude. The transitions between different conformations of a single motor occur in the range of $\mu$s – s. Somewhat unexpectedly, the actual mechanical step is quite rapid with a rate of $\sim 10^5\,\mathrm{s}^{-1}$. The corresponding movement of a motor head over 16 nm happens instantaneously on the timescale of the experimental resolution of about 30 $\mu$s [19] (see also the discussion in Ref. [15]). By contrast, the chemical transitions, which correspond to much smaller spatial reorientations, are slower with rates of $\sim 0.01\ \mathrm{s}^{-1}$ (see the set of rates collected in [48, 61]). The entire chemomechanical cycle takes on average 0.01 s at saturating ATP concentrations, corresponding to a motor velocity of 800 nm/s in the absence of a load force. Unbinding of a kinesin motor from a microtubule occurs on a timescale of two orders of magnitude larger ($\sim 1$ s), corresponding to a run length of $\sim 1\,\mu$m. For several motors, unbinding of motors is more frequent because all bound motors can unbind, so that the timescale of unbinding becomes smaller (and less separated from the stepping timescale). At the same time, unbinding of the cargo or the motor complex from the microtubule occurs on a longer timescale, as it requires unbinding of all motors. Estimates based on noninteracting motors lead to run times of many seconds or more. On such long timescales, additional effects become important, for example, the architecture of the cytoskeletal networks, because motors will often reach the end of a filament or filament–filament intersections. Using arrays of parallel isopolar microtubules large cargo particles have been shown to reach run lengths of millimeters, corresponding to runtimes of $\sim 10$ min [16].

## 3.2 Multiscale Computational Challenges

As discussed above, the dynamics of molecular motors and motor complexes involves movements on many different time and length scales. Therefore, typically different theoretical descriptions of the motors are used to study different aspects of their motility, dependent on the length and timescales on which the pertinent movements occur. The movements of molecular motors and motor complexes is often described using sets of discrete configurations or motor states, which may represent, for example, the chemical states of a motor or different mechanical configurations. Throughout most of this chapter we will follow the same strategy and describe systems of coupled motors by networks of discrete states and stochastic transitions between them. Such networks can however be constructed at many different levels of detail and we describe three of these below.

A key issue for the function of molecular motors is the coupling of mechanics and chemistry. At the level of a single motor, chemical (free) energy is converted into movement and work by the main chemomechanical cycle, in which hydrolysis of ATP in a motor head is followed by a mechanical movement of a motor head. An opposing load force can slow down the movement of the head, but may also induce backward steps and, via deformation of the motor head, affect the kinetics of the chemical processes such as ATP hydrolysis or ADP and phosphate release. In both cases, thermodynamic consistency imposes certain constraints relating the force-dependence of a rate to the force-dependence of the rate of the reverse process [61, 65]. The details of the chemomechanical cycle have consequences even on the largest time and length scales: Because the unbinding rate of a motor is dependent on its chemical state, changes in the nucleotide concentrations can modulate not only the motor velocity, but also the unbinding rate, and thus the run length. In a two-motor complex, such a modulation can shift the dominant mode of transport from a situation where transport is predominantly by a single motor bound to one where transport is predominantly by two motors [8, 96].

Specific to motor complexes is the question of coupling effects: If two or more motors are working cooperatively, will each of these motors work with the same characteristics as a single motor on its own or do motors interfere with each other? One generic reason for interference are forces between the motors that build up due to stochastic stepping: If coupled motors do not step in a synchronous fashion, the distance between the motors fluctuates over time and the linkers between the motors get stretched, thus mediating a fluctuating elastic force between the motors. If coupled motors interfere with each other, the next question is in what way do they interfere? Force between the motors may result in reduced stepping rates and thus a slow-down of the motor complex. In addition, however, a load force affects the unbinding rate of a motor, and thus its run lengths. Typically, the unbinding rate increases strongly with increasing force. As a consequence, a force between coupled motors could increase their unbinding rates and thus reduce the benefit of longer binding times (or run lengths) obtained from using several motors instead of just one. Indeed, both effects have been observed, with enhanced unbinding for a synthetic two-kinesin-1

motor complex [79] and reduced speed for a complex of two myosin V motors [66]. Reduced velocity has also been observed in microtubule gliding assays at high motor density with certain kinesin constructs with reduced flexibility [11, 24].

Our recent analysis of such interference effects has indicated the importance of the dynamic nature of these forces [7, 8]: Typically a motor will bind to the filament in a force-free fashion. The force between the motors is then built up by the stochastic stepping. The generation of forces of the order of the stall force (where a motor stops to step) or of the detachment force (the characteristic force scale for the unbinding rate) thus occurs over some characteristic timescales. These timescales have to be compared to the timescale for spontaneous unbinding, which provides a measure for the time the motors have to build up strain. If the time for spontaneous unbinding is very small, typically motors unbind before substantial strain is generated and thus interference effects are rather weak. A related issue arises when an external force is applied to a multi-motor complex: Only motors bound to the filament experience the load. When an additional motor binds to the filament, it will initially not experience any force and thus it will take some time until the force is actually shared equally among the bound motors. Equal force sharing is only reached if unbinding of motors is slower than the characteristic timescale for the equilibration of force sharing. Another question related to the stochastic stepping of the motors concerns the size of the observed steps. If the motors do not move in a synchronised fashion, steps that correspond to fractions of the single-motor step can be expected. This has indeed been observed in gliding assays for two motors, but not for three motors [58]. This observation has been attributed to nonequal force sharing between three motors [58] and to nonlinear elastic coupling between the motors [60].

Yet another longstanding challenge is the question how force is actually exerted on the molecules. This question is directly related to the spatial structure of the molecule. Force is typically exerted via the tail domain of the motor and somehow transmitted to the nucleotide binding pocket and to the microtubule binding site. How this force transmission occurs is not very clear. Important questions in this context are: Does the force experienced by the nucleotide binding pocket depend on the direction of the force in three dimensions? Is the commonly used one-dimensional description by a force along the direction of motion reasonably accurate? If not, which direction of force is characteristic in multi-motor complexes?

We conclude this section on the challenges to modeling and computation by a few general remarks. One rationale for using a palette of models at different scales, each appropriate for certain research questions, rather than a single model that describes everything, is the maxim attributed to Einstein to make things as simple as possible, but not simpler.[1] Doing so allows one to identify the key ingredients for certain phenomena to arise, while still being able to make quantitative predictions. This does not mean that further simplifications are useless. Further simplification may still be of use to provide a theoretical perspective on the core mechanisms. Nevertheless, one needs to keep in mind that every theoretical description is based on certain

[1] A discussion of the origin of the quote can be found at http://quoteinvestigator.com/2011/05/13/einstein-simple/#more-2363.

assumptions (which may be explicit or implicit) and should thus be expected to have a limited range of applicability. Outside this range its predictions may not be very reliable. As a matter of course, the construction of the model requires a careful choice of ingredients: Some results will not really be predictions, but rather rephrased statements of features of the model, as they have (explicitly or implicitly) been built into the model by way of its construction.

## 3.3 Methods

In the following we describe methods that have recently been developed for the theoretical and computational study of coupled molecular motors. We start with chemomechanical networks (Sect. 3.3.1) which provide a systematic framework for the description of individual motors that has very recently been extended to coupled motors [49]. We then discuss stochastic stepper approaches that are more coarse-grained in the sense that different chemical states of an individual motor are not distinguished and that movement is described by one or two effective stepping rates for forward and, possibly, backward steps (Sect. 3.3.2). The latter description can be further coarse-grained by characterizing the movement of a cargo by a set of velocities for different numbers of bound motors and not accounting for the individual steps of the motors. Finally, we briefly discuss approaches that describe the geometry of the motors and the cargo in some detail (Sect. 3.3.3). We conclude the discussion of the different methods with some general remarks and some comments on how the different methods can be integrated.

### *3.3.1 Chemomechanical Networks*

A detailed description of single molecular motors is given by chemomechanical networks [61], which provide a generalization of simple enzymatic cycles. The use of networks rather than a single chemomechanical cycle is necessary to account for complex coupling between ATP hydrolysis and stepping [20, 44, 61]. For example, backward steps of kinesin-1 under superstall forces have been observed to require ATP, indicating that ATP is hydrolyzed rather than synthesized during the backward stepping cycle [19, 20]. As a consequence, the backward stepping cycle is different from the forward stepping cycle run in reverse. The chemomechanical network approach explicitly incorporates the chemistry behind the stepping process, i.e., the different chemical configuration of the motor domains. This theoretical framework has been used successfully for a quantitative description of experimental observations for kinesin-1 [48, 49, 61] and myosin V motors [12, 13].

Cargo transport by a motor complex or a small team of motors (that may belong to the same or to different motor species) can also be studied with chemomechanical networks. Each motor of such a team can be described by its chemomechanical

network which contributes to the team network. Moreover, each motor in the team has a finite run length, after which it dissociates from the filament. As long as the cargo is still connected to the filament by the remaining motors, the inactive motor has a chance to rebind to the filament. As a consequence, the number of actively pulling motors fluctuates. In the following, we focus on two identical motors, using two coupled kinesin-1 motors as an example [49].

#### 3.3.1.1 Single Motor Network

The movement of a molecular motor on the filament is determined by the chemical reaction taking place within the catalytic domains of the motor which is coupled to a conformational change in the motor domains that causes translational motion of the motor. The dynamics of a molecular motor is described by a continuous-time Markov process on a discrete state-space or network [61, 65], the vertices of which represent the different chemical states of the two motor heads. The edges describe transitions between these states based on the network theory in enzyme kinetics introduced in [37]. The states of such a network are governed by certain dwell times that are exponentially distributed in a continuous-time Markov process [88]. The average dwell time in a certain state is given by the inverse of the sum of all transitions rates out of this state. The probability to find the motor in a certain state of such a network at a certain time is determined by the Master equation [88]. Our approach is based on identifying distinct motor states via the nucleotide occupancy of the two motor heads and (chemical as well as mechanical) stochastic transitions between these states.

The catalytic domain of each of the two motor heads of kinesin-1 can attain three different chemical configurations corresponding to the ATP-hydrolysis reaction: The binding pocket can be empty ($E$) or it can be occupied by ATP ($T$), by the cleavage products of the hydrolysis, ADP and phosphate ($\theta$), or, upon phosphate release, by ADP alone ($D$). This classification thus leads to four different chemical states. Combining the cleavage transition ($T \rightarrow \theta$) and the phosphate release transition ($\theta \rightarrow D$) into a single transition ($T \rightarrow D$), one obtains a reduced network in which a single motor head can attain the three states E, T, and D. These states are linked by six transitions, each of which corresponds to binding or release of certain nucleotides as shown in Fig. 3.1a.

The two-headed kinesin motor can then attain $3^2 = 9$ states, but not all of these states are relevant to describe the dynamics of kinesin motors as shown in [61]. Two of these states, namely ($EE$) and ($TT$), should not play any prominent role in the processive motion of kinesin because the motor head is strongly bound to the filament when the head is empty or contains ATP, whereas it is only loosely bound to the filament when it contains ADP [80]. As a consequence, the motor most likely dissociates from the ($DD$) state. Neglecting the strongly bound states leads to the 7-state network shown in Fig. 3.1b.

Kinesin motors move in a hand-over-hand fashion [100] which implies that a mechanical step requires the interchange of the positions of the leading and trailing head of the motor. In principle, there are several possibilities to fullfill this condition

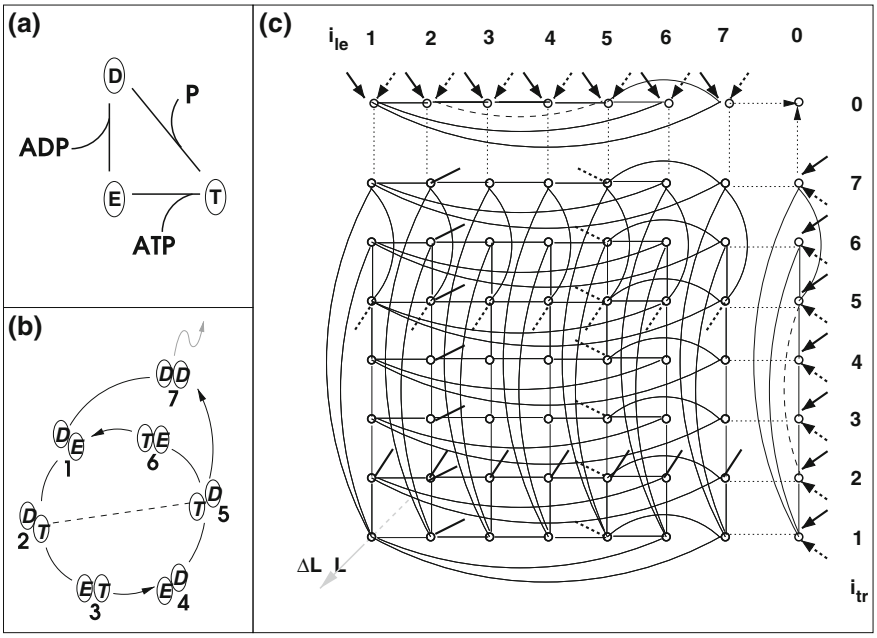


**Fig. 3.1** **a** Kinetic diagram of a single motor head, for which hydrolysis and phosphate release have been combined into a single transition. **b** Chemomechanical 7-state network of the kinesin-1 motor as introduced in [61]. The *dashed line* represents the mechanical step, the *black arrows* indicate the direction of the ATP hydrolysis and the *gray arrow* indicates dissociation. Figure adopted from Ref. [61]. **c** State-space of motor pair as described by three coordinates [49]: the motor states $i_{\rm le}$ and $i_{\rm tr}$ of the leading and the trailing motor, and the extension $\Delta L$ of the elastic spring (axis perpendicular to the plane of the figure). In general, the motor pair states form a stack of layers, each of which corresponds to a fixed value of $\Delta L$. Here, only the layer with $\Delta L = 0$ is shown. Open *circles* represent motor pair states, *thin lines* represent the chemical transitions between these states and *dashed lines* mechanical transitions during 1-motor runs. The thick stubs represent transitions to a neighboring $\Delta L$-layer. Full stubs correspond to forward steps and broken stubs describe backward steps of one of the motors. *Dotted lines* represent binding and unbinding events between the single motor states $i = 7$ and $i = 0$, the latter describes an inactive motor. The *black arrows* indicate unbinding events emanating from any other $\Delta L$-layer

for mechanical stepping, see Fig. 3.1b. The transition from $(DT)$ to $(TD)$ is taken to be the mechanical stepping transition [65], in agreement with single motor data.[2] The transition rates between two states $i$ and $j$ depend on the molar nucleotide concentrations $[X]$, with $X =$ ATP, ADP or P, and on the load force $F$. In general, these rates can be parameterized in the factorized form

$$\omega_{ij} = \omega_{ij,0}\, \Phi_{ij}(F) \quad \text{with} \quad \Phi_{ij}(0) \equiv 1, \tag{3.1}$$

[2] For backward steps, the transition between the states $(ED)$ and $(DE)$ may also play a role [44], a picture supported by recent experiments on mutant kinesins that are more prone to backward stepping [20]. The two different mechanical transitions were also studied in Ref. [63].

where the dependence on the nucleotide concentrations is embedded in the zero force rate $\omega_{ij,0}$ and the force dependence is described by the factor $\Phi_{ij}(F)$ [49, 61]. These factors are subject to constraints to fulfill detailed balance: For all chemical transitions, the force factors $\Phi_{ij}(F)$ satisfy $\Phi_{ij}(F) = \Phi_{ji}(F)$; for the mechanical stepping transitions between states $(DT)$ and $(TD)$ [states 2 and 5 in Fig. 3.1b], $\Phi_{25}(F) = \Phi_{52}(F) \times \exp(-F\ell/k_BT)$ with the step size $\ell$ [65].

Compared to a mechanical forward step, which is completed within μs, the chemical transitions are rather slow and take several ms. Thus, the chemical reaction paths are explicitly accessible to experiments and experimentally obtained reaction rates can be implemented as the transition rates of the network model [61]. One important property of these networks is that they involve several motor cycles, which provide the free energy transduction between ATP hydrolysis and mechanical work. As one varies the nucleotide concentrations and the external load force, the fluxes on these cycles change and different cycle fluxes dominate for different parameter regimes. In this sense, the chemomechanical networks of a single motor as introduced in [61] contain several competing motor cycles. Imposing cyclic balance conditions [62] on all motor cycles ensures that the network description satisfies both the first and second law of thermodynamics.

#### 3.3.1.2 Motor Pair Network

To extend the network description to coupled motors, we consider a pair of two kinesin-1 dimers that are attached to the same cargo and walk on the same filament. We refer to the two motors in the pair as the leading and the trailing motor, respectively, according to their relative positions in the direction of motion.

The modeling so far points to two key questions: What happens if one of the motors dissociates from the filament? And second, how does the translocation of one of the motors influence the motor pair system? For single motors, the answers are rather simple because the single motor run is terminated when the motor dissociates from the filament and the unbound motor is not spatially restricted. For the motor pair, unbinding from and rebinding to the filament provides an alternating sequence of 1-motor runs, where the cargo is pulled by one active motor, and 2-motor runs, where the cargo is actively pulled by both motors, as outlined in the upper row of Fig. 3.2. During 1-motor runs, the dynamics of the bound or active motor can be described by a random walk on the single motor network as discussed above. The only difference to the case of a single motor is that the average dwell time in any state $i$ now also involves the rebinding rate of the second (unbound or inactive) motor. A 1-motor run is terminated either by unbinding of the remaining motor, which corresponds to the termination of the motor pair walk, or by rebinding of the inactive motor, which initiates a 2-motor run. During 2-motor runs, the state-space consists of combinations of the 7 chemical states of the individual motors, i.e., $7^2 = 49$ states.

Concerning the coupling of the motor pair, we consider the flexible stalks of the kinesin motors as linear springs. Since both springs are only coupled via the cargo, which is taken to be rigid, we can effectively describe the system by one linear spring

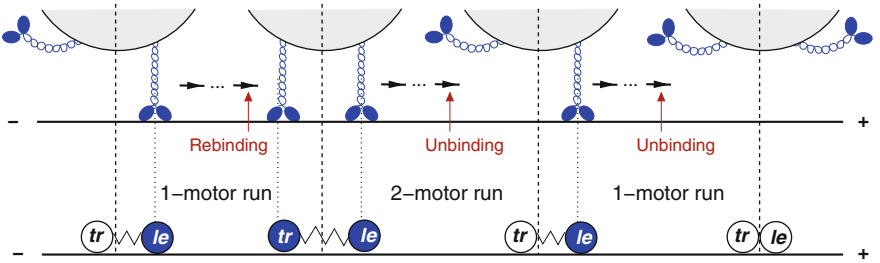


**Fig. 3.2** Motor pair walk for two kinesin motors (*blue*), each of which has two motor heads. Both motors are attached to the same cargo (*light gray*) and walk along the same filament (*black line*). A reduced representation describes such a system in terms of 2-motor 'particles' connected by an effective spring. As long as both motors are attached to the filament and, thus, active as indicated by the blue 'balls' they perform a 2-motor run. After unbinding from the filament, an active motor becomes inactive as indicated by the white 'balls'. If the cargo is pulled by only one active motor, the cargo performs a 1-motor run until it either unbinds as well, leading to an unbound motor pair, or until the inactive motor rebinds to the filament and the cargo starts another 2-motor run

as indicated in the bottom row of Fig. 3.2. As a result, we obtain a one-dimensional description of the motor pair, consisting now of two motor particles which are connected via one linear spring with an effective spring constant, the coupling parameter $K$, and the (dimensionless) spring extension $\Delta L$, which corresponds to the extension of the motor–motor separation (in multiples of the step size). This coupling generates the elastic force

$$F_{\mathrm{tr,le}} = -\Delta L \ell K = -F_{\mathrm{le,tr}} \tag{3.2}$$

$F_{\mathrm{tr,le}}$ between the two motors, as soon as one of these motors is spatially translocated, i.e., when it performs a mechanical step with the kinesin stepsize $\ell$. We consider this interaction force as an external load on the individual motor, which thus enters the transition rates, in the form

$$\begin{aligned} \omega_{ij,le} &= \omega_{ij,0}\, \Phi_{ij}(F_{\mathrm{le}}) \\ \omega_{ij,tr} &= \omega_{ij,0}\, \Phi_{ij}(F_{\mathrm{tr}}), \end{aligned} \tag{3.3}$$

compare Eq. (3.1). In these latter relations, we used the convention that resisting forces are positive, whereas assisting forces are negative. Therefore, the forces that enter these relations are $F = F_{\mathrm{le}}$ with $F_{\mathrm{le}} \equiv -F_{\mathrm{tr,le}}$ for the leading motor and $F_{\mathrm{tr}} \equiv -F_{\mathrm{le,tr}}$ for the trailing motor. Concerning the influence of coupling on the transition rates of the motor pair system, inspection of Eq. (3.3) shows that the force arising from a mechanical step of one motor during a 2-motor run affects *all* chemical and mechanical transition rates of *both* motors.

Three variables span the state-space of the motor pair, the individual motor states $i = i_{\mathrm{le}}$ and $i = i_{\mathrm{tr}}$ of the leading and the trailing motor, and the spring extension $\Delta L$ (which we define here as a dimensionless quantity, in multiples of the step size $\ell$), as shown in Fig. 3.1c. In general, the motor pair states form a stack of layers, each of which corresponds to a fixed value of $\Delta L$. For simplicity, only the single layer with

$\Delta L = 0$ is shown in Fig. 3.1c. All chemical transitions take place within this layer, but mechanical steps during 2-motor runs are transitions to a neighboring $\Delta L$-layer. Note that a forward step by the leading motor and a backward step by the trailing motor have the same effect on the spring extension. Rebinding and unbinding events take place between the single motor states $i = 7$ and $i = 0$ within this layer, whereas an unbinding event emanating from any other $\Delta L$-layer always leads to the $\Delta L = 0$-layer. As a result, we obtain a uniquely defined chemomechanical network for the motor pair. Although this network is rather complex and contains a large number of states, transitions, and motor cycles, it involves only two parameters in addition to the single motor parameters: the coupling parameter $K$ as well as the rebinding rate $\pi$ of a single motor.

In experimental studies, the values of these two parameters are typically not known, but can be deduced from the statistical properties of the trajectories [49]. This deduction is facilitated by the following separation of parameters: The properties of a 1-motor run depend on the rebinding rate, but not on the coupling parameter, whereas 2-motor runs depend on the coupling parameter, but not on the rebinding rate. This feature of the pair network also allows us to study the influence of these motor pair parameters separately in computational studies. Thus, on the one hand, an analysis of the statistical properties of the motor pair trajectories gives access to the motor pair parameters $K$ and $\pi$. On the other hand, it also allows to study the properties of the motor pair properties such as its average velocity, run length, and run time, once these two parameters are known (or as functions of these parameters). Because the chemomechanical network approach explicitly incorporates the different chemical configurations of the four motor heads, it also allows the calculation of quantities such as motor pair efficiency or operation regimes that are not directly accessible within other, more coarse-grained descriptions that we discuss next.

### *3.3.2 Stochastic Stepper Models*

To understand the dynamics of coupled motors, it has proven useful to use simplified descriptions of molecular motors as stochastic steppers. In such a description, the chemistry is effectively incorporated into a single stepping rate and the focus is on the coupling of the motors. The advantage of such a coarse-grained description is the reduced number of parameters, which can be obtained from experimental studies. This type of approach, which has been used in several studies of cooperative motors [7, 8, 17, 18, 26, 54, 93, 101] provides a powerful conceptual framework for analyzing experimental data as well as to address generic aspects of cooperative molecular motors.

#### 3.3.2.1 A Single Molecular Motor as a Stochastic Stepper

The dynamics of a single molecular motor consists of three basic processes, stepping along a filament as well as unbinding from and binding to this filament. To account for

the stochastic nature of these processes, each process is described by a transition rate.[3] In this way, the complex chemomechanical process of stepping is simplified into a single transition. However, the rate of that transition may be dependent on external control parameters that influence the chemomechanical cycle, such as an external load force or nucleotide concentrations. For example, the (forward) stepping rate $\alpha$ is typically force-dependent and can be related to the experimental force–velocity relation $v_{\mathrm{si}}(F)$ of a single motor via

$$\alpha \equiv \frac{v_{\mathrm{si}}(F)}{\ell} \tag{3.4}$$

with the step size $\ell$ of the motor. Likewise, unbinding from the filament is described by the force-dependent rate

$$\varepsilon_{\mathrm{si}}(F) \equiv \frac{1}{\langle t_{\mathrm{si}}(F)\rangle} \tag{3.5}$$

that can be determined from the measured average binding or attachment time $\langle t_{\mathrm{si}}\rangle$.[4] The third process, binding, is a rather complicated process, which depends on the precise geometry and other factors. Since very limited experimental data is available, it is often described by a force-independent rate $\pi$, based on the argument that typically elastic strain in the unbound motor is expected to relax upon unbinding. However, force-dependent binding rates have also been used, e.g., in Refs. [26, 66], see also the discussion in Ref. [8].

The general description introduced so far depends on the force velocity relation $v_{\mathrm{si}}(F)$, the step size $\ell$, the unbinding rate $\varepsilon(F)$, and the binding rate $\pi$ of a single motor. All these quantities can be measured and depend on the type of motor under consideration. Most of them have been measured for various motor species. Typical parameter values are summarized in Table 3.1. In the following, we use specific values as experimentally determined for kinesin-1 motors.

The force–velocity relation has been measured in optical trapping experiments. Typically, the velocity of the motor decreases with increasing load force $F$ until it vanishes under the so-called stall force $F_{\mathrm{s}}$ [19, 21, 32]. Here, we use the following sign convention of the force: load forces opposing the stepping direction of the motor are taken to be positive, whereas negative forces are assisting forces pulling in the direction of the motor's stepping. A good approximation for the force velocity relation of kinesin-1 is the piecewise linear function

[3] Thus, we implicitly assume an exponential dwell time distribution.

[4] The index 'si' is used to indicate explicitly the unbinding rate and average binding time of a single motor. The corresponding quantities for a single bound motor in a complex of several motors (e.g., in a motor pair as discussed below) are denoted by $\epsilon_1$ and $t_1$ respectively. These quantities are closely related to the single motor parameters, but there are some subtleties: While $\epsilon_1 = \epsilon_{\mathrm{si}}$, the dwell time in the 1-motor bound state (or the average duration of a 1-motor run) for cooperative motors also depends on the binding rate $\pi$ of the second motor or any other in a system with more than 2 motors, $t_1 = (\epsilon_1 + \pi)^{-1} < t_{\mathrm{si}}$.

**Table 3.1** Overview of parameters for the different molecular motors kinesin-1, dynein, myosin V, and myosin VI

| Parameter | kinesin-1 | dynein | myosin V | myosin VI |
|---|---|---|---|---|
| Binding rate $\pi$ [$s^{-1}$] | 4.7* [57], 5* [5, 57] | 1.6* [72] | – | – |
| Step size $\ell$ [nm] | 8 [91] | 8 [32] | 36 [21] | 36 [74] |
| Stall force $F_s$ [pN] | 6 [82, 85], 5 [23], 7 [19] | 7 [87] 1.1 [67] | 1.7 [21], 3 [70] | 2.8 [78] |
| (Force-free) velocity $v$ [nm/s] | 1,000 [82], 490 [79] | 650* [72], 700 [50] | 400 [21], 380 [1] | 150 [1], 291 [78] |
| (Force-free) unbinding rate $\epsilon_0$ [$s^{-1}$] | 1 [82], 0.6 [79] | 0.27* [72], 0.16 [68] | 0.48 [70], 0.3 [1] | 0.25 [1], 1.3 [78] |
| Detachment force $F_d$ [pN] | 3 [82] | 1.1* [72] | 4* [1] | 2.6* [1] |

The values marked by an asterisk are inferred indirectly by theoretical modeling of experimental data

$$v_{si}(F) \equiv \begin{cases} v & F < 0 \\ v(1 - F/F_s) & 0 \le F < F_s \\ 0 & F \ge F_s, \end{cases} \tag{3.6}$$

see Fig. 3.3b, but more complicated functional forms and parameterizations can also be used [7]. The force-dependence of the unbinding rate is described by the exponential form

$$\varepsilon_{si}(F) \equiv \varepsilon_0 \exp(|F|/F_d). \tag{3.7}$$

Note that by using the absolute value of the force, we do not distinguish between different pulling directions. This type of dependence is suggested on theoretical grounds according to Kramers' rate theory [53] and Bell's equation [6] and supported by measurements of the force-dependence of the run length [82]. The force-dependence of the unbinding rate is currently revisited by several labs for different types of motors. Deviations from this exponential increase have recently been reported for dynein motors, with an exponential increase for small forces but catch-bond-like behavior, i.e., a decrease in the unbinding rate, for forces around the stall force [55, 59].

Since it is difficult to measure the binding rate $\pi$ directly, its value has been determined by fitting theoretical models to experimental data. In this way, a binding rate $\pi \simeq 4.7\,s^{-1}$ is obtained from an experiment where kinesin-1 motors extract membrane nanotubes from vesicles [57]. A similar value has been reported in a study fitting the run length distribution of beads transported by several kinesin-1 motors [5]. For other types of motors, most of the parameters have also been determined experimentally; the corresponding parameter values are summarized in Table 3.1.

The simple stochastic stepper description of a single motor incorporates those properties of single motors that are relevant for large-scale cargo transport. Furthermore, the theoretical framework described here can easily be extended, for example,

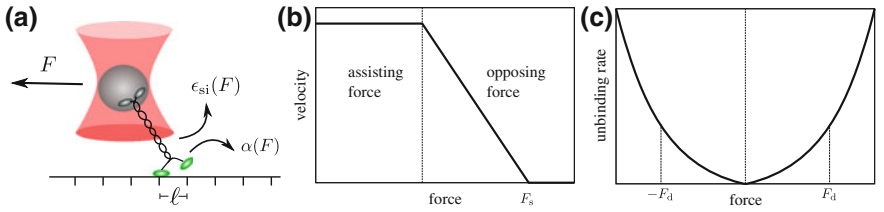


**Fig. 3.3** Force-dependent dynamics of a single motor: **a** Schematic setup of a typical single molecule experiment, in which a single kinesin is held with an optical trap that exerts the force $F$ on the motor in the direction opposite to its walking direction. The motor steps forward with the force-dependent stepping rate $\alpha(F)$ and the step size $\ell$. Force-dependent unbinding of the motor from the filament is described by the rate $\varepsilon_1(F)$. **b** Piecewise-linear parametrization of the force velocity relation $v_{si}(F)$, from which the stepping rate is determined via $\alpha(F) = v_{si}(F)/\ell$. **c** Parameterization of the force-dependent unbinding rate of the single motor. The stall force $F_s$ in (**b**) and the detachment force $F_d$ in (**c**) provide the basic force scales for the single motor behavior

to include backward steps or functional dependencies on other parameters such as the nucleotide concentrations [7]. Incorporating additional features of single motors usually requires additional parameters that need to be determined either directly from experiments or calculated from more microscopic models such as the chemomechanical networks described above. In the case of backward stepping, the forward stepping rate and the backward stepping rate can be determined from the force–velocity relation and the force-dependent ratio of forward to backward steps [8, 61]. The latter quantity has been measured for kinesin-1 [19].

### 3.3.2.2 Two Elastically Coupled Molecular Motors

In the following, we use the coarse-grained single motor description that we introduced above to study two elastically coupled molecular motors. As a generic case, we focus on two identical motors coupled via their stalks to a common cargo. Below, we use this model to determine the time $t_2$ that two motors stay simultaneously attached to the filament and the resulting velocity $v_2$ of the cargo, two key quantities for an even more coarse-grained description of transport by a motor pair as described at the end of this section. In general, these two quantities are expected to depend on the single motor dynamics and on the coupling. Because of the stochastic stepping of the motors, the elastic elements between them are stretched (or compressed) and relaxed. Thus strain forces are generated that in turn influence the stepping of the motors [7].

Assuming a linear force-extension relation of the elastic coupling, the only parameter, in addition to the single motor parameters, is again the coupling strength $K$. Since the motors step in a discrete manner, the induced strain forces have discrete values

$$F_i = i\ell K, \tag{3.8}$$

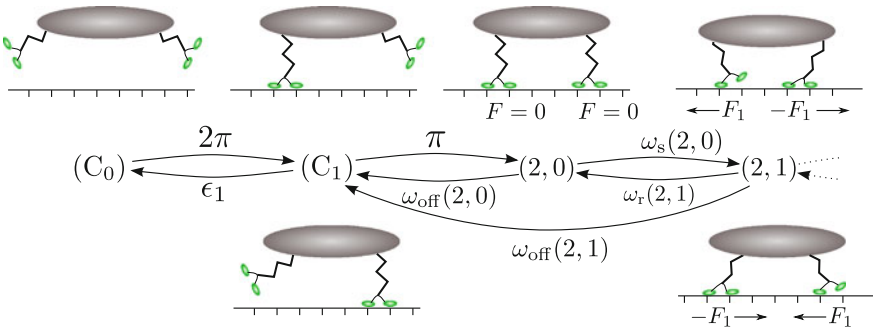


**Fig. 3.4** State-space of a cargo transported by two identical motors. In state $(C_1)$ the cargo is transported by only one motor. The other states $(2, i)$ correspond to different strain forces between two motors simultaneously pulling the cargo. In state $(2, 0)$, the motors are bound with relaxed linkers such that there is no force between them. When one of the motors performs a step, a strain force is generated between the two motors (the same strain is generated by stepping of either motor, therefore there are two configurations corresponding to the same state). Thus, stepping transitions between the states lead to the stretching or compression or to the relaxation of the elastic linkers. Unbinding of a motor occurs with rate $\omega_{\text{off}}$

where $\ell$ is the motor step size, $K$ the coupling strength and $i$ the distance (number of steps) between the motors.

The state of the two motors is now described by a discrete state-space, in which every state is characterized by the number of motors bound to the filament and, when both are bound, the discrete extension of the elastic linker between the motors (or the associated force), see Fig. 3.4. The states with no or one motor bound to the filament are denoted by $(C_0)$ and $(C_1)$, respectively. The states with two motors bound are denoted by $(2, i)$, where $i$ is the discrete distance between the motors.[5] Thus, in state $(2, 0)$, the linkers between the motors are relaxed. When one of the motors steps, the strain force $F_1 = \ell K$ is built up between them in such a way that one motor is pulled backwards with force $F_1$ and the other motor is pulled forwards with force $-F_1$, see state $(2, 1)$ in Fig. 3.4. Because we do not distinguish between the two motors, there are two configurations for this state.

Transitions between the different states $(2, 1)$ are associated with stepping of the motors. We denote the corresponding transition rates by $\omega_{\text{s}}(2, i)$ and $\omega_{\text{r}}(2, i)$, depending on whether the transition stretches (or compresses) or relaxes the linkers. These transition rates depend on the state of the motor pair and are related to the single motor stepping rates via

$$\omega_{\text{s}}(2, i) = \alpha(F_i) = v_{\text{si}}(F_i)/\ell \tag{3.9}$$

[5] It is convenient to introduce a highest state $(2, N)$ to reduce the network to a finite number of states. The state $(2, N)$ corresponds to a very large extension between the motor. Such a configuration is unlikely, because the motors typically unbind before reaching this state. Nevertheless, one has to check that the results do not depend on the choice of the value of $N$.

and

$$\omega_{\mathrm{r}}(2,i) = \alpha(-F_i) = v_{\mathrm{si}}(-F_i)/\ell. \tag{3.10}$$

for all states $(2,i)$ with $i > 0$ and

$$\omega_{\mathrm{s}}(2,0) = 2\alpha(0) = 2v_{\mathrm{si}}(0)/\ell \tag{3.11}$$

for state $(2,0)$. In these expressions, $v_{\mathrm{si}}(F)$ denotes the force-velocity relation of a single motor.

Transitions between the states $(C_0)$ and $(C_1)$ correspond to binding and unbinding of a motor, with rates given by the single-motor parameters. Unbinding of the bound motor in state $(C_1)$ occurs with the single-motor unbinding rate $\epsilon$ and leads to state $(C_0)$. The reverse transition is given by binding of one motor. Because either of the motors may bind, the rate for this transition is $2\pi$. Likewise, binding of the second motor occurs with rate $\pi$. We take this transition to lead to state $(2,0)$, i.e., we assume that the second motor binds in such a way that upon binding there is initially no strain between the motors. Finally, unbinding of one of the two bound motors, i.e., a transition to state $(C_1)$ may occur from any state $(2,i)$ and its rate is force-dependent,

$$\omega_{\mathrm{off}}(2,i) = 2\varepsilon_1(F_i). \tag{3.12}$$

#### 3.3.2.3 Effective Parameters of Transport by Two Bound Motors

While the dynamics of the motor pair can be studied using the model as described in the previous section, additional insight into the cargo transport can be obtained by lumping the states $(2,i)$ into one state $(C_2)$ with two motors bound to the filament and to determine an effective stepping rate or an average velocity $v_2$ for this state as well as an effective unbinding rate $\epsilon_2$ for one of the two motors, i.e., a transition rate to state $(C_1)$. The resulting coarse-grained description was originally proposed in Ref. [51], well before the more microscopic description. Coarse-graining of the microscopic model, however, now allows to obtain the parameters of state $(C_2)$ in a systematic way.

To determine the properties of the state $(C_2)$, we can focus on its substates $(2,i)$ and treat state $(C_1)$ as an absorbing state. Thus, all transitions associated to unbinding of a motor become transitions into the absorbing state with transition rates $\omega_{\mathrm{off}}(2,i)$. We then consider a Markov process on this network with the initial condition that all trajectories start immediately after binding of the second motor, i.e., in state $(2,0)$. The binding time or average dwell time in the two-motors-bound states is then obtained as the mean first passage time to absorption, the effective unbinding rate as the inverse of the binding time, and the velocity as the average stepping rate before absorption. We note that unbinding of motors is a mechanism for relaxing strain between the motors, because the unbinding rate increases with increasing force and rebinding occurs under zero load. Thus, simply neglecting unbinding, as done in some studies [93], will overestimate the probability of states $(2,i)$ with large $i$, i.e.,

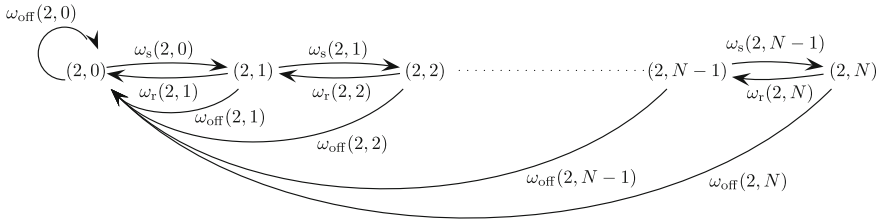


**Fig. 3.5** Closed network for calculating the probability distribution before unbinding of one motor: Starting from the network shown in Fig. 3.4, only the states $(2, i)$ in which both motors are simultaneously bound to the filament are considered and the state $(C_1)$ is treated as an absorbing state. The network is closed by redirecting all transitions that lead into the absorbing state back into the initial starting state $(2, 0)$

with large strain forces and therefore overestimate the effect of those forces. Indeed, neglecting unbinding typically leads to a strongly reduced velocity for two coupled kinesin-1 motors [47, 93], in contrast to what is found in the model with unbinding [7] and to what is observed experimentally [79].

An intuitive way to calculate the quantities characterizing state $(C_2)$ is based on a method proposed by Hill [38, 39]. The basic idea is to use the ensemble average instead of the time average, which makes it unnecessary to solve the time-dependent problem. To construct a network, whose steady state probability distribution is the steady state probability distribution before absorption of the original network, all transitions into the absorbing state are redirected to the initial state. Intuitively, this procedure can be understood as concatenating many trajectories, in the same way as one would do it in a computer simulation, namely by starting the next trajectory immediately after the one before has reached the absorbing state. Such a closed network is shown in Fig. 3.5. The probability distribution $P_{2,i}$ for the closed network is determined by solving the steady state of the master equation

$$\begin{aligned}
\partial_t P_{2,0} &= -[\omega_{\text{s}}(2,0) + \omega_{\text{off}}(2,0)]P_{2,0} + \omega_{\text{r}}(2,1)P_{2,1} + \sum_{j=0}^{N} \omega_{\text{off}}(2,j)P_{2,j} \\
\partial_t P_{2,i} &= \omega_{\text{s}}(2,i-1)P_{2,i-1} - [\omega_{\text{s}}(2,i) + \omega_{\text{r}}(2,i) + \omega_{\text{off}}(2,i)]P_{2,i} \\
&\quad + \omega_{\text{r}}(2,i+1)P_{2,i+1} \\
\partial_t P_{2,N} &= \omega_{\text{s}}(2,N-1)P_{2,N-1} - [\omega_{\text{r}}(2,N) + \omega_{\text{off}}(2,N)]P_{2,N},
\end{aligned} \tag{3.13}$$

where the middle equation is valid for $0 < i < N$. Here $P_{2,i}$ is the probability of being in state $(2, i)$ before absorption. Together with the normalization condition, the steady state of this set of equations can be solved with a backward substitution, since $P_{2,N}$ only depends on $P_{2,N-1}$. Now, the inverse mean first passage time or the effective unbinding rate (the rate of being absorbed), $\epsilon_2$, is given by the probability current into the absorbing state, i.e.,

$$\epsilon_2 = \frac{1}{t_2} = \sum_{i=0}^{N} \omega_{\text{off}}(2, i) P_{2,i}. \tag{3.14}$$

Averaging the stepping rates of both motors, weighted with the probabilities $P_{2,i}$, we obtain the velocity as

$$v_2 = \frac{\ell}{2} \sum_{i=0}^{N} [\alpha(F_i) + \alpha(-F_i)] P_{2,i}. \tag{3.15}$$

Once these two parameters have been obtained, the transport properties for a cargo pulled by two motors can be obtained using the theoretical framework of Ref. [51], which is discussed below. Specifically, the average velocity of the cargo, i.e., averaged over the states $(C_1)$ and $(C_2)$, is obtained as

$$v_{\text{ca}} = \frac{\pi v_2 + \epsilon_2 v_1}{\pi + \epsilon_2}, \tag{3.16}$$

where $v_1$ is the velocity when only one motor is bound. In the absence of an external force, $v_1 = v$, whereas in the presence of an external force, it s given by the force-velocity relation (3.6). Likewise, the average run length of the cargo, the distance moved before complete unbinding, is obtained as

$$\langle \Delta x_{\text{ca}} \rangle = \frac{\pi v_2 + \epsilon_2 v_1}{\epsilon_1 \epsilon_2}. \tag{3.17}$$

The advantage of using this combination of the explicit description of substates $(2, i)$ and the coarse grained description with states $(C_0)$, $(C_1)$ and $(C_2)$ is that different parameterizations for the single motors or different couplings can be implemented rather easily and their cooperative behavior can be deduced in a computationally inexpensive manner [7].

#### 3.3.2.4 Motility States of a Cargo and Semistochastic Approaches

Many experimental studies report trajectories (or kymographs) of labeled cargoes. Unless experimental methods with very high spatial and temporal resolution are used, e.g., [58, 98], discrete steps are not resolved and the cargo is seen to perform continuous motion with a velocity $v$, suggesting a deterministic description of the cargo movement of the cargo. Such a description [51] can be considered as resulting from the coarse-graining of a more microscopic description that replaces stochastic stepping by constant cargo velocities that characterize the different states of the cargo, for example, the states $(C_1)$ and $(C_2)$ discussed above.

The value of the cargo velocity is determined by the dynamics of the motors. If the cargo imposes a substantial load for the motors, for example in a viscous

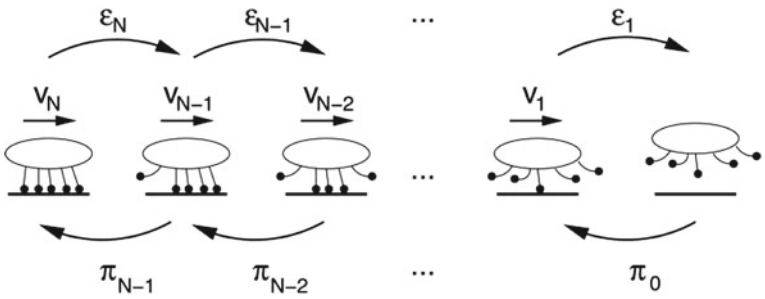


**Fig. 3.6** A cargo particle is transported by $N$ motors. Each state is characterized by the number of bound motors. In each state the cargo has velocity $v_n$, a motor unbinds from the filament with rate $\varepsilon_n$ and an additional motor binds to the filament with rate $\pi_n$ (reprinted from Ref. [51])

medium, a larger number of motors actively pulling on the cargo can result in higher speed [31, 51]. Since motors unbind and rebind to the filament, the velocity of such a cargo changes when the number of bound motors change. Therefore, a rather general coarse-grained description for cooperative cargo transport by molecular motors can be obtained by a discrete state-space with cargo states associated with the number of bound motors [51]. Transitions between these states correspond to binding and unbinding of motors, see Fig. 3.6. Thus, the model is semistochastic, describing the cargo movement (based on rapid steps) as a deterministic process and motor binding/unbinding, which happens on longer timescales, as stochastic processes. In principle, the parameters of this model, the velocities and unbinding rates can be obtained by systematic coarse-graining as described above. However, this has so far not been done for more than two motors. For cases with more than two motors, the rates have been obtained by making plausible assumptions such as weak coupling between the motors and equal sharing of load forces [51, 72]. This approach allows us to calculate dynamical properties of the cargo, like the run length and run time of a cargo transported by teams of motors. Such studies have been done for unidirectional transport by a single team of motors [51], for bidirectional transport by two teams of motors [72], for transport by motors with different velocities [56], and for combined directed and diffusive transport by active and inactive motors [10, 75].

If a cargo is transported by two teams of antagonistic motors, i.e., by motors that walk in opposite directions, the cargo is transported in a bidirectional manner, changing direction every few seconds. A theoretical description for this transport mode also starts by identifying discrete states associated with the numbers of bound motors of both types, see Fig. 3.7. Transitions between the states arise from binding and unbinding of the motors. Since the unbinding rate depends on the external force, motors can pull each other from the filament resulting in a tug-of-war. Such a tug-of-war displays a rich pattern of motility depending on the single motor parameters [71–73]. In particular, the analysis of this model showed that mechanical interactions of the motors mediated by the two teams pulling on each other is sufficient to generate rapid bidirectional movements [72]. No specialized coordination complex,

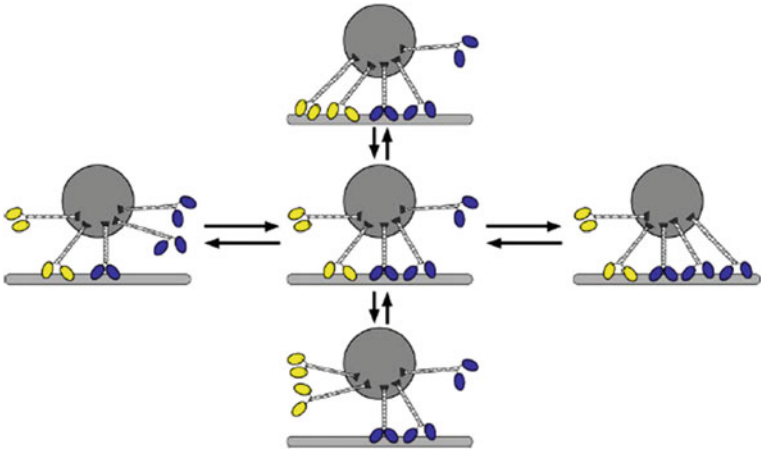

**Fig. 3.7** A cargo with 3 plus (*blue*) motors and 2 minus (*yellow*) motors is pulled by a fluctuating number of motors bound to the filament. The different states are defined by the number of bound motors. Only five of 12 possible states are displayed (reprinted from Ref. [72])

as proposed earlier (see, e.g., Ref. [95]), is required. Later experiments provided direct evidence for such mechanical interaction between motors [36, 84], which can be seen as an unavoidable physical constraint on the coordination of motors with opposite directionality. Some recent experimental studies also indicate that not all observations can be interpreted by mechanical interactions alone [55, 59], suggesting an additional layer of biochemical regulatory mechanisms regulating the tug-of-war, as emphasized in the theoretical studies [73].

The approach described so far can be extended to account for diffusive movements of the cargo along the filaments as observed experimentally [2]. For cargo states in which the motors diffuse, the velocity $v$ of the cargo vanishes. To account for the diffusive dynamics (or, likewise, for biased diffusive dynamics) one can describe the position of the cargo again in a stochastic fashion using an over-damped Fokker-Planck equation [77]. In this way, the motion of the spatial coordinate of the cargo in a state $(i)$ is described by a Fokker-Planck operator $\mathscr{L}_i$. Extending the master equation to account for the time evolution of this coordinate explicitly leads to

$$\partial_t p_i(x,t) = \sum_j \omega_{ji} p_j(x,t) - \sum_j \omega_{ij} p_i(x,t) + \mathscr{L}_i p_i(x,t). \tag{3.18}$$

Here $p_i(x,t)$ is the probability that the cargo is in state $(i)$ at the coordinate $x$ at time $t$. The transition rate from state $(i)$ to $(j)$ is given by $\omega_{ij}$. Within the framework of Fokker-Planck operators one can describe a wide range of motility patterns. Two important limiting cases are purely diffusive motion, which is represented by

$$\mathscr{L} = D\partial_x^2 \tag{3.19}$$

and deterministic motion with constant velocity $v$, represented by

$$\mathscr{L} = -\partial_x v. \tag{3.20}$$

If one is only interested in average values of observables such as the run length and the average binding time, one can avoid to explicitly solve the Fokker-Planck equation by using again the Hill method. This approach has been used in Ref. [10] to study how the presence of inactive, but diffusing motors enhances the processivity of actively pulling motors.

### *3.3.3 Explicit Descriptions of the Geometry of Motor–Cargo Complexes*

Finally, studying some aspects of molecular motor complexes requires geometric information about the system. A rather obvious example is effects of the arrangement of the motors on the cargo or in a multi-motor complex: Does it make a difference whether motors are attached to a cargo in one specific location or randomly distributed on a large cargo? What impact does the distance between two motors in a motor pair have? Does steric hindrance between motors play a role? These aspects have been studied in less detail than the stochastic network models discussed so far. Moreover, the construction of models that incorporate three-dimensional spatial information is less systematic than for the stochastic networks. In this section, we give a brief review of what has been done, without going into the technical details. We then discuss one such approach [52] in more detail to highlight some issues that arise in a geometric description of systems of cooperative motors.

In models that describe the spatial structure of the motor–cargo complex, motors are typically represented by a few degrees of freedom, namely their point of attachment to the filament (the 'head'), their point of attachment to the cargo and an elastic element between these two points, which may be a linear spring, a cable-like spring, or an empirically defined nonlinear spring. The position of the attachment point to the cargo is determined by the position and orientation of the cargo. Once the head is attached to the filament it moves like a stochastic stepper, but the force it experiences is now calculated according to a three-dimensional force balance. The movements of unbound heads are typically not described explicitly. Rather, unbound heads may bind to the filament according to a rate that depends on the relative location of the attachment point and the nearest sites on the filament, accounting for the distance to the filament and possibly for steric hindrance by the cargo or by other motors.

Approaches of this type have been used to address a number of issues. One study, in which our group was involved [52], has addressed the sharing of a viscous force among motors that are randomly distributed on a cargo and compared different elastic elements (linear and cable-like springs with different lengths). A similar study by Erickson et al. [28] investigated the impact of the geometric arrangement of motors

by comparing motors randomly distributed on a cargo and clustered motors and found that cooperation is more efficient in the clustered case, with larger run lengths. Finally, Driver et al. [26] used geometric force balance to determine transition rates in a Master equation approach used for a systematic comparison with optical trapping experiments on a two-kinesin-1 complex. The models used in these studies differ in various aspects, such as the description of the cargo (as simply the center of mass of the motors or as a diffusing particle), the choice of elastic element between the motor head and the cargo, and the inclusion of hydrodynamic effects and of steric hindrance. These differences make the comparison of the models quite difficult, and the relative importance of the various ingredients of these models remains to be elucidated.

We now describe the approach by Korn et al. [52] in some more detail in order to point out a few issues that arise in a description of the motor complex geometry. In that model, the motion of a spherical cargo particle is described using a Langevin equation with 6 degrees of freedom (its position in a three-dimensional space and its orientation) and with a position-dependent mobility matrix that accounts for hydrodynamic effects due to the presence of a wall (the coverslide on which the filament is immobilized). The motors are randomly distributed on the cargo and, when bound to the filament, move by stochastic stepping as described in Sect. 3.3.2 above. The motor "tail", the link between the motor head on the filament and the attachment point on the cargo, is described as an elastic element (either a linear spring or a cable-like spring). Thus, the cargo particle is subject to the forces mediated by the motor springs, viscous forces from the surrounding fluid and random forces that lead to the diffusion of the cargo particle around the equilibrium position given by the balance of the motor forces. External forces acting on the cargo can also be incorporated. In particular, because hydrodynamic effects are already incorporated in the mobility matrix, this approach is particularly suited to study hydrodynamic forces, arising, e.g., from shear flow.

Within this description of the motors, the elastic forces act along the direction of the springs, i.e., under an angle to the direction of motion. It is thus not entirely clear how this force should affect the stepping rates, as in the experiments the forces are typically exerted in the direction parallel to the filament. Therefore, an additional assumption has to be made at this point and simulations to validate this modeling assumption are required. In Ref. [52], the spring force was projected onto the direction of motion and the projected force was used in a linear force dependence of the stepping rate. This assumption led to a linear force-velocity relation in simulations mimicking an optical tweezers experiment with an external force applied to the cargo in the direction antiparallel to the direction of motion. Obviously, more complex force dependencies can be implemented, but in any case, the assumed force dependence needs to be validated by comparison to experimental data or to a desired simplified force-velocity relation.

A second issue that deserves a few comments is how binding of a motor to the filament is treated. In the approach of Korn et al. [52], the position of unbound motor heads is not described explicitly. Unbound motor heads perform rapid tethered diffusion with the ends of their tails fixed by the position of the cargo. Their rebinding

to the filament is therefore determined probabilistically with a rate that depends on two factors, a bare binding rate for a motor close to the filament and a probability that the motor is indeed close to the filament, i.e., within some capture distance to a free binding site on the filament. The latter distance can be determined by considering the overlap between the binding sites and the shell on which the tethered motor head diffuses.

### *3.3.4 General Modeling Strategy and Integration of Models on Different Scales*

We conclude our discussion of theoretical methods with some general remarks about the choice of a theoretical description and the construction of suitable models. The theoretical approaches described above provide different description of cooperative transport by several motors or of motor complexes, but they follow the same general modeling strategy.

The first step is to choose a level of theoretical description that is appropriate to study the questions of interest. This choice involves both the desired output of the model and the prior knowledge available as its input. The desired output determines how detailed the description needs to be and defines the time and length scales to be studied (if simulation time is a limiting issue, the latter may be a strong constraint). The available input, on the other hand, is critical for the feasibility by determining the number of unknown parameters. For the discrete stochastic models described above, the choice of a theoretical description ultimately leads to the identification of a set of states of the system described by a set of variables characterising these states. These variables are typically a combination of variables characterizing each individual motor (e.g., the chemomechanical states of the two motors) and variables characterizing their coupling (e.g., the force between the motors). While a motor or motor complex is in one such state, these parameters are taken to remain constant, so molecular movements on scales smaller than the chosen description are neglected.

In addition to the states, one needs to identify the transitions between the states (which are related to chemomechanical transitions of the configuration of a motor, stepping of a motor or binding/unbinding of a motor). For a multi-motor complex, these transitions are derived from the corresponding transitions of the single motors. Once the network of states linked by the allowed transition between them is set up, the transitions have to be associated with the corresponding transition rates. This is ideally done based on experimental data, but in many cases this step needs additional theoretical input. For cooperative motors, these transition rates can often be derived from the transition rates of individual motors under force, by incorporating forces arising from the coupling of the motors into the force experienced by that motor. Alternatively, one can calculate these rates from a more detailed model. An example is given by our calculation of $\epsilon_2$ in the stepper model in Sect. 3.3.2 that can be used in the semi-stochastic theoretical description of cargo movements. Yet another option

would be to use force-dependent single-motor transition rates, but determine the force from a detailed microscopic force balance. Thus, this step, the calculation of transition rates, provides an opportunity for true multiscale approaches.

Once the rates are known, the dynamics of the system can be solved either analytically or by simulations and observables can be determined and compared with experimental data. If necessary, the model is then adjusted. The latter comparison provides a consistency check in cases where the input of the model, the transition rates, is taken directly from experimental data, and a validation step for descriptions based on assumptions about the microscopic processes and interactions. Finally, quantitative predictions can be made with such a consistent theoretical description.

## 3.4 Results

The methods described above have been used extensively to study cooperative transport by molecular motors. Here we highlight some results where bridging the length and timescales has been crucial. Specifically, we discuss two issues: the effect of the coupling strength on motor cooperation and the different transport regimes that can emerge when different motor types are coupled.

### *3.4.1 Impact of Elastic Coupling*

#### 3.4.1.1 Varying Elastic Coupling in Chemomechanical Networks

Both the chemomechanical network and the stochastic stepper model as described above are based on a complete description of a single motor. In addition to the parameters characterizing the single motor, these models have only two parameters, the binding rate $\pi$ and the coupling parameter $K$.[6] Figure 3.8 shows some results obtained with the chemomechanical network approach for kinesin-1, systematically varying these two parameters. Figure 3.8a shows different activity regimes, regions in the parameter space, where transport is dominated by 1-motor runs and 2-motor runs, respectively. Which activity state is dominant during a motor pair walk obviously depends on the rebinding rate $\pi$, but also on the coupling parameter $K$, because $K$ influences the termination rate $\epsilon_2$ of 2-motor runs. The activity regime diagram in Fig. 3.8a shows the crossover line which separate the parameter regime in which 1-motor runs dominate the cargo run from the regime in which 2-motor runs are more likely. Along this line, both are equally probable. A small rebinding rate leads to a clear dominance of 1-motor runs for all values of the coupling parameter, whereas clear dominance of 2-motor runs is only found for relatively large rebinding rates and small coupling parameters.

[6] There may be more parameters for nonlinear couplings.

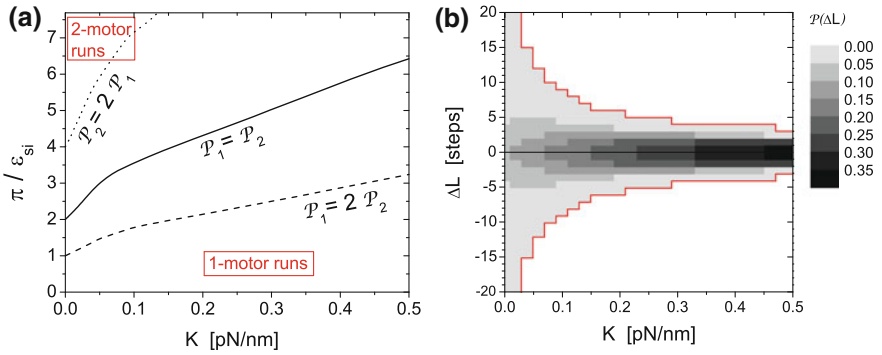


**Fig. 3.8** **a** Activity regimes of a motor pair in terms of the probabilities $\mathscr{P}_1$ and / $\mathscr{P}_2$ for 1-motor and 2-motor runs: The crossover *line* $\mathscr{P}_2 = \mathscr{P}_1$ separates the parameter regime, in which 1-motor runs dominate the cargo run from the regime in which 2-motor runs are more likely. The *dashed* and the *dotted lines* are the crossover lines at which $\mathscr{P}_1 = 2\mathscr{P}_2$ and $\mathscr{P}_2 = 2\mathscr{P}_1$, respectively. **b** Contour plot of the probability distribution $\mathscr{P}(\Delta L)$ for the extension $\Delta L$ of the motor-motor separation as a function of the coupling parameter $K$. The *red line* indicates maximal values of $\Delta L$ observed in the simulations

From trajectories of the individual motors within a motor pair, one can deduce the distribution of the extension $\Delta L$ of the motor-motor separation as shown in Fig. 3.8b. Since we define $\Delta L \equiv 0$ for 1-motor runs, this is a property of 2-motor runs. The probability distribution $\mathscr{P}(\Delta L)$ is symmetrically distributed around the average $\langle \Delta L \rangle = 0$ for all coupling parameters, which implies that the leading and trailing motor are interchangeable. The number of accessible $\Delta L$ values decreases with increasing coupling parameter $K$. Within the studied range for the coupling parameter, this number varies by one order of magnitude. Measuring the width and amplitude of the distribution for the deflection $\Delta L$ one can, for instance, determine the coupling parameter $K$. In principle, this distribution could also be used to reconstruct the full force–extension curve for a nonlinear spring that couples the motors. We note however that the distribution $\mathscr{P}(\Delta L)$ not only reflects the interaction potential of the two motors, but also depends on their unbinding, because unbinding from a state with large $\Delta L$ with subsequent relaxation and rebinding also provides a pathway to return to small extensions $\Delta L$.

### 3.4.1.2 Coupling Dependence in Stochastic Stepper Models

We briefly review the effect of varying the coupling strength in the stochastic stepper model and use this example as an illustration for how models at different scales and with different levels of detail can be integrated. Specifically, the detailed stochastic stepper model is used to determine parameters that enter the coarse-grained semi-stochastic description where all substates of the two-motor-bound state are lumped together.

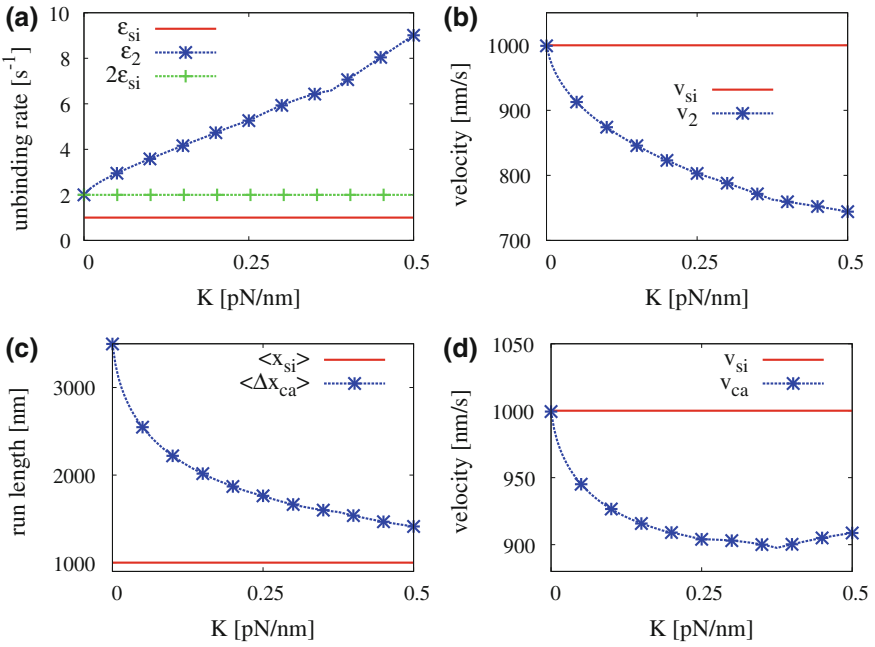


**Fig. 3.9** Transport properties of an elastically coupled kinesin pair: **a** Effective unbinding rate $\epsilon_2$, **b** average velocity $v_2$ of two bound motors, **c** run length and **d** average cargo velocity as functions of the coupling constant $K$. In all subfigures, the $K$-independent single motor properties are also included. The kinks in these *curves* are due to the discrete values of the force between the motors and arise when the stall force is an integer multiple of the strain force, i.e., for $K = F_s/(\ell n)$ with integer $n$. At these values of $K$, the number of states $(2, i)$ with forces *below* the stall force changes by 1

Figure 3.9a, b shows the effective unbinding rate $\epsilon_2$ and the effective velocity $v_2$ as functions of the coupling strength $K$ using parameters for kinesin-1 and assuming coupling by a linear spring. The two quantities, which are calculated via Eqs. (3.14) and (3.15), are characteristics of 2-motor runs and therefore independent of the binding rate $\pi$. The effect of coupling on the velocity is moderate with only about 15 percent reduction for strong coupling. The effect on unbinding is much more pronounced: For weak coupling, the motors unbind independently of each other, and the unbinding rate of one of them is thus twice the single-motor unbinding rate. With increasing coupling strength, the unbinding rate exhibits a strong increase, in agreement with experimental observations [79].

Using these results of the microscopic stepper model in the more coarse-grained semi-stochastic one, one can calculate the transport properties of the cargo such as the average velocity (averaged over 1-motor runs and 2-motors runs) and the cargo run length via Eqs. (3.16) and (3.17). These two quantities are plotted in Fig. 3.9c, d, also as functions of the coupling strength. Both quantities also depend on the binding rate. The dominant effect of coupling on the unbinding rate can also be seen

here: the run length decreases strongly with increasing coupling strength. The run length of the two-motor complex, however, is always larger than the run length of a single motor (which is approached for large coupling strength), i.e., the interference between the motors decreases the effect of motor cooperation, but does not reduce it below the level of a single motor. The average velocity shows even less reduction than the velocity $v_2$ of 2-motor runs and increases again for strong coupling, because with increasing coupling strength, 1-motor runs become more and more likely, and thus the reduced velocity of 2-motor runs contributes less and less to the average.

Nonlinear couplings have also been considered within the stochastic stepper approach [8]. For example, cable-like springs (that are linear springs with respect to stretching but exhibit no resistance to compression) leads to a much weaker effect because it takes longer to build up substantial strain forces between the two motors [8]. In addition, several studies have considered springs with a force-dependent spring constant, specifically, the case of a spring that is rather soft at low force and stiff at large forces. Such a spring can be characterized by two spring constants and is suggested by some experiments on the kinesin tail [3, 27]. The latter spring also leads to weaker coupling effects, indicating that the lower spring constant (for which building up strain requires some time) is dominant during 2-motor runs [8].

#### 3.4.1.3 Different Types of Elastic Coupling and Cargo Geometry

Finally, the impact of the type of spring was also studied in simulations of bead movements with explicit representation of the cargo geometry. Two different types of springs were studied, a linear spring and a cable-like (or semi-harmonic) spring that behaves as a linear spring when stretched, but does not resist compression. In addition, different rest lengths were used in both cases. For all cases, run length distributions were determined from extensive simulations. The distributions were approximately given by double-exponentials, and the average run length was found to increase almost exponentially with the number of motors attached to the cargo. For the same number of motors on the cargo, the average run length was found to be longer for longer springs [52]. This result can be explained by the observation that, in this case, more motors are bound to the filament simultaneously. This means that the longer spring rest length provides more flexibility to accommodate a larger number of motors on the filament. Moreover for all rest lengths, cable-like springs lead to longer run lengths than linear springs. This has been interpreted as an effect of the average distance between the cargo and the filament, which is expected to be smaller for cable-like motors, where the springs do not induce upward forces on the cargo, than for linear-spring motors [52]. However, our more recent discussion of interference effects for nonlinear springs suggests another explanation (not mutually exclusive with the first): For cable-like linkers, forces between the motors build up more slowly than for linear springs [8], so interference effects are less pronounced. Specifically, for linear springs, forces built up because of the nonsynchronous stochastic stepping of the motors, enhance unbinding, thus effectively reducing the number of bound motors.

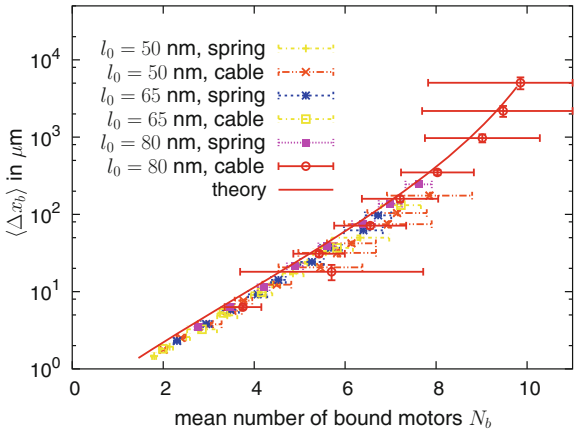


**Fig. 3.10** Run length of simulated beads transported by many kinesin motors: Data for the run lengths obtained with different elastic elements collapse onto a single master *curve*, when plotted against the average number of bound motors, indicating that the number of bound motors is what effectively determines the run length (reprinted from Ref. [52] with permission from AIP Publishing)

When the average run length is plotted against the average number of bound motors, the results for all spring models collapse on a single curve (Fig. 3.10). This master curve can also be described by the theoretical expectation based on the model of Ref. [51], if the maximal number of motors able to bind simultaneously is taken from a Poisson distribution, as indicated by the solid line in Fig. 3.10. This result shows that the dependence of the run length on the geometric details is fully mediated by a modulation of motor-filament binding and that additional factors such as modulation of the stepping rate or the movement of the cargo are of lesser importance.

### *3.4.2 Transport Regimes*

Finally, we briefly discuss some generic aspects of cooperative transport that can be understood based on the derivation of the effective parameters $\epsilon_2$ and $v_2$ of 2-motor runs from the microscopic stochastic stepper model. In the absence of an external force, the stepper model is characterized by three different force scales, the stall force $F_s$, the detachment force $F_d$, and the strain force $F_K$ that arise from coupling. The latter is defined by the force generated by a single step extending the elastic element between the motors. For a linear spring, $F_K = F_1 = \ell K$. If both force scales of the single motor, $F_s$ and $F_d$, are expressed as ratios to $F_K$, the two-motor parameters $\epsilon_2$ and $v_2$ can be calculated as functions of the two dimensionless force ratios $F_s/F_K$ and $F_d/K_K$, from which one can identify four different transport regimes [7]: when both force ratios are large, the coupling is weak and neither velocity nor unbinding rate is strongly affected by the coupling, i.e., $v_2 \approx v_1$ and $\epsilon_2 \approx 2\epsilon_1$ as for noninteracting motors (weak coupling regime). In the opposite limit, for which both force ratios are small, the coupling is strong, the velocity is reduced, and unbinding is enhanced (strong coupling regime). Furthermore, the motor pairs

exhibit two additional regimes, in which one of the two quantities is affected by coupling, while the other is not: A reduced velocity regime, in which the velocity is reduced, but the unbinding rate is (almost) unaffected by the strain force, is found for large $F_d/F_K$ and small $F_s/F_K$. In the opposite case, for small $F_d/F_K$ and large $F_s/F_K$, we have the enhanced unbinding regime, with an increased unbinding rate and a velocity that is unaffected.

The crossover lines between these regimes depend also on the dynamic parameters $v_1$ and $\epsilon_1$, because the force between the motors is built up dynamically by stepping. They can be understood based on the comparison of three timescales: the times to build up forces comparable to the stall force and the detachment force and time for spontaneous unbinding of a motor [7, 8]. If the time for spontaneous unbinding is the shortest, there is no time to build up a sufficiently large strain force to affect the motors' behavior, corresponding to the weak coupling regime. If one of the other two timescales (or both) is shorter than the time for spontaneous unbinding, the corresponding parameter ($\epsilon_2$, $v_2$ or both) is affected, resulting in the enhanced unbinding regime, the reduced velocity regime, or the strong coupling regime, respectively. We note that the presence of an external load force will provide an additional force scale, the external force itself, and additional timescales, such as the time it takes to equilibrate the distribution of the external force among the motors (force sharing).

Interestingly, which of the four regimes are accessed via a variation of the coupling strength is dependent on the motor species under consideration, because the force scales are characteristic parameters of these motors. For example, kinesin-1 motors are predicted to exhibit the strong and weak coupling regimes and, for intermediate coupling strength, the enhanced unbinding regime, while myosin V motors are predicted to be in the reduced velocity regime for intermediate couplings (in addition to also exhibiting the strong and weak coupling regimes) [7, 8]. This theoretical prediction was confirmed by experimental results: a pair of kinesin-1 motors was found to exhibit enhanced unbinding and little reduction of the velocity [79], while a reduced velocity was recently found for a pair of myosin V motors [66].

## 3.5 Open Questions

The cooperation of several molecular motor, specifically of well-defined small numbers of motors, is currently under intense investigation, mostly driven by new experimental techniques to couple molecular motors in a defined fashion, e.g., [25, 79]. These experiments address various aspects on different length scales, from molecular deformations on the scale of nanometers arising from elastic coupling-induced strains to increases in run lengths on the scale of many microns. These new experiments can be expected to lead to a rather detailed picture of motor cooperation in the near future, which will allow to address more detailed issues theoretically and to go beyond the coarse-grained descriptions of the motor configurations used so far. For example, we expect that precise empirical force dependencies of velocities and unbinding rates for a specific system can be used instead of the generic relations with

simple functional forms as employed in current studies. These improvements will, however, require fruitful interplay between model construction and experiments. One aspect that we hope can be addressed quite soon is the coupling to the chemistry of the motors, i.e. the interplay of nucleotide concentrations and forces in affecting the transport parameters of cooperatively pulled cargos. First steps in this direction have already been made, both from the experimental [96] and the theoretical sides [8, 49].

A key question will be what additional components are needed for certain patterns of movements. From the biochemical perspective, this is a question about additional molecular players such as regulatory components or proteins that modulate certain properties of the motors. Examples include the dynactin complex, which increases dynein's processivity and has been proposed as a candidate for regulating the interplay between kinesin and dynein motors [94], and the recently characterized regulators of dynein, NudE, and LIS1 [69]. From a theoretical perspective (where one tries to explain properties of a larger scale system, such as a complex of multiple motors, based on the known properties of its components, here the individual motors), these regulators modulate the parameters of the individual motors or of their coupling, so the question for regulatory factors can be addressed by studying the dynamic variation of parameters to explain observations that cannot be explained by fixed parameters characterizing the (unregulated) motors. For example, how would additional biochemical coordination have to affect a tug-of-war situation to result in the very long pauses that have been observed [55] or in directional memory after forced unbinding [59]. One example, in which such an extension of a tug-of-war is understood is the transport of early endosomes in the fungus *Ustilago maydis*, where a tug-of-war is controlled by the reversible binding and unbinding of a dynein motor to the moving cargo [83].

In order to understand transport in cells, it will also be necessary to consider the movements of motors on multiple levels of complexity (in addition to the different time and length scales discussed above). If single motors in vitro are considered as relatively simple systems,[7] complexity will increase and the space of possible dynamic behaviors extended by coupling motors in a defined way. These systems however are still relatively simple with respect to the number of different molecular components, which is relatively small. Moreover, all of these components are known. The system complexity increases further as one goes beyond the defined in vitro motility to movements in cell extracts and, finally, transport in vivo [4, 14]. Here, additional molecular players may modulate the properties of the motors and the possible existence of unknown components or of cross-talk and unknown interactions with other systems cannot easily be excluded. In this regard, theory can play an important role by bridging not only between different length and timescales but also between the different levels of complexity.

[7] Of course, the molecules themselves may also add a layer of complexity to the patterns of movements, for example if the motor has several different functional modes, as reported for dyneins [92].

## References


1. Ali, M.Y., Kennedy, G.G., Safer, D., Trybus, K.M., Sweeney, H.L., Warshaw, D.M.: Myosin Va and myosin VI coordinate their steps while engaged in an in vitro tug of war during cargo transport. Proc Natl Acad Sci U S A **108**, E 535–541 (2011).
2. Ali, M.Y., Krementsova, E.B., Kennedy, G.G., Mahaffy, R., Pollard, T.D., Trybus, K.M., Warshaw, D.M.: Myosin va maneuvers through actin intersections and diffuses along microtubules. Proc Natl Acad Sci U S A **104**, 4332–6 (2007).
3. Atzberger, P.J., Peskin, C.S.: A brownian dynamics model of kinesin in three dimensions incorporating the force-extension profile of the coiled-coil cargo tether. Bull Math Biol **68**, 131–60 (2006).
4. Barak, P., Rai, A., Rai, P., Mallik, R.: Quantitative optical trapping on single organelles in cell extract. Nat Methods **10**, 68–70 (2013).
5. Beeg, J., Klumpp, S., Dimova, R., Gracià, R.S., Unger, E., Lipowsky, R.: Transport of beads by several kinesin motors. Biophys J **94**, 532–41 (2008).
6. Bell, G.I.: Models for the specific adhesion of cells to cells. Science **200**, 618–627 (1978).
7. Berger, F., Keller, C., Klumpp, S., Lipowsky, R.: Distinct transport regimes of two elastically coupled molecular motors. Phys Rev Lett **108**, 208101 (2012).
8. Berger, F., Keller, C., Lipowsky, R., Klumpp, S.: Elastic coupling effects in cooperative transport by a pair of molecular motors. Cell Molec Bioeng **6**, 48–64 (2013).
9. Berger, F., Keller, C., Müller, M.J.I., Klumpp, S., Lipowsky, R.: Co-operative transport by molecular motors. Biochem Soc Trans **39**, 1211–5 (2011).
10. Berger, F., Müller, M.J.I., Lipowsky, R.: Enhancement of the processivity of kinesin-transported cargo by myosin V. Europhys Lett **87**, 28,002 (2009).
11. Bieling, P., Telley, I.A., Piehler, J., Surrey, T.: Processive kinesins require loose mechanical coupling for efficient collective motility. EMBO Rep **9**, 1121–7 (2008).
12. Bierbaum, V., Lipowsky, R.: Chemomechanical coupling and motor cycles of myosin V. Biophys J **100**, 1747–55 (2011).
13. Bierbaum, V., Lipowsky, R.: Dwell time distributions of the molecular motor myosin v. PLoS One **8**, e55366 (2013).
14. Blehm, B.H., Schroer, T.A., Trybus, K.M., Chemla, Y.R., Selvin, P.R.: In vivo optical trapping indicates kinesin's stall force is reduced by dynein during intracellular transport. Proc Natl Acad Sci U S A **110**, 3381–6 (2013).
15. Block, S.M.: Kinesin motor mechanics: Binding, stepping, tracking, gating, and limping. Biophys J **92**, 2986–95 (2007).
16. Böhm, K.J., Stracke, R., Mühlig, P., Unger, E.: Motor protein-driven unidirectional transport of micrometer-sized cargoes across isopolar microtubule arrays. Nanotechnology **12**, 238–244 (2001).
17. Bouzat, S., Falo, F.: The influence of direct motor-motor interaction in models for cargo transport by a single team of motors. Phys Biol **7**, 046009 (2010).
18. Campàs, O., Kafri, Y., Zeldovich, K.B., Casademunt, J., Joanny, J.F.: Collective dynamics of interacting molecular motors. Phys Rev Lett **97**, 038101 (2006).
19. Carter, N.J., Cross, R.A.: Mechanics of the kinesin step. Nature **435**, 308–12 (2005).
20. Clancy B.E., Behnke-Parks W.M., Andreasson J.O.L., Rosenfeld S.S., Block S.M.: A universal pathway for kinesin stepping. Nature Struct. Mol. Biol. **18** 1020–7 (2011).
21. Clemen, A.E.M., Vilfan, M., Jaud, J., Zhang, J., Bärmann, M., Rief, M.: Force-dependent stepping kinetics of myosin-V. Biophys J **88**, 4402–10 (2005).
22. Constantinou, P.E., Diehl, M.R.: The mechanochemistry of integrated motor protein complexes. J Biomech **43**, 31–7 (2010).
23. Coppin, C., Pierce, D., Hsu, L., Vale, R.: The load dependence of kinesin's mechanical cycle. Proc Natl Acad Sci U S A **94**, 8539–8544 (1997).
24. Crevenna, A.H., Madathil, S., Cohen, D.N., Wagenbach, M., Fahmy, K., Howard, J.: Secondary structure and compliance of a predicted flexible domain in kinesin-1 necessary for cooperation of motors. Biophys J **95**, 5216–27 (2008).

25. Derr, N.D., Goodman, B.S., Jungmann, R., Leschziner, A.E., Shih, W.M., Reck-Peterson, S.L.: Tug-of-war in motor protein ensembles revealed with a programmable dna origami scaffold. Science **338**, 662–5 (2012).
26. Driver, J.W., Jamison, D.K., Uppulury, K., Rogers, A.R., Kolomeisky, A.B., Diehl, M.R.: Productive cooperation among processive motors depends inversely on their mechanochemical efficiency. Biophys J **101**, 386–95 (2011).
27. Driver, J.W., Rogers, A.R., Jamison, D.K., Das, R.K., Kolomeisky, A.B., Diehl, M.R.: Coupling between motor proteins determines dynamic behaviors of motor protein assemblies. Phys Chem Chem Phys **12**, 10,398–405 (2010).
28. Erickson, R.P., Jia, Z., Gross, S.P., Yu, C.C.: How molecular motors are arranged on a cargo is important for vesicular transport. PLoS Comput Biol **7**, e1002,032 (2011).
29. Fisher, M.E., Kolomeisky, A.B.: Simple mechanochemistry describes the dynamics of kinesin molecules. Proc Natl Acad Sci USA **98**, 7748–7753 (2001).
30. Furuta, K., Furuta, A., Toyoshima, Y.Y., Amino, M., Oiwa, K., Kojima, H.: Measuring collective transport by defined numbers of processive and nonprocessive kinesin motors. Proc Natl Acad Sci U S A **110**, 501–6 (2013).
31. Gagliano, J., Walb, M., Blaker, B., Macosko, J.C., Holzwarth, G.: Kinesin velocity increases with the number of motors pulling against viscoelastic drag. Eur Biophys J **39**, 801–13 (2010).
32. Gennerich, A., Carter, A.P., Reck-Peterson, S.L., Vale, R.D.: Force-induced bidirectional stepping of cytoplasmic dynein. Cell **131**, 952 (2007).
33. Grant, B.J., Gheorghe, D.M., Zheng, W., Alonso, M., Huber, G., Dlugosz, M., McCammon, J.A., Cross, R.A.: Electrostatically biased binding of kinesin to microtubules. PLoS Biol **9**, e1001207 (2011).
34. Gross, S.P., Vershinin, M., Shubeita, G.T.: Cargo transport: two motors are sometimes better than one. Curr Biol **17**, R478–86 (2007).
35. Hancock, W.O., Howard, J.: Kinesin's processivity results from mechanical and chemical coordination between the ATP hydrolysis cycles of the two motor domains. Proc Natl Acad Sci USA **96**, 13147–13152 (1999).
36. Hendricks, A.G., Perlson, E., Ross, J.L., Schroeder 3rd, H.W., Tokito, M., Holzbaur, E.L.F.: Motor coordination via a tug-of-war mechanism drives bidirectional vesicle transport. Curr Biol **20**, 697–702 (2010).
37. Hill, T.: Free Energy Transduction in Biology. Academic Press, New York (1977).
38. Hill, T.L.: Interrelations between random walks on diagrams (graphs) with and without cycles. Proc Natl Acad Sci USA **85**, 2879–2883 (1988).
39. Hill, T.L.: Number of visits to a state in a random walk, before absorption, and related topics. Proc Natl Acad Sci USA **85**, 4577–4581 (1988).
40. Holmes, K.C.: Muscle contraction. In: L. Wolpert (ed.) The limits of reductionism in biology, Novartis Foundation Symposium **213**, pp. 76–92. Wiley, Chichester (1998).
41. Howard, J.: Mechanics of Motor Proteins and the Cytoskeleton. Sinauer Associates, Sunderland (Mass.) (2001).
42. Howard, J., Hudspeth, A.J., Vale, R.D.: Movement of microtubules by single kinesin molecules. Nature **342**, 154–158 (1989).
43. Hwang, W., Lang, M.J., Karplus, M.: Force generation in kinesin hinges on cover-neck bundle formation. Structure **16**, 62–71 (2008).
44. Hyeon, C., Klumpp, S., Onuchic, J.N.: Kinesin's backsteps under mechanical load. Phys Chem Chem Phys **11**, 4899–910 (2009).
45. Hyeon, C., Onuchic, J.N.: Mechanical control of the directional stepping dynamics of the kinesin motor. Proc Natl Acad Sci U S A **104**, 17,382–7 (2007).
46. Jülicher, F., Ajdari, A., Prost, J.: Modeling molecular motors. Rev Mod Phys **69**, 1269–1281 (1997).
47. Keller, C.: Coupled molecular motors. Diploma thesis, Humboldt-Universität, Berlin (2009).
48. Keller, C.: Coupled Molecular Motors: Network Representation & Dynamics of Kinesin Motor Pairs. Ph.D. thesis, Universität Potsdam (2013).

49. Keller, C., Berger, F., Liepelt, S., Lipowsky, R.: Network complexity and parametric simplicity for cargo transport by two molecular motors. J Stat Phys **150**, 205–234 (2013).
50. King, S.J., Schroer, T.A.: Dynactin increases the processivity of the cytoplasmic dynein motor. Nat Cell Biol **2**, 20 (2000).
51. Klumpp, S., Lipowsky, R.: Cooperative cargo transport by several molecular motors. Proc Natl Acad Sci U S A **102**, 17,284–9 (2005).
52. Korn, C.B., Klumpp, S., Lipowsky, R., Schwarz, U.S.: Stochastic simulations of cargo transport by processive molecular motors. J Chem Phys **131**, 245,107 (2009).
53. Kramers, H.: Brownian motion in a field of force and the diffusion model of chemical reactions. Physica **7**, 284 (1940).
54. Kunwar, A., Mogilner, A.: Robust transport by multiple motors with nonlinear force-velocity relations and stochastic load sharing. Phys Biol **7**, 16012 (2010).
55. Kunwar, A., Tripathy, S.K., Xu, J., Mattson, M.K., Anand, P., Sigua, R., Vershinin, M., McKenney, R.J., Yu, C.C., Mogilner, A., Gross, S.P.: Mechanical stochastic tug-of-war models cannot explain bidirectional lipid-droplet transport. Proc Natl Acad Sci U S A **108**, 18960–5 (2011).
56. Larson, A.G., Landahl, E.C., Rice, S.E.: Mechanism of cooperative behaviour in systems of slow and fast molecular motors. Phys Chem Chem Phys **11**, 4890–8 (2009).
57. Leduc, C., Campàs, O., Zeldovich, K.B., Roux, A., Jolimaitre, P., Bourel-Bonnet, L., Goud, B., Joanny, J.F., Bassereau, P., Prost, J.: Cooperative extraction of membrane nanotubes by molecular motors. Proc Natl Acad Sci USA **101**, 17096–17101 (2004).
58. Leduc, C., Ruhnow, F., Howard, J., Diez, S.: Detection of fractional steps in cargo movement by the collective operation of kinesin-1 motors. Proc Natl Acad Sci USA **104**, 10847–10852 (2007).
59. Leidel, C., Longoria, R.A., Gutierrez, F.M., Shubeita, G.T.: Measuring molecular motor forces in vivo: implications for tug-of-war models of bidirectional transport. Biophys J **103**, 492–500 (2012).
60. Li, X., Lipowsky, R., Kierfeld, J.: Critical motor number for fractional steps of cytoskeletal filaments in gliding assays. PLoS One **7**, e43219 (2012).
61. Liepelt, S., Lipowsky, R.: Kinesin's network of chemomechanical motor cycles. Phys Rev Lett **98**, 258102 (2007).
62. Liepelt, S., Lipowsky, R.: Steady-state balance conditions for molecular motor cycles and stochastic nonequilibrium processes. Europhys Lett **77**, 50002 (2007).
63. Liepelt, S., Lipowsky, R.: Impact of slip cycles on the operation modes and efficiency of molecular motors. J Stat Phys **141**, 1–16 (2010).
64. Lipowsky, R., Klumpp, S.: 'Life is motion' - multiscale motility of molecular motors. Physica A **352**, 53–112 (2005).
65. Lipowsky, R., Liepelt, S.: Chemomechanical coupling of molecular motors: Thermodynamics, network representations and balanced conditions. J Stat Phys 130, 39–67 (2008). Erratum: J Stat Phys **135**, 777–778 (2009).
66. Lu, H., Efremov, A.K., Bookwalter, C.S., Krementsova, E.B., Driver, J.W., Trybus, K.M., Diehl, M.R.: Collective dynamics of elastically coupled myosin V motors. J Biol Chem **287**, 27,753–61 (2012).
67. Mallik, R., Carter, B.C., Lex, S.A., King, S.J., Gross, S.: Cytoplasmic dynein functions as a gear in response to load. Nature **427**, 649 (2004).
68. Mallik, R., Petrov, D., Lex, S.A., King, S., Gross, S.: Building complexity: An in vitro study of cytoplasmic dynein with in vivo implications. Curr Biol **15**, 2075–2085 (2005).
69. McKenney, R.J., Vershinin, M., Kunwar, A., Vallee, R.B., Gross, S.P.: Lis1 and NudE induce a persistent dynein force-producing state. Cell **141**, 304–14 (2010).
70. Mehta, A.D., Rock, R.S., Rief, M., Spudich, J.A., Mooseker, M.S., Cheney, R.E.: Myosin-V is a processive actin-based motor. Nature **400**, 590–593 (1999).
71. Müller, M.J.I., Klumpp, S., Lipowsky, R.: Motility states of molecular motors engaged in a stochastic tug-of-war. J Stat Phys **133**, 1059–1081 (2008).

72. Müller, M.J.I., Klumpp, S., Lipowsky, R.: Tug-of-war as a cooperative mechanism for bidirectional cargo transport by molecular motors. Proc Natl Acad Sci USA **105**, 4609–4614 (2008).
73. Müller, M.J.I., Klumpp, S., Lipowsky, R.: Bidirectional transport by molecular motors: enhanced processivity and response to external forces. Biophys J **98**, 2610–8 (2010).
74. Ökten, Z., Churchman, L.S., Rock, R.S., Spudich, J.A.: Myosin VI walks hand-over-hand along actin. Nat Struct Mol Biol **11**, 884 (2004).
75. Posta, F., D'Orsogna, M.R., Chou, T.: Enhancement of cargo processivity by cooperating molecular motors. Phys Chem Chem Phys **11**, 4851–60 (2009).
76. Rice, S., Lin, A.W., Safer, D., Hart, C.L., Naber, N., Carragher, B.O., Cain, S.M., Pechatnikova, E., Wilson-Kubalek, E.M., Whittaker, M., Pate, E., Cooke, R., Taylor, E.W., Milligan, R.A., Vale, R.D.: A structural change in the kinesin motor protein that drives motility. Nature **402**, 778–84 (1999).
77. Risken, H.: The Fokker-Planck Equation. Springer, Berlin Heidelberg (1996).
78. Rock, R.S., Rice, S.E., Wells, A.L., Purcell, T.J., Spudich, J.A., Sweeney, H.L.: Myosin VI is a processive motor with a large step size. Proc Natl Acad Sci USA **98**, 13,655 (2001).
79. Rogers, A.R., Driver, J.W., Constantinou, P.E., Kenneth Jamison, D., Diehl, M.R.: Negative interference dominates collective transport of kinesin motors in the absence of load. Phys Chem Chem Phys **11**, 4882–9 (2009).
80. Romberg, L., Vale, R.: Chemomechanical cycle of kinesin differs from that of myosin. Nature **361**, 168–170 (1993).
81. Schliwa, M., Woehlke, G.: Molecular motors. Nature **422**, 759–765 (2003).
82. Schnitzer, M.J., Visscher, K., Block, S.M.: Force production by single kinesin motors. Nature Cell Biol. **2**, 718–723 (2000).
83. Schuster, M., Lipowsky, R., Assmann, M.A., Lenz, P., Steinberg, G.: Transient binding of dynein controls bidirectional long-range motility of early endosomes. Proc Natl Acad Sci U S A **108**, 3618–23 (2011).
84. Soppina, V., Rai, A.K., Ramaiya, A.J., Barak, P., Mallik, R.: Tug-of-war between dissimilar teams of microtubule motors regulates transport and fission of endosomes. Proc Natl Acad Sci U S A **106**, 19,381–6 (2009).
85. Svoboda, K., Block, S.M.: Force and velocity measured for single kinesin molecules. Cell **77**, 773 (1994).
86. Svoboda, K., Schmidt, C.F., Schnapp, B.J., Block, S.M.: Direct observation of kinesin stepping by optical trapping interferometry. Nature **365**, 721–727 (1993).
87. Toba, S., Watanabe, T.M., Yamaguchi-Okimoto, L., Toyoshima, Y.Y., Higuchi, H.: Overlapping hand-over-hand mechanism of single molecular motility of cytoplasmic dynein. Proc Natl Acad Sci USA **103**, 5741 (2006).
88. van Kampen, N.: Stochastic Processes in Physics and Chemistry. Elsevier, Amsterdam (1992).
89. Veigel, C., Coluccio, L.M., Jontes, J.D., Sparrow, J.C., Milligan, R.D., Molloy, J.E.: The motor protein myosin-I produces its working stroke in two steps. Nature **398**, 530–533 (1999).
90. Vershinin, M., Carter, B.C., Razafsky, D.S., King, S.J., Gross, S.P.: Multiple-motor based transport and its regulation by tau. Proc Natl Acad Sci U S A **104**, 87–92 (2007).
91. Visscher, K., Schnitzer, M.J., Block, S.M.: Single kinesin molecules studied with a molecular force clamp. Nature **400**, 184 (1999).
92. Walter, W.J., Koonce, M.P., Brenner, B., Steffen, W.: Two independent switches regulate cytoplasmic dynein's processivity and directionality. Proc Natl Acad Sci U S A **109**, 5289–93 (2012).
93. Wang, Z., Li, M.: Force-velocity relations for multiple-molecular-motor transport. Phys Rev E **80**, 041923 (2009).
94. Welte, M.A.: Bidirectional transport along microtubules. Curr Biol **14**, R525–37 (2004).
95. Welte, M.A., Gross, S.P.: Molecular motors: a traffic cop within? HFSP J **2**, 178–82 (2008).
96. Xu, J., Shu, Z., King, S.J., Gross, S.P.: Tuning multiple motor travel via single motor velocity. Traffic **13**, 1198–205 (2012).

97. Yildiz, A., Forkey, J.N., McKinney, S.A., Ha, T., Goldman, Y.E., Selvin, P.R.: Myosin V walks hand-over-hand: Single fluorophore imaging with 1.5-nm localization. Science **300**, 2061–2065 (2003).
98. Yildiz, A., Selvin, P.R.: Fluorescence imaging with one nanometer accuracy: application to molecular motors. Acc Chem Res **38**, 574–82 (2005).
99. Yildiz, A., Tomishige, M., Gennerich, A., Vale, R.D.: Intramolecular strain coordinates kinesin stepping behaviour along microtubules. Cell **134**, 1030–1040 (2008).
100. Yildiz, A., Tomishige, M., Vale, R.D., Selvin, P.R.: Kinesin walks hand-over-hand. Science **303**, 676–678 (2004).
101. Zhang, Y.: Cargo transport by several motors. Phys Rev E **83**, 011909 (2011).

# Chapter 4
# Biofilament Dynamics: Line-to-Rod-Level Descriptions

**Wonmuk Hwang**

**Abstract** Conformational dynamics of a biofilament is an essential aspect of its function. It can be considered in three different scales: Atomic level; rod level that considers the finite cross section of the filament and axial twist; and line level that only considers the filament's contour. I explain and compare basic concepts for the latter two levels of descriptions. At the line level, the contour length description is introduced, which is extended to the triad description at the rod level. Two case studies are presented, one on generation of the line-level contour in thermal equilibrium, the other on solving Kirchhoff's equations for bending of a clamped rod. As the experimental resolution in measuring the dynamics of biofilaments is improving, it is expected that applicability of these quantitative descriptions will increase.

## 4.1 Introduction: Describing Biofilament Behavior at Three Scales

The majority of our body's constituents have filamentous geometry: Proteins, polysaccharides, and nucleic acids are all biopolymers. Next in length scale in terms of filament diameter, F-actin in the cytoplasm and fibrillar collagen in the extracellular matrix, are among the most abundant proteins in the world [8, 28]. Higher order structures such as actin stress fibers and collagen fibers are formed and carry out crucial function. It is thus necessary to know the physical and mechanical aspects of biofilaments on different length scales: Interaction with other proteins or assembly of biofilaments occur via specific interactions at the atomic level. Here, "physical and mechanical aspects" refer to the dynamics of individual subunits forming the biofilament viewed as folded polypeptide chains. At the next level, bending and twisting behaviors of a biofilament, over length scales longer than its transverse

W. Hwang (✉)
Departments of Biomedical Engineering and Materials Science and Engineering,
Texas A&M University, College Station, TX, USA
e-mail: hwm@tamu.edu

W. Hwang
Korea Institute for Advanced Study, Seoul, Korea



S. De et al. (eds.), *Multiscale Modeling in Biomechanics and Mechanobiology*, DOI 10.1007/978-1-4471-6599-6_4

dimension, can be understood by approximating it as a continuum rod. The underlying assumption is that conformational fluctuation of individual subunits is in rapid local equilibrium compared to the timescale of the filament motion. At a still higher level, if we consider a much longer portion of the filament where its transverse dimension can be ignored altogether, and on timescales during which the longer portion moves, we ca use the line description.

While modeling the biofilament behavior on each of the above three scales is an actively evolving area of research, crossing these scales is far less explored. For the atomistic to rod levels, one can carry out molecular dynamics simulation using atomic structures of biofilaments and extract rod-level descriptors such as bending, stretching, and torsional stiffness [19, 24]. For the rod to line levels, the linkage is easier to make, since models at the two levels are already in the continuum domain. The distinction is made depending on whether internal motion of the rod's cross section can be ignored or not. However, for a student or a researcher who tries to study mechanics of biofilament at these two levels, the first practical challenge is learning extensively developed theories on respective scales. Elasticity of a rod, not necessarily biological, has a long history and is also a discipline of applied mathematics [6, 22]. The line-level polymer dynamics is a highly advanced field of physics and chemistry [5, 7]. While it is in principle possible to learn the two theories and apply them to modeling biofilaments, given the fact that mathematical theories have not permeated sufficiently in biological research, and with the worrisome trend that many students are becoming less diligent in learning and using mathematical methods, but instead rely more on ready-made computer softwares, even learning basics of a physical theory can be a significant burden.

Here I give a brief overview of the basic concepts and equations in the line- and rod-level filament mechanics. As an introductory tutorial, I present hands-on numerical schemes in two simple cases. Conceptual linkage between the line- and rod-level descriptions is given. While this chapter is aimed at entry-level graduate students and those alike, certain basic knowledge is assumed, which can be readily found in available textbooks [4, 14]. Yet, I derive most expressions step-by-step that are often skipped in the literature, conveniently replaced by phrases such as "It can be shown that…," or "It is straightforward to show …." Although the equations might look trivial to the authors, as a reader, sometimes I find it fairly difficult and time-consuming to derive or understand them. With the spirit of this "cookbook," I tried to make derivations accessible to those with undergraduate-level calculus knowledge.

## 4.2 Line-Level Mechanics

### *4.2.1 Description of the Contour*

The position vector of a point along a line or a curve is parametrized by the contour length $s$, $\boldsymbol{r} = \boldsymbol{r}(s)$ (Fig. 4.1a). We can also regard the contour as the trajectory of a point particle. In this case, $s$ corresponds to both the travel distance along the curve

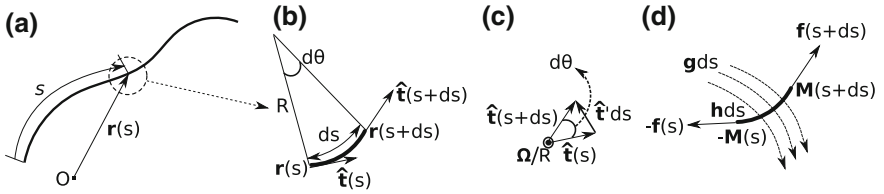


**Fig. 4.1** Contour length description of a filament as a line. **a** $\boldsymbol{r} = \boldsymbol{r}(s)$ is the position vector of a point on the filament relative to a fixed origin $O$, parametrized by the distance $s$ along the contour from one end of the filament. **b** An infinitesimal segment of length d$s$ approaches arc of a *circle* of radius $R$, with opening angle $\theta$. Tangential vectors at the two ends of the arc are $\boldsymbol{t}(s)$ and $\boldsymbol{t}(s + \mathrm{d}s)$. **c** $\boldsymbol{t}(s + \mathrm{d}s) - \boldsymbol{t}(s) \simeq \boldsymbol{t}'\mathrm{d}s$, so $\boldsymbol{t}'$ is normal to $\boldsymbol{t}$ and points to the center of the *circle* in (**b**). Since $|\boldsymbol{t}| = 1$, $d\theta = |\boldsymbol{t}'|\mathrm{d}s$, and from (b), $Rd\theta = \mathrm{d}s$. Combining these two, we get $|\boldsymbol{t}'| = \frac{1}{R}$, which is the curvature. The curvature vector $\frac{\boldsymbol{\Omega}}{R} = \boldsymbol{t} \times \boldsymbol{t}'$ is perpendicular to the page. **d** Forces and torques on a segment of length d$s$. $\boldsymbol{g}$ and $\boldsymbol{h}$ are external force and torque per unit length of the filament, respectively

and the travel time. Its "velocity" has magnitude 1 ($\boldsymbol{v} = \frac{\mathrm{d}\boldsymbol{r}}{\mathrm{d}s} \equiv \boldsymbol{r}'$, where $|\mathrm{d}\boldsymbol{r}| = \mathrm{d}s$), and it is in direction tangential to the contour at $\boldsymbol{r}(s)$. This defines the unit *tangential vector*:

$$\boldsymbol{t} = \frac{\mathrm{d}\boldsymbol{r}}{\mathrm{d}s} \tag{4.1}$$

Continuing with the analogy to a particle trajectory, since the velocity vector $\boldsymbol{t}$ has a constant magnitude, the "acceleration" $\boldsymbol{t}'$ will arise only from the change in direction, hence perpendicular to $\boldsymbol{t}$. Using $\boldsymbol{t}$ and $\boldsymbol{t}'$, we can define the *curvature vector*:

$$\boldsymbol{\kappa} = \frac{\boldsymbol{\Omega}}{R} \equiv \boldsymbol{t} \times \boldsymbol{t}'. \tag{4.2}$$

From Fig. 4.1c, $\boldsymbol{\Omega}$ is a unit vector perpendicular to the plane locally spanning the contour. The magnitude of $\boldsymbol{t} \times \boldsymbol{t}'$ is denoted by $R^{-1}$, with $R$ being the *radius of curvature*. The unit vectors $R\boldsymbol{t}'$ and $\boldsymbol{\Omega}$ are both perpendicular to the contour, and are respectively called *normal* and *binormal* vectors. The coordinate basis $\{R\boldsymbol{t}', \boldsymbol{\Omega}, \boldsymbol{t}\}$ (normal, binormal, tangential) is called the *Frenet basis* [3].

### *4.2.2 Dynamics of the Line-Level Filament*

In Fig. 4.1d, a segment of length d$s$ in the filament experiences internal forces $-\boldsymbol{f}(s)$ and $\boldsymbol{f}(s + \mathrm{d}s)$ at its ends. The sign of force is chosen such that it is positive in the direction of increasing $s$, so that the force $-\boldsymbol{f}(s)$ is the force applied by the portion of the filament with contour length less than $s$ on the cross section of the segment at $s$. $\boldsymbol{g}$ is the external force on the filament per unit length, for example, due to gravity, electric field, or viscous drag from the medium. The net force on the segment is

$\boldsymbol{f}(s+\mathrm{d}s)-\boldsymbol{f}(s)+\boldsymbol{g}\mathrm{d}s$. Denoting the linear mass density of the filament by $\rho$ (mass of the segment is $\rho \mathrm{d}s$) and the time derivative by a dot over a variable

$$\rho\ddot{\boldsymbol{r}} = \boldsymbol{f}' + \boldsymbol{g}. \tag{4.3}$$

In the case of rotation, we denote external torque per unit length by $\boldsymbol{h}$ At $s$, $-\boldsymbol{f}(s)$ has zero moment arm hence does not exert any torque on the segment. $\boldsymbol{f}(s+\mathrm{d}s)$ applies a torque $\boldsymbol{t}\mathrm{d}s \times \boldsymbol{f}(s+\mathrm{d}s) \simeq \boldsymbol{t} \times \boldsymbol{f}(s)\mathrm{d}s$ to the first order in $\mathrm{d}s$. The net torque on the segment is thus $\boldsymbol{M}'\mathrm{d}s + \boldsymbol{t} \times \boldsymbol{f}(s)\mathrm{d}s + \boldsymbol{h}\mathrm{d}s$ ($\boldsymbol{M}'$ arises in the same way as $\boldsymbol{f}'$ in Eq. 4.3). Denoting the moment of inertia of the segment by $J ds$, and angular velocity at $s$ by $\boldsymbol{\omega}$, we get

$$J\dot{\boldsymbol{\omega}} = \boldsymbol{M}' + \boldsymbol{t} \times \boldsymbol{f}(s) + \boldsymbol{h}. \tag{4.4}$$

In most cases where biofilaments undergo overdamped motion, the left-hand sides of Eqs. 4.3 and 4.4 can be set to zero, and $\boldsymbol{g}$ is the force due to viscous drag. In the length scale of biomolecules, rotational field is usually absent, so $\boldsymbol{h} = 0$. Equations 4.3 and 4.4 simplify to

$$\boldsymbol{f}' = -g, \qquad \boldsymbol{M}' = \boldsymbol{f} \times \boldsymbol{t}. \tag{4.5}$$

Furthermore, many biofilaments can be regarded as inextensible. This is because extension of covalent bonds results in much less deformation than by bending and dihedral motions of bonds [18, 19]. In the case of self-assembled filaments such as amyloid, F-actin, or microtubule, noncovalent interactions holding subunits are mostly short-ranged hydrogen bonds, which are again nearly inextensible [24]. Besides, while small amounts of local bending can lead to large conformational change of the filament as a whole, a small extension in length does not yield a noticeable difference in conformation. Once we approximate the filament as inextensible, the internal force $\boldsymbol{f}$ merely propagates along the filament, hence does not depend on its material property, which means an infinite extensional modulus. On the other hand, torque $\boldsymbol{M}$ depends not only on the curvature of the filament, but also depends on the material property—a stiffer filament bends less under a given torque. Unlike $\boldsymbol{f}$, a *constitutive relation* is thus required to find the filament deformation under $\boldsymbol{M}$. For this, we consider a case where the filament undergoes gentle deformation about its equilibrium shape. Since the potential energy profile around the minimum starts with the second order (harmonic) term, we can assume a linear behavior as

$$\boldsymbol{M} = K_f(\boldsymbol{\kappa} - \boldsymbol{\kappa}^u). \tag{4.6}$$

Here $K_f$ is *flexural rigidity* or *bending stiffness* of the filament, and $\boldsymbol{\kappa}$ and $\boldsymbol{\kappa}^u$ are respectively the current and the equilibrium (undeformed) curvature (Eq. 4.2). We also assume that the filament is isotropic, so that $K_f$ does not depend on the bending direction. Recalling that $\boldsymbol{t} = \boldsymbol{r}'$, the right-hand side of Eq. 4.6 involves up to second-order derivative of $\boldsymbol{r}$. Plugging Eq. 4.6 into Eq. 4.5 thus yields a pair of

partial differential equations for $\boldsymbol{r}$, first order in time (viscous drag $\boldsymbol{g}$ is proportional to the velocity of the segment, $\dot{\boldsymbol{r}}$) and third order in $s$. For given initial and boundary conditions, they can be integrated to yield $\boldsymbol{r}(s,t)$. Equations 4.5 and 4.6 have been widely studied and applied to different systems. Analytic solutions for simple static cases, such as bending and buckling, are found in standard textbooks on elasticity (for example, see chapter II of Ref. [22]). Reference [31] gives an excellent analysis of mechanically driven filaments such as bacterial flagellum.

Keeping the novice-minded approach, let us find the elastic energy stored upon bending the filament. From elementary mechanics, the work done by a torque $M$ in turning an object by an angle $d\theta$ is $Md\theta$. If $M = k\theta$ (linear), work done for turning the object to an angle $\theta$ is $\int_0^\theta Md\theta = \frac{k}{2}\theta^2$. By analogy, we work on a one-dimensional version of Eq. 4.6 with $\kappa_u = 0$ (a straight filament in equilibrium). In Fig. 4.1b, denote the length and bending angle of the segment as $\Delta s$ and $\Delta\theta$, respectively. We have

$$M = \frac{K_f}{R} = K_f \frac{\Delta\theta}{\Delta s} \tag{4.7}$$

The work $W$ done when bending the segment from straight to a bending angle $\Delta\theta$ is then $W = \frac{K_f}{2\Delta s}\Delta\theta^2 = \frac{K_f}{2R^2}\Delta s$ ($R\Delta\theta = \Delta s$). Thus, $\frac{W}{\Delta s} = \frac{K_f}{2R^2}$ is the *bending energy per unit length* of the segment. Using this for Eq. 4.6, we get

$$\frac{W}{\Delta s} = \frac{K_f}{2}(\boldsymbol{\kappa} - \boldsymbol{\kappa}^u)^2. \tag{4.8}$$

The equilibrium curvature $\boldsymbol{\kappa}^u$ serves as the reference configuration in the same way as a Hookean spring with stiffness $k$ and equilibrium length $x_0$ has energy $\frac{k}{2}(x - x_0)^2$.

### 4.2.3 Case Study: Filament Conformation in Thermal Equilibrium

Most biofilaments undergo thermal motion. Even for macroscopic collagen fibers, local thermal motion of individual collagen molecules forming the fiber is critical for their biological function. Random "thermal kicks" from the surrounding medium deform the filament. The characteristic length scale for the filament's thermal bending motion is given by the *persistence length* $l_p$. It is defined via the correlation function between two tangential vectors separated by a contour length $s$:

$$\langle \boldsymbol{t}(s_0) \cdot \boldsymbol{t}(s_0 + s) \rangle = e^{-s/l_p}. \tag{4.9}$$

Angular brackets on the left-hand side of Eq. 4.9 denote the *ensemble average*, meaning that average is made over a large number of identical filaments each undergoing different thermal motion. $s_0$ is an arbitrary reference point along the filament.

We consider a homogeneous filament so that the correlation function depends only on the distance $s$ between the two points, not $s_0$. Continuing the analogy between the filament contour and the trajectory of a moving particle, $l_p$ corresponds to the correlation time of a particle undergoing Brownian motion. At a given temperature $T$, a stiffer filament will remain straighter, hence $l_p$ will be longer. For a filament of a given stiffness, it will bend more at a higher temperature due to stronger thermal kicks. These two conditions combine to [5, 14]

$$l_p = \frac{K_f}{k_B T}. \tag{4.10}$$

Here, $k_B$ is the Boltzmann constant. We ca use a scaling argument to understand the origin of Eq. 4.10: Since thermal force bends the filament, the average elastic energy, $\frac{K_f}{l_p}$ ($\frac{K_f}{2l_p^2} l_p$, ignoring 2), should be equal to the thermal energy $k_B T$, yielding Eq. 4.10. If we follow a more rigorous derivation [5, 14], Eq. 4.10 is for filaments in three dimensions where the filament can bend in two orthogonal directions. In two dimensions, bending can occur only on a plane, so only half of the thermal energy can bend the filament, making it straighter: $l_p = 2\frac{K_f}{k_B T}$ (2-dim) [26].

The definition of $l_p$ (Eq. 4.9) involves an ensemble average, where we need to analyze many replicas of the filament. Let us ask a question on de-averaging: For a given $l_p$, how does a typical filament look? For this we use computer to generate example contours. For simplicity, we work in two dimensions. Take a segment of length $\Delta s$ and place it along the $x$-axis, with its left end at the origin (point $A$ in Fig. 4.2a). When it is bent to an angle $\theta_1$, the length $\Delta l_1$ of the line joining its two ends ($\overline{AB}$) is at an angle $\phi_1 = \theta_1/2$ relative to the $x$-axis. Also, $\Delta l_1 = 2R_1 \sin\frac{\theta_1}{2} = 2\frac{\Delta s}{\theta_1}\sin\frac{\theta_1}{2}$, so the coordinate of point $B$ is $(\Delta l_1 \sin\phi_1, \Delta l_1 \cos\phi_1)$. Next add the

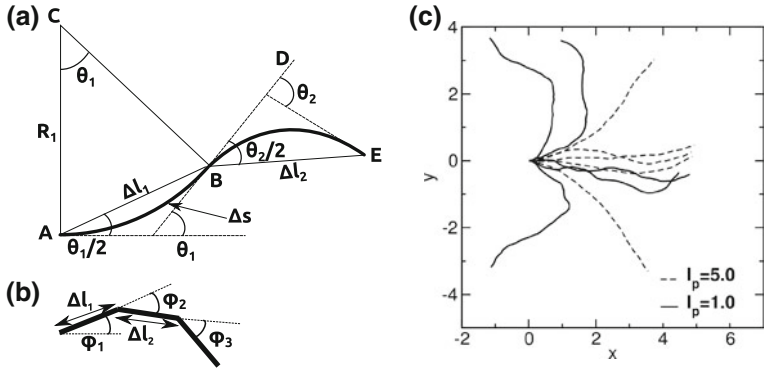


**Fig. 4.2** Generating a contour with a given persistence length $l_p$. **a** Two successive segments of length $\Delta s$ each. The local bending angle of segment $i$ is $\theta_i$ ($i = 1, 2, \ldots$). **b** Representing the contour using straight segments of length $\Delta l_i$. The angle $\phi_i$ between neighboring segments is $\frac{\theta_i}{2}$. **c** Sample contours starting horizontal at the origin. *Dashed* $l_p = 5$, and *thick solid* $l_p = 1.0$. The length of each contour is 5. $\Delta s = 0.01$ was used

second segment of length $\Delta s$ at $B$. If the equilibrium shape of the filament is straight, we need to work relative to the tangential line $\overline{BD}$. Suppose the new segment is bent to an angle $\theta_2$. It will be at an angle $\phi_2 = \theta_2/2$ relative to $\overline{BD}$. The end-to-end distance of the segment is, following a similar argument, $\Delta l_2 = 2\frac{\Delta s}{\theta_2}\sin\frac{\theta_2}{2}$. Relative to the $x$-axis, it will be at an angle $\theta_1 + \phi_2$, so the position of the point $D$ will be determined by adding the vector $(\Delta l_2 \cos(\theta_1 + \phi_2), \Delta l_2 \sin(\theta_1 + \phi_2))$ to $B$. Iterating this procedure, we can generate a contour with a given series of local bending angles $\{\theta_1, \theta_2, \ldots\}$ and segment length $\Delta l_i$. Let $\boldsymbol{r}_i$ $(i = 1, 2, \ldots)$ be the position vector of the end of the $i$-th segment. We have

$$\begin{aligned} &\boldsymbol{r}_i = \boldsymbol{r}_{i-1} + \Delta \boldsymbol{r}_i, \quad \Delta l_i = 2\frac{\Delta s}{\theta_i}\sin\frac{\theta_i}{2} \\ &\Delta \boldsymbol{r}_i = \left( \Delta l_i \cos\left[\sum_{j=0}^{i-1}\theta_j + \frac{\theta_i}{2}\right], \Delta l_i \sin\left[\sum_{j=0}^{i-1}\theta_j + \frac{\theta_i}{2}\right]\right) \\ &(i = 1, 2, \ldots;\ \boldsymbol{r}_0 \equiv (0,0), \theta_0 \equiv 0). \end{aligned} \tag{4.11}$$

What remains is to generate a set of angles $\{\theta_i\}$ that are consistent with the contour's persistence length $l_p$. This can be done via energy balance argument. When a segment $\Delta s$ is bent to an angle $\theta$, its bending energy is, as explained above Eq. 4.8, $\Delta E = \frac{K_f}{2}\frac{\theta^2}{\Delta s}$. From statistical thermodynamics, the probability distribution $P(\theta)$ that the segment bends to an angle $\theta$ at temperature $T$ follows the Boltzmann distribution

$$P(\theta) \sim e^{-\frac{\Delta E}{k_B T}} = e^{-\frac{K_f}{2k_B T}\frac{\theta^2}{\Delta s}} = e^{-\frac{l_p}{4\Delta s}\theta^2}. \tag{4.12}$$

where we used $l_p = 2K_f/k_B T$ for 2 dimensions. Equation 4.12 is a Gaussian distribution with zero mean and standard deviation $\sigma(\theta) = \sqrt{2\Delta s/l_p}$ (the variance $\sigma(\theta)^2$ of a Gaussian distribution is half the inverse of the prefactor for $\theta^2$ in the exponent). Thus, to generate a contour of persistence length $l_p$ in two dimensions with segment size $\Delta s$, generate Gaussian-distributed random numbers $\theta_i$ according to Eq. 4.12, and use them in Eq. 4.11.

Sample contours of length 5 generated in this way for two different values of $l_p$ are in Fig. 4.2c. While $l_p$ is typically considered as the length beyond which the memory of the initial filament direction is lost, when the contour length is equal to $l_p$, as for the case $l_p = 5.0$ in Fig. 4.2c, the filament is still fairly straight, i.e., semiflexible. It appears flexible only when the contour length is much greater than its persistence length.

For our approach be valid, $\Delta s$ must be sufficiently small so that its bent shape looks like an arc of a circle, not a random contour, as in Fig. 4.2a. This can be achieved by choosing $\Delta s/l_p \ll 1$, which in turn means the bending angle $\theta$ is small and narrowly distributed, $\sigma(\theta) \ll 1$. Among the examples in Fig. 4.2c, for $l_p = 1$ and $\Delta s = 0.01$, $\sigma(\theta) = \sqrt{2\Delta s/l_p} = 0.141$ rad $(=8.10°)$, which is reasonably small.

Equation 4.9 only tells how the correlation function behaves, and it does not require any particular probability distribution for the angle between $\boldsymbol{t}(s_0)$ and $\boldsymbol{t}(s_0 + s)$. Leveraging on the fact that bending of the filament occurs via thermal fluctuation, we used Eq. 4.12 for the probability distribution of the bending angles among discretized segments.

## 4.3 Rod-Level Mechanics

The main difference between line- and rod-level descriptions is that the latter considers finite cross section of the filament. As will be seen below, this makes the equations of motion significantly more complex. The price is worth to pay for, as it allows for describing more sophisticated behaviors of individual filaments, such as torsion-induced buckling, supercoiling, and perversion (note that sometimes there are a pair of kinks developed along a telephone cord, where the handedness of the cord is inverted between the kinks; check this for your landline phone!). Its relevance to a broad range of systems had led to the development of rod dynamics as a sub-discipline of mechanics or applied mathematics [9–12]. The earliest systematic treatment may be by Gustav Kirchhoff in the mid-nineteenth century [3, 6]. For this reason, an elastic rod is often called *Kirchhoff's rod*. The theory itself is simply a statement of force and torque balance along the rod. But applying it to different cases (meaning different initial and boundary conditions) is not easy both conceptually and computationally. Description of the equations of motion, strategies for solving them, and unfortunately, notations, differ among authors. These make it difficult for a beginner to learn this beautiful and powerful theory. The literature is divided roughly into two groups, one focused on theoretical aspect [3, 9–12], and the other on numerical implementation [1, 13, 16, 17]. The former tends to be intuitively and notationally clear, whereas the latter is easier or better at getting the results. Here I take the theoretical approach to introduce basic concepts and Kirchhoff's equations, then work out a simple example to explain how the equations are solved.

### *4.3.1 Triad Description*

The Frenet basis (Eqs. 4.1 and 4.2) is useful for describing the geometry of the filament contour. However, it provides little information about how much the filament is axially twisted, as the normal ($R\boldsymbol{t}'$) and binormal ($\boldsymbol{\Omega}$) vectors are determined by bending of the filament. Besides, when a region of a moving rod becomes locally straight, normal and binormal vectors become zero, losing orientational information of the cross section. This makes it necessary to use a coordinate frame that is attached to the material of the rod rather than the shape of the contour. The tangential vector $\boldsymbol{t}$ (Eq. 4.1) is well-defined for a rod if it possesses a continuous and differentiable

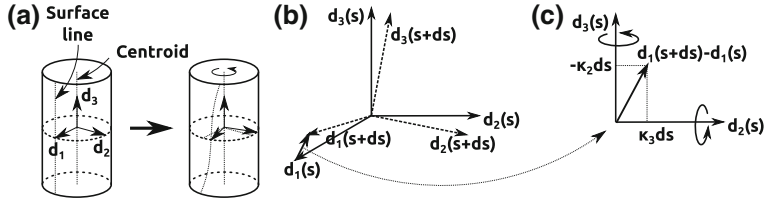


**Fig. 4.3** Triad description of a rod. **a** Material frame. The tangent vector along the rod's centroid line is $\boldsymbol{d_3}$. Perpendicular to it is $\boldsymbol{d_1}$ which points to a line fixed on the surface of the rod. When the rod twists, $\boldsymbol{d_1}$ rotates about $\boldsymbol{d_3}$ as the shape of the surface line changes. For this, $\boldsymbol{d_3}$ does not need to change direction, unlike the Frenet basis. **b**, **c** Meaning of the curvature vector $\boldsymbol{\kappa}$. **b** For a general deformation, triad at $s + \mathrm{d}s$ (*dashed arrows*) rotates relative to triad at $s$ (*solid arrows*). **c** For infinitesimal $\mathrm{d}s$, $\boldsymbol{d_1}(s+\mathrm{d}s) - \boldsymbol{d_1}(s) = \boldsymbol{d_1'}\mathrm{d}s$ is perpendicular to $\boldsymbol{d_1}$, hence lies on the $d_2 d_3$-plane. $\kappa_3 ds$ is the $\boldsymbol{d_2}$-component as $\boldsymbol{d_1}$ rotates about $\boldsymbol{d_3}$. Similarly, $-\kappa_2 ds$ is the $\boldsymbol{d_3}$-component of $\boldsymbol{d_1'}\mathrm{d}s$ for rotation of $\boldsymbol{d_1}$ about $\boldsymbol{d_2}$. The negative sign is because the right-handed rotation of $\boldsymbol{d_2}$ leads to a decrease in the $\boldsymbol{d_3}$-component of $\boldsymbol{d_1'}\mathrm{d}s$

centroid that corresponds to the contour in the line-level description. Herein we call it as $\boldsymbol{d_3}(s)$. Describing the twisting motion of the rod about $\boldsymbol{d_3}$ is conceptually simple: Draw a line on the surface of the rod parallel to the contour (centroid). At each point along the contour, erect a unit vector $\boldsymbol{d_1}$ locally perpendicular to the contour, toward the surface line. If the rod twists, the surface line will change its shape, so will the direction of $\boldsymbol{d_1}$ (Fig. 4.3a). Assigning $\boldsymbol{d_1}$ and $\boldsymbol{d_3}$ fixes $\boldsymbol{d_2} \equiv \boldsymbol{d_3} \times \boldsymbol{d_1}$. The local coordinate basis $\{\boldsymbol{d_1}(s), \boldsymbol{d_2}(s), \boldsymbol{d_3}(s)\}$ forms a *triad* that describes local conformation of the rod. It is also called the *material frame*. Some authors use the notation $\boldsymbol{T} = \boldsymbol{d_3}$, and call $\boldsymbol{d_1}$ and $\boldsymbol{d_2}$ respectively as $\boldsymbol{U}$ and $\boldsymbol{V}$, and re-order them to $\{\boldsymbol{T}, \boldsymbol{U}, \boldsymbol{V}\}$ [1, 20]. Here, we use $\boldsymbol{d_i}$ [3, 9] as it enables the index notation in algebraic operations. One can remember $\boldsymbol{d_i}$ as *d*irectional basis.

Note that any choices for $\boldsymbol{d_1}$ and $\boldsymbol{d_2}$ work as long as they are perpendicular and lie on the local cross section of the rod. A popular choice is using the two principal axes of the cross section, which makes the constitutive relation simpler. To be more precise, the cross section may change shape or warp as the rod deforms [22], which makes it difficult to maintain orthonormality of the triad. However, as long as such changes are small, we can assume the cross section to be planar and has a fixed shape. References [3, 6] give an in-depth discussion of higher order corrections to Kirchhoff's theory. We do not consider them here since the lowest order theory is already useful and complex enough in most cases. Besides, applying Kirchhoff's theory to a biofilament is a gross idealization anyway (e.g., the DNA double helix is often described as a cylindrical rod). Our main goal is getting a semi-quantitative and intuitive picture, which is not altered significantly by higher order corrections.

To describe local deformation of a rod, we need only three degrees of freedom; two directions of bending and axial twist. Three unit vectors forming the triad are thus more than necessary, and other descriptions have been proposed [2, 20]. Although some of them might be more economical, the triad description makes

the deformation and mechanics easier to understand, hence we stick to this more traditional way.

Orthonormality of the triad can be written as $\boldsymbol{d_i} \cdot \boldsymbol{d_j} = \delta_{ij}$, where $\delta_{ij} = 0\,(i \neq j)$ or $1\,(i = j)$, is the Kronecker-delta. Differentiating this relation with $s$ gives ($\delta_{ij}$ is independent of $s$)

$$\boldsymbol{d}_i' \cdot \boldsymbol{d_j} + \boldsymbol{d_i} \cdot \boldsymbol{d}_j' = 0 \tag{4.13}$$

Analogous to Fig. 4.1c, $\boldsymbol{d}_i'$ is perpendicular to $\boldsymbol{d_i}$, which can also be seen from Eq. 4.13 by setting $j = i$. If we decompose $\boldsymbol{d}_i'$ using the triad, $\boldsymbol{d}_i' = \sum_k K_{ik}\boldsymbol{d_k}$, we get $K_{ii} = 0$. Equation 4.13 also suggests $K_{ij} + K_{ji} = 0$, so that $K_{ij}$ is an antisymmetric matrix with zero diagonal elements. In other words, we can write

$$\boldsymbol{d}_i' = \boldsymbol{\kappa} \times \boldsymbol{d_i} \tag{4.14}$$

This generalizes Eq. 4.2 for the line-level description. We call $\boldsymbol{\kappa}$ again as the *curvature* vector. Since the triad is also a function of time, $\boldsymbol{d_i} = \boldsymbol{d_i}(s, t)$, we can apply the same argument to the time derivative of $\boldsymbol{d_i} \cdot \boldsymbol{d_j}$, and introduce the *spin* vector $\boldsymbol{\omega}$:

$$\dot{\boldsymbol{d}}_i = \boldsymbol{\omega} \times \boldsymbol{d_i}. \tag{4.15}$$

Note that $\boldsymbol{\kappa} = \boldsymbol{\kappa}(s, t)$ and $\boldsymbol{\omega} = \boldsymbol{\omega}(s, t)$. To better understand these expressions, let us take an example, $\boldsymbol{d}_1' = \kappa_3 \boldsymbol{d_2} - \kappa_2 \boldsymbol{d_3}$. As shown in Fig. 4.3c, $\kappa_3$ relates to the rate of rotation of $\boldsymbol{d_1}$ about $\boldsymbol{d_3}$, and similarly, $\kappa_2$ is about $\boldsymbol{d_2}$. We can thus see that $\kappa_i$ and $\omega_i$ are rotation rates of the triad about $\boldsymbol{d_i}$ in $s$ and $t$, respectively: $\kappa_{1,2}$ and $\omega_{1,2}$ are for bending of the rod about the two principal axes, and $\kappa_3$ and $\omega_3$ are for twist. To find the relation between $\boldsymbol{\kappa}$ and $\boldsymbol{\omega}$, we use the condition $\partial^2 \boldsymbol{d_i}/\partial s \partial t = \partial^2 \boldsymbol{d_i}/\partial t \partial s$, and use Eqs. 4.14 and 4.15:

$$\begin{aligned} \frac{\partial}{\partial s}\frac{\partial \boldsymbol{d_i}}{\partial t} &= \frac{\partial}{\partial s}(\boldsymbol{\omega} \times \boldsymbol{d_i}) = \boldsymbol{\omega}' \times \boldsymbol{d_i} + \boldsymbol{\omega} \times (\boldsymbol{\kappa} \times \boldsymbol{d_i}) \\ &= \boldsymbol{\omega}' \times \boldsymbol{d_i} + \omega_i \boldsymbol{\kappa} - (\boldsymbol{\omega} \cdot \boldsymbol{\kappa})\boldsymbol{d_i}. \end{aligned} \tag{4.16}$$

For the last line, we used the vector identity $\boldsymbol{A} \times (\boldsymbol{B} \times \boldsymbol{C}) = \boldsymbol{B}(\boldsymbol{A} \cdot \boldsymbol{C}) - \boldsymbol{C}(\boldsymbol{A} \cdot \boldsymbol{B})$. Also note that $\boldsymbol{d_i}$ is the $i$-th basis vector of the triad, whereas $\omega_i = \boldsymbol{\omega} \cdot \boldsymbol{d_i}$ is the $i$-th component of $\boldsymbol{\omega}$, which is a scalar. We can obtain a similar expression for the other derivative

$$\partial^2 \boldsymbol{d_i}/\partial t \partial s = \dot{\boldsymbol{\kappa}} \times \boldsymbol{d_i} + \kappa_i \boldsymbol{\omega} - (\boldsymbol{\omega} \cdot \boldsymbol{\kappa})\boldsymbol{d_i}. \tag{4.17}$$

Apply $(\sum_{i=1}^{3} \boldsymbol{d_i} \times\,)$ to Eqs. 4.16, 4.17, and equate:

$$\sum_{i=1}^{3} \boldsymbol{d_i} \times (\boldsymbol{\omega}' \times \boldsymbol{d_i}) + \sum_{i=1}^{3} \omega_i \boldsymbol{d_i} \times \boldsymbol{\kappa} = 3\boldsymbol{\omega}' - \sum_i (\boldsymbol{\omega}')_i \boldsymbol{d_i} + \boldsymbol{\omega} \times \boldsymbol{\kappa} = 2\boldsymbol{\omega}' + \boldsymbol{\omega} \times \boldsymbol{\kappa}$$

$$\sum_{i=1}^{3} \boldsymbol{d_i} \times (\dot{\boldsymbol{\kappa}} \times \boldsymbol{d_i}) + \sum_{i=1}^{3} \kappa_i \boldsymbol{d_i} \times \boldsymbol{\omega} = 3\dot{\boldsymbol{\kappa}} - \sum_i (\dot{\boldsymbol{\kappa}})_i \boldsymbol{d_i} + \boldsymbol{\kappa} \times \boldsymbol{\omega} = 2\dot{\boldsymbol{\kappa}} + \boldsymbol{\kappa} \times \boldsymbol{\omega}$$

$$\therefore \quad \boldsymbol{\omega}' - \dot{\boldsymbol{\kappa}} = \boldsymbol{\kappa} \times \boldsymbol{\omega}. \tag{4.18}$$

Equation 4.18 is called the *compatibility condition*.

### 4.3.2 Equation of Motion

As for the line-level description, let $\boldsymbol{r}(s)$ be the position vector of the rod's centroid at contour length $s$ (Fig. 4.1a). The position vector $\boldsymbol{X}$ of a point within the rod is expressed as $\boldsymbol{X}(s, x_1, x_2, t) = \boldsymbol{r}(s, t) + x_1 \boldsymbol{d_1}(s, t) + x_2 \boldsymbol{d_2}(s, t)$, with $x_1$ and $x_2$ as components of $\boldsymbol{X}$ on the cross section of the rod at $s$. For force balance, integrating the internal stress over the rod's cross section yields the internal force $\boldsymbol{f}$ that we introduced in line-level mechanics. As in Fig. 4.1d, if we consider a segment of the rod with length d$s$, the net internal force at $s$ and $s + \mathrm{d}s$ is $\boldsymbol{f}'\mathrm{d}s$. Similarly, $\boldsymbol{g}(s)\mathrm{d}s$ is the net external force on the center of mass of the segment. Let $\rho_V$ be the volumetric mass density of the rod. Newton's second law of dynamics becomes, as for Eq. 4.3,

$$\int_A \rho_V \ddot{X} dA = \boldsymbol{f}' + \boldsymbol{g} \tag{4.19}$$

We now make two assumptions: Let the rod be homogeneous so $\rho_V$ is constant. Also assume that the rod's cross section has a fixed shape and is symmetric relative to the principal axes, so that $\int_A x_{1,2} dA = 0$. These assumptions, although only approximately valid in real biofilaments, make equations more tractable. The left-hand side of Eq. 4.19 becomes: $\rho_V \int_A \ddot{X} dA = \rho_V \int_A (\ddot{\boldsymbol{r}} + x_1 \ddot{\boldsymbol{d}}_1 + x_2 \ddot{\boldsymbol{d}}_2) dA = \rho_V A \ddot{\boldsymbol{r}} = \rho \ddot{\boldsymbol{r}}$ ($A$: cross sectional area, $\rho \equiv \rho_V A$: linear mass density of the rod). In the homogeneous and symmetric case, Eq. 4.19 thus becomes identical to Eq. 4.3. In fact, Eqs. 4.3 and 4.4 implicitly make these two assumptions. To proceed further, differentiate Eq. 4.3 relative to $s$, and use $\boldsymbol{r}' = \boldsymbol{d_3}$ to get

$$\rho \ddot{\boldsymbol{d}}_3 = \boldsymbol{f}'' + \boldsymbol{g}' \tag{4.20}$$

With the triad description, the torque balance equation becomes, as for Eq. 4.4,

$$\begin{aligned} \boldsymbol{M}' + \boldsymbol{d_3} \times \boldsymbol{f} + \boldsymbol{h} &= \int_A \rho_V \left[ (x_1 \boldsymbol{d_1} + x_2 \boldsymbol{d_2}) \times (x_1 \ddot{\boldsymbol{d}}_{\boldsymbol{1}} + x_2 \ddot{\boldsymbol{d}}_{\boldsymbol{2}}) \right] dA \\ &= \int_A \rho_V \left( x_1^2 \boldsymbol{d_1} \times \ddot{\boldsymbol{d}}_{\boldsymbol{1}} + x_2^2 \boldsymbol{d_2} \times \ddot{\boldsymbol{d}}_{\boldsymbol{2}} \right) dA \quad \leftarrow \quad \int x_1 x_2 dA = 0 \\ &= \rho_V \left( I_1 \boldsymbol{d_1} \times \ddot{\boldsymbol{d}}_{\boldsymbol{1}} + I_2 \boldsymbol{d_2} \times \ddot{\boldsymbol{d}}_{\boldsymbol{2}} \right). \end{aligned} \tag{4.21}$$

For the last line, $I_{1,2} \equiv \int_A x_{1,2}^2 dA$ is the second moment of inertia of the cross section. Equation 4.21 is applicable for a rod whose cross section is symmetric in respective principal axes, such as an ellipse. If we further assume equivalence of the two principal axes such as in a cylinder, $I_1 = I_2 \equiv I$, and we get

$$\boldsymbol{M}' + \boldsymbol{d_3} \times \boldsymbol{f} + \boldsymbol{h} = \rho_V I \left( \boldsymbol{d_1} \times \ddot{\boldsymbol{d}}_{\boldsymbol{1}} + \boldsymbol{d_2} \times \ddot{\boldsymbol{d}}_{\boldsymbol{2}} \right). \tag{4.22}$$

Eqs. 4.20 and 4.22 are the equations of motion for the rod, also called *Kirchhoff's equations*. Unless the rod has internal chemical reactions that generate active force (this is possible for a bundle of filaments driven by motors, such as muscle fibers or cilia), and if we assume inextensibility as in the line-level mechanics, the internal force $\boldsymbol{f}(s,t)$ arises as a reaction force. On the other hand, the torque $\boldsymbol{M}$ depends on deformation, for which we need a constitutive law. The most widely used one is, as for the line-level description, the linear law. If we expand $\boldsymbol{M}$ using the triad, $\boldsymbol{M} = \sum_{i=1}^{3} M_i \boldsymbol{d_i}$,

$$M_1 = EI(\kappa_1 - \kappa_1^u), \qquad M_2 = EI(\kappa_2 - \kappa_2^u), \qquad M_3 = \mu J(\kappa_3 - \kappa_3^u), \tag{4.23}$$

where $E$ is Young's modulus, $\mu$ is the shear modulus, and $J$ is the axial moment of inertia (*cf.*, Eq. 4.4). For a circular cross section, $J = 2I$ [22]. The vector $\boldsymbol{\kappa}^u = \sum_{i=1}^{3} \kappa_i^u \boldsymbol{d_i}$ is the equilibrium curvature of the rod. For a straight rod, $\boldsymbol{\kappa}^u = 0$. Components of the torque in $\boldsymbol{d_i}$ do not mix together since we chose $\boldsymbol{d_1}$ and $\boldsymbol{d_2}$ as principal axes ($M_1$ is independent of $\kappa_2$, and *vice versa*).

When is the linear (harmonic) constitutive law applicable? For a well-folded biofilament, conformational fluctuation is around the energy minimum (equilibrium shape). In this case, linear behavior is usually guaranteed for small local deformations (which can still change the rod's overall shape significantly), as explained above. Larger deformations can be approximated as linear as long as they lie within the basin of attraction of the minimum. If deformation is even larger and the system moves to other local energy minima, the case has to be treated with multiple equilibrium conformations, where small deformation from each minimum can be locally treated harmonic. Also note that, linearity in the constitutive law does not imply linearity in the conformational behavior of the rod. Equation 4.22 is nonlinear ($\boldsymbol{d}_i$ and $\boldsymbol{f}$ are functions of $s$ and $t$), so the resulting motion can be quite complex. Although the linear constitutive law has wide range of applicability, if the biofilament locally denatures so that there is no well-defined energy minimum, the rod behaves flexible. In such cases, one needs to determine whether the denatured region(s) can

be treated as flexible joints while applying continuum elasticity to the well-folded portions.

For numerical implementation, let us de-dimensionalize variables. The answers are given in, for example, Refs. [3, 9]. Here we show how it's done. For simplicity, below we consider the case $\boldsymbol{g} = 0$, $\boldsymbol{h} = 0$, and $\boldsymbol{\kappa}^u = 0$. Let $a_t$, $a_s$, $a_f$, and $a_M$ be respectively characteristic time, length, force, and torque of the rod. We scale the corresponding dimensionful quantities

$$t = a_t t_0, \quad s = a_s s_0, \quad \boldsymbol{f} = a_f \boldsymbol{f_0}, \quad \boldsymbol{M} = a_M \boldsymbol{M_0}, \tag{4.24}$$

where we use a subscript 0 to denote dimensionless variables (later we will drop it). Time and $s$-derivatives can then be expressed as $\frac{\partial}{\partial t} = \frac{1}{a_t}\frac{\partial}{\partial t_0}$, and $\frac{\partial}{\partial s} = \frac{1}{a_s}\frac{\partial}{\partial s_0}$. From Eq. 4.20 (with $\boldsymbol{g} = 0$),

$$\frac{\rho_V A}{a_t^2}\ddot{d}_3 = \frac{a_f}{a_s^2} f_0'' \quad \rightarrow \quad \left(\frac{a_t}{a_s}\right)^2 = \frac{\rho_V A}{a_f}. \tag{4.25}$$

Here, derivatives are by dimensionless variables $t_0$ and $s_0$. We similarly de-dimensionalize Eq. 4.22:

$$\begin{aligned} \frac{a_M}{a_s}\boldsymbol{M}_0' + a_f \boldsymbol{d_3} \times \boldsymbol{f}_0 &= \frac{\rho_V I}{a_t^2}\left(\boldsymbol{d_1} \times \ddot{\boldsymbol{d}}_1 + \boldsymbol{d_2} \times \ddot{\boldsymbol{d}}_2\right) \\ \rightarrow \quad a_f = \frac{a_M}{a_s} &= \frac{\rho_V I}{a_t^2}. \end{aligned} \tag{4.26}$$

From Eq. 4.14, the dimension of $\boldsymbol{\kappa}$ is the inverse of length ($\boldsymbol{d_i}$ is a unit vector, hence dimensionless). Equation 4.23 can be de-dimensionalized as

$$\begin{aligned} a_M \boldsymbol{M}_{10} = \frac{EI}{a_s}\kappa_{10}, \quad a_M \boldsymbol{M}_{20} = \frac{EI}{a_s}\kappa_{20}, \quad a_M \boldsymbol{M}_{30} = \frac{\mu J}{a_s}\kappa_{30} \\ \rightarrow \quad a_M = \frac{EI}{a_s}. \end{aligned} \tag{4.27}$$

Inserting $a_f = \rho_V I / a_t^2$ (Eq. 4.26) into Eq. 4.25 yields $a_s = \sqrt{I/A}$. We plug this to Eq. 4.27, to get $a_M = E\sqrt{AI}$. Inserting these back to Eq. 4.26 gives $a_f = AE$ and $a_t = \sqrt{\rho_V I / AE}$, completing de-dimensionalization. The $\boldsymbol{d_3}$-component of Eq. 4.27 becomes $M_{30} = \frac{\mu J}{EI}\kappa_{30}$. Below we work only with de-dimensionalized variables and drop the subscript 0. The de-dimensionalized Kirchhoff's equations are

$$\ddot{\boldsymbol{d}}_3 = \boldsymbol{f}'' \tag{4.28a}$$

$$\boldsymbol{M}' + \boldsymbol{d_3} \times \boldsymbol{f} = \boldsymbol{d_1} \times \ddot{\boldsymbol{d}}_1 + \boldsymbol{d_2} \times \ddot{\boldsymbol{d}}_2 \tag{4.28b}$$

$$\boldsymbol{M} = \kappa_1 \boldsymbol{d_1} + \kappa_2 \boldsymbol{d_2} + \Gamma \kappa_3 \boldsymbol{d_3} \tag{4.28c}$$

Here, $\Gamma \equiv \mu J/EI$ is the only number that differs between systems. For a cylindrical rod, $\Gamma = 2\mu/E$. We also treat Eqs. 4.14 and 4.15 as dimensionless.

### 4.3.3 Numerical Implementation of Kirchhoff's Equations

The main idea underlying Kirchhoff's equations is to express vectors using the triad, a material frame following the rod, so that we can focus on conformational motion, not the center of mass rotation and translation of the rod as a whole. However, solving them is nontrivial. Most literature reach the point of showing Kirchhoff's equations or the corresponding equations, then jump to results of their calculations, sometimes only briefly mentioning about the method they used to integrate the equations. As will become clearer below, the difficulty lies not only in the use of integration algorithms, but more fundamentally, the approach depends on the problem under consideration. By analogy, knowing Newton's second law of dynamics ($\boldsymbol{F} = m\boldsymbol{a}$) is not enough to design a bridge or a bicycle. Keeping the novice spirit, here we take more steps to see *how* the equations are solved.

Since $\boldsymbol{d_i}$ depends on $s$ and $t$, derivatives of a vector ($\boldsymbol{f}$, $\boldsymbol{M}$, $\boldsymbol{\kappa}$, and $\boldsymbol{\omega}$) projected on the triad generate derivatives of the triad as well. We use this in expressing each component of Eq. 4.28. For notational simplicity, below we use the Einstein convention where the summation symbol $\sum_{i=1}^{3}$ is omitted if the same index appears more than twice in a term, so that $a_i b_i$ means $\sum_i a_i b_i$. Let us start with the left-hand side of Eq. 4.28a. Using Eq. 4.15,

$$\begin{aligned}\dot{\boldsymbol{d_3}} &= \boldsymbol{\omega} \times \boldsymbol{d_3} = \omega_i \boldsymbol{d_i} \times \boldsymbol{d_3} = \omega_2 \boldsymbol{d_1} - \omega_1 \boldsymbol{d_2} \\ \ddot{\boldsymbol{d_3}} &= \dot{\omega}_2 \boldsymbol{d_1} - \dot{\omega}_1 \boldsymbol{d_2} + \omega_2(\boldsymbol{\omega} \times \boldsymbol{d_1}) - \omega_1(\boldsymbol{\omega} \times \boldsymbol{d_2}).\end{aligned} \tag{4.29}$$

Component-wise,

$$(\ddot{\boldsymbol{d_3}})_1 = \dot{\omega}_2 + \omega_1\omega_3 \tag{4.30a}$$

$$(\ddot{\boldsymbol{d_3}})_2 = -\dot{\omega}_1 + \omega_2\omega_3 \tag{4.30b}$$

$$(\ddot{\boldsymbol{d_3}})_3 = -(\omega_1^2 + \omega_2^2). \tag{4.30c}$$

For the right-hand side of Eq. 4.28a, use Eq. 4.14,

$$\begin{aligned}\boldsymbol{f}' &= f_i' \boldsymbol{d_i} + f_i(\boldsymbol{\kappa} \times \boldsymbol{d_i}) \\ \boldsymbol{f}'' &= f_i'' \boldsymbol{d_i} + 2f_i'(\boldsymbol{\kappa} \times \boldsymbol{d_i}) + f_i(\boldsymbol{\kappa}' \times \boldsymbol{d_i}) + f_i(\boldsymbol{\kappa} \times [\boldsymbol{\kappa} \times \boldsymbol{d_i}]) \\ &= f_i'' \boldsymbol{d_i} + 2f_i'(\boldsymbol{\kappa} \times \boldsymbol{d_i}) + f_i([\kappa_m' \boldsymbol{d_m} + \kappa_m\{\boldsymbol{\kappa} \times \boldsymbol{d_m}\}] \times \boldsymbol{d_i}) + f_i(\kappa_i \boldsymbol{\kappa} - \kappa^2 \boldsymbol{d_i}) \\ &= f_i'' \boldsymbol{d_i} + 2f_i'(\boldsymbol{\kappa} \times \boldsymbol{d_i}) + f_i\kappa_m'(\boldsymbol{d_m} \times \boldsymbol{d_i}) - f_i\kappa_m(\boldsymbol{d_i} \times \{\boldsymbol{\kappa} \times \boldsymbol{d_m}\}) \\ &\quad + (\boldsymbol{f} \cdot \boldsymbol{\kappa})\boldsymbol{\kappa} - \kappa^2 f_i \boldsymbol{d_i}\end{aligned}$$

$$
\begin{aligned}
&= (f_i'' - \kappa^2 f_i)\boldsymbol{d_i} + 2f_i'(\kappa \times \boldsymbol{d_i}) + f_i\kappa_m'(\boldsymbol{d_m} \times \boldsymbol{d_i}) - f_i\kappa_m(\delta_{im}\boldsymbol{\kappa} - \kappa_i \boldsymbol{d_m}) \\
&\quad + (\boldsymbol{f} \cdot \boldsymbol{\kappa})\kappa \\
&= (f_i'' - \kappa^2 f_i)\boldsymbol{d_i} + 2f_i'(\kappa \times \boldsymbol{d_i}) + f_i\kappa_m'(\boldsymbol{d_m} \times \boldsymbol{d_i}) + (\boldsymbol{f} \cdot \boldsymbol{\kappa})\boldsymbol{\kappa}. \qquad (4.31)
\end{aligned}
$$

In the last, we used, $f_i\kappa_m(\delta_{im}\boldsymbol{\kappa} - \kappa_i \boldsymbol{d_m}) = (\boldsymbol{f} \cdot \boldsymbol{\kappa})\boldsymbol{\kappa} - (\boldsymbol{f} \cdot \boldsymbol{\kappa})\boldsymbol{\kappa} = 0$. Equating Eqs. 4.31 and 4.30 yields,

$$f_1'' - \kappa^2 f_1 - 2f_2'\kappa_3 + 2f_3'\kappa_2 + f_3\kappa_2' - f_2\kappa_3' + (\boldsymbol{f} \cdot \boldsymbol{\kappa})\kappa_1 = \dot{\omega}_2 + \omega_1\omega_3 \qquad (4.32a)$$

$$f_2'' - \kappa^2 f_2 - 2f_3'\kappa_1 + 2f_1'\kappa_3 + f_1\kappa_3' - f_3\kappa_1' + (\boldsymbol{f} \cdot \boldsymbol{\kappa})\kappa_2 = -\dot{\omega}_1 + \omega_2\omega_3 \qquad (4.32b)$$

$$f_3'' - \kappa^2 f_3 - 2f_1'\kappa_2 + 2f_2'\kappa_1 + f_2\kappa_1' - f_1\kappa_2' + (\boldsymbol{f} \cdot \boldsymbol{\kappa})\kappa_3 = -(\omega_1^2 + \omega_2^2). \qquad (4.32c)$$

Next work on Eq. 4.28b. From Eq. 4.28c,

$$
\begin{aligned}
\boldsymbol{M}' &= \kappa_1'\boldsymbol{d_1} + \kappa_2'\boldsymbol{d_2} + \Gamma\kappa_3'\boldsymbol{d_3} + \kappa_1(\boldsymbol{\kappa} \times \boldsymbol{d_1}) + \kappa_2(\boldsymbol{\kappa} \times \boldsymbol{d_2}) + \Gamma\kappa_3(\boldsymbol{\kappa} \times \boldsymbol{d_3}) \\
(\boldsymbol{M}')_1 &= \kappa_1' + (\Gamma - 1)\kappa_2\kappa_3, \\
(\boldsymbol{M}')_2 &= \kappa_2' - (\Gamma - 1)\kappa_1\kappa_3, \\
(\boldsymbol{M}')_3 &= \Gamma\kappa_3' \qquad (4.33)
\end{aligned}
$$

and

$$\boldsymbol{d_3} \times \boldsymbol{f} = f_1\boldsymbol{d_2} - f_2\boldsymbol{d_1}. \qquad (4.34)$$

For the right-hand side of Eq. 4.28b, we follow a procedure similar to Eq. 4.29,

$$
\begin{aligned}
\ddot{\boldsymbol{d}}_{\boldsymbol{1}} &= \dot{\omega}_3\boldsymbol{d_2} - \dot{\omega}_2\boldsymbol{d_3} + \omega_3(\boldsymbol{\omega} \times \boldsymbol{d_2}) - \omega_2(\boldsymbol{\omega} \times \boldsymbol{d_3}) \\
\ddot{\boldsymbol{d}}_{\boldsymbol{2}} &= \dot{\omega}_1\boldsymbol{d_3} - \dot{\omega}_3\boldsymbol{d_1} + \omega_1(\boldsymbol{\omega} \times \boldsymbol{d_3}) - \omega_3(\boldsymbol{\omega} \times \boldsymbol{d_1}), \qquad (4.35)
\end{aligned}
$$

so that

$$
\begin{aligned}
\boldsymbol{d_1} \times \ddot{\boldsymbol{d}}_{\boldsymbol{1}} &= \dot{\omega}_3\boldsymbol{d_3} + \dot{\omega}_2\boldsymbol{d_2} - \omega_3\omega_1\boldsymbol{d_2} + \omega_2\omega_1\boldsymbol{d_3} \\
\boldsymbol{d_2} \times \ddot{\boldsymbol{d}}_{\boldsymbol{2}} &= \dot{\omega}_1\boldsymbol{d_1} + \dot{\omega}_3\boldsymbol{d_3} - \omega_1\omega_2\boldsymbol{d_3} + \omega_3\omega_2\boldsymbol{d_1}. \qquad (4.36)
\end{aligned}
$$

Inserting Eqs. 4.33, 4.34, and 4.36 into Eq. 4.28b yields

$$\kappa_1' + (\Gamma - 1)\kappa_2\kappa_3 - f_2 = \dot{\omega}_1 + \omega_3\omega_2 \qquad (4.37a)$$

$$\kappa_2' - (\Gamma - 1)\kappa_1\kappa_3 + f_1 = \dot{\omega}_2 - \omega_3\omega_1 \qquad (4.37b)$$

$$\Gamma\kappa_3' = 2\dot{\omega}_3. \qquad (4.37c)$$

Equations 4.32 and 4.37 are component forms of Eqs. 4.28a and 4.28b. They are easier to work with since no derivatives of the triad are present. To use them for

a given system, we must know the initial and boundary conditions. Regarding the initial condition, the position (shape) and velocity of each point on the rod at $t = 0$ must be given. When using the triad, these correspond to prescribing $\boldsymbol{\kappa}(s, 0)$ for shape and $\boldsymbol{\omega}(s, 0)$ for velocity. Suppose we found $\boldsymbol{\kappa}(s, t)$ and $\boldsymbol{\omega}(s, t)$ at $t > 0$. To find them at $t + dt$, we need to calculate $f_i$, $f_i'$, $f_i''$, and $\dot{\omega}_i$ in Eqs. 4.32 and 4.37. If $f(s)$ is known, its derivatives are also known. So we need to find $f_i$ and $\dot{\omega}_i$, hence 6 equations with 6 unknowns. To make them more manageable, express $\dot{\omega}_i$ in Eq. 4.37:

$$\dot{\omega}_1 = \kappa_1' + (\Gamma - 1)\kappa_2\kappa_3 - f_2 - \omega_3\omega_2 \tag{4.38a}$$

$$\dot{\omega}_2 = \kappa_2' - (\Gamma - 1)\kappa_1\kappa_3 + f_1 + \omega_3\omega_1 \tag{4.38b}$$

$$\dot{\omega}_3 = \frac{1}{2}\Gamma\kappa_3'. \tag{4.38c}$$

Plug $\dot{\omega}_1$ and $\dot{\omega}_2$ in Eq. 4.32:

$$f_1'' - (1 + \kappa^2)f_1 - 2f_2'\kappa_3 + 2f_3'\kappa_2 + f_3\kappa_2' - f_2\kappa_3' + (\boldsymbol{f} \cdot \boldsymbol{\kappa})\kappa_1 = \kappa_2' - (\Gamma - 1)\kappa_1\kappa_3 + 2\omega_1\omega_3 \tag{4.39a}$$

$$f_2'' - (1 + \kappa^2)f_2 - 2f_3'\kappa_1 + 2f_1'\kappa_3 + f_1\kappa_3' - f_3\kappa_1' + (\boldsymbol{f} \cdot \boldsymbol{\kappa})\kappa_2 = -\kappa_1' - (\Gamma - 1)\kappa_2\kappa_3 + 2\omega_2\omega_3 \tag{4.39b}$$

$$f_3'' - \kappa^2 f_3 - 2f_1'\kappa_2 + 2f_2'\kappa_1 + f_2\kappa_1' - f_1\kappa_2' + (\boldsymbol{f} \cdot \boldsymbol{\kappa})\kappa_3 = -(\omega_1^2 + \omega_2^2). \tag{4.39c}$$

If we know $\kappa_i(s, t)$ and $\omega_i(s, t)$, Eq. 4.39 is a set of second order differential equations for $f_i$. After solving it, we can plug the results into Eq. 4.38 to get $\dot{\omega}_i(s, t)$. Using $\omega_i(s, t)$, we can get $\boldsymbol{d_i}(s, t + dt)$ (Eq. 4.15), hence $\boldsymbol{\kappa}(s, t + dt)$ (Eq. 4.14). From $\dot{\omega}_i(s, t)$, we can also get $\omega_i(s, t + dt)$. Since we now know $\kappa_i(s, t + dt)$ and $\omega_i(s, t + dt)$, the procedure can be iterated over time. What we have done is to rewrite Eqs. 4.32 and 4.37 to Eqs. 4.38 and 4.39, so that derivatives of $f_i$ and $\omega_i$ can be evaluated sequentially rather than simultaneously. Equation 4.39 can be written in matrix form

$$\begin{pmatrix} f_1'' \\ f_2'' \\ f_3'' \end{pmatrix} + \begin{pmatrix} 0 & -2\kappa_3 & 2\kappa_2 \\ 2\kappa_3 & 0 & -2\kappa_1 \\ -2\kappa_2 & 2\kappa_1 & 0 \end{pmatrix} \begin{pmatrix} f_1' \\ f_2' \\ f_3' \end{pmatrix} + \begin{pmatrix} -(1 + \kappa_2^2 + \kappa_3^2) & \kappa_1\kappa_2 - \kappa_3' & \kappa_1\kappa_3 + \kappa_2' \\ \kappa_1\kappa_2 + \kappa_3' & -(1 + \kappa_1^2 + \kappa_3^2) & \kappa_2\kappa_3 - \kappa_1' \\ \kappa_1\kappa_3 - \kappa_2' & \kappa_2\kappa_3 + \kappa_1' & -(\kappa_1^2 + \kappa_2^2) \end{pmatrix} \begin{pmatrix} f_1 \\ f_2 \\ f_3 \end{pmatrix} = \begin{pmatrix} \kappa_2' - (\Gamma - 1)\kappa_1\kappa_3 + 2\omega_1\omega_3 \\ -\kappa_1' - (\Gamma - 1)\kappa_2\kappa_3 + 2\omega_2\omega_3 \\ -(\omega_1^2 + \omega_2^2) \end{pmatrix} \tag{4.40}$$

If $f_i$ and $f_i'$ at $s = 0$ are provided as boundary conditions, Eq. 4.40 can be integrated to yield $f_i$ for $s > 0$. However, boundary conditions in many cases come in different forms, and it is not immediately clear what $f_i(s = 0)$ and $f_i'(s = 0)$ are. The next section is a tutorial on approaching this problem.

### 4.3.4 Case Study: Static Bending of a Clamped Rod

Consider an undergraduate-level mechanics problem: A rod of length $L$ is clamped at $s = 0$ to the Cartesian coordinate origin, aligned along the $z$-axis. Its two major axes of cross section are aligned to the $x$- and $y$-axes. An external force $f_e$ applies in the $y$-direction to the tip ($s = L$), and bends the rod on the $yz$-plane. What is the shape of the bent rod? If we ignore changes in the rod's cross section upon bending, the problem can easily be solved using the line-level description [22]. Using Kirchhoff's equations for this simple system may be an overkill, but it is a good exercise.

Since this is a problem of statics, $\boldsymbol{\omega} = 0$. Also, since all deformations occur on the $yz$-plane, $\boldsymbol{d_1} = \boldsymbol{x}$ and $f_1 = 0$ for all $s$. Considering that $\kappa_i$ relates to the rotation about $\boldsymbol{d_i}$ (Fig. 4.3c), there are no rotations about $\boldsymbol{d_2}$ or $\boldsymbol{d_3}$ for bending on the $yz$-plane, hence $\kappa_2 = \kappa_3 = 0$. Equation 4.40 then reduces to

$$\begin{pmatrix} f_2'' \\ f_3'' \end{pmatrix} + \begin{pmatrix} 0 & -2\kappa_1 \\ 2\kappa_1 & 0 \end{pmatrix} \begin{pmatrix} f_2' \\ f_3' \end{pmatrix} + \begin{pmatrix} -(1+\kappa_1^2) & -\kappa_1' \\ \kappa_1' & -\kappa_1^2 \end{pmatrix} \begin{pmatrix} f_2 \\ f_3 \end{pmatrix} = \begin{pmatrix} 0 \\ 0 \end{pmatrix} \tag{4.41}$$

In Eq. 4.41, $\kappa_1$, $f_2$, and $f_3$ are unknown along the rod, so we have to solve for them with given boundary conditions. At $s = 0$, the triad aligns with the Cartesian coordinate basis: $\{\boldsymbol{d_1}, \boldsymbol{d_2}, \boldsymbol{d_3}\} = \{\boldsymbol{x}, \boldsymbol{y}, \boldsymbol{z}\}$. The wall holding the rod applies force and torque to keep it clamped. The force must be $-f_e \boldsymbol{y}$, since the net force on the rod must be zero. From the rod's point of view, this means $\boldsymbol{f}(0) = f_e \boldsymbol{d_2}(0)$. The sign reverts as explained regarding Fig. 4.1d. On the other hand, we do not know $f_i'(0)$ $(i = 2, 3)$ nor $\kappa_1(0)$. If we denote the $z$-coordinate of the rod's tip as $z_L$, $\boldsymbol{M}(0) = -f_e z_L \boldsymbol{d_1}$, so $\kappa_1(0) = -f_e z_L$. But we don't know $z_L$ yet. Now let us consider boundary conditions at $s = L$. Although $f(L) = f_e \boldsymbol{y}$, due to tilting of the tip, the triad does not align with the Cartesian coordinate system so the components $f_2(L)$ and $f_3(L)$ are not individually known. Note that, with $\ddot{\boldsymbol{X}} = 0$ and $\boldsymbol{g} = 0$ in Eq. 4.19, $\boldsymbol{f}' = 0$, so $\boldsymbol{f} = f_e \boldsymbol{y}$ (constant) along the rod. However, since $\boldsymbol{d_2}$ and $\boldsymbol{d_3}$ vary with $s$, the components $f_2$ and $f_3$ also depend on $s$:

$$\begin{aligned} \boldsymbol{f}' &= f_2' \boldsymbol{d_2} + f_3' \boldsymbol{d_3} + f_2(\boldsymbol{\kappa} \times \boldsymbol{d_2}) + f_3(\boldsymbol{\kappa} \times \boldsymbol{d_3}) \\ &= (f_2' - \kappa_1 f_3)\boldsymbol{d_2} + (f_3' + \kappa_1 f_2)\boldsymbol{d_3} = 0 \\ &\therefore \quad f_2' = \kappa_1 f_3, \quad f_3' = -\kappa_1 f_2. \end{aligned} \tag{4.42}$$

Since there is no torque on the rod's tip, $\kappa_1(L) = 0$, so that $f_2'(L) = f_3'(L) = 0$. For a general $s$, since $\boldsymbol{d_1}$ is independent of $s$, $\boldsymbol{M} = \kappa_1 \boldsymbol{d_1} \rightarrow \boldsymbol{M}' = \kappa_1' \boldsymbol{d_1}$. On the other

hand, from Eq. 4.28b, $\boldsymbol{M}' = \boldsymbol{f} \times \boldsymbol{d_3} = f_2 \boldsymbol{d_1}$. This gives $\kappa_1' = f_2$, which, together with $f_2^2 + f_3^2 = f_e^2$ and Eq. 4.42, can be used to rewrite Eq. 4.41 separately for $f_2$ and $f_3$:

$$f_2'' = f_2 \left( 1 - \kappa_1^2 + \sqrt{f_e^2 - f_2^2} \right) \tag{4.43a}$$

$$f_3'' = f_3 (f_3 - \kappa_1^2) - f_e^2. \tag{4.43b}$$

For solving Eq. 4.43, neither $s = 0$ nor $s = L$ has $f_i$ and $f_i'$ completely specified. Summarizing boundary conditions discussed above, at $s = 0$, $f_i$ is known ($f_2(0) = f_e$, $f_3(0) = 0$), while at $s = L$, $f_i'$ is known ($f_2'(L) = f_3'(L) = 0$). We can thus solve Eq. 4.43 in two ways. The first is to integrate from $s = 0$. In this case, we use trial values for $f_i'(0)$. After integrating to $s = L$, check if $f_i'(L) = 0$. If not, vary $f_i'(0)$ until the boundary condition at $s = L$ is met. The second way goes in the opposite direction, where we vary $f_i(L)$ and integrate Eq. 4.43 from $s = L$ to 0 until $\boldsymbol{f}(0)$ matches with $f_e \boldsymbol{y}$. The computational technique of varying the unknown boundary condition at one end of the integration range to match the known boundary condition at the other end is in general called the *shooting method* [25]. Conceptually, whether to start the integration from $s = 0$ or $L$ does not make any difference. One can choose whichever direction that is easier to write into a computer program, or is less prone to roundoff error. Numerically solving boundary value problems, or scientific computing in general, is an art where accuracy and efficiency are two major factors to consider. Discussion of how to actually integrate Eq. 4.43 would be a separate topic by itself, for which I refer the readers to the excellent hands-on book *Numerical Recipes* [25]. Here, we integrate from $s = L$ to 0. Only either one of Eqs. 4.43a and 4.43b needs to be solved, since the three vectors of the triad are

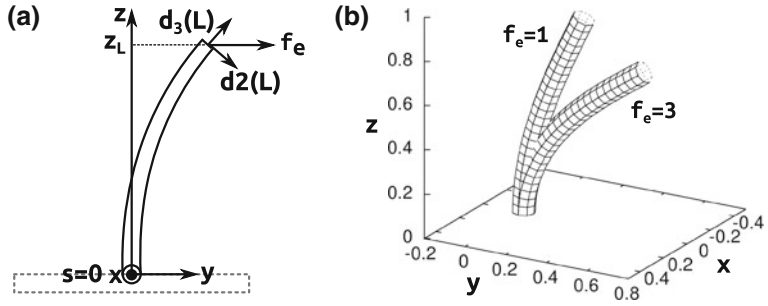


**Fig. 4.4** Bending of a clamped rod. **a** Schema of the system. At $s = 0$. the rod is clamped and aligned along the Cartesian $z$-axis. At $s = L$, an external force $f_e$ applies in the $y$-direction. Due to bending, the $z$-coordinate of the rod at $s = L$ is $z_L$. Bending occurs only on the $yz$-plane. The triad corresponds to the Cartesian coordinate basis at $s = 0$, and changes direction for $s > 0$ due to bending. **b** Solution of Eq. 4.43b for $f_e = 1$ and 3. We used $L = 1$ and the integration interval was $\Delta s = 0.001$. The rod's actual diameter is irrelevant, since it is absorbed into the length scale after de-dimensionalization. Besides, there are no lateral interactions in this problem

not mutually independent ($\boldsymbol{d_3} = \boldsymbol{d_1} \times \boldsymbol{d_2}$). We choose Eq. 4.43b. With $\kappa_1(s)$ known, using $\boldsymbol{d_2}(0) = \boldsymbol{y}$, $\boldsymbol{d_3}(0) = \boldsymbol{z}$, $\boldsymbol{d_2'}(s) = \kappa_1 \boldsymbol{d_3}$, and $\boldsymbol{d_3'}(s) = -\kappa_1 \boldsymbol{d_2}$, we can calculate $\boldsymbol{d_2}(s)$ and $\boldsymbol{d_3}(s)$.

Figure 4.4b shows two cases with $f_e = 1$ and 3. One way of checking the accuracy of calculation is to compare $M(0) = \kappa_1(0)$ with $f_e z_L$ (ignoring signs). In the case of $f_e = 1$, $M(0) = 0.9420$ and $f_e z_L = 0.9439$ ($z_L = 0.9439$). For $f_e = 3$, $M(0) = 2.2345$ and $f_e z_L = 2.2396$ ($z_L = 0.7465$). These are about 0.2 % accuracy, which is good enough for the purpose of this chapter. When carrying out more involved calculations, however, it is necessary to check the result in multiple angles to make sure that it is not infested by numerical artifacts.

## 4.4 Conclusion

Between the line- and rod-level descriptions of biofilaments, the former is simpler and is of widespread use when detailed conformational behavior of a filament is not measured in experiments. Good examples are mechanical unfolding of a protein [21] or analysis of filament bending motion [15]. The *worm-like chain* model [23] may be viewed as a version of the line-level description that emphasizes statistical aspects arising from thermal fluctuation. By comparison, the rod-level description has been the most extensively used perhaps for DNA [16, 29]. This may be because it has long been known that DNA conformation is crucial for the cellular machinery. However, the same is most likely to hold for other biofilaments, i.e., the conformational behavior and mechanics of a biofilament are essential for its biological function. Taking fibrillar collagen as an example, the increasingly available imaging data show large conformational variability depending on tissue type [27] or the amount of load [30]. Dynamic organization of the cytoskeleton is, of course, key to cellular function. As the experimental resolution is steadily increasing in both space and time, it is expected that the rod-level description will play a greater role.

Although it can capture more detailed conformational behavior, the rod-level description is difficult to use. As demonstrated by the simple bending of a rod, one needs to have a good understanding of the system in order to figure out boundary conditions, which can be fairly sophisticated in cases when the filament has nonzero equilibrium curvature, or if the system contains multiple interacting filaments. In such cases, the traditional approach of solving Kirchhoff's equations as an initial-boundary value problem can be impractical. Recent approaches treat the system as discrete from the outset, rather than relying solely on the continuum formulation [17], and even utilizes the relatively new mathematical theory of discrete differential geometry [1]. These approaches are somewhere between molecular dynamics simulation and continuum mechanics. After all, continuum description is an idealization that is suitable mainly for macroscopic and homogeneous systems. With the increasing need to simulate mesoscale, near-atomic resolution biofilaments, discrete description may be computationally more advantageous. However, a unique advantage of the continuum description is the physical insight it provides—Biofilaments

are ultimately a discrete collection of atoms. Computers are digital. The neurons in our brains make distinct and finite connections and fire signals. However, our thoughts are hardly discretized.

## References


1. Bergou, M., Wardetzky, M., Robinson, S., Audoly, B., Grinspun, E.: Discrete elastic rods. ACM Transactions on Graphics **27**(3), article 63 (2008)
2. Bishop, R.L.: There is more than one way to frame a curve. Amer. Math. Month. **82**(3), 246–251 (1975)
3. Coleman, B.D., Dill, E.H., Lembo, M., Lu, Z., Tobias, I.: On the dynamics of rods in the theory of kirchhoff and clebsch. Arch. Rat. Mech. Anal. **121**(4), 339–359 (1993)
4. Daune, M., Duffin, W.J.: Molecular biophysics: structures in motion. Oxford University Press (1999)
5. de Gennes, P.G.: Scaling Concepts in Polymer Physics. Cornell University Press, Ithaca, NY (1979)
6. Dill, E.H.: Kirchhoff's theory of rods. Arch. Hist. Exact Sci. **44**(1), 1–23 (1992)
7. Doi, M., Edwards, S.F.: The theory of polymer dynamics, vol. 73. Oxford University Press (1988)
8. Ellis, R.J.: The most abundant protein in the world. Trends Biochem. Sci. **4**(11), 241–244 (1979)
9. Goriely, A., Tabor, M.: Nonlinear dynamics of filaments I. Dynamical instabilities. Physica D **105**(1), 20–44 (1997)
10. Goriely, A., Tabor, M.: Nonlinear dynamics of filaments II. nonlinear analysis. Physica D **105**(1), 45–61 (1997)
11. Goriely, A., Tabor, M.: Nonlinear dynamics of filaments. III. Instabilities of helical rods. Proc. Roy. Soc. London A **453**(1967), 2583–2601 (1997)
12. Goriely, A., Tabor, M.: Nonlinear dynamics of filaments. IV Spontaneous looping of twisted elastic rods. Proc. Roy. Soc. London A **454**(1980), 3183–3202 (1998)
13. Goyal, S., Perkins, N.C., Lee, C.L.: Nonlinear dynamics and loop formation in Kirchhoff rods with implications to the mechanics of DNA and cables. J. Comp. Phys. **209**(1), 371–389 (2005)
14. Howard, J.: Mechanics of Motor Proteins and the Cytoskeleton. Sinauer, Sunderland, MA, USA (2001)
15. Janson, M.E., Dogterom, M.: A bending mode analysis for growing microtubules: evidence for a velocity-dependent rigidity. Biophys. J. **87**(4), 2723–2736 (2004)
16. Klapper, I.: Biological applications of the dynamics of twisted elastic rods. J. Comp. Phys. **125**(2), 325–337 (1996)
17. Ladd, A.J., Misra, G.: A symplectic integration method for elastic filaments. J. Chem. Phys. **130**, 124,909 (2009)
18. Lakkaraju, S.K., Hwang, W.: Critical buckling length versus persistence length: What governs a biofilament conformation? Phys. Rev. Lett. **102**(11), 118,102 (2009)
19. Lakkaraju, S.K., Hwang, W.: Modulation of elasticity in functionally distinct domains of the tropomyosin coiled-coil. Cell. Molec. Bioeng. **2**, 57–65 (2009)
20. Langer, J., Singer, D.A.: Lagrangian aspects of the kirchhoff elastic rod. SIAM Rev. **38**(4), 605–618 (1996)
21. Li, H., Linke, W.A., Oberhauser, A.F., Carrion-Vazquez, M., Kerkvliet, J.G., Lu, H., Marszalek, P.E., Fernandez, J.M.: Reverse engineering of the giant muscle protein titin. Nature **418**, 998–1002 (2002)
22. Lifshitz, E.M., Landau, L.D.: Statistical Physics Part 1, 3rd edn. Butterworth-Heinemann (1984)
23. Marko, J.F., Siggia, E.D.: Stretching DNA. Macromolec. **28**, 8759–8770 (1995)

24. Park, J., Kahng, B., Kamm, R.D., Hwang, W.: Atomistic simulation approach to a continuum description of self-assembled $\beta$-sheet filaments. Biophys. J. **90**, 2510–2524 (2006)
25. Press, W.H., Teukolsky, S.A., Vetterling, W.T., Flannery, B.P.: Numerical Recipes in C, 2nd ed. Cambridge University Press, Cambridge, U.K. (1999)
26. Rivetti, C., Guthold, M., Bustamante, C.: Scanning force microscopy of dna deposited onto mica: Equilibration versus kinetic trapping studied by statistical polymer chain analysis. J. Mol. Biol. **264**(5), 919–932 (1996)
27. Ushiki, T.: Collagen fibers, reticular fibers and elastic fibers. A comprehensive understanding from a morphological viewpoint. Arch. Histol. Cytol. **65**(2), 109–126 (2002)
28. Vakonakis, I., Campbell, I.D.: Extracellular matrix: from atomic resolution to ultrastructure. Curr. Op. Cell Biol. **19**(5), 578–583 (2007)
29. Vologodskii, A.V., Cozzarelli, N.R.: Supercoiling, knotting, looping and other large-scale conformational properties of dna. Curr. Op. Struct. Biol. **4**(3), 372–375 (1994)
30. Wicker, B.K., Hutchens, H.P., Wu, Q., Yeh, A.T., Humphrey, J.D.: Normal basilar artery structure and biaxial mechanical behaviour. Comput. Methods Biomech. Biomed. Eng. **11**(5), 539–551 (2008)
31. Wiggins, C.H., Riveline, D., Ott, A., Goldstein, R.E.: Trapping and wiggling: Elastohydrodynamics of driven microfilaments. Biophys. J. **74**(2), 1043–1060 (1998)

# Part II
# Multiscale Modeling Around the Cellular and Tissue Level

# Chapter 5
# Multiscale Modeling of Primary Cilia

**Y.-N. Young, Lina C. Espinha, An M. Nguyen and Christopher R. Jacobs**

**Abstract** Primary cilia are nonmotile, solitary organelles that protrude from the apical surface of nearly every mammalian cell. Discovered over a century ago, the primary cilium has been identified as a multifunctional antenna, sensing both mechanical (fluid flow, pressure, touch, vibration) and chemical changes in the extracellular environment. Furthermore, the primary cilium has also been implicated as a complex signaling center for the cell, regulating key signaling pathways during development such as Hedgehog and Wnt. In this article we summarize recent theoretical approaches for modeling primary cilium bending mechanics. By combining theoretical modeling and detailed experimental observations, we construct a model for the primary cilium as an elastic slender beam with a nonlinear rotational stiffness at the base that accounts for the behavior of the basal anchorage. The importance of incorporating the detailed basal anchorage in multiscale modeling of the primary cilium is highlighted by good quantitative agreement between cilium bending under flow and experimental observation. New observations further illustrate how the microtubule network connected to the basal body responds to mechanical stress from the bending of the primary cilium. We discuss how to use the current model as a foundation to construct a more realistic multiscale model that incorporates coupling with the cytoplasmic microtubule network.

Y.-N. Young (✉)
Department of Mathematical Sciences and Center for Applied Mathematics and Statistics, New Jersey Institute of Technology, Newark, NJ 07102, USA
e-mail: yyoung@njit.edu

L.C. Espinha · A.M. Nguyen · C.R. Jacobs
Department of Biomedical Engineering, Columbia University, New York, NY 10027, USA

L.C. Espinha
LAETA, Instituto Superior Técnico, Universidade de Lisboa, Lisbon, Portugal



S. De et al. (eds.), *Multiscale Modeling in Biomechanics and Mechanobiology*, DOI 10.1007/978-1-4471-6599-6_5

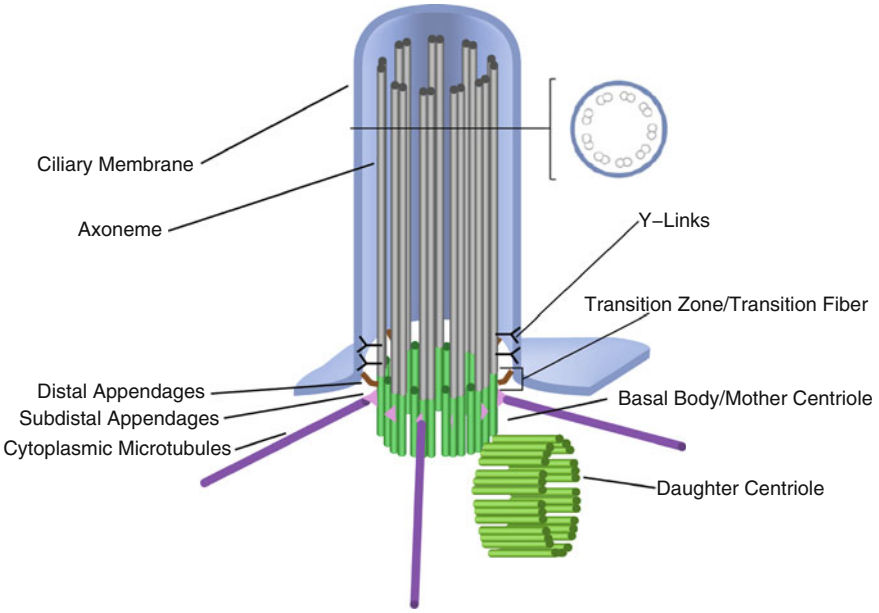


**Fig. 5.1** Schematic diagram of primary cilium (adopted from Temiyasathi et al. [3])

## 5.1 Introduction: Structures and Functions of Primary Cilia

The primary cilium is a solitary nonmotile, microtubule-based organelle found ubiquitously in many nonmitotic mammalian cells [1, 2]. As a hair-like protrusion from the apical cell membrane into the extracellular space (Fig. 5.1), the core structure of the primary cilium is a membrane-enclosed axoneme containing nine microtubule doublets that originate from the basal body. The ciliary membrane is a continuation of the plasma membrane [4], and experimental findings suggest that there are physiological differences between the two, such as lipid compositions [5, 6], electrical resistance [7], ion-binding, and osmotic behavior [8, 9]. The axonemal base is connected to the cilium basal body, a protein-based structure consisting of nine triplet microtubules arranged circumferentially.

When cells are not involved in mitosis, the centrioles (the central component of the microtubule organizing center) migrate to the cell membrane and one (the mother centriole) acts as a template for ciliogenesis and the anchoring basal body for the ciliary axoneme [6, 10]. The basal body includes structures such as the distal and subdistal appendages. The distal appendages attach it to the cell membrane. Below this, it is coupled to the cytoskeletal microtubule network at the subdistal appendages also known as the basal feet [11], which extend laterally to form attachment points for cytoskeletal microtubules. Extending into the cytoplasm are striated rootlets, a collection of filamentous structures with periodic striations that radiate

from the proximal end of the basal body. It has been suggested that these rootlets act as "nanomachines" for muscle-like contraction [12], highways for the transport of proteins from the Golgi apparatus to the plasma membrane [13], or anchorage for the basal body/primary cilium complex by interacting with the cell's cytoskeleton [14].

Between the axoneme and the basal body is a transition zone (TZ) (see Fig. 5.1) where the transition fibers (right below the Y-links, also called the ciliary necklace [8]), link the TZ microtubules with the ciliary membrane. These connectors distribute around the TZ microtubules in an almost symmetrical fashion. The transition zone is also closely associated with various proteins and molecular transport around the ciliary pocket [4, 6, 15, 16].

Primary cilia differ from the better-understood motile cilia in several important aspects. Despite similarities in the axonemal structure which consists of nine microtubule doublets, there are significant differences: motile cilia and flagella have two additional central microtubules, which are attached to each of the surrounding doublets by radial spokes. Therefore, motile cilia are commonly referred to as $9 + 2$ cilia in contrast to the $9 + 0$ arrangement for primary cilia. In addition, the doublets of the $9 + 2$ cilium are connected via nexin links, which (in combination with the radial spokes) reinforce the axoneme rigidity, resulting in an order of magnitude larger resistance to bending (flexural rigidity) relative to the primary cilium. Unlike motile cilia, there is only a single primary cilium per cell. Motile cilia are expressed only on specialized cells, while primary cilia are found in virtually every cell type. Furthermore, primary cilia have multiple basal feet and striated rootlets distributed evenly around their basal bodies, while the basal feet of beating cilia are aligned with the beating direction [17].

Although initial morphological descriptions of primary cilia date back over a century, their function has only recently begun to be unraveled. Initially the focus had been on the role of primary cilia in cellular development where they are known to be involved in establishment of the left–right axis and anterior–posterior limb bud patterning [18–24] via sensing of the Hedgehog and Wnt families of morphogens. As a sensory organelle, the primary cilium enables the cell to interrogate its environment over a distance and has emerged as a central site of cell signal coordination and integration.

More recently, the mechanosensing role of primary cilia was discovered. Praetorious and Spring found a dramatic extracellular calcium-dependent increase in intracellular calcium by using fluid flow or a micropipette to bend the primary cilia of kidney epithelial cells. They also found that this response was lost with removal of primary cilia [25, 26]. It has been suggested that this response occurs via a cationic channel that localizes to the base of the cilium known as polycystin 2 [27, 28]. This mechanism has also been found in liver cholangiocytes in response to fluid flow [29]. In addition to calcium signaling, fluid flow in bile ducts also activates the second messenger cAMP [29]. The response of the primary cilium to the external load is observed to be more than mechanical bending and transfer of stress, but also molecular alterations. For example, proteins of the linker density may undergo

conformational changes as a result of $Ca^{2+}$ binding, which increases the stiffness of stereocilia [30] and also increases the rate of depolymerization of microtubules [31, 32].

Defective or malfunctional primary cilia have been linked to pathologies [33–37] such as arthritis, osteoporosis, polycystic kidney disease, heart failure, obesity, and cancer. For example, it is well known that when bone is exposed to repeated mechanical loading in vivo it loses its sensitivity to subsequent mechanical loading [38, 39]. This reduced sensitivity is refractory and is gradually reversed over a period of minutes. Furthermore, it coincides with a loss of cellular responsiveness [40]. Interestingly, there is also evidence that primary cilia degrade with loading [41].

Recent state-of-the-art measurements have uncovered detailed equilibrium shape and dynamics of the ciliary axoneme under flow. These experimental results are summarized in Sect. 5.2, where we also explain that multiscale modeling is the key to advancement in modeling of primary cilia. We refined a drag-force/cantilevered-beam model to incorporate large rotation at the ciliary base (Sect. 5.3.1). We have recently further extended our model and used slender-body theory to consistently address the fluid–structure interaction between the the fluid and ciliary axoneme with nonlinear rotational stiffness of the basal body (Sect. 5.3.2). Our modeling results and quantitative comparisons with experiments indicate that the mechanical details of the basal anchorage are essential to capturing the mechanical characteristics and understanding the behaviors of the primary cilium. In Sect. 5.5 we summarize recent findings on the morphological changes in the microtubule network connected to the basal body. In Sect. 5.6 we discuss the challenges in multiscale modeling of primary cilia that incorporate the mechanical coupling between the axoneme and the underlying microtubule network.

## 5.2 Multiscale Modeling and Computational Challenges

Models of the primary cilium should incorporate the bending (characterized by axonemal length and bending rigidity) and positional characteristics (characterized by axonemal orientation at the base and its position on the cell) observed for different cells. The axonemal length is a dynamic quantity that depends on regulated intraflagellar transport (IFT) [6, 42]. It is not clear if there exists an optimal length for mechanotransduction, nor is it understood if this length may vary over different cell types. The three-dimensional axonemal orientation varies by cell type, and it has been reported that a well-defined axonemal orientation can be observed for a population of cells [43]. The axonemal position has been found to be critical for establishing tissue organization in highly anisotropic tissues [43].

The complex sub-axonemal compartment is often simplified in models for motile cilia and beating flagella. As a paradigm for studying biological swimming and propulsion in biophysics and applied mathematics, motile cilia and flagella are examples where, once the biomechanics of an organelle is properly formulated in mathematical terms, advancements in multiscale modeling and direct numerical

simulations lead to quantitative understanding of biological functions that may be beyond reach of experiments alone. These advances have also stimulated a series of experiments focusing not just on more detailed investigations of motile cilia, but also synthesis of artificial beating cilia that are designed to perform the biological function of moving mucus [44, 45]. Following Lighthill's early work [46, 47] Gueron et al. adopted similar approaches to investigate the fluid flow induced by a beating cilium/flagellum [48–50]. Slender-body theory has been widely used to investigate the interaction between the beating cilium/flagellum and the viscous fluid.

Multiscale modeling of a motile cilium that incorporates the beating kinematics in the immersed boundary framework [51–56] has shed light on the bio-fluid mechanics of beating cilia and flagellated swimmers in viscous fluid [55, 56]. The internal structures of a beating cilium such as the elasticity of the microtubule doublets and connectivity between the doublets are incorporated into these models [51]. Multiple beating cilia interact with each other nonlocally through hydrodynamic interactions, as each one of them beats according to its own internal stress generated by the central microtubule doublet. In all of these studies the role of the basal body and the coupling to the cytoskeleton membrane have been ignored. However, recent studies have shown the importance of the basal body anchorage in swimming by flagellum undulation [57].

Compared to motile cilia and flagella, much less theoretical modeling and numerical simulations of primary cilia have been reported. Schwartz et al. [58] developed a mathematical model based on a small-deformation elastic beam formulation. This model assumed a constant velocity and drag profile along the cilium, not valid under high flow conditions. Resnick et al. [59] applied a similar formulation to study small deflections in cylindrical Poiseuille flow. Liu et al. [60] used a more precise model of the fluid flow around an array of cilia by numerically solving Stokes equations. They assumed small rotation at the cilium base although they computed the drag on cilium axoneme consistently from Stokes equations. Rydholm et al. [61] conducted computational fluid dynamics simulations of the bending of an elastic filament connected to an elastic membrane. From their simulations they found the stress distribution along a filament under flow with the maximum stress at the axoneme base, even though flexibility of the anchorage at the sub-axonemal compartments was not included in their simulations. They also conducted experiments illustrating the cilium bending and the subsequent variation in the intracellular calcium concentration. Although they did not provide any validation of their simulations by comparing against their experiments.

Three-dimensional (3D) imaging of primary cilia under steady fluid flow allowed Downs et al. to investigate the mechanical properties of primary cilia in detail [62]. Results from the experiments revealed several patterns of primary cilia deflection and different post-flow relaxation patterns [62]. The vast majority exhibited a smooth bending curve similar to those previously reported (Fig. 5.2a–c). Occasionally deflections without axoneme bending were observed, see Fig. 5.2d. These straight deflections were characterized by large rotations at the cilium base and relatively little bending along the axoneme, perhaps indicative of a decreased degree of cilium anchorage and axonemal stiffening. At higher flow rates another behavior

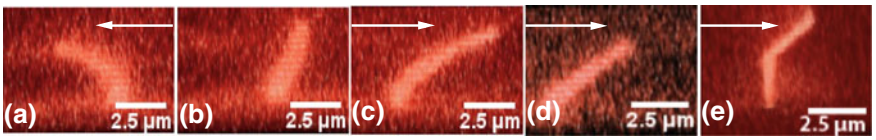


**Fig. 5.2** **a**–**c** 2D profiles of a smooth *bending curve* from a 3D z-stack. *Arrows* indicate the flow direction. **b** is the configuration prior to flow. **d** 2D profile of a deflected *straight curve* from a 3D z-stack. **e** 2D profile of a kinked cilium at high flow rate. Adapted from results in [62]

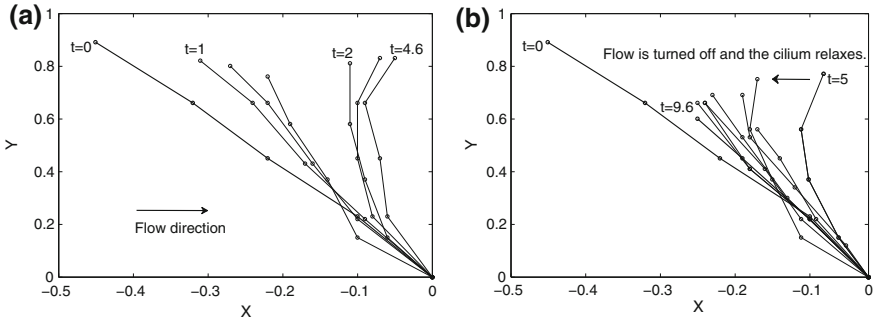


**Fig. 5.3** Dynamics of cilium bending under flow. Panel **a** The flow is turned on at $t = 0$. As time progresses to $t \sim 4.6$ the cilium bends and reaches maximum bending. Panel **b** The flow is turned off and the cilium relaxes from the curve labeled at $t = 5$ to the nonstressed profile at $t = t_f \sim 9.6$ s. The cilium length is 2.7 μm at $t = 0$. Reproduced from [63] with permission fr om the Biophysical Society

was observed: A kinked cilium characterized by two linear segments of low bending joined by a localized region of high curvature (Fig. 5.2e). After flow was stopped, some cilia did not return to the pre-flow shape. Other cilia displayed a recovery towards the original pre-flow position (see Fig. 5.3). This would indicate that primary cilia are capable of undergoing both elastic and plastic deformation.

High-speed confocal microscopy can also acquire two-dimensional (2D) images of the dynamic primary cilia bending under flow. For a flow velocity that corresponds to 0.1–1.5 Pa wall shear stress, the cilium bends and reaches an equilibrium position within $\mathcal{O}(1)$ s. Such dynamical processes can be captured by high-speed imaging, as shown in Fig. 5.3a where the flow is turned on at $t = 0$ and the cilium bends as time progresses. In Fig. 5.3b the flow is stopped at $t \sim 5$ s and the cilium relaxes to the profile labeled at $t \sim 9.6$ s. Both 2- and 3-D cilium profile data are obtained by high-speed z-stack scanning of the fluorescence proteins on the ciliary membrane. Consequently, significant noise is often un-avoidable and the estimated cilium length may not be the same for a single cilium over the duration of 10 s (Fig. 5.3). In addition, we observed that the initial nonstressed cilium profile in Fig. 5.3 is not upright.

These experimental results provide the potential for quantitative comparisons between modeling and experiments. The first challenges for successful theoretical modeling are (1) reproduce the equilibrium profile of the ciliary axoneme under flow,

(2) explain the large rotation at the cilium base, (3) explain why the primary cilium does not always recover to the same pre-flow profile, and (4) capture the dynamics of ciliary bending under a steady or oscillatory fluid flow.

Detailed quantitative understanding of the mechanical behavior of primary cilia has been lacking due to the biological complexity of ciliary structures. Although the ciliary axoneme is structurally simpler in primary cilia than motile cilia, the sub-axonemal compartment (consisting of basal body and the anchorage from the surrounding microtubule network) is much more complex. In addition, we need to take into account the disparity in the characteristic length and timescales associated with the biological complexity of primary cilia: The length of the ciliary axoneme ($L$) ranges from one to several μm's. The radius of cross section of the basal body $r \sim 200$ nm. Proteins involved in the mechano-sensing are no larger than several nanometers. Ciliogenesis is often completed within 24 h, while the ciliary bending in a physiologically realistic flow is of the order of seconds. The activation time for intracellular calcium influx is a few seconds [25, 26, 28, 61, 64, 65].

Currently, it is not feasible to simulate the bending dynamics of primary cilia using molecular dynamics (MD) computations, coarse-grained calculations, or direct numerical simulations of a continuum model that considers the underlying physics on distinct space and timescales, let alone the subsequent signaling processes over several microns and several tens of seconds. However, MD simulations can provide quantitative understanding of the connection between the mechanical behavior of the primary cilium and its molecular configuration. For example, the conformation of acetylated tubulin may promote binding of MAPs (microtubule associated proteins) and hence alter the flexural rigidity of the axoneme. A normal mode analysis [66] of the MD simulations of such molecular alterations under stress can be obtained from the continuum model, and will provide a flexural rigidity that varies along the axoneme. This may, in turn, be fed to a continuum model for a better estimate of stress distribution. Success of such coupling between MD simulations and continuum modeling hinges on developing a physically consistent continuum model that can capture all the essential primary cilium mechanical behaviors.

To construct a multi-physics model of primary cilium mechanics some questions should be considered: (1) How many degrees of freedom are associated with axonemal bending in response to fluid flow? Is the ciliary axoneme, because of its radial symmetry, capable of a bending response equally in all possible directions? Are the same signaling pathways activated in response to fluid flow from different directions? (2) How do we quantitatively describe the mechanical behavior of the primary cilium under hydrodynamic load? (3) What is the relation between ciliary mechanical behavior, its 3D orientation and location on the membrane? (4) How should we understand the mechanosensing processes in terms of coupling the mechanical behavior of the primary cilium to the rest of the cell through signaling pathways? (5) Is there a threshold of bending required to activate signal transduction? Are the same pathways activated at different degrees of bending? Is the system toggled and/or does it undergo a refractory period after bending?

From our experience in modeling primary cilia, we have found that the interaction between fluid flow and the primary cilium axoneme should be accurately considered

to reproduce the equilibrium profiles of primary cilia under flow [62]. We further find that the cilium base behaves like a nonlinear rotational spring, and this may be modeled with coupling between the cilium axoneme and an elastic shell with a local torque at the contact point [63]. This particular result shows that, due to the multiscale structures of the primary cilium, a multiscale model is necessary to capture the essential mechanics and dynamics of the primary cilium and the connected microtubule network.

The long-term goal for modeling of primary cilia is to decipher coupling between their mechanical behavior (such as bending under a hydrodynamic load) with biochemical processes (initiated by their responses to mechanical loads), such as the opening of ion channels or cascades of cellular (or intercellular) signals. For example, is it possible that IFT is affected by the load on the axoneme through bending? Is it possible to construct a multiscale model that will couple the mechanics of an elastic axoneme to the cellular signaling as in the case of the cochlear amplifier and sensory hair cells [67, 68]? It is not clear how mechanosensitive channels open in response to the deflection of the ciliary axoneme and/or the displacement of the ciliary membrane around the basal body. It is also not clear if the deflection at the ciliary tip may be more important than at the base when it comes to mechanotransduction. Numerical simulations suggest that the maximum strain on the ciliary membrane is at the base [61]. Yet without a detailed description of the distributions and responses of the mechanosensitive channels, this information is insufficient for further understanding of the biological functions of primary cilia.

In the cochlear amplifier, displacements of the hair cells and the hair cell bundles are coupled to the basilar membrane and the organ of corti through the electromotility of the outer hair cells and the gating of the mechanosensitive channels associated with the outer hair cell bundles (see review [69] and references therein). The mechanically gated ion channels (MET channels) located near the tips of stereocilia in the hair cell bundle are known to be responsible for the influx of $K^+$ ions into the hair cell [70]. Upon deflection of the hair cell bundle toward the largest row of stereocilia, tension in the tip links increases and induces the opening of MET channels, giving rise to an intracellular $K^+$ current. Such detailed depiction of the signaling processes associated with primary cilia is not yet available. As will be shown in Sect. 5.6, the continuum model that we developed can incorporate the change in IFT traffic due to the basal membrane strain, which then in turn alters the cilium length as it bends under flow. However, the molecular details need to be provided. Once such details are available, we can then make direct connection to the mechanical behavior of the primary cilium to its biological function(s) in a given cell.

## 5.3 Large-Rotation Formulations: Drag Force Model and Slender-Body Theory

For a primary cilium in viscous flow under physiological conditions, the Reynolds number (ratio of inertial forces to viscous forces) is of the order of $10^{-4}$ with a characteristic length of 1 $\mu$m and a characteristic flow velocity of 1 cm/s. Consequently, we

ignore the inertia effects and focus on the Stokes flow regime. In 2012 we advanced previous models [58, 60] by taking into account the large rotation at the cilium base and a consistent hydrodynamic drag force [62]. Later, we used the slender-body theory (SBT) to compute the hydrodynamic interaction more accurately with large deformation of the cilium under a planar shear flow [63]. Within the SBT framework we incorporated a rotational stiffness at the axoneme base to model the basal anchorage, and we obtained good quantitative agreement in the dynamics of cilium bending under flow with experiments. We further used this model to investigate the ciliary dynamics with a more complex temporally periodic flow (see Sect. 5.4.2.2), and the bending dynamics of a cilium with a time-varying length that depends on the balance between axonemal assembly and dissemble rates (see Sect. 5.6).

### *5.3.1 Drag Force Model*

Downs et al. [62] modeled the primary cilium axoneme as an elastic, homogeneous beam with a uniform cross-section along the centerline. Under load the bending of such an elastic beam can be described by Euler-Bernoulli beam theory:

$$\frac{\mathrm{d}\theta}{\mathrm{d}s} = \frac{M(s,\theta)}{E\mathrm{I}}, \tag{5.1}$$

where $\theta$ is the angle between the tangent and the vertical, $M$ is the bending moment, $s$ is the arclength along the beam from the tip to the base, $E$ is Young's modulus, and $I$ is the second moment of inertia. In this formulation they assume an infinitesimal strain, and make no assumption about the axoneme angle at the free end to allow for large deflection at equilibrium.

At equilibrium the governing equation for the angle $\theta(s)$ is

$$E\mathrm{I}\frac{d^2\theta}{\mathrm{d}s^2} = \frac{\mathrm{d}M}{\mathrm{d}s} = Q_x(s)\sin\theta(s) - Q_y(s)\cos\theta(s), \tag{5.2}$$

where $Q_x$ and $Q_y$ are the total forces in the $x$ and $y$ directions, respectively. In this model the main focus is on a unidirectional flow in the $y$ direction, and force-free condition is assumed in the $x$-direction. Thus the governing equation for $\theta(s)$ is

$$E\mathrm{I}\frac{d^2\theta}{\mathrm{d}s^2} = -Q_y(s)\cos(\theta(s) - \theta_0), \tag{5.3}$$

where $\theta(s) - \theta_0$ is the difference in angle from $\theta_0$, the basal angle of the initial shape of the nonstressed beam. The cantilevered beam boundary conditions with a specified rotation $\theta_{\text{base}}$ at the fixed end are used: $\theta(L) = \theta_{\text{base}}$ and a zero bending moment at the free end, $\frac{\mathrm{d}\theta}{\mathrm{d}s}|_{s=0} = 0$.

In the experimental component of the work, cells were placed at the bottom of a laminar flow chamber where a fluid flow with a shear stress of 0.25 Pa (corresponding to a flow rate of 500 μl/min) was applied with a syringe pump [62]. Along the length of the ciliium, it is safe to assume that the laminar flow velocity increases linearly with distance from the bottom surface. The force is thus approximated as the 2D planar drag force acting on a cylinder in low Reynolds number Stokes flow

$$Q(h) = \frac{2\pi h\tau}{\ln(L/2r)}, \tag{5.4}$$

where $\tau$ is the wall shear stress, $h$ is the distance between the cilium and the wall, $r$ is the diameter, and $L$ is the contour length of the primary cilium. The distance $h(s)$ can be computed as $h(s,\theta) = H - \int_0^s s' \cos(\theta(s'))\mathrm{d}s'$, where $H$ is the height from the tip of the cilium to the cell surface. Equation 5.4 is the drag force acting on a beam that is slightly deformed. When the elastic beam is highly deformed, the slender-body theory (see Sect. 5.3.2) can better capture the drag force [63]. In addition to the above closed-form approach they also conducted a computational study using the commercial finite-element code COMSOL to simulate the interaction between a viscous fluid and a cylinder (a model for a section of a cilium) in a low Reynolds number planar flow [62]. The angle between the cylinder and the vertical was veried from 0° to 80° and total drag was determined at each angle and fit with a polynomial regression. Convergence was verified by creating a refined mesh of 85,000 elements and observing less than a 15 % change in predicted drag.

The flexural rigidity $E$I of the axoneme is a parameter of this model. [62] developed a numerical algorithm to find the $E$I that best fit experiment data. First, the nonstressed configuration and $\theta_{\text{base}}$ were calculated from the experimental observation. They then calculated the $E$I that would give the best-fit solution to the equilibrium profile with the 2D analytic drag approximation, and the drag from the 3D finite element simulation was used to refine the estimate for $E$I. The nonlocal differential Eq. 5.3 was solved numerically. In this model the basal body support is not included. Instead the basal angle at equilibrium from the experiments is used ito find the best-fit equilibrium cilium profile [62]. This assumption will be relaxed in the slender-body model (Sect. 5.3.2).

### *5.3.2 Slender-Body Theory*

The ratio ($\epsilon$) of axonemal radius $r$ to length $L$ of primary cilia is often in the range $10^{-2} \leq \epsilon \leq 10^{-1}$, consequently, the relevant physics underlying the primary cilium dynamics under flow is the bending of a supported elastic slender filament under a hydrodynamic load. The elastic slender-body formulation [48, 50, 71, 72] is adopted to model the bending of the ciliary axoneme under flow [63]. First, the force distribution along the slender-body centerline is decomposed (as $\mathbf{F} = F^t(s)\hat{t} + F^n(s)\hat{n}$) in the tangential $\hat{t}$ and the normal $\hat{n}$ directions with $s \in [s_0, s_e]$ the arclength.

The curvature $\kappa$ is assumed to be linearly proportional to the moment $M$: $M = E_B\kappa$. The external load $\mathbf{P}(s) = P^t\hat{t} + P^n\hat{n}$ is related to the force by $\frac{\mathrm{d}\mathbf{F}}{\mathrm{d}s} + \mathbf{P} = \mathbf{F}_s + \mathbf{P} = 0$. The moment and the force density are related as $\frac{\mathrm{d}M}{\mathrm{d}s} = M_s = F^n$. Denoting the filament centerline $\mathbf{x} = (x(s), y(s))$ and $\hat{t} = (t_1(s), t_2(s))$, the governing dimensionless equations are obtained by force balance for an elastic filament of constant length, see [63] for a detailed derivation. The external hydrodynamic load $\mathbf{P}$ is computed from the local SBT as

$$\mathbf{P} = -\frac{\eta\left(\partial\mathbf{x}/\partial t - U\right)}{(1+2\beta)\,\mathbf{I} + (1-2\beta)\,\mathbf{x}_s \otimes \mathbf{x}_s}, \tag{5.5}$$

where $U$ is the fluid velocity at the location $\mathbf{x}$ in the absence of the elastic filament, $\beta = 1/(-\ln(\epsilon^2 e))$ is the filament slenderness and $\eta = \frac{8\pi\mu\dot{\gamma}L^4\beta}{E_B}$ is the effective viscosity with $\mu$ the fluid viscosity and $\dot{\gamma}$ the characteristic flow rate. The parameter $\eta$ quantifies the magnitude of the viscous force relative to the restoring elastic force. This formulation is also generalized for time-dependent dynamics of an inextensible elastic filament under flow in [63].

At the free filament end ($s = s_e$), the force-free and torque-free conditions give

$$F^t(s_e) = 0, \quad F^n(s_e) = 0, \quad \kappa(s_e) = 0. \tag{5.6}$$

At the basal body ($s = s_0$) the filament is fixed: $x(s_0) = 0$ and $y(s_0) = 0$. The basal anchorage behaves like a nonlinear rotational spring that couples the axoneme to an elastic shell [63]. Assuming axial symmetry for the elastic shell, the shell surface is parametrized as $(r(l), z(l))$ with $l \in [l_0, l_e]$ the arc-length along the elastic sheet. $\psi$ is the angle between the elastic shell normal vector $\mathbf{n}$ and the $r$-axis, see Fig. 5.4a. The elastic filament is coupled to a small patch of an inextensible elastic sheet [73, 74]. The elastic sheet has a bending rigidity $E_T \equiv \lambda E_B$ with $\lambda \sim \mathcal{O}(1)$. The interested readers are referred to [63] for the governing equations of the elastic sheet with axial symmetry. At the junction where the elastic shell is connected to the filament base, the unit tangent vector is reasonably assumed to be continuous from the filament base to the elastic shell [63]. Secondly, the force distribution and the curvature are also assumed to be continuous at the junction.

As explained in Sect. 5.1, the axonemal anchorage consists of support from the Y-links and various distal appendages in a very small region. To model the complex basal anchorage, we assume that the mechanical support from the basal anchorage can be treated as a localized finite torque on the elastic cylindrical shell at $l = l_0$. The equation for the moment along the ciliary axoneme is then

$$\frac{\mathrm{d}M}{\mathrm{d}s} = F^n(s) + h\delta\left(s - s_0\right), \tag{5.7}$$

where $h$ is the torque magnitude and $\delta(s - s_0)$ is the Kronecker-delta function at $s_0$. Integrating over a small interval around $s_0$, we find that the localized torque (from the TZ fibers) induces a jump in the moment

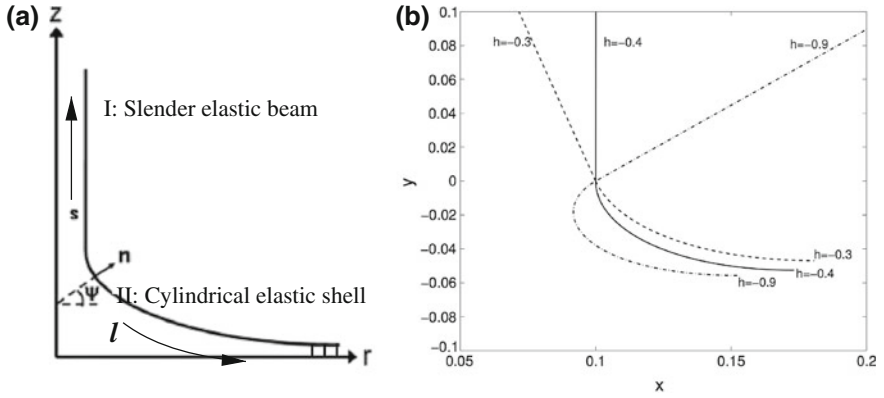


**Fig. 5.4** Panel **a** Coordinate system for the *cylindrical shell* in the transition zone. Region I is the elastic slender beam, and region II is the transition zone that is bound to the distal appendages (*small vertical bars* on the right end, where $\psi = \pi/2$ is fixed). Panel **b** Profiles of the beam-shell system in a quiescent flow ($\eta = 0$) with different values for the torque $h$ at the base. Reproduced from [63] with permission from the Biophysical Society

$$M\left(s_0^+\right) = M\left(s_0^-\right) + h \rightarrow \kappa\left(s_0^+\right) = \kappa\left(s_0^-\right) + \frac{h}{E_B} = \frac{h}{E_B}, \tag{5.8}$$

which, in turn, induces a curvature at the base. At the junction the radius of the elastic sheet is taken to be the radius of the cilium, and the height of the transition membrane is assumed to be of the same order as the filament radius. At the opposite end, the elastic sheet is assumed to be connected to the cell membrane in a flat angle such that $\psi(l_e) = \pi/2$.

In their beam-shell model the torque $h$ represents the total mechanical support from the basal anchorage [63]. Figure 5.4b illustrates the cilium-transition zone profiles for different values of $h$. A nonzero $h$ is needed to maintain the axoneme in the upright position in the absence of flow. This is because the unforced equilibrium is a flat horizontal shell coupled to a horizontal straight beam. As the cilium basal body is mechanically connected to the ciliary membrane through the distal appendages, it seems physiologically feasible that $h$ is not zero. Numerically, we find that the value of $h$ required to support the upright cilium axoneme is proportional to $\lambda$, and in dimensionless units $h = -0.145$ when $\lambda = 1/10$ and $h = -0.402$ when $\lambda = 1/3.6$.

## 5.4 Summary of Results

### *5.4.1 Results from Drag Force Model*

Figure 5.5a depicts an example of the best-fit from the drag-force model. For the six individual cilia examined under physiological flow conditions, the average basal

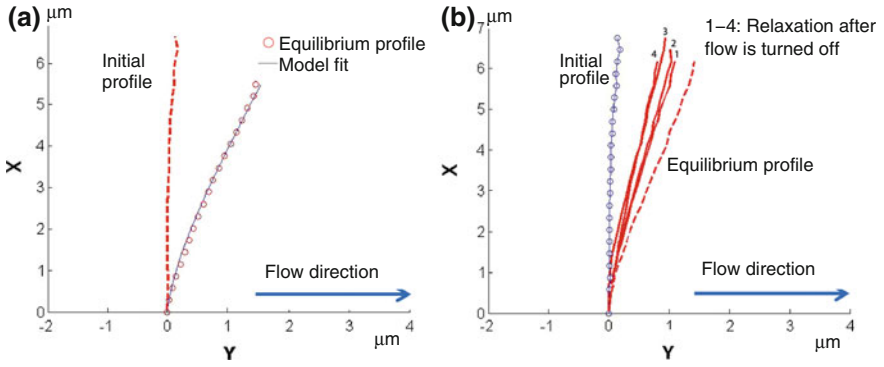


**Fig. 5.5** Panel **a** best-fit to a deflected equilibrium primary cilium profile under flow, in the direction of the *arrows* in the figure. Panel **b** An example of cilium relaxation after the flow is turned off. The deflected profile (*dashed line*) is at equilibrium. *Curve* 1 is the first time point taken at time 0 min, and *curve* 4 is the last at time 2 min with a 30-s interval between each point. Adapted from results in [62]

rotation was found to be $10.1° \pm 2.8°$. The averaged best-fit $EI$ from the drag model is $\sim 3.1 \pm 0.7 \times 10^{-22}$ Nm$^2$, while a slightly lower value is obtained with the finite element approach $\sim 2.1 \pm 0.45 \times 10^{-22}$ Nm$^2$. Interestingly, some primary cilia subjected to the 3 ml/min flow rate did not return to the same nonstressed, pre-flow position after flow had ceased as shown in Fig. 5.5b. Other cilia displayed a slight recovery toward the original nonstressed position after flow had ceased, but did not fully recover (see Fig. 5.2).

## *5.4.2 Results from Slender-Body Theory*

### 5.4.2.1 Steady Shear Flow

Young et al. [63] developed a systematic procedure to find the best-fit equilibrium ciliary profile and the corresponding bending rigidity [63], and applied this procedure to a set of 80 cilia. Almost 70 % of the data set falls in the range of $1 \times 10^{-23}$ Nm$^2$ $\leq EI \leq 5 \times 10^{-23}$ Nm$^2$. The average value is $EI \sim 8.4 \times 10^{-23}$ Nm$^2$, which is higher than reported in [58] and lower than results from the drag force model in Sect. 5.4.1.

Young et al. [63] also applied the beam-shell model to the dynamics of cilium bending under flow. The high-speed imaging system can capture the bending dynamics in 2D, and an example is shown Fig. 5.3. The comparison between experimental and computational findings is summarized in Fig. 5.6. The cilium bends and quickly reaches the equilibrium position. The flow is stopped at $t \sim 5$ and the cilium relaxes to a position close to the initial one. Despite the noise, results indicate that cilium

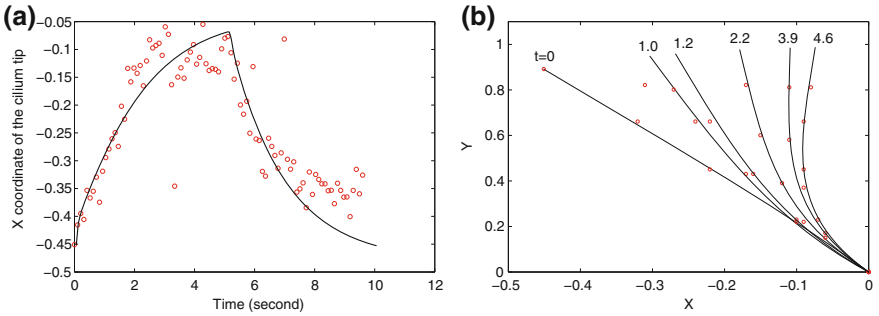


**Fig. 5.6** Comparison between model (*solid lines*) and experiment results (*symbols*). The unit for time is second and the cilium length is 2.7 μm at $t = 0$. Panel **a** plots the $x$-coordinate of cilium tip versus time, and panel **b** compares the cilium profiles at different times. Reproduced from [63] with permission from the Biophysical Society

bending and relaxation are well approximated by our simple model incorporating viscous stress, rotational stiffness and residual stress [63].

#### 5.4.2.2 Periodic Flow

We recently applied the elastic beam-shell model to examine the dynamics of a primary cilium under a periodic flow with a sinusoidal temporal variation. Such a periodic flow is motivated by the physiological conditions in kidney and bone marrow, where primary cilia are thought to undergo repetitive bending. It has also been observed that the basal anchorage may deteriorate due to repeated bending over a long time. This observation illustrates the complex nature of the basal body and the surrounding cytoskeletal structures.

Here we focus on the periodic ciliary bending dynamics with different values of axonemal rigidity and the basal orientation. Small effective viscosity $\eta$ represents a stiff axoneme while large $\eta$ means the axoneme is flexible. In our beam-shell model the basal orientation of the axoneme is determined by the balance of moments at the connection between the beam and the shell. By adjusting the torque $h$, keeping everything else fixed, the basal orientation varies from upright to tilted, as shown in Fig. 5.4b.

Figure 5.7 shows the bending dynamics for an axoneme with $\eta = 0.1$ in panel a and $\eta = 20$ in panel b. For both panels the flow periodicity is fixed at 10. At $t = 0$ the cilium profile is the upright thick solid curve at the center. For $0 \leq t \leq 5$ the beam bends toward the left in the first half of the cycle. For $5 \leq t \leq 10$ the beam bends toward the right, and then returns to the center at the completion of a full cycle. Figure 5.8a shows the basal angle versus time for different axonemal stiffnesses, and the corresponding angle at the free end is depicted in panel b. During the first cycle (from $t = 0$ to $t = 10$) the maximum cilium bending is reached before the reversal of flow. After the first cycle the cilium bending is more symmetric between

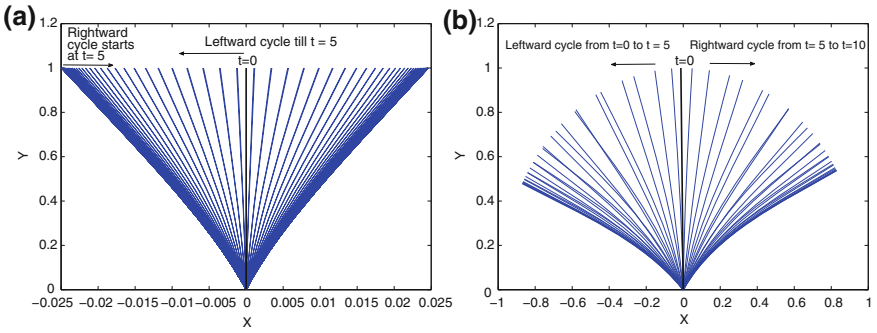


**Fig. 5.7** **a** Repeated bending of a stiff beam ($\eta = 0.1$) under a periodic flow. **b** Repeated bending of a flexible beam ($\eta = 20$). The leftward flow occurs from $t = 0$ till $t = 5$, and turns to the rightward flow for $5 < t \leq 10$

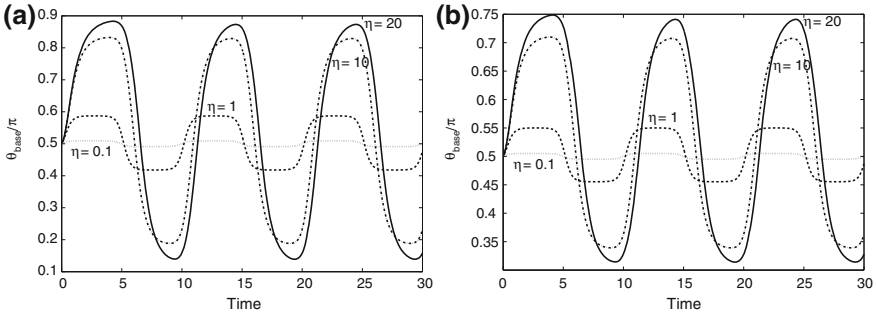


**Fig. 5.8** **a** Basal angle versus time for four values of $\eta$ as labeled in the figure. **b** The corresponding axoneme angle at the free end

the rightward and leftward cycles. In Fig. 5.8b we also observe that the more flexible axoneme is taking longer to reverse its orientation.

We also carried out the calculations of a tilted cilium under the same periodic flow. The initial ciliary profile is tilted with a basal angle $\sim 0.38\,\pi$. The bending dynamics are depicted in Fig. 5.9a for a stiff beam, and Fig. 5.9b for a more flexible beam. Figure 5.10 shows the corresponding angle at the base (Fig. 5.10a) and at the free end (Fig. 5.10b) for four values of $\eta$ as labeled. We observe that the axoneme spends more time on the left to the initial profile than on the right for more flexible cases. Such asymmetry is negligible for a stiff axoneme. It will be interesting to compare these results with experimental observations from the oscillatory flow chamber and make quantitative connections with the morphological changes of the cytoskeletal network that is in contact with the basal body.

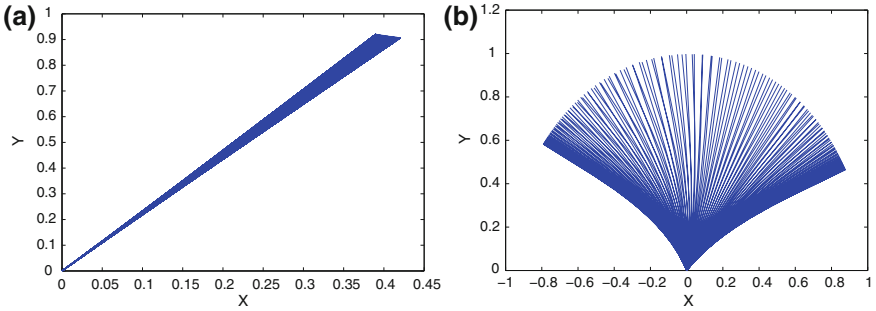


**Fig. 5.9** Repeated bending of an initially tilted cilium. **a** A stiff beam ($\eta = 0.1$) under a periodic flow. **b** A more flexible beam ($\eta = 20$). The leftward flow starts from $t = 0$ till $t = 5$, and turns to the rightward flow for $5 < t \leq 10$

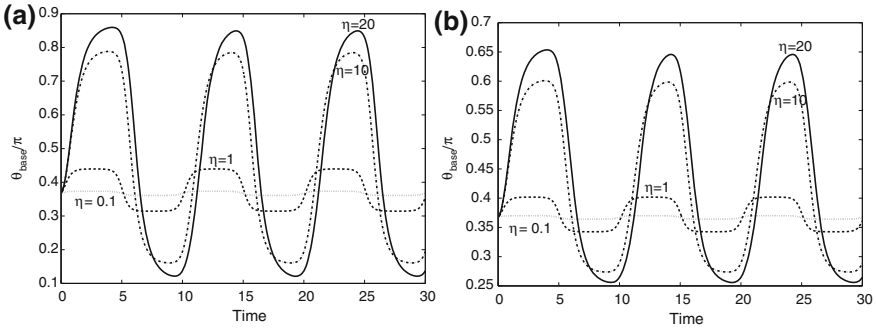


**Fig. 5.10** **a** Basal angle versus time for four values of $\eta$ as labeled in the figure. **b** The corresponding axoneme angle at the free end

## 5.5 Microtubule Network

Results summarized in Sects. 5.4.1 and 5.4.2 demonstrate the importance of incorporating the basal body anchorage into the multiscale modeling of primary cilia. [75] pointed out that very little is known about the subciliary compartment and the details of the basal support. Structurally, the majority of microtubules contributing to the anchoring of the primary cilium assemble and emanate from around the basal body, which is a modified form of the microtubule organizing center (MTOC) [20, 76]. Modifying the microtubule attachment of primary cilia would change primary cilia mechanics and, possibly, their mechanosensitivity [77]. Several attempts have been made to count the number of microtubules emanating from the basal body and the results are found to depend on the cell type [78, 79]. It has also been shown that the cellular response to shear stress depends on microtubular integrity [80]. In our preliminary results we find an increase in microtubules around primary cilia and a

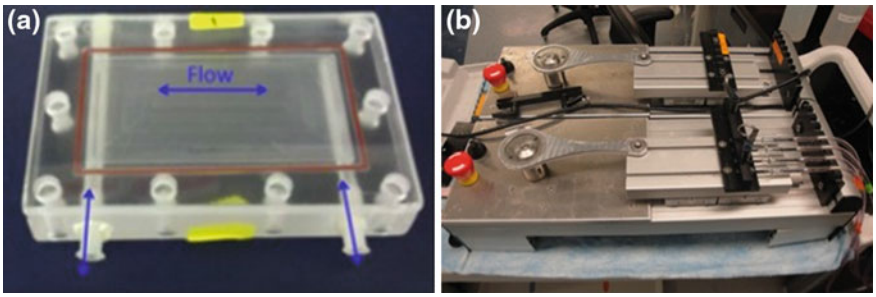


**Fig. 5.11** **a** Parallel plate flow chamber used to apply the mechanical stimulus. **b** Mechanical loading device used to apply oscillatory fluid flow to cells

conformation change within the microtubule network in response to oscillatory fluid flow (OFF) stimulation (more details can be found in [81]).

In a series of preliminary experiments, the IMCD-SSTR3 cell line (inner medullary collecting duct cells, stably transfected with a somatostatin receptor-3 green florescent protein (GFP) fusion protein) was used and cultured following the procedures in [82]. Oscillatory fluid flow was applied to cells using a parallel plate flow chamber (see Fig. 5.11a) which has been described previously [83]. The flow rate was selected to yield peak shear stress of 1 Pa. Cells were exposed to this type of mechanical stimulus for one hour. After oscillatory fluid flow, cells were fixed immediately [81].

Full 3D images of cells were obtained using a confocal microscope. Slices were collected into a z-stack, with approximately 0.08 μm spacing. The open-source platform Fiji [84] and one of its plugins (Simple Neurite Tracer [85]) were used to analyze the image stacks. Using this approach we could count the number of microtubules around primary cilia. These experiments were repeated using the MLO-Y4 cell line, which has characteristics similar to osteocytes.

Preliminary results show that oscillatory fluid flow (with a frequency of 0.5, 1.0 and 2.0 Hz and a peak shear stress of 1 Pa for 1 h) increases the number of microtubules attached to the base of primary cilia. As illustrated in Fig. 5.12, more dense structures are also evident. For IMCD-SSTR3 cells the number of MT around the basal body increased from ∼6 to ∼15 on average. For MLO-Y4 cells the number increased from ∼10 to ∼16. This suggests that the cell may modulate the number of microtubules anchoring primary cilia, which may change cilium mechanics and affect mechanosensation.

We are currently working to replace the elastic shell in the beam-shell model [63] with a cross-linked semi-flexible polymer network to model the cytoskeletal network that is connected with the cilium basal body. The mechanical transduction of such a random, semi-flexible, cross-linked biopolymer network is a very challenging subject because its in vivo properties are expected to be highly dependent on the length and timescales on which they are being probed. The static mechanical properties of such networks have been investigated in the linear response regime [86–88]. Such networks can be constructed by sequential random deposition of monodisperse

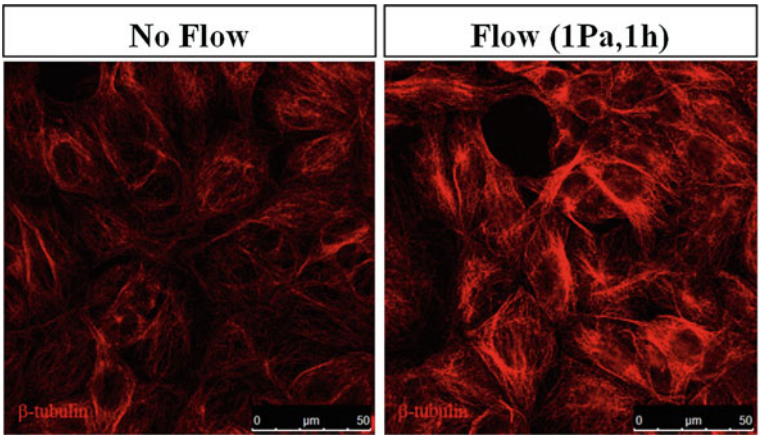


**Fig. 5.12** Effects of oscillatory fluid flow (1 Pa for 1 h) in microtubule morphology for IMCD-SSTR3 cells. Both images were taken with the same intensity. Images are produced from experiments in [81]

filaments into a two-dimensional box. Since the position and orientation of filaments are uniformly distributed over the allowed ranges, the networks are isotropic and homogeneous on sufficiently large scales. Each intersection between filaments is a cross link. The elastic moduli can be computed from the discrete Hamiltonian that consists of both the discrete bending energy and compression/extensional energy [89–91].

## 5.6 Conclusions and Open Questions

The mechanics of the primary cilium has been extensively investigated experimentally. Several attempts have been made to theoretically model its bending mechanics. From our modeling approaches we find that it is essential to capture the fluid–structure interaction between fluid flow and the elastic ciliary axoneme. The slender-body theory is modified to incorporate the basal body anchorage, which behaves like a nonlinear rotational spring. With such rotational stiffness at the cilium base, the slender-body model reproduces the experimentally observed bending dynamics, and sheds light on the repetitive bending of primary cilia.

The primary cilium has been known to play an important mechanosensory role in numerous tissues across many species and organisms [92]. The cilium's ability to do so depends on its adaptation to different situations. For example, the primary cilium is able to dynamically modulate its length, and thus, fine tune its sensitivity to the extracellular environment. By blocking calcium ion entry and increasing intracellular cAMP (cyclic adenosine monophosphate), Besschetnova et al. recently demonstrated that the length of the primary cilium (in a mammalian epithelia and

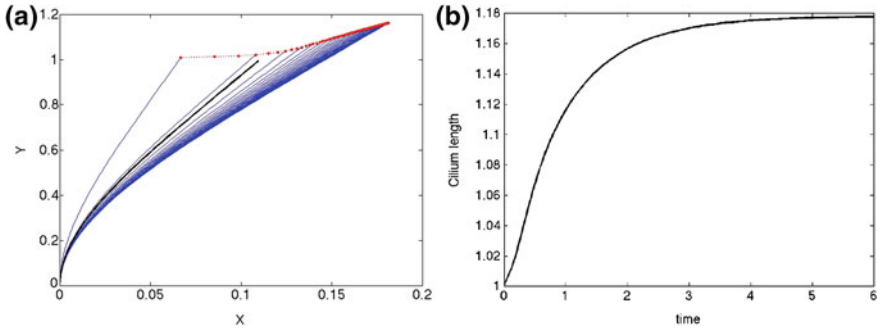


**Fig. 5.13** **a** Bending of a primary cilium with a variable length. The *thick solid line* is the equilibrium profile for the cilium with a fixed length of unity. **b** The corresponding cilium length over time

mesenchymal cells) increased two-fold in 3 h [32]. After the application of fluid shear, which is known to increase intracellular $Ca^{2+}$ and decrease intracellular cAMP, the average cilia length decreased by 20–35 %. Furthermore, it has been demonstrated that overloading of chondrocytes results in a decrease in cilia length and conversely stress deprivation in tendon cells results in an immediate and significant increase in length [93, 94].

The slender-body model can incorporate the change of length due to the molecular alterations that are part of the cilium dynamics under load. From the molecular description we first have an empirical model for the cilium length [95]

$$\frac{\mathrm{d}L}{\mathrm{d}t} = \frac{a}{L} - b, \tag{5.9}$$

and the fluid velocity $U$ in Eq. 5.5 should be replaced with $U + \frac{\mathrm{d}L}{\mathrm{d}t}\mathbf{x}_s$. Coefficients $a$ and $b$ are related to the assembly rate and disassociation rate at the cilium tip, respectively. If we assume that $a$ increases with the stress at the cilium base and $b$ remains constant, we find that (1) the cilium deflected more and (2) the cilium length can increase almost 16 % before an equilibrium profile is reached, see Fig. 5.13.

Another phenomenon that requires more experimental observations for accurate multiscale modeling is the varying circumferential arrangement of the microtubule doublets along the axoneme [96, 97]. Although the cause of this nonhomogeneous organization is unclear, it is most likely due to the lack of interconnecting attachments such as nexin links between axonemal doublets. The mechanical consequence of the disrupted circumferential organization may give rise to inhomogeneous bending rigidity along the length of the cilium.

**Acknowledgments** YNY acknowledges helpful discussion with Jung-Chi Liao, and partial support of NSF from grants CBET-0853673, DMS-0708977, and DMS-0420590 for the computing cluster at NJIT. AMN acknowledges support from NIH through grant AR59038. CRJ is supported by NIAM/NIH through grants AR45989, AR54156 and AR62177 and New York State Stem Cell Research Grant N08G-210.

## References


1. Robert A. Bloodgood, "From central to rudimentary to primary: The history of an underappreciated organelle whose time has come. the primary cilium." in *Methods in Cell Biology, Vol. 94: Primary Cilia*, edited by Roger D. Sloboda (Academic Press, San Diego, California, USA, 2009) pp. 3–52.
2. P. Satir, L. B. Pedersen, and S. T. Christensen, "The primary cilium at a glance," J. Cell Sci. **123**, 499 (2010).
3. S. Temiyasathit and C. R. Jacobs, "Osteocyte primary cilium and its role in bone mechanotransduction," Ann. N. Y. Acad. Sci. **1192**, 422–428 (2010).
4. Rajat Rohatgi and William J. Snell, "The ciliary membrane," Current Opinion in Cell Biology **22**, 541–546 (2010).
5. Gregory J. Pazour and Robert A. Bloodgood, "Targeting proteins to the ciliary membrane," (Academic Press, San Diego, USA, 2008) pp. 116–151.
6. Hiroaki Ishikawa and Wallace F. Marshall, "Ciliogenesis: building the cell's antenna," Nature Review **12**, 222 (2011).
7. N. R. Silvester, "The cilia of tetrahymena pyriformis: X-Ray diffraction by the ciliary membrane," Journal of Molecular Biology **8**, 11–19 (1964).
8. N. B. Gilula and P. Satir, "The ciliary necklace. a ciliary membrane specialization," Journal of Cell Biology 53, 494–509 (1972).
9. P. Satir and N. B. Gilula, "The cell junction in a lamelibranch gill ciliated epithelium: localization of pyroantimonate precipitate," Journal of Cell Biology **47**, 468–487 (1970).
10. W. F. Marshall, "Basal bodies: Platforms for building cilia," (Academic Press, San Diego, USA, 2008) pp. 2–23.
11. G. Albrecht-Buehler and A. Bushnell, "The ultrastructure of primary cilia in quiescent 3t3 cells," Experimental Cell Research **126**, 427–437 (1980).
12. D. N. Wheatley, "Nanobiology of the primary cilium-paradigm of a multifunctional nanomachine complex," Methods in Cell Biology **90**, 139–156 (2008).
13. R. N. Fariss, R. S. Molday, S. K. Fisher, and B. Matsumoto, "Evidence from normal and degenerating photoreceptors that two outer segment integral membrane proteins have separate transport pathways," Journal of Comparative Neurology **387**, 148–156 (1997).
14. N. Kobayashi and N. Hirokawa, "Cytoskeletal architechture and immunocytochemical localization of fordin in the terminal web of the ciliated epithelial cell," Cell Motility and the Cytoskeleton **11**, 167–177 (1988).
15. F. R. Garcia-Gonzalo and J. F. Reiter, "Scoring a backstage pass: Mechanisms of ciliogenesis and ciliary access," J. Cell Biol. **11**, 697–709 (2012).
16. L. B. Pedersen, J. M. Schroder, P. Satir, and S. T. Christensen, "The ciliary cytoskeleton," Comprehensive Physiology **2**, 779–803 (2012).
17. Z. Mirzadeh, Y.-G. Han, M. Soriano-Navarro, HJ. M. Garcia-Verdugo, and A. Alvarez-Buylla, "Cilia organize ependymal planar polarity," J. Neuroscience **30**, 2600–2610 (2010).
18. H. W. Ehlen, L. A. Buelens, and A. Vortkamp, "Hedgehog signaling in skeletal development," Birth Defects Res C Embryo Today **78**, 267–279 (2006).
19. C. J. Haycraft and R. Serra, "Cilia involvement in patterning and maintenance of the skeleton," Curr. Top Dev Biol **85**, 303–332 (2008).
20. J. R. Marszalek, P. Ruiz-Lozano, E. Roberts, K. R. Chien, and L. S. Goldstein, "Situs inversus and embryonic ciliary morphogenesis defects in mouse mutants lacking the kif3a subunit of kinesin-ii," Proc. Natl Acad Sci USA **114**, 205–212 (1999).
21. N. Hirokawa, Y. Tanaka, Y. Okada, and S. Takeda, "Nodal ow and the generation of left-right asymmetry," Cell **125**, 33–45 (2006).
22. B. Basu and M. Brueckner, "Cilia: Multifunctional organelles at the center of vertebrate left-right asymmetry," (Academic Press, San Diego, USA, 2008) pp. 152–261.
23. Y.-G. Han and A. Alvarez-Buylla, "Role of primary cilia in brain development and cancer," Current Opinion in Neurobiology **20**, 58–67 (2010).

24. M. A. Willaredt, E. Tasouri, K. L. Tucker, "Primary cilia and forebrain development," Mech. Devel. **online**, in press (2012).
25. H. A. Praetorius and K. R. Spring, "Bending the mdck cell primary cilium increases intracellular calcium," J. Membr. Biol. **184**, 71–79 (2001).
26. H. A. Praetorius and K. R. Spring, "Removal of the mdck cell primary cilium abolishes ow sensing," J. Membr. Biol. **191**, 69–76 (2003).
27. E. J. Arnsdorf, P. Tummala, and C. R. Jacobs, "Wnt signaling and n-cadherin related betacatenin signaling play a role in mechanically induced osteogenic cell fate," PLoS One **4**, e5388 (2009).
28. S. M. Nauli, F. J. Alenghat, Y. Luo, E. Williams, P. Vassilev, X. Li, A. E. Elia, W. Lu, E. M. Brown, S. J. Quinn, D. E. Ingber, and J. Zhou, "Polycistins 1 and 2 mediate mechanosensation in the priimary cilium of kidney cells," Nat Genet **33**, 129–137 (2003).
29. A. I. Masyuk, T. V. Masyuk, P. L. Splinter, B. Q. Huang, A. J. Stroope, and N. F. LaRusso, "Cholangiocyte cilia detect changes in luminal uid ow and transmit them into intracellular Ca2+ and cAMP signaling," Gastroenterology **131**, 911–920 (2006).
30. S. S. Pae and J. C. Saunders, "Intra- and extracellular calcium modulates stereocilia stiffness on chick cochlear hair cells," Proceedings of the National Academy of Sciences **91**, 1153–1157 (1994).
31. E. T. OBrien, E. D. Salmon, and H. P. Erickson, "How calcium causes microtubule depolymerization," Cell Motility and Cytoskeleton **36**, 125–135 (1997).
32. T. Y. Besschetnova, E. Kolpakova-Hart, Y. Guan, J. Zhou, B. R. Olsen, and J. V. Shah, "Identification of signaling pathways regulating primary cilium length," Current Biology **20**, 182–187 (2010).
33. I. Ibanez-Tallon, N. Heintz, and H. Omran, "To beat or not to beat: roles of cilia in development and disease," Hum. Mol. Genet. **12**, R27–R35 (2003).
34. J. L. Badano, N. Mitsuma, P. L. Beales, and N. Katsanis, "The ciliopathies: an emerging class of human genetic disorders," Annu. Rev. Genomics Hum. Genet. **7**, 125–148 (2006).
35. M. Adams, U. M. Smith, C. V. Logan, and C. A. Johnson, "Recent advances in the molecular pathology, cell biology and genetics of ciliopathies," J. Med. Genet. **45**, 257–267 (2008).
36. I. R. Veland, A. Awan, L. B. Pedersen, B. K. Yoder, and S. T. Christensen, "Primary cilia and signaling pathways in mammalian development, health and disease," Nephron. Physiol. **111**, 39–53 (2009).
37. F. Hildebrandt, T. Benzing, and N. Katsanis, "Ciliopathies," N. Engl. J. Med. **364**, 1533–1543 (2011).
38. A. G. Robling, D. B. Burr, and C. H. Turner, "Partitionin a daily mechanical stimulus into discrete loading bouts improves the osteogenic response to loading," J. Bone Miner Res. **15**, 1596–1602 (2000).
39. L. K. Saxon, A. G. Robling, A. B. Castillo, S. Mohan, and C. H. Turner, "The skeletal responsiveness to mechanical loading is enchanced in mice with a null mutation in estrogen receptor-beta," Am. J. Physiol. Endocrinol. Metab. **293**, E484–491 (2007).
40. T. L. Donahue, T. R. Haut, C. E. Yellowley, H. J. Donahue, and C. R. Jacobs, "Mechanosensitivity of bone cells to oscillating uid ow induced shear stress may be modulated by chemotransport," J. Biomech. **36**, p1363–1371 (2003).
41. K. Van der Heiden, B. P. Hierck, R. Krams, R. de Crom, C. Chen, M Baiker, M. J. Pourquie, F. E. Alkemade, M. C. Deruiter, A. C. Tittenberger de Groot, and R. E. Poelmann, "Endothelial primary cilia in areas of distrubed ow are at the base of atherosclerosis," Atherosclerosis **196**, 542–50 (2008).
42. Ko Miyoshi, Kyosuke Kasashara, Ikuko Miyazaki, and Masato Asanuma, "Factors that in uence primary cilium length," Acta Med. Okayama **65**, 279–285 (2011).
43. Cornelia E. Farnum and Norman J. Wilsman, "Axonemal positioning and orientation in three-dimensional space for primary cilia: What is known, what is assumed, and what needs clarification," Developmental Dynamics **240**, 2405–2431 (2011).
44. A. R. Shield, B. L. Fiser, B. A. Evans, M. R. Falvo, S.Washburn, and R. Superfine, "Biomimetic cilia arrays generate simultaneous pumping and mixing regimes," Proc. Nat. Sci. USA 107, 15670 (2010).

45. N. Coq, A. Bricard, F.-D. Delapierre, L. Malaquin, O. Du Roure, M. Fermigier, and D. Bartolo, "Collective beating of artificial microcilia," Phys. Rev. Lett. **107**, 014501 (2011).
46. M. J. Lighthill, Mathematical Biofluiddynamics, Regional conference series in applied mathematics, Vol. 17 (Society for Industrial and Applied Mathematics, 1975).
47. M. J. Lighthill, "Flagellar hydrodynamics," SIAM Rev. **18**, 161–230 (1976).
48. S. Gueron and N. Liron, "Ciliary motion modeling, and dynamic multicilia interactions," Biophysical Journal **63**, 1045–1058 (1992).
49. S. Gueron and K. Levit-Gurevich, "The three-dimensional motion of slender filaments," Math. Methods Appl. Sci. **24**, 1577–1603 (2001).
50. S. Gueron and K. Levit-Gurevich, "A three-dimensional model for ciliary motion based on the internal 9+2 structure," Proc. R. Soc. Lond. B **268**, 599–607 (2001).
51. R. H. Dillon and L. J. Fauci, "An integrative model of internal axoneme mechanics and external fluid dynamics in ciliary beating," Journal of Theoretical Biology **207**, 415–430 (2000).
52. R. H. Dillon, L. J. Fauci, and C. Omoto, "Mathematical modeling of axoneme mechanics and fluid dynamics in ciliary and sperm motility," Dynamics of Continuous, Discrete and Impulsive Systems Series A: Mathematical Analysis **10**, 745–757 (2003).
53. R. H. Dillon, L. J. Fauci, C. Omoto, and X. Yang, "Fluid dynamic models of agellar and ciliary beating," Annals of the New York Academy of Sciences **1101**, 494–505 (2007).
54. R. H. Dillon, L. J. Fauci, and X. Yang, "Sperm motility and multicilliary beating: An integrative mechanical model," Computers and Mathematics with Applications **52**, 749–758 (2006).
55. L. J. Fauci and R. Dillon, "Bio uidmechanics of reproduction," Annual Review of Fluid Mechanics **38**, 371–394 (2006).
56. X. Yang, R. H. Dillon, and L. J. Fauci, "An integrative computational model of multiciliary beating," Bull. Math. Bio. **70**, 1192–1215 (2008).
57. H. Shum and E. A. Gaffney, "The effects of agellar hook compliance on motility of monotrichous bacteria: A modeling study," Phys. Fluids **24**, 061901 (2012).
58. Eric A. Schwartz, Michelle L. Leonard, Rena Bizios, and Samuel S. Bowser, "Analysis and modeling of the primary cilium bending response to uid shear," Am. J. Physiol. **272**, F132–F138 (1997).
59. Andrew Resnick and Ulrich Hopfer, "Mechanical stimulation of primary cilia," Frontiers in Bioscience **13**, 1665–1680 (2008).
60. W. Liu, N. s. Murica, Y. Duan, s. Weinbaum, B. K. Yoder, E. Schwiebert, and L. M. Satlin, "Mechanoregulation of intracellular ca2+ concentration is attenuated in collecting duct of monocilium-impaired orpk mice," Am. J. Physiol. Renal Physiol. **289**, F978–988 (2005).
61. S. Rydholm, G. Zwartz, J. M. Kowalewski, P. Kamali-Zare, T. Frisk, and H. Brismar, "Mechanical properties of primary cilia regulate the response to uid ow," Am. J. Physiol. **298**, F1096–F1102 (2010).
62. Matthew E. Downs, An M. Nguyen, Florian A. Herzog, David A. Hoey, and Christopher R. Jacobs, "An experimental and computational analysis of primary cilia de ection under fluid flow," Computer Methods in Biomechanics and Biomedical Engineering **iFirst**, 1–9 (2012).
63. Y.-N. Young, M. Downs, and C. R. Jacobs, "Dynamics of the primary cilium in shear flow," Biophys. J. **103**, 629–639 (2012).
64. X. Jin, A. M. Mohieldin, B. S. Muntean, J. A. Green, J. V. Shah, K. Mykytyn, and S. M. Nauli, "Cilioplasm is a cellular compartment for calcium signaling in response to mechanical and chemical stimuli," Cell. Mol. Life Sci. **in press**, 1–14 (2013).
65. S. Su, S. C. Phua, R. DeRose, S. Chiba, K. Narita, P. N. Kalugin, T. Katada, K. Kontani, S. Takeda, and T. Inoue, "Genetically encoded calcium indicator illuminates calcium dynamics within primary cilia," Nat. Methods **10**, 1105–1107 (2013).
66. W. Zheng, J.-C. Liao, B. Brooks, and S. Doniach, "Toward the mechanism of dynamical couplings and translocation in hepatitis c virus ns3 helicase using elastic network model," Proteins: Structure, Function, and Bioinformatics **67**, 886–896 (2007).
67. B. Nadrowski, P. Martin, and F. Julicher, "Active hair-bundle motility harnesses noises to operate near an optimum of mechanosensitivity," Proc. Nat. Acad. Sci. **101**, 12195–12200 (2004).

68. J-Y. Tinevez, F. Julicher, and P. Martin, “Unifying the various incarnations of active hairbundle motility by the vertebrate hair cell,” Biophys. J. **93**, 4053–4067 (2007).
69. J. Ashmore, P. Avan, W. E. Brownell, P. Dallos, K. Dierkes, R. Fettiplace, K. Grosh, C. M.Hackney, A. J. Hudspeth, F. Julicher, B. Lindner, P. Martin, J. Meaud, C. Petit, J. R. Santos Sacchi, and B. Canlon, “The remarkable cochlear amplifier,” Hearing Research **266**, 1–17 (2010).
70. A. B. Neiman, K. Dierkes, B. Lindner, L. Han, and A. L. Shilnikov, “Spontaneous voltage oscillations and response dynamics of a Hodgkin-Huxley type model of sensory hair cells,” J. Mathematical Neuroscience **1**, 1–11 (2011).
71. C. Pozrikidis, “Shear ow over cylindrical rods attached to a substrate,” Fluids and Structures **26**, 393–405 (2010).
72. C. Pozrikidis, “Shear ow past slender elastic rods attached to a plane,” International Journal of Solids and Structures **48**, 137–143 (2011).
73. Aleksander S. Popel, Bahman Anvari, William E. Brownell, and Alexander A. Spector, “Modeling the mechanics of tethers pulled from the cochlear outer hair cell membrane,” J. Biomechanical Eng. **130**, 031007 (2008).
74. Kristopher R. Schumacher, Aleksander S. Popel, Bahman Anvari, William E. Brownell, and Alexander A. Spector, “Computational analysis of the tether-pulling experiment to probe plasma membrane-cytoskeleton interaction in cells,” Phys. Rev. E **80**, 041905 (2009).
75. David A. Hoey, Matthew E. Downs, and Christopher R. Jacobs, “The mechanics of the primary cilium: An intricate structure with complex function,” Journal of Biomechanics **45**, 17–26 (2012).
76. H. Hagiwara, A. Kano, T. Aoki, and N. Ohwada, “Immunocytochemistry of the striated rootlets associated with solitary cilia in human oviductal secretory cells," Histochem. Cell Biol. **114**, 205–212 (2000).
77. N. Sharma, Z. A. Kosan, J. E. Stallworth, N. F. Berbari, and B. K. Yoder, “Soluble levels of cytosolic tubulin regulate ciliary length control," Mol. Biol. Cell **22**, 806–816 (2011).
78. I. B. Alieva, E. A. Vaisberg, E. S. Nadezhdina, and I. A. Vorobjev, “Microtubule and intermediate filament patterns around the centrosome in interphase cells,” Centrosome **15**, 103–129 (1992).
79. I. A. Vorobjev, T. M. Svitkina, and G. G. Borisy, “Cytoplasmic assembly of microtubules in cultured cells,” Journal of Cell Science **110**, 2635–2645 (1997).
80. B. P Hierck, K. Van Der Heiden, F. E. Alkemade, S. Van de Pas, J. V. Van Thienen, B. C. C. Croenendijk, W. H. Bax, A. Van der Laarse, M. C. DeRuiter, A. J. G. Horrevoets, and R. E. Poelmann, “Primary cilia sensitize endothelial cells for uid shear stress,” Developmental Dynamics **237**, 725–735 (2008).
81. L. C. Espinha, D. A. Hoey, P. R. Fernandes, H. C. Rodrigues and C. R. Jacobs,“Oscillatory fluid flow influences primary cilia and microtubule mechanics,” Cytoskeleton **71**, 435-445 (2014).
82. H. B. Ruhfus, G. Bauernschmitt, and R. K. H. Kinne, “Properties of a polarized primary culture from rat renal inner medullary collecting duct (imcd) cells,” In vitro Cell Dev Biol - Animal **34**, 227–231 (1998).
83. C. R. Jacobs, C. E. Yellowley, B. R. Davis, Z. Zhou, J. M. Cimbala, and H. J. Donahue, “Differential effect of steady versus oscillating ow on bone cells,” J. Biomech. **31**, 969–976 (1998).
84. J. Schindelin, I Arganda-Carreras, E. Frise, V. Kaying, M. Longair, T. Pietzsch, S. Pietzsch, C. Rueden, S. Saalfeld, and B. Schmid, “Fiji: an open-source platform for biological-image analysis,” Nature Methods **9**, 676–682 (2012).
85. M. H. Longair, D. A. Baker, and J. D. Armstrong, “Simple Neurite Tracer: open source software for reconstruction, visualization and analysis of neuronal processes,” Bioinformatics **27**, 2453–2454 (2011).
86. D. A. Head, A. J. Levine, and F. C. MacKintosh, “Deformation of cross-linked semi exible polymer networks,” Phys. Rev. Lett. **91**, 108102 (2003).
87. D. A. Head, A. J. Levine, and F. C. MacKintosh, “Distinct regimes of elastic response and deformation modes of cross-linked cytoskeletal and semi exible polymer networks,” Phys. Rev. E **68**, 061907 (2003).

88. A. Shahsavari and R. C. Picu, "Model selection for athermal cross-linked fiber networks," Phys. Rev. E **86**, 011923 (2012).
89. M. Bai, A. R. Missel, A. J. Levine, and W. S. Klug, "On the role of the filament length distribution in the mechanics of semi exible networks," Acta Biomaterialia **7**, 2109–2118 (2011).
90. D. A. Head, A. J. Levine, and F. C. MacKintosh, "Mechanical response of semi exible networks to localized perturbations," Phys. Rev. E **72**, 061914 (2005).
91. R. C. Picu, "Mechanics of random fiber networks - a review," Soft Matter **7**, 6768–6785 (2012).
92. A. K. T.Wann, C. Thompson, and M. K. Knight, "The role of the primary cilium in chondrocyte response to mechanical loading," Mechanosensitivity in Cells and Tisseus **6**, 405–426 (2013).
93. S. R. McGlashan, M. M. Knight, T. T. Chowdhury, P. Joshi, C. G. Jensen, S. Kennedy, and C. A. Poole, "Mechanical loading modulates chondrocyte primary cilia incidence and length," Cell Biology International **34**, 441–446 (2010).
94. K. Gardner, S. P. Arnoczky, and M. Lavagnino, "Effect of in vitro stress-deprivation and cyclic loading on the length of tendon cell cilia in situ," Journal of Orthopaedic Research **29**, 582–587 (2011).
95. P. C. Bressloff, "Stochastic model of intra agellar transport," Phys. Rev. E **73**, 061916 (2006).
96. D. L. Odor and R. J. Blandau, "Observation on the solitary cilium of rabbit oviductal epithelium: its motility and ultrastructure," American Journal of Anatomy **174**, 437–453 (1985).
97. M. Yamamoto and K. Kataoka, "Electron microscopic observation of the primary cilium in the pancreatic islets," Archivum Hisologicum Japonicum **49**, 449–457 (1986).

# Chapter 6
# Reduced-Order Network Models for Biological Scaffolding

**T.I. Zohdi**

## 6.1 Introduction

Many types of biological soft tissues possess a microstructure comprised of embedded fibers which, collectively, are load bearing components. A direct simulation of a continuum model, with a detailed discretization and meshing, for example, using the Finite Element method, of the fibrous microstructure, would result in literally billions of numerical degrees of freedom. Furthermore, incorporating damage and rupture effects *at finite strains* make such problem difficult for "everyday" use by researchers in biomechanics, which motivates so-called "reduced-order" models. In this work, we present a framework for reduced-order models for fiber-laden tissue, that is relatively simple and robust, and which can be implemented with minimal effort by researchers in the biomechanics community. The advantages of reduced-order fiber network models are

- the simplicity of the constitutive laws at the fiber level, for example one-dimensional Fung material laws,
- the ability to easily incorporate effects such as fiber damage and fracture and
- the amenability of the model to extremely rapid numerical simulation,

The presentation is purposely made to be as transparent and simple as possible.

T.I. Zohdi (✉)
Department of Mechanical Engineering, University of California, Berkeley,
6117 Etcheverry Hall, Berkeley, CA 94720-1740, USA
e-mail: zohdi@berkeley.edu



S. De et al. (eds.), *Multiscale Modeling in Biomechanics and Mechanobiology*, DOI 10.1007/978-1-4471-6599-6_6

## 6.2 The Basic Model Reduction Approach

We consider a model problem of a structure comprised of an initially undeformed planar surface network of one-dimensional fibers (Fig. 6.1). The structure is capable of deforming in three dimensions (in and out of the initial plane), in response to loading on its surface. The fibers are joined at the nodes (as pin-joints), in other words, they are sutured together at those locations to form a network. While the structure is relatively simple, compared with real biological tissue, the primary purpose here is simply to illustrate how the approach works, since it is quite flexible and adaptable to specific applications. The salient points of the model reduction for this class of problems are:

- The "weave" is reduced to a truss-like network,
- The truss components are connected by pin-joints,
- The truss components experience only axial strains (stretches), although they can displace and rotate in three dimensions,
- The stress–stretch constitutive relations are one-dimensional,
- The mass of the system is lumped at weave suture point (at the nodes), and
- The nodes displace by the action of the external forces and surrounding fiber stretch, which requires solving a coupled system of ordinary differential equations.

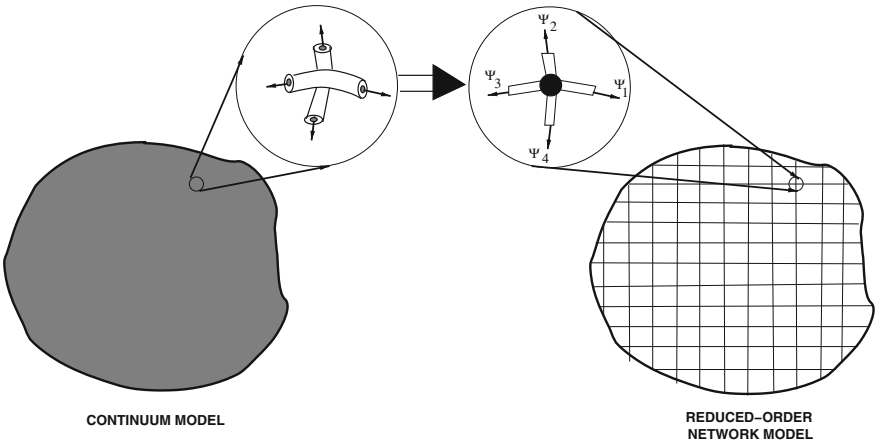


**Fig. 6.1** The process of model reduction: **a** the "weave" is reduced to a truss-like network, **b** the truss components are connected by pin-joints, **c** the truss components experience only axial strains (stretches), although they can displace and rotate in three dimensions, **d** the stress-stretch constitutive relations are one-dimensional, **e** the mass of the system is lumped at weave suture point (at the nodes), and **f** the nodes displace by the action of the external forces and surrounding fiber stretch, which requires solving a coupled system of ordinary differential equations

In the present analysis, any surrounding soft tissue contribution to the response is considered negligible relative to that of the relatively stiff load carrying fibers.[1] By employing enough of these simple structural elements, one can build an entire macroscale sheet of fibrous tissue, as shown in Fig. 6.1.

*Remark 1* The use of pin-joints, i.e., not allowing moments at each node, greatly speeds up the computation in this approach. Bending can be taken into account, and adds a degree of complexity that may be warranted in certain applications. Probably, there are situations where the adopted simplification could be adequate, and others where it is not. Also, as mentioned previously, we ignore buckling phenomena and consider cases where compressive stresses are of somewhat less importance than tensile states. The objective of this work is simply to illustrate the main modeling and solution techniques, without overly complicating issues. In other words, this model and solution techniques serve as a starting point for more in-depth analyses.

## 6.3 Fiber-Segment Network Representation

For the mechanical portion of the modeling of network structures, we assume that: (1) the fiber segments are quite thin, experiencing a uniaxial-stress condition, whereby the forces only act along the length of the fiber segments, (2) the fiber segments remain (macroscopic) straight, undergoing a homogeneous (axial) stress state, (3) the compressive response of a fiber segment is insignificant (relative to tensile states), and (4) fiber-segment buckling phenomena are ignored. We write one-dimensional constitutive laws in terms of a one-dimensional scalar Piola–Kirchhoff-like stresses (mimicking 3-D approaches), defined by

$$P = \frac{\text{force on referential area}}{\text{referential area}}, \tag{6.1}$$

and then transform the result to a scalar second Piola–Kirchhoff-like stress via $P = US$, where $U = \frac{L}{L_o}$ is the stretch ratio, $L$ is the deformed length of the fiber segment, $L_o$ is its original length and where we note that for a relaxed model, when $U \leq 1$ (compression), we enforce $P = 0$. A standard constitutive relation $S = \mathcal{F}(U)$ is then employed, with the primary objective being to extract the force carried in the fiber segment ($\boldsymbol{\Psi}^{\text{fiber}}$), which is needed later for the dynamics of the lumped masses. Specifically,

[1] At the end of this chapter, we shall return to this issue, and indicate how soft tissue–fiber interaction can be computed.

$$P = \frac{\psi^{\text{fiber}}}{A_o} \Rightarrow \psi^{\text{fiber}} = USA_o = \frac{L}{L_o} SA_o. \tag{6.2}$$

One could adopt a simple one-dimensional model for the stored energy, $W = \frac{1}{2}\mathbb{E}E^2$, where $\mathbb{E}$ is Young's modulus and $E \overset{\text{def}}{=} \frac{1}{2}(U^2 - 1)$ is the Green-Lagrange strain, with the second Piola–Kirchhoff-like stress given by $\frac{\partial W}{\partial E} = S = \mathbb{E}E$. Thus, for the fiber segment,

$$P = \frac{\psi^{\text{fiber}}}{A_o} \Rightarrow \psi^{\text{fiber}} = USA_o = \frac{L}{L_o} SA_o = \frac{L}{2L_o}\mathbb{E}\left(\left(\frac{L}{L_o}\right)^2 - 1\right)A_o. \tag{6.3}$$

We will consider more appropriate constitutive laws shortly.

*Remark 2* As a result of the previous analysis, $\boldsymbol{\Psi}_{I_i}^{\text{fiber}} = U_I S_I A_o \mathbf{a}_{I_i}$ ($A_o$ is the undeformed cross-sectional area of the fiber), where the unit axial fiber direction is given by $\mathbf{a}_{I_i} = \frac{\mathbf{r}_I^+ - \mathbf{r}_I^-}{||\mathbf{r}_I^+ - \mathbf{r}_I^-||}$, where $\mathbf{r}_I^+$ denotes the position vector of the endpoint connected to the lumped mass and $\mathbf{r}_I^-$ denotes the endpoint that is connected to it neighboring mass.[2]

*Remark 3* Assumption (3) in the previous section is the adoption of a relaxed-type model, *whereby a zero-stress state is enforced for a compressive state.* Relaxed models have a long history, and we refer the reader to works dating back to Pipkin [49], Buchholdt et al. [3], Pangiotopoulos [45], Bufler and Nguyen-Tuong [4], Papadrakakis [46], Cannarozzi [5, 6], Steigmann [60], Haseganu and Steigmann [17–19], and Atai and Steigmann [1, 2]. Relaxed formulations have served as a foundation for computational models describing rupture of ballistic fabric shielding in Zohdi [66, 75, 79], Zohdi and Steigmann [67], Zohdi and Powell [73], and Powell and Zohdi [50, 51] and are the basis for the present approach.

*Remark 4* Consistent with the assumed one-dimensional deformation of the fiber segments, we have the following relations, between the deformed and undeformed states for the fiber segment length ($U_I(t) = \frac{L_I(t)}{L_I(t=0)}$), cross-sectional area, and volume:

$$\frac{V_I(t)}{V_I(t=0)} = \frac{A_I(t)L_I(t)}{A_I(t=0)L_I(t=0)} = U_I(t), \tag{6.4}$$

which renders $V_I(t) = V_I(t=0)U(t)$ and $A_I(t) = A_I(t=0)$ (the cross-sectional area remains constant). For other alternative possibilities for one-dimensional reduced-order model behavior, see Zohdi and Steigmann [67].

[2] $||\cdot||$ indicates the Euclidean norm in $R^3$.

*Remark 5* While it is generally not true that the compressive response of fibrous tissues is always of little interest, in this work we formulate only a compression-free model, primarily because we are interested in tensile tearing type failure of soft tissue. However, it is important to note that, for example, cartilage researchers believe that the difference between the tensile and compressive properties of that fibrous tissue are the keys to understanding its response to dynamic loading. For example, one of the more important problems in tendon mechanics is understanding the tendon-to-bone insertion (especially its repair), which most surgeons believe places the tendon under compression. The natural loading state of pressurized structures such as arteries and the heart places the tissue in radial compression, and this is sometimes important to the mechanics (especially as it relates to wall thickening in the heart). Thus, there are clearly many biomechanics applications where compression can play a role, and the method developed can be extended to those regimes with relatively minor modifications.

## 6.4 An Example: The Fung Material Model

As an example material, we start by considering a form of the well-known three-dimensional Fung material model (isotropic stiffening "soft" tissue, Fung [12–14]):

$$W = \frac{1}{2}\mathbf{E} : \mathbb{H} : \mathbf{E} + I\!D \left(e^{Q} - 1\right), \tag{6.5}$$

where $\mathbf{E} = \frac{1}{2}\left(\mathbf{F}^T \cdot \mathbf{F} - \mathbf{1}\right)$ is the Green-Lagrange strain tensor, $Q = \frac{\mathbf{E}:\mathbb{B}:\mathbf{E}}{2}$ and $\mathbb{H}$, $I\!D$ and $\mathbb{B}$ are material parameters.

### *6.4.1 Interpretation of Material Constants*

The material constants in a finite deformation material law must match the infinitesimal deformation response, Hooke's Law, $\boldsymbol{\sigma} = \mathbb{E} : \boldsymbol{\epsilon}$, where $\boldsymbol{\sigma}$ is the Cauchy stress, $\mathbb{E}$ is the linear elasticity tensor, and $\boldsymbol{\epsilon}$ is the infinitesimal strain tensor, when perturbed around the undeformed configuration. In the case of isotropy, one can express the Kirchhoff-St. Venant constitutive law in terms of the bulk $\kappa$ and shear moduli $\mu$:

$$\boldsymbol{\sigma} = \mathbb{E} : \boldsymbol{\epsilon} = 3\kappa \frac{tr(\boldsymbol{\epsilon})}{3}\mathbf{1} + 2\mu\boldsymbol{\epsilon}', \tag{6.6}$$

where $\boldsymbol{\epsilon}' = \boldsymbol{\epsilon} - \frac{tr(\boldsymbol{\epsilon})}{3}\mathbf{1}$. In order to match the Fung material law to the linearized response at infinitesimal strains, we compute

$$\mathbf{S} = \frac{\partial W}{\partial \mathbf{E}} = \mathbb{H} : \mathbf{E} + \mathbb{D} e^{Q} \frac{\partial Q}{\partial \mathbf{E}} = \mathbb{H} : \mathbf{E} + \mathbb{D} e^{\frac{\mathbf{E}:\mathbb{B}:\mathbf{E}}{2}} \mathbb{B} : \mathbf{E} \tag{6.7}$$

and

$$\begin{aligned} \mathbb{E}^{\tan} = \frac{\partial^2 W}{\partial \mathbf{E}^2} &= \mathbb{H} + \mathbb{D} e^{Q} \left( \frac{\partial Q}{\partial \mathbf{E}} \otimes \frac{\partial Q}{\partial \mathbf{E}} + \frac{\partial^2 Q}{\partial \mathbf{E}^2} \right) \\ &= \mathbb{H} + \mathbb{D} e^{\frac{\mathbf{E}:\mathbb{B}:\mathbf{E}}{2}} \left( (\mathbb{B} : \mathbf{E}) \otimes (\mathbb{B} : \mathbf{E}) + \mathbb{B} \right). \end{aligned} \tag{6.8}$$

As $\mathbf{E} \rightarrow \mathbf{0}$ we must have $\mathbb{H} + \mathbb{D}\mathbb{B} \rightarrow \mathbb{E}$, in order to match linearized response at infinitesimal strains (by matching the tangent moduli). In the analysis to follow, we choose $\mathbb{H} = \mathbf{0}$.

*Remark 6* For overviews of a wide variety of soft tissue models, we refer the reader to the extensive works of Holzapfel [21, 22] or Humphrey [25, 26]. The material constants used in the present analysis are *effective parameters*. Generally, these types of materials will contain a large number of microscale inhomogeneities. A detailed analysis of the response of the microstructure to loading is beyond the scope of this chapter. There are a number of methods to estimate the overall macroscopic properties of materials consisting of a matrix, containing a distribution of inhomogeneities, pores, or cracks, in terms of microstructural parameters. The literature on this topic is quite extensive, dating back to the early works of Maxwell [41, 42] and Lord Rayleigh [53]. For an wide-ranging overview of random heterogeneous media, we refer the reader to Torquato [61], while for more mathematical homogenization aspects, see Jikov et al. [27]. For solid-mechanics aspects, we refer the reader to the works of Hashin [20], Markov [40], Mura [43], Nemat-Nasser and Hori [44], Huet [23, 24]. Finally, for the analyses of defect-laden, porous and cracked media, one may refer to Kachanov [29], Kachanov, Tsukrov and Shafiro [30], Kachanov and Sevostianov [31], Sevostianov and Kachanov [58], Sevostianov, Gorbatikh and Kachanov [57], while for computational aspects, see Zohdi and Wriggers [77].

### 6.4.2 Adaptation to the Network Model

Adapting the Fung model, as well as the assumptions for the reduced-order model introduced earlier, for a one-dimensional fiber segment, we have

$$W = \mathbb{D}(e^{Q} - 1), \tag{6.9}$$

where $Q = \frac{1}{2}\mathbb{B}E^2$, $\mathbb{B}$ and $\mathbb{D}$ are material constants, $E \overset{\text{def}}{=} \frac{1}{2}(C - 1)$ is the Green-Lagrange strain, $C \overset{\text{def}}{=} U^2$ is the right Cauchy-Green strain and $U = \frac{L}{L_o}$ is the stretch ratio. The exponential term phenomenologically describes a stiffening effect, due to a progressive reduction in fibrous microscale "slack," which is prevalent in many types biological tissue. A second Piola–Kirchhoff-like stress is given by

$$S = \frac{\partial W}{\partial E} = c\frac{\partial Q}{\partial E}e^{Q} = I\!D\,I\!B\,E e^{I\!B\,E^2}, \tag{6.10}$$

and the tangent stiffness is

$$I\!E^{\tan} = \frac{\partial^2 W}{\partial E^2} = I\!D e^{Q}\left(\left(\frac{\partial Q}{\partial E}\right)^2 + \frac{\partial^2 Q}{\partial E^2}\right) = I\!B\,I\!D e^{Q}(I\!B\,E^2 + 1). \tag{6.11}$$

As $E \to 0$, $I\!D\,I\!B \to I\!E^{\tan}$. We assume that $I\!D$ and $I\!B$ are both positive.

*Remark 7* This relaxed (tensile-strain only) one-dimensional model is convex in terms of the stretch ratio $U$. By computing two derivatives of $W(U)$, we obtain

$$\frac{\partial^2 W}{\partial U^2} = I\!D e^{Q}\left(\left(\frac{\partial Q}{\partial U}\right)^2 + \frac{\partial^2 Q}{\partial U^2}\right) > 0. \tag{6.12}$$

*Remark 8* An alternative starting point for the material model could be

$$W = \frac{1}{2}\kappa(E(q))^2, \tag{6.13}$$

where $\kappa > 0$ and $q$ are material constants, $E(q) \overset{\text{def}}{=} \frac{1}{2q}(U^{2q} - 1)$ is the generalized Green-Lagrange (Seth) strain. The second Piola–Kirchhoff-like stress, $S$, is given by

$$S = \frac{\partial W}{\partial E} = \kappa E(q) U^{2(q-1)}. \tag{6.14}$$

The exponent $q$ phenomenologically describes a stiffening effect, due to a progressive reduction in fibrous slack, which is prelavent in many biological tissues. We note that $q = 1$ produces the classical Kirchhoff–St. Venant law, when $\kappa$ is interpreted as the Young's modulus.

*Remark 9* Models which explicitly account for the presence of fibers in biological tissue date back, at least, to Lanir [32], who formulated continuum models based on the existence of fiber families. For reviews of fiber-like models, we refer the reader to Sacks and Sun [55], Costa et al. [8] and recent the works of Barocas and co-workers (Zhang et al. [64] and Hadi and Barocas [16]).

*Remark 10* The simplest approach to describe failure of a fiber is to check whether a critical stretch has been attained, $U(t) \geq U_{\text{crit},I}$. If this condition is met, then the fiber is deemed inactive. However, it is more realistic to have the fiber gradually rupture. In order to track the progressive damage for the $I$th fiber, a single damage variable, $\alpha_I$, is used. The damage variable $\alpha_I$ can, for example, represent the fraction of smaller scale fibrils that are *not ruptured*, within the $I$th fiber.[3] Thus, for a fiber

[3] This topic, which is relevant in a multiscale setting, has been explored in depth in Zohdi and Steigmann [67] and Zohdi and Powell [73].

that is undamaged, $\alpha_I = 1$, while for an fiber that is completely damaged, $\alpha_I = 0$. Probably, the simplest damage representation is, with $\alpha_I(t=0) = 1$,

$$\alpha_I(t) = \min\left(\alpha_I(0 \leq t^* < t), e^{(-\lambda(\frac{U_I(t)-U_{\text{crit},I}}{U_{\text{crit},I}}))}\right), \tag{6.15}$$

where $U_I(t)$ is the stretch of the fiber at time $t$, and where $0 \leq \lambda$ is a rate parameter. The above relation indicates that damage is irreversible, i.e., $\alpha_I$ is a monotonically decreasing function. As $\lambda \rightarrow \infty$, the type of failure tends toward sudden rupture, while as $\lambda \rightarrow 0$, then there is no damage generated.

## 6.5 Simulation of Network Dynamics

A natural way to simulate the dynamics of such tissue is to consider a lumped mass model, where the lumped masses are located at the suture (criss-cross) points (Fig. 6.1). In order describe the overall time-stepping scheme, we first start with the dynamics of a single ($i$th) lumped mass. The equation of motion is given by

$$m_i \dot{\mathbf{v}}_i = \boldsymbol{\psi}_i^{\text{tot}}, \tag{6.16}$$

where $\boldsymbol{\psi}_i^{\text{tot}}$ is the total force provided from interactions with the external environment (fiber, loading, etc.). Employing the trapezoidal-like rule ($0 \leq \phi \leq 1$)[4]

$$\mathbf{v}_i(t+\Delta t) = \mathbf{v}_i(t) + \frac{\Delta t}{m_i}\left(\phi \boldsymbol{\psi}_i^{\text{tot}}(t+\Delta t) + (1-\phi)\boldsymbol{\psi}_i^{\text{tot}}(t)\right) \tag{6.17}$$

and for the position

$$\begin{aligned} \mathbf{r}_i(t+\Delta t) &= \mathbf{r}_i(t) + \mathbf{v}_i(t+\phi\Delta t)\Delta t \\ &= \mathbf{r}_i(t) + \left(\phi \mathbf{v}_i(t+\Delta t) + (1-\phi)\mathbf{v}_i(t)\right)\Delta t, \end{aligned} \tag{6.18}$$

or, explicitly combining the expressions,

$$\mathbf{r}_i(t+\Delta t) = \mathbf{r}_i(t) + \mathbf{v}_i(t)\Delta t + \frac{\phi(\Delta t)^2}{m_i}\left(\phi \boldsymbol{\psi}_i^{\text{tot}}(\mathbf{r}_i(t+\Delta t)) + (1-\phi)\boldsymbol{\psi}_i^{\text{tot}}(\mathbf{r}_i(t))\right), \tag{6.19}$$

where if $\phi = 1$, then Eq. (6.19) becomes the (implicit) Backward Euler scheme, which is very stable, dissipative and $\hat{\mathcal{O}}(\Delta t)^2 = \mathcal{O}(\Delta t)^2$ locally in time, if $\phi = 0$, then Eq. (6.19) becomes the (explicit) Forward Euler scheme, which is conditionally stable and $\hat{\mathcal{O}}(\Delta t)^2 = \mathcal{O}(\Delta t)^2$ locally in time and if $\phi = 0.5$, then Eq. (6.19)

[4] For a derivation, refer to the Appendix.

becomes the (implicit) Midpoint scheme, which is stable and $\hat{\mathcal{O}}(\Delta t)^2 = \mathcal{O}(\Delta t)^3$ locally in time. [5] Equation (6.19) can be solved recursively by recasting the relation as

$$\mathbf{r}_i^{L+1,K} = \mathcal{G}(\mathbf{r}_i^{L+1,K-1}) + \mathcal{R}_i, \tag{6.20}$$

where $K = 1, 2, 3, ...$ is the index of iteration within time step $L + 1$ and $\mathcal{R}_i$ is a remainder term that does not depend on the solution, i.e., $\mathcal{R}_i \neq \mathcal{R}_i(\mathbf{r}_1^{L+1}, \mathbf{r}_2^{L+1} ...\mathbf{r}_N^{L+1})$. The convergence of such a scheme is dependent on the behavior of $\mathcal{G}$. Namely, a sufficient condition for convergence is that $\mathcal{G}$ is a contraction mapping for all $\mathbf{r}_i^{L+1,K}$, $K = 1, 2, 3...$ In order to investigate this further, we define the iteration error as

$$\varpi_i^{L+1,K} \stackrel{\text{def}}{=} \mathbf{r}_i^{L+1,K} - \mathbf{r}_i^{L+1}. \tag{6.21}$$

A necessary restriction for convergence is iterative self-consistency, i.e., the "exact" (discretized) solution must be represented by the scheme

$$\mathcal{G}(\mathbf{r}_i^{L+1}) + \mathcal{R}_i = \mathbf{r}_i^{L+1}. \tag{6.22}$$

Enforcing this restriction, a sufficient condition for convergence is the existence of a contraction mapping

$$||\underbrace{\mathbf{r}_i^{L+1,K} - \mathbf{r}_i^{L+1}}_{\varpi_i^{L+1,K}}|| = ||\mathcal{G}(\mathbf{r}_i^{L+1,K-1}) - \mathcal{G}(\mathbf{r}_i^{L+1})|| \leq \eta^{L+1,K}||\mathbf{r}_i^{L+1,K-1} - \mathbf{r}_i^{L+1}||,$$

where, if $0 \leq \eta^{L+1,K} < 1$ for each iteration $K$, then $\varpi_i^{L+1,K} \to \mathbf{0}$ for any arbitrary starting value $\mathbf{r}_i^{L+1,K=0}$, as $K \to \infty$. This type of contraction condition is sufficient, but not necessary, for convergence. Explicitly, the recursion is

$$\mathbf{r}_i^{L+1,K} = \underbrace{\mathbf{r}_i^L + \mathbf{v}_i^L \Delta t + \frac{\phi(\Delta t)^2}{m_i}\left((1-\phi)\boldsymbol{\psi}_i^{\text{tot},L}\right)}_{\mathcal{R}_i} + \underbrace{\frac{\phi(\Delta t)^2}{m_i}\left(\phi\boldsymbol{\psi}_i^{\text{tot},L+1,K-1}\right)}_{\mathcal{G}(\mathbf{r}_i^{L+1,K-1})} \tag{6.23}$$

[5] In order to streamline the notation, we drop the cumbersome $\mathcal{O}(\Delta t)$-type terms.

where

$$\boldsymbol{\psi}_i^{\text{tot},L} = \boldsymbol{\psi}_i^{\text{tot},L}(\mathbf{r}_1^L, \mathbf{r}_2^L ... \mathbf{r}_N^L) \tag{6.24}$$

and

$$\boldsymbol{\psi}_i^{\text{tot},L+1,K-1} = \boldsymbol{\psi}_i^{\text{tot},L+1,K-1}(\mathbf{r}_1^{L+1,K-1}, \mathbf{r}_2^{L+1,K-1} ... \mathbf{r}_N^{L+1,K-1}). \tag{6.25}$$

According to Equation, convergence is scaled by $\eta \propto \frac{(\Delta t)^2}{m_i}$, and that the contraction constant of $\mathcal{G}$ is (1) directly dependent on the magnitude of the interaction forces, (2) inversely proportional to the lumped masses $m_i$ and (3) directly proportional to $\Delta t$. Thus, if convergence is slow within a time step, the time step size, which is adjustable, can be reduced by an appropriate amount to increase the rate of convergence. It is also desirable to simultaneously maximize the time-step sizes to decrease overall computing time, while obeying an error tolerance on the numerical solution's accuracy. In order to achieve this goal, we follow an approach found in Zohdi [70–78], originally developed for continuum thermochemical multifield problems where (1) one approximates $\eta^{L+1,K} \approx S(\Delta t)^p$ ($S$ is a constant) and (2) one assumes that the error within an iteration to behave according to $(S(\Delta t)^p)^K \varpi^{L+1,0} = \varpi^{L+1,K}$, $K = 1, 2, ...$, where $\varpi^{L+1,0}$ is the initial norm of the iterative error and $S$ is intrinsic to the system.[6] The objective is to meet an error tolerance in exactly a preset number of iterations. To this end, one writes $(S(\Delta t_{\text{tol}})^p)^{K_d} \varpi^{L+1,0} = TOL$, where $TOL$ is a tolerance and where $K_d$ is the number of desired iterations.[7] If the error tolerance is not met in the desired number of iterations, the contraction constant $\eta^{L+1,K}$ is too large. Accordingly, one can solve for a new smaller step size, under the assumption that $S$ is constant,

$$\Delta t_{\text{tol}} = \Delta t \left( \frac{(\frac{TOL}{\varpi^{L+1,0}})^{\frac{1}{pK_d}}}{(\frac{\varpi^{L+1,K}}{\varpi^{L+1,0}})^{\frac{1}{pK}}} \right). \tag{6.26}$$

The assumption that $S$ is constant is not crucial, since the time steps are to be recursively refined and unrefined throughout the simulation. The expression in Eq. (6.26) can also be used for time step enlargement, to reduce computational effort, if convergence is met in less than $K_d$ iterations. Numerous parameter studies of this algorithm can be found in Zohdi [70–78].

An implementation of the procedure is as follows:

[6] For the class of problems under consideration, due to the quadratic dependency on $\Delta t$, $p \approx 2$.

[7] Typically, $K_d$ is chosen to be between five to ten iterations.

(1) GLOBAL FIXED − POINT ITERATION : (SET i = 1 AND K = 0) :
(2) IF i > N THEN GO TO (4) (N = # OF NODES)
(3) IF i ≤ N THEN :
($a$) COMPUTE MASS POSITION :$\mathbf{r}_i^{L+1,K}$
($b$) GO TO (2) AND NEXT MASS (i = i + 1)
(4) COMPUTE/UPDATE FORCES $\boldsymbol{\psi}_i^{\text{tot},K}$ AND FIBER DAMAGE :$\alpha_I$
(5) ERROR MEASURE :

$$(a)\ \varpi_K \overset{\text{def}}{=} \frac{\sum_{i=1}^{N} ||\mathbf{r}_i^{L+1,K} - \mathbf{r}_i^{L+1,K-1}||}{\sum_{i=1}^{N} ||\mathbf{r}_i^{L+1,K} - \mathbf{r}_i^{L}||} \quad \text{(normalized)}$$

$$(b)\ Z_K \overset{\text{def}}{=} \frac{\varpi_K}{TOL_r}$$

$$(c)\ \Phi_K \overset{\text{def}}{=} \left( \frac{(\frac{TOL}{\varpi_0})^{\frac{1}{pK_d}}}{(\frac{\varpi_K}{\varpi_0})^{\frac{1}{pK}}} \right)$$

(6) IF TOLERANCE MET ($Z_K \leq 1$) AND $K < K_d$ THEN :
($a$) CONSTRUCT NEW TIME STEP : $\Delta t = \Phi_K \Delta t$
($b$) SELECT MINIMUM : $\Delta t = MIN(\Delta t^{\text{lim}}, \Delta t)$
($c$) INCREMENT TIME : $t = t + \Delta t$ AND GO TO (1)
(7) IF TOLERANCE NOT MET ($Z_K > 1$) AND $K = K_d$ THEN :
($a$) CONSTRUCT NEW TIME STEP :$\Delta t = \Phi_K \Delta t$
($b$) RESTART AT TIME = t AND GO TO (1) (6.27)

*Remark 11* At the implementation level in Box 6.27, normalized (nondimensional) error measures were used. As with the unnormalized case, one approximates the error within an iteration to behave according to

$$(\gamma(\Delta t)^p)^K \underbrace{\frac{||\mathbf{r}^{L+1,1} - \mathbf{r}^{L+1,0}||}{||\mathbf{r}^{L+1,0} - \mathbf{r}^{L}||}}_{\varpi_0} = \underbrace{\frac{||\mathbf{r}^{L+1,K} - \mathbf{r}^{L+1,K-1}||}{||\mathbf{r}^{L+1,K} - \mathbf{r}^{L}||}}_{\varpi_K}, \tag{6.28}$$

$K = 2, ...$, where the normalized measures characterize the ratio of the iterative error within a time step to the difference in solutions between time steps. Since both $||\mathbf{r}^{L+1,0} - \mathbf{r}^{L}|| = \mathcal{O}(\Delta t)$ and $||\mathbf{r}^{L+1,K} - \mathbf{r}^{L}|| = \mathcal{O}(\Delta t)$ the approach has roughly the same rates of convergence, and the adaptive scheme remains the same. The normalized measures are preferred since they have a clear meaning.

*Remark 12* We note that the model presented is flexible enough to capture static or dynamic loading. Although quasi-static loading are appropriate for many biomechanical applications, there are cases, for example, blunt trauma-type loading, where dynamic loading is important. Clearly, if the inertial terms are made small, by allowing $m \rightarrow 0$, the response will resemble a quasistatic solution, if that is desired. As mentioned previously, this type of approach is sometimes referred to as a dynamic relaxation technique to solve quasistatic problems. For details, we refer the reader to Steigmann and coworkers (Steigmann [60], Haseganu and Steigmann [17, 18] and [19], Atai and Steigmann [1, 2], Papadrakakis [46].

## 6.6 A Numerical Example: Pressurized Loading

As an idealized model problem, following an example provided in Zohdi [75], consider a planar rectangular sheet, composed of the fiber network, clamped on all four edges. We consider gradually increasing forces due to pressure loading underneath the tissue, for each node, of the form

$$\mathcal{F} = \frac{f_o d^2 e^{qt}}{N}, \tag{6.29}$$

where $f_o$ is a pressure force constant, $d$ is the length of a side of the square ($d \times d$) exterior membrane boundary, $q$ is a loading rate parameter ,and where $N$ is the total number of nodes. The unit normal at a node is computed by taking the cross-product of the vectors connecting the nodes before and after the node in question, and normalizing the result by the magnitude. The pressure is then projected onto this normal, $\mathbf{n}$. Thus, this is *live loading*, since each nodal $\mathbf{n}$ is a function of the deformation. In order to illustrate the robustness of the approach, the tissue was given some heterogeneity from fiber to fiber: a 50 % variation from a mean value overall value of the material constant $I\!D$ for the fibers (Fig. 6.2). Also, an initially softened elliptical region was placed slightly off center in the tissue (Fig. 6.2). A $50 \times 50$ network was used. The specific parameters employed were:

- The initial radii of the fibers were $r_o = 10^{-5}$ m,
- The dimensions of the domain were $0.025\,\text{m} \times 0.025\,\text{m}$,
- The starting time step value, $\Delta t = 0.005\,\text{s}$
- The iterative stopping tolerance, $TOL_r = 0.001$,
- The total simulation time, $T = 10\,\text{s}$,
- The desired number of iterations, $K_d = 20$,
- The upper bound on the time step size, $\Delta t^{\text{lim}} = 0.01\,\text{s}$,
- The initial pressure, $f_o = 0.00001$ Pa,
- The pressure rate, $q = 1.0$,
- The damage rate, $\lambda = 1$,
- The critical stretch, $U_{\text{crit}} = 1.25$,

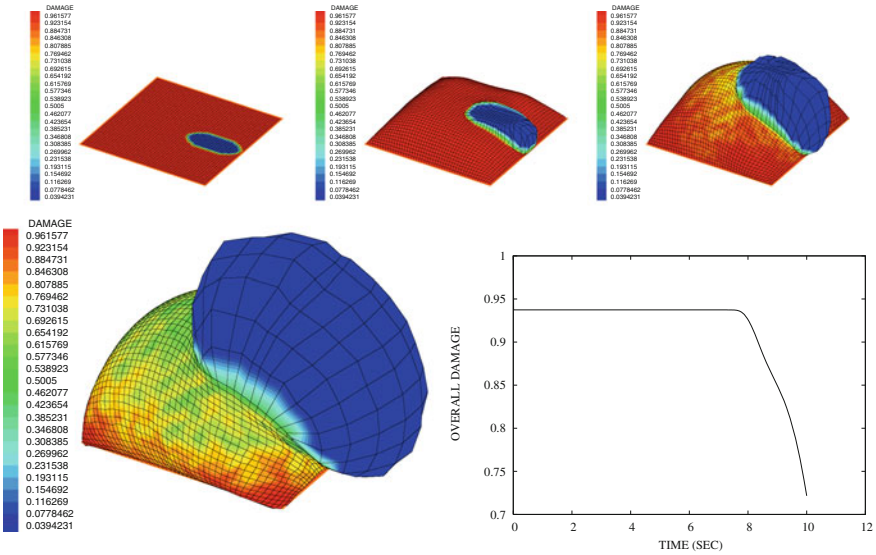


**Fig. 6.2** *TOP LEFT TO RIGHT* Successive frames of the pressurized loading leading to rupture. The graphics indicate the average damage in the surrounding fibers. *BOTTOM* A zoom on the final configuration and a plot of the overall damage, $\langle \alpha \rangle_\Omega \stackrel{\text{def}}{=} \frac{1}{|\Omega|} \int_\Omega \alpha \, d\Omega$, of the tissue as a function of time. *Note* there was approximately 7 % initial damage due to the initially softened elliptical region in the tissue (Zohdi [75])

- The Fung material parameters were $\mathbb{D} = (1 \pm 0.5) \times 10^5$ Pa and $\mathbb{B} = 10^{-3}$,
- The first Fung material parameter in the weakened elliptical region was one-hundredth of the nominal; $\mathbb{D} = (1 \pm 0.5) \times 10^4$ Pa ($H$ was the same),
- The major radius of the elliptical softened region was 0.005 m, while the minor radius of the elliptical softened region was 0.0025 m.

As Fig. 6.2 indicates, it takes some time for the critical stretch to be met before damage starts to occur. Thus, in the beginning, the time step sizes are enlarged, automatically by the algorithm, until the (finite difference) discretization error upper limit (set to $\Delta t^{\text{lim}} = 0.01$) was met. Thereafter, when damage initiates, inhomogeneously (Fig. 6.2), the steps are refined and unrefined to meet the iterative error tolerance. At this stage in the deformation, the iterative error tolerance dictates time-step sizes which are required, by the adaptive algorithm, to be smaller than the step-size dictated by the discretization limit. Clearly, the method can handle extraordinarily large, inelastic, deformations that would be difficult to formulate with an anisotropic continuum theory, and an accompanying finite element discretization, due to large element distortion. The total simulation time was on the order of 45 s on a standard laptop.

*Remark 13* This example was motivated by the simulation of diseased fibrous cap tissue which forms during plaque growth associated with the vascular disease of

atherosclerosis. Myocardial infarction and stroke can result from fibrous plaque cap rupture and subsequent release of highly thrombogenic material and lipids into the blood stream. Lesions (plaque caps) with a high risk of rupture are termed *vulnerable* (Fuster [15]), and are responsible, along with other micromorphological characteristics, such as lipid core size, for many sudden life-threatening cardiovascular events. For overviews, we refer the reader to Shah [59], Virmani et al. [62], van der Wal and Becker [63], Chyu and Shah [7], Libby and Aikawa [36], Libby [37], Richardson et al. [54], Loree et al. [39] and Davies et al. [9].

## 6.7 Summary and Future Work

The purpose of this chapter was to present an accessible, straightforward, modeling approach, which can be numerically implemented with minimal effort by researchers interested in the simulation of fibrous biological tissue. The advantages of such a fiber network approach are that the constitutive laws at the (one-dimensional) fiber level are simple and that the damage and rupture therein is straightforward to characterize, with the further caveat that the model is amenable to extremely rapid numerical simulation. Finally, we remark that while the response of the surrounding soft tissue was neglected, it can be accounted for via staggering techniques whereby, at a time-step, the load that the fibers induce on the tissue are applied as a (momentarily) fixed load and the deformation of the fibers are computed and updated to provide a new reaction load on the soft tissue (by projecting the fiber response onto a discretization mesh of the soft tissue). The process is repeated until convergence. Staggering schemes are clearly ideal to simulate such processes. We refer readers to Park and Felippa [47], Schrefler [56], Zienkiewicz [65], Lewis et al. [34], Lewis and Schrefler [33], Piperno [48], Doltsinis [10, 11] and Zohdi [70–83] for details of staggering schemes. For simple cases involving coupled fields associated with atherosclerosis, we refer the reader to Zohdi et al. [68] and Zohdi [69]. Generally, such schemes proceed, within a discretized time step, by solving each field equation individually, allowing only the corresponding primary field variable to be active. This effectively decouples the system of differential equations. After the solution of each field equation, the primary field variable is updated, and the next field equation is solved in a similar manner, with only the corresponding primary variable being active. For accurate numerical solutions, the approach requires small time steps, primarily because the staggering error accumulates with each passing increment. Generally, such computations will require time-step adaptivity, perhaps, for example, using schemes such as the one presented in this work. We note that this staggering-type approach could be used for systems with two families of interacting fibers, representing two types of tissue, for example elastin and collagen.

Finally, because the distribution of water, biological fluids, and chemical species within such tissue are dependent on the deformation of the solid, coupled multi-field computations are necessary to realistically simulate such systems. For example, in many models involving fibrous biological tissue, it is usually assumed that the

response depends on the concentration of a chemical species present, denoted $s$, for example, intracellular calcium $Ca^{2+}$, and the stretch $U$ of the tissue fiber, relative to a reference sarcomere length. A basic form suggested is $\sigma = \sigma(s, U)$, where $\sigma$ is the total Cauchy stress (active and passive), which combines the mechanical (passive) contribution and the actively generated muscle tension. There exist several models for incorporating the effects of a chemical species into the response of biotissue. For example, one could consider a representation where $\sigma = \sigma^{\text{mech}} + \sigma^{\text{chem}}(Ca^{2+}, U)$, where $\sigma$ is the total Cauchy stress (active and passive), $\sigma^{\text{mech}}$ is the usual mechanical (passive) contribution, $\sigma(Ca^{2+}, U)$ is the actively generated muscle tension, and where $U$ is the stretch along the muscle fiber. We refer the reader to Rachev and Hayashi [52], Humphrey [25] or [26] for reviews.[8] A proto-typical coupled system involves (a) fluid mechanics, involving the concentration of suspensions, which are nominally convected with the fluid, (b) fluid-solid interaction at wall/fluid interfaces, leading to penetration or absorption of suspensions into the biotissue, and (c) growth of the tissue and an accompanying buildup of stress and/or possible damage. Staggering schemes are clearly ideal to simulate such fluid–solid processes, and have been applied in Zohdi [74] for related systems.

## Appendix: Temporal Discretization

In order to motivate the time-stepping scheme, we first start with the dynamics of a single lumped mass. The equation of motion is given by

$$m_i \dot{\mathbf{v}}_i = \boldsymbol{\psi}_i^{\text{tot}}, \tag{6.30}$$

where $\boldsymbol{\psi}_i^{\text{tot}}$ is the total force provided from interactions with the external environment (fiber, etc.). Expanding the velocity in a Taylor series about $t + \phi\Delta t$ we obtain,

$$\mathbf{v}_i(t+\Delta t) = \mathbf{v}_i(t+\phi\Delta t) + \frac{d\mathbf{v}_i}{dt}|_{t+\phi\Delta t}(1-\phi)\Delta t + \frac{1}{2}\frac{d^2\mathbf{v}_i}{dt^2}|_{t+\phi\Delta t}(1-\phi)^2(\Delta t)^2 + \mathcal{O}(\Delta t)^3 \tag{6.31}$$

and

$$\mathbf{v}_i(t) = \mathbf{v}_i(t+\phi\Delta t) - \frac{d\mathbf{v}_i}{dt}|_{t+\phi\Delta t}\phi\Delta t + \frac{1}{2}\frac{d^2\mathbf{v}_i}{dt^2}|_{t+\phi\Delta t}\phi^2(\Delta t)^2 + \mathcal{O}(\Delta t)^3 \tag{6.32}$$

Subtracting the two expressions yields

$$\frac{d\mathbf{v}_i}{dt}|_{t+\phi\Delta t} = \frac{\mathbf{v}_i(t+\Delta t) - \mathbf{v}_i(t)}{\Delta t} + \hat{\mathcal{O}}(\Delta t), \tag{6.33}$$

[8] The system presented in this work can be considered a relatively simple coupled system, coupling equilibrium and damage equations.

where $\hat{\mathcal{O}}(\Delta t) = \mathcal{O}(\Delta t)^2$, when $\phi = \frac{1}{2}$. Thus, inserting this into the equations of equilibrium yields

$$\mathbf{v}_i(t+\Delta t) = \mathbf{v}_i(t) + \frac{\Delta t}{m_i}\boldsymbol{\psi}_i^{\text{tot}}(t+\phi\Delta t) + \hat{\mathcal{O}}(\Delta t)^2. \tag{6.34}$$

Note that adding a weighted sum of Eqs. (6.31) and (6.32) yields

$$\mathbf{v}_i(t+\phi\Delta t) = \phi\mathbf{v}_i(t+\Delta t) + (1-\phi)\mathbf{v}_i(t) + \mathcal{O}(\Delta t)^2, \tag{6.35}$$

which will be useful shortly. Now expanding the position of the center of mass in a Taylor series about $t+\phi\Delta t$ we obtain

$$\mathbf{r}_i(t+\Delta t) = \mathbf{r}_i(t+\phi\Delta t) + \frac{d\mathbf{r}_i}{dt}|_{t+\phi\Delta t}(1-\phi)\Delta t + \frac{1}{2}\frac{d^2\mathbf{r}_i}{dt^2}|_{t+\phi\Delta t}(1-\phi)^2(\Delta t)^2 + \mathcal{O}(\Delta t)^3 \tag{6.36}$$

and

$$\mathbf{r}_i(t) = \mathbf{r}_i(t+\phi\Delta t) - \frac{d\mathbf{r}_i}{dt}|_{t+\phi\Delta t}\phi\Delta t + \frac{1}{2}\frac{d^2\mathbf{r}_i}{dt^2}|_{t+\phi\Delta t}\phi^2(\Delta t)^2 + \mathcal{O}(\Delta t)^3. \tag{6.37}$$

Subtracting the two expressions yields

$$\frac{\mathbf{r}_i(t+\Delta t) - \mathbf{r}_i(t)}{\Delta t} = \mathbf{v}_i(t+\phi\Delta t) + \hat{\mathcal{O}}(\Delta t). \tag{6.38}$$

Inserting Eq. (6.35) yields

$$\mathbf{r}_i(t+\Delta t) = \mathbf{r}_i(t) + \left(\phi\mathbf{v}_i(t+\Delta t) + (1-\phi)\mathbf{v}_i(t)\right)\Delta t + \hat{\mathcal{O}}(\Delta t)^2. \tag{6.39}$$

and thus using Eq. (6.34) yields

$$\mathbf{r}_i(t+\Delta t) = \mathbf{r}_i(t) + \mathbf{v}_i(t)\Delta t + \frac{\phi(\Delta t)^2}{m_i}\boldsymbol{\psi}_i^{\text{tot}}(t+\phi\Delta t) + \hat{\mathcal{O}}(\Delta t)^2. \tag{6.40}$$

The term $\boldsymbol{\psi}_i^{\text{tot}}(t+\phi\Delta t)$ can be approximated by $\boldsymbol{\psi}_i^{\text{tot}}(t+\phi\Delta t) \approx \phi\boldsymbol{\psi}_i^{\text{tot}}(\mathbf{r}_i(t+\Delta t)) + (1-\phi)\boldsymbol{\psi}_i^{\text{tot}}(\mathbf{r}_i(t))$. Thus, we have the following for the velocity[9]

$$\mathbf{v}_i(t+\Delta t) = \mathbf{v}_i(t) + \frac{\Delta t}{m_i}\left(\phi\boldsymbol{\psi}_i^{\text{tot}}(t+\Delta t) + (1-\phi)\boldsymbol{\psi}_i^{\text{tot}}(t)\right) \tag{6.41}$$

and for the position

[9] In order to streamline the notation, we drop the cumbersome $\mathcal{O}(\Delta t)$-type terms.

$$\begin{aligned}\mathbf{r}_i(t+\Delta t) &= \mathbf{r}_i(t) + \mathbf{v}_i(t+\phi\Delta t)\Delta t \\ &= \mathbf{r}_i(t) + (\phi\mathbf{v}_i(t+\Delta t) + (1-\phi)\mathbf{v}_i(t))\,\Delta t,\end{aligned} \tag{6.42}$$

or, explicitly combining the expressions,

$$\mathbf{r}_i(t+\Delta t) = \mathbf{r}_i(t) + \mathbf{v}_i(t)\Delta t + \frac{\phi(\Delta t)^2}{m_i}\left(\phi\boldsymbol{\psi}_i^{\text{tot}}(t+\Delta t) + (1-\phi)\boldsymbol{\psi}_i^{\text{tot}}(t)\right). \tag{6.43}$$

## References


1. Atai, A. A. and Steigmann, D. J. (1997). On the nonlinear mechanics of discrete networks. Archive of Applied Mechanics. 67, 303–319.
2. Atai, A. A. and Steigmann, D. J. (1998). Coupled deformations of elastic curves and surfaces. Int. J. Solids Structures. 35, No. 16, 1915–1952.
3. Buchholdt, H. A. Davies, M. Hussey, M. J. L. (1968). The analysis of cable nets. J. Inst. Maths. Applics. 4 339–358.
4. Bufler, H. and Nguyen-Tuong, B. (1980). On the work theorems in nonlinear network theory. Ing. Arch. 49 275–286.
5. Cannarozzi, M. (1987). A minimum principle for tractions in the elastostatics of cable networks. Int. J. Solids Struct. 23, 551–568.
6. Cannarozzi, M. (1985). Stationary and extremum variational formulations for the elastostatics of cable networks. Meccanica. 20, 136–143.
7. Chyu, K. Y. and Shah, P. K. (2001) The role of inflammation in plaque disruption and thrombosis, Rev. Cardiovas. Med., 2, 82–91.
8. Costa, K. D., Holmes J. W., McCulloch A. D. (2001) Modeling cardiac mechanical properties in three dimensions. Phil Trans R Soc Lond A 359:1233–1250.
9. Davies, M. J., P. D. Richardson, N. Woolf and D. R. Katz and J. Mann. (1993). Risk of thrombosis in human atherosclerotic plaques: role of extracellular lipid, macrophage, and smooth muscle cell content, Br. Heart Journal, 69, 377–381.
10. Doltsinis, I. St. (1993). Coupled field problems-solution techniques for sequential & parallel processing. In Solving large-scale problems in mechanics. M. Papadrakakis editor.
11. Doltsinis, I. St. (1997). Solution of coupled systems by distinct operators. Engineering Computations, 14, 829–868.
12. Fung, Y. C. (1967). Elasticity of soft tissues in simple elongation. Am. J. Physiol. 28, 1532–1544.
13. Fung, Y. C. (1973). Biorheology of soft tissues. Biorheology 10, 139–155.
14. Fung, Y. C. (1983). On the foundations of biomechanics. ASME J. Appl. Mech. 50, 1003–1009.
15. Fuster, V. (2002), Assessing and Modifying the Vulnerable Atherosclerotic Plaque, Futura publishing company.
16. Hadi, M. F. and Barocas, V. H. (2013). Microscale fiber network alignment affects macroscale failure behavior in simulated collagen tissue analogs Journal of Biomechanical Engineering. 2013;135(2).
17. Haseganu, E. M. and Steigmann, D. J. (1994a). Analysis of partly wrinkled membranes by the method of dynamic relaxation. Computational Mechanics. 14, 596–614.
18. Haseganu, E. M. and Steigmann, D. J. (1994b). Theoretical flexural response of a pressurized cylindrical membrane. Int. J. Solids Struct. 31, 27–50.
19. Haseganu, E. M. and Steigmann, D. J. (1996). Equilibrium analysis of finitely deformed elastic networks. Computational Mechanics. 17, 359–373.

20. Hashin, Z. (1983) Analysis of composite materials: a survey. ASME Journal of Applied Mechanics. 50, 481–505.
21. Holzapfel, G. A. (2001). Biomechanics of soft tissue. The handbook of materials behavior models. Volume III, Multiphysics behaviors, Chapter 10, Composite Media, Biomaterials. Edited by J. Lemaitre, Academic Press, Boston, 1049–1063.
22. Holzapfel, G. A. and Ogden, R. W. (2009). Biomechanical modeling at the molecular, cellular and tissue levels. Springer-Verlag.
23. Huet, C. (1982) Universal conditions for assimilation of a heterogeneous material to an effective medium. Mechanics Research Communications. 9 (3), 165–170.
24. Huet, C. (1984) On the definition and experimental determination of effective constitutive equations for heterogeneous materials. Mechanics Research Communications. 11 (3), 195–200.
25. Humphrey, J. D. (2003). Continuum biomechanics of soft biological tissues. Proceedings of the Royal Society, Vol. 459, No. 2029, 3–46.
26. Humphrey, J. D. (2002). Cardiovascular Solid Mechanics. Cells, Tissues, and Organs. Springer-Verlag, New York.
27. Jikov, V. V., Kozlov, S. M., Olenik, O. A. (1994) Homogenization of differential operators and integral functionals. Springer-Verlag.
28. Kachanov, L. M. (1986) Introduction to continuum damage mechanics. Martinus Nijoff, Dordricht.
29. Kachanov, M. (1993) Elastic solids with many cracks and related problems. Advance Applied Mechanics, vol. 30. Academic Press, New York, p. 259.
30. Kachanov, M., Tsukrov, I. and Shafiro, B. (1994). Effective moduli of solids with cavities of various shapes. Appl. Mech. Rev. 47, S151–S174.
31. Kachanov, M. and Sevostianov, I. (2005) On the quantitative characterization of microstructures and effective properties. International Journal of Solids and Structures. 42, 309–336.
32. Lanir, Y. (1983). Constitutive equations for fibrous connective tissues. J. Biomech. 16:1, 1–12.
33. Lewis, R. W. & Schrefler, B. A. (1998). The finite element method in the static & dynamic deformation & consolidation of porous media, 2nd ed. Wiley Press.
34. Lewis, R. W., Schrefler, B. A. & Simoni, L. 1992. Coupling versus uncoupling in soil consolidation. Int. J. Num. Anal. Metho. Geomech., 15, 533–548.
35. Libby, P. (2001), Current Concepts of the Pathogenesis of the Acute Coronary Syndromes, Circ., 104, 365–372.
36. Libby, P. (2001), The Vascular Biology of Atherosclerosis, E. Braunwald and D. P. Zipes and P. Libby, Heart Disease. A Textbook of Cardiovascular Medicine, Philadelphia, W. B. Saunders Company, sixth, Chapter 30, 995–1009.
37. Libby, P., Ridker, P. M. and Maseri, A. (2002), Inflammation and Atherosclerosis, Circ., 105,1135–1143.
38. Libby, P. and Aikawa, M. (2002), Stabilization of atherosclerotic plaques: new mechanisms and clinical targets, Nat. Med., 8, 1257–1262.
39. Loree, H. M., Kamm, R. D., Stringfellow, R. G. and Lee, R. T. (1992), Effects of Fibrous Cap Thickness on Peak Circumferential Stress in Model Atherosclerotic Vessels, Circ. Res., 71, 850–858.
40. Markov, K. Z. (2000). Elementary micromechanics of heterogeneous media. In Heterogeneous Media: Micromechanics Modeling Methods and Simulations (K. Z. Markov, and L. Preziozi, Eds.), pp. 1162. Birkhauser, Boston.
41. Maxwell, J. C. (1867) On the dynamical theory of gases. Philos. Trans. Soc. London. 157, 49.
42. Maxwell, J. C. (1873) A treatise on electricity and magnetism. 3rd. Ed. Clarendon Press, Oxford.
43. Mura, T. (1993) Micromechanics of defects in solids, 2nd edition. Kluwer Academic Publishers.
44. Nemat-Nasser, S. and Hori, M. (1999) Micromechanics: overall properties of heterogeneous solids. 2nd edition. Elsevier, Amsterdam.
45. Pangiotopoulos, P. D. (1976). A variational inequality approach to the inelastic stress-unilateral analysis of cable structures. Comput. Struct. 6 133–139.

46. Papadrakakis, M. (1980). A method for the automatic evaluation of the dynamic relaxation parameters. Computer Methods in Applied Mechanics & Engineering. 25 35–48.
47. Park, K. C. & Felippa, C. A. (1983). Partitioned analysis of coupled systems. In Computational methods for transient analysis. T. Belytschko & T. J. R. Hughes, editors.
48. Piperno, S. (1997). Explicit/implicit fluid/structure staggered procedures with a structural predictor & fluid subcycling for 2D inviscid aeroelastic simulations. Int. J. Num. Meth. Fluids. 25, 1207–1226.
49. Pipkin, A. C. (1986). The relaxed energy density for isotropic elastic membranes. IMA Journal of Applied Mathematics. 36, 297–308.
50. Powell, D. and Zohdi, T. I. (2009) Attachment mode performance of network-modeled ballistic fabric shielding. Composites Part B: Engineering. Volume 40, Issue 6, Pages 451–460.
51. Powell, D. and Zohdi, T. I. (2009) A note on flaw-induced integrity reduction of structural fabric. The International Journal of Fracture/Letters in Micromechanics. Vol. 158, L89–L96.
52. Rachev, A. and Hayashi, K. (1999). Theoretical study of the effects of vascular smooth muscle contraction on strain and stress distributions in arteries. Ann. Biomed. Engng 27, 459–468.
53. Rayleigh, J. W. (1892) On the influence of obstacles arranged in rectangular order upon properties of a medium. Phil. Mag. 32, 481–491.
54. Richardson, P. D. and Davies, M. J. and Born, G. V. R. (1989), Influence of plaque configuration and stress distribution on fissuring of coronary atherosclerotic plaques, Lancet, 2(8669) 941–944.
55. Sacks, M. S. and Sun, W. (2003). Multiaxial mechanical behavior of biological materials. Annual Review of Biomedical Engineering, Vol. 5: 251–284.
56. Schrefler, B. A. (1985). A partitioned solution procedure for geothermal reservoir analysis. Comm. Appl. Num. Meth., 1, 53–56.
57. Sevostianov, I., Gorbatikh, L. and Kachanov, M. (2001). Recovery of information of porous/microcracked materials from the effective elastic/conductive properties. Materials Science and Engineering. A 318, 1–14.
58. Sevostianov, I and Kachanov, M. (2008). Connections between Elastic and Conductive Properties of Heterogeneous Materials. Advances in Applied Mechanics. Volume 42, 69–253.
59. Shah, P. K. (1997), Plaque disruption and coronary thrombosis: New insight into pathogenesis and prevention, Clinical Cardiology, 20 (Suppl. II). II-38-II-44.
60. Steigmann, D. J. (1990). Tension field theory. Proceedings of the Royal Society London A. Vol. 429, 141–173.
61. Torquato, S. (2002) Random Heterogeneous Materials: Microstructure and Macroscopic Properties Springer-Verlag, New York.
62. Virmani, R. and F. D. Kolodgie and A. P. Burke and A. Farb and S. M. Schwartz (2000), Lessons from sudden coronary death: A comprehensive morphological classification scheme for atherosclerotic lesions, Arterioscl. Thromb. and Vasc. Biol., 20, 1262–1275.
63. van der Wal, A. C. and A. E. Becker (1999), Atherosclerotic plaque rupture - pathologic basis of plaque stability and instability, Cardiovasc. Res., 41, 334–344.
64. Zhang, L., Lake, S. P., Lai, V. K., Picu, C. R., Barocas, V. H. and Shephard, M. S. (2013). A coupled fiber-matrix model demonstrates highly inhomogeneous microstructural interactions in soft tissues under tensile load Journal of Biomechanical Engineering. 135(1).
65. Zienkiewicz, O. C. (1984). Coupled problems & their numerical solution, in R. W. Lewis, P. Bettes & E. Hinton (eds) Numerical methods in coupled systems Wiley, Chichester, 35–58.
66. Zohdi, T. I. (2002a). Modeling and simulation of progressive penetration of multilayered ballistic fabric shielding. Computational Mechanics. 29, 61–67.
67. Zohdi, T. I. and Steigmann, D. J. (2002b). The toughening effect of microscopic filament misalignment on macroscopic fabric response. The International Journal of Fracture. 115, L9–L14.
68. Zohdi, T. I., Holzapfel, G. A. and Berger, S. A. (2004). A phenomenological model for atherosclerotic plaque growth and rupture. The Journal of Theoretical Biology. Vol. 227, Issue 3, pp. 437–443.

69. Zohdi, T. I. (2005). A simple model for shear stress mediated lumen reduction in blood vessels. Biomechanics and Modeling in Mechanobiology. Volume 4, Number 1, p 57–61.
70. Zohdi, T. I. (2004a). Modeling and direct simulation of near-field granular flows. The International Journal of Solids and Structures. Vol 42/2 pp 539–564.
71. Zohdi, T. I. (2004b). A computational framework for agglomeration in thermo-chemically reacting granular flows. Proceedings of the Royal Society. Vol. 460. Num. 2052, 3421–3445.
72. Zohdi, T. I. (2005). Charge-induced clustering in multifield particulate flow The International Journal of Numerical Methods in Engineering. Volume 62, Issue 7, Pages 870–898.
73. Zohdi, T. I. and Powell, D. (2006). Multiscale construction and large-scale simulation of structural fabric undergoing ballistic impact. Computer Methods in Applied Mechanics and Engineering. Volume 195, Issues 1–3, 1 January 2006, Pages 94–109.
74. Zohdi, T. I. (2007a) Computation of strongly coupled multifield interaction in particle-fluid systems. Computer Methods in Applied Mechanics and Engineering. Volume 196, 3927–3950.
75. Zohdi, T. I. (2007b). A computational framework for network modeling of fibrous biological tissue deformation and rupture. Computer Methods in Applied Mechanics and Engineering. Volume 196, 2972–2980.
76. Zohdi, T. I. (2007c). Introduction to the modeling and simulation of particulate flows. SIAM (Society for Industrial and Applied Mathematics).
77. Zohdi, T. I. and Wriggers, P. (2008). Introduction to computational micromechanics. Second Reprinting. Springer-Verlag.
78. Zohdi, T. I. (2009) Microfibril-based estimates of the ballistic limit of multilayered fabric shielding. The International Journal of Fracture/Letters in Micromechanics. Vol. 158, L81–L88.
79. Zohdi, T. I. (2010a). High-speed impact with electromagnetically sensitive fabric and induced projectile spin. Computational Mechanics. 46, 399–415.
80. Zohdi, T. I. (2010b). Simulation of coupled microscale multiphysical-fields in particulate-doped dielectrics with staggered adaptive FDTD. Computer Methods in Applied Mechanics and Engineering. Volume 199, 79–101.
81. Zohdi, T. I. (2011a). Dynamics of clusters of charged particulates in electromagnetic fields. The International Journal of Numerical Methods in Engineering. 85, 1140–1159.
82. Zohdi, T. I. (2011b). Electromagnetically-induced deformation of functionalized fabric. The Journal of Elasticity. Volume 105, Numbers 1–2. 381–398.
83. Zohdi, T. I. (2012) Modeling and simulation of electrification delivery in functionalized textiles in electromagnetic fields. Computer Methods in Applied Mechanics and Engineering. Volumes 245246, Pages 206–216.

# Chapter 7
# Transport Phenomena: Computational Models for Convective and Diffusive Transport in Capillaries and Tissue

**Milos Kojic, Miljan Milosevic, Nikola Kojic, Velibor Isailovic, Dejan Petrovic, Nenad Filipovic, Mauro Ferrari and Arturas Ziemys**

**Abstract** A review of computational procedures for convective and diffusive transport, developed by the authors, is presented in this chapter. The presented finite element computational framework is directed to transport within capillaries and tissue. The convective transport includes modeling of motion of deformable bodies within fluid flow. It is based on a strong coupling concept and remeshing procedure. It was found by the authors that this approach has advantages in reliability and accuracy with respect to others available in literature, although it is not computationally efficient. A hierarchical multiscale model for diffusion couples molecular dynamics and continuum FE method by evaluating equivalent continuum diffusive parameters; these parameters include commonly used diffusion coefficients, but also parameters which account for physicochemical interactions between diffusing molecules and microstructural solid surfaces. A numerical homogenization is used in this multiscale model. Coupled convective and diffusive transport is also considered. A number of typical solved examples illustrate generality, robustness, and accuracy of the presented computational methodology.

**Keywords** Finite element method · Strong coupling · Remeshing procedure · Multiscale diffusion model · Numerical homogenization · Biomedical applications

M. Kojic (✉) · M. Ferrari · A. Ziemys
Houston Methodist Research Institute, Houston, TX, USA
e-mail: mkojic42@gmail.com

M. Kojic · M. Milosevic · V. Isailovic · D. Petrovic · N. Filipovic
Belgrade Metropolitan University – Research and Development Center for Bioengineering BioIRC, Kragujevac, Serbia

N. Filipovic
Faculty of Technical Sciences, University of Kragujevac, Kragujevac, Serbia

N. Kojic
Center for Engineering in Medicine and Surgical Services, Massachusetts General Hospital, Harvard Medical School, Boston, MA 02114, USA



S. De et al. (eds.), *Multiscale Modeling in Biomechanics and Mechanobiology*, DOI 10.1007/978-1-4471-6599-6_7

## 7.1 Introduction

Transport phenomena are a vital part of life, found in biology, in technology, and in our environment. One might observe transport on scales from macro to nano, like ocean streams, flow in tap water pipes, or microfluidics. Reducing the scales to the micro and below the flow in mass transport decreases and diffusion transport becomes more important. In systems where the Peclet number becomes small, diffusion may start to dominate mass transport, or be as important as flow at least. Transport phenomena involving diffusion are common in nature [8, 58], industrial processes [12, 22, 23] or biology [2, 11].

Most of research is focused on the macro-scale, where fundamental laws, such as Fick's or Darcy's law, describe movement of a given substance through a medium. However, in heterogeneous structures or materials the scale and interfaces may alter the transport. For example, in nanofluidic and nanoporous materials, new material properties and transport phenomena emerge that are exploited in biomedical and industrial applications, including drug delivery [20, 51], catalysis [14, 55] and molecular filtering [24]; here, a substantial deviation occurs from the traditional phenomenological transport laws.

Classical continuum theories of diffusion through homogenous media use Fick's law:

$$\mathbf{J} = -D\nabla c \tag{7.1}$$

where

$$D = \frac{k_B T}{6\pi \mu r} \tag{7.2}$$

$\mathbf{J}$ is the mass flux along the concentration gradient $\nabla c$ with diffusion coefficient (diffusivity) $D$. The Stokes–Einstein equation (7.2) shows that $D$ for an ideal solution is inversely proportional to viscosity $\mu$ and radius $r$ of the diffusing molecule. In further discussions we will refer to Fickian diffusion where D is a constant, or D(const). However, experiments often deal with non-ideal solutions, where D depends on concentration, i.e., D = D(c) [5, 12].

Systems, where the interface starts dominating over volume properties, alter diffusion because of interactions of the diffusing particles with solid media [30, 47]; also, both fluid and solute properties could be altered at the interface [26, 56]. In view of the above, diffusion transport predictions by Eq. 7.1 may become inaccurate, because the homogeneity of diffusion environment is violated [64]. Therefore, in modeling diffusive mass transport, it is important not to neglect the interactions between diffusion particles with the microstructure.

Accurate and reliable prediction of mass transport is important in biomedical application, for example in predicting mass distribution in tissue microenvironment or designing drug delivery material for optimal drug release kinetics. We here

describe a multiscale mass transport modeling framework that relies on basic physical laws and employs modern computational tools; it includes particle flow, molecule diffusion, or the combination of both, and is robust and general.

## 7.2 Convective Transport of Particles and Cells

### *7.2.1 A Review of Methods*

In many technological processes, in living organisms, and in nature, motion of rigid and deformable solids within fluid is commonly present. This motion has been the subject of experimental and theoretical investigations over centuries. Regarding mathematical modeling, analytical formulations originally were used which triggered development of mathematical methods. In the era of computer technology, numerical methods have been introduced offering solutions of very complex problems. We here give a brief overview of computational methods relevant to the methodology adopted in our research.

In the so-called Stokes dynamics, the effects of particle motion on fluid flow are neglected, while forces and torques acting on particles are evaluated to compute motion of particles [15, 31, 45, 52]. Coupling particle motion and fluid flow was further considered and we cite several methods, such as integral equation for particle motion and the boundary element method, [49, 50]; fictitious domain approach [18, 19]; arbitrary Lagrangian-Eulerian (ALE) formulation [28]; Lagrange multiplier method [18, 53]; immerse boundary finite element method [1, 59]; finite element method with remeshing in an explicit–implicit procedure, called direct simulation [27]. Finally, we here note a few recent references related to motion of particles within channels, which is important in microchip devices used in cell biology; there, the shape of particle trajectory depends on the lift (lateral) force generated during particle motion [9, 60].

We have found that the most accurate and robust methodology is the finite element method (FE), where a strong coupling approach with remeshing procedure is used [29, 40]. Also, our approach employs an implicit incremental-iterative computational scheme [34, 36].

### *7.2.2 Remeshing Procedure*

The FE method used in our models relies on the fundamental laws of balance of linear momentum (i.e., Newton's Second Law); in case of fluid, mass balance is also used. We here first summarize the basic equations in the differential form and in the FE format, and then describe the remeshing procedure. The balance of linear momentum for fluid can be written in the form of the Navier–Stokes equations [36]:

$$\rho_f \left( \frac{\partial v_i}{\partial t} + \frac{\partial v_i}{\partial x_k} v_k \right) = -\frac{\partial p}{\partial x_i} + \mu \frac{\partial^2 v_i}{\partial x_k \partial x_k} + f_i^V \quad i = 1, 2, 3; \quad \text{sum on } k: \ k = 1, 2, 3 \tag{7.3}$$

where $v_i$ are fluid velocities, $p$ is pressure, $f_i^V$ are volumetric forces; and $\rho_f$ and $\mu$ are fluid density and dynamic viscosity. It should be noted that these equations are derived assuming the Eulerian description of motion and using constitutive law for viscous fluid: $\sigma_{ij}^{\text{viscous}} = \mu \left( \partial v_i / \partial x_j + \partial v_j / \partial x_i \right)$. We will only consider flow of incompressible fluid, for which the continuity (mass balance) equation can be expressed as:

$$\frac{\partial v_i}{\partial x_i} \equiv \frac{\partial v_x}{\partial x} + \frac{\partial v_y}{\partial y} + \frac{\partial v_z}{\partial z} = 0 \tag{7.4}$$

By implementing a weighted procedure (Galerkin method [36]), a weak form of the above equations can be derived. Within an incremental-iterative computational scheme, the equations of balance related to one finite element (which include both Eqs. (7.3) and (7.6)), for a time step $n$ of size $\Delta t$ and iteration $i$, can be written in a form:

$$\begin{bmatrix} \frac{1}{\Delta t}\mathbf{M} + {}^{n+1}\tilde{\mathbf{K}}_{\text{vv}}^{(i-1)} & \mathbf{K}_{\text{vp}} \\ \mathbf{K}_{\text{vp}}^T & \mathbf{0} \end{bmatrix} \begin{Bmatrix} \Delta \mathbf{V}^{(i)} \\ \Delta \mathbf{P}^{(i)} \end{Bmatrix} = \begin{Bmatrix} {}^{n+1}\mathbf{F}_{\text{ext}}^{(i-1)} \\ 0 \end{Bmatrix} - \begin{bmatrix} \frac{1}{\Delta t}\mathbf{M} + {}^{n+1}\mathbf{K}_{\text{vv}}^{(i-1)} & \mathbf{K}_{\text{vp}} \\ \mathbf{K}_{\text{vp}}^T & 0 \end{bmatrix} \begin{Bmatrix} {}^{n+1}\mathbf{V}^{(i-1)} \\ {}^{n+1}\mathbf{P}^{(i-1)} \end{Bmatrix} + \begin{Bmatrix} \frac{1}{\Delta t}\mathbf{M}^n\mathbf{V} \\ 0 \end{Bmatrix} \tag{7.5}$$

where matrix $\mathbf{M}$ corresponds to the local velocity derivatives $\partial v_i / \partial t$; matrices ${}^{n+1}\tilde{\mathbf{K}}_{\text{vv}}^{(i-1)}$ and ${}^{n+1}\mathbf{K}_{\text{vv}}^{(i-1)}$ include convective velocity derivatives $\frac{\partial v_i}{\partial x_k} v_k$ and viscous terms; $\mathbf{K}_{\text{vp}}$ is the matrix coupling velocities and pressure; $\mathbf{F}_{\text{ext}}$ are external nodal forces corresponding to volumetric forces and action of the surrounding elements; $\mathbf{V}$ and $\mathbf{P}$ are nodal velocity and pressure vectors; left upper indices $n$ and $n$+1 indicate start and end of the time step; and the right upper indices $i$ and $i$-1 denote the current and previous equilibrium iteration within the time step. These equations are assembled into a system of equations for the entire fluid domain, using the stationary fluid mesh, since the equations assume the Eulerian description. The time integration procedure is implicit, therefore the overall system of balance equations are satisfied at the end of time step, and iterations continue until selected convergence criteria are satisfied. Details about matrices and computations are given elsewhere [36].

Motion of the solid is described according to the Lagrangian description. Then, the differential equation of balance of linear momentum is:

$$\rho_s \frac{\partial v_i}{\partial t} = \frac{\partial \sigma_{ik}}{\partial x_k} + f_i^V \, i = 1, 2, 3; \quad \text{sum on } k: \ k = 1, 2, 3 \tag{7.6}$$

where $\rho_s$ is density of solid, and $\sigma_{ik}$ are stresses. Besides these equations, constitutive law for material behavior must be included; in case of elastic solid the constitutive law

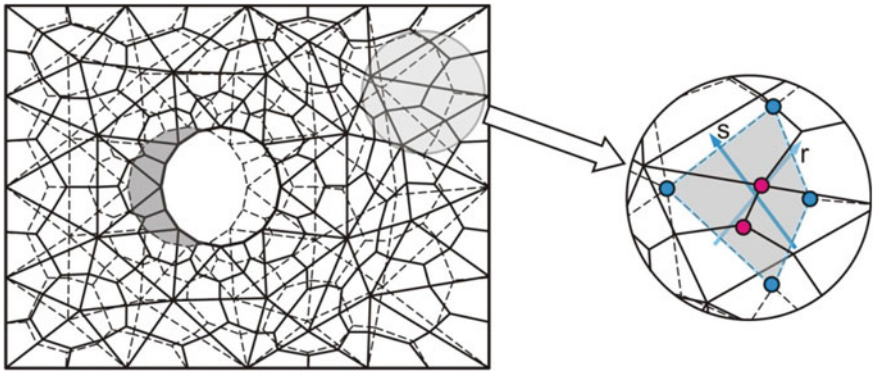


**Fig. 7.1** Schematics of the remeshing procedure. After the solution for the current time step is obtained, the solid is displaced, a new fluid mesh is generated (with common solid and fluid nodes at the solid boundary) and solutions from the old mesh are mapped to the new mesh [29]

is: $\sigma_i = C^E_{ij} e_j$ where $C^E_{ij}$ is elastic matrix, with the one-index notation for stresses and strains $e_j$. Balance equations which follow from Eq. (7.6) can be written in the form

$$\left(\frac{1}{\Delta t}\mathbf{M}^s + \Delta t^{n+1}\mathbf{K}^{s(i-1)}\right)\Delta\mathbf{V}^s = {}^{n+1}\mathbf{F}^{s(i-1)}_{\text{ext}} - {}^{n+1}\mathbf{F}^{s(i-1)}_{\text{int}} - \frac{1}{\Delta t}\mathbf{M}^s\left({}^{n+1}\mathbf{V}^{s(i-1)} - {}^{n}\mathbf{V}^s\right) \tag{7.7}$$

where $\mathbf{M}^s$ and $\mathbf{K}^s$ are the mass and stiffness matrix of the solid, $\mathbf{V}^s$ is the nodal velocity vector; $\mathbf{F}^s_{\text{ext}}$ are external nodal forces which also include volumetric forces and nodal forces from other elements (together with forces from fluid elements for common solid–fluid nodes); and $\mathbf{F}^s_{\text{int}}$ are internal nodal forces arising from stresses within solid [6, 34]. Note that we use the term $\Delta t^{n+1}\mathbf{K}^{s(i-1)}$ since we are solving for velocities instead of displacements usually used in modeling solids.

We use a remeshing procedure [29, 40] which assumes that the boundary nodes of the particle mesh and of the fluid are the same for the current step, hence these nodes have the same velocities. When convergence is reached, we displace all solid nodes for $\Delta\mathbf{U}^s = \Delta t\mathbf{V}^s$ (graphically shown in Fig. 7.1). Then, we generate a new fluid mesh, with common nodes at the displaced solid boundary nodes. Besides a purely geometrical change in the mesh, it is necessary to map solutions from the previous mesh to the new mesh. We search over all new fluid nodes, find the element in the previous mesh to which the node belongs, and use isoparametric interpolation from the element nodes of the old mesh to find the velocity and pressure at the new node.

We have implemented the above described methodology into our FE program PAK-FS [35]. Details of this methodology and its implementation are given in [29]. Solution accuracy of the computational method and software has been tested on various examples available in the literature [29, 37].

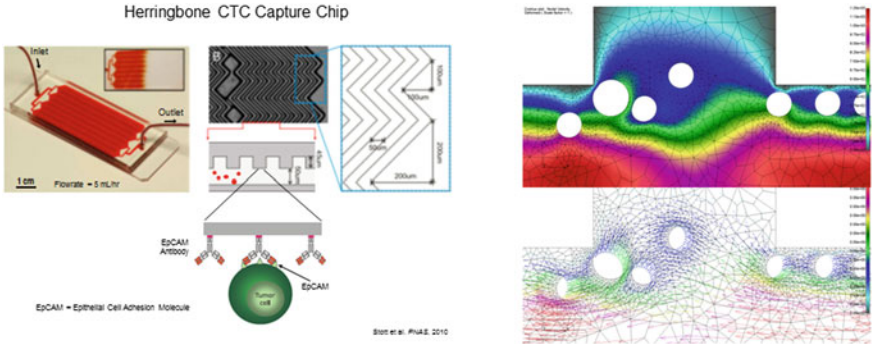


**Fig. 7.2** Herringbone chip for capturing tumor cells [54] (*left*) and velocity field calculated using the solid-fluid interaction FE model (*right*)

### *7.2.3 Modeling Motion of Cells Within a Herringbone Chip*

Model of herringbone chip is shown in Fig. 7.2 (left panel) [54]. This chip is designed to capture rare circulating tumor cells (CTC) in blood. It applies passive mixing of blood cells through the generation of microvortices to significantly increase the number of interactions between target CTCs and the antibody-coated chip surface. A simplified 2D FE model, which includes normal and cancer cells, is developed and velocity field is shown in Fig. 7.2 (right panel).

## 7.3 Diffusion—Multiscale Models

In this section diffusion models are presented. After the introduction about significance of diffusion processes in biological media, we describe our basic hierarchical model and then introduce a general multiscale model for diffusion in composite media. Selected examples illustrate validation and applicability of our computational models.

The fundamental equation of diffusion, which represents the mass balance equation at a material point of the continuum (composed of solvent and solute), can be written as

$$-\frac{\partial c}{\partial t}+\frac{\partial}{\partial x_i}\left(D_{ij}\frac{\partial c}{\partial x_j}\right)+q^V=0 \tag{7.8}$$

where $c\,(x_i,t)$ is concentration, $D_{ij}$ are components of the diffusion tensor, and $q^V\,(x_i,t)$ is a source term. The constitutive relation, represented by the Fick's law,

$$\mathbf{J}=-\mathbf{D}\nabla c \quad \text{or} \quad J_i=-D_{ij}\frac{\partial c}{\partial x_j} \tag{7.9}$$

is included in Eq. (7.8), where $\mathbf{J}$ is the mass flux, and summation on the repeated index is implied ($j = 1, 2, 3$). In case of isotropic diffusion, the diffusion tensor is diagonal,

$$\mathbf{D} = D\mathbf{I} \tag{7.10}$$

where $\mathbf{I}$ is the identity tensor.

### 7.3.1 Characteristics of Diffusion Within Nanospace

Transport by diffusion represents one of the most fundamental processes in biological systems [3, 11]. Mathematical models of transport on the macro-scale within composite media rely on the phenomenological laws, such as Fick's or Darcy's law. Diffusion, which is the subject of this study, depends not only on the porosity and the size of the moving particles or molecules, but also on the physico-chemical interactions between the particles and solid surface occurring at the molecular level. This is particularly significant in case of diffusion within biological media where the spatial dimensions of pore space are comparable to the diffusing particles or molecules [64, 65]. Then, Fick's law does not accurately describe diffusion and the surface interaction at the molecular level must be taken into account. We employ the Molecular Dynamics (MD) method to include surface effects into our continuum macro-scale diffusion models, as presented below.

### 7.3.2 Hierarchical Model of Diffusion

We here introduce a hierarchical diffusion model which couples MD and FE methods. This model represents the basis for the formulation of our multiscale model, formulated in the next section. It is assumed that the chemical interaction occurs between the transported particles or molecules and surrounding solid surfaces. Then, trajectories of particles are altered due this interaction and the overall diffusion is affected in the vicinity of the surfaces.

The diffusion near the surfaces differs from the free diffusion and is characterized as hindered diffusion. This hindered diffusion is more pronounced in case of small, nanosize dimensions of the diffusive space. The interaction effects are illustrated in Fig. 7.3a, b for diffusion within a nanochannel with a height $h$ comparable to the particle size. MD is used to quantify the surface interaction effects by calculating the effective diffusion coefficient $D$ in terms of the distance from the solid surface and the concentration $c$. The function $D(h, c)$ is further used within finite element (FE) models in our hierarchical diffusion computational model, as is described in the text below [39, 40, 65].

#### 7.3.2.1 MD Simulations

MD has been used for many decades and is well described in many texts, as for example [4, 16]. MD is based on statistical mechanics, where motion of particles or molecules is described according to Newtonian mechanics:

$$m_i \dot{\mathbf{v}}_i = \mathbf{F}_i \tag{7.11}$$

where $m_i$, $\dot{\mathbf{v}}_i$ and $\mathbf{F}_i$ are mass, acceleration and resulting force (including interaction forces from the neighboring particles and external forces), respectively. The interaction forces include bonded (repulsive-attractive, bending and torsion) and non-bonded (electrostatic, van der Waals) terms, $E_{\text{intra}}$ and $E_{\text{inter}}$, respectively. The Force Field (FF) represents a functional form of the behavior of chemical structures and is evaluated from potential energy function. There are many popular FFs available and they differ by parameterization and available chemical space. CHARMM FF [41] is a good illustration of a general and well adopted FF that is also used in our MD models:

$$E_{\text{intra}} = \sum_{\text{bonds}} K_b \left(b - b_0\right)^2 + \sum_{\text{angles}} K_\theta \left(\theta - \theta_0\right)^2 + \sum_{\text{torsions}} K_\phi \left(1 + \cos\left(n\phi + \delta\right)\right) \tag{7.12}$$

$$E_{\text{inter}} = \sum_{\text{electrostatics}} \frac{q_i q_j}{r_{ij}} + \sum_{\text{VDW}} \varepsilon_{ij} \left[ \left( \frac{R_{\min,ij}}{r_{ij}} \right)^{12} + 2 \left( \frac{R_{\min,ij}}{r_{ij}} \right)^{6} \right] \tag{7.13}$$

Material parameters of the intra-molecular potential $E_{\text{intra}}$ are given by the force constants $K_b$, $K_\theta$ and $K_\phi$, equilibrium values of bonds and angles $b_0$ and $\theta_0$, and equilibrium torsion constants—dihedral multiplicity $n$ and dihedral phase $\delta$. Inter-molecular potential sums are electrostatic and van der Waals (VDW) terms, where $\varepsilon_{ij}$ is VDW potential depth, $R_{\min}$ is atom radius, and $q_i$, $q_j$ are partial atomic charge. These parameters of FF are introduced to represent certain chemical classes of compounds in order to reproduce experimental physico-chemical properties.

MD simulations for calculating diffusivities were carried out using NAMD 2.6 [48] with a TIP3P water model [32] and NVT (fixed number of particles $N$, pressure $P$, volume $V$) ensemble. CHARMM compatible amorphous silica force field [10] was employed to model the silica nanochannel, which is modeled by charged hydrophilic amorphous silica phase to match the silica properties after the fabrication process. Details of MD simulations related to diffusion in silica channels are published in [61, 62]. Calculating the diffusion of Rhodamine 6G, the same tools were used as for silica channel systems. All molecules involved in the model, including $\beta$-D-glucose and rhodamine 6G, were simulated with the CHARMM22 FF [46, 57]. The agarose fiber model was composed of glucose molecules positions in a rod-structure with $2 \times 2 \times 6$ molecules and were constrained to maintain rod structures. The fiber model was hydrated in an approximately $4 \times 10 \times 10$ nm box and filled with water. Six molecules of Rhodamine 6G were added at random location in water phase.

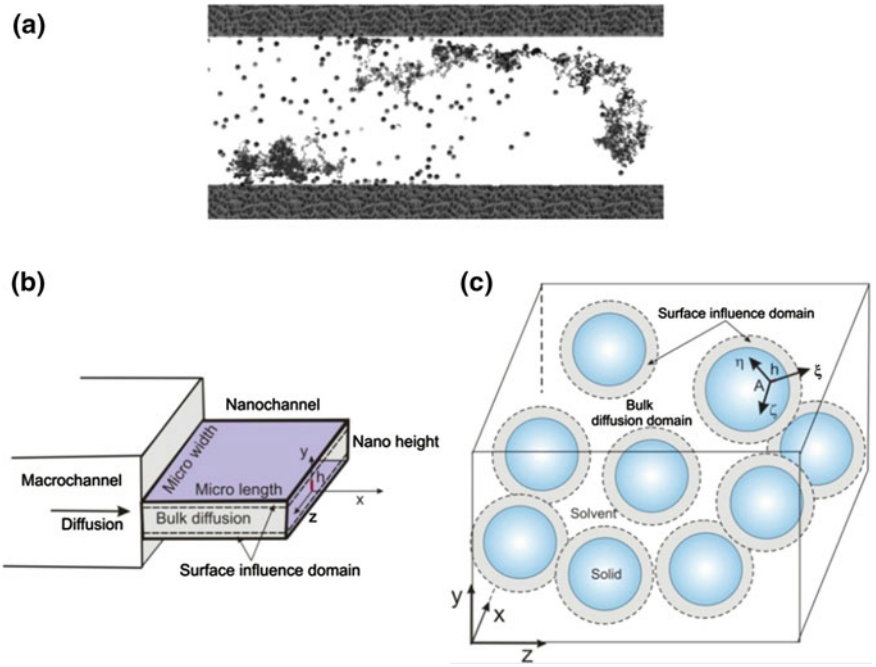


**Fig. 7.3** Representation of diffusion within confined space. **a** Trajectories of diffusing molecules (*dark spheres*) within a nanochannel illustrate surface effect which reduces diffusivity of molecules at proximity to surface; **b** Diffusion within nannochannel with bulk domain (free diffusion) and diffusion domain affected by interaction with surface in case of nanochannel of (nano) height $h$ ; **c** A porous medium with bulk diffusion domain and surface influence domain

Periodic boundary conditions were applied in all directions. The whole model was minimized, equilibrated and later production simulation executed over 20 ns using 2 fs integration step.

Diffusion was analyzed studying center-of-mass displacement of target molecules (glucose, Rhodamine 6G) and calculating diffusivity dependence on proximity to the fiber or silica wall like in [42, 63]. Diffusion coefficients were calculated from trajectories by using the mean square displacement $\langle r^2 \rangle$:

$$\langle r^2 \rangle = 2\mathrm{d}Dt \tag{7.14}$$

where the factor $d = 1, 2, 3$ depends on the dimensionality of the space, and $t$ is time. The diffusivity along the surface normal was evaluated from the surface of the fiber or silica wall to distances at which the diffusivity value saturates. The time window $t$ for $\langle r^2 \rangle$ was chosen as 20 ps, which is small enough to catch local displacements within 0.5 nm thick slabs. Values of $\langle r^2 \rangle$ were collected to bins according to the center of mass of molecules and their initial position. Molecules could leave the bin in which $\langle r^2 \rangle$ is computed in order to avoid restricted ensembles. The diffusivity results

include dependence on distance from the solid surface for glucose and Rhodamine 6G at different concentrations (Fig. 7.4).

For easier implementation within the FE models, and also for the generality of this methodology, we introduce scaling functions as material characteristics for the considered particle-surface pair. Namely, the MD calculated diffusivity is normalized with respect to the "bulk" value $D_{\text{bulk}}$ corresponding to diffusivity far from the surface, where influence of the surface is negligible, such that

$$D = s\, D_{\text{bulk}} \tag{7.15}$$

where

$$s = s\,(h, c)\,, \quad 0 \leq s \leq 1 \tag{7.16}$$

is the scaling function which depends on the distance from the wall surface $h$ and concentration $c$. Example of scaling functions for different concentrations are shown in Fig. 7.4b [65] and Fig. 7.4d, assuming diffusion within a nanochannel with silica walls. For the examples shown here we have chosen glucose molecules according to [17].

Further, it is straightforward to extend calculation of the scaling function to any microstructural geometry. The assumption is that the surface size is large when compared with the particle/molecule. Then, using MD as in case of nanochannel we can determine diffusion coefficients $D_{\xi\xi}$, $D_{\eta\eta}$, $D_{\zeta\zeta}$ (or scaling functions $s_\xi$, $s_\eta$, $s_\varsigma$) in the local system $\xi$, $\eta$, $\zeta$ (Fig. 7.3c), where $\xi$ is in the direction normal to the surface, and $\eta$, $\zeta$ lie in the tangential plane:

$$\begin{aligned} D_{\xi\xi} &= s_\xi\, D_{\text{bulk}} \\ D_{\eta\eta} &= s_\eta\, D_{\text{bulk}} \\ D_{\zeta\zeta} &= s_\zeta\, D_{\text{bulk}} \end{aligned} \tag{7.17}$$

where $D_{\text{bulk}}$ can depend on concentration, i.e., $D_{\text{bulk}} = D_{bulk}\,(c)$. It is shown in Fig. 7.3c that there are two domains in a microstructure: the domain with surface effects with the so-called hindered diffusion, and the bulk diffusion domain. Diffusion tensor in the global coordinate system can be obtained by the tensorial transformation,

$$\mathbf{D} = \mathbf{T}\mathbf{D}_{\xi\eta\varsigma}\mathbf{T}^T \tag{7.18}$$

where $\mathbf{D}_{\xi\eta\varsigma}$ is the diagonal tensor with components given in Eq. (7.17), while $\mathbf{T}$ is the transformation matrix containing cosines of angles between local and global coordinate systems [36]. The three scaling functions are the same $s_\xi = s_\eta = s_\varsigma = s\,(h, c)$ in case of isotropic conditions, and the diffusion tensor is diagonal,

$$\mathbf{D} = \mathbf{D}_{\xi\eta\varsigma} = s\,(h, c)\, D_{bulk}\mathbf{I} \tag{7.19}$$

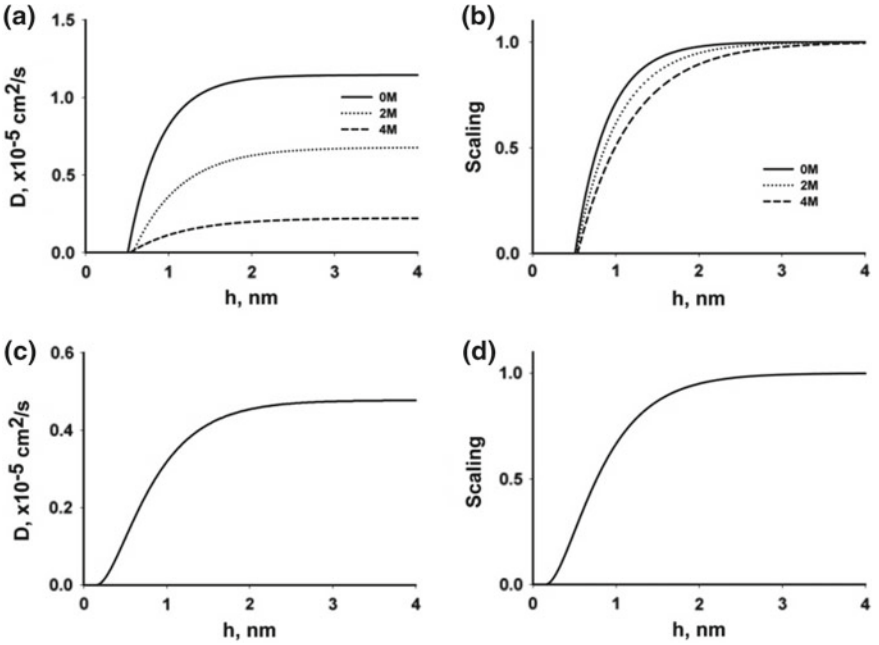


**Fig. 7.4** Diffusion coefficient and corresponding scaling functions for glucose [65] and Rhodamine 6G, calculated using MD and presented with exponential fits. **a** Glucose diffusion coefficient as a function of distance from silica surface for different glucose concentrations; **b** Diffusion scaling functions, with the segment of zero diffusivity corresponding to statistical molecular radius; **c** Rhodamine 6G diffusion coefficient as a function of distance form agarose fiber; **d** Rhodamine 6G scaling function

#### 7.3.2.2 Finite Element Model

As in case of fluid (Sect. 7.2.2), a Galerkin procedure can be used and the nonlinear differential equation (7.8) can be transformed into the incremental-iterative system of linear balance equations for a finite element [36],

$$\left(\frac{1}{\Delta t}\mathbf{M} + {}^{n+1}\mathbf{K}^{(i-1)}\right)\Delta\mathbf{C}^{(i)} = {}^{n+1}\mathbf{Q}^{S(i-1)} + {}^{n+1}\mathbf{Q}^{V(i)} - {}^{n+1}\mathbf{K}^{(i-1)}\,{}^{n+1}\mathbf{C}^{(i-1)} - \frac{1}{\Delta t}\mathbf{M}\left({}^{n+1}\mathbf{C}^{(i-1)} - {}^{n}\mathbf{C}\right) \tag{7.20}$$

where $\mathbf{C}$ is the vector of nodal concentrations; $\mathbf{Q}^S$ and $\mathbf{Q}^V$ are surface and volumetric nodal fluxes for the element; and components of the matrices $\mathbf{M}$ and $\mathbf{K}$ are

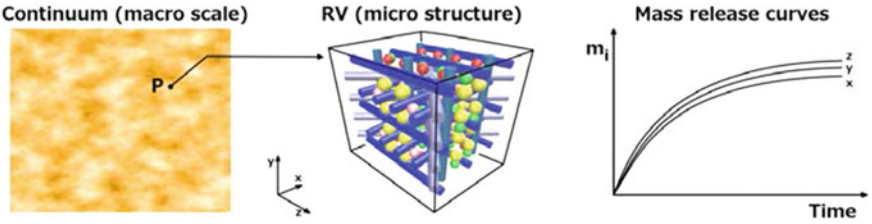


**Fig. 7.5** Numerical homogenization concept. At a point P of the continuum we specify a small—reference volume (RV) and calculate mass release curves $m_i$(t) within RV for coordinate directions $x, y, z$. A microstructural model for diffusion within the RV is generated, with detailed description of the microstructure and spatial field of the diffusion tensor obtained from MD

$$M_{IJ} = \int_V N_I N_J \mathrm{d}V \tag{7.21}$$

$$^{n+1}K_{IJ}^{(i-1)} = \int_V {}^{n+1}D_{ij}^{(i-1)} N_{I,i} N_{J,j} \mathrm{d}V \tag{7.22}$$

Here $N_I$ and $N_J$ are the interpolation functions, and $^{n+1}D_{ij}^{(i-1)}$ are components of the diffusion tensor corresponding to the last known concentration $^{n+1}c^{(i-1)}$ at a point within the finite element.

The described hierarchical model has been verified by comparison of computed results for mass release in nanochannels with experiments [13, 65]. In Sect. 7.3.4 we demonstrate the effects of molecule-surface interaction.

### *7.3.3 Multiscale MD-FE Model*

The hierarchical model described in the previous section involves detailed evaluation of the field of the diffusion tensor, which for the case of complex microstructure requires significant effort in generating the internal microstructural geometry and evaluation of the scaling functions. We call this diffusion model the microstructural model. The model is practically not adequate for large domains, as, for example, is a micron size domain for diffusion within biological tissues. It follows that a macroscale model with equivalent diffusion parameters is desirable for applications. We here describe a continuum macroscale diffusion model with equivalent parameters using the microstructural model and a numerical homogenization procedure [39, 43].

#### 7.3.3.1 Numerical Homogenization Procedure

Our homogenization procedure relies on the condition that mass release curves for the detailed microstructural and continuum models are the same (within a numerical tolerance). Practically, we proceed as follows. We select a small reference volume (RV) at a material point and calculate mass release curves for three coordinate directions according to the microstructural model formulation. Then we seek for equivalent diffusion parameters of the continuum to obtain the same mass release curves (schematic is shown in Fig. 7.5). Note that the mass fluxes in the coordinate directions,

$$J_i = \frac{\partial m_i}{\partial t}, \qquad i = 1, 2, 3 \tag{7.23}$$

are geometrically represented by the slope on the mass release curves, as indicated in Fig. 7.5. If the equivalent parameters are determined under the condition that mass release curves are the same for both microstructural and continuum model, then the mass fluxes for the microstructural and continuum models are the same at any time during the diffusion process. Hence, diffusion characteristics will be the same for both models and the governing Eq. (7.8), written using fluxes:

$$-\frac{\partial c}{\partial t} - \frac{\partial J_i}{\partial x_i} + q^V = 0 \qquad \text{sum on } i : \; i = 1, 2, 3 \tag{7.24}$$

will have the same solutions. Of course, the microstructural model requires MD calculation of the scaling functions for diffusing particles in the microstructure and a very fine FE mesh for discretization of the RV.

The equivalent continuum model includes two sets of equivalent diffusion parameters:

(a) equivalent diffusion coefficients $\bar{D}_i$
(b) equivalent distances $\bar{h}_i$ from solid surfaces

for the three coordinate directions. The first set corresponds to the bulk diffusion within microstructure, and has been used in the past in homogenization procedures for diffusion [7, 25]. The new parameters $\bar{h}_i$ take into account surface interactions within the microstructure.

Practical evaluation of the equivalent parameters consists of the following steps:

1. Find mass release curves for the microstructural model while neglecting surface interaction effects within microstructure (Fickian diffusion);
2. Determine equivalent diffusion coefficients $\bar{D}_i$ using these mass release curves;
3. Evaluate scaling functions for the microstructure and determine mass release curves for the microstructural model using these scaling functions and the bulk diffusion coefficient $D_{\text{bulk}}$;
4. Find equivalent distances $\bar{h}_i$ by employing mass release curves from step 3 and diffusion coefficients $\bar{D}_i$ from step 2.

Details of the practical implementation of these steps are given in references [38, 39, 43].

A proof that the equivalent diffusion parameters (for a given solute)—equivalent diffusion coefficients and equivalent distances from surface—depend only on the geometry of the microstructure and its material characteristics, is given in references [38, 39, 43].

We note that RVs can be specified at various points of the continuum and the equivalent diffusion parameters can be interpolated to capture variability of material properties within a macro-domain.

## *7.3.4 Case Studies*

### 7.3.4.1 Simple Diffusion Domain

A simple case of diffusion is selected to illustrate interface effects (Fig. 7.6). This example was investigated in detail in [65]. Diffusion through a nanochannel of width $W = 3\ \mu$m, length $L = 500$ nm and height (H) is computed. Diffusion can be considered two-dimensional (width is very large)—the same in all planes parallel to the shaded plane in Fig. 7.6b, so that a 2D rectangular domain bounded by nanochannel length and height is used in the FE model. Two diffusion domains can be distinguished in the FE model: central and interface domain. Diffusion in the central diffusion domain is not affected by the interface, therefore diffusion coefficient is represented by $D_{\text{bulk}}$ and may depend only on concentration. Interface domain spans from the wall (with zero-value of the scaling function and diffusion coefficient) to a distance where scaling functions become equal to 1 and local diffusion coefficient reaches the bulk value. A fine mesh in FE model was used in the interface domain to capture the interface effects on the diffusivity, while a coarser mesh was employed in the central domain where material properties are homogeneous. Diffusivity $D_{\text{bulk}}$ linearly changes from $1.0 \cdot 10^{-6}$ cm$^2$/s at zero concentration to $0.5 \cdot 10^{-6}$ cm$^2$/s at 1M (Fig. 7.6a). The nanochannel connects inlet and outlet reservoirs with $1 \cdot 10^{-6}$ $\mu$l volume each; initially, the inlet reservoir is filled with 1M solution, while the other reservoir has 0 M concentration. Diffusion is calculated until concentrations in both inlet and outlet reservoirs become equal (=0.5 M) (then, the diffusion gradient reaches zero value) (Fig. 7.7a).

The interface effects can be seen from results in Fig. 7.7, where diffusion through nanochannels of height 5 and 50 nm is computed. As shown in Fig. 7.4, the interface domain spans up to 2–3 nm for the case of diffusion of glucose molecule and silica surface. In case of the 5nm nanochannel, majority of channel volume is be affected by surface effect and hindered diffusion dominates over free diffusion. On the other hand, the interface effect has small influence on release through 50 nm channel, since free diffusion prevails. It is worth noting that, for a given transported molecule, interface effects could be changed by changing chemistry of channel structure, e.g., if highly charged molecular species are diffusing at the wall surface.

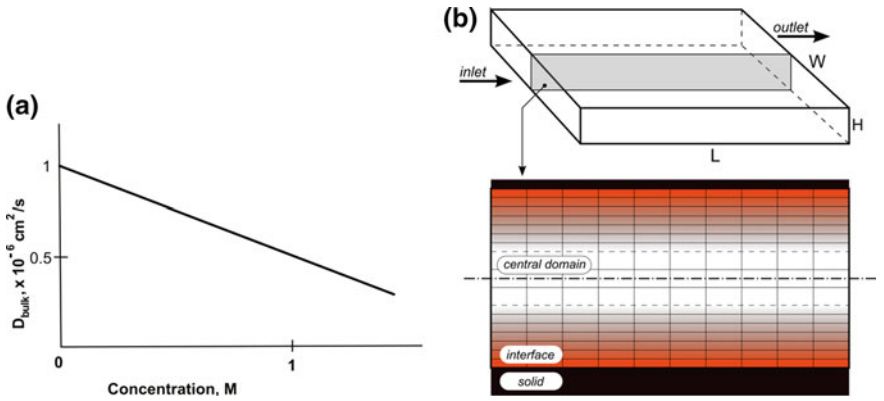


**Fig. 7.6** A simple diffusion model as studied in [65]. **a** Dependence of bulk diffusion coefficient $D_{\text{bulk}}$ on concentration; **b** *Top* the diffusion domain of nanochannel (nano-slit) with 2D conditions, where concentration gradient is developed between inlet and outlet. Nanochannel dimensions are width $W = 3\ \mu\text{m}$, length $L = 500\,\text{nm}$ and height ($H$), where $H$ is much smaller than $W$ and $L$. *Bottom* 2D Finite Element model with two diffusion domains: interface and central, with spatial distribution of diffusivity. Interface effect on diffusivity is illustrated by gradient of color; in the central domain diffusivity is equal to the bulk value

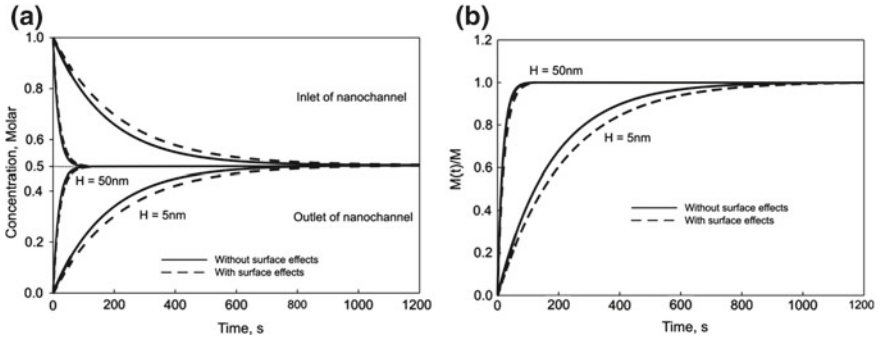


**Fig. 7.7** Diffusion from the inlet to the outlet reservoir through nanochannels of height 5 and 50 nm. **a** Concentration versus time in the *inlet* and *outlet* reservoir of equal volume; the final steady-state is reached when concentrations at the reservoirs become equal; **b** Normalized cumulative mass release *curves*; $M$ is total released mass. Diffusion kinetics is much more affected by surface interaction for nanochannel with height 5 than with 50 nm

### 7.3.4.2 Polymeric Solution

Multiscale microstructural and continuum models were applied to model diffusion through an agarose polymeric solution of Rhodamine 6G molecule that is frequently used for diffusion studies [44]. The internal structure of agarose hydrogel ($0.934 \times 0.934\ \mu\text{m}$) was adopted from [21], which was imaged by using TEM. Fibers are discretized using "Agarose Fibers" interface software developed in R&D Center for

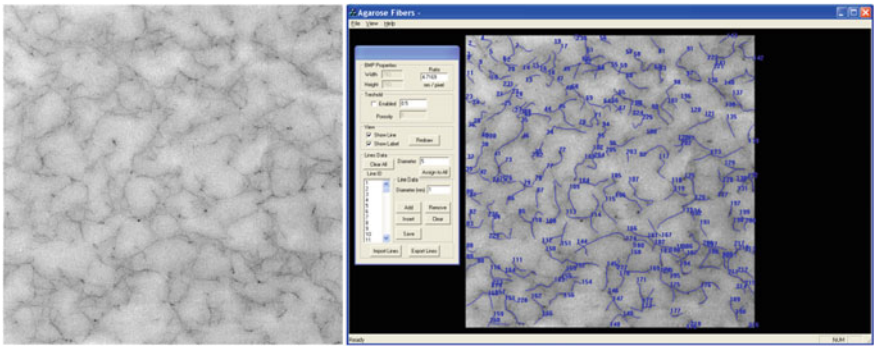


**Fig. 7.8** Internal microstructure obtained by imaging, *left panel*, according to [21]. Fiber recognition software developed at R&D Center for Bioengineering BioIRC

Bioengineering BioIRC, Kragujevac, Serbia (Fig. 7.8). The bulk diffusion coefficient is $D_{\text{bulk}} = 286\ \mu\text{m}^2/\text{s}$, while the scaling functions are calculated using MD procedure; porosity of the agarose gel is 97 %.

Mass release curves and flux (for the entire outlet cross-section) change over time are shown in Fig. 7.9 (lower right panel), for both microstructural and continuum models, considering the diffusion domain as a reference volume (RV). It can be seen that the microstructural and continuum models give the same results. In order to gain further insight into diffusion within this complex microstructure of polymer gel, we examine mass flux and concentration distributions within the RV. The upper left panel shows distribution of mass fluxes in the direction of diffusion at the end of the first time step, time $t = 0.5\,\text{s}$. The field displays variation of the flux due to agarose fibers, with zero-values within the fibers and at the fiber surfaces. Diagrams of concentration and mass flux along the coordinate axes are shown in the lower-left and upper-right panels. Continuum solutions show that concentration decreases approximately linearly along x-direction (diffusion direction), and remains constant along vertical cross-section (y-axis); flux-x is roughly constant along x-direction, and flux-y is equal to zero along vertical cross-section. On the other hand, microstructural solutions have variations, with zero-values at the points corresponding to fibers. Besides these variations occurring within microstructure, we have that the continuum model incorporates the microstructural flux fluctuations and gives the same overall mass fluxes through RV; therefore, microstructural and equivalent continuum display the same diffusion characteristics.

To validate the multiscale model we have experimentally measured R6G diffusion through a 1 and 3 % agarose hydrogel membrane. Mass release curves are calculated using the equivalent continuum model, based on the above microstructural model and the homogenization procedure. Figure 7.10 shows experimental and computational curves normalized by the maximum released mass $M_\infty$, as $M(t)/M_\infty$. Without inclusion of surface effects the release curves are practically the same for 1 and 3 %

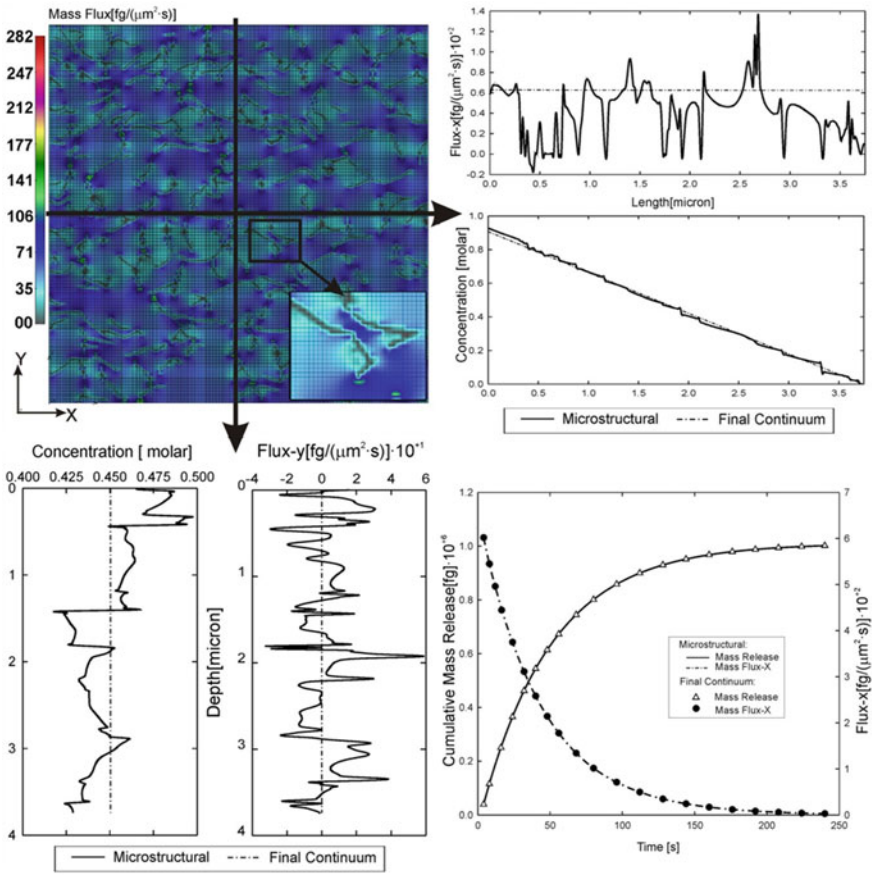


**Fig. 7.9** Diffusion within an agarose polymer gel. *Upper left panel* Mass flux-x distribution at time $t = 0.5$ s; dark domains within the field show zero-flux at fiber areas. *Upper right panel* distribution of mass flux and concentration in x-direction, microstructural (*full line*) and continuum (*dashed line*) along horizontal cross-section. *Lower left panel* distribution of mass flux and concentration in the y-direction, microstructural (*solid line*) and continuum (*dashed line*) along vertical cross-section. *Lower right panel* change of both cumulative mass release and flux-x over time for microstructural and continuum models [44]

agarose hydrogels. But slower release is found for release profiles for both 1 and 3 % agarose films.

### 7.3.4.3 Tissue

A diffusion model can be developed to analyze mass distribution around vessels. Figure 7.11 illustrates an example of doxorubicin drug extravasation around vessel

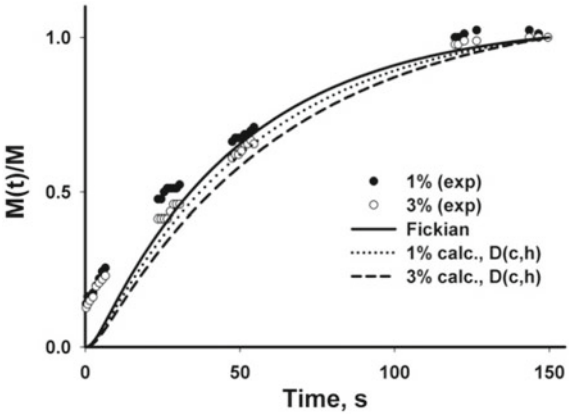


**Fig. 7.10** Comparison of Rhodamine 6G mass release through 1 and 3 % agarose hydrogel films, obtained by experiments and multiscale diffusion model. Interface effects lead to differences in release kinetics in 1 and 3 % agarose gels. Notation in the figure: Fickian—without surface effects, D(c,h)—with surface effects, exp—experimental results

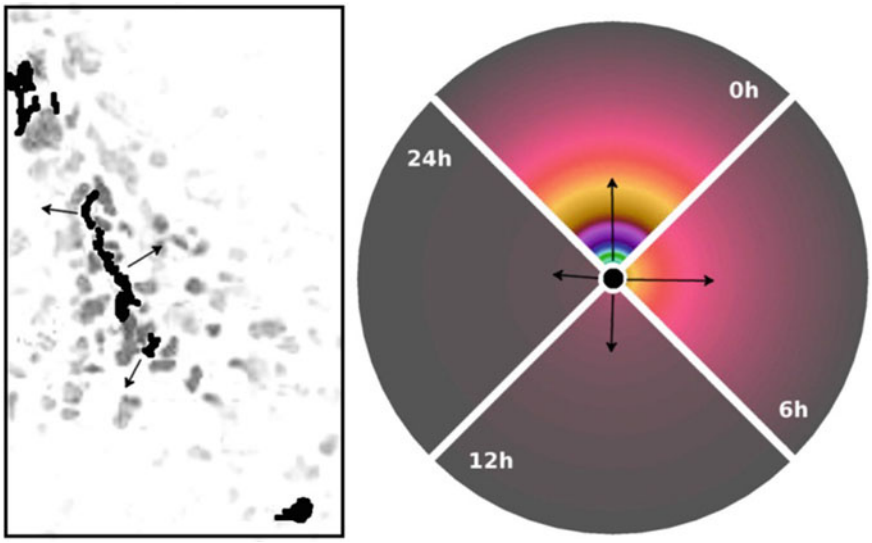


**Fig. 7.11** Calculated drug concentration field around blood vessel. *Left* concentration field of doxorubicin (*grey*) around vessel (*black*) in 4T1 tumor from tissue imaging. *Right* Calculated concentration distribution within vessel wall (diameter of capillary is 10 μm) at four different time points. The *arrows* show the direction of diffusion, where the experimentally determined doxorubicin field spans up to 50–100 μm on average from the vessel

in 4T1 tumor tissues at 24 h after drug injection. The simplified model can incorporate a vessel lumen as a source of drug concentration, the vessel wall, and the surrounding cellular media. Here, we only consider diffusion through vessel wall which was modeled by a collagen sleeve in the basal membrane of vessel. By using different phenomenological diffusion coefficients for pure doxorubicin and doxorubicin in liposomal formulations, differences in extravasation kinetics can be evaluated.

In our example, we have used the experimental concentration profiles in plasma similar to data from Ref. [33]. The results presented in Fig. 7.11 show that liposomal formulation can potentially develop more sustainable gradients of the drug because of reduced diffusivity, while pure drug as small molecule can be washed away fast from media surrounding vessel lumen.

## 7.4 Flow and Diffusion

Here, we summarize the basic equations for coupled convective-diffusion transport in differential and FE formulations and then give solutions for typical problems of transport in biological media.

### *7.4.1 Fundamentals and Computational Methodology*

The above listed basic equations for convective and diffusion mass transport are now coupled. It is assumed that diffusion occurs within flowing fluid and within transported solids. Also, it is considered that concentration of diffusing particles/molecules (solute) does not affect the fluid flow. Under these conditions, the fundamental equations for diffusion within moving solid remain the same, while the mass balance equation for the solute within fluid must be modified to account for the convection. The mass balance Eq. (7.8) for diffusion within fluid now becomes:

$$-\frac{\partial c}{\partial t}-\frac{\partial c}{\partial x_j}v_j+\frac{\partial}{\partial x_i}\left(D_{ij}\frac{\partial c}{\partial x_j}\right)+q^V=0 \qquad \text{sum on } j:\ j=1,2,3 \tag{7.25}$$

where $\left(\partial c/\partial x_j\right)v_j$ represents the convective term, with the fluid velocity $v_j$.

These equations can be transformed into the FE format so that the system of Eqs. (7.3) and (7.25) can be written in a form:

$$\begin{bmatrix}\mathbf{K}^{vv} & \mathbf{0}\\ \mathbf{K}^{cv} & \mathbf{K}^{cc}\end{bmatrix}\begin{bmatrix}\Delta\bar{\mathbf{V}}\\ \Delta\mathbf{C}\end{bmatrix}=\begin{bmatrix}\mathbf{F}^{v}\\ \mathbf{F}^{c}\end{bmatrix} \tag{7.26}$$

where $\mathbf{K}^{vv}$, $\mathbf{K}^{cv}$ and $\mathbf{K}^{cc}$ are the equivalent convective-diffusion matrices, and $\mathbf{F}^{v}$ and $\mathbf{F}^{c}$ are the unbalanced force nodal vectors; in increments $\Delta\bar{\mathbf{V}}$ are included fluid velocities and pressures. Of course, in case of motion of solids with diffusion within the solids, Eqs. (7.7) and (7.20) for the solid must be added to the system (7.26).

Boundary conditions for the solid and fluid domain are imposed in a standard manner [6, 36]. As we use the remeshing procedure, it is taken (in general) that concentration at the common nodes at the solid-fluid boundary nodes are the same. However, the boundary of two materials may lead to different partitioning of molecules based on physicochemical similarity of molecules to both material phases, which is characterized by partition coefficient $P$. Frequently logP is used to characterize

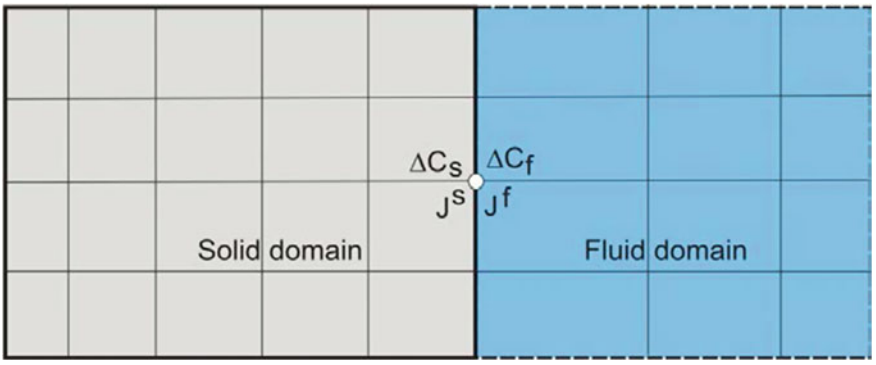


**Fig. 7.12** The partitioning of molecules between solid and fluid domain as used in the implementation of molecular hydrophobicity; $J^f$ and $J^s$ are fluid and solid FE nodes at the same spatial position, and $\Delta C_f$ and $\Delta C_s$ are increments of concentration in fluid and solid

molecules by measuring the partitioning between water and octanol phases. In other words, it describes hydrophobicity of molecules: e.g., the more positive logP, the more hydrophobic the molecule. The simplest way to include this phenomenon in our diffusion models is to take that, within a time step, the ratio between number of molecules passing the boundary between solid and fluid is a constant $P$:

$$\Delta N_s / \Delta N_f = P \tag{7.27}$$

where $\Delta N_s$ and $\Delta N_f$ are the numbers at the solid and fluid side of the boundary. For convenience, we use the inverse value

$$p = 1/P \tag{7.28}$$

Implementation of this condition is as follows. Instead of the ratio of number of molecules we can use increments of concentration at the common point,

$$\Delta C_f = p \Delta C_s, \quad C_f = p C_s \tag{7.29}$$

Graphical illustration of these relations is shown in Fig. 7.12. From these relations follow the corresponding corrections in the FE balance equations. The corrections are included into our solvers [35] and the effects of hydrophobicity are illustrated in the selected applications.

### *7.4.2 Transport of Drugs in Capillaries and in Tumor Tissue*

By coupling diffusion and convective transports one can study systems like drug release and distribution around capillaries and surrounding environment. Figure 7.13

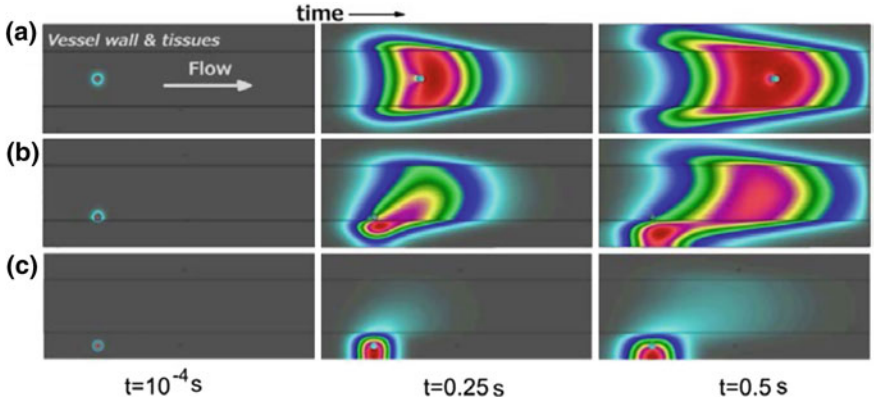


**Fig. 7.13** Diffusion of drug from a microparticle to flowing fluid in capillary and surrounding tissue. Data: dimensions of capillary $10 \times 50$ μm, tissue wall thickness 5 μm, entering fluid velocity 50 μm/s, initial concentration is equal to zero except within the particle $C_0 = 1$M; fluid density $\rho_f = 1 \times 10^{-6}$μgr/μm$^3$, viscosity $\mu = 10^{-3}$ Pas, diffusion coefficient $D_f = 100$ μm$^2$/s; particle density $\rho_s = 1 \times 10^{-6}$ μgr/μm$^3$, diffusion coefficient $D_s = 10$ μm$^2$/s. Concentration field at times: $t = 10^{-4}$, 0.25, 0.5 s is shown for cases: **a** particle is carried by fluid, **b** particle is attached to the wall, and **c** particle is internalized into vessel wall

shows the capillary model of $10 \times 50$ μm dimensions and 50 μm/s flow, surrounded by 5 μm of tissue or vessel wall, and a microparticle serving as drug source. In the FE model, transport properties of individual materials may be derived using multi-scale approach as described in Sect. 7.3.3; that is applicable to any drug vector. We have selected material parameters as given in caption of Fig. 7.13. Figure 7.13 shows concentration field at time $t = 1$ s and illustrates payload release form microparticle for three different initial locations: Fig. 7.13a the middle of the capillary, with the particle transported by liquid phase; Fig. 7.13b at the surface of capillary wall, attached as it would be in case of adsorbtion, and Fig. 7.13c internalized into vessel wall by means of active biological transport. In the last two cases the microparticle is not moving. The case Fig. 7.13a shows that concentration field is traveling with microparticle itself, while in other two cases the concentration field expands over time within tissue and fluid, and is carried away or smeared by flow. The case of internalized particle shows that the majority of payload released from microparticle is caught in tissues and is slowly washed out by adjacent flow in the capillary.

Figure 7.14 displays payload (drug) released into bottom vessel wall under various conditions. Accumulated mass over time for three particle positions (a, b, c in Fig. 7.13 is shown in Fig. 7.14a. It can be noticed that the largest amount of payload found in vessel wall is in case of internalized particle, but gets depleted over time by the flow. Since hydrophobicity of molecules may be an important factor for release kinetics, we show in Fig. 7.14b the effects of hydrophobicity by implementing partitioning of payload between microparticle and fluid phase as described above. It is assumed that the particle is attached to the wall (case b). Four cases are

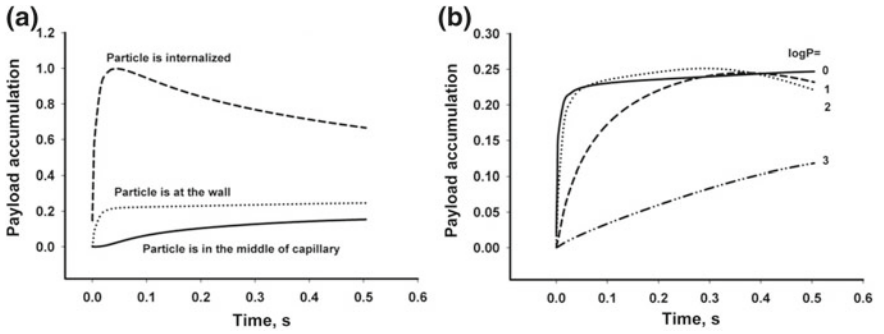


**Fig. 7.14** The normalized (with respect to the total mass in microparticle at $t = 0$) payload accumulation into the *bottom* wall. Data are as in Fig. 7.13. **a** Three different particle location in capillary model (a, b, c, see Fig. 7.13); **b** Four values of partitioning between solid and fluid phases (logP) when the particle is at the wall

considered, with $\log P = 0, 1, 2$, and 3, revealing that most hydrophobic payload is released substantially slower than hydrophilic compounds. Therefore, in situations where payload is hydrophobic, inclusion of partitioning in the computational model maybe as important as accounting for interface effects.

## 7.5 Summary and Expected Results in Near Future

This chapter presents a review of computational procedures developed by the authors. We offer a computational framework for modeling convective-diffusive mass transport with the emphasis on biomedical applications. This framework is based on our own experience gained over a number of years and effort to develop a robust and accurate computational scheme. Our methodology relies on the idea of coupling the basic physico-chemical processes occurring on the small—molecular scale with the outcome measured on the large—macro (continuum) scale. These multiscale methods of transport are efficient since they only employ MD calculations for evaluation of the constitutive parameters for the larger scale, where the macro domains are modeled by a robust, efficient and reliable numerical FE method.

Regarding the computational methodology, a number of issues remain challenging. For example, handling enormous systems—measured in millions of equations—in an efficient way has to be improved, as well as interpretation of the results. Generation of computational models, which assumes creation of 3D FE mesh from imaging (3D reconstruction), requires significant effort; this is particularly important in medical applications.

We believe that novel computational tools will support advances in in-vitro and in-vivo experiments in bioengineering and medicine, and in other fields, such as optimal design of complex materials. The main benefit of using these computational

models is that they provide insight into the physics of the fundamental processes and replace the traditional phenomenological models obtained by fitting of parameters through experimental or clinical investigations. Therefore, these models offer a bridge between the events on the smallest scale and the larger measurable macroscale. We mention that, for example, new materials or devices with desired features rely on certain physics which can be captured by the introduced multiscale computational models. We anticipate a stronger and seamless multiscale method integration with imaging for creation of novel and robust computational tools in medicine or material characterization.

**Acknowledgments** This work has been partially supported with the Methodist Research Institute, by the grants OI 174028 and III 41007 of the Serbian Ministry of Education and Science, and City of Kragujevac - Serbia. Authors also acknowledge partial supports from the following funding sources: the Ernest Cockrell Jr. Distinguished Endowed Chair (M.F.), US Department of Defense (W81XWH-09-1-0212) (M.F.), National Institute of Health (U54CA143837, U54CA151668) (M.F.).

## References

1. Adriani G, Tullio MD, Ferrari M, Hussain F, Pascazio G, Liu X, Decuzzi P (2012) The preferential targeting of the diseased microvasculature by disk-like particles. Biomaterials 33: 5504–5513.
2. Alber F, Dokudovskaya S, Veenhoff LM, Zhang W, Kipper J, Devos D, Suprapto A, Karni-Schmidt O, Williams R, Chait BT (2007) Determining the architectures of macromolecular assemblies. Nature 450: 683–694.
3. Alber F, Dokudovskaya S, Veenhoff LM, Zhang W, Kipper J, Devos D, Suprapto A, Karni-Schmidt O, Williams R, Chait BT (2007) Determining the architectures of macromolecular assemblies. Nature 450 (7170): 683–694.
4. Allen MP, Tildesley DJ (1989). Computer simulation of liquids, Oxford university press.
5. Alpert S, Banks G (1976) The concentration dependence of the hemoglobin mutual diffusion coefficient. Biophys. Chem. 4(3): 287–296.
6. Bathe KJ (1996). Finite Element Procedures. Englewood Cliffs, N.J., Prentice-Hall, Inc..
7. Boutin C, Geindreau C (2010) Periodic homogenization and consistent estimates of transport parameters through sphere and polyhedron packings in the whole porosity range Phys. Review E 82( ): 036311–036318.
8. Boving TB, Grathwohl P (2001) Tracer diffusion coefficients in sedimentary rocks: correlation to porosity and hydraulic conductivity. J. Contam. Hydrol. 53 (1–2): 85–100.
9. Carlo DD, Irimia D, Tompkins RG, Toner M (2007) Continuous inertial focusing, ordering, and separation of particles in microchannels. PNAS 104 (48): 18892–18897.
10. Chu-Cruz ER, Aksimentiev A, Schulten K (2006) Water silica force field for simulating nanodevices. J. Phys. Chem. B 110(43): 21497–21508.
11. Desai TA, Hansford DJ, Kulinsky L, Nashat AH, Rasi G, Tu J, Wang Y, Zhang M, Ferrari M (1999) Nanopore technology for biomedical applications. Biomed. Microdev. 2(1): 11–40.
12. English A, Dole M (1950) Diffusion of sucrose in supersaturated solutions. J. Am. Chem. Soc. 72(7): 3261–3267.
13. Fine D, Grattoni A, Hosali S, Ziemys A, Rosa ED, Gill J, Medema R, Hudson L, Kojic M, Milosevic M, Ferrari M (2010) A robust nanofluidic membrane with tunable zero-order release for implantable dose specific drug delivery. Lab Chip DOI: 10.1039/c0lc00013b.
14. Forster P, Cheetham A (2003) Hybrid Inorganic-Organic Solids: An Emerging Class of Nanoporous Catalysts. Top. Catal. 24(1): 79–86.

15. Freeman B (1985) The motion of rigid ellipsoidal particcles in slow flows. Tecfonophysics 113: 163–183.
16. Frenkel D, Smit B (2001). Understanding molecular simulation: from algorithms to applications, Access Online via Elsevier.
17. Gladden JK, Dole M (1953) Diffusion in supersaturated solution II: glucose solutions. J. Am. Chem. Soc. 75: 3900–3904.
18. Glowinski R, Pan TW, Hesla TI, Joseph DD, Periaux J (2001) A fictitious domain approach to the direct numerical simulation of incompressible viscous flow past moving rigid bodies: application to particulate flow. J. Comput. Physics 169: 363–426.
19. Goano CD, Minev PD, Nandakumar K (2003) A fictitious domain/finite element method for particulate flows. J. Comput. Physics 192: 105–123.
20. Grattoni A, Shen H, Fine D, Ziemys A, Gill J, Hudson L, Hosali S, Goodall R, Liu X, Ferrari M (2011) Nanochannel Technology for Constant Delivery of Chemotherapeutics: Beyond Metronomic Administration. Pharm. Res. 28(2): 292–300.
21. Griess GA, Guiseley KB, Serwer P (1993) The relationship of agarose gel structure to the sieving of spheres during agarose gel electrophoresis. Biophys. J. 65(1): 138–148.
22. H. Cao ZY, J. Wang, J. Tegenfeldt, R. Austin, E. Chen, W. Wu, S. Chou (2002) Fabrication of 10 nm enclosed nanofluidic channels. Appl. Phys. Lett. 81.
23. H. Gardeniers AB (2004) Micro-and nanofluidic devices for environmental and biomedical applications. Int. J. Envir. Analyt. Chemistry 84(11): 809–819.
24. Han J, Fu J, Schoch R (2008) Molecular sieving using nanofilters: past, present and future. Lab Chip 8(1): 23.
25. Hashin Z (1968) Assessment of the self consistent scheme approximation: conductivity of particulate composites. J. Composite Materials 2: 284–300.
26. Hosoda M, Sakai K, Takagi K (1998) Measurement of anisotropic Brownian motion near an interface by evanescent light-scattering spectroscopy. Phys. Rev. E 58(5): 6275–6280.
27. Hu HH, Joseph DD, Crochet MJ (1992) Direct simulation of fluid particle motions. Theoret. Comput. Fluid Dynamics 3: 285–306.
28. Hu HH, Patankar NA, Zhu MY (2001) Direct numerical simulations of fluid-solid systems using the arbitrary Lagrangian-Eulerian technique. J. Comput. Physics 169: 427–462.
29. Isailovic V (2012). Numerical modeling of motion of cells, micro- and nano- particles in blood vessels. Information Tchnology. Belgrade, Metropolitan University. Ph. D.
30. Israelachvili J, Wennerström H (1996) Role of hydration and water structure in biological and colloidal interactions. Nature 379: 219–225.
31. Jayageeth C, Sharma VI, Singh A (2009) Dynamics of short fiber suspensions in bounded shear flow. Int. J. Multiphase Flow 35: 261–269.
32. Jorgensen WL, al. e (1983) Comparison of simple potential functions for simulating liquid water. J. Chem. Physics 79(2): 926–935.
33. Junping W, Maitani Y, Takayama K, Nagai T (2000) In vivo evaluation of doxorubicin carried with long circulating and remote loading proliposome. Int. J. Pharm. 203(1): 61–69.
34. Kojic M, Bathe KJ (2005). Inelastic Analysis of Solids and Structures. Heildelberg - Berlin, Springer-Verlag.
35. Kojic M, Filipovic N, Slavkovic R, Zivkovic M, Grujovic N (1998, 2009). PAK-FS - Finite Element Program for Fluid Flow and Fluid-Solid Interaction Kragujevac, Serbia, University of Kragujevac and R&D Center for Bioengineering, Kragujevac, Serbia.
36. Kojic M, Filipovic N, Stojanovic B, Kojic N (2008). Computer Modeling in Bioengineering - Theoretical Background, Examples and Software. Chichester, England, John Wiley and Sons.
37. Kojic M, Isailovic V, Filipovic N, Kojic N, Savovic S, Petrovic D, Ziemys A, Ferrari M (2013) A numerical study of motion of circular and elliptical micro- and nano-particles in microchannels. Microfluidcs and Nanofluidics (under review).
38. Kojic M, Milosevic M, Kojic N, Ferrari M, Ziemys A (2011) On diffusion in nanospace. J. Serbian Soc. Comp. Mechanics 5(1): 84–109.
39. Kojic M, Milosevic M, Kojic N, Kim K, Ferrari M, Ziemys A (2013) A multiscale MD-FE model of diffusion in composite media with internal surface interaction based on numerical homogenization procedure. Comp. Meth. Appl. Mech. Engrg. (under review).

40. Kojic M, Ziemys A, Milosevic M, Isailovic V, Kojic N, Rosic M, Filipovic N, Ferrari M (2011) Transport in biological systems. J. Serbian Soc. Comp. Mechanics, Vol. 5 (2): 101–128.
41. MacKerell A, al. e (1998) All-atom empirical potential for molecular modeling and dynamics studies of proteins. J. Phys. Chem. B 102(18): 3586–3616.
42. Mahadevan T, Kojic M, Ferrari M, Ziemys A (2013) Mechanisms of Reduced Solute Diffusivity at Nanoconfined Solid-Liquid Interface. Chem. Phys.
43. Milosevic M (2012). Numerical Modeling of Diffusion within Composite Media. Faculty of Tchnical Sciences. Kragujevac, University of Kragujevac, Serbia. Ph. D.
44. Milosevic M, Kojic M, Kojic N, Ferrari M, Ziemys A (2013). Multiscale modeling of molecular diffusion in tissue. SEECCM III - 3rd South-East European Conference on Computational Mechanics - an ECCOMAS and IACM Special Interest Conference, Kos Island, Greece, ECCOMAS and IACM.
45. Nott PR, Brady JF (1994) Pressure-driven flow of suspensions : simulation and theory. J. Fluid Mech. 275: 157–199.
46. Palma R, Himmel ME, Liang G, Brady JW (2001). Glycosyl Hydrolases in Biomass Conversion. ACS Symp Series. Himmel ME, Americal Chemical Society. 769 : 112–130.
47. Parida SK, Dash S, Patel S, Mishra B (2006) Adsorption of organic molecules on silica surface. Adv. Colloid Interface Sci. 121(1–3): 77–110.
48. Phillips JC, al. e (2005) Scalable molecular dynamics with NAMD. J. Comput. Chem. 26(16): 1781–1802.
49. Pozrikidis C (2006) Flipping of an adherent blood platelet over a substrate. J. Fluid Mech. 568: 161–172.
50. Pozrikidis C (2006) Interception of two spheroidal particles in shear flow. J. Non-Newtonian Fluid Mech. 136: 50–63.
51. Qiu Y, Park K (2001) Environment-sensitive hydrogels for drug delivery. Adv. Drug Delivery. Rev. 53(3): 321–339.
52. Singh A, Nott PR (2000) Normal stresses and microstructure in bounded sheared suspensions via Stokesian Dynamics simulations. J. Fluid Mech. 412: 279–301.
53. Singh P, Hesla TI, Joseph DD (2003) Distributed Lagrange multiplier method for particulate flows with collisions. Int. J. Multiphase Flow 29: 495–509.
54. Stott LS, Toner M (2010) Isolation of circulating tumor cells using a microvortex - generating herringbone-chip. PNAS 107(43): 18392–18397.
55. Thomas J, Raja R (2001) Nanopore and nanoparticle catalysts. The Chemical Record 1(6): 448–466.
56. Topgaard D, Söderman O (2001) Diffusion of water absorbed in cellulose fibers studied with 1H-NMR. Langmuir 17(9): 2694–2702.
57. Vanommeslaeghe K, Hatcher E, Acharya C, Kundu S, Zhong S, Shim J, Darian E, Guvench O, Lopes P, Vorobyov I (2010) CHARMM general force field: A force field for drug-like molecules compatible with the CHARMM all-atom additive biological force fields. J. Comput. Chem. 31(4): 671–690.
58. Zhang H, Selim HM (2011) Second-order modeling of arsenite transport in soils. J. Contam. Hydrol. 126 121–129.
59. Zhang L, Gerstenberger A, Wang X, Liu WK (2004) Immersed finite element method. Comput. Methods Appl. Mech. Engrg. 193: 2051–2067.
60. Zhou J, Papautsky I (2013) Fundamentals of inertial focusing in microchannels. Lab Chip 13: 1121–1132.
61. Ziemys A, al. e (2010) Confinement effects on monosaccharide transport in nanochannels. The Journal of Physical Chemisstry B: 132–137.
62. Ziemys A, Ferrari M, Cavasotto CN (2009) Molecular modeling of glucose diffusivity in silica nanochannels. Journal of Nanoscience and Nanotechnology 9: 6349–6359.
63. Ziemys A, Grattoni A, Fine D, Hussain F, Ferrari M (2010) Confinement Effects on Monosaccharide Transport in Nanochannels. The Journal of Physical Chemistry B 114(34): 11117–11126.

64. Ziemys A, Kojic M, Milosevic M, Ferrari M (2012) Interfacial effects on nanoconfined diffusive mass transport regimes. Phys. Rev. Lett. 108(23): 5.
65. Ziemys A, Kojic M, Milosevic M, Kojic N, Hussain F, Ferrari M, Grattoni A (2011) Hierarchical modeling of diffusive transport through nanochannels by coupling molecular dynamics with finite element method. J. Comput. Phys. 230(14): 5722–5731.

# Part III
# Multiscale Modeling Around the Organ Level

# Chapter 8
# Tendons and Ligaments: Current State and Future Directions

**Shawn P. Reese and Jeffrey A. Weiss**

## 8.1 Background

### *8.1.1 Introduction*

Tendons and ligament are soft connective tissues that transmit load and support movement and joint articulation within the musculoskeletal system. The primary load-bearing constituent of these tissues is type I collagen, which self-assembles into a complex arrangement of fibrils, fibers, and fascicles via the process of fibrillogenesis [1–3]. Fibrillogenesis is mediated by populations of fibroblasts, which are the dominant cell type within these tissues. Fibroblasts detect the microscale strain environment within the tissue, and this mechanotransduction process guides the process of adaption, healing, and remodeling [4–7]. Fibroblasts also respond to various chemical factors (growth factors, inflammatory cytokines, etc.), which also guide these processes [8, 9].

The normal function of these tissues requires a complex interplay between macroscopic and microscopic mechanical requirements. At the macroscopic level, these connective tissues must withstand substantial impact and loading forces. As such, they must simultaneously be able to absorb energy and maintain a high static tensile strength. At the microscopic level, they must maintain an environment conducive to cellular homeostasis and tissue remodeling. Concurrent with these demands is the need to facilitate nutrient transport through both active (i.e., vasculature) and passive (i.e., diffusion) mechanisms. To meet these demands, tendons and ligaments have evolved a complex organization of collagen and other tissue constituents that spans numerous physical scales, including the nanometer scale of individual tropocollagen monomers and self-assembled fibrils, the micrometer scale of collagen fibers

S.P. Reese
Department of Bioengineering, Scientific Computing and Imaging Institute,
Salt Lake City, UT, USA

J.A. Weiss (✉)
Department of Orthopaedics and School of Computing, University of Utah,
Salt Lake City, UT, USA
e-mail: jeff.weiss@utah.edu



S. De et al. (eds.), *Multiscale Modeling in Biomechanics and Mechanobiology*, DOI 10.1007/978-1-4471-6599-6_8

and fibroblast and the millimeter scale of collagen fascicles and bundles [10, 11]. Numerous organizational motifs exist at these scales, including bundled fibrils, crimped fibers, and sliding fascicles. From this perspective, tendons and ligaments can be viewed as "smart materials" with a complex multiscale organization, highly adapted to simultaneously meeting the opposing demands of macroscopic mechanical integrity and microscopic cellular function and nutrient transport.

The normal multiscale function of connective tissues is of central importance to the etiology and healing of injured and diseased tissues. This information will be essential in developing new methods and techniques for treatment. A range of pathologies can affect tendons and ligaments, including genetic diseases, degenerative diseases, chronic overuse injuries, and traumatic injuries. Genetic diseases such as Ehlers-Danlos syndrome result in altered collagen fibril formation which, through as of yet unknown mechanisms, results in weakened connective tissues [12, 13]. Degenerative disorders such as tendinosis arise from a complex interplay of collagen damage and cellular, vascular, and neurological alterations [14–18]. Chronic overuse injuries such as jumper's knee arise from an imbalance in the accrual of microdamage and tendon repair [19]. Traumatic tendon and ligament injury (tears and ruptures) are sometimes a result of previous damage accumulation or tendon disease and abnormal joint loading resulting from physiological abnormalities [20, 21].

Although we are still in the early stages of understanding the normal and diseased behavior of these tissues, the highly coupled, multiphysics nature of their function suggests that mathematical modeling will play a crucial role. Principles of continuum mechanics can be applied to the study of force transmission across scale and between cells and their substrates [22]. Principles of chemistry and thermodynamics can be applied to the study of nutrient transport and fibrillogenesis [23]. Linking of these two modeling types can yield insights into the interactions between physical structure and biological function. To date, the mechanical modeling of tissue structures has been the primary focus of the study. As such, this will be the primary focus of this chapter. In particular, emphasis will be placed on modeling strategies that describe interactions between physical scales. Although considerable work has been done regarding one-dimensional continuum based approaches, focus will be placed on two- and three-dimensional approaches that discretize the spatial domain of interest. To set the stage, an in-depth discussion of the macroscale function, microstructural organization, and biological function of tendons and ligaments is presented. This will be followed by a detailed description of some of the prominent challenges that researchers either currently or will soon face when implementing multiscale models of tendon and ligament. Given this basis, current and proposed methods for multiscale modeling (with an emphasis on mechanical modeling) will be presented, as well as a number of results of such methods from the literature. The chapter will close with a discussion of the many significant open questions and challenges that remain to be addressed by future research.

### 8.1.2 Ligament Function

Ligaments are soft, fibrous tissues that connect bone to bone at the joints. They help to guide and limit the motion of the bones, so that the joint articulates with no separation or only a limited separation of the bones. Ligaments are passive stabilizers and work in conjunction with other passive stabilizers, including the articulating surfaces of the bones and, in most diarthrodial joints (major joints—knee, hip, and shoulder), other soft tissues such as the meniscus in the knee and the labrum in the shoulder and hip. In diarthrodial joints, ligaments are primarily banded or cordlike. For instance, the medial collateral ligament (MCL) of the knee is a banded ligament, while the anterior cruciate ligament (ACL) is a cordlike ligament. These knee ligaments resist motion along a single line of action and transmit tensile load, but also experience shear, transverse, and compressive loads [24–37]. The ligaments in the shoulder and hip form thin, dense bands of tissue around the joint capsule and are known as capsular ligaments. The inferior glenohumeral ligament (IGHL), for example, is a capsular ligament in the shoulder. While it can be argued that capsular ligaments resist motion primarily in one direction, they are thought to constrain more complex motions than knee ligaments through their connection with the rest of the capsule [38–45].

Although ligaments are considered passive stabilizers, there are stresses in the tissue when the joint is in a neutral position [46]. These in situ stresses are responsible for the stability of the joint when muscle forces are not acting across the joint. Due to the difficulty in measuring in situ stresses, in situ strains are usually measured [32, 47]. Ligament in situ strains are inhomogeneous, subject-specific, and vary depending on joint position [32, 47]. Previous research has shown that ligament in situ strains must be taken into account in order to accurately measure or predict ligament strains and stresses due to external loading [32].

Ligaments attach to bone at insertion sites. There are two types of insertion sites: direct and indirect insertions. Direct insertion sites occur over a distance of less than 1 mm [37], and consist of a distinct right-angle boundary where deep collagen fibrils extend out of the ground substance matrix and become fibrocartilage tissue, mineralized fibrocartilage tissue and then bone [48]. Indirect insertion sites occur over a larger area where superficial collagen fibrils gradually blend into the periosteum at more acute angles. Deep collagen fibrils also make attachments at indirect insertion sites, but the connections are fewer than at direct insertion sites, occur at more acute angles and without the fibrocartilagenous transitional zone observed in direct insertions [49].

### 8.1.3 Tendon Function

Tendons connect muscles to bones and transmit the forces generated by the muscles to the bones. Tendons generally stretch more than ligaments during use, with some tendons being very efficient at storing and recovering energy [50–59]. These elastic properties allow tendons to passively modulate forces during locomotion, providing

additional stability with no active work [53, 55, 56, 60]. The length of a tendon significantly contributes to these characteristics. Shorter tendons allow for more muscle mass [61, 62], but longer tendons provide more elastic recovery of stored energy [53, 55, 58, 59, 63–66]. The primary function of positional tendons like the rotator cuff, finger tendons, and animal extensor tendons is to transfer load generated by their associated muscles [50, 62, 66–71]. In contrast, tendons like the Achilles tendon and animal flexor tendons store substantial amounts of energy and are thought to act like biological springs [53, 55, 58, 59, 63–66]. Structure and composition vary between different tendons and between different locations within individual tendons [10, 69, 72]. Similar to ligaments, tendons connect to bones with either direct or indirect insertion sites. These attachments are complex, are often the site of injury and as such are an area of extensive continued research [57, 73–83].

### *8.1.4 Hierarchical Structure of Tendon and Ligament*

Tendons and ligaments are multiphase biological composites. The extracellular matrix (ECM) is composed of a fluid phase and a solid phase. The solid phase consists primarily of type I collagen, which is organized into a complex hierarchy-where tropocollagen monomers form fibrils at the nanoscale, fibrils form fibers at the microscale, fibers form fascicles at the mesoscale and fascicles form the whole tendon or ligament at the macroscale (Fig. 8.1).

The ECM of ligaments and tendons is formed by self-assembly of cell-secreted proteins and consists of approximately 70 % water [69]. The solid phase of these tissues is primarily composed of type I collagen (60–80 %), with the remainder consisting of elastin, proteoglycans and glycosaminoglycans (GAGs), other types of

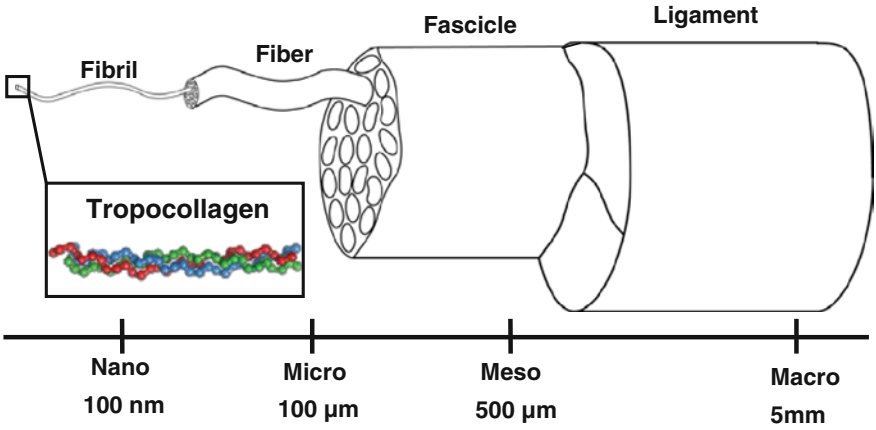


**Fig. 8.1** Hierarchical organization of ligament from the molecular level to the macroscopic organ level

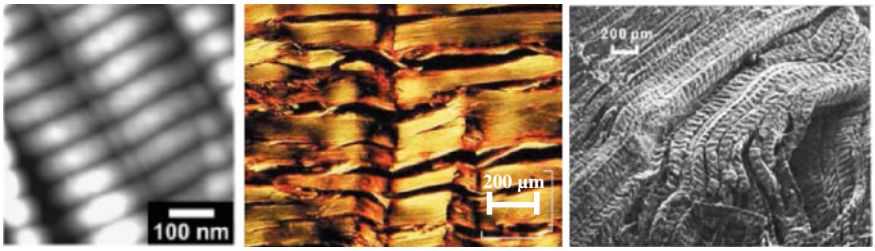


**Fig. 8.2** Unique structural motifs exist at multiple scale level. At the nanoscale, 67 nm d-banding is observed (*Left*), at the microscale, fiber crimp is present (*Middle*), and at the macroscale, fascicles align in a parallel fashion (*Right*). Note that crimp is generally in register within fascicles. (reproduced with permission from [85, 90, 112])

collagen (types III, IV, V, VI), fibrillin, and other proteins [6, 10, 84]. Type I collagen exhibits different organizational motifs at each scale (Figs. 8.1 and 8.2) [10]. At the *nanoscale*, tropocollagen monomers are assembled to form **fibrils** (50–200 nm dia.), which display a characteristic d-banding period (67 nm) [10, 85–87]. Tropocollagen monomers are held together by a combination of hydrogen, ionic, and covalent bonds [6, 84]. Fibrils are spaced regularly within healthy tissue and predominantly aligned in parallel [3, 88, 89]. At the *microscale*, fibrils are assembled into **fibers** (20–50 μm dia.) [90, 91]. Fibroblasts and tenocytes (a specialized type of fibroblast) (10 μm width × 60 μm length) are located in the interfiber space [10, 84]. Fibroblasts are responsible for regulating the ECM in response to loading and injury, and mechanotransduction plays a major role in their function [92]. The characteristic crimp pattern is visible at the fiber level, with a period of 50–200 μm [91, 93]. Fibers are arranged in a largely parallel fashion [10]. At the *mesoscale*, fibers are assembled into **fascicles** (100–500 μm dia) [6, 10, 90]. To at least some extent, crimp is registered between fibers [11, 94]. Fascicles are organized in parallel [95]. Fascicles and fibers are surrounded by a thin fascia (referred to as endotenon or interfascicular matrix) [10, 67, 96, 97]. At the *macroscale*, groups of fascicles are organized into functional bands (100 μm–1 mm dia) [90].

Noncollagenous ECM constituents include proteoglycans (PGs) such as decorin (~1 %/wt), biglycan (~0.5 %/wt) and others (fibromodulin, lumican, aggrecan, versican), fibrillin [1, 84, 98–102], and elastin (1–2 %/wt) [10, 84, 96, 103]. The large PGs (e.g., aggrecan) contribute to the apparent viscoelastic material behavior of these tissues by controlling water content and flux [98]. The mechanical role of small PGs (decorin, biglycan) is debated [104, 105], but our own research demonstrated that their GAG side chains have a negligible contribution to tissue-level mechanics in ligament [100, 102, 106, 107]. Elastin and fibrillin are thought to contribute to the toe region of the stress–strain curve in ligament and tendon [108–111].

Structurally, ligaments and tendons share the same hierarchical organization and structural motifs. However, there are significant differences in fibril diameter distributions, fiber diameter and crimp morphologies, metabolic activity, and the relative percentage of certain components, such as water, PGs, and types I and III collagen [10, 84, 113, 114].

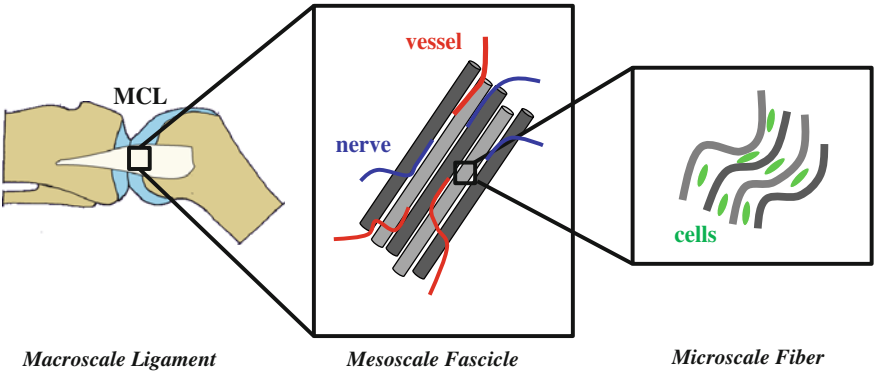


**Fig. 8.3** Multiscale force transmission. Force transmission within a macroscale tissue structure (e.g., an MCL, shown on the *left*) is mediated at the mesoscale by fascicles (*Center*) and at the microscale by fibers (*Right*)

### *8.1.5 Force Transfer Within Tendons and Ligaments*

The mechanical behavior of tendons and ligaments has both a time-independent (or equilibrium) response and a time-dependent (or viscoelastic) response. The equilibrium elastic response is experimentally measured using slow strain rates or stress relaxation and creep testing, whereby step displacements or loading are applied and equilibrium values are obtained [102]. The elastic response arises primarily from stretching and interactions of the solid phase components. However, the level of hydration also modulates equilibrium elastic response [115]. The viscoelastic response is experimentally measured by performing mechanical testing at varied strain rates, stress relaxation testing, creep testing, and harmonic testing [100, 116–118]. The viscoelastic response is attributed to both fluid flow-dependent and fluid flow-independent effects. Flow-independent effects refer to an intrinsic viscoelasticity of the solid phase (e.g., a viscous sliding of fibrils), while flow-dependent effects refer to the pressure driven transport of free water through a permeable tissue (e.g., described using biphasic theory, discussed in Sect. 3.3) [34, 119–122].

Force transfer at the macroscale (e.g., between the two insertion points of a ligament) is mediated by a number of complex and poorly understood mechanisms that span numerous physical scales. Initial force transfer occurs within individual fascicles (Fig. 8.3). Although it was once thought that fascicles spanned the entire ligament or tendon unit, recent evidence suggests that fascicles may be discontinuous and connected via lateral force transfer through an interfascicular membrane [67, 123]. Force within individual fascicles is transferred via crimped fibers. Confocal studies on fascicles subject to tensile loading reveal highly complex microscale interactions, where shearing and sliding deformations result from the uncrimping of these fibers [124–127]. Force within fibers is transmitted via collagen fibrils, and force within collagen fibrils is transmitted via assembled tropocollagen monomers.

The material properties of each scale level have been found to be markedly different with specialized methods of testing being required for each scale level.

### *8.1.6 Macroscopic Mechanical Behavior*

In this chapter, the macroscale is defined as tissue structures that are within the range of millimeters to centimeters, most commonly consisting of whole ligament and tendon preparations or subsamples that are dissected or punched out [68, 102, 128–130]. The 3D elastic response of ligament and tendon tissue is complex and difficult to fully characterize. The material response is highly dependent on the predominant alignment of the collagen fiber families. Although some capsular ligaments appear to have an isotropic fiber distribution (e.g., glenohumeral capsule [43, 44]), the material symmetry of most ligaments and tendonsis reasonably described by transverse isotropy, with the collagen fibers predominantly aligned locally with the direction of in vivo loading [34, 120]. To fully characterize the elastic material response of these tissues, a combination of tensile, compression, and shear testing must be performed in parallel and transverse directions to the predominate fiber family [116, 129, 131, 132].

Tensile testing in the fiber direction reveals a nonlinear stress–strain response consisting of a so-called "toe region" and a linear region [34, 116] (Fig. 8.4, left). It has been hypothesized that the nonlinear toe region results from the uncrimping and/or successive recruitment of the aligned collagen fibers [109, 133, 134]. The reported linear modulus varies widely between tissue types, location, and studies [37, 116, 129, 135–137]. The tensile response in the direction transverse to the fiber axis is nearly linear and an order of magnitude more compliant than the longitudinal response (Fig. 8.4, left). The shear response is nonlinear, with a tangent stiffness that is three orders of magnitude less than the fiber stiffness (Fig. 8.4, middle). Ligament stiffness is lowest when tested in unconfined compression transverse to the fiber axis, yielding a nonlinear response with a tangent compressive modulus nearly four orders of magnitude less than the tensile modulus of the fiber family (Fig. 8.4, right). The elastic volumetric response describes the change in volume in response to tensile or compressive loading. This has most commonly been reported as the Poisson's ratio (which is a linear measure of volume change), and less commonly as the Poisson's function (which is a nonlinear measure of volume change) [133, 138]. The Poisson's ratio (or function) is a kinematic measure that relates the axially applied strain to the laterally induced strain [138]. Experimentally measured Poisson's ratios for uniaxial tensile testing in the fiber direction have revealed values ranging from 1.0 in capsular ligament to 3.0 for flexor tendon [129, 139]. These values exceed the thermodynamic limit of 0.5 for isotropic tissues and are indicative of volume loss under tensile loading. This volume loss is generally understood to be the result of fluid exudation during tensile loading, which has been reported in the literature [140, 141]. The elastic response at the macroscale, mesoscale, and microscale is not spatially homogenous when subjected to tensile loading [123, 124, 126, 127, 129]. Strain measurements techniques such as speckle tracking and digital image correlation have shown that

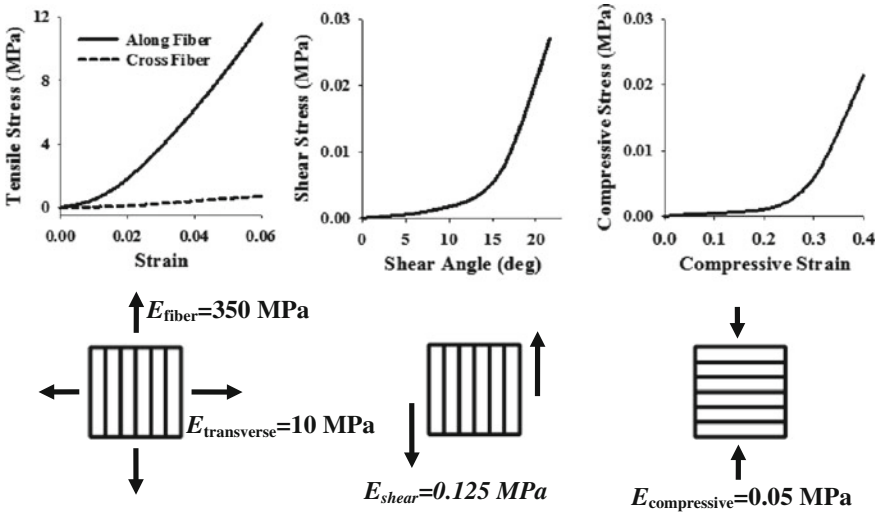


**Fig. 8.4** The elastic behavior of ligament is anisotropic and nonlinear. The tensile stiffness along the fiber direction is an order of magnitude stiffer than in the transverse direction (*Left*) [116, 147]. In shear, ligament is two orders of magnitude more compliant than in the transverse direction (*Center*) [131]. In compression, ligament is over three times more compliant than in tension, indicating compression-tension nonlinearity (*Right*) [148]. Approximate linear modulus ($E$) is shown for each test type along with the testing directions and fiber direction

strains are highly inhomogeneous during tensile loading [142–145]. Although the origins of this behavior are unclear, it may be due in part to variation in the tissue mechanical properties [146], clamping artifacts, or an uneven fascicle stiffness and preload [34, 123]. It appears that spatial inhomogeneity within strain distribution may be an intrinsic property of ligament and tendon tissue.

The viscoelastic response of ligament and tendon is believed to play an important role in the normal function of these tissues [116]. It is manifested as stress relaxation under a step displacement, creep under a step loading, hysteresis, and a phase shift during harmonic loading [149]. Stress relaxation testing of ligament and tendon reveals a dependence of both the relaxation rate and magnitude of relaxation on the strain level [100, 128, 150, 151]. Similarly, the creep rate and creep magnitude are also strain dependent [152]. The tensile modulus is strain rate dependent, while the damping is relatively independent of strain rate [34, 35, 120, 153]. During high rate loading, the volumetric behavior of ligament and tendon appears to be incompressible [34, 133, 154]. Although viscoelastic testing is most commonly reported for uniaxial tensile testing in the fiber direction, both viscoelastic tensile testing in the transverse direction and in shear have been reported [116]. The magnitude of stress relaxation is relatively large for testing in the axial, transverse, and shear directions, with times to equilibrium on the order of ten minutes or more [100, 128, 129, 150]. Because of the considerable importance of the fluid phase to tissue viscoelasticity, it comes as little surprise that the viscoelastic response is significantly altered by varied levels of

tissue hydration [102]. There is also an observed effect of temperature on the elastic and viscoelastic material response [115].

### *8.1.7 Mesoscale Mechanical Behavior*

Fascicles are the primary load-bearing mesoscale structure found within ligament and tendon, and range in diameter from 100 to 500 μm [6, 10, 90]. Experimental studies at the mesoscale have interrogated the fascicle response by testing both isolated individual fascicles as well as fascicles in situ. Rat tail tendons have often been used in such studies because they are readily available, have large aspect ratios, and their fascicles are relatively easy to isolate from the intact tendon. A number of studies have reported both elastic and viscoelastic properties of rat tail tendon fascicles [72, 155, 156]. The qualitative elastic and viscoelastic response is similar to that observed for macroscopic tissue, with a nonlinear toe region and a large stress relaxation.

Several studies have performed tensile testing on progressively divided tendons (e.g., into half and quarter sections) as well as individually isolated fascicles and fascicle bundles [67, 123, 137, 157]. In a study by Yamamoto et al. uniaxial tensile testing was performed on whole tendons, split tendons, and isolated individual fascicles from rabbit patellar tendons [137]. A comparison of quasistatic stress–strain curves indicated that the intact tendons were stiffer than split tendons, which were in turn stiffer than individually isolated tendon fascicles. Stress relaxation testing revealed that whole tendons had a larger stress relaxation magnitude and lower stress relaxation rate compared to individual fascicles. A similar study reported that whole porcine cruciate ligaments were stiffer than split ligaments and isolated fascicles [157]. The results of these studies seem counterintuitive, in that macroscopic structures were stiffer than the constituents. A parallel spring model was proposed to explain this, but this awaits experimental verification [157]. Likewise, in a study by Thorpe et al., the stress within macroscopic tendon samples was found to be higher than that in isolated fascicles strained to a similar level [67].

The opposite trend was observed in similar studies performed on human tendons. In a study by Atkinson et al, human patellar tendons were sectioned into half, quarter, and individual fascicles [158]. A comparison of the elastic modulus, relaxation magnitude and rate revealed a strong dependence on cross-sectional area. As the sample cross-sectional area decreased, the linear modulus increased and the rate and magnitude of stress relaxation decreased. This result is supported by another study by Komolafe et al., in which macroscopic human Achilles tendon samples were clamped and subjected to multiple quasistatic tensile testing experiments [123]. For each test, a fascicular bundle was severed and another stress–strain test was performed. The construct stiffness increased as the cross-sectional area decreased. Another finding from this study was that fascicles within the tissue did not appear to bear load evenly, with some fascicles carrying considerably more load than others. This may explain the macroscale observation of inhomogeneity in strain distribution.

The preceding paragraphs highlight a discrepancy in the literature regarding the variation of stiffness across scale levels. Some studies report increasing stiffness with increasing scale level (e.g., [137, 157, 159]), while others report the opposite (e.g., [123, 158]) Although the cause of this discrepancy is unclear, differences may arise from clamping methods and methods used for sectioning and separating the tendons [67]. In the study by Thorpe et al. it was suggested that the simple act of removing a fascicle from the tissue causes swelling, which artificially increases the cross-sectional area of the fascicle and makes them appear less stiff. In either case, it is clear that the uniaxial tensile behavior in tendon depends on the physical scale.

It has also been shown that the shear behavior displays a scale dependence [95]. In this study, two adjacent fascicles in human patellar tendon were isolated from the whole tendon. The preparations were subjected to repeated tensile loading. On the first cycle, both fascicles were intact. On the second cycle, a single fascicle was cut on one end. On the last cycle, the second fascicle was cut on the opposing end such that force could only be transmitted through an interfascicle shearing mechanism. The results indicated that very little load was transferred through shearing of adjacent fascicles, suggesting that fascicles of some tissues may be free sliding and largely independent in the transmission of tensile forces across the tendon.

### *8.1.8 Microscale Mechanical Behavior*

The collagen fiber is the primary load-bearing tissue constituent in ligaments and tendons at the microscale. Located between collagen fibers are specialized fibroblasts which are often referred to as tenocytes in tendons. These cells are responsible for secreting collagen and other ECM materials in order to maintain the mechanical integrity of the tissue [6]. It is well-established that fibroblasts respond to local strain fields via mechanotransduction, making the study of microscale force transfer particularly important [68]. Both direct (e.g., isolating individual fibers) and indirect (e.g., confocal imaging of loaded tissue) studies have been performed.

Only one study has directly examined the stress–strain response of individual fibers [159]. In this study, individual fibers ($\sim$1 $\mu$m in diameter) were isolated from rabbit patellar tendon and subjected to uniaxial tensile loading. The reported stiffness was compared to the fascicle and whole tendon data from a previous study [137]. The individual fibers were less stiff than both individual fascicles and whole tendons. This result implies that the macrostructures are stiffer than their constituents. As with the mesoscale fascicle test data discussed in Sect. 1.7, this result awaits a satisfactory explanation.

Confocal imaging of rat tail tendon fascicles has yielded considerable insight into the microscale strain environment of collagen fibers and fibroblasts. In these studies, single rat tail tendon fascicles were stained for collagen and cell nuclei, subjected to tensile loading and imaged using confocal microscopy [124, 126, 127]. These studies revealed that the local strain field within fascicles is highly inhomogeneous. In response to uniaxial tensile loading, the predominant mode of microscale

deformation is shearing, whereby individual fibers slide relative to adjacent fibers. As a result, local fiber strains are much smaller in magnitude than applied tensile strains. In one study, the local fiber strain was ~1 % in response to an applied fascicle strain of 6 % [126]. Resulting fibroblast strains were also inhomogeneous, with tensile loading inducing both tensile strains and large shearing strains.

These experiments have also yielded insights into the microscale viscoelastic response. Two microscale mechanisms of viscoelasticity have been observed: a time-dependent shearing of adjacent fascicles, and a time-dependent stretching of individual fibers. The interfiber sliding response displayed a much larger magnitude of stress relaxation than the individual fibers, suggesting that microscale shearing may play an important role in the solid phase viscoelastic component of tendon. Although the source of the microscale strain inhomogeneity and large interfiber shear is still under investigation, it has been suggested that this may result from the uncrimping of the ubiquitous collagen crimping pattern [126, 127].

### *8.1.9 Nanoscale Mechanical Behavior*

The collagen fibril is the primary load-bearing structure at the nanoscale. A number of methods have been employed to study the behavior of ligament and tendon fibrils, including direct testing of isolated fibrils, atomic force microscopy of fibrils, and the use of X-ray diffraction techniques. Numerous studies have isolated individual collagen fibrils and subjected them to uniaxial tensile testing (e.g., [160–163]). The stiffness of fibrils varied between studies and was dependent on hydration, mounting method, cross-linking, and strain rate. Single fibrils tested in this manner display viscoelastic behavior such as strain rate dependence, hysteresis on unloading and stress relaxation [164]. In another study, AFM was performed on strained fibrils within murine Achilles tendon tissue, revealing that the local fibril strain was considerably less than the applied macroscale strain (~2 % fibril strain for an applied 10 % macroscale strain). A large lateral contraction (corresponding to a Poisson's ratio of ~0.8) was also observed [165]. Mechanical testing of single tropocollagen molecules has also been reported [166, 167]. In these studies, force–extension relationships were measured and analyzed by fitting the data to a worm-like chain elasticity model.

It is believed that other nanoscale components may also contribute to the macroscopic mechanical behavior of ligament and tendon, including PGs such as decorin, biglycan [84, 98, 102], and elastin [168]. Although not a direct test of multiscale interactions, a number of knockout studies in mice have been performed that suggest macroscale effects from the altered expression of various nanoscale constituents [72, 105]. For instance, decorin deficient mice have been found to have mechanically inferior tendon fascicles [72]. In vitro studies have also been used to investigate the role of nanoscale constituents such as decorin. In a number of studies, samples of human MCL were subjected to tensile testing before and after decorin digestion (via incubation in chondroitinase ABC, ChABC) and no significant changes in mechanical

behavior were found [100, 102, 128]. However, in similar studies that utilized single rat tail tendon fascicles, a change in mechanical behavior was found in response to digestion incubation in ChABC. This suggests that perhaps the mechanical function of certain PGS may vary between tissue types and scale levels [125, 169]. Still, the changes in mechanical behavior were minimal. Although there were some trends towards incubation decreasing the stiffness and ultimate strength of the fascicles, the increased strain at the onset of visible fiber sliding was the only significant difference found in the tensile test data from both studies [125, 169].

### *8.1.10 Biological Function*

Within tendon and ligament tissue, there exists a balance between mechanical and biological function. Mechanically, they must maintain elastic and viscoelastic material behavior to absorb shock while maintaining strength to resist rupture. However, their structure and material properties must also support vascularization, cellularity, and cellular function. Tendon tissue subjected to cyclic loading, even at relatively small force levels, will accumulate damage [170–172]. Alterations in joint loading patterns lead to a need for structural remodeling and damage resulting from injury must be repaired. Therefore, cellular metabolism must be regulated and populations of fibroblasts must be capable of remodeling and repairing damaged tissue. Fibroblast mediated remodeling is guided by complex interactions of mechanical and chemical factors. Cellular response to mechanical loading is known as mechanotransduction. Mechanotransduction is mediated through a number of mechanisms, including stretch sensitive ion channels, cytoskeletal stretch transduction, and stretch sensitive nuclear pores, amongst others [4, 6–8]. Studies have shown that stress shielding leads to a decrease in synthesis of ECM proteins, such as type I collagen, and an increase in proteolytic activity, while strain up to a certain point leads to an increase in the transcription of ECM proteins, growth factors (e.g., IGF-1) and collagen synthesis [22, 173]. Strain past this point leads to damage and inflammatory cytokines are released, as are certain proteases, growth factors, and ECM proteins. The release of cytokines leads to inflammation, cell infiltration (e.g., monocytes), and vascular proliferation. The presence of these various chemical factors (herein defined as growth factors, inflammatory cytokines, proteases, protease inhibitors, and ECM proteins) will in turn modify the ECM and the fibroblast response. This generates a feedback loop whereby mechanical and chemical signals are closely linked in the regulation of ECM organization and fibroblasts apoptosis, homeostasis, and proliferation (Fig. 8.5).

A finding of critical importance is that the macroscopic strain field within tendon and ligament is not representative of the microscale strain field within fascicles and fibers. As previously discussed, confocal studies have shown that homogeneous macroscale tensile strain of tendon fascicles results in microscale fiber strains that are highly inhomogeneous [124, 127]. Although applied macroscale strains were tensile, microscale strains were manifested as the sliding and uncramping of adjacent fibers. The actual fiber strain in response to an applied load of 8 % was on the order of 2 % (Fig. 8.6). Since fibroblasts are attached to fibers, the measured cellular strains

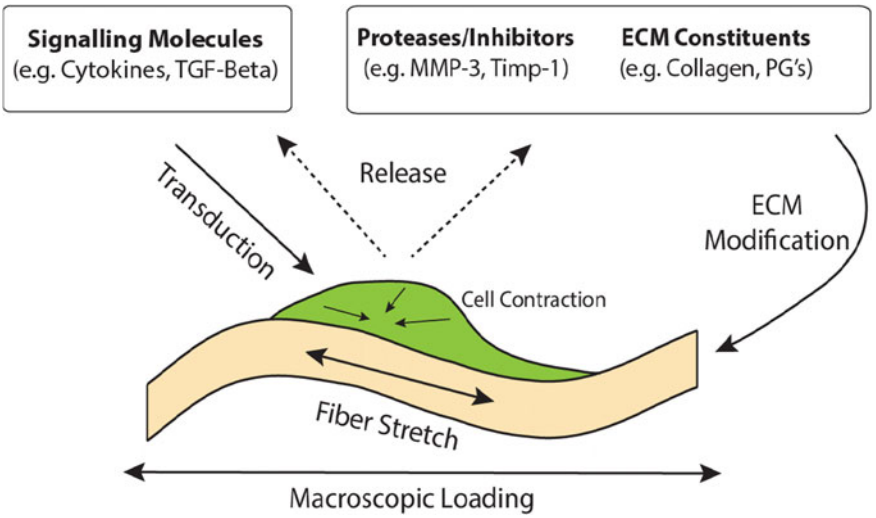


**Fig. 8.5** ECM remodeling feedback loop. Fibroblasts (*green*) are attached to collagen fibers (tan) at the microscale. Macroscopic loading creates stretch within the fibers, which induces mechanotransduction within the fibroblasts. This leads to the excretion of ECM constituents, as well proteases and protease inhibitors. These, in turn, modify the ECM structures (e.g., collagen fibers) via degradation or deposition. Mechanotransduction may also lead to the release of certain signaling molecules, which are transduced by adjacent fibroblasts and may stimulate further release of ECM constituents or proteases. Fibroblasts may also generate internal forces, which can further modify the feedback loop

were similar. This highlights the importance of microscale structure on fibroblast mechanotransduction. In the absence of fiber crimp, fibroblasts would experience much larger strains. If the crimp angle is increased or fiber organization is less aligned (as in scar tissue), the fibroblast strains could be smaller. If the crimp was absent, the fibroblast strains could be significantly larger. It has been suggested that fiber crimp may play the role of a "shock absorber" at the macroscale. These results suggest that fiber crimp may also play a role at the microscale by protecting fibroblasts from excess strains. Although additional research is needed, it is clear that microscale fiber organization affects strain transmission from the macroscale to the microscale, and that this has a profound impact on fibroblasts mechanotransduction and associated remodeling.

## 8.2 Multiscale Computational Challenges

Given the relatively early stage of multiscale mechanical modeling and its application to biological problems, significant challenges remain to be addressed. These challenges include modeling the mechanics of force transmission across scales, the mechanisms of nutrient transport and the biological functions of mechanotransduction, cellular proliferation and tissue healing and remodeling. Further challenges are

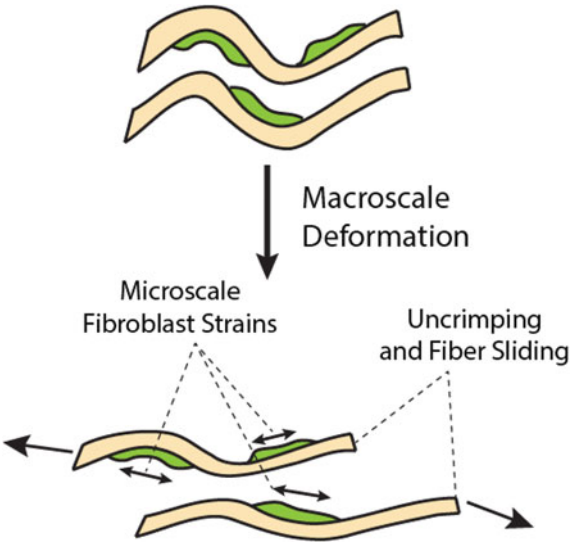


**Fig. 8.6** Microscale mechanotransduction in ligament and tendon. Macroscale tensile strain leads to inhomogeneous strains at the microscale, where fiber sliding and uncrimping are the dominant modes of deformation. As a result, the strains transduced by fibroblasts are less than those applied at the macroscale

related to coupling these models (e.g., mechanical modeling coupled to mechanotransduction and cellular function). In accordance with the scope of this chapter, only the multiscale transmission of force will be addressed.

### *8.2.1 Force Transfer Across Scales*

As discussed in the Introduction, force transmission between scales is highly complex. Given that mechanotransduction occurs at the microscale, the interaction between the macroscale and microscale is particularly relevant. Although this problem is often treated as a macro-micro problem, with representation of only the link between the macro- and microscale, this may not be a sufficient methodology for many problems of biological interest. Mounting experimental evidence suggests that force transfer between the macro- and microscales is mediated by complex interactions at the mesoscale fascicle level. Interestingly, the level of strain measured within fascicles is generally much less than that measured at the macroscale. It has been suggested that fascicles may not span the entire length of the tendon, thus macroscopic force transfer is actually mediated via the shearing of the more compliant interfascicular matrix. In a comparison of the macroscopic strains and mesoscale fascicle strains for two different tendon types (a positional tendon and a load bearing tendon), the fascicle strains were the same for both tendon types, but the load-bearing tendon had much larger macroscale strains [67]. The difference was attributed to the fact that the interfascicular matrix was much thicker in the load-bearing tendons, which then led to greater shearing. Not only does it appear that load may be transferred

between fascicles via shearing of the interfascicular matrix, but it appears that the load sharing between fascicles is highly inhomogeneous. Strains within individual fascicles of an Achilles tendon sample were highly variable, even when the applied macroscopic loading was constant [123]. To date, very little research has addressed modeling the mesocale fascicle interactions, thus this remains as an open modeling challenge. Given that vascular perfusion and innervation occur at this level [84, 174], the need for further research and development in this area is particularly high.

Force transmission from the mesocale fascicle level to the microscale fiber level has been the subject of a number of experimental studies. As previously discussed, strain at the microscale fiber level is highly inhomogeneous, with uncrimping and sliding of adjacent fibers being the dominant modes of deformation. In fact, strains resulting from sliding of adjacent fibers actually exceeded that of strains measured within individual fibers. As a result, the fiber strain was considerably less than the macroscopic fascicles strain. Given this information, it appears that the largest strains are experienced at the macroscale, followed by the mesoscale fascicle and again followed by the microscale fiber. Since fibroblasts anchor to individual or multiple fibers, this suggests that even large macroscale tendon strains may result in relatively low microscale fiber, and thus fibroblast strains. As mechanotransduction occurs within individual fibroblast, modeling both the meso- and microscale interactions may be a necessity. The explicit representation of fibroblast cell bodies may prove especially insightful, as they will provide the mechanical environment "seen" by cells in response to macroscale joint loading, which can then yield insights into cellular mechanotransduction.

There has been very little investigation of force transmission within individual fibers. This is a result of challenges related to the extremely small physical scale of fibers. Unlike fascicles, fibers are difficult to isolate [159]. If fibers are isolated successfully, they may be damaged by the process. Furthermore, the diffraction limit of light limits the achievable resolution of optical imaging modalities, making it difficult to study the interaction of individual fibrils in a dynamically strained fiber. Most information regarding force transmission within fibers has been inferred from SEM and TEM microscopy. In TEM, the distribution and shapes of fibril cross sections have been studied, indicating both modal and bimodal distributions of fibril diameters [10, 87, 175]. TEM has also been used to study the distribution of PGs (e.g., decorin) within tendon and ligament tissue, as they have been hypothesized to play a role as cross-linkers and spacers between adjacent fibrils [105, 106, 176–181]. Although a number of studies have refuted their role as cross-linking agents [100, 102], their role as mechanical spacers may still be significant. SEM imaging has revealed that fibrils appear to be very long and display minimal amounts of splitting, weaving, and merging [93]. Several studies have measured the change in D-band of fibrils resulting from macroscopic loading using synchrotron radiation and found that fibril strains are correlated with applied macroscopic strains [182]. In order to accurately model the force transfer within single fibers, more experimental information will be needed regarding the morphology of fibrils (e.g., the extent of interweaving and crossing) as well as possible cross-linking mechanisms. This will be particularly relevant for studies that seek to understand how certain genetic diseases (e.g., Ehlers-Danlos

syndrome) affect the mechanical properties of fibers via their altered structural characteristics.

Force transmission within individual fibrils concerns the organization of tropocollagen monomers within fibrils, as well as the mechanical behavior of individual tropocollagen monomers. Questions regarding the exact organization of tropocollagen within fibrils remains open ended. It has been hypothesized that there exists microfibrils within individual fibrils, but this has been a subject of controversy [86, 87]. Molecular dynamics simulations are possible for individual tropocollagen molecules, and coupling this to the behavior of entire fibrils is an active area of research [183, 184].

### *8.2.2 Multiscale Validation*

Validation of computational models is fundamentally important if the models are to be interpreted in a meaningful way [185, 186]. Validation of macroscale computational models of ligaments and tendons consists of comparing macroscale FE simulations to experimentally measured metrics such as joint reactions forces and in situ tissue strains, and there are a number of examples in the literature (e.g., [32, 120]). Validation of multiscale models proceeds in a similar way, but ideally, experimental validation would occur at each scale level that is simulated (e.g., the macroscale and microscale). Because of the important role of validation in interpreting the results of computational studies, it is desirable to develop multiscale simulation strategies and experimental validation methods concurrently. Although macroscale validation methods have been described for macroscopic tendon and ligament [185, 186], microscale validation methods are still in need of improvement and development. In order to validate microscale models, data regarding stress and strain at lower scale levels (e.g., within fascicles, fibers, and fibrils) must be obtained. One possible route involves isolating and mechanically testing individual tissue constituents, such as those described in Sects. 1.7–1.9. However, such methods have yielded widely variable results, likely due to the difficulty in consistently isolating substructures without causing tissue damage [67]. Microscopic imaging studies, such as the confocal studies described in Sect. 1.8, provide considerable promise for use in validation of microscale models.

## 8.3 Methods

Continuum mechanics provide the foundation for modern multiscale modeling techniques. Based on the notion of a continuum, constitutive models are proposed for describing the stress–strain behavior of a material. For complex geometries and loading patterns, computational methods must be used to solve the equations of motion. For multiscale materials, the constitutive behavior may be described using

a homogenization procedure. These methods utilize an explicit microstructure as a means for both obtaining the macroscopic stress–strain behavior and for reconstructing the microscale stress–strain problem. A number of homogenization schemes have been proposed, each with a specific use. In this section, a brief summary and discussion of the preceding topics will be provided.

### 8.3.1 Continuum Mechanics

The presence of a continuum assumes that the length scale of microstructures is infinitesimally small in comparison to the macroscale, and that the deformation gradient, and thus strain and stress, can be defined uniquely at every point within the domain. This latter point implies an affine deformation map in which an infinitesimal line element $\boldsymbol{dX}$ in the reference configuration is mapped to the current configuration $\boldsymbol{dx}$:

$$\boldsymbol{dx} = \boldsymbol{F} \cdot \boldsymbol{dX} + \boldsymbol{X_0}, \tag{8.1}$$

in which $\boldsymbol{dX}$ is an infinitesimal material line element in the reference configuration, $\boldsymbol{dx}$ is the deformed version of the same infinitesimal material line element, and $\boldsymbol{X_0}$ represents a rigid body translation vector. $\boldsymbol{F}$ is the (nonsymmetric) deformation gradient:

$$\boldsymbol{F} = \frac{\partial \boldsymbol{x}}{\partial \boldsymbol{X}}. \tag{8.2}$$

A number of second-order strain measurement tensors are computed from the deformation gradient, including the right Cauchy deformation gradient ($\boldsymbol{C}$), the Green-Lagrange strain ($\boldsymbol{E}$) and the engineering or infinitesimal strain ($\boldsymbol{e}$):

$$\boldsymbol{C} = \boldsymbol{F}^{\boldsymbol{T}}\boldsymbol{F}\,, \tag{8.3}$$

$$\boldsymbol{E} = \frac{1}{2}\left(\boldsymbol{C} - \boldsymbol{1}\right), \tag{8.4}$$

$$\boldsymbol{e} = \frac{1}{2}\left[(\boldsymbol{F} - \mathbf{1}) + (\boldsymbol{F} - \mathbf{1})^{\boldsymbol{T}}\right]. \tag{8.5}$$

The engineering strain is used extensively for linear elasticity, but is generally of limited use for the finite deformations seen in biological tissues. A useful concept in the study of aligned collagenous tissue is the notion of a unit vector to describe the fiber direction, which is denoted $\boldsymbol{a}_0$ in the reference configuration. This fiber vector is rotated and stretched by the deformation gradient, $\lambda \boldsymbol{a} = \boldsymbol{F} \cdot \mathbf{a_0}$, where $\lambda$ is the fiber stretch and $\boldsymbol{a}$ is a new unit vector describing the rotated orientation of the fiber direction. The concept of strain invariants is of particular importance in

biosolid mechanics, since they provide an objective measure of strain that is invariant to rotation and rigid body motion [187, 188].

### 8.3.2 Continuum Based Constitutive Models

In order to compute a stress from the aforementioned strain measures, a constitutive model is required. In the case of linear elasticity, this constitutive model defines the Cauchy stress, $\boldsymbol{\sigma}$, to bethe inner product of the engineering strain, $\boldsymbol{\varepsilon}$, and the fourth order elasticity tensor, $\mathcal{C}$ , such that: $\boldsymbol{\sigma} = \mathcal{C} : \boldsymbol{\varepsilon}$. Due to the inherent nonlinearity of ligament and tendon tissue, strain energy approaches (referred to as hyperelasticity) based on the invariants of the deformation tensor ($I_1$, $I_2$, $I_3$, $I_4$, $I_5$), are commonly utilized. Such an approach is particularly attractive because it automatically satisfies a number of constraints, such that the formulation will be objective (i.e., invariant to rigid body rotation and displacement) and the tangent elasticity tensor (i.e., the linearization) will be positive definite for a polyconvex strain energy function [187]. In this approach, a scalar strain energy function ($W$) is defined, which is typically (but not necessarily) a function of the strain invariants. The Cauchy stress tensor is computed by taking the derivative of the strain energy function with respect to the right Cauchy deformation tensor $\boldsymbol{C}$:

$$\boldsymbol{\sigma} = \frac{2}{J}\boldsymbol{F}\left(\frac{\partial W}{\partial \boldsymbol{C}}\right)\boldsymbol{F}^T. \tag{8.6}$$

The fourth-order elasticity tensor (necessary for the linearization and subsequent nonlinear analysis in numerical methods) is found by taking the second derivative:

$$\mathcal{C} = 4\frac{\partial^2 W}{\partial \boldsymbol{C}\partial \boldsymbol{C}}, \tag{8.7}$$

where $\mathcal{C}$ is the elasticity tensor in the material frame, which is pushed forward to the spatial frame in most practical implementations.

Hyperelastic, invariant-based, anisotropic continuum models have proved successful in modeling the macroscale behavior of ligament and tendon [34, 120]. A relatively simple formulation that has been used successfully to model the macroscopic stress–strain behavior of ligament can be described as [29, 32–34, 120, 132, 189]:

$$W = W_m(I_1, I_2) + W_f(\lambda) + U(J). \tag{8.8}$$

Here, $W$ is the total strain energy, $W_m$ is the strain energy for the interfiber matrix, $W_f$ is the strain energy for the collagen fibers, and $U$ represents a volumetric strain energy. $I_1$ and $I_2$ are the invariants of the right Cauchy deformation tensor $\boldsymbol{C}$, $\lambda$ is the stretch along the fiber direction, and $J = \det(\boldsymbol{F})$ is the volume ratio. The fiber strain energy term ($W_f$) is defined to capture the toe region and linear region of the

stress–strain curve for ligaments, and to represent the relatively small compressive stiffness:

$$\lambda \frac{\partial W_f}{\partial \lambda} = \left\{ \begin{array}{cc} 0 & \lambda \leq 1 \\ c_2 \left( e^{c_3(\lambda - 1)} - 1 \right) & 1 < \lambda < \lambda^* \\ c_4 \lambda + c_5 & \lambda \geq \lambda^* \end{array} \right\}. \tag{8.9}$$

This formulation represents a structurally motivated constitutive model, as it specifies strain energy terms for the collagen fiber family and the interfiber matrix. Numerical implementation of hyperelastic constitutive models in finite element (FE) codes often make use of an additive decomposition of the strain energy into volumetric and deviatoric parts based on the multiplicative decomposition of the deformation gradient $\boldsymbol{F}$ [34, 120, 187]. This requires a small modification of the equations above. The uncoupled strain energy equations are advantageous for representing these tissues in FE software because they can make use of element formulations that allow for nearly and fully incompressible material behavior without element locking [34, 120].

### *8.3.3 Constitutive Modeling of Viscoelasticity*

Ligament and tendon viscoelasticity has most commonly been represented by quasilinear viscoelastic (QLV) [34, 120, 150, 190–192] and nonlinear viscoelastic constitutive models [151, 193–195]. The QLV theory postulates that the time response and the elastic response are independent [149]. The time response is described using a relaxation function, while the elastic stress response is typically described using a hyperelastic constitutive model [196]. The time-dependent stress is then obtained by convolving the relaxation function with the elastic stress. According to QLV theory, the relaxation function is implicitly related to the creep function via a convolution [117]. Thus, an experimentally measured relaxation function should predict an experimentally measured creep function. Although a number of studies have applied the QLV theory successfully to describe the time- and rate-dependent material behavior of ligaments and tendons [83, 192, 197–199], several studies have suggested that these materials do not strictly behave as quasilinear viscoelastic materials [200–203]. This has motivated the development of nonlinear viscoelastic models [193, 195, 200].

The apparent viscoelasticity of ligament and tendon can also be described using biphasic theory [22, 121, 122, 204]. Biphasic theory postulates an interaction between a porous, elastic solid phase, and an incompressible fluid phase. Loading of the biphasic material induces volumetric changes in the elastic phase. This creates pressure gradients, which drive a time-dependent fluid flux through the porous matrix. Diffusive drag and thus energy dissipation is induced by the local difference in velocity between the solid and fluid phases. Biphasic materials exhibit stress relaxation, creep, and hysteresis. A necessary component of the field equations for the biphasic theory is the introduction of additional degrees of freedom related to

the time and spatially varying fluid pressure field (or fluid velocity), thus making analytical solutions more difficult to compute than for standard viscoelastic constitutive models. Because of this, quasianalytic solutions to biphasic problems have only been obtained for simplified geometries and loading scenarios [119, 205]. These include the confined and unconfined loading of a cylinder subjected to ramp loading, step loading, and harmonic loading [119, 205] for linear material behavior, and for certain nonlinear materials [206, 207]. Both flow-dependent (e.g., biphasic material) and flow-independent mechanisms may be needed to accurately describe and predict the apparent viscoelasticity of some biological soft tissues [207, 208]. Poroviscoelastic formulations have been proposed that utilize a viscoelastic continuum model within the solid phase. These approaches have found utility in the field of cartilage mechanics [207–209].

### *8.3.4 Computational Modeling*

Analytical solutions to the equations of motion for the mechanics of ligaments and tendons can only be obtained for simplified geometries and loading scenarios (e.g., uniaxial tension-compression). For complex geometries and loading patterns such as simulation of the mechanics of a ligament within an intact joint, the geometry and governing equations must be discretized and solved numerically [34, 120]. The FE method is by far the most commonly used numerical method in the field of biosolid mechanics. Commercial and freely available software packages support preprocessing, solution, and postprocessing ofthe nonlinear FE problems. Many studies in the literature have used FE methods for the simulation of ligament and tendon mechanics (e.g., [29, 32, 44, 120]). In addition to elastic problems, the FE method can also be used to solve viscoelastic problems and biphasic problems. In the past, addressing these types of problems was more difficult due to the lack of a FE framework specifically designed for biological applications. To address this issue, our lab developed FEBio, a nonlinear implicit finite element framework designed specifically for analysis in computational solid biomechanics (www.febio.org) [210].

### *8.3.5 Homogenization*

Although continuum-based constitutive models are useful for describing macroscopic behavior, they do not address the mechanical behavior that occurs at lower length scales and are not always useful for the study of structure–function relationships between the microscale and the macroscale. Because of the multiscale structure of ligaments and tendons, it is sometimes desirable to use models that can simultaneously describe both macroscale and microscale behavior. This is the goal of multiscale modeling in mechanics, and homogenization is part of the foundation of multiscale modeling. Homogenization is the process of obtaining a macroscopic stress–strain

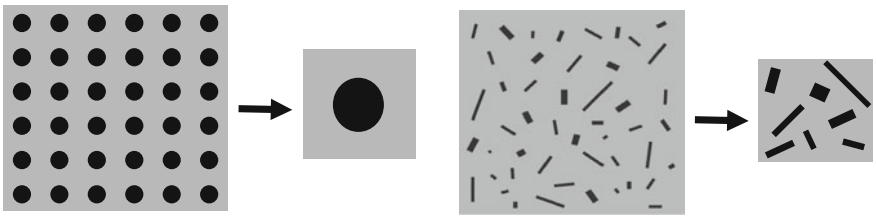


**Fig. 8.7** Comparison of a unit cell and an RVE. For materials with a periodic microstructure, such as a lattice of spheres embedded in a matrix material (*Left*), a unit cell (*Middle Left*) can be defined that describes the microscale geometry. For the case of media with random microstructures (*Middle Right*), a volume element representative of the microstructure, called an RVE (*Right*), can be defined

response from a material with a known heterogeneous microstructure [211–213]. It is based on the concept of a representative volume element (RVE), which can be considered representative of the continuum [214–216] (Fig. 8.7). An RVE must be large enough to be statistically representative of the material microstructure, but it must still satisfy the continuum assumption that its dimensions are much smaller than the macroscale dimension [214]. For the case of a perfectly periodic microstructure (e.g., a lattice of spherical particles), the RVE reduces to a unit cell [217]. In a homogenization, the RVE is subjected to the appropriate boundary conditions and then simulated macroscopic loading is used to compute the effective material response. For a periodic unit cell, the exact homogenized effective material properties are obtained. If the RVE is statistically representative of the material microstructure, the "apparent material properties" are obtained [217, 218].

The concept of homogenization is based upon the Hill principle [219], which states that the volume averaged strain energy at the macroscale is equal to the volume averaged strain energy at the microscale (i.e., energy is conserved):

$$\langle \boldsymbol{\sigma} : \boldsymbol{\varepsilon} \rangle = \langle \boldsymbol{\sigma} \rangle : \langle \boldsymbol{\varepsilon} \rangle \ . \tag{8.10}$$

Special boundary conditions must be applied to satisfy the Hill condition. For a periodic unit cell, they are periodic boundary conditions [217, 220]. The periodic boundary conditions enforce the constraints that opposing faces of the unit cell must deform identically, and that the traction forces on opposing faces must be antiperiodic [213, 217, 220]:

$$\begin{aligned} \boldsymbol{u}^{k+}\left(\boldsymbol{x}^{+}\right) - \boldsymbol{u}^{k-}\left(\boldsymbol{x}^{-}\right) &= \varepsilon_0\left(\boldsymbol{x}^{+} - \boldsymbol{x}^{-}\right) \\ \boldsymbol{t}^{k+}\left(\boldsymbol{x}^{+}\right) &= -\boldsymbol{t}^{k-}\left(\boldsymbol{x}^{-}\right) \end{aligned} \quad \text{on } \Gamma \ , \tag{8.11}$$

where $\boldsymbol{u}^{k+}$ and $\boldsymbol{u}^{k-}$ are the displacements on opposing faces and $\boldsymbol{t}^{k+}$ and $t^{k-}$ are traction forces on opposing faces (both on the boundary $\Gamma$), $\varepsilon_0$ is the applied strain and $\boldsymbol{x}^{+}$ and $\boldsymbol{x}^{-}$ are the position vectors on opposing faces.

Historically, homogenization approaches have been primarily used to analyze linear material behavior, with the effective coefficients of the linear elasticity tensor being computed. Analytical methods, which obtain homogenized coefficients via closed form solutions, have been applied to problems that feature simple RVE geometries (e.g., a homogenization of annulus fibrosis [221], also refer to [211] for a summary of such methods in engineering applications). However, homogenization techniques based on analytical methods lack the ability to address the complex 3D microstructural features in ligament and tendon. Thus, methods based on FE discretization are particularly appealing.

For a properly discretized RVE, the FE method can be used to perform the homogenization. In the linear case, FE simulations are used to obtain the unknown coefficients of the elasticity tensor. To obtain a full set of homogenized material coefficients, a sufficient number of loading conditions must be applied. Depending on the type of homogenization and the underlying material symmetry, this may include simulated tensile testing in orthogonal directions and shear testing in orthogonal shearing directions. For a unit cell with an orthotropic symmetry, a total of six unique loading simulations must be performed to obtain the nine independent coefficients in the elasticity tensor [222]. For a FE simulation, the periodic displacement boundary conditions (Eq. 8.11) must be enforced explicitly [220]. This can be achieved by converting the periodic boundary equations into a set of linear constraint equations (e.g., via a master node approach) within the FE solver [133]. The application of periodic boundary conditions typically requires that the FE mesh has identical nodal distributions on opposing faces and edges (i.e., the faces and edges are conformal). For homogenizations that utilize a RVE that does not have conformal faces, other permissible boundary conditions must be used. These include kinematic boundary conditions, traction boundary conditions, and mixed boundary conditions [217]. For these cases, the resulting homogenization is not exact.

Although homogenization methods have historically been applied to linear material behavior and kinematics, they can also be applied to nonlinear materials and nonlinear kinematics [219]. In the linear case, a finite number of loading scenarios can be used to solve for the unknown coefficients. In the nonlinear case, this methodology cannot be used because the functional form of the stress–strain response is unknown. For example, there is no combination of loading scenarios that can directly resolve whether a stress–strain response is quadratic, exponential, or some other function. Strain energy-based approaches have been suggested that curve fit an assumed functional response or populate a lookup table for interpolation [223]. However, they have yet to find widespread use.

An attractive alternative for nonlinear homogenizations is the use of a micromechanical model in combination with the appropriate boundary conditions. A micromechanical model can be subjected to loading scenarios that are of interest (e.g., uniaxial tensile loading of a tendon) in combination with periodic boundary conditions, and the homogenized response can be examined. This has proven useful in several studies that have sought to examine microscale forces and structure–function relationships in ligaments and tendons [224, 225]. See Sect. 8.4 for a discussion of these models.

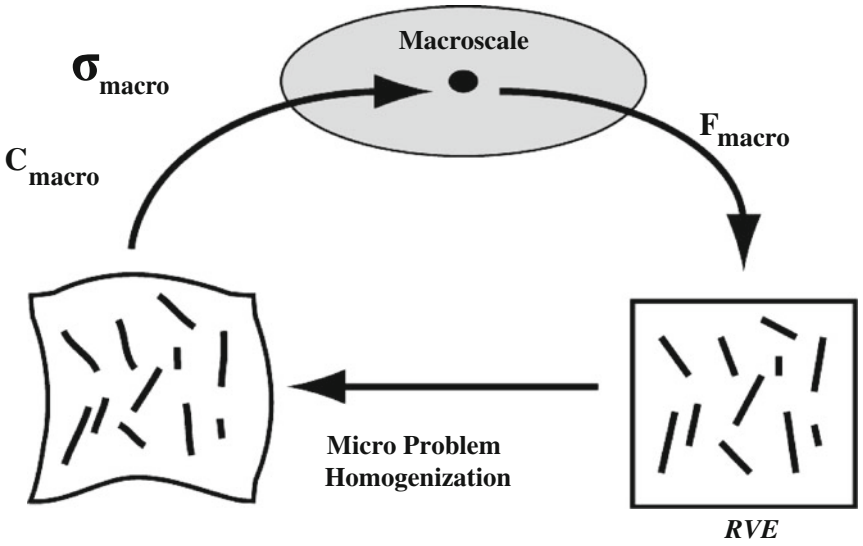


**Fig. 8.8** $FE^2$ homogenization algorithm. The $FE^2$ method solves a nested FE problem, in which the deformation gradient $\mathbf{F}_{\text{macro}}$ computed at a macroscale point is passed to the microscale RVE or unit cell. A homogenization is performed using the deformation gradient coupled with suitable boundary conditions, and the resulting stress tensor ($\boldsymbol{\sigma}_{\mathbf{macro}}$) and elasticity tensor $\mathcal{C}_{\mathbf{macro}}$ are passed back to the macroscale. Figure adapted from [226]

However, micromechanical models are limited to very specific loading scenarios and do not provide a general homogenized response. In order to provide a more general homogenization, the $FE^2$ method has been proposed. $FE^2$ based homogenization utilizes a nested FE problem that consists of a macroscale boundary value problem and a microscale boundary value problem [211, 212, 226–230]. A macroscale mesh is defined in the normal fashion. When the stress or elasticity tensor for the macroscale model is needed during the nonlinear FE solution procedure, the macroscale deformation gradient is passed to the microscale problem and a homogenization is performed on a discretized RVE (Fig. 8.8). Thus, the constitutive model is itself an FE problem. This framework provides a generalized strategy for performing a nonlinear homogenization on an arbitrarily defined RVE. The primary downside to this methodology is the substantial increase in computational demand. However, increased computing power coupled with parallelization methods will make future $FE^2$ considerably faster [231].

A fundamental assumption for the aforementioned homogenization approaches is that the RVE is infinitesimally small in comparison to the macroscale. Under this assumption, a homogenous deformation is described via the deformation gradient (Eq. 8.2). Since the deformation gradient is computed by taking a first order derivative, continuum-based homogenization methods are referred to as 1st order methods. Some homogenization problems, however, feature RVEs that are not infinitesimally small in comparison to the macroscale. In these cases, microstructural size effects

**Table 8.1** Summary of homogenization methods

| Homogenization | Number of simulations | Purpose |
|---|---|---|
| Linear | Finite number, based on number of unknowns in linear elasticity tensor | Homogenized linear material coefficients |
| Micromechanical | Finite number, based on model application | Investigate nonlinear behavior and structure–function relationships |
| 1st order $FE^2$ | Simulation every time stress and tangent stiffness are evaluated within macro model | Nonlinear homogenization for infinitesimally small microstructures |
| 2nd order $FE^2$ | Simulation every time stress and tangent stiffness are evaluated within macro model | Nonlinear homogenization that incorporates size effects |

The method of homogenization used is dependent on the intended purpose of the model

must be taken into account [232, 233]. This is particularly relevant in the study of damage initiation as size effects play a critical role in this field [211, 234]. The most generalized approach to accounting for these size effects is to utilize 2nd order $FE^2$ strategies. In these methods, a microscale RVE problem is still used. However, the homogenization utilizes a quadratic version of the deformation map. In this method, a Taylor series expansion is used to express the infinitesimal material line element $\boldsymbol{dx}$ as:

$$\boldsymbol{dx} = \boldsymbol{F} \cdot \boldsymbol{dX} + \frac{1}{2}\left(\boldsymbol{dX} \cdot {}^{3}\boldsymbol{G} \cdot \boldsymbol{dX}\right) + \boldsymbol{X_0}, \tag{8.12}$$

where the 3rd-order tensor ${}^{3}\boldsymbol{G} = \nabla \boldsymbol{F}$ is used. This method explicitly accounts for the length scale through the size of the RVE, and thus allows for computational homogenization of materials for which the assumptions of the 1st order method are not appropriate. Second-order methods are particularly attractive for biological materials as physical scales are often not separated sufficiently in size. As an example, the microstructures in ligament and tendon have similar physical dimensions to the macroscale. Fascicles, for instance, have a diameter of $\sim 250\,\mu$m, which is only 1–2 orders of magnitude less than ligament and tendon widths, which are ~5–30 mm (refer to Sect. 2.3). For a comparison of homogenization techniques, refer to Table 8.1.

## 8.4 Results

The field of multiscale mechanical modeling, and the multiscale modeling of ligament and tendon in particular, is in its relative infancy. For example, there seems to be no clear consensus on the very definition of multiscale modeling, as it has been applied to a large number of models that vary as to what scales are included and how the scales are linked. For the purposes of this section, a multiscale model is defined as

a model that addresses two or more physical scales. This implies that both macroscale and microscale stress and strain are computed from a single simulation. Furthermore, this requires that there is some form of linking between scale levels. This linking is based on the appropriate application of boundary conditions, which may include periodic boundary conditions, prescribed boundary conditions, homogenous boundary conditions, and a mixture thereof. This definition includes micromechanical models in which both a macroscale response and microscale response is described, as well as full nonlinear homogenizations (e.g., $FE^2$ methods). It is important to note that this definition does not include structurally motivated constitutive models, which may utilize the notion of microstructural features (e.g., uncrimping of collagen fibers [235, 236], fiber recruitment [237], or fiber families embedded within a ground substance [238]). This definition also precludes models that utilize generalized continuums, which address microscale size effects but do not specifically define microscale stress and strain [234]. This section reviews the state of the art in multiscale modeling and multiscale model validation as they relate to ligament and tendon.

### *8.4.1 Micromechanical Modeling of Ligament and Tendon*

We define a micromechanical model as a 2D or 3D model that specifies a microscale geometry (e.g., a unit cell), applies macroscale boundary conditions (e.g., simulated tensile loading combined with periodic boundary conditions) and solves the governing equations over the simulation domain. Such a model yields both a microscale response (e.g., within the unit cell) and a macroscale response (e.g., reaction force of a unit cell subjected to tensile deformation). Since even simple 2D geometries do not generally have tractable solutions, these models almost exclusively rely on computational methods, most commonly the FE method. Models within the literature are primarily 2D and focused on equilibrium elasticity, although a biphasic model and 3D models have been proposed [22, 133]. Boundary conditions include fixed boundary conditions (e.g., zero displacement on a model edge), prescribed boundary conditions (e.g., a prescribed load or displacement on a model edge), periodic boundary conditions, and a combination of these. Both linear and nonlinear micromechanical models have been proposed for biological tissues. Linear models (ubiquitous in the study of trabecular bone, e.g., [217, 239–242]) generally seek to obtain homogenized coefficients of the linear elastic stiffness tensor. Due to the nonlinear nature of ligament and tendon, most micromechanical models for this application are nonlinear and seek to explore nonlinear behavior as the primary goal, although some studies have reported homogenized linear coefficients as well (e.g., [133]). The utility of microscale models is found in a number of ways. Some models are used to study certain structure–function relationships (e.g., how certain microscale structures affect macroscale behavior) [133, 243]. Other models are used to study microscale damage mechanisms [224], and still others investigate microscale mechanotransduction [22].

Micromechanical models have been used to examine the structure–function relationship between fibril shape, fibril aspect ratio, the stiffness of fibrils and the

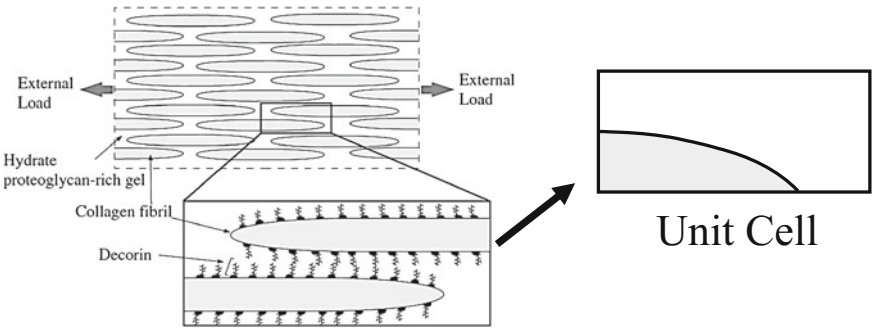


**Fig. 8.9** Collagen fibril micromechanical model [243]. A model put fourth for collagen fibers consisted of fibrils of a finite length and with tapered tips connected via proteoglycan matrix material (*Left*). A quarter symmetric micromechanical model was defined (*Right*) and subjected to simulated loading. Figure adapted from [243]

interfibril matrix [243, 244]. In these studies, a 2D plane strain model was used to examine force transfer between adjacent collagen fibrils via an interfiber matrix [243]. A unit cell was created that consisted of a discretized fibril embedded within a matrix material (Fig. 8.9). The fibrils were given cylindrical or tapered endpoints [244]. The unit cell was subjected to homogenous boundary conditions, in which a displacement was applied to the sides of the model. The aspect ratio of the fiber and applied load were varied parametrically and their influence on the fibril stress, interfiber force transfer and strain was examined. Simulations revealed that fiber strain displayed a dependency on the end shape of the fibril, on the fibril aspect ratio and the ratio of the fibril stiffness to the matrix stiffness. The effect of tapered fibril ends was to decrease stress within fibers. The effect of increasing the stiffness of the inter fibril matrix was to increase load sharing between fibril and the matrix, which yielded decreased fibril strains. By utilizing a unit cell approach, this study was able to examine the influence of structure–function relationships that would be difficult if not impossible to investigate using experimental or analytical approaches. Within these studies, the concept of an interfiber matrix material was utilized. The matrix material is thought to consist of PGs, elastin and other ECM proteins that may mechanically couple collagen. Such a concept has been used in numerous studies (e.g., [132, 133, 238, 245, 246]) and is used to describe the substance that mechanically couples collagen fibrils and fibers within tendon and ligament.

One area that shows great promise in the field of multiscale modeling is the study of stress and strain localization as it pertains to damage initiation. Although no studies have yet utilized micromechanical models to study damage initiation in tendon, they have been utilized in studying microscale strain patterns in the myotendinous junction (MTJ), which displays similarities to tendon and ligament tissue. In one such study, a 2D micromechanical model was used to explore microscale strain distributions within the MTJ, a common location for musculoskeletal injuries [224]. At the MTJ, muscle fibers taper as they insert into the tendon via the endomysium,

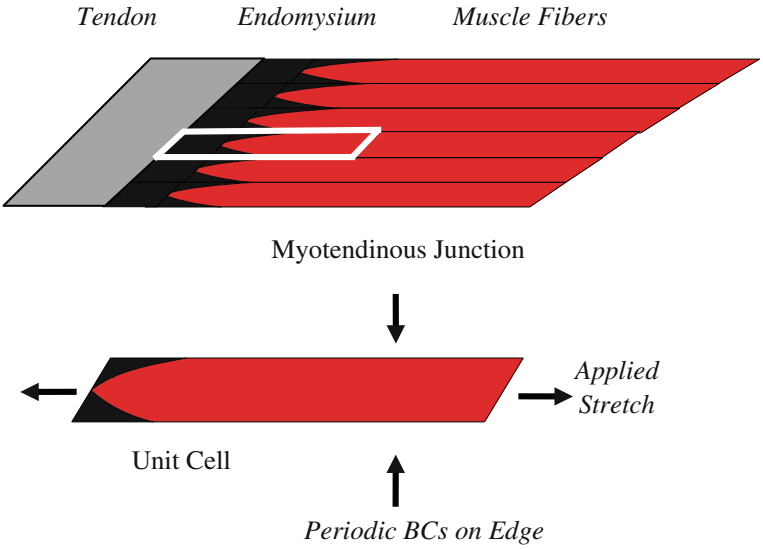


**Fig. 8.10** Myotendinous junction (MTJ) micromechanical model [224]. (*Top*) The MTJ consists of muscle fibers (*red*) that insert into tendon tissue (*gray*) via the endomysium (*black*). A micromechanical model was made of the MTJ by creating a unit cell (outlined in a *white* polygon and shown on *bottom*) and subjecting it to periodic boundary on the edge and prescribed boundary conditions on the ends. Figure adapted from [224].

creating a potential location for strain concentration and damage initiation. By utilizing a microscale unit cell model, this study sought to investigate strain concentrations within this region. The unit cell consisted of a single tapered muscle fiber inserting into tendon at a pennation angle of 37° (Fig. 8.10). The endomysium was given a transversely isotropic constitutive model similar to that presented in Sect. 4.2 and the muscle fiber was given an active contraction material model developed for muscle tissue [224]. The unit cell was subjected to prescribed displacement along the fiber direction corresponding to a 24 % strain. The edges of the unit cell were given periodic boundary conditions, which simulated a fiber embedded in macroscopic tissue. Simulations were run with both passive and active fiber recruitment. Model validation was performed by comparing the predicted fiber strains to those experimentally measured for relaxed and strained muscle fibers. More specifically, the deflection of the A-bands within the muscle fibers were experimentally measured and compared to those obtained from the FE models (refer to [224] for more detail regarding validation methods).

The most significant result of this study was that the FE micromechanical model predicted stress concentration and microscale strains that were significantly larger than the macroscale strains. This suggests that origins of damage mechanisms may initiate within the MTJ, demonstrating the utility of micromechanical models in the study of damage initiation. The FE models predicted the experimentally

measured deflection of the A-bands of muscle fibers. Although not a direct validation of the 2D strains within the unit cell, this validation provides evidence of the accuracy of the FE simulations. By creating micromechanical FE simulations driven by macroscopic loading, this study was able to utilize modeling as a means for investigating microscale strain concentrations, something that would have been difficult using experimental methods alone.

The aforementioned studies utilized 2D simulations. In our own research, we have used 3D micromechanical FE models to study structure–function relationships in tendon and ligament tissue [133]. The aim of this research was to examine how fibril organization contributes to the elastic volumetric response. The volumetric response is quantified using the Poisson's ratio in linear theory and the Poisson's function in nonlinear theory. Experimentally observed Poisson's ratios range from 1.0 to 3.0 for tendon and ligament [129, 139], yet the structural underpinnings for these large values are not known. It was hypothesized that a planar, crimped arrangement of fibrils would not account for these large Poisson's ratios, while a helical organization of fibrils would.

To test this hypothesis, 3D unit cells were created that explicitly modeled collagen fibrils embedded within a matrix material (Fig. 8.11, top). The fibrils were given crimped, helical, and combined crimped with a superhelical organization (Fig. 8.11, top). The models were given periodic boundary conditions and subjected to simulated tensile loading in the fiber direction, which yielded a homogenized macroscale stress–strain response and a homogenized Poisson's function. For a subset of models, tensile strains of 8 % were applied and the nonlinear stress–strain response and the Poisson's function were obtained (Fig. 8.10, bottom). For all other models, small strains (0.5 %) were applied and homogenized Poisson's ratios were obtained.

Models with planar crimp (both with and without a helical twist) could generate the classic nonlinear response, but only models with a helical twist could generate large Poisson's ratios (Fig. 8.11, bottom). This suggests that helical twisting of fibrils (which has been observed histologically [247, 248]) may contribute to the large experimentally measured Poisson's ratios. A parametric study which varied crimp angle, helical twist, the number of fibrils, and the stiffness of the fibrils and matrix suggested that the large Poisson's ratios were predicted across a range of physiologically relevant values for the these parameters. This study highlights the utility of homogenized micromechanical models in testing structure function based hypothesis that are otherwise difficult to address. Furthermore, it demonstrates the use of 3D until cells with a nonrectangular cross section for the use of nonlinear homogenization.

In the previously discussed studies, boundary conditions on the micromechanical model were applied a priori to the microscale models. In a recent study, micromechanical models were combined with a macroscale simulation to solve the localization problem [249]. In a localization problem, a macroscale deformation (generally computed from a continuum-based FE simulation) is applied to an RVE, which is then solved in order to obtain the microscale stress and strain [211]. In this study, an analytically based homogenization was used as the constitutive model for a macroscopic FE simulation. Briefly, the analytical homogenization modeled

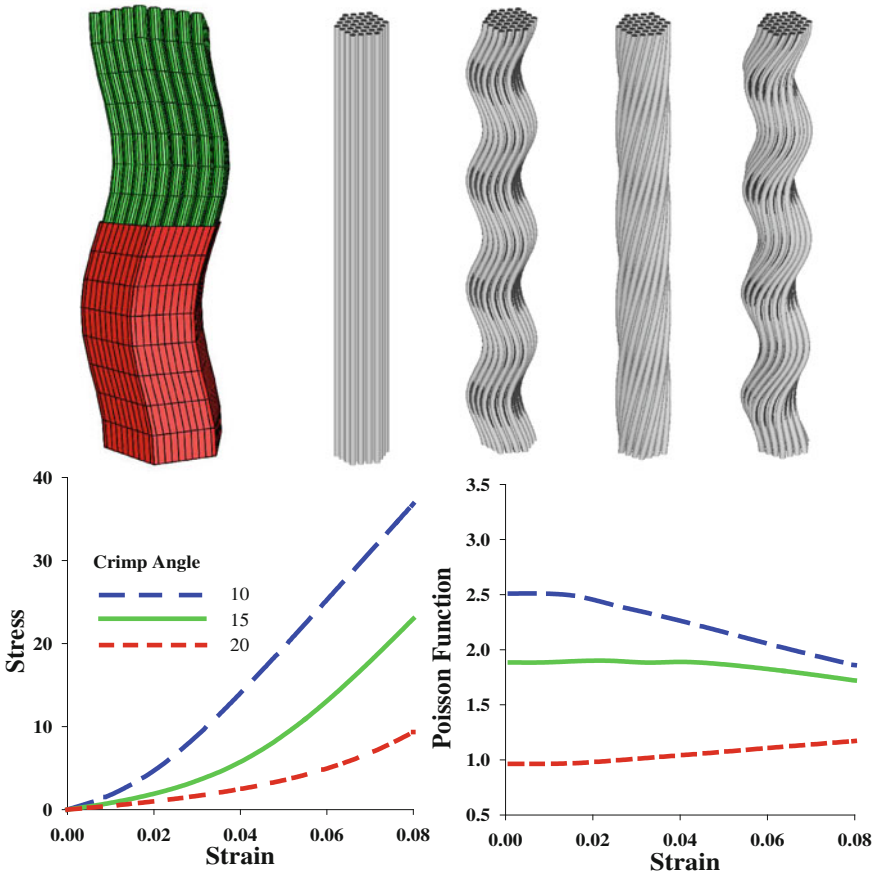


**Fig. 8.11** 3D micromechanical models with crimped and helical fiber organization [133]. *Top left*—a micromechanical FE model shows fibrils (*green*) embedded within the matrix material (*red*). *Top right*—straight, crimped, helical, and helically crimped fibril organizations were modeled. *Bottom Left*—Crimped models were able to reproduce both the toe and linear regions typical for tensile loading of tendon. *Bottom right*—Crimped models with a constant helical pitch predicted both the nonlinear stress–strain behavior and the large, nonlinear Poisson's function

collagen cross-links at the nanoscale and collagen fiber uncrimping at the microscale to specify a macroscopic continuum response. The homogenization was not based on an explicit microstructural organization, therefore no microscale strains were computed. A macroscale cube was subjected to a tensile loading (Fig. 8.12, left), which yielded a macroscale deformation within each element. This macroscale deformation from an element in the interior of the macroscale mesh was applied to a microscale RVE (Fig. 8.12, right), which was solved using an FE simulation. The microscale FE results revealed a heterogeneous distribution of stress and strain at the microscale. Although this study was primarily the presentation of a new method, it demonstrates

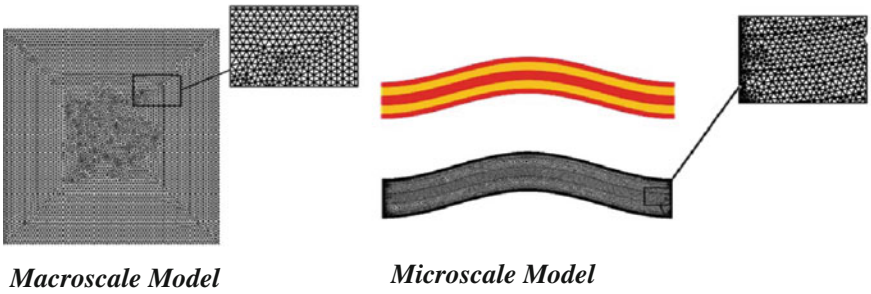


**Fig. 8.12** Microscale stress and strain localization of tendon [249]. A macroscale model consisting of a cube of tendon tissue (mesh shown on *Left*) was subjected to simulated loading and the macroscale deformation was computed. This deformation was then applied to the microscale model (*Right*). The microscale model consisted of fibers (shown on the *upper right* in *red*) connected via an interfiber matrix (shown in *yellow*). A close-up of the macroscopic and microscopic model mesh is shown in the breakout boxes. Figure adapted from [249, 250]

the utility of micromechanical models in solving the localization problem by applying the results of a macroscale simulation to a microscale RVE.

The aforementioned models were limited to quasistatic elastic simulations only. However, models that can incorporate the time dependence and biphasic nature of these tissues are desirable. In one study, a macroscopic biphasic FE model was combined with a microscopic biphasic FE model in order to examine the link between macroscale loading and microscale mechanotransduction [22]. To facilitate this, a macroscopic nonlinear biphasic model of a rat tail tendon fascicle was first solved. The macroscopic model utilized nonlinear springs to represent the transversely isotropic symmetry and nonlinear stress–strain behavior of tendon fascicles (Fig. 8.13, left). The springs were embedded in a porous matrix that had a transversely isotropic porosity. The model was subjected to uniaxial loading under a constant strain rate, and the computationally obtained macroscale stress–strain curve was validated against experimental stress–strain data of rat tail tendon fascicles. The deformation and fluid flux obtained from this model was then used to generate boundary conditions for the microscale model, which featured an ovoid shaped fibroblast aligned with the collagen matrix (Fig. 8.13, right). Finally, the predicted microscale fluid shear and microscale cell membrane deformation was correlated to collagenase mRNA levels that were experimentally measured in rat tail tendon fascicles. Briefly, fresh rat tail tendon fascicles were subjected to loading scenarios identical to those applied to the simulations. Four loading scenarios were utilized, including low strain, high strain, low strain rate, and high strain rate. After each experiment, collagenase mRNA levels (MMP-13) were measured using real time quantitative PCR.

The macroscale models predicted a stress–strain response that was in good agreement with experimentally measured values. The microscale models predicted significant cell membrane strains and fluid shear stress on the embedded cell for the high strain rate and large strain models. The strains and shear stress correlated to a decreased expression of mRNA for collagenase. Experimentally, it can be

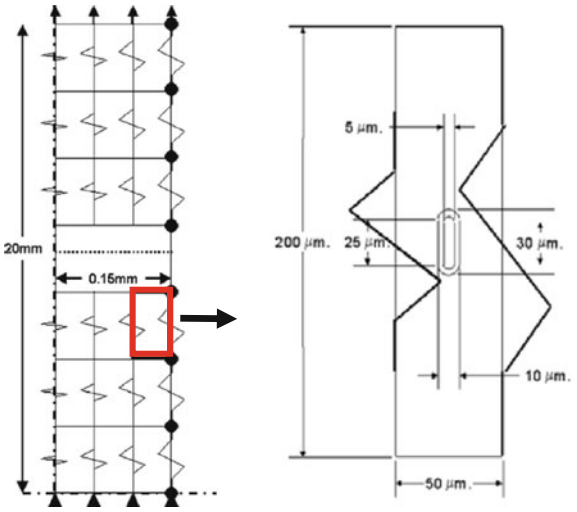


**Fig. 8.13** Two level-biphasic simulation of a tendon fascicle [22]. A biphasic axisymmetric macroscale model was created that contained nonlinear springs (mesh, springs, and model dimensions shown on *left*). The resulting strains and fluid flux was applied to a microscale model (*red box* on the *left* and shown on the *right*) that contained nonlinear springs and an ovoid shaped fibroblast. Figure adapted from [22]

concluded that decreased loading results in increased collagenase activity. By utilizing a computational micromechanical model, estimates of fluid shear stress on fibroblasts as well as cell membrane strains were able to be correlated to these experimental results. No tractable experimental methods currently have been proposed for obtaining microscale values of this sort, highlighting the important role that such modeling studies can play in extending our understanding of mechanotransduction within tendon tissue.

### *8.4.2 1st Order FE$^2$ Methods*

The aforementioned micromechanical models report both macroscale and microscale measures, but are limited to a specific set of loading conditions. A more general approach is offered by the 1st order FE$^2$ homogenization method described in Sect. 4.5. To date, no FE$^2$ models have been proposed for the simulation of ligament and tendon. However, an FE$^2$ approach has been developed and applied to model collagen hydrogels, which have characteristics in common with connective tissues [251–253]. In this research, FE$^2$ models were made of type I collagen gels that were molded into a cruciform shape. The gels were seeded with fibroblasts and

were allowed to undergo cell-mediated compaction of the fibril network. The gels were subjected to biaxial testing and the macroscopic stress and strain was measured. Additionally, polarametric fiber alignment imaging (PFAI) was used to measure fibril orientations during testing. A quarter symmetric macroscopic FE model was constructed that mimicked the geometry and loading conditions of the experimentally tested cruciform gels. The fibril orientation (e.g., the angular distribution of fibrils) measured in the reference position was used in order to generate 3D RVE models that consisted of beam elements, which represented collagen fibrils within the gel. A constitutive model specific to collagen fibrils was developed for use in the RVEs. The macroscopic FE model utilized an $FE^2$ methodology described in Sect. 4.5, whereby the RVE homogenization was utilized as the constitutive model for the macroscopic simulation. The results of the FE simulations generated both macroscopic stress and strain as well as microscopic stress and strain within the fibril network. The FE predicted principle angles for fiber orientation were extracted from the microscale RVE simulations and compared to the experimentally obtained principle angles (via PFAI). There was good agreement between the predicted and measured orientation of the fibrillar network, which provided validation of the methodology. The microscale RVE simulations revealed realignment of the fibrillar network with applied strain. A considerable percentage of the fibrils were subjected to compressive buckling, revealing microscale inhomogeneity in response to a homogenous macroscale deformation. Collagen hydrogels are substantially different from tendon and ligament; however, this same microscale heterogeneity has been observed in tendon fascicles [126] (refer to Sects. 1.7 and 1.8). Although not directly applicable to tendon and ligament, this study provides a template for how first order $FE^2$ methodologies could be applied to connective tissues such as tendon and ligament.

### *8.4.3 Multiscale Model Validation*

Validation of computational models is fundamentally important if the models are to be interpreted in a meaningful way [185, 186]. Validation of macroscale computational models of ligaments and tendons consist of comparing macroscale FE simulations to experimentally measured metrics such as joint reactions forces and in situ tissue strains, with a number of examples being present in the literature (e.g., [32, 120]). Validation of multiscale models proceeds in a similar model, but ideally, experimental validation would occur at each scale level simulated (e.g., the macroscale and microscale). In a number of the aforementioned studies, validation of the mechanical simulations were performed at a single-scale level (e.g., at the micro level for the unit cells of the myotendinous junction [224], and at the macro level for the biphasic tendon model [22]). To our knowledge, only one model relevant to tendons and ligaments has been validated at two scale levels [251]. This study, described in the preceding section, validated macroscale results via stress–strain data and validated microscale results via polarametric fiber alignment imaging.

Because of the important role validation plays in interpreting the results of computational studies, it is desirable to develop multiscale simulation strategies and experimental validation methods concurrently. Although macroscale validation methods have been described, microscale validation methods are still in need of improvement and development. In order to validate microscale models, data regarding stress and strain at lower scale levels (e.g., within fascicles, fibers and fibrils) must be obtained. One possible route involves isolating and mechanically testing individual tissue constituents, such as those described in Sects. 1.6–1.9. However, such methods have yielded widely variable results, likely due to the difficulty in consistently isolating substructures without causing tissue damage. Microscopic imaging studies, such as the confocal studies described in Sect. 1.8, provide considerable promise for use in validation of microscale models. However, the highly inhomogeneous strain fields and the complex microscale fiber structure make this a challenging starting point [124, 126, 127]. In order to address these challenges, our lab has developed a surrogate material for use as a physical model to aid in the development of multiscale modeling and validation methods [254]. A physical model reduces the number of uncontrolled variables related to the structural organization of ligaments and tendons. To create the physical surrogates, dense (∼25 % collage/wt), extruded collagen fibers were embedded within a collagen gel matrix (∼0.5 % collagen/wt). Surrogates served as physical models to emulate features of ligament and tendon tissuein a controlled and reproducible manner. Two different colors of fluorescent beads were embedded in the fibers and gel matrix (Fig. 8.14, top left) for use as microscopic fiducial markers. 3D micromechanical FE models of the surrogates were then constructed (Fig. 8.14, middle-left and bottom). A constitutive model based on a continuous elliptical fiber distribution was used to describe the mechanical behavior of the collagen gel and embedded fibers [255]. This constitutive model emulated the reorganization of fibrils with applied strain. The model was curve fit to tensile testing data for isolated gel and extruded fiber samples and was found to accurately model both the uniaxial stress–strain behavior and the 2D strain behavior (i.e., the nonlinear Poisson's function). Micromechanical FE models were subjected to uniaxial strain, and the macroscale and microscale stress and 2D strain were determined. FEBio was used for all analysis (http://www.febio.org) [210]. To validate the FE models, the physical surrogates were subjected to tensile loading in a custom testing apparatus on an inverted confocal microscope. Confocal images were acquired at 6 strain increments at both 4X and 10X, while force was measured simultaneously. Texture correlation was used to measure strain at the macroscale and to measure strain within the fibers and strain in the interfiber matrix at the microscale [256].

The microscopic 2D strains were inhomogeneous, and the macroscopic 2D strain was not representative of the microscopic 2D strain (Fig. 8.14, right). The magnitude of the transverse strain in the fibers greatly exceeded the macroscopic transverse strain, while the magnitude of the transverse matrix strain was significantly less than the macroscopic strain. The macroscopically measured Poisson's ratio was $1.72 \pm 0.26$, which is comparable to experimentally measured values for tendon and ligament [129, 139]. The micromechanical FE model was able to simultaneously predict the macroscopic stress–strain behavior and the 2D macroscale and microscale

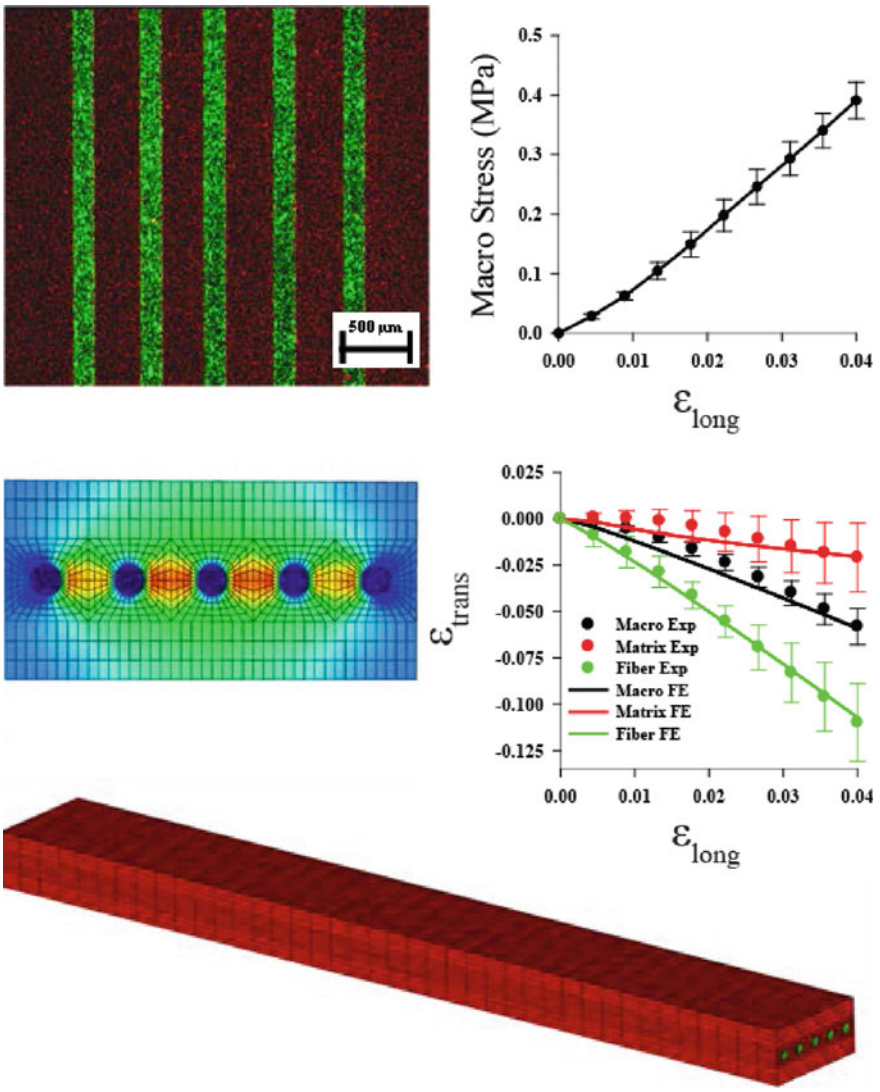


**Fig. 8.14** Multiscale validation of a micromechanical FE model. (*Upper Left*) A dual channel 4X confocal image of a collagen surrogate construct shows the red fluorescent beads in the gel matrix and the green fluorescent beads in the fiber that were used for microscopic and macroscopic strain measurements. (*Upper Right*) Micromechanical FE model stress–strain predictions were in excellent agreement with the experimental data ($\varepsilon_{\text{long}}$ denotes strain in the testing direction, which was parallel to the fibers). (*Middle Left*) The constrained surrogate model displayed considerable heterogeneity in transverse strain ($\varepsilon_{\text{trans}}$). (*Middle Right*) Microscopic and macroscopic strain measurement results show that the macroscopic transverse strain (*black line*) was not representative of the microscopic fiber strain (*green line*) or matrix strain (*red line*). For all strain measures, the FE model (*solid lines*) was in excellent agreement with the experimental data (*solid circles*). The error bars represent the standard deviation computed for all samples. (*Bottom*) Micromechanical FE model of the surrogate. *Green* elements represent the fibers and red elements represent the gel matrix

strains (Fig. 8.14, right). The predicted macroscopic stress and macroscopic transverse strain closely matched the experimentally measured values with normalized root mean square (NRMSE) values of 0.015 and 0.085, respectively. The predicted microscopic transverse fiber strain was closely matched by the experimentally measured values (NRMSE = 0.018), while predictions for the microscopic transverse matrix strain were reasonable but not as accurate (NRMSE = 0.190). When simulations were performed using coefficients that varied by a single standard deviation, all of the predictions were closely bounded by this uncertainty. A sensitivity study was then performed, in which the interfiber spacing and the interfiber matrix material properties were varied.

The results of this work indicate that the micromechanical model was able to accurately predict the strains at both the macroscopic and microscopic level, demonstrating the utility of this approach for the study of fibrous biological composites. The use of physical surrogate materials provides a means for developing and validating more complex and physiologically relevant micromechanical and multiscale mechanical models. This study illustrates the feasibility of simultaneous validation at macro- and micro-scales that could be extended to the validation of micromechanical or $FE^2$ models of nativeligament or tendon [257, 258].

## 8.5 Open Questions

Applications of multiscale mechanical modeling to the study of the hierarchical mechanical behavior of ligaments and tendons are just beginning to surface. Major questions remain about which scales in the tissue organization are most important to represent in a mechanical multiscale model, and as discussed above, whether these scales present sufficient separation to allow use of 1st order homogenization. This area represents the most immediate need in the field. As discussed in this chapter, validation of multiscale models remains difficult, and new approaches are needed to address this difficulty. Once these technical issues are resolved, we can begin to address a number of interesting and physiologically relevant questions regarding force transfer between scales, and we can study alterations in force transfer due to structural changes at different levels.

Although the majority of the most relevant questions regarding multiscale mechanics of connective tissues relate to force transfer at the level of the collagen fibril and higher, there are some questions that will require coupling to molecular level models to address. There are methodological and computational challenges associated with coupling molecular models to multiscale continuum and/or micromechanical models that will need to be addressed, and most of the challenges are not unique to multiscale modeling of ligaments and tendons.

Validated multiscale models can be extended in the future to include capabilities for modeling biophysical aspects of cellular processes, including mechanotransduction. A natural framework for this is the law of mass action, which allows modeling of receptor-ligand binding and chemical reaction kinetics. The FEBio software suite

has recently been expanded to include these capabilities [259]. Further enhancements can include the incorporation of growth and remodeling, diffusive processes, and even interaction with the microvasculature.

In the future, multiscale models of ligaments and tendons offer many possible applications. Perhaps the most immediate need, as detailed in this chapter, is the investigation of structure and function across physical scales as it related to mechanics. Additional lines of inquiry related to structure–function relationships include the role of different noncollagenous constituents such as elastin [168] and the small leucine-rich PGs [102, 106, 107, 176, 177]. Once multiscale models with the major structural features and components have been constructed and validated, they offer the opportunity to provide substantial insight into the mechanical and biological processes associated with injury, healing, immobilization, optimization of treatment regimens, and the engineering of replacement tissues.

## References

1. Banos CC, Thomas AH, Kuo CK. Collagen fibrillogenesis in tendon development: current models and regulation of fibril assembly. Birth Defects Res C Embryo Today. 2008;84(3):228–244.
2. Birk DE, Trelstad RL. Extracellular compartments in tendon morphogenesis: collagen fibril, bundle, and macroaggregate formation. J Cell Biol. 1986;103(1):231–240.
3. Birk DE, Zycband EI, Woodruff S, Winkelmann DA, Trelstad RL. Collagen fibrillogenesis in situ: fibril segments become long fibrils as the developing tendon matures. Dev Dyn. 1997;208(3):291–298.
4. Chen CS. Mechanotransduction - a field pulling together? J Cell Sci. 2008;121(Pt 20):3285–3292. doi:10.1242/jcs.023507.
5. Sharir A, Zelzer E. Tendon homeostasis: the right pull. Curr Biol. 2011;21(12):R472–R474. doi:10.1016/j.cub.2011.05.025.
6. Wang JH. Mechanobiology of tendon. J Biomech. 2006;39(9):1563–1582. doi:10.1016/j.jbiomech.2005.05.011.
7. Wang JH, Guo Q, Li B. Tendon biomechanics and mechanobiology-a minireview of basic concepts and recent advancements. J Hand Ther. 2012;25(2):133–140; quiz 41. doi:10.1016/j.jht.2011.07.004.
8. Chiquet M, Gelman L, Lutz R, Maier S. From mechanotransduction to extracellular matrix gene expression in fibroblasts. Biochim Biophys Acta. 2009;1793(5):911–920. doi:10.1016/j.bbamcr.2009.01.012.
9. Rees JD, Stride M, Scott A. Tendons - time to revisit inflammation. Br J Sports Med. 2013. doi:10.1136/bjsports-2012-091957.
10. Kannus P. Structure of the tendon connective tissue. Scand J Med Sci Sports. 2000;10(6):312–320.
11. Kastelic J, Galeski A, Baer E. The multicomposite structure of tendon. Connect Tissue Res. 1978;6(1):11–23.
12. Royce PM, Steinmann B. Connective Tissue and Its Heritable Disorders: Molecular, Genetic, and Medical Aspects. 2nd Edition ed. New York: John Wiley and Sons; 2002.
13. Tsipouras P, Ramirez F. Genetic disorders of collagen. Journal of medical genetics. 1987;24(1):2–8.
14. Glazebrook MA, Wright JR, Jr., Langman M, Stanish WD, Lee JM. Histological analysis of achilles tendons in an overuse rat model. J Orthop Res. 2008;26(6):840–846. doi:10.1002/jor.20546.

15. Kongsgaard M, Qvortrup K, Larsen J, Aagaard P, Doessing S, Hansen P et al. Fibril morphology and tendon mechanical properties in patellar tendinopathy: effects of heavy slow resistance training. Am J Sports Med. 2010;38(4):749–756. doi:10.1177/0363546509350915.
16. Nakama LH, King KB, Abrahamsson S, Rempel DM. Evidence of tendon microtears due to cyclical loading in an in vivo tendinopathy model. J Orthop Res. 2005;23(5):1199–1205. doi:10.1016/j.orthres.2005.03.006.
17. Fredberg U, Stengaard-Pedersen K. Chronic tendinopathy tissue pathology, pain mechanisms, and etiology with a special focus on inflammation. Scand J Med Sci Sports. 2008;18(1):3–15. doi:10.1111/j.1600-0838.2007.00746.x.
18. Maffulli N, Khan KM, Puddu G. Overuse tendon conditions: time to change a confusing terminology. Arthroscopy. 1998;14(8):840–843.
19. Sharma P, Maffulli N. Tendon injury and tendinopathy: healing and repair. The Journal of Bone and Joint Surgery (American Volume). 2005;87(1):187–202. doi:10.2106/JBJS.D.01850.
20. Bunata RE, Brown DS, Capelo R. Anatomic factors related to the cause of tennis elbow. J Bone Joint Surg Am. 2007;89(9):1955–1963. doi:10.2106/jbjs.f.00727.
21. Beynnon BD, Shultz SJ. Anatomic alignment, menstrual cycle phase, and the risk of anterior cruciate ligament injury. J Athl Train. 2008;43(5):541–542. doi:10.4085/1062-6050-43.5.541.
22. Lavagnino M, Arnoczky SP, Kepich E, Caballero O, Haut RC. A finite element model predicts the mechanotransduction response of tendon cells to cyclic tensile loading. Biomech Model Mechanobiol. 2008;7(5):405–416.
23. Parkinson J, Kadler KE, Brass A. Simple physical model of collagen fibrillogenesis based on diffusion limited aggregation. J Mol Biol. 1995;247(4):823–831. doi:10.1006/jmbi.1994.0182.
24. Ahmed AM, Burke DL, Duncan NA, Chan KH. Ligament tension pattern in the flexed knee in combined passive anterior translation and axial rotation. Journal of Orthopaedic Research. 1992;10(6):854–867.
25. Ahmed AM, Hyder A, Burke DL, Chan KH. In vitro ligament tension pattern in the flexed knee in passive loading. J Orthop Res. 1987;5(2):217–230.
26. Bach JM, Hull ML, Patterson HA. Direct measurement of strain in the posterolateral bundle of the anterior cruciate ligament. J Biomech. 1997;30(3):281–283.
27. Berns GS, Hull ML, Patterson HA. Strain in the anteromedial bundle of the anterior cruciate ligament under combination loading. J Orthop Res. 1992;10(2):167–176.
28. Blankevoort L, Kuiper JH, Huiskes R, Grootenboer HJ. Articular contact in a three-dimensional model of the knee. Journal of Biomechanics. 1991;24(11):1019–1031.
29. Ellis BJ, Lujan TJ, Dalton MS, Weiss JA. Medial collateral ligament insertion site and contact forces in the ACL-deficient knee. Journal of orthopaedic research : official publication of the Orthopaedic Research Society. 2006;24(4):800–810. doi:10.1002/jor.20102.
30. Butler DL, Noyes FR, Grood ES. Ligamentous restraints to anterior-posterior drawer in the human knee. Journal of Bone and Joint Surgery (Am). 1980;62:259–270.
31. Daniel DM, Akeson WH, O'Connor JJ. Knee Ligaments: Structure, Function, Injury and Repair. New York: Raven Press; 1990.
32. Gardiner JC, Weiss JA. Subject-specific finite element analysis of the human medial collateral ligament during valgus knee loading. Journal of Orthopaedic Research. 2003;21:1098–1106.
33. Gardiner JC, Weiss JA, Rosenberg TD. Strain in the human medial collateral ligament during valgus loading of the knee. Clin Orthop. 2001;391:266–274.
34. Weiss JA, Gardiner JC. Computational modeling of ligament mechanics. Crit Rev Biomed Eng. 2001;29(3):303–371.
35. Woo SL-Y. Biomechanics of tendons and ligaments. Frontiers in Biomechanics. New York 1986. p. 180–195.
36. Woo SL-Y, An K-N, Arnoczky SP, Wayne JS, Fithian DC, Myers BS. Anatomy, Biology, and Biomechanics of Tendon, Ligament and Meniscus. In: Simon S, editor. Orthopaedic Basic Science. American Academy of Orthopaedic Surgeons; 1994. p. 47–74.
37. Woo SL-Y, Weiss JA, MacKenna DA. Biomechanics and morphology of the medial collateral and anterior cruciate ligaments. In: Mow VaR, A and Woo, SL-Y, editor. Biomechanics of Diarthrodial Joints, Volume 1. 1990. p. 63–103.

38. Debski RE, Weiss JA, Newman WJ, Moore SM, McMahon PJ. In-situ force, stress and strain distribution in the glenohumeral capsule. Journal of Shoulder and Elbow Surgery. 2003;In Review.
39. Debski RE, Weiss JA, Newman WJ, Moore SM, McMahon PJ. Stress and strain in the anterior band of the inferior glenohumeral ligament during a simulated clinical examination. Journal of shoulder and elbow surgery/American Shoulder and Elbow Surgeons [et al]. 2005;14(1 Suppl S):24S–31S. doi:10.1016/j.jse.2004.10.003.
40. Debski RE, Wong EK, Woo SL, Sakane M, Fu FH, Warner JJ. In situ force distribution in the glenohumeral joint capsule during anterior-posterior loading. J Orthop Res. 1999;17(5):769–776.
41. Drury NJ, Ellis BJ, Weiss JA, McMahon PJ, Debski RE. The impact of glenoid labrum thickness and modulus on labrum and glenohumeral capsule function. Journal of biomechanical engineering. 2010;132(12):121003. doi:10.1115/1.4002622.
42. Drury NJ, Ellis BJ, Weiss JA, McMahon PJ, Debski RE. Finding consistent strain distributions in the glenohumeral capsule between two subjects: implications for development of physical examinations. Journal of biomechanics. 2011;44(4):607–613. doi:10.1016/j.jbiomech.2010.11.018.
43. Ellis BJ, Debski RE, Moore SM, McMahon PJ, Weiss JA. Methodology and sensitivity studies for finite element modeling of the inferior glenohumeral ligament complex. Journal of biomechanics. 2007;40(3):603–612. doi:10.1016/j.jbiomech.2006.01.024.
44. Ellis BJ, Drury NJ, Moore SM, McMahon PJ, Weiss JA, Debski RE. Finite element modelling of the glenohumeral capsule can help assess the tested region during a clinical exam. Computer methods in biomechanics and biomedical engineering. 2010;13(3):413–418. doi:10.1080/10255840903317378.
45. Moore SM, Ellis B, Weiss JA, McMahon PJ, Debski RE. The glenohumeral capsule should be evaluated as a sheet of fibrous tissue: a validated finite element model. Annals of biomedical engineering. 2010;38(1):66–76. doi:10.1007/s10439-009-9834-7.
46. Abdel-Rahman E. Three-dimensional dynamic anatomically based model of the human tibiofemoral joint [Ph.D.]. Toledo: University of Toledo; 1995.
47. Woo SL-Y, Weiss JA, Gomez MA, Hawkins DA. Measurement of changes in ligament tension with knee motion and skeletal maturation. J Biomech Eng. 1990;112(1):46–51.
48. Cooper RR, Misol S. Tendon and ligament insertion. A light and electron microscopic study. Journal of Bone and Joint Surgery (Am). 1970;52:1–20.
49. Benjamin M, Evans EJ, Copp L. The histology of tendon attachments to bone in man. Journal of Anatomy. 1986;149:89–100.
50. Batson EL, Paramour RJ, Smith TJ, Birch HL, Patterson-Kane JC, Goodship AE. Are the material properties and matrix composition of equine flexor and extensor tendons determined by their functions? Equine veterinary journal. 2003;35(3):314–318.
51. Butler DL, Kay MD, Stouffer DC. Comparison of material properties in fascicle-bone units from human patellar tendon and knee ligaments. Journal of biomechanics. 1986;19(6):425–432.
52. Cui L, Maas H, Perreault EJ, Sandercock TG. In situ estimation of tendon material properties: differences between muscles of the feline hindlimb. Journal of biomechanics. 2009;42(6):679–685. doi:10.1016/j.jbiomech.2009.01.022.
53. Fukunaga T, Kubo K, Kawakami Y, Fukashiro S, Kanehisa H, Maganaris CN. In vivo behaviour of human muscle tendon during walking. Proceedings Biological sciences / The Royal Society. 2001;268(1464):229–233. doi:10.1098/rspb.2000.1361.
54. Heinemeier KM, Kjaer M. In vivo investigation of tendon responses to mechanical loading. Journal of musculoskeletal & neuronal interactions. 2011;11(2):115–123.
55. Ishikawa M, Komi PV, Grey MJ, Lepola V, Bruggemann GP. Muscle-tendon interaction and elastic energy usage in human walking. Journal of applied physiology. 2005;99(2):603–608. doi:10.1152/japplphysiol.00189.2005.
56. Lichtwark GA, Wilson AM. In vivo mechanical properties of the human Achilles tendon during one-legged hopping. The Journal of experimental biology. 2005;208(Pt 24):4715–4725. doi:10.1242/jeb.01950.

57. Maganaris CN, Narici MV, Maffulli N. Biomechanics of the Achilles tendon. Disability and rehabilitation. 2008;30(20–22):1542–1547. doi:10.1080/09638280701785494.
58. Malvankar S, Khan WS. Evolution of the Achilles tendon: The athlete's Achilles heel? Foot. 2011;21(4):193–197. doi:10.1016/j.foot.2011.08.004.
59. Shadwick RE. Elastic energy storage in tendons: mechanical differences related to function and age. Journal of applied physiology. 1990;68(3):1033–1040.
60. Jung HJ, Fisher MB, Woo SL. Role of biomechanics in the understanding of normal, injured, and healing ligaments and tendons. Sports medicine, arthroscopy, rehabilitation, therapy & technology : SMARTT. 2009;1(1):9. doi:10.1186/1758-2555-1-9.
61. Payne RC, Crompton RH, Isler K, Savage R, Vereecke EE, Gunther MM et al. Morphological analysis of the hindlimb in apes and humans. I. Muscle architecture. Journal of anatomy. 2006;208(6):709–724. doi:10.1111/j.1469-7580.2006.00563.x.
62. Pollock CM, Shadwick RE. Relationship between body mass and biomechanical properties of limb tendons in adult mammals. The American journal of physiology. 1994;266(3 Pt 2):R1016–R1021.
63. Magnusson SP, Narici MV, Maganaris CN, Kjaer M. Human tendon behaviour and adaptation, in vivo. The Journal of physiology. 2008;586(1):71–81. doi:10.1113/jphysiol.2007.139105.
64. Birch HL. Tendon matrix composition and turnover in relation to functional requirements. International journal of experimental pathology. 2007;88(4):241–248. doi:10.1111/j.1365-2613.2007.00552.x.
65. Maganaris CN, Paul JP. Tensile properties of the in vivo human gastrocnemius tendon. Journal of biomechanics. 2002;35(12):1639–1646.
66. Pollock CM, Shadwick RE. Allometry of muscle, tendon, and elastic energy storage capacity in mammals. The American journal of physiology. 1994;266(3 Pt 2):R1022–R1031.
67. Thorpe CT, Udeze CP, Birch HL, Clegg PD, Screen HR. Specialization of tendon mechanical properties results from interfascicular differences. J R Soc Interface. 2012;9(76):3108–3117. doi:10.1098/rsif.2012.0362.
68. Benjamin M, Kaiser E, Milz S. Structure-function relationships in tendons: a review. J Anat. 2008;212(3):211–228. doi:10.1111/j.1469-7580.2008.00864.x.
69. Benjamin M, Ralphs JR. Tendons and ligaments-an overview. Histol Histopathol. 1997;12(4):1135–1144.
70. Karas V, Cole BJ, Wang VM. Role of biomechanics in rotator cuff pathology: North American perspective. Medicine and sport science. 2012;57:18–26. doi:10.1159/000328871.
71. Zajac FE. How musculotendon architecture and joint geometry affect the capacity of muscles to move and exert force on objects: a review with application to arm and forearm tendon transfer design. The Journal of hand surgery. 1992;17(5):799–804.
72. Robinson PS, Huang TF, Kazam E, Iozzo RV, Birk DE, Soslowsky LJ. Influence of decorin and biglycan on mechanical properties of multiple tendons in knockout mice. J Biomech Eng. 2005;127(1):181–185.
73. Maganaris CN, Narici MV, Almekinders LC, Maffulli N. Biomechanics and pathophysiology of overuse tendon injuries: ideas on insertional tendinopathy. Sports medicine. 2004;34(14):1005–1017.
74. Thomopoulos S, Hattersley G, Rosen V, Mertens M, Galatz L, Williams GR et al. The localized expression of extracellular matrix components in healing tendon insertion sites: an in situ hybridization study. Journal of orthopaedic research : official publication of the Orthopaedic Research Society. 2002;20(3):454–463. doi:10.1016/S0736-0266(01)00144-9.
75. Edelstein L, Thomas SJ, Soslowsky LJ. Rotator cuff tears: what have we learned from animal models? Journal of musculoskeletal & neuronal interactions. 2011;11(2):150–162.
76. Andarawis-Puri N, Kuntz AF, Ramsey ML, Soslowsky LJ. Effect of supraspinatus tendon repair technique on the infraspinatus tendon. Journal of biomechanical engineering. 2011;133(3):031008. doi:10.1115/1.4003326.
77. Wurgler-Hauri CC, Dourte LM, Baradet TC, Williams GR, Soslowsky LJ. Temporal expression of 8 growth factors in tendon-to-bone healing in a rat supraspinatus model. Journal of shoulder and elbow surgery / American Shoulder and Elbow Surgeons [et al]. 2007;16(5 Suppl):S198–203. doi:10.1016/j.jse.2007.04.003.

78. Gimbel JA, Van Kleunen JP, Lake SP, Williams GR, Soslowsky LJ. The role of repair tension on tendon to bone healing in an animal model of chronic rotator cuff tears. Journal of biomechanics. 2007;40(3):561–568. doi:10.1016/j.jbiomech.2006.02.010.
79. Gimbel JA, Van Kleunen JP, Williams GR, Thomopoulos S, Soslowsky LJ. Long durations of immobilization in the rat result in enhanced mechanical properties of the healing supraspinatus tendon insertion site. Journal of biomechanical engineering. 2007;129(3):400–404. doi:10.1115/1.2721075.
80. Yokota A, Gimbel JA, Williams GR, Soslowsky LJ. Supraspinatus tendon composition remains altered long after tendon detachment. Journal of shoulder and elbow surgery / American Shoulder and Elbow Surgeons [et al]. 2005;14(1 Suppl S):72S–78S. doi:10.1016/j.jse.2004.09.021.
81. Barton ER, Gimbel JA, Williams GR, Soslowsky LJ. Rat supraspinatus muscle atrophy after tendon detachment. Journal of orthopaedic research : official publication of the Orthopaedic Research Society. 2005;23(2):259–265. doi:10.1016/j.orthres.2004.08.018.
82. Gimbel JA, Mehta S, Van Kleunen JP, Williams GR, Soslowsky LJ. The tension required at repair to reappose the supraspinatus tendon to bone rapidly increases after injury. Clinical orthopaedics and related research. 2004(426):258–265.
83. Thomopoulos S, Williams GR, Gimbel JA, Favata M, Soslowsky LJ. Variation of biomechanical, structural, and compositional properties along the tendon to bone insertion site. J Orthop Res. 2003;21(3):413–419.
84. Kjaer M. Role of extracellular matrix in adaptation of tendon and skeletal muscle to mechanical loading. Physiol Rev. 2004;84(2):649–698. doi:10.1152/physrev.00031.2003.
85. Venturoni M, Gutsmann T, Fantner GE, Kindt JH, Hansma PK. Investigations into the polymorphism of rat tail tendon fibrils using atomic force microscopy. Biochem Biophys Res Commun. 2003;303(2):508–513.
86. Ottani V, Raspanti M, Ruggeri A. Collagen structure and functional implications. Micron. 2001;32(3):251–260.
87. Ottani V, Martini D, Franchi M, Ruggeri A, Raspanti M. Hierarchical structures in fibrillar collagens. Micron. 2002;33(7–8):587–596.
88. Vidal DC. Image analysis of tendon helical superstructure using interference and polarized light microscopy. Micron. 2003;34(8):423–432.
89. Starborg T, Lu Y, Huffman A, Holmes DF, Kadler KE. Electron microscope 3D reconstruction of branched collagen fibrils in vivo. Scand J Med Sci Sports. 2009;19(4):547–552. doi:10.1111/j.1600-0838.2009.00907.x.
90. Danylchuk KD, Finlay JB, Krcek JP. Microstructural organization of human and bovine cruciate ligaments. Clin Orthop Relat Res. 1978(131):294–298.
91. Jarvinen T, Jarvinen TL, Kannus P, Jozsa L, Jarvinen M. Collagen fibres of the spontaneously ruptured human tendons display decreased thickness and crimp angle. Journal of Orthopaedic Research. 2004;22(6):1303–1309.
92. Wang CJ, Walker PS, Wolf B. The effects of flexion and rotation on the length patterns of the ligaments of the knee. Journal of Biomechanics. 1973;6:587–596.
93. Hurschler C, Provenzano PP, Vanderby R, Jr. Scanning electron microscopic characterization of healing and normal rat ligament microstructure under slack and loaded conditions. Connect Tissue Res. 2003;44(2):59–68.
94. Niven H, Baer E, Hiltner A. Organization of collagen fibers in rat tail tendon at the optical microscope level. Coll Relat Res. 1982;2(2):131–142.
95. Haraldsson BT, Aagaard P, Qvortrup K, Bojsen-Moller J, Krogsgaard M, Koskinen S et al. Lateral force transmission between human tendon fascicles. Matrix Biol. 2008;27(2):86–95.
96. Smith KD, Vaughan-Thomas A, Spiller DG, Innes JF, Clegg PD, Comerford EJ. The organisation of elastin and fibrillins 1 and 2 in the cruciate ligament complex. J Anat. 2011;218(6):600–607. doi:10.1111/j.1469-7580.2011.01374.x.
97. Gotoh T, Murashige N, Yamashita K. Ultrastructural observations on the tendon sheath of the rat tail. J Electron Microsc (Tokyo). 1997;46(3):247–252.
98. Ilic MZ, Carter P, Tyndall A, Dudhia J, Handley CJ. Proteoglycans and catabolic products of proteoglycans present in ligament. Biochem J. 2005;385(Pt 2):381–388. doi:10.1042/bj20040844.

99. Lujan TJ, Dalton MS, Thompson BM, Ellis BJ, Weiss JA. Effect of ACL deficiency on MCL strains and joint kinematics. Journal of biomechanical engineering. 2007;129(3):386–392. doi:10.1115/1.2720915.
100. Lujan TJ, Underwood CJ, Jacobs NT, Weiss JA. Contribution of glycosaminoglycans to viscoelastic tensile behavior of human ligament. J Appl Physiol. 2009;106(2):423–431.
101. Neame PJ, Kay CJ, McQuillan DJ, Beales MP, Hassell JR. Independent modulation of collagen fibrillogenesis by decorin and lumican. Cell Mol Life Sci. 2000;57(5):859–863.
102. Lujan TJ, Underwood CJ, Henninger HB, Thompson BM, Weiss JA. Effect of dermatan sulfate glycosaminoglycans on the quasi-static material properties of the human medial collateral ligament. J Orthop Res. 2007;25(7):894–903. doi:10.1002/jor.20351.
103. Rosenbloom J. Elastin: Biosynthesis, structure, degradation, and role in disease processes. Connective Tissue Research. 1982;10:73–91.
104. Pins GD, Christiansen DL, Patel R, Silver FH. Self-assembly of collagen fibers. Influence of fibrillar alignment and decorin on mechanical properties. Biophys J. 1997;73(4):2164–2172.
105. Zhang G, Ezura Y, Chervoneva I, Robinson PS, Beason DP, Carine ET et al. Decorin regulates assembly of collagen fibrils and acquisition of biomechanical properties during tendon development. J Cell Biochem. 2006;98(6):1436–1449.
106. Henninger HB, Maas SA, Shepherd JH, Joshi S, Weiss JA. Transversely isotropic distribution of sulfated glycosaminoglycans in human medial collateral ligament: a quantitative analysis. J Struct Biol. 2009;165(3):176–183.
107. Henninger HB, Underwood CJ, Ateshian GA, Weiss JA. Effect of sulfated glycosaminoglycan digestion on the transverse permeability of medial collateral ligament. Journal of biomechanics. 2010;43(13):2567–2573. doi:10.1016/j.jbiomech.2010.05.012.
108. Black LD, Brewer KK, Morris SM, Schreiber BM, Toselli P, Nugent MA et al. Effects of elastase on the mechanical and failure properties of engineered elastin-rich matrices. J Appl Physiol. 2005;98(4):1434–1441.
109. Lanir Y. Structure-Strength Relationships in Mammalian Tendon. Biophysical Journal. 1978;24:541–554.
110. Nakagawa H, Mikawa Y, Watanabe R. Elastin in the human posterior longitudinal ligament and spinal dura. A histologic and biochemical study. Spine. 1994;19(19):2164–2169.
111. Uitto J. Biochemistry of the elastic fibers in normal connective tissues and its alterations in diseases. J Invest Dermatol. 1979;72(1):1–10.
112. Franchi M, Fini M, Quaranta M, De Pasquale V, Raspanti M, Giavaresi G et al. Crimp morphology in relaxed and stretched rat Achilles tendon. J Anat. 2007;210(1):1–7. doi:10.1111/j.1469-7580.2006.00666.x.
113. Amiel D, Frank C, Harwood F, Fronek J, Akeson W. Tendons and ligaments: a morphological and biochemical comparison. Journal of Orthopaedic Research. 1984;1(3):257–265.
114. Rumian AP, Wallace AL, Birch HL. Tendons and ligaments are anatomically distinct but overlap in molecular and morphological features-a comparative study in an ovine model. J Orthop Res. 2007;25(4):458–464.
115. Ciccone WJ, 2nd, Bratton DR, Weinstein DM, Elias JJ. Viscoelasticity and temperature variations decrease tension and stiffness of hamstring tendon grafts following anterior cruciate ligament reconstruction. The Journal of bone and joint surgery American volume. 2006;88(5):1071–1078. doi:10.2106/JBJS.E.00576.
116. Bonifasi-Lista C, Lake SP, Small MS, Weiss JA. Viscoelastic properties of the human medial collateral ligament under longitudinal, transverse and shear loading. J Orthop Res. 2005;23(1):67–76.
117. Lakes RS, Vanderby R. Interrelation of creep and relaxation: a modeling approach for ligament. Journal of Biomechanical Engineering. 1999;121(6):612–615.
118. Woo SL-Y. Mechanical properties of tendons and ligaments I. Quasi-static and nonlinear viscoelastic properties. Biorheology. 1982;19:385–396.
119. Cohen B, Lai WM, Mow VC. A transversely isotropic biphasic model for unconfined compression of growth plate and chondroepiphysis. J Biomech Eng. 1998;120(4):491–496.

120. Weiss JA, Gardiner JC, Ellis BJ, Lujan TJ, Phatak NS. Three-dimensional finite element modeling of ligaments: technical aspects. Medical engineering & physics. 2005;27(10):845–861. doi:10.1016/j.medengphy.2005.05.006.
121. Weiss JA, Maakestad BJ. Permeability of human medial collateral ligament in compression transverse to the collagen fiber direction. J Biomech. 2006;39(2):276–283.
122. Yin L, Elliott DM. A biphasic and transversely isotropic mechanical model for tendon: application to mouse tail fascicles in uniaxial tension. J Biomech. 2004;37(6):907–916.
123. Komolafe OA, Doehring TC. Fascicle-scale loading and failure behavior of the Achilles tendon. J Biomech Eng. 2010;132(2):021004. doi:10.1115/1.4000696.
124. Screen HR, Lee DA, Bader DL, Shelton JC. An investigation into the effects of the hierarchical structure of tendon fascicles on micromechanical properties. Proc Inst Mech Eng [H]. 2004;218(2):109–119.
125. Screen HR, Shelton JC, Chhaya VH, Kayser MV, Bader DL, Lee DA. The influence of noncollagenous matrix components on the micromechanical environment of tendon fascicles. Ann Biomed Eng. 2005;33(8):1090–1099. doi:10.1007/s10439-005-5777-9.
126. Screen HRC, Bader DL, Lee DA, Shelton JC. Local Strain Measurement within Tendon. Strain 2004. p. 157–163.
127. Screen HRC, Cheng VWT. The Micro-structural Strain Response of Tendon. Journal of Material Science 2007. p. 1–2.
128. Lafortune MA, Cavanagh PR, Sommer HJ, III, Kalenak A. Three-dimensional kinematics of the human knee during walking. J Biomechanics. 1992;25:347–357.
129. Lynch HA, Johannessen W, Wu JP, Jawa A, Elliott DM. Effect of fiber orientation and strain rate on the nonlinear uniaxial tensile material properties of tendon. Journal of biomechanical engineering. 2003;125(5):726–731.
130. Yamamoto E, Hayashi K, Yamamoto N. Effects of stress shielding on the transverse mechanical properties of rabbit patellar tendons. J Biomech Eng. 2000;122(6):608–614.
131. Weiss JA, Gardiner JC, Bonifasi-Lista C. Ligament material behavior is nonlinear, viscoelastic and rate-independent under shear loading. Journal of Biomechanics. 2002;35:943–950.
132. Weiss JA. A constitutive model and finite element representation for transversely isotropic soft tissues [Ph.D.]. Salt Lake City: University of Utah; 1994.
133. Reese SP, Maas SA, Weiss JA. Micromechanical models of helical superstructures in ligament and tendon fibers predict large Poisson's ratios. Journal of biomechanics. 2010;43(7):1394–1400. doi:10.1016/j.jbiomech.2010.01.004.
134. Lanir Y. Constitutive equations for fibrous connective tissues. Journal of Biomechanics. 1983;16(1):1–12.
135. Babuska I. The finite element method with Lagrangian multipliers. Num Math. 1973;20:179–192.
136. Woo SL-Y, Hollis JM, Adams DJ, Lyon RM, Takai S. Tensile properties of the human femur-anterior cruciate ligament-tibia complex. The effects of specimen age and orientation. Amer J Sports Med. 1991;19:217–225.
137. Yamamoto E, Hayashi K, Yamamoto N. Mechanical properties of collagen fascicles from the rabbit patellar tendon. J Biomech Eng. 1999;121(1):124–131.
138. Beatty MF, Stalnaker DO. The Poisson function of finite elasticity. Journal of applied mechanics 1986;53(4):807–813.
139. Hewitt J, Guilak F, Glisson R, Vail TP. Regional material properties of the human hip joint capsule ligaments. J Orthop Res. 2001;19(3):359–364.
140. Hannafin JA, Arnoczky SP. Effect of cyclic and static tensile loading on water content and solute diffusion in canine flexor tendons: an in vitro study. Journal of Orthopaedic Research. 1994;12:350–356.
141. Helmer KG, Nair G, Cannella M, Grigg P. Water movement in tendon in response to a repeated static tensile load using one-dimensional magnetic resonance imaging. J Biomech Eng. 2006;128(5):733–741.
142. Matsumoto H, Suda Y, Otani T, Niki Y, Seedhom BB, Fujikawa K. Roles of the anterior cruciate ligament and the medial collateral ligament in preventing valgus instability. Journal of Orthopaedic Science. 2001;6(1):28–32.

143. Defrate LE, van der Ven A, Boyer PJ, Gill TJ, Li G. The measurement of the variation in the surface strains of Achilles tendon grafts using imaging techniques. J Biomech. 2006;39(3):399–405. doi:10.1016/j.jbiomech.2004.12.021.
144. Lake SP, Miller KS, Elliott DM, Soslowsky LJ. Effect of fiber distribution and realignment on the nonlinear and inhomogeneous mechanical properties of human supraspinatus tendon under longitudinal tensile loading. J Orthop Res. 2009;27(12):1596–1602. doi:10.1002/jor.20938.
145. Doehring TC, Kahelin M, Vesely I. Direct measurement of nonuniform large deformations in soft tissues during uniaxial extension. J Biomech Eng. 2009;131(6):061001. doi:10.1115/1.3116155.
146. Mommersteeg TJ, Blankevoort L, Kooloos JG, Hendriks JC, Kauer JM, Huiskes R. Nonuniform distribution of collagen density in human knee ligaments. J Orthop Res. 1994;12(2):238–245.
147. Quapp KM, Weiss JA. Material characterization of human medial collateral ligament. J Biomech Eng. 1998;120:757–763.
148. Weiss JA, editor. Behavior of human medial collateral ligament in unconfined compression. Othopaedic Research Society 46th Annual Meeting; 2000 March 12–15; Orlando, FL: ORS.
149. Lakes RS. Viscoelastic Materials. New York, NY: Cambridge University Press; 2009.
150. Abramowitch SD, Clineff TD, Withrow JD, Papageorgiou CD, Woo SL. The quasilinear viscoelastic properties of the healing goat medial collateral ligament: an experimental & analytical approach. 23rd annual meeting of the American Society of Biomechanics. 1999.
151. Provenzano P, Lakes R, Keenan T, Vanderby R, Jr. Nonlinear ligament viscoelasticity. Ann Biomed Eng. 2001;29(10):908–914.
152. Thornton GM, Oliynyk A, Frank CB, Shrive NG. Ligament creep cannot be predicted from stress relaxation at low stresses: A biomechanical study of the rabbit medial collateral ligament. Journal of Orthopaedic Research. 1997;15:652–656.
153. Waggett AD, Ralphs JR, Kwan AP, Woodnutt D, Benjamin M. Characterization of collagens and proteoglycans at the insertion of the human Achilles tendon. Matrix Biol. 1998;16(8):457–470.
154. Reese SP, Weiss JA. Tendon fascicles exhibit a linear correlation between poisson's ratio and force during uniaxial stress relaxation. J Biomech Eng. 2013;135(3):34501. doi:10.1115/1.4023134.
155. Hansen KA, Weiss JA, Barton JK. Recruitment of Tendon Crimp With Applied Tensile Strain. ASME; 2002. p. 72.
156. Race A, Amis AA. The mechanical properties of the two bundles of the human posterior cruciate ligament. J Biomech. 1994;27(1):13–24.
157. Hirokawa S. An experimental study of the microstructures and mechanical properties of swine cruciate ligaments. JSME International Journal. 2003;46(4):1417–1425.
158. Atkinson TS, Ewers BJ, Haut RC. The tensile and stress relaxation responses of human patellar tendon varies with specimen cross-sectional area. J Biomech. 1999;32(9):907–914.
159. Miyazaki H, Kozaburo H. Tensile tests of collagen fibers obtained from the rabbit patellar tendon. Biomedical Microdevices. 1999;2(2):151–157.
160. van der Rijt JA, van der Werf KO, Bennink ML, Dijkstra PJ, Feijen J. Micromechanical testing of individual collagen fibrils. Macromol Biosci. 2006;6(9):697–702. doi:10.1002/mabi.200600063.
161. Wenger MP, Bozec L, Horton MA, Mesquida P. Mechanical properties of collagen fibrils. Biophys J. 2007;93(4):1255–1263.
162. Yang L, van der Werf KO, Fitie CF, Bennink ML, Dijkstra PJ, Feijen J. Mechanical properties of native and cross-linked type I collagen fibrils. Biophys J. 2008;94(6):2204–2211. doi:10.1529/biophysj.107.111013.
163. Yang L, van der Werf KO, Koopman BF, Subramaniam V, Bennink ML, Dijkstra PJ et al. Micromechanical bending of single collagen fibrils using atomic force microscopy. J Biomed Mater Res A. 2007;82(1):160–168. doi:10.1002/jbm.a.31127.
164. Svensson RB, Hassenkam T, Hansen P, Peter Magnusson S. Viscoelastic behavior of discrete human collagen fibrils. J Mech Behav Biomed Mater. 3(1):112–115.

165. Rigozzi S, Stemmer A, Muller R, Snedeker JG. Mechanical response of individual collagen fibrils in loaded tendon as measured by atomic force microscopy. J Struct Biol. 2011;176(1):9–15. doi:10.1016/j.jsb.2011.07.002.
166. Bozec L, Horton M. Topography and mechanical properties of single molecules of type I collagen using atomic force microscopy. Biophysical journal. 2005;88(6):4223–4231. doi:10.1529/biophysj.104.055228.
167. Sun YL, Luo ZP, Fertala A, An KN. Direct quantification of the flexibility of type I collagen monomer. Biochemical and biophysical research communications. 2002;295(2):382–386.
168. Henninger HB, Underwood CJ, Romney SJ, Davis GL, Weiss JA. Effect of elastin digestion on the quasi-static tensile response of medial collateral ligament. J Orthop Res. 2013;31(8):1226–1233. doi:10.1002/jor.22352.
169. Screen HR, Chhaya VH, Greenwald SE, Bader DL, Lee DA, Shelton JC. The influence of swelling and matrix degradation on the microstructural integrity of tendon. Acta Biomater. 2006;2(5):505–513. doi:10.1016/j.actbio.2006.05.008.
170. Fung DT, Wang VM, Andarawis-Puri N, Basta-Pljakic J, Li Y, Laudier DM et al. Early response to tendon fatigue damage accumulation in a novel in vivo model. J Biomech. 2010;43(2):274–279. doi:10.1016/j.jbiomech.2009.08.039.
171. Neviaser A, Andarawis-Puri N, Flatow E. Basic mechanisms of tendon fatigue damage. J Shoulder Elbow Surg. 2012;21(2):158–163. doi:10.1016/j.jse.2011.11.014.
172. Andarawis-Puri N, Flatow EL. Tendon fatigue in response to mechanical loading. J Musculoskelet Neuronal Interact. 2011;11(2):106–114.
173. Killian ML, Cavinatto L, Galatz LM, Thomopoulos S. The role of mechanobiology in tendon healing. J Shoulder Elbow Surg. 2012;21(2):228–237. doi:10.1016/j.jse.2011.11.002.
174. Fenwick SA, Hazleman BL, Riley GP. The vasculature and its role in the damaged and healing tendon. Arthritis Res. 2002;4(4):252–260.
175. Lavagnino M, Arnoczky SP, Frank K, Tian T. Collagen fibril diameter distribution does not reflect changes in the mechanical properties of in vitro stress-deprived tendons. J Biomech. 2005;38(1):69–75. doi:10.1016/j.jbiomech.2004.03.035.
176. Henninger HB, Lujan TJ, Underwood CJ, Weiss JA, editors. Distribution and mechanical implications of dermatan sulfate in human medial collateral ligament. ASME Summer Bioengineeing Conference,; 2006; Amelia Island, FL.
177. Henninger HB, Maas SA, Underwood CJ, Whitaker RT, Weiss JA. Spatial distribution and orientation of dermatan sulfate in human medial collateral ligament. J Struct Biol. 2007;158(1):33–45.
178. Scott JE. Collagen-proteoglycan interactions. Localization of proteoglycans in tendon by electron microscopy. The Biochemical journal. 1980;187(3):887–891.
179. Scott JE. Proteoglycan-fibrillar collagen interactions. Biochem J. 1988;252(2):313–323.
180. Scott JE. Proteoglycan-collagen interactions and sub-fibrillar structure in collagen fibrils: implications in the development and remodelling of connective tissues. Biochem Soc Trans. 1990;18(3):489–490.
181. Scott JE. Proteoglycan: collagen interactions in connective tissues. Ultrastructural, biochemical, functional and evolutionary aspects. Int J Biol Macromol. 1991;13(3):157–161.
182. Sasaki N, Shukunami N, Matsushima N, Izumi Y. Time-resolved X-ray diffraction from tendon collagen during creep using synchrotron radiation. J Biomech. 1999;32(3):285–292.
183. Buehler MJ, Wong SY. Entropic elasticity controls nanomechanics of single tropocollagen molecules. Biophys J. 2007;93(1):37–43. doi:10.1529/biophysj.106.102616.
184. Buehler MJ. Nature designs tough collagen: explaining the nanostructure of collagen fibrils. Proc Natl Acad Sci U S A. 2006;103(33):12285–12290. doi:10.1073/pnas.0603216103.
185. Anderson AE, Ellis BJ, Weiss JA. Verification, validation and sensitivity studies in computational biomechanics. Comput Methods Biomech Biomed Engin. 2007;10(3):171–184. doi:10.1080/10255840601160484.
186. Henninger HB, Reese SP, Anderson AE, Weiss JA. Validation of computational models in biomechanics. Proc Inst Mech Eng H. 2010;224(7):801–812.

187. Holzapfel GA. Nonlinear Solid Mechanics. Chichester, United Kingdom: John Wiley and Sons, Ltd; 2000.
188. Spencer AJM. Continuum Mechanics. New York, NY: Dover Publications; 1980.
189. Weiss JA, Maker BN, Govindjee S. Finite element implementation of incompressible, transversely isotropic hyperelasticity. Comp Meth Appl Mech Eng. 1996;135:107–128.
190. Funk JR, Hall GW, Crandall JR, Pilkey WD. Linear and quasi-linear viscoelastic characterization of ankle ligaments. J Biomech Eng. 2000;122(1):15–22.
191. Puso MA, Weiss JA. Finite element implementation of anisotropic quasilinear viscoelasticity. Journal of Biomechanical Engineering. 1998;120(1):62–70.
192. Elliott DM, Robinson PS, Gimbel JA, Sarver JJ, Abboud JA, Iozzo RV et al. Effect of altered matrix proteins on quasilinear viscoelastic properties in transgenic mouse tail tendons. Annals of biomedical engineering. 2003;31(5):599–605.
193. Pena E, Pena JA, Doblare M. On modelling nonlinear viscoelastic effects in ligaments. Journal of biomechanics. 2008;41(12):2659–2666. doi:10.1016/j.jbiomech.2008.06.019.
194. Lakes RS, Vanderby R. Interrelation of creep and relaxation: a modeling approach for ligaments. J Biomech Eng. 1999;121(6):612–615.
195. Provenzano PP, Lakes RS, Corr DT, R R, Jr. Application of nonlinear viscoelastic models to describe ligament behavior. Biomech Model Mechanobiol. 2002;1(1):45–57.
196. Puso MA, Weiss JA. Finite element implementation of anisotropic quasi-linear viscoelasticity using a discrete spectrum approximation. J Biomech Eng. 1998;120(1):62–70.
197. Funk JR, Hall GW, Crandall JR, Pilkey WD. Linear and quasi-linear viscoelastic characterization of ankle ligaments. Journal of biomechanical engineering. 2000;122(1):15–22.
198. Johnson GA, Tramaglini DM, Levine RE, Ohno K, Choi NY, Woo SL. Tensile and viscoelastic properties of human patellar tendon. Journal of orthopaedic research : official publication of the Orthopaedic Research Society. 1994;12(6):796–803. doi:10.1002/jor.1100120607.
199. Thomopoulos S, Williams GR, Soslowsky LJ. Tendon to bone healing: differences in biomechanical, structural, and compositional properties due to a range of activity levels. Journal of biomechanical engineering. 2003;125(1):106–113.
200. Provenzano P, Lakes R, Keenan T, Vanderby R, Jr. Nonlinear ligament viscoelasticity. Annals of biomedical engineering. 2001;29(10):908–914.
201. Thornton GM, Oliynyk A, Frank CB, Shrive NG. Ligament creep cannot be predicted from stress relaxation at low stress: a biomechanical study of the rabbit medial collateral ligament. Journal of orthopaedic research : official publication of the Orthopaedic Research Society. 1997;15(5):652–656. doi:10.1002/jor.1100150504.
202. Duenwald SE, Vanderby R, Jr., Lakes RS. Viscoelastic relaxation and recovery of tendon. Annals of biomedical engineering. 2009;37(6):1131–1140. doi:10.1007/s10439-009-9687-0.
203. Einat R, Yoram L. Recruitment viscoelasticity of the tendon. Journal of biomechanical engineering. 2009;131(11):111008. doi:10.1115/1.3212107.
204. Rausch MK, Reese S, Maas S, Weiss JA. Can poroelasticity predict the cyclic tensile viscoelastic behavior of ligament? Proc 55th Annual Meeting of the Orthopaedic Research Society. 2009.
205. Armstrong CG, Lai WM, Mow VC. An analysis of the unconfined compression of articular cartilage. J Biomech Eng. 1984;106(2):165–173.
206. Ateshian GA, Warden WH, Kim JJ, Grelsamer RP, Mow VC. Finite deformation biphasic material properties of bovine articular cartilage from confined compression experiments. J Biomech. 1997;30(11–12):1157–1164.
207. Huang CY, Soltz MA, Kopacz M, Mow VC, Ateshian GA. Experimental verification of the roles of intrinsic matrix viscoelasticity and tension-compression nonlinearity in the biphasic response of cartilage. J Biomech Eng. 2003;125(1):84–93.
208. Huang CY, Mow VC, Ateshian GA. The role of flow-independent viscoelasticity in the biphasic tensile and compressive responses of articular cartilage. J Biomech Eng. 2001;123(5):410–417.
209. Mak AF. Unconfined compression of hydrated viscoelastic tissues: a biphasic poroviscoelastic analysis. Biorheology. 1986;23(4):371–383.

210. Maas SA, Ellis BJ, Ateshian GA, Weiss JA. FEBio: finite elements for biomechanics. Journal of biomechanical engineering. 2012;134(1):011005. doi:10.1115/1.4005694.
211. Kanouté P, Boso D, Chaboche J, Schrefler B. Multiscale Methods for Composites: A Review. Archives of Computational Methods in Engineering. 2009;16(1):31–75. doi:10.1007/s11831-008-9028-8.
212. Geers MGD, Kouznetsova VG, Brekelmans WAM. Multi-scale computational homogenization: Trends and challenges. Jnl Comp Appl Math. 2010;234:2175–2182.
213. Suquet PM. Elements of homogenization theory for inelastic solid mechanics. In: Sanchez-Palencia E, Zaoui A, editors. Homogenization Techniques for Composite Media. Berlin: Springer; 1985.
214. Gitman IM, Askes H, Sluys LJ. Representative volume: Existence and size determination. Engineering Fracture Mechanics. 2007;74(16):2518–2534. doi:10.1016/j.engfracmech.2006.12.021.
215. Gusev AA. Representative volume element size for elastic composites: A numerical study. Journal of the Mechanics and Physics of Solids. 1997;45(9):1449–1459. doi:10.1016/s0022-5096(97)00016-1.
216. Kanit T, Forest S, Galliet I, Mounoury V, Jeulin D. Determination of the size of the representative volume element for random composites: statistical and numerical approach. International Journal of Solids and Structures. 40(13–14):3647–3679. doi:10.1016/s0020-7683(03)00143-4.
217. Pahr DH, Zysset PK. Influence of boundary conditions on computed apparent elastic properties of cancellous bone. Biomech Model Mechanobiol. 2008;7(6):463–476.
218. Hazanov S. On apparent properties of nonlinear heterogeneous bodies smaller than the representative volume Acta Mechanica. 1998;134(3–4):1619–6937.
219. Hazanov S. Hill condition and overall properties of composites. Archive of Applied Mechanics 1998. p. 385–294.
220. Xia Z, Zhou C, Yong Q, Wang X. On selection of repeated unit cell model and application of unified periodic boundary conditions in micro-mechanical analysis of composites. International Journal of Solids and Structures. 2006;43(2):266–278.
221. Yin L, Elliott DM. A homogenization model of the annulus fibrosus. J Biomech. 2005;38(8):1674–1684.
222. Garnich MR, Karami G. Finite Element Micromechanics for Stiffness and Strength of Wavy Fiber Composites. Journal of Composite Materials. 2004;38(4):273.
223. Yvonnet J, Gonzalez D, He QC. Numerically explicit potentials for the homogenization of nonlinear elastic heterogeneous materials. Computer Methods in Applied Mechanics and Engineering. 2009;198(33–36):2723–2737. doi:10.1016/j.cma.2009.03.017.
224. Sharafi B, Ames EG, Holmes JW, Blemker SS. Strains at the myotendinous junction predicted by a micromechanical model. J Biomech. 2011;44(16):2795–2801. doi:10.1016/j.jbiomech.2011.08.025.
225. Reese SP, Weiss JA, editors. Measurement of Poisson's Ratio and Transverse Strain in Rat Tail Tendon During Stress Relaxation. Proc. of the 56th Annual Meeting of the Orthopaedic Research Society; 2010 March 5–9; New Orleans, LA.
226. Kouznetsova V, Geers MGD, Brekelmans WAM. Multi-scale constitutive modelling of heterogeneous materials with a gradient-enhanced computational homogenization scheme. International Journal for Numerical Methods in Engineering. 2002;54(8):1235–1260. doi:10.1002/nme.541.
227. Kouznetsova V, Brekelmans WAM, Baaijens FPT. An approach to micro-macro modeling of heterogeneous materials. Computational Mechanics. 2001;27(1):37–48. doi:10.1007/s004660000212.
228. Feyel F. A multilevel finite element method (FE2) to describe the response of highly nonlinear structures using generalized continua. Computer Methods in Applied Mechanics and Engineering. 2003;192(28–30):3233–3244. doi:10.1016/s0045-7825(03)00348-7.
229. Yuan Z, Fish J. Toward realization of computational homogenization in practice. International Journal for Numerical Methods in Engineering. 2008;73(3):361–380. doi:10.1002/nme.2074.

230. Tawhai M, Bischoff J, Einstein D, Erdemir A, Guess T, Reinbolt J. Multiscale modeling in computational biomechanics. IEEE Eng Med Biol Mag. 2009;28(3):41–49.
231. Okada J-i, Washio T, Hisada T. Study of efficient homogenization algorithms for nonlinear problems. Computational Mechanics. 2010;46(2):247–258. doi:10.1007/s00466-009-0432-1.
232. Kouznetsova VG, Geers MGD, Brekelmans WAM. Multi-scale second-order computational homogenization of multi-phase materials: a nested finite element solution strategy. Computer Methods in Applied Mechanics and Engineering. 2004;193(48–51):5525–5550. doi:10.1016/j.cma.2003.12.073.
233. Buechner PM, Lakes RS. Size effects in the elasticity and viscoelasticity of bone. Biomech Model Mechanobiol. 2003;1(4):295–301. doi:10.1007/s10237-002-0026-8.
234. Vernerey FJ, Kabiri M. An adaptive concurrent multiscale method for microstructured elastic solids. Computer Methods in Applied Mechanics and Engineering. 2012;241–244(0):52–64. doi:10.1016/j.cma.2012.04.021.
235. Freed AD, Doehring TC. Elastic model for crimped collagen fibrils. J Biomech Eng. 2005;127(4):587–593.
236. Grytz R, Meschke G. Constitutive modeling of crimped collagen fibrils in soft tissues. J Mech Behav Biomed Mater. 2009;2(5):522–533.
237. Hurschler C, Loitz-Ramage B, Vanderby R, Jr. A structurally based stress-stretch relationship for tendon and ligament. Journal of biomechanical engineering. 1997;119(4):392–399.
238. Ault HK, Hoffman AH. A composite micromechanical model for connective tissues: Part II - Application to rat tail tendon and joint capsule. Journal of Biomechanical Engineering. 1992;114(1):142–146.
239. Müller R, Rüegsegger P. Three-dimensional finite element modelling of non-invasively assessed trabecular bone structures. Medical engineering & physics. 1995;17(2):126–133.
240. Podshivalov L, Fischer A, Bar-Yoseph PZ. 3D hierarchical geometric modeling and multiscale FE analysis as a base for individualized medical diagnosis of bone structure. Bone. 2011;48(4):693–703. doi:10.1016/j.bone.2010.12.022.
241. Sanz-Herrera JA, Garcia-Aznar JM, Doblare M. On scaffold designing for bone regeneration: A computational multiscale approach. Acta Biomater. 2009;5(1):219–229. doi:10.1016/j.actbio.2008.06.021.
242. Varga P, Dall'ara E, Pahr DH, Pretterklieber M, Zysset PK. Validation of an HR-pQCT-based homogenized finite element approach using mechanical testing of ultra-distal radius sections. Biomech Model Mechanobiol. 2010. doi:10.1007/s10237-010-0245-3.
243. Goh KL, Meakin JR, Aspden RM, Hukins DW. Stress transfer in collagen fibrils reinforcing connective tissues: effects of collagen fibril slenderness and relative stiffness. J Theor Biol. 2007;245(2):305–311. doi:10.1016/j.jtbi.2006.10.008.
244. Goh KL, Meakin JR, Aspden RM, Hukins DW. Influence of fibril taper on the function of collagen to reinforce extracellular matrix. Proceedings Biological sciences / The Royal Society. 2005;272(1575):1979–1983. doi:10.1098/rspb.2005.3173.
245. Ault HK, Hoffman AH. A composite micromechanical model for connective tissues: Part I - Theory. Journal of Biomechanical Engineering. 1992;114(1):137–141.
246. Lake SP, Barocas VH. Mechanical and Structural Contribution of Non-Fibrillar Matrix in Uniaxial Tension: A Collagen-Agarose Co-Gel Model. Annals of biomedical engineering. 2011. doi:10.1007/s10439-011-0298-1.
247. Vidal BC. Crimp as part of a helical structure. C R Acad Sci III. 1995;318(2):173–178.
248. Yahia LH, Drouin G. Microscopical investigation of canine anterior cruciate ligament and patellar tendon: collagen fascicle morphology and architecture. J Orthop Res. 1989;7(2):243–251.
249. Marino M, Vairo G. Stress and strain localization in stretched collagenous tissues via a multiscale modelling approach. Comput Methods Biomech Biomed Engin. 2012. doi:10.1080/10255842.2012.658043.
250. Schulze-Tanzil G, Al-Sadi O, Wiegand E, Ertel W, Busch C, Kohl B et al. The role of pro-inflammatory and immunoregulatory cytokines in tendon healing and rupture: new insights. Scand J Med Sci Sports. 2011;21(3):337–351. doi:10.1111/j.1600-0838.2010.01265.x.

251. Sander EA, Stylianopoulos T, Tranquillo RT, Barocas VH. Image-based multiscale modeling predicts tissue-level and network-level fiber reorganization in stretched cell-compacted collagen gels. Proc Natl Acad Sci U S A. 2009;106(42):17675–17680.
252. Chandran PL, Barocas VH. Deterministic material-based averaging theory model of collagen gel micromechanics. J Biomech Eng. 2007;129(2):137–147. doi:10.1115/1.2472369.
253. Sander EA, Tranquillo RT, Barocas VH. Image-based multiscale structural models of fibrous engineered tissues. Conference proceedings : Annual International Conference of the IEEE Engineering in Medicine and Biology Society IEEE Engineering in Medicine and Biology Society Conference. 2009;2009:4270-4272. doi:10.1109/IEMBS.2009.5334586.
254. Reese SP, Ellis BJ, Weiss JA. Micromechanical model of a surrogate for collagenous soft tissues: development, validation and analysis of mesoscale size effects. Biomech Model Mechanobiol. 2013;12(6):1195–1204. doi:10.1007/s10237-013-0475-2.
255. Ateshian GA, Rajan V, Chahine NO, Canal CE, Hung CT. Modeling the matrix of articular cartilage using a continuous fiber angular distribution predicts many observed phenomena. J Biomech Eng. 2009;131(6):061003.
256. Upton ML, Gilchrist CL, Guilak F, Setton LA. Transfer of macroscale tissue strain to microscale cell regions in the deformed meniscus. Biophys J. 2008;95(4):2116-21-24. doi:10.1529/biophysj.107.126938.
257. Reese SP, Maas SA, Weiss JA, editors. A bottom-up approach to construction and validation of multiscale models for aligned collagenous tissues. Workshop on Microscale Modeling in Biomechanics and Mechanobiology; 2011.
258. Reese SP, Weiss JA, editors. Multiscale micromechanical model of a collagen-based composite: development and validation. Multiscale Methods and Validation in Medicine and Biology; 2012.
259. Ateshian GA, Nims RJ, Maas SA, Weiss JA. Computational modeling of chemical reactions and interstitial growth and remodeling involving charged solutes and solid-bound molecules. Biomechanics and Modeling in Mechanobiology. 2014; In Press.

# Chapter 9
# Arteries: Mechanics, Mechanobiology, and the Need for a New Class of Models

**J.D. Humphrey and J.S. Wilson**

**Abstract** Constitutive relations for describing the biomechanical behavior of arteries have continued to progress since the late 1960s and we now have considerable ability to understand and predict many mechanical and mechanobiological processes. Nevertheless, advances in both genetics and cell and matrix biology have revealed new needs with regard to describing the biomechanics. In this chapter, we briefly review arterial structure and prior biomechanical constitutive approaches and then discuss a growing appreciation of the details of the arterial extracellular matrix and the need to include such detail in future constitutive relations. As it will be seen, much has been learned, yet much remains to be accomplished in the formulation of constitutive relations for arteries that can provide true predictive capability with regard to mechanobiological aspects of the development, maintenance, adaptation, disease progression, and responses to injury.

## 9.1 Introduction

Vascular disease is a leading cause of morbidity and mortality in industrialized nations and its impact continues to increase worldwide. That mechanics is fundamental to understanding arterial health and disease is obvious—these vessels serve as structural conduits and loss of structural integrity can result in a life-threatening hemorrhage. Just as important, however, mechanics influences the workload on the heart and it affects fundamental cellular activities that influence the development, maintenance, adaptation, and repair of arteries in diverse physiologic and pathophysiologic circumstances. Hence, there is strong motivation to understand both the mechanics and the mechanobiology.

There have been tremendous advances over the past four decades in arterial biomechanics (cf. [22]), yet recent advances in genetics and cell and matrix biology demand that we advance further our biomechanical understanding of arterial

J.D. Humphrey (✉) · J.S. Wilson
Department of Biomedical Engineering, Malone Engineering Center,
Yale University, 55 Prospect Street, New Haven, CT 06520, USA
e-mail: jay.humphrey@yale.edu



S. De et al. (eds.), *Multiscale Modeling in Biomechanics and Mechanobiology*, DOI 10.1007/978-1-4471-6599-6_9

function and dysfunction. In this chapter, we will first review basic arterial structure and prior constitutive approaches for describing observed biomechanical behaviors of arteries. With this as a background, we will then briefly review more detailed information on arterial microstructure and, within the context of an illustrative example, suggest that there is a need for a new class of multiscale biomechanical models for arterial mechanics. The latter is motivated primarily by the recently discovered importance of structural constituents within the wall that have not been included explicitly in prior constitutive modeling. The general implications of such modeling are much farther reaching, however.

## 9.2 Basic Arterial Structure

Arteries are generally classified as either elastic or muscular. Elastic arteries are found closer to the heart and function to store elastic energy during systole that can be used to work on the blood during diastole. This elastic response decreases the work load on the heart, augments coronary perfusion by aiding retrograde flow during diastole, and promotes a continuous flow in the microcirculation that aids in gas and nutrient exchange. Muscular arteries are found near or in target organs and tissues such as the heart, brain, kidneys, and skeletal muscle; via a strong smooth muscle contractile response, they regulate local blood pressure and flow. Both types of arteries consist of three layers: intima, media, and adventitia. The innermost layer, or intima, consists primarily of a monolayer of endothelial cells that adhere to an underlying basement membrane that consists largely of type IV collagen and laminin. Albeit not structurally significant in young healthy individuals, this layer can thicken in aging, particular diseases, and responses to injury primarily due to an accumulation of synthetic cells and deposition of abundant collagen and proteoglycans. The middle layer, or media, is the parenchymal layer of the arterial wall. It consists of abundant smooth muscle cells as well as elastic fibers, fibrillar collagens, and proteoglycans. In elastic arteries, the smooth muscle cells reside within concentric layers of elastic fibers that are organized into fenestrated sheets, or laminae. In muscular arteries, the smooth muscle cells reside within a more diffuse plexus of elastic fibers, collagen fibers, and proteoglycans, typically with overall delimiting inner and outer elastic laminae. The outermost layer, or adventitia, consists primarily of fibroblasts and the plexus of collagen fibers that they synthesize and maintain along with admixed elastic fibers and proteoglycans.

In summary, despite regional differences that serve local functionality, the arterial wall consists primarily of three layers, three cell types (endothelial, smooth muscle, and fibroblasts), and three primary types of structural constituents (elastic fibers, fibrillar collagens, and proteoglycans)—see Wagenseil and Mecham [44] for an excellent review. Of particular note, all three cell types are highly mechanosensitive [5, 6, 32], hence understanding arterial mechanics is important for two reasons. First, arteries are subjected to continuous loading, including pulsatile blood pressure, and their structural integrity is fundamental to their function as conduits for

blood flow; internal tears or fissures can lead to life threatening blood clots whereas dissections and transmural ruptures can lead to life-threatening bleeding. Second, because vascular cells are mechanosensitive, understanding the mechanical stimuli to which they are subjected is fundamental to understanding many of their biological responses, including migration, proliferation, differentiation, and apoptosis. Indeed, for this reason, the mechanics is fundamental to arterial development, homeostasis, adaptation, disease progression, and response to injury [25].

## 9.3 Constitutive Relations—A Historical Perspective

As noted many years ago by Y.C. Fung, one of the most important needs in biomechanics is identification of nonlinear constitutive equations for tissues that experience multiaxial loads in vivo (cf. [11]). Arteries are prototypical of such tissues.

*Phenomenological Relations*. The first class of stress–strain (constitutive) relations developed for arteries can be classified as phenomenological, that is, relations that describe observed responses primarily in pressure-diameter and axial force-length tests. Because of the ubiquitous nonlinear material behavior exhibited by arteries over finite deformations, an important advance realized in the late 1960s and the early 1970s was the use of the theory of finite elasticity to quantify arterial behavior. Early contributors in this regard included H. Demiray, Y.C. Fung, I. Mirsky, B. Simon, R. Vaishnav, and R. Vito, among others (cf. [22]). Briefly, in each case, these investigators sought to identify a strain energy function $W$ that depended on an appropriate measure of the finite deformation, as, for example, the right Cauchy-Green tensor $\mathbf{C}$ or the Green strain tensor $\mathbf{E}$. That is, given a functional form for $W(\mathbf{C})$ or $W(\mathbf{E})$, one could then compute the associated stress via established, general (e.g., based on the entropy inequality) constitutive relations, namely

$$\mathbf{t} = \frac{2}{\det\mathbf{F}}\mathbf{F}\frac{\partial W}{\partial \mathbf{C}}\mathbf{F}^T$$

where $\mathbf{F}$ is the deformation gradient tensor (with $\mathbf{C} = \mathbf{F}^{\mathrm{T}}\mathbf{F}$ and $\mathbf{E} = (\mathbf{C} - \mathbf{I})/2$). One of the most popular phenomenological relations is that due to Fung, which can be written as $W = c(\mathrm{e}^{Q} - 1)$ where $Q$ is typically written as a quadratic function of Green strain (note: by using a quadratic form, one can exploit material symmetry arguments from linearized elasticity, which is recovered directly in the limit as the strain becomes small). Although such relations can provide excellent estimates of the transmural distribution of wall stress, and indeed were fundamental in the discovery of the importance of residual stresses in arteries [7], values of the best-fit material parameters (typically determined via nonlinear regression) do not have any physical meaning, which limits the interpretive value when comparing relations as a function of species, genotype, arterial location, age, adaptation, or disease status.

*Structurally Motivated Relations*. For this reason, there was further motivation to pursue structurally motivated constitutive relations. Toward this end, there have been

two basic approaches, both founded on the basic tenet that the overall stored energy $W$ equals the sum of the energy stored in the structurally significant constituents that constitute the artery. First, building on the seminal paper by Lanir [31], some groups have sought to develop constitutive relations that include mass fractions and distribution functions for the orientations of the fibrous constituents (e.g., elastic and collagen fibers) as well as possible functions that capture fiber undulation. A recent example of such an approach is Hollander et al. [15]. Given the microstructural complexity of arteries, as revealed by light, multiphoton, and scanning electrom microscopy, such models necessarily include many simplifying assumptions such as Gaussian distribution functions and lack of intra- and interconstituent interactions.

Indeed, given the complexity of the microstructure, [19] suggested a "hybrid approach" wherein phenomenological relations can be prescribed for individual constituents. This approach evolved to include single- [20], two- [17], and four- [3] fiber family constitutive models; there does not appear to be any advantage to including additional families of fibers for arteries [52]. For example, the overall stored energy function $W$ is often assumed to result from energy stored in an amorphous matrix plus that stored in locally parallel families of fibers, usually thought to be dominated by collagen. An initial motivation for such models was to correct a fundamental deficiency in so-called fiber-in-fluid models (cf. [4]); an additional advantage is that such models also capture, with fewer parameters, the net effects of Gaussian distributions of fiber orientations (i.e., the preferred directions) and undulations (i.e., the exponential stiffening with stretch) as envisioned by Lanir [31]. Indeed, these fiber family models easily admit the inclusion of distributions of fiber orientations as desired (cf. [18, 45]), yet even without adding such capabilities these models have proven able to yield insight into constituent-dependent behaviors (cf. [9, 10]).

*Extension to Growth and Remodeling*. Of particular importance here, the structure of these "hybrid" fiber family models allowed a straightforward extension to model the ability of an artery to grow and remodel in response to sustained changes in mechanical and chemical stimuli [23]. By growth we mean a change in mass; by remodeling we mean a change in structure [2, 41]. For example, such growth and remodeling (G&R) models can be constructed by assuming that the overall stored energy$W$is a sum of the energy stored in each structurally significant constituent as its turns over—that is, energy is stored in constituents until they are removed. For example, Valentin et al. [43] suggested a form of $W$, where

$$W(s) = \sum \left( \frac{\rho^\alpha(0) Q^\alpha(s)}{\rho} W^\alpha \left( \mathbf{F}^\alpha_{n(0)}(s) \right) + \int_0^s \frac{m^\alpha(\tau) q^\alpha(s,\tau)}{\rho} W^\alpha \left( \mathbf{F}^\alpha_{n(\tau)}(s) \right) \mathrm{d}\tau \right)$$

at any G&R time $s$ (with time $\tau \in [0, s]$). Here, $\rho^\alpha$ is the mass density of constituent $\alpha = 1, 2, \ldots N$, the survival function $Q^\alpha \in [0, 1]$ tracks the amount of constituent $\alpha$ that was present at G&R time 0 and survives to time $s$, $W^\alpha$, is the energy stored in constituent $\alpha$, which depends on its individual deformation $\mathbf{F}^\alpha_{n(\text{G\&R time})}$, where

"G&R time" denotes the configuration at G&R time $\tau \in [0, s]$ at which the constituent was incorporated within the extant matrix, $m^\alpha$ is the mass density production rate for constituent $\alpha$, and the survival function $q^\alpha(s, \tau) \in [0, 1]$ tracks the amount of constituent $\alpha$ that was present at G&R time $\tau$ and survives to time $s$. In this way, the constitutive challenge expands to include the identification of specific functional forms for both the constituent-specific production ($m^\alpha$) and removal (or survival, $q^\alpha(s, \tau)$), not just energy storage ($W^\alpha$). Of particular importance, production and removal can depend on both mechanical and chemical stimuli. Regarding the former, although cells cannot sense directly the stress or strain, these continuum metrics remain useful, correlates for mechanobiological responses [21], which thereby allows one to exploit many advances in continuum biomechanics [24]. Regarding the latter, one can often solve coupled reaction-diffusion type relations for soluble factors, including growth factors, cytokines, and proteases, which in turn can inform the constitutive relations for production and removal [27]. In this way, one obtains a natural coupling between macroscale solid mechanics and microscale chemical kinetics, that is, a multiscale model that allows incorporation of considerable information on the molecular and cell biology. Indeed, one can even couple such G&R models to standard fluid mechanical models to create multiscale fluid-solid-growth models [26] or to combined agent based-cell signaling models to create models that exploit advances in systems biology [13].

*An Illustrative Example*. Here, we review briefly a G&R analysis of the enlargement of an idealized (fusiform) abdominal aortic aneurysm (AAA) to reveal both the types of constitutive relations that one must formulate and the types of insight that can be gleaned from such models. Briefly (cf. [28]), AAAs are pathologic dilatations ($\geq$50 % of the original diameter) of the infrarenal abdominal aorta that typically occur in elderly men, particularly those who smoke. The initial stages of aneurysm development are clinically silent; the lesion is typically discovered in its more advanced stages as a result of clinical symptoms (e.g., pain), targeted screening studies (usually by ultrasound), or imaging studies performed for other reasons. The most critical complication of AAAs is their propensity to rupture, which carries as much as a 90 % fatality rate. The only treatment options currently available are surgical, either by open replacement with a synthetic graft or endovascular placement of an endograft. A primary challenge for clinicians is to estimate the risk of rupture for a given AAA and to weigh that against the inherent risks of surgical intervention for a given patient. Unfortunately, accurately predicting patient-specific rupture risk remains challenging, and clinicians generally rely upon the maximum diameter ($>$5 to 5.5 cm) or expansion rate ($>$1 cm/yr) of the lesion to determine operative timing. Nevertheless, some smaller aneurysms rupture while some larger aneurysms may remain unruptured throughout a patient's remaining life. There is, therefore, a pressing need for a more accurate method of quantifying rupture risk in individual patients, which could reduce the morbidity and mortality associated with both the ruptures and potentially unnecessary surgeries in elderly patients.

In the final analysis, AAAs rupture when wall stress exceeds wall strength. It has been shown that calculating wall stress via finite element models based on patient-specific geometries (and using phenomenological stress–strain relations) may

yield a better estimate of rupture risk than the current metric of maximum diameter alone. This finding was an important advance, yet a patient-specific calculation of wall stress does not depend on luminal geometry alone. Stress depends on material properties and wall thickness, each of which may vary with location. Whereas one might be able to measure wall thickness by high-resolution imaging, defining the heterogeneous properties of the wall is much more difficult. As a first estimate, many investigators (see review by Humphrey and Holzapfel [28]), assume uniform isotropic properties in the lesion and surrounding nondilated aorta. Furthermore, they assumed population-averaged material parameters based on in vitro biomechanical tests on AAA samples obtained from a small group of individuals, each at an unknown time during the natural history of the lesion. Of course, overall geometry (including thickness), properties, and hemodynamic loads also tend to evolve, hence calculating stresses based on a current medical image of a lesion (that has not yet ruptured) need not provide the most important information (cf. [26]), that is, the potential risk of rupture in the near future (e.g., within the 6-12 months until the next imaging session).

In contrast, a G&R model conceptually has the potential both to recover the current geometry (i.e., to match imaging data) and properties as well as to predict the future geometry of an AAA from an initially nondilated aorta while naturally evolving local wall stiffness and thickness consistent with observed changes in the evolving histology. There is, therefore, considerable motivation to develop such models [28]. As a first step toward this goal, we constructed a G&R model of idealized fusiform AAAs by beginning with an initially straight, nondilated aortic segment consisting of three primary load-bearing constituents: collagen, elastin, and smooth muscle [3]. The collagen mass was distributed into four families consistent with an aforementioned structurally motivated constitutive relation, with circumferential, axial, and paired symmetrically diagonal fibers. The elastin-dominated matrix was assumed to be amorphous whereas smooth muscle was oriented circumferentially. Mass fractions for each constituent (and fiber family) were then prescribed based on estimates from available histology and best fits to mechanical data [47]. Associated strain energy functions were also prescribed for each constituent, parameters for which were determined via nonlinear regressions of data. For example, the elastin was modeled via a neoHookean relation and the fibrillar collagen and smooth muscle were modeled using Fung-exponentials.

An advantage of using constituent-specific relations is that one can numerically investigate contributions by individual constituents to the gross behavior. For example, one can study effects of stiffening the collagen via increased lysyl oxidase activity or glycosylation as in aging, remembering that AAAs typically present in elderly individuals. That is, mechanical properties of constituents, as represented by values of the material parameters, may be linked to a patient's medical history (e.g., risk factors) and be allowed to evolve during the G&R process according to general relationships. In particular, it is also hoped that once specific functional forms for the stored energy functions and associated ranges for the parameter values are well known from detailed biaxial data on selected specimens, patient-specific values may then be able to be inferred from the limited clinical data that will be

available. To increase patient-specificity, data from which the ranges of parameters are obtained should come from samples covering the appropriate sex, age, smoking status, blood pressure, and so forth. One of the key challenges, nonetheless, will be assigning properties for the nonaneurysmal aorta from which the lesion developed given information after the patient presents with an AAA. Thus, there is also a need to correlate properties of the nonaneurysmal infrarenal aorta with more proximal sections.

Once an appropriate data set is selected and the initial in vivo blood pressure and diameter are prescribed to establish an in vivo homeostatic reference configuration, nonlinear regression may be used to find best-fit values for the parameters of interest. A fundamental assumption of this approach is that a nonaneurysmal aorta will seek to maintain or restore a preferred homeostatic mechanical state (cf. [25]). That is, just as a cell seeks to establish and maintain a preferred chemical state via ion channels and pumps, we hypothesize that cells also synthesize, reorganize, and/or degrade structural constituents to establish, maintain, or restore a preferred mechanical state. Specifically, for our model, we assume that each constituent seeks to maintain a preferred Cauchy stress. Since our initial geometry is assumed to be a "healthy" initially nondilated aorta, we assume the constituents are initially at their respective homeostatic stresses. Moreover, because many proteins, notably collagen, are turning over constantly, we assume that the new collagen is incorporated within extant matrix at its preferred stress as the old collagen is removed.When such production and removal balance in an unchanging configuration, we call this tissue maintenance (or homeostasis). Because the original mass fractions, geometry, loads, and strain energy functions are all known, the appropriate "deposition stretch" for each constituent can be calculated from biaxial mechanical data along with the material parameters. It is then assumed that subsequently produced constituents will generally retain the same deposition stretch. Whereas the fibrillar collagen and smooth muscle turn over continuously throughout life, load-bearing elastic fibers within the elastic laminae are produced primarily during the perinatal period. Thus, the "deposition stretch" for elastin includes not only its initial deposition stretch, but also contributions due to somatic growth during development, maturation, and aging up to the time the simulation is to be initiated.

The second class of constitutive relations must describe the new mass production. Based on the concept of preferred, or homeostatic, stress, we hypothesized that cells generate new constituents in proportion to the deviation of their current stress from the homeostatic level. That is, if cells "sense" an increase in stress during the progression of the AAA, new material will be produced at a greater rate in an attempt to reduce the stress back toward the homeostatic level. A gain-type parameter captures the robustness of this new mass production. As noted earlier, such G&R models can also depend on effects due to far field stresses (e.g., smooth muscle cell production can depend on changes in wall shear stress on endothelial cells due to their altered production of nitric oxide or endothelin-1, which in turn affect smooth muscle production of collagen—see [43]). Alternatively, one could couple reaction-diffusion models to the production models to account directly for mechano- and chemo-mediated changes in a host of molecules, including angiotensin-II, transforming growth factor—beta,

and so forth, all of which affect smooth muscle production of collagen. Because collagen production and removal are continuous, even in the homeostatic state, a basal production rate must be included. This value is theoretically required to balance the basal degradation rate to ensure tissue maintenance under normal conditions and thus can be prescribed with some confidence. Finally, to account for the potential increase in the number of cells capable of producing collagen or smooth muscle, one could consider an additional term to augment production. For example, we have used the ratio of current mass to original mass (which assumes a near constant cell density), though more complex relationships could account for cellular proliferation, hypertrophy, or phenotypic changes. Overall, this constitutive relation for production provides a useful method for proposing and testing a number of competing hypotheses, from simple to complex, as to how cells transduce biochemomechanical stimuli into the production of load-bearing constituents.

The final key class of constitutive relations is mass removal, which can include apoptosis/anoikis and degradation/damage. For healthy arteries, the basal degradation rate must balance the basal turnover. More challenging, however, is determination of increases in degradation rate in pathological conditions like AAA formation. Marked increases in serine proteases and matrix metalloproteinases have been observed in AAAs, which need not be uniform throughout the lesion. We have considered two general methods of removing mass heterogeneously: stress-dependent mechanical failure and enzymatic degradation. A basic relation to account for mechanical failure can be written as a function of a maximum stretch, stress, or strain energy that a constituent can bear. Beyond the defined maximum, the material is considered fragmented and unable to bear load. Since collagen and smooth muscle are constantly turning over during aneurysmal enlargement, these materials may be somewhat protected from mechanical failure as new material may replace older fibers prior to their reaching the higher loads. In rapidly expanding aneurysms, however, collagen may reach its failure point before it is removed. Clearly, if significant collagen mass is lost, the risk of rupture can increase significantly. On the other hand, elastin is considered not to turnover. As a result, it is much more susceptible to mechanical failure in an AAA, which can increase in diameter more than threefold. While elastin is difficult to isolate, the literature suggests an ultimate stretch of about 2.2, hence potential mechanical failure must be included. While our initial models assumed that elastin is removed completely upon mechanical failure, it is possible that fragmented elastin may continue to bear some load as well as occupy space (and thus contribute to wall thickness and affect stress) because of its highly cross-linked and interconnected structure. In fact, histological examination of large AAA samples have revealed regions still containing elastin, and some stress–strain data from mechanical tests of AAAs show an initially linear relationship in the low strain range that is classically attributed to the presence of elastic fibers. Interestingly, small fragments of elastin often referred to as elastin degradation products may also exert significant biological effects on surrounding cells by recruiting inflammatory cells, activating fibroblasts, and promoting angiogenesis [49]. Clearly, further research and modeling efforts are needed to capture better these complexities.

As briefly mentioned earlier, degradation of matrix proteins is accomplished by a variety of enzymes (e.g., matrix metalloproteinases, elastases, and cathepsins). As a useful first approximation, we modeled such degradation using a first-order type decay defined as a function of half-life. It is reported that elastin has a normal half-life of approximately 50 to 70 years, though much shorter in pathological states like AAAs. While we often prescribe an initial spatial loss of elastin to initiate AAA development [47], the remaining elastin continues to degrade according to the prescribed first-order decay. Potentially, the relationship defining the half-life of this decay could be a function of the distribution and activation of particular elastases, such as neuthrophil elastase derived from inflammatory cells infiltrating the wall and located within the luminal layer of the often present intraluminal thrombus, as well as other elastases released by macrophages and smooth muscle cells within the wall. Similarly, we have allowed smooth muscle to turnover via a first-order relation. Losses of smooth muscle should include the phenomenon of anoikis, in which cells undergo apoptosis in response to lost connections with their surrounding matrix. In AAAs, anoikis may be of particular importance as the elastic laminae, in which the smooth muscle cells are normally in intimate contact, are proteolytically degraded or mechanically damaged. Indeed, smooth muscle cell apoptosis is a key pathological feature of AAAs. Thus, in addition to the first-order decay, we also allow the loss of SMCs to be proportional to the loss of elastin.

Finally, a critical component to the integrity of the aortic wall is the rate of degradation of collagen, particularly in aneurysms where the majority of the elastin and SMCs have been lost. Three main components have been considered in the enzymatic degradation of collagen. First, we include a baseline degradation rate that is balanced by the baseline production rate. Second, modification of this baseline rate due to effects from the production of collagenases by inflammatory cells, such as in the intraluminal thrombus or invading from the vasa vasorum [48]. Third, changes in this rate may be due to changes in the current stress state of the collagen fibers; that is, underloading (or potentially overloading) collagen may affect the rate at which collagenases are able to attack the molecule. There is, however, a need for improved understanding and quantification of the many biochemomechanical factors in the degradation of collagen, including identification of relevant collagenases, diffusion rates of these enzymes, kinematic relationships for enzymatic effectiveness as a function of stress and other factors.

Defining the evolving properties of the aortic wall on the level of individual constituents, as opposed to a static description of the whole wall as a single material, potentially allows a greater understanding of the processes that govern the growth and remodeling of healthy and diseased arteries. In addition, defining the strain energies, productions, and removals as separate functions (each drawing from quantifiable biochemical and biomechanical data) can yield a modular design to the model that allows new ideas to be included easily, interchanged, and tested computationally. Hence, G&R models can be powerful tools for gaining insight into the complex, evolving processes that govern arterial biomechanics, for evaluating competing hypotheses, and potentially for providing new prognostic information to improve clinical outcomes. For example, our models have suggested that the initial mechanical state of

the aorta (e.g., its biological, not chronological, age) prior to the development of an AAA may be particularly important in determining its subsequent progression [47] and that G&R parameters controlling collagen turnover (e.g., mass production, removal, stiffness, and prestretch) appear to be critical in determining the outcome of the aneurysm (i.e., stabilization, continued expansion, or rupture; [49]). Nevertheless, much remains to be elucidated about this complex disease process, such as the biochemomechanical role of the intraluminal thrombus within AAAs, contributions to the mechanics due to the presence and later loss of glycosaminoglycans, the roles of different subtypes of collagen, the interactions and cross-linking of the various constituents, and the quantities and distributions of key regulating enzymes. As future G&R models incorporate these added complexities, their usefulness to clinical decision-making will continue to grow.

## 9.4 Toward a New Class of Models

At this juncture, we recall another line of multiscale biomechanical investigation. Note, for example, that the type I collagen fibers that endow the arterial wall with considerable strength consist of a hierarchical structure. The collagen molecule is approximately 1.5 nm in diameter and 300 nm in length. These molecules are organized into quarter-staggered microfibrils on the order of 4 to 8 nm in diameter. These microfibrils, in turn, are organized into fibrils that may have diameters on the order of 100 to 500 nm, which are brought together to form collagen fibers that may have diameters on the order of 1 to 10 μm. Finally, these fibers can be organized into networks or parallel families that exist on the macroscale and are visible in confocal or light microscopy. There have been a number of attempts to develop multiscale models of this type of hierarchical structure. In particular, see Tang et al. [42] who propose a model for collagen fibers from nano- to macroscales, the latter of which relates to the aforementioned fiber family models. See, too, Matufi and Gasser [34] who employ similar methods to study macroscopic behaviors of the aorta. We will return to this line of study below.

Herein, however, it is suggested that we must continue to expand such efforts to develop yet a new class of multiscale constitutive relations for arteries that incorporate contributions not only of the primary structural constituents (e.g., collagen fibers), but also the many accessory proteins, glycoproteins, and proteoglycans that contribute to the microscale and macroscale mechanical properties of individual fibers and hence the tissue as a whole. Indeed, because of the increasing realization that genetic mutations affect directly the macroscopic mechanical behavior of arteries [30], our mechanical models need to account directly for expected changes in mechanical behavior given specific genetic mutations and related changes to matrix composition. In order to set the stage for such modeling, let us first consider in more detail the three primary structural constituents: elastic fibers, collagen fibers, and proteoglycans.

*Elastic Fibers*. Although we often read in the literature that elastin is one of the three primary structural constituents within the arterial wall, it is actually the

elastic fiber that is structurally important. Elastic fibers consist of a core of elastin (which constitutes 90 % of a fiber) that is surrounded by so-called microfibrils (mainly fibrillin-1) and microfibril associated glycoproteins (including fibulin-4,5; microfibril associated glycoprotein-1, or MAGP-1; elastin microfibril interface located protein-1, or Emilin-1; and latent transforming growth factor binding proteins, or LTBPs). Fibrillin-1 has a diameter on the order of 10 nm; it appears to be fundamental to elastogenesis and structural integrity, and thus morphogenesis and homeostasis [38]. It has also been suggested that fibrillin-1 is two orders of magnitude stiffer than elastin, hence it may serve to reinforce the composite fiber [40]. Fibulin-4,5 belong to the class of "short" fibulins; they appear to be particularly important in elastogenesis for they preferentially bind tropoelastin rather than polymerized elastin [51]. MAGP-1 are components of the microfibrils that appear to be important in homeostasis, not elastogenesis. Like Emilin-1 [37], MAGP-1 also appears to be involved in the regulation of transforming growth factor—beta (TGF-β), a cytokine that is important in controlling many aspects of smooth muscle and fibroblast phenotype. The aforementioned LTBP similarly associates with the microfibrils and serve to control TGF-β activity. The extracellular matrix is thus an important source of both structural integrity and instructional cues for the cells.

Amongst the many matrix components, fibrillin-1 appears to play a particularly important role in the the long-term mechanical stability of elastic fibers. In humans, for example, the half-life of normal elastic fibers appears to be on the order of 50 years to 70 [1]. This long-term stability is fundamental to the mechanical function of these fibers for they tend to be deposited primarily during the perinatal period and, thereafter, must suffer on the order of 30 million cycles of loading per year in humans. Thus, of the many structural constituents, elastic fibers alone are subject to a fatigue-induced damage as well as the normal and pathological proteolytic insults and mechanical overloading experienced by other intramural constituents. Mutations in the fibrillin 1 gene (*FBN1*), which cause Marfan syndrome, lead to aortic root / ascending aortic aneurysms and possible dissections. It appears that part of the pathogenic process is indeed an accelerated fatigue of the elastic fibers, which may appear as an accelerated aging of the wall prior to the extreme dilatation or intramural separation seen in later stages of the disease.

In contrast, it appears that the short fibulins (fibulin-4,5) contribute to the elastogenesis, that is, the initial organization of the elastic fibers during the perinatal period. Mutations in the fibulin 4 and 5 genes (*EFEMP2* and *DANCE*) have also been associated with thoracic aortic aneurysms in humans, though this does not appear to be a common phenotype. In mice, knockout of *Fbln4* results in thoracic aneurysms whereas knockout of *Fbln5* leads to increased aortic stiffening [16, 50]. The latter appears to manifest early on and not to be progressive [45]. It is not yet known structurally why mutations that code two very similar glycoproteins result in such different aortic phenotypes. Clearly, there is a need to understand better the mechanical consequences of these genetic mutations.

*Collagen Fibers*. There are many members of the family of proteins called collagen, but the members of primary importance in arteries are fibrillar types I, III, and V and network forming type IV (Wagenseil and Mecham 2009). Of these, types I

and III are most abundant within the arterial wall: type I constitutes nearly 70 % and type III nearly 30 % of all arterial collagen. Whereas elastic fibers endow arteries primarily with resilience, and thus elastic recoil, fibrillar collagens endow arteries with stiffness and strength.

Collagen I is thought to be the primary collagen endowing the arterial wall with strength; it has a heterotrimeric triple helical structure consisting of two alpha1 (coded by *COL1A1*) and one alpha 2 (coded by *COL1A2*) helices. One mutation to a gene coding collagen I results in a condition known as osteogenesis imperfecta. As implied by this term, one of the main phenotypes is fragile bones. Nevertheless, an osteogenesis imperfecta *Col1a2* null mouse also presents with reduced thoracic aortic integrity, due in part to reduced functional collagen [35]. Indeed, another mouse model with a *Col1a1* mutation is susceptible to both aortic dissection and rupture [36]. Collagen III is thought to contribute to the elasticity of the arterial wall; it has a homotrimeric triple helical structure consisting of three alpha1 helices. Mutations to the gene coding collagen III *(COL3A1)* cause vascular Ehlers-Danlos syndrome (vEDS). This syndrome is characterized by fragile arteries and aneurysms that may arise in many arterial locations. This finding is not unexpected from the perspective that collagen III represents nearly 30 % of the collagen in the normal aorta, much of it found in the media. It has thus long been recognized as an important contributor to the structural integrity of the wall. Not surprisingly, the *Col3a1* haploinsufficient mouse also recapitulates the vEDS phenotype [8]. In contrast to collagen I and III, collagen V is typically regarded as a "minor" collagen in arteries. It appears to play an important structural role nonetheless, that is, it is important in collagen I fibrillogenesis by helping to organize the fibrils into fibers. Collagen V has a heterotrimeric helical structure consisting of two alpha1 (coded by *COL5A1*) and one alpha2 (coded by *COL5A2*) helices. The Col5a1 haploinsufficient mouse also results in a vEDS phenotype, with decreased aortic stiffness and strength [46]. In particular, there was a lower density of collagen fibrils in the collagen V deficient arteries, and the existing fibrils exhibited highly irregular cross-sectional shapes. It is interesting to note, therefore, that collagen III and collagen V both contribute to collagen I fibrillogenesis (cf. [33]).

*Proteoglycans*. Although typically constituting only 2–5 % of the extracellular matrix in arteries, glycosaminoglycans (GAGs) and proteoglycans (PGs) play fundamental roles in the structural integrity. PGs consist of a protein core to which are attached multiple GAG chains. The four primary classes of GAGs are hyaluronan, chondroitin sulfate/dermatan sulfate, heparan sulfate, and keratan sulfate. Of particular interest herein, are the small lucine-rich proteoglycans (SLRPs), biglycan, and decorin. Both of these SLRPs aid in collagen fibrillogensis and they bind TGF-β, a key promoter of collagen synthesis. It has been shown [14, 44], for example, that biglycan deficiency in a BALB/cA mouse line results in spontaneous aortic dissection and rupture despite baseline aortic stiffness being near normal. Of particular note, wall strength was lower, collagen fibers exhibited irregular diameters, and dissection occurred between the media and adventitia not unlike in the collagen III mutant noted earlier.

*Further Extracellular Matrix Interactions*. Extensive cross-links and physical entanglements contribute significantly to the overall integrity of the arterial wall.

Cross-links are formed primarily via two classes of enzymes, the lysyl oxidases and transglutaminases[12], but nonenzymatic glycation cross-links can also become important in both aging and diabetes. Notwithstanding the fundamental importance of intra- and inter-constituent interactions, associated mechanical data remain scant.

## 9.5 Discussion and Directions

Historically, we have seen constitutive formulations for arteries transition from inappropriate linear elastic relations to more appropriate nonlinearly elastic, viscoelastic, and poroelastic relations. Moreover, these nonlinear relations have appropriately transitioned from phenomenological to microstructurally motivated, the latter of which include multiscale constituent and growth and remodeling relations. Each class of nonlinear relation has different advantages and we are reminded that constitutive relations do not describe materials; rather, they describe the response of a material to applied loads under conditions of interest, thus different classes of relations can be equally useful depending on the particular question of importance. That said, advances in genetics have revealed that mutations to many genes that code structural constituents within the extracellular matrix can lead to an altered ability of an artery to adapt to changing hemodynamics or to an increased risk of lethal conditions such as aneurysms and dissections. There is, therefore, a pressing need to broaden our constitutive modeling efforts to include multiscale effects of constituent interactions, both at an individual fiber and an integrated matrix level.

We have seen, for example, that G&R models that account for seaparate mechanical properties, natural (stress-free) configurations, and rates of turnover of individual constituents can provide significantly more information, indeed emergent results not possible with traditional relations. There is, however, an opportunity to incorporate within both classical constitutive (stress–strain) relations and contemporary growth and remodeling models increasing multiscale information that accounts for additional proteins, glycoproteins, and glycosaminoglycans that are parts of the primary structural constituents. For example, we must understand better and model structural roles of fibrillin-1, fibulin-4, and fibulin-5 and how they affect the structural integrity, including fatigue resistance, of elastic fibers. As noted earlier, compromised elastic fibers due to deficiencies in any of these three glycoproteins can lead to arterial stiffening, lengthening, dilatation (e.g., aneurysm), or dissections. Similarly, we must understand better and model roles of collagen III, collagen V, and biglycan in collagen I fibrillogenesis. Structurally competent collagen I is essential for maintaining sufficient arterial strength and thereby to prevent rupture [39]. Because interactions amongst these different biomolecules occur at a nano- to micro-level and yet manifest at a macro-level as clinically important changes in arterial integrity, multiscale models are clearly needed. Without such models, we will not be able to predict maladaptations or disease progression due to particular genetic mutations; we will similarly not be able to design optimal treatment strategies. Indeed, multiscale models will also be needed to quantify microstructural damage and degradation,

both of which are important for understanding altered structural integrity and cellular responses. For example, cells respond to "cryptic sites" on molecules that are exposed when the molecule is deformed or disrupted (cf. [29]). Mechanics must play a role in understanding such structurally based cell responses.

In summary, advances in genetics as well as matrix and cell biology have revealed the fundamental importance to arterial integrity and adaptability of what have been previously considered as "minor" extracellular matrix constituents. Given the "major" roles played by these constituents, our constitutive relations must begin to incorporate their status directly, which will require multiscale approaches.

**Acknowledgments** This work was supported, in part, by grants to JDH from the NIH (HL086418, HL105297) and National Marfan Foundation as well as by a predoctoral fellowship to JSW from the American Heart Association-Founders Affiliate.

## References

1. Arribas SM, Hinek A, Gonzalez MC (2006) Elastic fibres and vascular structure in hypertension. Pharma & Therapeut 111: 771–791.
2. Baaijens F, Bouten C, Driessen N (2010) Modeling collagen remodeling. J Biomech 43: 166–175.
3. Baek S, Rajagopal KR, Humphrey JD (2006) A theoretical model of enlarging intracranial fusiform aneurysms. ASME J Biomech Engr 128: 142–149.
4. Chadwick RS (1982) Mechanics of the left ventricle. Biophys J 39: 279–288.
5. Chiquet M, Gelman L, Lutz R, Maier S (2009) From mechanotransduction to extracellular matrix gene expression in fibroblasts. Biochim et Biophys Acta 1793: 911–920.
6. Chiu JJ, Chien S (2011) Effects of disturbed flow on vascular endothelium: Pathophysiologic basis and clinical perspectives. Physiol Rev 91: 327–387.
7. Choung CJ, Fung YC (1986) On residual stress in arteries. J Biomech Engr 108: 189–192.
8. Cooper TK, Zhong Q, Krawczyk M, Tae H-J, Muller GA, Schubert R, Myers LA, Dietz HC, Talan MI, Briest W (2010) The haploinsufficient Co13a1 mouse as a model for vascular Ehlers-Danlos syndrome. Vet Path 47: 1028–1039.
9. Eberth JF, Cardamone L, Humphrey JD (2011) Altered mechanical properties of carotid arteries in hypertension. J Biomech 44: 2532–2537.
10. Ferruzzi J, Collins MJ, Yeh AT, Humphrey JD (2011) Mechanical assessment of elastin integrity in fibrillin-1 deficient carotid arteries: Implications for Marfan syndrome. Cardiovasc Res 92: 287–295.
11. Fung YC (1981) Biomechanics: Mechanical Properties of Living Tissues. Springer, NY.
12. Griffin M, Casadio R, Bergamini CM (2002) Transglutaminases: nature's biological glues. Biochem J 368: 377–396.
13. Hayenga HN, Thorne BC, Papin JA, Peirce SM, Humphrey JD (2012) Multiscale Computational Modeling in Vascular Biology: From Molecular Mechanisms to Tissue-Level Structure and Function. In: Multiscale Computer Modeling in Biomechanics and Biomedical Engineering (A Gefen, ed). Springer, NY, pp. 209–240.
14. Heegaard A-M, Corsi A, Danielsen CC, Nielsen KL, Jorgenssen HL, Riminucci M, Young MF, Bianco P (2007) Biglycan deficiency causes spontaneous aortic dissection and rupture in mice. Circ 115: 2731–2738.
15. Hollander Y, Durban D, Lu X, Kassab GS, Lanir Y (2011) Experimentally validated microstructural 3D constitutive model of coronary arterial media. J Biomech Engr 133: 1–14.

16. Huang J, Davis EC, Chapman SL, Budatha M, Marmorstein LY, Word RA, Yanagisawa H (2010) Fibulin-4 deficiency results in ascending aortic aneurysms. Circ Res 106: 583–592.
17. Holzapfel GA, Gasser TC, Ogden RW (2000) A new constitutive relation for arterial wall mechanics and a comparative study of material models.J Elast 61: 1–48.
18. Holzapfel GA, Ogden RW (2010) Constitutive modeling of arteries. Proceed R Soc A 466: 1551–1597.
19. Humphrey JD, Yin FCP (1987) A new constitutive formulation for characterizing the mechanical behavior of soft tissues. Biophys J 52:563–570.
20. Humphrey JD, Strumpf RK, Yin FCP (1990) Determination of a constitutive relation for passive myocardium: I. A new functional form. ASME J Biomech Engr 112:333–339.
21. Humphrey JD (2001) Stress, strain, and mechanotransduction in cells. ASME J Biomech Engr 123: 638–641.
22. Humphrey JD (2002) Cardiovascular Solid Mechanics: Cells, Tissues, and Organs, Springer, NY.
23. Humphrey JD, Rajagopal KR (2002) A constrained mixture model for growth and remodeling of soft tissues. Math Model Meth Appl Sci 12: 407–430.
24. Humphrey JD (2003) Continuum thermomechanics and the treatment of disease and injury.Appl Mech Rev 56: 231–260.
25. Humphrey JD (2008) Vascular adaptation and mechanical homeostasis at tissue, cellular, and sub-cellular levels. Cell Biochem Biophys 50: 53–78. PMID 18209957.
26. Humphrey JD, Taylor CA (2008) Intracranial and abdominal aortic aneurysms: Similarities, differences, and need for a new class of computational models. Ann Rev Biomed Engr 10: 221–246.
27. Humphrey JD (2012) Multiscale Modeling of Arterial Adaptations: Incorporating Molecular Mechanisms in Continuum Biomechanical Models. In: Computer Models in Biomechanics: From Nano to Macro (GA Holzapfel, E Kuhl, eds), Springer, Berlin pp. 119–128.
28. Humphrey JD, Holzapfel GA (2012) Mechanics, mechanobiology, and modeling of human abdominal aorta and aneurysms. J Biomech 45: 805–814.
29. Karsdal MA, Nielsen MJ, Sand JM, Henriksen K, Genovese F, Bay-Jensen A-C, Victoria S, Adamkewicz JI, Christiansen C, Leeming DJ (2012) Extracellular matrix remodeling: the common denominator in connective tissue diseases. ASSAY and Drug Dev Tech.
30. Lacolley P, Challande P, Osborne-Pellegrin M, Regnault V (2009) Genetics and pathophysiology of arterial stiffness. Cardiovasc Res 81: 637–648.
31. Lanir Y (1979) A structural theory for the homogeneous biaxial stress-strain relationships in flat collagenous tissues. J Biomech 12: 423–436.
32. Li C, Xu Q (2007) Mechanical stress-initiated signal transduction in vascular smooth muscle cells in vitro and in vivo. Cell Signal 19: 881–891.
33. Liu X, Wu H, Byrne M, Krane S, Jaenisch R (1997) Type III collagen is crucial for collagen I fibrillogenesis and for normal cardiovascular development. Proc Natl Acad Sci 94: 1852–1856.
34. Martufi G, Gasser TC (2011) A constitutive model for vascular tissue that integrates fibril, fiber and continuum levels with application fo the isotropic and passive properties of the infrarenal aorta. J Biomech 44: 2544–2550.
35. Pfeiffer BJ, Franklin CL, Hsieh F-H, Bank RA, Phillips CL (2005) Alpha 2(I) collagen deficient oim mice have altered biomechanical integrity, collagen content, and collagen crosslinking of their thoracic aorta. Mat Biol 24: 451–458.
36. Rahkonen O, Su M, Hakovirta H, Koskivirta I, Hormuzdi SG, Vuorio E, Bornstein P, Penttinen R (2004) Mice with a deletion in the first intron of the Col1A1 gene develop age-dependent aortic dissection and rupture. Circ Res 94: 83–90.
37. Raman M, Cobb MH (2006) TGF-beta regulation by Emilin1: new links in the etiology of hypertension. Cell 124: 893–895.
38. Ramirez F, Pereira L (1999) The fibrillins. Intl J Biochem & Cell Biol 31: 255–259.
39. Rodriguez-Feo JA, Sluijter JPG, de Kleijn DPV, Pasterkamp G (2005) Modulation of collagen turnover in cardiovascular disease. Curr Pharm Des 11: 2501–2514.

40. Sherratt MJ, Baldock C, Haston JL, Holmes DF, Jones CJP, Shuttleworth CA, Wess TJ, Kielty CM (2003) Fibrillin microfibrils are stiff reinforcing fibres in compliant tissues. J Mol Biol 332: 183–193.
41. Taber LA (1995) Biomechanics of growth, remodeling, and morphogenesis.Appl Mech Rev 48: 487–545.
42. Tang H, Buehler MJ, Moran B (2009) A constitutive model of soft tissue: from nanoscale collagen to tissue continuum. Ann Biomed Engr 37: 1117–1130.
43. Valentin A, Cardamone L, Baek S, Humphrey JD (2009) Complementary vasoactivity and matrix remodeling in arterial adaptations to altered flow and pressure. J Roy Soc Interface 6:293–306.
44. Wagenseil JE, RP Mecham (2009) Vascular extracellular matrix and arterial mechanics. Physiol Rev 89:957–989.
45. Wan W, Gleason RL, (2013) Dysfunction in elastic fiber formation in fibulin-5 null mice abrogates the evolution in mechanical response of carotid arteries during maturation. Am J Physiol Heart Circ Physiol 304: 674–686.
46. Wenstrup RJ, Florer JB, Davidson JM, Phillips CL, Pfeiffer BJ, Menezes DW, Chervoneva I, Birk DE (2006) Murine model of the Ehlers-Danlos syndrome. J Biol Chem 281: 12888–12895.
47. Wilson JS, Baek S, Humphrey JD (2012) Importance of initial aortic properties on the evolving regional anisotropy, stiffness, and wall thickness of human abdominal aortic aneurysms. J Roy Soc Interface 9: 2047–2058.
48. Wilson JS, Virag L, Karsaj I, Humphrey JD (2013) Biochemomechanics of intraluminal thrombus in abdominal aortic aneurysms. ASME J Biomech Engr 135: 021011.
49. Wilson JS, Baek S, Humphrey JD (2012) Parametric study of effects of collagen turnover in human abdominal aortic aneurysms. Proceed R Soc Lond A 469: 20120556.
50. Yanagisawa, G, Davis EC, Starcher BC, Ouchi T, Yanagisawa M, Richardson JA, Olson EN (2002) Fibulin-5 is an elastin-binding protein essential for elastic fibre development in vivo. Nat 415: 168–171.
51. Yanagisawa H, Davis EC (2010) Unraveling the mechanism of elastic fiber assembly: the roles of short fibulins. Intl J Biochem & Cell Biol 42: 1084–1093.
52. Zeinali-Davarani S, Choi J, Baek S (2009) On parameter estimation for biaxial mechanical behavior of arteries. J Biomech 42: 524–530.

# Chapter 10
# Mitral Valves: A Computational Framework

**Chung-Hao Lee, Rouzbeh Amini, Yusuke Sakamoto, Christopher A. Carruthers, AnkushAggarwal, Robert C. Gorman, Joseph H. Gorman III and Michael S. Sacks**

**Abstract** The mitral valve (MV) is one of the four heart valves which locates in between the left atrium and left ventricle and regulates the unidirectional blood flow and normal functioning of the heart during cardiac cycles. Alternation of any component of the MV apparatus will typically lead to abnormal MV function. Currently, 40,000 patients in the United States receive MV repair or replacement annually according to the American Heart Association. Clinically, this can be achieved iteratively by surgical repair that reinstates normal annular geometry (size and shape) and restores mobile leaflet tissue, resulting in reduced annular and chordae force distribution. High-fidelity computer simulations provide a means to connect the cellular function with the organ-level MV tissue mechanical responses, and to help the design of optimal MV repair strategies. As in many physiological systems, one can approach heart valve biomechanics from using multiscale modeling (MSM) methodologies, since mechanical stimuli occur and have biological impact at the organ, tissue, and cellular levels. Yet, MSM approaches of heart valves are scarce, largely due to the major difficulties in adapting conventional methods to the areas where we simply do not have requisite data. There also remains both theoretical and computational challenges to applying traditional MSM techniques to heart valves. Moreover, existing physiologically realistic computational models of heart valve function make many assumptions, such as a simplified microstructural and anatomical representation of the MV apparatus, and thorough validations with in-vitro or in-vivo data are still

C.-H. Lee · Y. Sakamoto · A. Aggarwal · M.S. Sacks (✉)
Department of Biomedical Engineering, Center for Cardiovascular Simulation, Institute for Computational Engineering and Sciences (ICES), The University of Texas at Austin, Austin, TX 78752, USA
e-mail: msacks@ices.utexas.edu

R. Amini
Department of Biomedical Engineering, University of Akron, Akron, OH 44325, USA

C.A. Carruthers
Department of Bioengineering, University of Pittsburgh, Pittsburgh, PA 15260, USA

R.C. Gorman · J.H. Gorman III
Gorman Cardiovascular Research Group, University of Pennsylvania, Philadelphia, PA 19104, USA



S. De et al. (eds.), *Multiscale Modeling in Biomechanics and Mechanobiology*, DOI 10.1007/978-1-4471-6599-6_10

limited. In the following, we present the details of the state of the art of mitral valve modeling techniques, with an emphasis on what is known and investigated at various length scales.

## 10.1 Background

The mitral valve (MV) is one of the four heart valves which locates in between the left atrium and left ventricle and regulates the blood flow and normal functioning of the heart during cardiac cycles. The mitral valve apparatus has four primary subcomponents: the anterior and posterior leaflets (MVAL and MVPL), the papillary muscles (PMs) that project from the left ventricular wall, the chordae tendineae that provide connections between the papillary muscles and the MV leaflets, and the annulus that is part of the conceptual transition between the MV leaflets and left atrium. During systole of the cardiac cycle, the MV leaflets close to prevent blood backflow from the left ventricle, which accompanied by the shrinkage of the MV annulus, ventricular contraction of the PMs, and the tightening of the MV chordae tendineae. The opening of the mitral valve allows blood flow from the left atrium to left ventricle in diastole. According to the previous studies [49, 81], the mitral valve leaflets can be considered as a four-layered structure: the atrialis (A) facing the atrium, the ventricularis (V) on the ventricular side, the inner spongiosa (S), and fibrosa (F) layers. The fibrosa is the thickest layer that consists mainly of a dense network of type I collagen fibers and is the primary load-bearing layer. The ventricularis and atrialis layers are composed of a dense network of collagen fibers and radially aligned elastin fibers, which provide sufficient resistance to large radial strains when the MV is fully open. The central spongiosa layer contains a high concentration of hydrated glycosaminoglycans (GAGs) and proteoglycans (PGs) as the lubricant of shear deformation between the fibrosa and ventricularis layers. Each of these four layers has its distinct microstructure and mechanical properties, leading to highly nonlinear, anisotropic, and pseudoelastic tissue-level mechanical behaviors of the mitral valve.

Alternation of any component of the MV apparatus will typically lead to abnormal MV function. Currently 40,000 patients in the United States receive MV repair or replacement annually according to the American Heart Association [18]. Moreover, after two decades of emphasis on valve replacement, cardiac surgeons have been gradually turning to MV repair [14] rather than replacement of the MV to treat valvular dysfunctions such as mitral regurgitation (MR), which is caused by systolic traction on the mitral leaflets secondary to ventricular distortion, or stenosis [1, 66]. Promising MV repair concepts include leaflet augmentation to restore leaflet mobility [20, 44, 77] and saddle-shaped annuloplasty to restore normal annular shape [57, 58]. As collective experience has increased, many surgeons have come to view MV repair as the treatment of choice in patients with mitral regurgitation and post infarction ventricular remodeling (ischemic mitral regurgitation—IMR, Fig. 10.1). However, recent long-term studies have indicated that the recurrence of significant

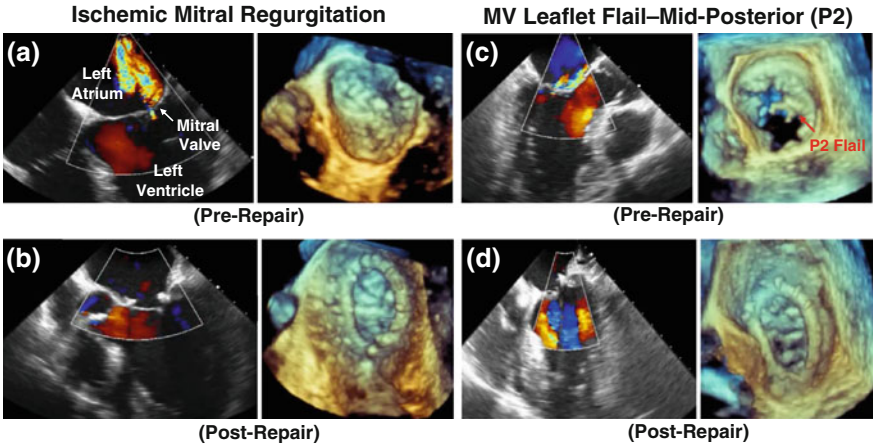


**Fig. 10.1** Assessment of the mitral valve disease and repair using 3D echocardiography and automatic reconstruction techniques for ischemic mitral regurgitation (IMR): **a** pre-repair and **b** post-repair, and for mitral valve posterior leaflet flail: **c** pre-repair and **d** post-repair

MR after surgical repair may be much higher than previously believed, particularly in patients with IMR [11, 29, 30], and it has been suggested that excessive tissue stress and the resulting strain-induced tissue failure are important etiological factors [11]. These repair-induced altered stresses lead to changes in MV interstitial cell (MVIC) metabolism and biosynthesis, and are important in understanding the biomechanical responses at the organ, tissue, and cellular levels. We then hypothesize that restoration of homeostatic normal MV leaflet tissue stresses in IMR repair techniques ultimately leads to improved repair durability through restoration of normal MVIC biosynthetic responses. Clinically, this can be achieved iteratively by surgical repair that reinstates normal annular geometry (size and shape) and restores mobile leaflet tissue, resulting in reduced annular and chordae force distribution. Alternatively, high-fidelity computational simulations could provide a means to connect the cellular function with the organ-level MV tissue mechanical responses, and to help the optimal design of MV repair strategies.

## 10.2 Challenges in Multiscale Computational Modeling of the MV

We are now entering a level of knowledge about the MV function, wherein computational approaches begin to be realistically applied. For modeling of the mitral valve, the pioneering anatomic sectioning and finite element (FE) simulation work by Kunzelman et al. [48, 51, 75, 76] has clearly demonstrated how computational modeling of MV function can help gaining insight into the relationship between the

variation of the MV components and MV functioning. Einstein et al. [21–23] integrated this developed FE model into the fluid-structure interaction (FSI) framework to early acoustic simulations for better understanding of MV diseases. Prot et al. [69, 70] proposed both the transversely isotropic membrane shell model and nonlinear solid element model with heterogeneous layer properties for the analyses of the MV apparatus. More recently, FE simulations have been utilized as a tool toward in-vivo and patient-specific modeling as well as surgical repair remodeling [19, 54, 98, 99], by incorporating the in-vivo measured transvalvular pressure, dynamic boundaries, and patient-specific geometry. The FE computational modeling tools have also been applied to investigating the in-vivo stress estimate of the MVAL for better understanding of surgical repair-induced stress variations on the MV function [45, 46].

Although these models render an important first step in developing physiologically realistic computational models of heart valve function, many assumptions were made, such as a simplified microstructural and anatomical representation of the MV apparatus, and thorough validations with in-vitro or in-vivo data are still limited. Therefore, there is a need for the development of an anatomically and microstructural accurate finite element model, which has been carefully validated, in order to make insightful connection between the mechanical responses of the MV tissue and the organ-level mitral valve behavior under physiological loading or surgical repair intervention.

## 10.3 Multiscale Modeling Approaches for the Functioning MV

As in many physiological systems, one can approach heart valve biomechanics from using multiscale modeling (MSM) approaches, since mechanical stimuli occur and have biological impact at the organ, tissue, and cellular scales (Fig. 10.2). For example, we have reported that valve interstitial cells (VICs) from the aortic valve (AV) and MV were significantly stiffer than the pulmonary valve (PV) and tricuspid valve (TV) VICs [62]. These findings suggest that VICs respond to local tissue stress by altering cellular stiffness through valvular remodeling and valvular pathologies. On the other hand, valvular endothelium, which is directly exposed to shear stress, responds to the local shear stress changes [13]. Another key point is that valvular extracellular matrix (ECM) is composed of dense network of collagen, elastin, and GAGs, and is thus functionally and mechanically very different from other cardiovascular structures (e.g., blood vessels, myocardium) [83, 87]. In fact, valvular ECM behaves mechanically much more like the dense planar connective tissues of the musculoskeletal system [8, 80]. They are unique in that they must function within a blood contacting environment and are thus coated with endothelial cell (VEC) monolayer. Moreover, there is evidence that VEC/VIC communication may play an important role in valve ECM homeostasis.

Yet, despite its clinical importance, the unique and demanding valvular biological/biomechanical environment is relatively unexplored. MSM approaches of heart valves are scarce, largely due to the major difficulties in adapting conventional MSM

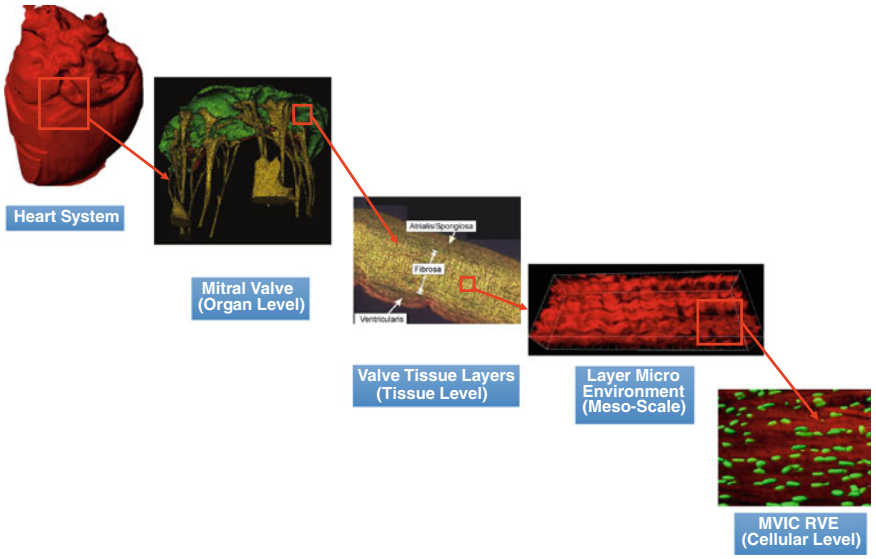


**Fig. 10.2** Multiscale hierarchical structure for the heart system and the associated computational paradigm for modeling the functional mitral valves with integration of tissue, layer, and cellular-level mechanical responses into the organ-level macroscopic simulation

to the areas where we simply do not have requisite data. Moreover, there remains both theoretical and practical challenges to applying traditional MSM techniques to heart valves. For example, even defining something as basic as the representative volume element (RVE) is problematic due to the presence of a larger number of relevant length scales whose magnitudes are not always amenable for MSM approaches. For example, if the RVE is too small it will not statistically represent the VIC cell spatial distributions and orientations. Alternatively, if the RVE is too large the strain distribution will vary greatly within the RVE and will not adequately represent the local response. Chen et al. [17] applied second-order homogenization (SOH) theory of Ponte-Castañeda et al. [56, 67, 68] to arterial mechanics, which belong to the same class of biological tissues as heart valves, including unique mechanical properties due to wavy fibrous collagen and elastin microstructure. The authors addressed an assumption of current microstructural models of blood vessels via affine deformation, i.e., the deformation of each fiber is assumed to be identical to the macroscopic deformation of the tissue. This uniform-field (UF) assumption leads to the macroscopic (or effective) strain energy of the tissue that is the volumetric sum of the contributions of the tissue components. In their work, a micromechanics-based constitutive model of fibrous tissue is developed to remove the affine assumption and to take into consideration of the heterogeneous interactions between the fibers and the ground substance. The theory takes into account for the waviness, orientations and spatial distribution of the fibers, as well as the material nonlinearity at finite-strain deformation. However, full trans-scale models are clearly needed for better understanding of the mitral valve functioning as well as the mechanical

behaviors in response to external loading (Fig. 10.2). In the following, we present the details of the state of the art of mitral valve modeling techniques, with an emphasis on what is known and investigated at various length scales.

## 10.4 State-of-the-Art Studies on Multiscale Computational Modeling of the Mitral Valve

### *10.4.1 3D Organ-Level Reconstruction of the MV Finite Element Model*

A modified left heart simulator [72] was used for acquisition of the in-vitro mitral valve deformations at stress-free (referential), pressure loaded (∼30 mm Hg), and fully loaded (∼70 mm Hg) states. The modular left heart allows for precise control of annular and subvalvular mitral valve geometry. Ebony fiducial beads (0.2–0.4 mm in diameter) were glued to the mitral leaflets in a regular array (110 and 166 markers for the MVAL and MVPL, respectively). The native ovine mitral annulus was sutured to a sized 32 Carpentier-Edwards Physio annuloplasty ring (Edwards Lifesciences Corp, CA) and mounted onto an acrylic plate in between the atrial and ventricular chambers. The papillary muscles were mounted onto mechanical positioning rods in the left ventricle and carefully positioned to produce physiological MV function. The left ventricle was fixed to the Micro-CT gantry using a custom adapter plate, and the mitral valve was scanned in air for all three conditions using a vivaCT 40 system (Scanco Medical AG, Switzerland) at 39 μm resolution with isotropic voxels using scanning parameters for low density soft tissues [10]. For all conditions, the annulus and papillary muscle positions were undisturbed in the left ventricular chamber.

The stack of three-dimensional Micro-CT images were then segmented semi-automatically using ScanIP (Simpleware Ltd. United Kingdom) to acquire micro-anatomically accurate geometry of the MV apparatus at the stress-free, 30 mm Hg pressure loaded, and 70 mm Hg pressure loaded states, with the following key components: MV leaflets, annulus, chordae tendineae, and papillary muscles (Fig. 10.3a). The three-dimensional positions of the fiducial markers at the above three states were obtained via a mask with gray-scale threshold in ScanIP. The segmented MV geometry at each state was imported into Geomagic Studio (Morrisville, NC) for generation of the corresponding finite element model (Fig. 10.3b, 6,528 four-node shell elements, in which 2,176 and 4,352 elements are for the MVAL and MVPL, respectively). The 3D locations of the key points for representation of the MV chordae tendineae, such as MV PM attaching points, chordal branching points, and MV leaflet attaching points, were quantified for realistic reconstruction of chordae tendineae (297 three-dimensional truss elements, Fig. 10.3b). Moreover, spatially varied and anatomically accurate MV leaflet thicknesses were determined from the Micro-CT data.

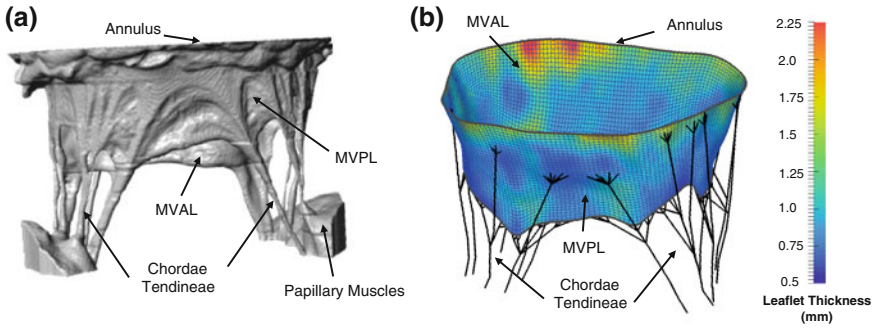


**Fig. 10.3** **a** 3D reconstruction of anatomically accurate geometry of the mitral valve from high-solution Micro-CT images, and **b** the corresponding finite element model (thin-shell elements for the MV leaflets and 3D truss elements for the MV chordae) with MV leaflet thicknesses determined based on the Micro-CT measurements

### *10.4.2 Mapping of the Bulk Collagen Fiber Architecture*

Both the anterior and posterior leaflets were then dissected and prepared for the measurement of the tissue collagen gross fiber orientation using the small angle light scattering (SALS) technique [82]. Briefly, the MV leaflet tissue was placed in glycerol for dehydration and then scanned in the SALS device, which utilizes a continuous unpolarized 4 mW HeNe laser ($\lambda = 632.8$ nm, Uniphase, Manteca, CA). The measured diffraction patterns were analyzed to quantify the local preferred fiber direction $\phi_f$ and the strength of fiber alignment indicated by an orientation index (OI). The OI is defined as one half of the area under the quantified collagen fiber angular distribution $\Gamma(\theta)$, that is, $\int_{\phi_f - \frac{OI}{2}}^{\phi_f + \frac{OI}{2}} \Gamma(\theta) d\,\theta = 0.5$.

In order to incorporate the collagen fiber microstructural information measured at the excised state into the 3D finite element mesh, we developed the following mapping algorithm. First, to account for the transformation between the excised state $\Omega_{SALS}$ and in-vitro fully loaded configuration $\Omega_t$, the fiber dispersion distributions for the MV anterior leaflet and posterior leaflet were determined by assuming an affine transformation [7]:

$$\Gamma(\beta) = \Gamma(\theta) \frac{\mathbf{N}(\theta) \cdot \mathbf{C}\mathbf{N}(\theta)}{\mathbf{J}_{2D}} = \frac{\lambda_{\mathbf{N}}^2}{\mathbf{J}_{2D}} \tag{10.1}$$

where $\Gamma(\beta)$ and $\Gamma(\theta)$ are the fiber angular dispersion functions at the in-vitro fully loaded and excised configurations, respectively, $\mathbf{N}(\theta)$ denotes the unit vector of the preferred fiber direction at the excised configuration, $J_{2D}$ is the determinant of the in-plane components of the deformation gradient tensor (computed from the fiducial marker positions at these two configurations), $\lambda_N$ is the collagen fiber stretch

ratio in the direction of $\mathbf{N}$, and $\mathbf{C} = ({}_{SALS}{}^{t}\mathbf{F})^{T}\,{}_{SALS}{}^{t}\mathbf{F}$ is the right Cauchy-Green deformation tensor. Once $\Gamma(\beta)$ was determined, the new values of the mean $\mu$ and standard deviation $\sigma$ in the deformed configuration were directly computed. Next, the measured preferred fiber direction at the excised state was used to determine the local material axes at the fully loaded configuration by

$$\mathbf{e}_1(\beta) = {}_{SALS}{}^{t}\mathbf{F}\cdot\begin{Bmatrix}\cos(\mu)\\ \sin(\mu)\\ 0\end{Bmatrix}, \quad \text{and} \quad \mathbf{e}_2(\beta) = {}_{SALS}{}^{t}\mathbf{F}\cdot\begin{Bmatrix}-\sin(\mu)\\ \cos(\mu)\\ 0\end{Bmatrix} \tag{10.2}$$

Noted that the collagen fiber architecture was measured at the pressure loaded state $\Omega_t$, whereas the stress-free state $\Omega_0$ was chosen as the initial/reference configuration for the FE simulation. The collagen fiber microstructural information associated with the reference configuration was then determined via the affine-transformation reverse mapping approach using the deformation gradient between the fully loaded and stress-free states for Eqs. (10.1)–(10.2). The mapped collagen fiber architecture was further incorporated into an anisotropic hyperelastic model for the MV leaflets:

$$\begin{aligned}\Psi^{\text{leaflet}}(I_1, I_4) &= \Psi^{\text{leaflet}}_{\text{iso}}(I_1) + \Psi^{\text{leaflet}}_{\text{aniso}}(I_4)\\ &= C_{10}(I_1 - 3) + \frac{c_0}{2}\left\{(1-\delta)\exp\left[c_1(I_1-3)^2\right] + \delta\exp\left[c_2(I_4-1)^2\right] - 1\right\}\end{aligned} \tag{10.3}$$

where $\Psi^{\text{leaflet}}(I_1, I_4)$ is the strain energy density function of the leaflet tissues that consists of an isotropic term $\Psi^{\text{leaflet}}_{\text{iso}}(I_1)$ and a transversely isotropic term $\Psi^{\text{leaflet}}_{\text{aniso}}(I_4)$, $I_1 = \text{tr}(\mathbf{C})$ and $I_4 = \mathbf{N}\cdot\mathbf{CN}$ are the invariants, $C_{10}$ and $c_i$ are the material parameters quantified by fitting to the biaxial data, and $\delta$ is a parameter governing the level of material anisotropy.

The collagen fiber microstructural information, including the preferred fiber direction $\phi_f$ and OI value, was mapped onto the finite element model (Fig. 10.4a and b), accounting for the transformation/deformation between the excised $\Omega_{SALS}$ and in-vitro fully load state $\Omega_t$. Noted that the collagen fibers were fairly continuous for the MVAL and MVPL, which provide smooth local material axes for contiguous leaflet finite elements; better aligned collagen fibers were observed in the belly regions of both leaflets which sustain the greater amount of stretching under pressure loadings. The collagen fiber architecture associated with the FE mesh at the reference configuration (stress-free state) $\Omega_0$ was determined by the affine-transformation reverse mapping (Fig. 10.4c and d). It is clear that the collagen fibers were less aligned at the stress-free (fully open) state whereas the fibers were re-oriented according to the deformations of the MV leaflets and become much well aligned as the stretches in both the circumferential and radial directions increase at the fully loaded state.

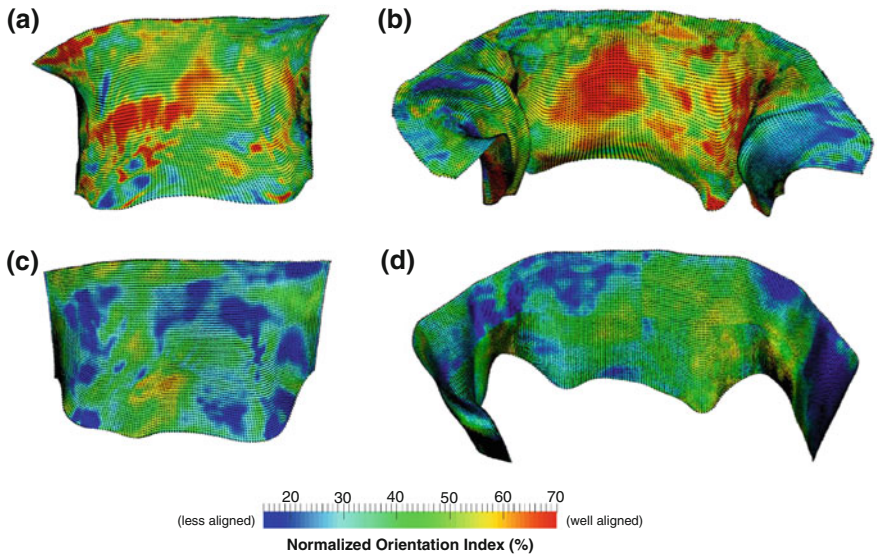


**Fig. 10.4** Mapping of the collagen fiber microstructural architecture onto the 3D finite element mesh at the deformed (*fully loaded*) configuration $\Omega_t$: **a** MVAL and **b** MVPL, and at the reference (*stress-free*) configuration $\Omega_0$: **c** MVAL and **d** MVPL

### *10.4.3 Finite Element Simulations of MV Closure*

Simulations of the MV systolic closure were performed in the FE commercial software ABAQUS 6.11 (SIMULIA, Providence, RI) by utilizing:

(i) the four-node shell elements for the MV leaflets and 3D tension-only truss elements for the MV chordae tendineae,
(ii) user material subroutine `VUMAT` for implementation of the material models for MV leaflets and chordae,
(iii) `QUASI-STATIC` option in the implicit dynamic analysis with automatic time stepping,
(iv) `ORIENT` feature and user subroutine VUSDFLD for defining the element-based local coordinate system with the preferred fiber direction and orientation index obtained from the mapping technique,
(v) `THICKNESS TABLE` feature for assigning spatially varied MV leaflet thicknesses quantified based on the Micro-CT images,
(vi) general frictionless self-contact algorithm for handling the contact behavior of the MV leaflets,
(vii) user subroutine `VDISP` for prescribing displacement boundary conditions accounting for the MV annulus and papillary muscles dynamics due to left ventricle contraction, and
(viii) `AMPLITUDE` feature for defining the transvalvular pressure loadings.

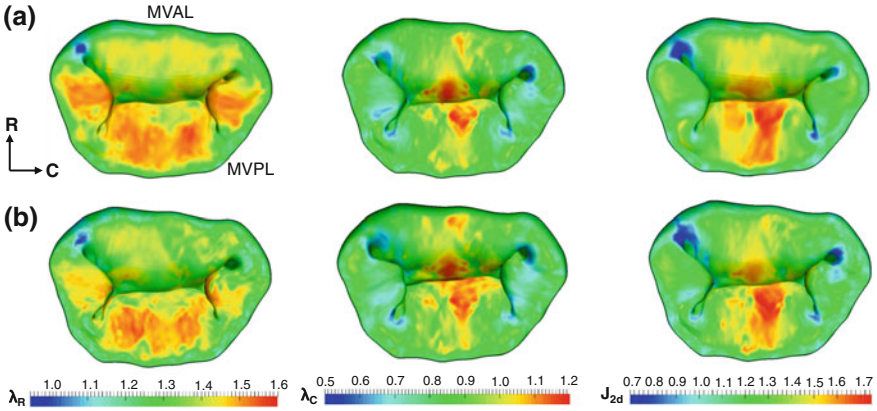


**Fig. 10.5** Comparison of the principal stretches ($\lambda_C$ and $\lambda_R$) and in-plane Jacobian (J2d) at the fully loaded state: **a** in-vitro measurements and **b** numerical results via FE simulations

Nodal displacements and rotations, elemental strain, and stress fields were the primary output from the FE simulations. The deformed leaflet geometry, principal stretches, and in-plane Jacobian were compared to the in-vitro measurements at transvalvular pressures of 30 and 70 mm Hg.

The numerical predictions of the deformed geometry in general agreed well with the in-vitro experimental data, with the total displacement errors of 13.72 and 14.93 mm evaluated at the total 266 fiducial markers under pressures of 30 and 70 mm Hg. The differences in marker displacements between the numerical results and experimental data were $0.388 \pm 0.236$ and $0.261 \pm 0.192$ mm at 30 mm Hg, and $0.537 \pm 0.336$ and $0.411 \pm 0.349$ mm at 70 mm Hg for the MVAL and MVPL, respectively. Moreover, the principal stretches in the radial and circumferential directions and in-plane Jacobian were captured well by the numerical simulations (Fig. 10.5). The predicted maximum values of $\lambda_C$, $\lambda_R$, and $J_{2d}$ were 1.589, 1.216, 1.617 for the MVAL and 1.689, 1.208, 1.702 for the MVPL at 70 mm Hg in comparison with the in-vitro measurements: $\lambda_C = 1.601$, $\lambda_R = 1.234$, and $J_{2d} = 1.631$ for the MVAL and $\lambda_C = 1.655$, $\lambda_R = 1.224$, and $J_{2d} = 1.695$ for the MVPL.

### *10.4.4 Parametric Studies: Effects of Material Model Forms, Local Fiber Directions, Mechanical Anisotropy, Leaflet Tissue Thicknesses, and Chordae Geometry*

We performed the parametric studies in the following four categories to investigate the effect of each model perturbation on the numerical predictions. In brief, we first investigated the appropriate constitutive model form for reasonable predictions of the highly nonlinear and anisotropic mechanical responses of the MV as well the MV

deformations. Second, we compared the high-fidelity FE model presented previously with simplified collagen fiber mapping and different representations of the material anisotropy. We next examined the effect of the MV leaftlet thickness, which is closely relate to the stiffness of the MV apparatus, on the predictions of the MV deformations. Finally, various chordae representations were studied to determine the most suitable chordae realization in the FE simulations. The detailed results of each parametric study category are summarized as follows:

(1) *Effect of the constitutive model forms*: Three constitutive model forms were considered: (i) Neo-Hookean material, (ii) exponential-type isotropic material, and (iii) full collagen fiber mapped transversely isotropic material. Substantially larger discrepancies of the MV deformed geometry, errors of the fiducial marker displacements and in-plane Jacobian (Table 10.1) were observed between the Neo-Hookean and transversely isotropic materials, whereas the exponential-type isotropic material yielded the predictions with ∼25–45 % greater errors compared to the transversely isotropic material (Table 10.1), indicating that the transversely anisotropic model produced the most accurate results and is a more realistic pseudo-hyperelastic material model form for the MV tissues [60].

(2) *Effect of the local fiber directions and degrees of material anisotropy*: Smaller discrepancies of the MV deformed geometry and displacement errors (∼15–20 % greater, Table 10.1) were shown in this sensitivity analysis group. However, distinct differences in the local deformation fields in terms of the principal stretches and in-plane Jacobian were observed between the curvilinear mapped and full collagen fiber mapped local fiber directions and between the structural tensor approach and the linear relationship for $\delta$ values.

(3) *Effect of the MV leaflet thicknesses*: The comparison of the numerical results between uniform leaflet thicknesses of 50, 100, and 200 % mean thicknesses of MVAL and MVPL and the spatially varied Micro-CT quantified one were made (Table 10.1). The case of uniform mean leaflet thicknesses produced fairly accurate predictions with ∼30 % greater displacement errors compared with the full-blown model, while it yielded less accurate local deformation field ($J_{2d}$). This suggests that incorporation of anatomically accurate leaflet thicknesses would be necessary for accurate simulation of the MV apparatus.

(4) *Effect of the MV chordae representations*: In this group of sensitivity analysis, we investigated the effect of various representations of chordae on the numerical results (Table 10.1). There were significant discrepancies between the commonly adopted chordae representation (all marginal chordae) in literature [19, 48, 99] and the Micro-CT reconstructed ones. Although the Micro-CT reconstructed chordae with single attached node reasonable results compared to the Micro-CT reconstructed chordae with multiple attached nodes, there exhibited stress concentration near the attaching regions for the former case, suggesting that the Micro-CT reconstructed chordae with multiple attached nodes is a more appropriate representation of the MV chordae.

**Table 10.1** Error comparisons of the displacements and in-plane Jacobian evaluated at the fiducial marker positions between the numerical predictions and in-vitro measurements

| Parametric study category | Case | Pressure of 30 mm Hg | | Pressure of 70 mm Hg | |
|---|---|---|---|---|---|
| | | Displacement error (mm)[a] | Error of $J_{2d}$[b] | Displacement error (mm)[a] | Error of $J_{2d}$[b] |
| (1) Effect of material model forms | Neo-Hookean model | 48.99 | 10.19 | 52.31 | 19.09 |
| | Exponential-type isotropic model | 17.18 | 8.69 | 24.78 | 9.44 |
| | Full collagen fiber mapped transversely isotropic model[c] | 13.72 | 5.84 | 14.93 | 7.01 |
| (2) Effect of local material axes and degrees of anisotropy | Curvilinear mapped fiber directions | 16.26 | 7.98 | 18.01 | 8.15 |
| | Mapped fiber directions from SALS + Linear relationship for $\delta$ | 15.67 | 7.19 | 19.48 | 8.85 |
| | Mapped fiber directions from SALS + Structural tensor for $\delta$[c] | 13.72 | 5.84 | 14.93 | 7.01 |
| (3) Effect of leaflet thicknesses | 50 % of mean leaflet thicknesses[d] | 31.81 | 11.23 | 36.28 | 13.09 |
| | 100 % of mean leaflet thicknesses[d] | 18.14 | 9.89 | 20.72 | 10.42 |
| | 200 % of mean leaflet thicknesses[d] | 34.37 | 12.01 | 45.16 | 19.23 |
| | Micro-CT-based leaflet thicknesses[c] | 13.72 | 5.84 | 14.93 | 7.01 |
| (4) Effect of chordae representations | All marginal | 14.17 | 6.92 | 17.35 | 9.01 |
| | Micro-CT reconstructed chordae with single-attached node | 56.50 | 12.89 | 51.61 | 14.36 |
| | Micro-CT reconstructed chordae with multiple-attached node[c] | 13.72 | 5.84 | 14.93 | 7.01 |

[a] Displacement error = $\sum_{I=1}^{N_{\text{marker}}} ||\mathbf{u}_I^{\text{in-vitro}} - \mathbf{u}_I^{\text{numerical}}||$, where $\mathbf{u}_I$ denotes the displacements associated with fiducial marker $I$

[b] In-plane Jacobian error = $\sum_{I=1}^{N_{\text{marker}}} |(J_{2d})_I^{\text{in-vitro}} - (J_{2d})_I^{\text{numerical}}|$

[c] The full-blown FE model for the mitral valve with highest fidelity

[d] Uniform thicknesses: MVAL = 1.1 mm and MVPL = 0.92 mm

### *10.4.5 Estimation of the In-Vivo Valvular Stresses*

Estimation of regional tissue stresses in the functioning heart valve remains an important goal in our understanding of normal valve function and in developing novel engineered tissue strategies for valvular repair and replacement. Methods to accurately estimate regional tissue stresses are thus needed for this purpose, and in particular to develop accurate, statistically informed means to validate computational models of valve function. We thus estimated the regional tissue stresses of the MVAL based on in-vivo three-dimensional deformational data by utilizing a finite element (FE) modeling approach for stress analysis, in which an average structure of the MVAL was incorporated. In order to characterize the in-vivo mechanical properties of the MV constitutive models, an inverse FE modeling approach via the genetic algorithm was employed. The following assumptions were made in the numerical studies:

- The viscous and any related time-dependent effects were ignored and only the functional, quasi-elastic behaviors of the MV tissues were considered [36, 37].
- MVAL tissue was modeled as a pseudo-hyperelastic material [33].
- The region of interest (ROI) $\Omega$ was defined by the 2 by 2 sonocrystal marker array with an additional center marker (Fig. 10.6a).
- The local kinematics of the MVAL was represented by the prescribed in-vivo measured displacement data on the four edges.
- The FE simulation for stress analysis was carried from the reference configuration to the end of isovolumic relaxation, and the fully loaded state was chosen for the statistical analysis of the MVAL regional stresses.

In this integrated modeling/experimental scenario, we sought to develop an estimate of the ROI stress tensor by averaging the stress at each point within the ROI. We noted that in developing our approach, variations in the resulting local tissue stresses can arise from the following sources within the ROI:

(1) Heterogeneities of the local deformation, resulting in $\mathbf{F} = \mathbf{F}(\mathbf{X}, t)$, where $\mathbf{X}$ is the local position vector and $t$ is time over the cardiac cycle.
(2) Variations in local tissue microstructure.
(3) Variations in local fiber mechanical properties.

The first two items can be directly quantified from experimental data: $\mathbf{F}$ can be determined at each point in the marker array by bilinear interpolation and tissue microstructure can be quantified using available experimental techniques, as we have done using small angle light scattering (SALS). It is the last item, the mechanical properties, which must be computed from the experimental data. Thus, we conducted a study to determine the average key fiber microstructural features from extant microstructural data on the MVAL. This key piece of information, when incorporated in the simulations, allowed us to quantify not only the mean ROI stress but also its variation from a single experimental run. This further allowed us to set confidence limits for the computed mean stresses from individual test specimens under a single set of experimental conditions.

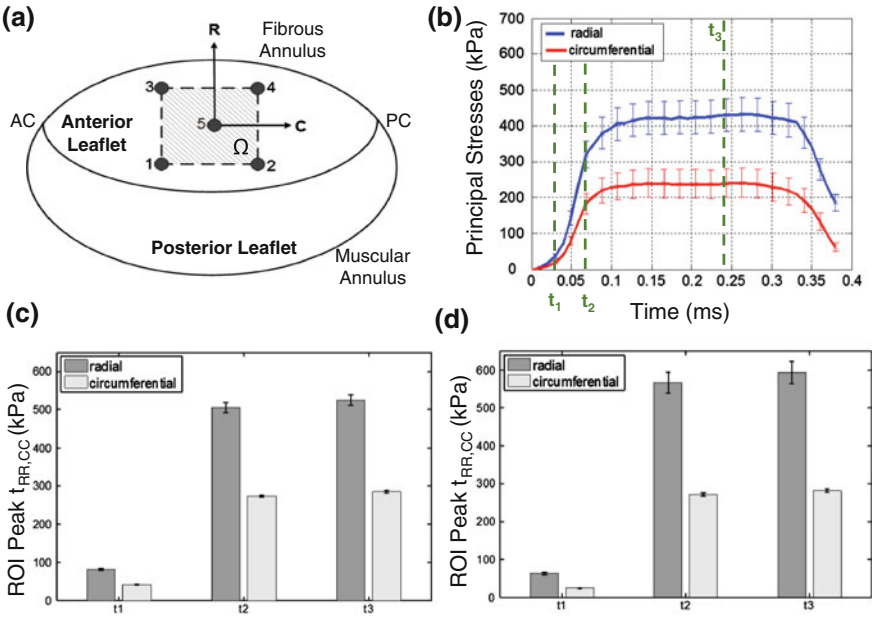


**Fig. 10.6** **a** Schematic of the ovine mitral valve anterior and posterior leaflets and the sonocrystal marker array for in-vivo measurements, **b** estimated mean principal stresses and the variation ($t_{\mathrm{RR,CC}} \pm \mathrm{SD}_{t\mathrm{RR,CC}}$) over the region of interest ($\Omega$) in the radial and circumferential directions during a cardiac cycle, and estimated ROI peak principal stresses and associated sample variations ($n = 10$) at various time instants ($t_1$, $t_2$, $t_3$) considering: **c** the variation in the local fiber directions, and **d** variations in both the local fiber directions and degrees of material anisotropy (figures modified from [52])

We employed the following inverse modeling approach to characterize the in-vivo mechanical response for the MVAL. We utilized a global optimization technique, the genetic algorithm [93], for finding an optimal set of material parameters which minimizes the error norm of displacement field between the in-vivo measurements [3, 52] and FE solutions:

$$\text{Objective function: } \min_{\mathbf{x}} f(\mathbf{x}) = \frac{1}{n_{\mathrm{data}}} \sum_{I=1}^{n_{\mathrm{data}}} \left\| \mathbf{u}_I^{\mathrm{in-vivo}} - \mathbf{u}_I^{\mathrm{FEM}} \right\| \tag{10.4}$$

where $n_{\mathrm{data}} = 40$ is the number of time points of the 3D sonocrystal positional data during the cardiac cycle. Given a set of material parameters, an ABAQUS input file was generated for the simulation of the MVAL subjected to external pressure loading. The nodal displacements were obtained from the ABAQUS output file to construct the displacement vector, and the fitness function for each genome population was evaluated. The optimization process terminated when the change of the objective function is less than the set tolerance (TOL $= 10^{-6}$).

To analyze the stress field in the ROI, the MVAL surface was discretized into $40 \times 40$ thin-shell elements with the characterized in-vivo constitutive model. The boundary nodes were prescribed with the displacement boundary conditions based on the five sonocrystal measured data; transvalvular pressures were applied on the element surfaces; FE simulations of the MVAL during a cardiac cycle were performed, and stress output data were obtained using a `Python` post-processing script. The calculated stresses were averaged over the 1,600 elements and regional variation of the stresses was estimated.

Stress-time profile during a cardiac cycle predicted was fairly regular in shape and smooth (Fig. 10.6b), provided the anisotropic in-vivo stretches, with a similar pattern of rapid increasing followed by a plateau, in both radial and circumferential directions. Interestingly, we also noted that the full collagen fiber mapped transversely isotropic produces estimates with substantially larger stresses in the radial direction ranging from 380 to 480 kPa and the circumferential stresses ranging from 200 to 280 kPa given the radial stretch of 32 % and circumferential stretch of 11 %. The predicted ROI peak stresses at the fully loaded state ($t_3$) were ∼520 and ∼285 kPa for the radial and circumferential components, respectively, for the numerical experiments with *variations in the local fiber directions* (Fig. 10.6c), whereas the peak stress components of ∼600 and ∼280 kPa in the radial and circumferential directions were reported by considering *variations in both the local fiber directions and degrees of material anisotropy* (Fig. 10.6d). The resulting radial stress variations in the latter case are expectedly larger (by ∼5 %) than the former situation (∼2.4 %) due to introducing additional fiber microstructural. However, this additional variation led to very small deviations of the estimated peak circumferential stress component.

### *10.4.6 Tissue Microstructure and Mechanics of the MV Leaflets*

The ultimate success of the tissue models utilized in the above studies relies on an in-depth understanding of the underlying tissue fibrous and cellular constituents, and of how they rearrange under physiological loading. Critical to heart valve tissue homeostasis is the valve interstitial cells (VICs), which reside in the interstitium and maintain the extracellular matrix (ECM) through both protein synthesis and enzymatic degradation [94]. There is also scant experimental data on the alterations of the mitral valve fiber network reorganization as a function of load, which is critical for implementation of computational strategies that attempt to link this meso-micro scale phenomenon. The observed large-scale deformations experienced by VICs could be implicated in mechanotransduction [101], i.e., translation of mechanical stimuli into synthetic levels.

The MV leaflets are composed of collagen, elastin, glycosaminoglycans (GAGs), and interstitial cells [55]. Collagen (∼71.7 % Type I + ∼29.3 % Type III) constitutes ∼59.2 % of the leaflet dry weight [49, 55]. Morphologically, the MV leaflet has a multilayered structure: the atrialis/spongiosa, the fibrosa, and the ventricularis [91]. The fibrosa, which mainly consists of collagen fibers and accounts for ∼68 % of

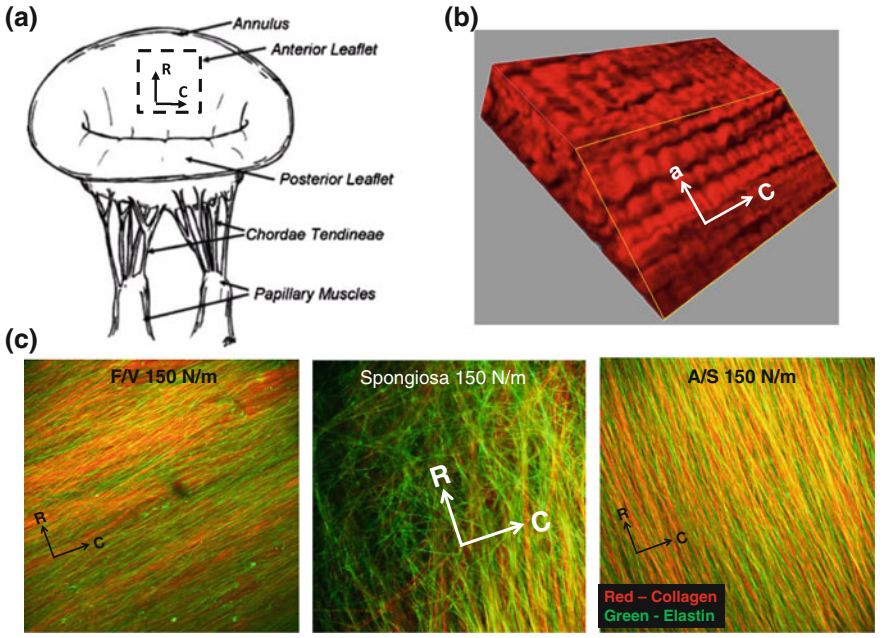


**Fig. 10.7** **a** Schematic diagram of the mitral valve showing the ~10 mm × 10 mm anterior leaflet region where the tissue section was removed for analysis, **b** 3D rendering of the fibrosa collagen structure showing the high degree of compacted collagen structure, and **c** enface images of the MV leaflet tissue in the major layers, with collagen in *red* and elastin in *green*. Noted that changes in both preferential alignment and degree of orientation in the layers, indicative of the complex structure of the mitral valve

the whole leaflet thickness [49], likely has the greatest influence on the mechanical properties of valve leaflets. We have previously shown in heart valve tissues that mechanical response is dominated by reorientation and rotation of the collagen fibers and that rotation is responsible for large radial strains [7–9]. In addition, it is likely that the interactions between collagen fibrils and matrix constituents (mainly proteoglycans and water) affect the tissue mechanical properties [15, 24, 35]. Clearly, knowledge of mechanical properties and kinematics of MV at fiber level is necessary to fully understand the structural basis for its unique elastic mechanical behavior.

We have recently looked into the microstructure of the mitral valve anterior leaflet utilizing a laser scanning confocal imaging system (LSCM). Ovine anterior MV leaflets, approximately 35 kg in size, were acquired, and a 1 cm by 1 cm sample (Fig. 10.7a) was mounted into a miniature biaxial testing system and loaded to 150 N/m. Samples were fixed at the desired tension level and were then split into two pieces with long-axis oriented along the circumferential direction. The first piece was embedded into optimal cutting tempature (OCT) for transverse sectioning. A 7-μm cryosection was taken for Movat's Pentachrome staining to distinguish the leaflet layers (Fig. 10.2). A 30-μm cryosection was also taken for LSCM to identify collagen fibers from second harmonic generation (SHG). The second

intact piece was taken for LSCM to identify collagen fibers from SHG and elastin fibers from autoflourescence at 830-μm wavelength (Fig 10.7b). Samples were imaged enface to 50 μm deep on both the atrialis and ventricularis surfaces. From the enface image stacks, a *z*-projection was formed and the elastin network was detected. Results for the fibrosa layer, which is the main load-bearing layer, revealed the typical dense, undulated collagen type-I fiber network oriented in a planar arrays (Fig 10.7b). However, we noted that the undulations are largely in sync and the presence of noticeable spaces between the major fiber bundles. Interestingly, close examination of the layers revealed major orientation variations (Fig 10.7c). We noted first that the ventricularis and fibrosa layers demonstrated the usual circumferentially orientation for both collagen and elastin fibers. However, the spongiosa layer revealed a more random arrangement, followed by a radially oriented collagen and elastin fiber network in the atrialis layer. These layer differences in layer-specific fibrous organization, and the intricate interrelationship between ECM planar organizations are necessary to account for micro-meso scale phenomena when developing MV finite element models. The long-term goal for these findings is to provide insight into VIC mechanobiology as a function of ECM architecture under organ-level loads. ECM architecture has been shown to change with age, disease, and repair with procedures such as annuloplasty and resection.

These experimental findings clearly motivate a structurally accurate MV constitutive model, which incorporates layer-specific ECM planar organization under organ-level loading. Thus, while phenomenological constitutive models, such as Eq. (10.3), provide a good description of the effective behavior of the bulk tissue, considering the fiber architecture and mechanical behavior of valvular tissues (Figs. 10.4 and 10.7), a structural approach is clearly most suitable for the formulation of a constitutive model for valvular tissues. We have developed a series of these models, the most basic presented [9, 27, 34, 78, 92]. In brief, the tissue's total strain energy is assumed to be the sum of the individual fiber strain energies, linked through an affine transformation from the fiber coordinate to the global tissue coordinates as depicted in Eq. (10.1). We started by noting that, like all soft biological tissues, valvular tissues have primarily two major load-bearing components: the collagen and elastin fibrous network and the non-fibrous (or amorphous) ground matrix, which is composed mainly of GAGs and water. We thus assumed that the planar biaxial mechanical properties of the leaflet can be represented as a planar array of collagen and elastin fibers. Anatomically, these collagen fibers most closely represent the dense, highly aligned collagen fibers in the fibrosa layer. Based on works by Fung [33], soft tissues are considered as hyperelastic composite elastomeric materials. Next, the following comprehensive set of assumptions were considered for modeling the heart valve soft tissues:

(1) Both elastin and collagen fibers bear load only along their fiber axes and have negligible resistance to compressive forces.
(2) The elastin-collagen mechanical interactions were ignored and the overall tissue response is considered to be the sum of the individual constituent responses.

(3) The load required to straighten the collagen fibers is negligible compared to the load transmitted by elastin or stretched collagen. Thus, collagen bears load only when completely straightened.
(4) Elastin fibers bear load immediately upon strain and do not exhibit any recruitment.
(5) Contributions from non-load-bearing constituents are assumed to mechanically contribute to tissue incompressibility.

The tissue-level hyperelastic strain energy density $\Psi$ [33] of the RVE is thus assumed to result from the contribution of elastin (e), collagen (c), which includes the sparse elastic sheet or lamina, and smooth muscle cells, weighted by their respective volume fractions $\phi$'s:

$$\Psi(\mathbf{C}) = \phi_c \Psi_c(\mathbf{C}) + \phi_e \Psi_e(\mathbf{C}) + \phi_m \Psi_m(\mathbf{C}) \tag{10.5}$$

The resulting tissue-level response in terms of the second Piola-Kirchhoff stress tensor $\mathbf{S}$ is derived by

$$\mathbf{S} = \frac{\partial \Psi}{\partial \mathbf{E}} - \mathbf{p} \cdot \mathbf{C}^{-1} = \phi_c \frac{\partial \Psi_c}{\partial \mathbf{E}} + \phi_e \frac{\partial \Psi_e}{\partial \mathbf{E}} + \phi_m \frac{\partial \Psi_m}{\partial \mathbf{E}} - \mathbf{p} \cdot \mathbf{C}^{-1} \tag{10.6}$$

Here, $\mathbf{E}$ is the Green strain tensor, and the Lagrange multiplier p, which accounts for the incompressibility, is assumed to be associated with the ground matrix constituents of the tissue as stated above. A structurally based modeling approach is employed for the collagen and elastin strain energy functions. The novelty of this study is the approach to model the elastin network as discrete fibers like collagen fibers, rather than a material phase as in [42]. This has been made possible by the quantification of the elastin structure using two-photon imaging in [26]. Thus, the contributions of both collagen and elastin fiber ensembles acting in a given direction $\mathbf{N}(\theta) = \cos(\theta)\mathbf{X}_C + \sin(\theta)\mathbf{X}_R$ at the reference configuration, summed over all fiber orientations, are obtained by

$$\Psi_e(\mathbf{E}) = \phi_e \int_\theta \Gamma_e(\theta)\, \Psi_e^f(\mathbf{E})\, d\theta \quad \text{and} \quad \Psi_c(\mathbf{E}) = \phi_c \int_\theta \Gamma_c(\theta)\, \Psi_c^{ens}(\mathbf{E})\, d\theta \tag{10.7}$$

where the functions $\Gamma_c$ and $\Gamma_e$ describe the planar angular distributions of collagen and elastin fibers, respectively, and $\Psi_e^f$ and $\Psi_c^{ens}$ are the elastin fiber and collagen fiber ensemble strain energy functions, respectively. The non-fibrous components are modeled as a Neo-Hookean material with a shear modulus of ~50 kPa based on recent data [12].

The results from Fata et al. [26] and related studies [41, 42, 102] suggested that the elastin fibers can be represented using a linear **S-E** relation. Therefore, we utilized the following elastin fiber strain energy

$$\Psi_e^f(\mathbf{E}) = \frac{\kappa_e}{2}\varepsilon^2 \tag{10.8}$$

Under the usual affine transformation assumption, the elastin fiber strain is derived from the bulk tissue strain using $\varepsilon = \mathbf{N}^{\mathrm{T}}\mathbf{E}\,\mathbf{N}$. As stated above, unlike collagen, elastin fibers do not appear to undergo any type of recruitment, so the total elastin stress is simply

$$\mathbf{S}_{\mathrm{e}}(\mathbf{E}) = \phi_{\mathrm{e}} \frac{\partial \Psi_{\mathrm{e}}}{\partial \varepsilon} \frac{\partial \varepsilon}{\partial \mathbf{E}} = \phi_{\mathrm{e}} \int_{\theta} \Gamma_{\mathrm{e}}(\theta)\, S_{\mathrm{e}}^{\mathrm{f}}(\varepsilon) \frac{\partial \varepsilon}{\partial \mathbf{E}} \mathrm{d}\theta \tag{10.9}$$

To model $\Gamma_{\mathrm{e}}(\theta)$ from the multiphoton imaging data (Fig. 10.7c), our experimental findings suggested two orthogonally placed, normally distributed fiber populations aligned to the circumferential (C) and radial (R) directions, respectively, with low splay values ($\sim 10^{\circ}$). Hence, the total fiber orientation distribution function is given by $\Gamma_{\mathrm{e}}(\theta) = \Gamma_{\mathrm{e}}^{\mathrm{C}}(\theta) + \Gamma_{\mathrm{e}}^{\mathrm{R}}(\theta)$, and the corresponding elastin stress phase can be determined by

$$\mathbf{S}_{\mathrm{e}} = \phi_{\mathrm{e}} \kappa_{\mathrm{e}} \int_{\theta} \Gamma_{\mathrm{e}}(\theta)\, \varepsilon(\mathbf{N} \otimes \mathbf{N}) \mathrm{d}\theta \tag{10.10}$$

with $\phi_{\mathrm{e}}$ and $\Gamma_{\mathrm{e}}$ taken from known measurements and $\kappa_{\mathrm{e}}$ estimated from the biaxial mechanical data.

Next, as for the collagen fiber phase, the collagen ensemble strain energy is considered to be the sum of individual fiber strain energies $\Psi_{\mathrm{c}}^{\mathrm{f}}$ weighted by the angular probability function $\Gamma_{\mathrm{c}}$

$$\Psi_{\mathrm{c}}^{\mathrm{ens}}(\mathrm{E_f}) = \int_{0}^{\mathrm{E_f}} \Gamma_{\mathrm{c}}(\mathrm{E}) \Psi_{\mathrm{c}}^{\mathrm{f}}(\mathrm{E})\, \mathrm{dE} \tag{10.11}$$

As in our work for pericardium [79], we assumed a linear fiber stress strain relationship based on the second Piola-Kirchhoff stress and Green-Lagrange strain, $S_{\mathrm{c}}^{\mathrm{f}} = \kappa_{\mathrm{c}} E_{\mathrm{t}}$, where $\kappa_{\mathrm{c}}$ is the elastic modulus of individual straight collagen fibers, and $E_t$ is the true fiber strain defined by $E_{\mathrm{t}} = (E_{\mathrm{f}} - E_{\mathrm{s}})/(1 + 2E_{\mathrm{s}})$. The collagen fiber strain energy is simply

$$\Psi_{\mathrm{c}}^{\mathrm{f}} = \frac{\kappa_{\mathrm{c}}}{2} E_{\mathrm{t}}^2 \tag{10.12}$$

and the total collagen fiber phase 2nd Piola-Kirchhoff stress is given by

$$\begin{aligned} \mathbf{S}_{\mathrm{c}} &= \phi_{\mathrm{c}} \int_{\theta} \Gamma_{\mathrm{c}}(\theta) \frac{\partial \Psi_{\mathrm{c}}^{\varepsilon}}{\partial \mathbf{E}} \mathrm{d}\theta \\ &= \phi_{\mathrm{c}} \kappa_{\mathrm{c}} \int_{\theta} \Gamma_{\mathrm{c}}(\theta) \left[ \int_{0}^{E_{\mathrm{ens}}(\theta)} D(x) \frac{E_{\mathrm{ens}} - x}{(2x+1)^2} \mathrm{d}x \right] \mathbf{N} \otimes \mathbf{N} \mathrm{d}\theta \end{aligned} \tag{10.13}$$

To facilitate numerical integration, we simulated the measured collagen fiber orientation distribution using a Beta probability distribution function, with a mean $\mu$ and the standard deviation $\sigma$, with a span from $E_s \in [0, E_{ub}]$, where $E_{ub}$ represents the ensemble strain level where all the collagen fibers have been recruited.

Finally, we represented the ground matrix using a Neo-Hookean model as

$$\mathbf{S}_m = \phi_m \frac{\kappa_m}{2} (I_1 - 3) \tag{10.14}$$

Furthermore, the water content were assumed to be responsible for the incompressibility of the tissue, and are used to solve for the Lagrange multiplier p. With Eqs. (10.10), (10.13), and (10.14), we have the final complete expression of **S** for the MV leaflet tissues as

$$\begin{aligned} \mathbf{S} = {} & \phi_c \kappa_c \int_\theta \Gamma_c(\theta) \left[ \int_0^{E_{ens}(\theta)} D(x) \frac{E_{ens} - x}{(2x+1)^2} dx \right] \mathbf{N} \otimes \mathbf{N} d\theta \\ & + \phi_e \kappa_e \int_\theta \Gamma_e(\theta) \varepsilon \mathbf{N} \otimes \mathbf{N} d\theta + \phi_m \frac{\kappa_m}{2} (I_1 - 3) - p\mathbf{C}^{-1} \end{aligned} \tag{10.15}$$

When applied to the mitral valve anterior leaflet biaxial mechanical data, the model fit quite well (Fig. 10.8a). This included the representation of the long-toe region found in the radial component. Moreover, when the respective contribution of the each tissue component was plotted along the experimental data, one can see how the elastin dominates the low strain region, and then transitions to the expected collagen dominated phase (Fig. 10.8b). An important aspect of the structural approach is that the two distinguishing aspects of the heart valve leaflet biaxial behavior, namely the extreme mechanical anisotropy and the strong mechanical coupling between the axes, can be explained by the angular distribution of fibers. While this modeling approach worked well, it should be noted that the use of this level of homogenized formulation ignores the layer-specific mechanical contributions and the implicit nonuniformity of the transmural stress distribution. Such work is currently under investigation in our lab.

### *10.4.7 Affine Deformation of the MV Collagen Fiber Network*

Collagen has a complex, three-dimensional hierarchical structure, with both collagen Type I and III molecules consisting of triple helix amino acid chains stabilized by hydrogen bonds [65]. Rod-like collagen molecules covalently self-assembled into long fibrils with 64–68 nm D-period (or D-spacing) that are visible under electron microscopy [16, 33, 40, 90] (Fig. 10.10a). According to the Hodge-Petruska model (also called quarter-stagger model), the D-period consists of a gap region of ~0.6D

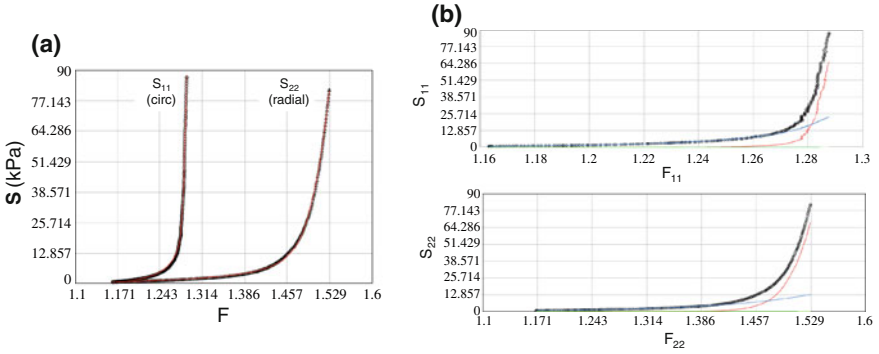


**Fig. 10.8** **a** Representative biaxial stress-strain curves of the mitral valve anterior leaflet under *equibiaxial curves* (*symbols*) and the fit of the structural model, showing excellent agreement, including the long-toe region in the radial direction. **b** Same data but showing respective contributions of the collagen (*red*), elastin (*blue*), and matrix (*green*) phases. Note how the elastin phase is responsible for entire low stress regions, whereas the collagen becomes dominant at high stresses. While similar observations have been made for many soft tissues, the very large strains that the leaflets undergo before the collagen becomes dominant is more specific to valvular tissues

and an overlap region 0.4 D [40]. Collagen fibrils are discontinuous and with a large aspect ratio (length/diameter) up to ~2,000 [96, 97]. At the higher hierarchical level, collagen fibrils are bounded together by small proteoglycans and form the collagen fibers [88, 100]. The structure of the formed collagen fiber networks tends to be tissue specific [33, 43, 90]. For example, in tissues such as tendon collagen fibers are uniaxially aligned, while in planar tissues such as skin they are aligned multidirectionally in two-dimensional sheets [89].

Polarized light microscopy [38, 39], small angle light scattering (SALS) [47, 82], and X-ray scattering [4, 6, 25, 85] techniques have been applied to intact tissues to nondestructively characterize the collagen crimp structure, collagen fiber orientation, and mechanical properties of collagen at the fibril/molecular levels. Among them, small angle X-ray scattering (SAXS) remains an ideal tool to characterize the collagen fibril orientation and stretch, as demonstrated in many applications under uniaxial stretch [31, 32, 71, 84, 86]. We have carried out the first study of the kinematics of collagen fibrils under *controlled biaxial stretch* [53]. As expected, the collagen fibril kinematics under biaxial stretch was found to be more complex than those under uniaxial deformation. The D-period strain of collagen fibrils was found to be a fraction of tissue strain and with a delayed onset [53]. Moreover, alignment and orientation of collagen fibrils changed with the applied biaxial loads [53]. These findings underscored the importance of quantifying the collagen fibril kinematics under biaxial stretch in planar collagenous tissues. Here, we investigated the kinematics and mechanical properties of collagen fibrils in the MVAL under biaxial stretch using SAXS. Our goal was to gain insight into the mechanisms underlying the MVAL quasi-elastic properties. The biaxial stretching device using for SAXS measurements [53] was redesigned to allow for simultaneous force measurements. This modification allowed determination of the fibrillar modulus. Collagen fibril angular distribution of

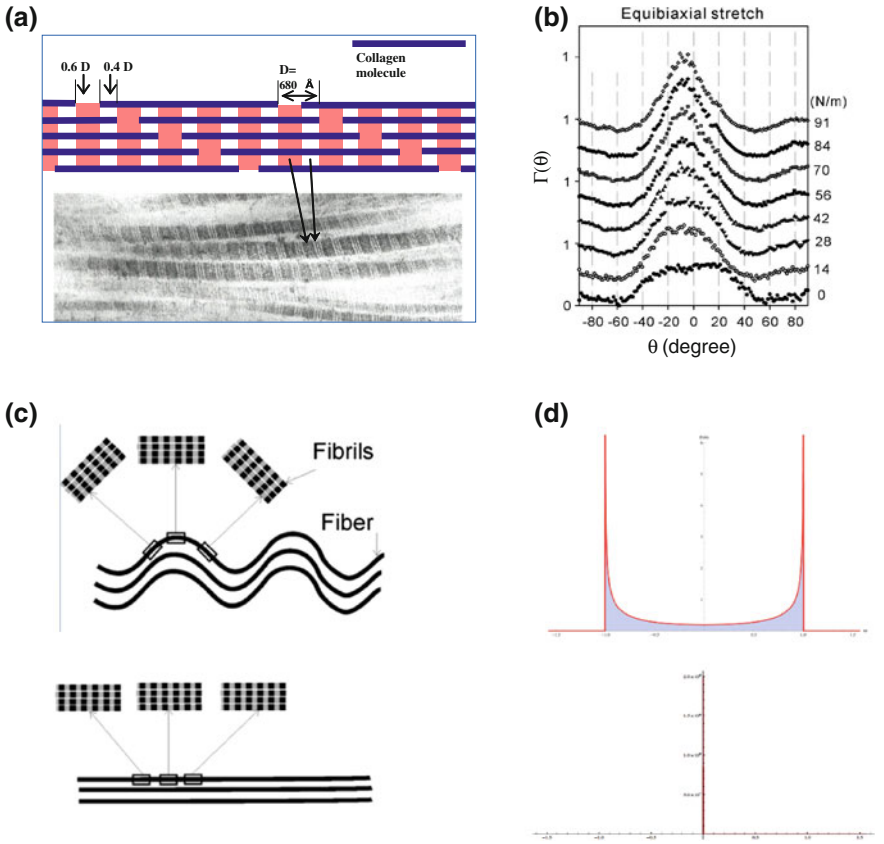


**Fig. 10.9** **a** Schematic diagram of the structure of the collagen molecule showing the characteristic "*D*" spacing and the actual electron microscope image. **b** Successive SAXS orientation distribution *curves* for a mitral valve anterior leaflet tissue under increasing levels of equi-biaxial loading, showing an increased order (i.e., reduced splay). Illustration of how a single collagen fibril angular distribution is affected by the uncrimping resulting from straightening: **c** crimped and straight collagen fibrils, **d** the resulting angular distribution

collagen fibrils were measured under biaxial stretch (Fig. 10.9b). *This unique dataset allows an opportunity to evaluate the key assumption of the structural models, i.e., the fiber network deform under an affine rule* as shown in Eq. (10.1). In the following, we utilized the SAXS data and the collagen fiber amplitude and crimp period measured from the SHG images (Fig. 10.9b) to simulate the rotation and stretch of the MV collagen fibril network. It should be emphasized that the SAXS measurements are restricted to collagen fibrils only, and are not affected by the presence of the elastin and other components. This makes them ideal for the present studies.

We started by assuming that the collagen fibers of the mitral valve can be represented by a planar sinusoids (Fig 10.9c), with an amplitude $a$ and a period $p$. Based on the SHG measurements, we determined that the MV anterior leaflet in the unloaded

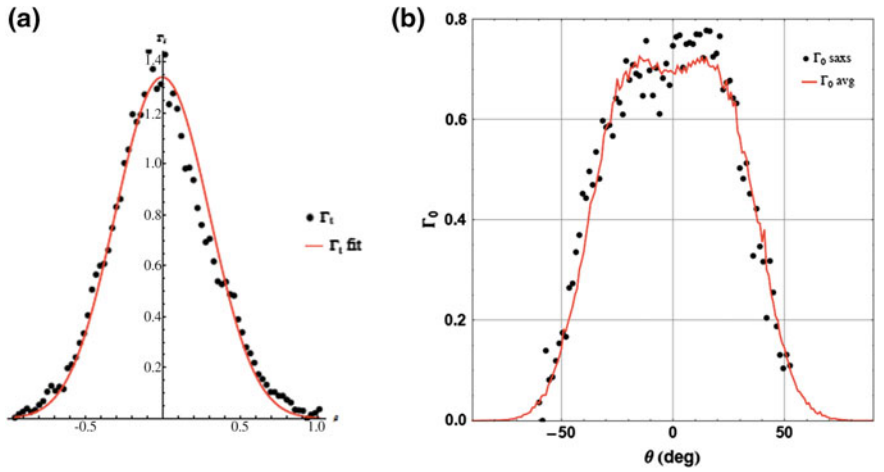


**Fig. 10.10** **a** The orientation distribution function fit using a Beta distribution in the loaded state, and **b** results of the complete model simulated 10,000 sinusoidal fibers showing excellent agreement. These results suggest that, at the tissue level, the collagen fibers of the mitral valve leaflet follow affine transformation kinematic behavior

state has a mean amplitude of 2.10 μm and a mean period of 22.85 μm. Next, since the SAXS technique actually measures the combined effects of fiber undulations and overall orientation (Fig. 10.9c), we can represent the orientation distribution function $\Gamma_{\text{single fiber}}(\theta)$ for a single sinusoidal fiber using

$$\Gamma_{\text{single fiber}}(\theta) = \frac{p}{\pi \cos(\theta)^2 \sqrt{4\pi^2 a^2 - p^2 \tan(\theta)^2}} \tag{10.16}$$

This leads to a dual peaked distribution (Fig. 10.9d). As the fiber stretches, the amplitude decreases and the distribution will collapse to a delta function $\delta\ (\theta = 0)$ (Fig. 10.9d). It should be noted here that the actual measured $\Gamma(\theta)$ (Fig. 10.9b) is the sum of the overall fiber orientation of the fiber normal **N**, $\Gamma_N(\theta)$, and the sinusoidal geometry of each fiber, given by Eq. (10.16). Thus, as the MV leaflet is stretched, $\Gamma(\theta)$ will change due to both the rotation of the fibers according to the anisotropic stretch patterns (Fig. 10.8a) and the straightening of the constituent collagen fibers. Since, the collagen is preferentially oriented along the circumferential direction of the leaflet (Fig. 10.7a and b) and the leaflet experiences much higher strains in the radial direction, the overall fiber splay will tend to increase. However, this effect is counteracted by the simultaneous alignment of the individual collagen fibrils as they straighten (Fig. 10.9c and d). As observed, it is the later effect that dominates the SAXS pattern (Fig. 10.9b). In essence, the *proof* of the affine deformation assumption is our ability to obtain the unloaded fiber measured splay from the SAXS measurements, $\Gamma_0(\theta)$ (Fig. 10.10b), by separating these effects using the following model.

We simulated the MV collagen fiber network using 10,000 fibers (the approximate number contained in a transmural section of the tissue). Sinusoidal collagen fibrils

with an orientation distribution were represented by a Beta function for $\Gamma_N(\theta)$, with $\theta \in [-90°, 90°]$, a mean of 0°, and a standard deviation determined by fitting the SAXS data (Fig. 10.10b). From our SHG measurements, we noted that the collagen fibers were completely straightened under physiological loading. By inverting Eq. (10.1), we fitted the deformed distribution under full load by estimating the $\Gamma_N(\theta)$ using the measured deformation gradient tensor **F** from the experimental data, resulting in a fit of 14.51° with an $r^2 = 0.97$ (Fig. 10.10a). Next, we utilized this value and the measured amplitude as well as the crimp period values in Eq. (10.16) to simulate the total $\Gamma(\theta)$ as measured in SAXS by summing the contributions of all 10,000 fibers and renormalizing to unit area. When compared to the measured SAXS measurements, $\Gamma_0(\theta)$ (Fig. 10.10b), the model fit the data quite well, with an $r^2 = 0.96$. *This remarkable result suggests that, at the homogenized tissue-level scale of* ∼1 mm, *the collagen fiber network in the mitral valve anterior leaflet deforms according to the affine model as shown in* Eq. (10.1). *Moreover, the result serves as the foundation for supporting the use of structural models for the heart valve tissues that require an affine fiber kinematic basis.*

### *10.4.8 Mechanical Properties of Valve Interstitial Cells*

Within the layers of all heart valve leaflet tissues, there resides a heterogenic population of valve interstitial cells [28, 63, 64, 94]. The heterogeneity of the interstitial cells is made up of fibroblasts, smooth muscle cells, and myofibroblasts, which have characteristics of both fibroblasts and smooth muscle cells. Studies of the interstitial cell population in both human and porcine subjects have revealed that the cell population was not localized to any single region or layer of the leaflet, but was presented throughout the tissue [5, 62]. Interest in the myofibroblast cells (typically referred to as VICs) has grown in recent years, as they are believed to be critically important in valve pathophysiology. Primarily, VICs serve to maintain the structural integrity of the leaflet tissue by remodeling via protein synthesis and enzymatic degradation. Their phenotype (which ranges from fibroblast-like to myo-like) is believed to be plastic and reversible, as VICs of normal, healthy valves were quiescent. In developing, diseased, and remodeling valves, the VICs were activated and contractile [73, 74]. While their dualistic nature is not fully understood, the VIC's multifunctionality may be used for cell-cell communication, tissue remodeling, wound healing, and contraction [64]. Further, it is believed that when the phenotype of the resident VIC population is myo-like, the cells are actively remodeling the ECM. This indicates that the VIC phenotypic state at any given time is likely related to the current remodeling demands of the tissue [74]. Porcine aortic VIC (AVIC) contractility has been qualitatively studied with cultured cells on silicone substrates in the presence of multiple contractile chemical agents [28, 63]. In both studies, contraction occurred for most agents within 3 min and reached a plateau within 10 min. Additionally, Messier et al. [63] found that the few cells with no initial basal tonus did not respond to the administered vasoconstriction drugs. Isoproterenol was used to elicit relaxation

from active cells, from which all cells recovered their previous basal tonus within 25 min. While not quantitative, these findings were the first examples demonstrating an AVIC contractile response.

One major indicator of VIC phenotype is the level of $\alpha$ smooth muscle actin ($\alpha$-SMA), which dramatically affects the cell stiffness. To address this question, we have isolated ovine VICs from the four heart valves and subjected them to micropipette aspiration to assess cellular stiffness [95], and cytoskeletal composition and collagen biosynthesis were quantified using surrogates $\alpha$-(SMA) [62]. Results revealed that VICs from the aortic and mitral valves were significantly stiffer ($p < 0.001$) than the pulmonary and tricuspid VICs (Fig. 10.11a). Additionally, left side isolated VICs contained significantly more ($p < 0.001$) SMA and Hsp47 than the right side VICs. Mean VIC stiffness correlated well ($r = 0.973$) with TVP; $\alpha$-(SMA) and Hsp47 also correlated well ($r = 0.996$) with one another. Moreover, assays were repeated for VICs in situ, and as with the in-vitro results, the left side VIC protein levels were significantly greater ($p < 0.05$). We have also explored AVIC viscoelastic behavior using the micropipette aspiration technique [61]. We then modeled the resulting time-length data over the 100 s test period using a standard linear solid (SLS) model, which includes Boltzmann superposition. We concluded that while VIC viscoelastic effects are negligible during valve closure, they likely contribute to the time-history of AVIC deformations during diastole.

However, such models are only a first step. Clearly, it is important to investigate the mechanical properties of the VICs and their cellular structures as well as the mechanical interactions with their environments. Numerical results from our simulations may play an important role in elucidating how the mechanical properties of VICs cause the pathological responses to the heart valve tissue. Recently, we have developed a 3D mixture model for VICs and specialized for 2D axisymmetric geometry of a micropipette aspiration experiment (Fig. 10.11b). We considered the VIC as a multiphasic continuum mixture that constitutes viscous fluid phase for cytosol and a solid phase for different constituents of cytoskeleton. The interactions between the fluid and solid phases were described by Darcy's Law. Next, we considered basal (non-oriented) cytoskeleton, which can be either hyperelastic or hyperviscoelastic and oriented $\alpha$-SMA fibers as solid phases. The VIC can be activated due to the contraction of $\alpha$-SMA fibers and deactivated as necessary. Moreover, we simulated both poroelastic response, which consists of hyperelastic cytoskeleton, and poroviscoelastic response, which consists of hyperviscoelastic cytoskeleton. The micropipette aspiration simulations were carried out using the open source finite element solver, FEBio [59]. Results to date indicated that while a poroelastic model was able to capture the long-term model response, the poroviscoelastic model was required to completely match the entire cellular response (Fig. 10.11c). This multiphasic model of the VICs was developed first time to analyze the mechanical properties of the VICs as well as the micromechanical effects of $\alpha$-SMA fibers. We will further develop our model to simulate not only an isolated VIC under micropipette aspirations, but also in the native tissue. Consequently, we will be able to investigate how the mechanical properties of the VICs interact with the heart valves as a whole.

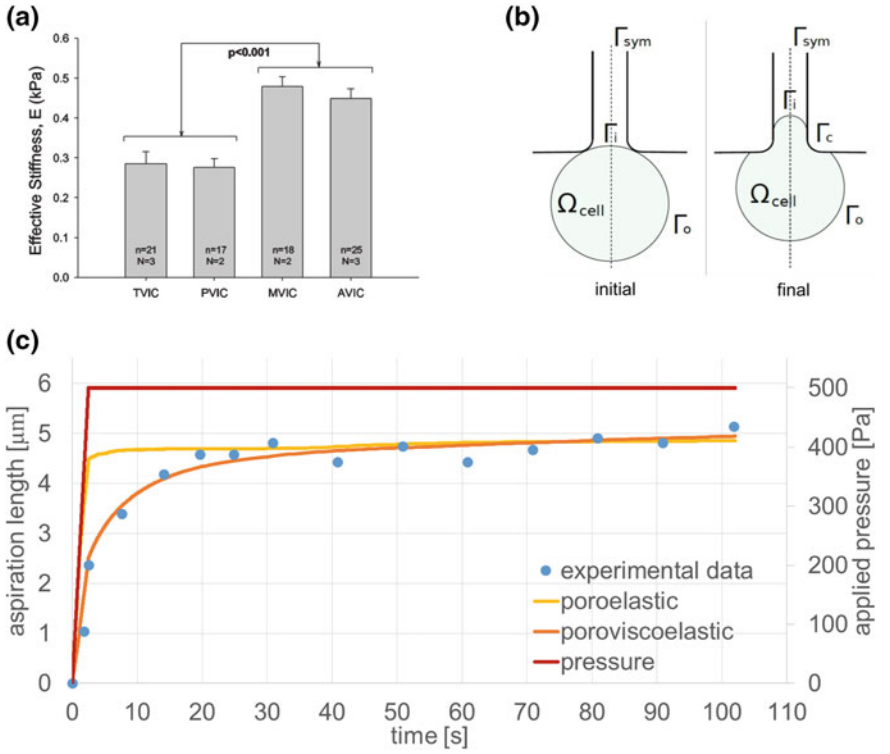


**Fig. 10.11** **a** Results from micropipette aspiration studies showing (using the Theret's formula) the effective stiffness of the four heart valve interstitial cells, with the left side valves exhibit 60 % greater stiffness than the right side valve cells, **b** schematic of the micropipette aspiration finite element study, and **c** the mixture model simulation of the micropipette aspiration experiment showing how the poro-viscoelastic model is required to obtain the best agreement with the experimental aspiration length data

## 10.5 Conclusion and Future Directions

As mentioned in the beginning of this chapter, we are now entering a level of knowledge of MV function, wherein computational approaches begin to be realistically applied. We have demonstrated that there is a need of the development of an anatomically and microstructural accurate finite element model in order to make insightful connection to the mechanical responses of the MV tissues with the organ-level mitral valve behaviors under physiological loadings or due to surgical repair intervention.

However, simulations of normal and pathological valves requires the correct input data for them to be meaningful and realistic. This necessitates the integration of patient-specific data, which is generally not available on an individual basis.

Another approach is to utilize statistical descriptors of valve function from human sources. To this end, we have recently demonstrated that such information can be successfully integrated into a mapping procedure to produce average maps of heart

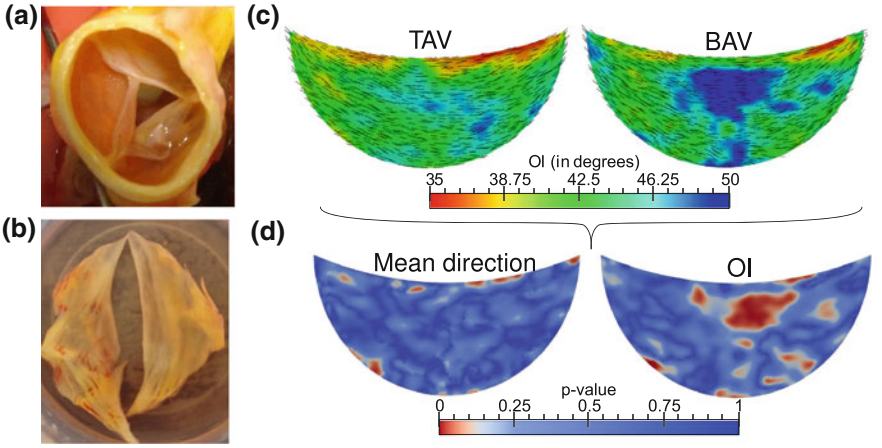


**Fig. 10.12** Micrographs of **a** normal and **b** bicuspid heart valve leaflets. Collagen fiber architectural measurements of human explants were used to determine the microstructure and then averaged to obtain the mean microstructure maps as shown in (**c**). Subsequent statistical analysis shown in (**d**) on mean fiber directions (*left*) and orientation index (OI) (*right*) shows important differences in the belly region for the OI but the mean fiber directions are similar in two cases

valve structure. The bicuspid aortic valve (Fig. 10.12a and b) is the most common cardiac congenital anomaly and has been found to be a significant risk factor for developing calcific aortic valve disease. We quantified the structure of human normal and bicuspid leaflets in the early disease stage. From these individual leaflet mappings, average fiber structure maps were generated using a novel spline-based technique to a total of six normal (tricuspid) and six bicuspid human explanted non-diseased aortic valves. A common template of the simulated heart valve geometry was used and a spline surface was fitted to this template geometry (RMSD of fitting $<0.04$ mm). The common template allows us to calculate the average fiber structure of the sampled tricuspid data (Fig. 10.12c and d), clearly showing the difference in the fiber microstructure. Interestingly, we found statistically different and consistent regional structures between the normal and bicuspid valves [2]. The regularity in the observed microstructure was a surprising finding, especially for the pathological BAV leaflets and is an essential cornerstone of any predictive modeling of the heart valves.

Ultimately, we would like to connect the organ-scale simulations to evaluate our understanding of the VIC mechanotransduction. To this end, it would be beneficial to develop a VIC phenotypic/biosynthetic model linked to organ-level deformations. For example, in the aortic valve leaflet transvalvular pressures above $\sim$5 mm Hg predominately result in ECM compaction as the collagen fibers become uncrimped and taut. From this ECM compaction, significant VIC shape changes have been observed with increasing pressures. Even a phenomenological model could, thus, simulate the VIC population with mechanical inputs (quantified by the deformation of the VIC nuclei) and cytokine activity. It could then be possible to predict the phenotypic and biosynthetic response of VICs under altered stress conditions.

The overall endpoint will be to quantitatively establish the degree which restoration of normal tissue stress leads to recovered tissue homeostasis, laying the basis for the rational and optimal design of surgical repairs and novel repair strategies, and will represent a major step towards patient-specific MV repair design-based on sound engineering and biological science.

**Acknowledgments** The funding from the National Institutes of Health (NIH) grants R01 HL119297, HL108330, HL63054, HL73021, and F32 HL110651 was greatly appreciated. Dr. C.H. Lee was supported in part by the American Heart Association Southwest Affiliate Postdoctoral Fellowship (14POST18160013) and the ICES Postdoctoral Fellowship. Dr. A. Aggarwal was supported by the American Heart Association Southwest Affiliate Postdoctoral Fellowship (14POST18720037).

## References

1. Adams, D.H., Rosenhek, R., Falk, V. (2010) Degenerative mitral valve regurgitation: best practice revolution. Eur Heart J 31 (16):1958–1966.
2. Aggarwal, A., Ferrari, G., Joyce, E., Daniels, M. J., Sainger, R., Gorman I.I.I., J. H., Gorma, R.C., Sacks, M. S. (2014) Architectural trends in the human normal and bicuspid aortic valve leaflet and its relevance to valve disease. Ann Biomed Eng 42 (5):986–998.
3. Amini, R., Eckert, C.E., Koomalsingh, K., McGarvey, J., Minakawa, M., Gorman, J.H., Gorman, R.C., Sacks, M.S. (2012) On the in vivo deformation of the mitral valve anterior leaflet: effects of annular geometry and referential configuration. Ann Biomed Eng 40 (7):1455–1467.
4. Aspden, R.M., Bornstein, N.H., Hukins, D.W. (1987) Collagen organisation in the interspinous ligament and its relationship to tissue function. J Anat 155:141–151.
5. Bairati, A., DeBiasi, S. (1981) Presence of a smooth muscle system in aortic valve leaflets. Anatomy and Embryology 161 (3):329–340.
6. Bigi, A., Incerti, A., Leonardi, L., Miccoli, G., Re, G., Roveri, N. (1980) Role of the orientation of the collagen fibers on the mechanical properties of the carotid wall. Boll Soc Ital Biol Sper 56 (4):380–384.
7. Billiar, K.L., Sacks, M.S. (1997) A method to quantify the fiber kinematics of planar tissues under biaxial stretch. J Biomech 30 (7):753–756.
8. Billiar, K.L., Sacks, M.S. (2000a) Biaxial mechanical properties of the natural and glutaraldehyde treated aortic valve cusp-Part I: Experimental results. Journal of Biomechanical Engineering 122 (1):23–30.
9. Billiar, K.L., Sacks, M.S. (2000b) Biaxial mechanical properties of the native and glutaraldehyde-treated aortic valve cusp: Part II-A structural constitutive model. Journal of Biomechanical Engineering 122 (4):327–335.
10. Bouxsein, M.L., Boyd, S.K., Christiansen, B.A., Guldberg, R.E., Jepsen, K.J., Müller, R. (2010) Guidelines for assessment of bone microstructure in rodents using micro-computed tomography. J Bone Miner Res 25 (7):1468–1486.
11. Braunberger, E., Deloche, A., Berrebi, A., Abdallah, F., Celestin, J.A., Meimoun, P., Chatellier, G., Chauvaud, S., Fabiani, J.N., Carpentier, A. (2001) Very long-term results (more than 20 years) of valve repair with carpentier's techniques in nonrheumatic mitral valve insufficiency. Circulation 104 (12 Suppl 1):I8–11.
12. Buchanan, R.M., Sacks, M.S. (2013) Interlayer micromechanics of the aortic heart valve leaflet. Biomech Model Mechanobiol 3 (4):1–4.
13. Butcher, J.T., Penrod, A.M., Garcia, A.J., Nerem, R.M. (2004) Unique morphology and focal adhesion development of valvular endothelial cells in static and fluid flow environments. Arterioscler Thromb Vasc Biol 24 (8):1429–1434.

14. Carpentier, A., Chauvaud, S., Fabiani, J.N., Deloche, A., Relland, J., Lessana, A., D'Allaines, C., Blondeau, P., Piwnica, A., Dubost, C. (1980) Reconstructive surgery of mitral valve incompetence: ten-year appraisal. J Thorac Cardiovasc Surg 79 (3):338–348.
15. Cavalcante, F.S., Ito, S., Brewer, K., Sakai, H., Alencar, A.M., Almeida, M.P., Andrade, J.S., Jr., Majumdar, A., Ingenito, E.P., Suki, B. (2005) Mechanical interactions between collagen and proteoglycans: implications for the stability of lung tissue. J Appl Physiol 98 (2):672–679.
16. Chapman, J.A., Hulmes, D.J.S. (1984) Electron microscopy of the collagen fibril. In: Ruggeri, A., Motto, P.M. (eds) Ultrastructure of the Connective Tissue Matrix. Martinus Nijhoff, Boston, pp 1–33.
17. Chen, H., Liu, Y., Zhao, X., Lanir, Y., Kassab, G.S. (2011) A micromechanics finite-strain constitutive model of fibrous tissue. J Mech Phys Solids 59 (9):1823–1837.
18. Condado, J.A., Velez-Gimon, M. (2003) Catheter-Based Approach to Mitral Regurgitation. Journal of interventional cardiology 16 (6):523–534.
19. Dal Pan, F., Donzella, G., Fucci, C., Schreiber, M. (2005) Structural effects of an innovative surgical technique to repair heart valve defects. J Biomech 38 (12):2460–2471.
20. de Varennes, B., Chaturvedi, R., Sidhu, S., Cote, A.V., Shan, W.L., Goyer, C., Hatzakorzian, R., Buithieu, J., Sniderman, A. (2009) Initial results of posterior leaflet extension for severe type IIIb ischemic mitral regurgitation. Circulation 119 (21):2837–2843.
21. Einstein, D.R., Del Pin, F., Jiao, X., Kuprat, A.P., Carson, J.P., Kunzelman, K.S., Cochran, R.P., Guccione, J.M., Ratcliffe, M.B. (2010) Fluid-Structure Interactions of the Mitral Valve and Left Heart: Comprehensive Strategies, Past, Present and Future. International journal for numerical methods in engineering 26 (3–4):348–380.
22. Einstein, D.R., Kunzelman, K.S., Reinhall, P.G., Cochran, R.P., Nicosia, M.A. (2004) Haemodynamic determinants of the mitral valve closure sound: a finite element study. Med Biol Eng Comput 42 (6):832–846.
23. Einstein, D.R., Kunzelman, K.S., Reinhall, P.G., Nicosia, M.A., Cochran, R.P. (2005) The relationship of normal and abnormal microstructural proliferation to the mitral valve closure sound. J Biomech Eng 127 (1):134–147.
24. Elliott, D.M., Robinson, P.S., Gimbel, J.A., Sarver, J.J., Abboud, J.A., Iozzo, R.V., Soslowsky, L.J. (2003) Effect of altered matrix proteins on quasilinear viscoelastic properties in transgenic mouse tail tendons. Ann Biomed Eng 31 (5):599–605.
25. Farkasjahnke, M., Synećek, V. (1965) Small-angle x-ray diffraction studies on rat-tail tendon. Acta Physiol Acad Sci 28 (1):1–17.
26. Fata, B., Carruthers, C.A., Gibson, G., Watkins, S.C., Gottlieb, D., Mayer, J.E., Sacks, M.S. (2013) Regional structural and biomechanical alterations of the ovine main pulmonary artery during postnatal growth. J Biomech Eng 135 (2):021022.
27. Fata, B., Gottlieb, D., Mayer, J.E., Sacks, M.S. (2013) Estimated in vivo postnatal surface growth patterns of the ovine main pulmonary artery and ascending aorta. J Biomech Eng 135 (7):71010–71012.
28. Filip, D.A., Radu, A., Simionescu, M. (1986) Interstitial cells of the heart valve possess characteristics similar to smooth muscle cells. Circulation Research 59 (3):310–320.
29. Flameng, W., Herijgers, P., Bogaerts, K. (2003) Recurrence of mitral valve regurgitation after mitral valve repair in degenerative valve disease. Circulation 107 (12):1609–1613.
30. Flameng, W., Meuris, B., Herijgers, P., Herregods, M.-C. (2008) Durability of mitral valve repair in Barlow disease versus fibroelastic deficiency. The Journal of thoracic and cardiovascular surgery 135 (2):274–282.
31. Folkhard, W., Geercken, W., Knorzer, E., Mosler, E., Nemetschek-Gansler, H., Nemetschek, T., Koch, M.H. (1987) Structural dynamic of native tendon collagen. J Mol Biol 193 (2):405–407.
32. Fratzl, P., Misof, K., Zizak, I., Rapp, G., Amenitsch, H., Bernstorff, S. (1998) Fibrillar structure and mechanical properties of collagen. J Struct Biol 122 (1–2):119–122.
33. Fung, Y.C. (1993) Biomechanics: Mechanical Properties of Living Tissues. 2nd edn. Springer Verlag, New York.
34. Gilbert, T.W., Wognum, S., Joyce, E.M., Freytes, D.O., Sacks, M.S., Badylak, S.F. (2008) Collagen fiber alignment and biaxial mechanical behavior of porcine urinary bladder derived extracellular matrix. Biomaterials 29 (36):4775–4782.

35. Grande-Allen, K.J., Griffin, B.P., Calabro, A., Ratliff, N.B., Cosgrove, D.M., 3rd, Vesely, I. (2001) Myxomatous mitral valve chordae. II: Selective elevation of glycosaminoglycan content. J Heart Valve Dis 10 (3):325–332; discussion 332–323.
36. Grashow, J.S., Sacks, M.S., Liao, J., Yoganathan, A.P. (2006) Planar biaxial creep and stress relaxation of the mitral valve anterior leaflet. Ann Biomed Eng 34 (10):1509–1518.
37. Grashow, J.S., Yoganathan, A.P., Sacks, M.S. (2006) Biaixal stress-stretch behavior of the mitral valve anterior leaflet at physiologic strain rates. Ann Biomed Eng 34 (2):315–325.
38. Hansen, K.A., Weiss, J.A., Barton, J.K. (2002) Recruitment of tendon crimp with applied tensile strain. J Biomech Eng 124 (1):72–77.
39. Hilbert, S.L., Sword, L.C., Batchelder, K.F., Barrick, M.K., Ferrans, V.J. (1996) Simultaneous assessment of bioprosthetic heart valve biomechanical properties and collagen crimp length. J Biomed Mater Res 31 (4):503–509.
40. Hodge, A.J., Petruska, J.A. (1963) Recent studies with the electron microscope on ordered aggregates of the tropocollagen molecule, vol 289–300. Aspects of Protein Chemistry. Academic Press, London.
41. Hunter, K.S., Lanning, C.J., Chen, S.Y., Zhang, Y., Garg, R., Ivy, D.D., Shandas, R. (2006) Simulations of congenital septal defect closure and reactivity testing in patient-specific models of the pediatric pulmonary vasculature: A 3D numerical study with fluid-structure interaction. J Biomech Eng 128 (4):564–572.
42. Kao, P.H., Lammers, S., Tian, L., Hunter, K., Stenmark, K.R., Shandas, R., Qi, H.J. (2011) A microstructurally-driven model for pulmonary artery tissue. Journal of biomechanical engineering 133 (5):051002.
43. Kastelic, J., Galeski, A., Baer, E. (1978) The multicomposite structure of tendon. Connect Tissue Res 6 (1):11–23.
44. Kincaid, E.H., Riley, R.D., Hines, M.H., Hammon, J.W., Kon, N.D. (2004) Anterior leaflet augmentation for ischemic mitral regurgitation. Ann Thorac Surg 78 (2):564–568; discussion 568.
45. Krishnamurthy, G., Ennis, D.B., Itoh, A., Bothe, W., Swanson, J.C., Karlsson, M., Kuhl, E., Miller, D.C., Ingels, N.B., Jr. (2008) Material properties of the ovine mitral valve anterior leaflet in vivo from inverse finite element analysis. Am J Physiol Heart Circ Physiol 295 (3):H1141–H1149.
46. Krishnamurthy, G., Itoh, A., Bothe, W., Swanson, J.C., Kuhl, E., Karlsson, M., Craig Miller, D., Ingels, N.B., Jr. (2009) Stress-strain behavior of mitral valve leaflets in the beating ovine heart. J Biomech 42 (12):1909–1916.
47. Kronick, P.L., Buechler, P.R. (1986) Fiber Orientation in Calfskin by Laser Light Scattering or X-ray Diffraction and Quantitative Relation to Mechanical Properties. Journal of the American Leather Chemists Association 81:221–229.
48. Kunzelman, K.S., Cochran, R.P., Chuong, C., Ring, W.S., Verrier, E.D., Eberhart, R.D. (1993) Finite element analysis of the mitral valve. J Heart Valve Dis 2 (3):326–340.
49. Kunzelman, K.S., Cochran, R.P., Murphree, S.S., Ring, W.S., Verrier, E.D., Eberhart, R.C. (1993) Differential collagen distribution in the mitral valve and its influence on biomechanical behaviour. J Heart Valve Dis 2 (2):236–244.
50. Kunzelman, K.S., Quick, D.W., Cochran, R.P. (1998) Altered collagen concentration in mitral valve leaflets: biochemical and finite element analysis. Ann Thorac Surg 66 (6 Suppl):S198–205.
51. Kunzelman, K.S., Reimink, M.S., Cochran, R.P. (1997) Annular dilatation increases stress in the mitral valve and delays coaptation: a finite element computer model. Cardiovasc Surg 5 (4):427–434.
52. Lee, C.H., Amini, R., Gorman, R.C., Gorman, J.H., Sacks, M.S. (2014) An inverse modeling approach for stress estimation in mitral valve anterior leaflet valvuloplasty for in-vivo valvular biomaterial assessment. J Biomech 47 (9):2055–2063.
53. Liao, J., Yang, L., Grashow, J., Sacks, M.S. (2005) Molecular orientation of collagen in intact planar connective tissues under biaxial stretch. Acta Biomaterialia 1 (1):45–54.

54. Lim, K.H., Yeo, J.H., Duran, C.M. (2005) Three-dimensional asymmetrical modeling of the mitral valve: a finite element study with dynamic boundaries. J Heart Valve Dis 14 (3):386–392.
55. Lis, Y., Burleigh, M.C., Parker, D.J., Child, A.H., Hogg, J., Davies, M.J. (1987) Biochemical characterization of individual normal, floppy and rheumatic human mitral valves. Biochem J 244 (3):597–603.
56. Lopez-Pamies, O., Castañeda, P.P. (2004) Second-order homogenization estimates incorporating field fluctuations in finite elasticity. Mathematics and Mechanics of Solids 9 (3):243–270.
57. Mahmood, F., Gorman, J.H., 3rd, Subramaniam, B., Gorman, R.C., Panzica, P.J., Hagberg, R.C., Lerner, A.B., Hess, P.E., Maslow, A., Khabbaz, K.R. (2010) Changes in mitral valve annular geometry after repair: saddle-shaped versus flat annuloplasty rings. Ann Thorac Surg 90 (4):1212–1220.
58. Mahmood, F., Subramaniam, B., Gorman, J.H., 3rd, Levine, R.M., Gorman, R.C., Maslow, A., Panzica, P.J., Hagberg, R.M., Karthik, S., Khabbaz, K.R. (2009) Three-dimensional echocardiographic assessment of changes in mitral valve geometry after valve repair. Ann Thorac Surg 88 (6):1838–1844.
59. Maas, S.A., Ellis, B.J., Ateshian, G.A., Weiss, J.A. (2012) FEBio: finite elements for biomechanics. J Biomech Eng 134:011005.
60. May-Newman, K., Yin, F.C. (1998) A constitutive law for mitral valve tissue. J Biomech Eng 120 (1):38–47.
61. Merryman, W.D., Bieniek, P.D., Guilak, F., Sacks, M.S. (2009) Viscoelastic properties of the aortic valve interstitial cell. J Biomech Eng 131 (4):041005.
62. Merryman, W.D., Youn, I., Lukoff, H.D., Krueger, P.M., Guilak, F., Hopkins, R.A., Sacks, M.S. (2006) Correlation between heart valve interstitial cell stiffness and transvalvular pressure: implications for collagen biosynthesis. Am J Physiol Heart Circ Physiol 290 (1):H224–231.
63. Messier, R.H., Jr., Bass, B.L., Aly, H.M., Jones, J.L., Domkowski, P.W., Wallace, R.B., Hopkins, R.A. (1994) Dual structural and functional phenotypes of the porcine aortic valve interstitial population: characteristics of the leaflet myofibroblast. Journal of Surgical Research 57 (1):1–21.
64. Mulholland, D.L., Gotlieb, A.I. (1996) Cell biology of valvular interstitial cells. Canadian Journal of Cardiology 12 (3):231–236.
65. Nimni, M.E. (1980) The molecular organization of collgen and its role in determining the biophysical properties of the connective tissues. Biorheology 17:51–82.
66. Nowicki, E.R., Weintraub, R.W., Birkmeyer, N.J., Sanders, J.H., Dacey, L.J., Lahey, S.J., Leavitt, B., Clough, R.A., Quinn, R.D., O'Connor G, T. (2003) Mitral valve repair and replacement in northern New England. Am Heart J 145 (6):1058–1062.
67. Ponte Castañeda, P. (2002) Second-order homogenization estimates for nonlinear composites incorporating field fluctuations: I–theory. J Mech Phys Solids 50 (4):737–757.
68. Ponte Castañeda, P., Tiberio, E. (2000) A second-order homogenization method in finite elasticity and applications to black-filled elastomers. J Mech Phys Solids 48 (6):1389–1411.
69. Prot, V., Skallerud, B. (2009) Nonlinear solid finite element analysis of mitral valves with heterogeneous leaflet layers. Comput Mech 43 (3):353–368.
70. Prot, V., Skallerud, B., Holzapfel, G. (2007) Transversely isotropic membrane shells with application to mitral valve mechanics. Constitutive modelling and finite element implementation. Int J Numer Methods Eng 71 (8):987–1008.
71. Purslow, P.P., Wess, T.J., Hukins, D.W. (1998) Collagen orientation and molecular spacing during creep and stress-relaxation in soft connective tissues. J Exp Biol 201 (Pt 1):135–142.
72. Rabbah, J.-P., Saikrishnan, N., Yoganathan, A.P. (2013) A novel left heart simulator for the multi-modality characterization of native mitral valve geometry and fluid mechanics. Ann Biomed Eng 41 (2):305–315.
73. Rabkin-Aikawa, E., Farber, M., Aikawa, M., Schoen, F.J. (2004) Dynamic and reversible changes of interstitial cell phenotype during remodeling of cardiac valves. J Heart Valve Dis 13 (5):841–847.
74. Rabkin, E., Hoerstrup, S.P., Aikawa, M., Mayer, J.E., Jr., Schoen, F.J. (2002) Evolution of cell phenotype and extracellular matrix in tissue-engineered heart valves during in-vitro maturation and in-vivo remodeling. Journal of Heart Valve Disease 11 (3):308–314; discussion 314.

75. Reimink, M.S., Kunzelman, K.S., Cochran, R.P. (1996) The effect of chordal replacement suture length on function and stresses in repaired mitral valves: a finite element study. J Heart Valve Dis 5 (4):365–375.
76. Reimink, M.S., Kunzelman, K.S., Verrier, E.D., Cochran, R.P. (1995) The effect of anterior chordal replacement on mitral valve function and stresses. A finite element study. Asaio J 41 (3):M754–762.
77. Robb, J.D., Minakawa, M., Koomalsingh, K.J., Shuto, T., Jassar, A.S., Ratcliffe, S.J., Gorman, R.C., Gorman, J.H., 3rd (2011) Posterior leaflet augmentation improves leaflet tethering in repair of ischemic mitral regurgitation. European journal of cardio-thoracic surgery : official journal of the European Association for Cardio-thoracic Surgery.
78. Sacks, M.S. A structural model for natural and chemically treated bovine pericardium. In: Atluri, S., O'Donoghue, P. (eds) Modeling and simulation based engineering, Atlanta, GA, 1998. Tech Science Press, pp 1574–1579.
79. Sacks, M.S. (2003) Incorporation of experimentally-derived fiber orientation into a structural constitutive model for planar collagenous tissues. J Biomech Eng 125 (2):280–287.
80. Sacks, M.S., Chuong, C.J. (1992) Characterization of Collagen Fiber Architecture in the Canine Central Tendon. Journal of Biomechanical Engineering 114:183–190.
81. Sacks, M.S., Merryman, W.D., Schmidt, D.E. (2009) On the biomechanics of heart valve function. J Biomech 42 (12):1804–1824.
82. Sacks, M.S., Smith, D.B., Hiester, E.D. (1997) A small angle light scattering device for planar connective tissue microstructural analysis. Ann Biomed Eng 25 (4):678–689.
83. Sacks, M.S., Smith, D.B., Hiester, E.D. (1998) The aortic valve microstructure: effects of transvalvular pressure. Journal of Biomedical Materials Research 41 (1):131–141.
84. Sasaki, N., Odajima, S. (1996) Elongation mechanism of collagen fibrils and force-strain relations of tendon at each level of structural hierarchy. J Biomech 29 (9):1131–1136.
85. Sasaki, N., Odajima, S. (1996) Stress-strain curve and Young's modulus of a collagen molecule as determined by the X-ray diffraction technique. Journal of Biomechanics 29:655–658.
86. Sasaki, N., Shukunami, N., Matsushima, N., Izumi, Y. (1999) Time resolved X-ray diffraction from tendon collagen during creep using synchrotron radiation. Journal of Biomechanics 32:285–292.
87. Schoen, F. (1997) Aortic valve structure-function correlations: Role of elastic fibers no longer a stretch of the imagination. Journal of Heart Valve Disease 6:1–6.
88. Scott, J.E. (1991) Proteoglycan: collagen interactions in connective tissues. Ultrastructural, biochemical, functional and evolutionary aspects. Int J Biol Macromol 13 (3):157–161.
89. Silver, F.H. (1987) Biological Materials: Structure, Mechanical Properties, and Modeling of Soft Tissues. New York University Press, New York and London.
90. Silver, F.H., Freeman, J.W., Seehra, G.P. (2003) Collagen self-assembly and the development of tendon mechanical properties. J Biomech 36 (10):1529–1553.
91. Silverman, M.E., Hurst, J.W. (1968) The mitral complex. Interaction of the anatomy, physiology, and pathology of the mitral annulus, mitral valve leaflets, chordae tendineae, and papillary muscles. Am Heart J 76 (3):399–418.
92. Stella, J.A., Sacks, M.S. (2007) On the biaxial mechanical properties of the layers of the aortic valve leaflet. J Biomech Eng 129 (5):757–766.
93. Storn, R., Price, K. (1997) Differential evolution—A simple and efficient heuristic for global optimization over continuous spaces. J Global Optim 11 (4):341–359.
94. Taylor, P.M., Batten, P., Brand, N.J., Thomas, P.S., Yacoub, M.H. (2003) The cardiac valve interstitial cell. International Journal of Biochemistry and Cell Biology 35 (2):113–118.
95. Theret, D.P., Levesque, M.J., Sato, M., Nerem, R.M., Wheeler, T. (1988) The application of a homogeneous half-space model in the analysis of endothelial cell micropipette measurements. J Biomech Eng 110:190–199.
96. Trotter, J.A., Koob, T.J. (1989) Collagen and proteoglycan in a sea urchin ligament with mutable mechanical properties. Cell Tissue Res 258 (3):527–539.
97. Trotter, J.A., Thurmond, F.A., Koob, T.J. (1994) Molecular structure and functional morphology of echinoderm collagen fibrils. Cell Tissue Res 275 (3):451–458.

98. Votta, E., Le, T.B., Stevanella, M., Fusini, L., Caiani, E.G., Redaelli, A., Sotiropoulos, F. (2013) Toward patient-specific simulations of cardiac valves: state-of-the-art and future directions. J Biomech 46 (2):217–228.
99. Votta, E., Caiani, E., Veronesi, F., Soncini, M., Montevecchi, F.M., Redaelli, A. (2008) Mitral valve finite-element modelling from ultrasound data: a pilot study for a new approach to understand mitral function and clinical scenarios. Philos Transact A Math Phys Eng Sci 366 (1879):3411–3434.
100. Weber, I.T., Harrison, R.W., Iozzo, R.V. (1996) Model structure of decorin and implications for collagen fibrillogenesis. J Biol Chem 271 (50):31767–31770.
101. Xing, Y., Warnock, J.N., He, Z., Hilbert, S.L., Yoganathan, A.P. (2004) Cyclic pressure affects the biological properties of porcine aortic valve leaflets in a magnitude and frequency dependent manner. Ann Biomed Eng 32 (11):1461–1470.
102. Zhang, Y., Dunn, M.L., Hunter, K.S., Lanning, C., Ivy, D.D., Claussen, L., Chen, S.J., Shandas, R. (2007) Application of a microstructural constitutive model of the pulmonary artery to patient-specific studies: validation and effect of orthotropy. J Biomech Eng 129 (2):193–201.

# Chapter 11
# Biological Systems: Multiscale Modeling Based on Mixture Theory

**Yusheng Feng, Sarah J. Boukhris, Rakesh Ranjan and Raul A. Valencia**

**Abstract** Scientific understanding of complex biological systems has recently benefited from mathematical and computational modeling. Classical biological studies are focused on observation and experimentation. However, mathematical modeling and computer simulation can provide useful guidance and insightful interpretations for experimental studies. Mathematical modeling can also be used to characterize complex biological phenomena, such as cell migration, cancer metastasis, tumor growth, bone remodeling, and wound healing. Since these phenomena occur over varying spatial and temporal scales, it is necessary to use multiscale modeling approaches. This book chapter provides an overview of multiscale mathematical methods for developing models for aforementioned biological phenomena based on so-called mixture theory. In Sect. 11.1, we cover the background about multiscale modeling in general applications as well as biology specific applications, Sect. 11.2 presents the multiscale computational methods and the challenges associated with modeling complex biological systems and processes, Sect. 11.3 presents theories and their applications of four example model problems, and Sect. 11.4 concludes with open questions in multiscale mathematical modeling, especially in biomedical areas.

## 11.1 Background

Although microscale and nanoscale systems are becoming more prevalent in many engineering and biological applications, our ability to create predictive and informative mathematical models of these systems is limited [1]. For systems that cannot

Y. Feng (✉) · S.J. Boukhris · R. Ranjan · R.A. Valencia
The University of Texas at San Antonio, One UTSA Circle San Antonio, TX 78249, USA
e-mail: yusheng.feng@utsa.edu

S.J. Boukhris
e-mail: bcr625@my.utsa.edu

R. Ranjan
e-mail: rakesh.ranjan@utsa.edu

R.A. Valencia
e-mail: raul.valencia@upb.edu.co



S. De et al. (eds.), *Multiscale Modeling in Biomechanics and Mechanobiology*, DOI 10.1007/978-1-4471-6599-6_11

be modeled by continuum or molecular methods alone (e.g., too small or too large), multiscale methods can be implemented. Multiscale methods involve the use of information at various scales, which requires mathematics and computation to simulate a physical or biological system at more tha one scale [1]. These methods are mainly divided into two types of approaches: hierarchical and concurrent. The hierarchical approach to multiscale modeling directly uses the information at small length scales and inputs it into larger length scales via an averaging process. The more popular concurrent multiscale methods, in contrast, utilize information at differing scales simultaneously.

Multiscale modeling techniques have relevant uses in many fields of study such as engineering and biology. Materials science has benefited from multiscale methods in the realm of solid mechanics. Studying fluid flow effects in microfluidic devices requires analysis at two or more spatial and temporal scales with coupled chemistry, electrochemistry, and fluid motion [1].

For decades, advances in biology had little to do with contribution from sophisticated mathematical modeling. Biology was mainly based on observation and experimentation and it was not possible to simulate large complex systems. However, now in the age of computers and seemingly endless computational capabilities, there is an avenue for collaboration among biologists, mathematicians, and computational scientists to establish relevant models based on experiments. No longer are there strict limitations in tools and resources to examine life at many scales, which represents the difficulty in modeling biology. It is well known that biological systems are complicated to mathematically model because they involve many interrelated processes across many scales [2]. Each scale level in a biological system, both temporal and spatial, contains information from levels either above or before [3]. The general hierarchy of scales in biological systems follows the order of atom, molecule, macromolecule, organelle, cell, tissue, organ, individual, to population. These complex scales have also been broken up into specific fields of study (i.e., molecular biology, cellular biology, organism studies, and population studies).

In the field of cancer research, the ultimate goal of mathematical modeling and simulation is to aid in development of personalized therapies thereby decreasing patient suffering while increasing treatment effectiveness [4]. Mathematical and computational models, therefore, are needed to quantify the links between 3D tumors and migration, invasion, proliferation, and microscale cellular and environmental characteristics [4]. This task is best accomplished using multiscale methods.

## 11.2 Multiscale Computational Methods and Challenges

Multiscale methods are specially geared to develop models that are capable of linking molecular, cellular, and tissue continuum scales. The common approach taken in constructing a mathematical model is to begin with a simple model. This model will preserve enough biology to be meaningful, but will include less parameters [3] as to not over complicate the modeling process. The advantage of this approach is that the model can be applied to understand many different biological systems.

A mathematical model that incorporates multiple scales can serve at least two purposes: (1) when detailed information about the biological system is known, the model can be used to conduct in silico experiments in lieu of in vitro or in vivo experiments; and (2) when details are unknown, the model can serve as a tool to test a hypothesis and create a prediction. Extensions and complications can be included into the mathematical model, in the form of additional parameters, to better resemble the biological system [3]. However, it is necessary to avoid overcomplicating the model.

The ultimate goal of multiscale mathematical modeling is to couple discrete particle methods (e.g., molecular dynamics) with models at the continuum level. However, coupling of these two methods is difficult because of the interaction between the interfaces between molecular dynamics and continuum regions. When applying the energy-conservation formulation, this discrepancy is amplified by causing heat generation in the molecular dynamics regime thereby polluting the solution. Another issue in coupling molecular dynamics and continuum methods is in connecting timescales in each region. Several researchers have developed multiscale methods to account for these issues to efficaciously bridge between temporal and spatial scales. The following is a brief overview of commonly used multiscale modeling approaches in the literature.

### *11.2.1 Bridging Scale Method*

The bridging scale method is a concurrent multiscale method that couples the atomistic and continuum simulation methods [1]. The feature of this method is that it is general and can be used in a full three-dimensional domain. At its basic level, the bridging scale method includes the numerical calculation of the time history kernel in multiple dimension so that a two-way coupled coarse and fine molecular dynamics boundary condition is determined. This approach is particularly suitable for dynamics systems with finite temperature.

### *11.2.2 Bridging Domain Method*

The bridging domain method uses molecular dynamics in localized regions then couples it with a continuum region that surrounds the atomistic region [5, 6]. A spatial region contains overlapping continuum and atomistic regions which is best demonstrated by two-dimensional wave and crack propagation scenarios [1].

### *11.2.3 Quasi-Continuum Method*

Using the Cauchy-Born rule [7], which assumes that the continuum energy density can be estimated using an atomistic potential, the analysis at the atomic level is

coupled to the continuum in the Quasi-Continuum method [8]. This approach is similar to an adaptive finite element method [9] which requires that the restriction that the deformation of the lattice of continuum point must be homogeneous.

### *11.2.4 Coupled Atomistics and Discrete Dislocation*

Coupled atomistics and discrete dislocation (CADD) is a method for quasi-static coupling [1]. This approach to multiscale modeling couples molecular statics with discrete dislocation plasticity [10–12], thus making it an especially useful tool in fracture mechanics. Defects such as dislocations generated within the atomistic region pass through to the continuum region where they are characterized by discrete dislocation mechanics [1, 13].

### *11.2.5 Macroscopic, Atomistic, ab Initio Dynamics*

The macroscopic, atomistic, ab initio dynamics (MAAD) multiscale method concurrently links tight binding, molecular dynamics, and finite element methods [14]. All three methods are computed simultaneously and dynamically share and receive information. The approach decreases the mesh size of the finite element mesh until it is on the order of the atomic spacing. Atomic dynamic are then governed by molecular dynamics, then tight binding is used to simulate the atomic bond breaking processes at an area of interest such as a crack tip [1].

### *11.2.6 Course-Grained Molecular Dynamics*

Coarse-grained molecular dynamics (CGMD) is a multiscale approach similar to MAAD but instead couples only finite element and molecular dynamics [15]. It is possible to eliminate the tight binding analysis because the coarse-grained energy approximation converges to the exact atomic energy that is used to derive the governing equations of motion [1].

## 11.3 Theories and Applications

### *11.3.1 Multiscale Cell Migration Simulation*

Biological studies indicate that abnormal gene mutations in healthy cells may disrupt their regulatory mechanisms that control growth, proliferation, and apoptosis [16]. The uncontrolled growth of these cancer cells creates an avascular tumor mass [17].

Avascular tumors receive nutrients and oxygen via diffusion from nearby vessels [16], but as the tumor grows the demand for nutrients and oxygen increases. When the tumor reaches a critical size, a small amount of cancer cells within the core of the tumor will become necrotic due to the limited nutrient and oxygen supply from diffusion thus initiating cell responses to hypoxia and inducing angiogenesis [18]. The now vascularized tumor creates a pathway that allows for the tumor cells to migrate out of the primary tumor. These circulating tumor cells have the ability to be deposited at a distant site and proliferate to produce secondary tumors [18]. Unfortunately, it is difficult to clinically treat patients with metastatic cancer, in part, because of our limited understanding of the mechanisms of cancer metastasis. Therefore, it is in both scientific and practical healthcare interests to study cell migration and nanoparticle transport in living tissues. However, it is very challenging to quantify cellular motion and nanoparticle transport in an in vivo environment. Mathematical and computational models may provide insight into mechanisms that govern the mass transport and cell migration and possibly identify major influencing factors in the process. We introduce a multiscale approach to simulate a simple system that consists of a single fluid channel surrounded by hydrogel matrix with porous structure, which reflects an in vitro 3D cell culture apparatus [16]. Cancer cells, nanoparticles, and nutrients are immersed in the fluid, which mimics particle transport in a blood vessel or a lymphatic vessel. The current model considers three kinds of particle mass (cells, nanoparticles, and nutrients) transport driven by the flow inside a channel.

Transport of biochemical species and cellular microfluidics depends on the velocity of the carrier flow and on the size and nature of the biological species [19]. Mass transport can be divided into two types in the circulatory system: (1) transport dominated by convection and (2) transport dominated by diffusion. In the first type of mass transport, cell and nutrient transport within the human vasculature is governed by the local haemodynamics (macro-scale). The second type is the transport within the wall of both the artery and vascular graft (micro-scale). Properties such as permeability, porosity, tortuosity, and diffusivity define how mass are transported within vessel walls. In order to accurately model mass transport through a vessel wall, it is necessary to understand the micro-structure of the wall [20].

It is important to analyze different length and timescales, since, specific consideration may apply at the macro-scale but not at the micro-scale. Usually, the fluid flows by pressure gradient effects and sometimes by electric forces (electro-osmotic flow) at micro-scale. The Knudsen number is useful for determining whether continuum mechanics or statistical mechanics formulation of fluid dynamics should be used [19].

Different physicochemical phenomena of the blood flow and cell migration are associated at different time and length scales. Some of these phenomena are consumption and transport of oxygen and nutrients, osmosis, generation of waste by cells, mechanical loading of cells, electrochemical, chemo-mechanical, and electro-mechanical phenomena, among others. For example, the time for cell synthetize is about weeks while the cell adhesion is about hours. In the same way, the length scale of the hydrogel is about millimeters, while the length of adhesion points of cells is about is few nanometers [21].

#### 11.3.1.1 Mathematical Formulation

The coupling with hydrodynamics consists of a system with five unknown variables: velocity ($u$, $v$, $w$), pressure ($p$), and concentration ($c$). The known parameters are the fluid density ($\rho$), fluid dynamic viscosity ($\mu$), the diffusion constant of the species $D$, and two external actions on the fluid: the body force per unit volume $F$ and the concentration source or sink per unit volume $S$. At the macro-scale, the system considers the Navier-Stokes equation and convection-diffusion equation.

$$\frac{\partial \rho}{\partial t} + \nabla \cdot (\rho \mathbf{U}) = 0 \tag{11.1}$$

$$\rho \frac{\partial \mathbf{U}}{\partial t} + \rho \mathbf{U} \cdot \nabla \mathbf{U} = -\nabla p + \mu \triangle \mathbf{U} + \mathbf{F} \tag{11.2}$$

$$\frac{\partial c}{\partial t} + \mathbf{U} \cdot \nabla c = \nabla \cdot (D \nabla c) + S \tag{11.3}$$

The system is under the condition that the concentration of nutrients is sufficiently small as to not affect the carrier fluid viscosity and density. Usually in a microfluidics system, the flow of the carrier fluid is assumed to be steady state and only the nutrient concentration changes with time. In such case, parameters $\rho$, $\mu$, and $D$ are constant, there is no cell growth ($S = 0$) and there are no body forces (gravity is negligible in very small systems), the system would thus become:

$$\nabla \cdot \mathbf{U} = 0 \tag{11.4}$$

$$\mathbf{U} \cdot \nabla \mathbf{U} = -\frac{1}{\rho} \nabla p + \nu \triangle \mathbf{U} \tag{11.5}$$

$$\frac{\partial c}{\partial t} + \mathbf{U} \cdot \nabla c = D \triangle c \tag{11.6}$$

where $\nu$ is the kinematic viscosity. At the macro-scale level, fluid flow through the porous hydrogel matrix is described by the Brinkman equation:

$$\nabla \cdot \mathbf{U} = 0 \tag{11.7}$$

$$\frac{\rho}{\varepsilon} \left[ \frac{\partial \mathbf{U}}{\partial t} + (\mathbf{U} \cdot \nabla) \frac{\mathbf{U}}{\varepsilon} \right] = -\nabla p + \nabla \cdot \frac{\mu}{\varepsilon} [\nabla \mathbf{U} + (\nabla \mathbf{U})^T] - \frac{\overline{\mu}}{k} \mathbf{U} + \mathbf{F} \tag{11.8}$$

where $\varepsilon$ is the porosity, $\mu$ is the dynamic viscosity, $\overline{\mu}$ is the effective viscosity of the medium, and $k$ is the permeability of the media. One approach to calculating the local permeability is the Kozeny-Carman equation below, which relates the porosity to the permeability of the structure [22]:

$$k = \frac{r^2 \varepsilon^3}{4k_k(1-\varepsilon)^2} \tag{11.9}$$

where $r$ the radius of the cylinders, $k_k$ is the Kozeny-Carman constant, and $\varepsilon$ is the porosity of the structure. Kozeny calculated an approximate value of 2 for $k_k$ and Carman suggested a value of 5 based on experimental evidence on an assumed isotropic medium [23].

For the effective viscosity of the medium, Brinkman simply took [21]:

$$\overline{\mu} = \mu \tag{11.10}$$

while Seyam et al. took [24]:

$$\frac{\overline{\mu}}{\mu} = \frac{1}{\varepsilon}\tau \tag{11.11}$$

with $\tau$ as the tortuosity of the medium defined below. For the case of this model, we consider Brinkman's simplification to the effective viscosity of a medium.

$$\tau = \sqrt{\varepsilon} \tag{11.12}$$

If the hypothesis of a creeping flow is valid at micro-scale, the system collapses to the linear system [19]:

$$\nabla \cdot \mathbf{U} = 0 \tag{11.13}$$

$$\nabla p = \nu \triangle \mathbf{U} \tag{11.14}$$

The cell motion was tracked using the Newtonian formulation:

$$\frac{\mathrm{d}}{\mathrm{d}t}(m_p v_p) = F_D + F_g + F_{ext} \tag{11.15}$$

$F_D$ is the drag force from the fluid, which is described as:

$$\mathbf{F}_D = m_p F_d(\mathbf{U} - \mathbf{v}_p) \tag{11.16}$$

where $m_p$ is the individual cell mass and $F_d$ is the drag force per unit mass on the cell. Assuming that the cells take spherical shape, $F_d$ is defined as:

$$F_d = \frac{18\mu}{\rho_p d_p^2} \tag{11.17}$$

where $\rho_p$ is the cell mass density and $d_p$ is the cell diameter. The gravity force $F_g$ is usually negligible in very small systems and $F_{ext}$ is defined as:

$$F_{ext} = M\nabla c - K\mathbf{v}_p \tag{11.18}$$

The first term on the right side, $M\nabla c$, is the attraction to nutrients (based on chemotaxis) and the second term, $K\mathbf{v}_p$, is the drag force exerted by the porous media. $M$[J m$^3$/mol] and $K$[N s/m] are two constants that will be determined experimentally. The shear stress for laminar flow of a Newtonian fluid is linearly related to the shear rate ($\mathrm{d}V/\mathrm{d}r$) in terms of cylindrical coordinates [25, 26]:

$$\tau = -\mu \frac{\mathrm{d}V}{\mathrm{d}r} \tag{11.19}$$

where $V$ is the velocity [m/s] at radial position $r$ [m] and $\mu$ [N s/m$^2$] is the dynamic viscosity of the fluid. Wall shear stress for turbulent flow is large compared to laminar flow. For either case, laminar or turbulent, the wall shear stress can be determined from:

$$\tau = -\frac{d}{4}\frac{\triangle p}{L} \tag{11.20}$$

Wall shear stress of Newtonian fluids in tubular vessels can be calculated as a function of volumetric flow rate:

$$\tau = \frac{4\mu Q}{\pi r^3} \tag{11.21}$$

based on Hagen-Poseuille equation:

$$\triangle p = 128\frac{\mu L Q}{\pi d^4} \tag{11.22}$$

The diffusion constant in the fluid for nutrients was estimated by the Stokes-Einstein diffusivity equation for diffusion of spherical particles through liquid with a low Reynolds number [20, 27]:

$$D = \frac{k_B T}{6\pi\,\mu\, r} \tag{11.23}$$

where $k_B$ is the Boltzmann's Constant, $T$ is the absolute temperature and $r$ is the radius of the spherical particles. $r$ was estimated from the assumed molecular weight and the following equation for a sphere:

$$r = \left(\frac{3 \cdot M_w \cdot V_p}{4\,\pi\, N_A}\right)^{\frac{1}{3}} \tag{11.24}$$

where $V_p$ is the molecule's specific volume, $M_w$ is the molecular weight, and $N_A$ is Avogadro's number. The characteristic Knudsen Number (Kn) is defined as [19]:

$$Kn = \frac{\lambda}{L} \tag{11.25}$$

where $\lambda$ is the mean free path of the molecules and $L$ is the characteristic dimension of the channel.

Weak Formulation

For this study, fluid was assumed to be Newtonian, homogeneous, and incompressible. The equations solved were:

$$\nabla \cdot \sigma = \rho(\mathbf{u} \cdot \nabla \mathbf{u}) \text{ in } \Omega \tag{11.26}$$

$$\nabla \cdot \mathbf{u} = 0 \quad \text{in } \Omega \tag{11.27}$$

Given the strong form, the boundary conditions and weak form can be described as follows:

$$\mathbf{u} = \tilde{\mathbf{u}} \quad \text{on} \quad \Gamma_D \tag{11.28}$$

$$\sigma \cdot \mathbf{n} = \tilde{\mathbf{h}} \quad \text{on} \quad \Gamma_N \tag{11.29}$$

The weak form is obtained by taking the scalar product of the momentum equations with a vector test function $\mathbf{v}$ belonging to a functional space $\mathbf{V} = \left\{\mathbf{v} | \mathbf{v} \in \mathbf{H}^1(\Omega), \quad \mathbf{v}|_{\Gamma_D} = 0\right\}$, integrating over $\Omega$ and applying the Green integration formula.

Similarly, the continuity equation is operated by multiplying by a function $q \in \mathbf{Q} = \left\{q | q \in \mathbf{H}^1(\Omega)\right\}$.

$$\int_\Omega (\nabla \cdot \sigma) \cdot \mathbf{v} d\Omega - \int_\Omega \rho(\mathbf{u} \cdot \nabla \mathbf{u}) \cdot \mathbf{v} \, d\Omega = 0 \tag{11.30}$$

$$\int_\Omega (\nabla \cdot \mathbf{u}) \, \mathbf{q} \, d\Omega = 0 \tag{11.31}$$

Substituting the identity $(\nabla \cdot \sigma) \cdot \mathbf{v} = \nabla \cdot (\sigma \cdot \mathbf{v}) - \sigma : \nabla \mathbf{v}$:

$$\int_\Omega (\nabla \cdot \sigma) \cdot \mathbf{v} d\Omega = \int_\Omega (\nabla \cdot (\sigma \cdot \mathbf{v}) - \sigma : \nabla \mathbf{v}) \, d\Omega \tag{11.32}$$

$$\int_\Omega (\nabla \cdot \sigma) \cdot \mathbf{v} \, d\Omega = \int_\Omega \nabla \cdot (\sigma \cdot \mathbf{v}) \, d\Omega - \int_\Omega \sigma : \nabla \mathbf{v} \, d\Omega \tag{11.33}$$

Applying Green integration:

$$\int_{\Omega} (\nabla \cdot \sigma) \cdot \mathbf{v} \mathrm{d}\Omega = \int_{\Gamma} (\sigma \cdot \mathbf{v}) \cdot n \, \mathrm{d}\Gamma - \int_{\Omega} \sigma : \nabla \mathbf{v} \, \mathrm{d}\Omega \tag{11.34}$$

Applying $(\sigma \cdot \mathbf{v}) \cdot \mathbf{n} = (\sigma \cdot \mathbf{n}) \cdot \mathbf{v}$ due to $\sigma$ is a symmetric tensor:

$$\int_{\Omega} (\nabla \cdot \sigma) \cdot \mathbf{v} \, \mathrm{d}\Omega = \int_{\Gamma} (\sigma \cdot \mathbf{n}) \cdot \mathbf{v} \, \mathrm{d}\Gamma - \int_{\Omega} \sigma : \nabla \mathbf{v} \, \mathrm{d}\Omega \tag{11.35}$$

Substituting:

$$\int_{\Gamma} (\sigma \cdot \mathbf{n}) \cdot \mathbf{v} \, \mathrm{d}\Gamma - \int_{\Omega} \sigma : \nabla \mathbf{v} \, \mathrm{d}\Omega - \int_{\Omega} \rho (\mathbf{u} \cdot \nabla \mathbf{u}) \cdot \mathbf{v} \, \mathrm{d}\Omega = 0 \tag{11.36}$$

Taking the first term and applying the boundary conditions:

$$\int_{\Gamma} (\sigma \cdot \mathbf{n}) \cdot \mathbf{v} \, \mathrm{d}\Gamma = \int_{\Gamma} \tilde{\mathbf{h}} \cdot \mathbf{v} \, \mathrm{d}\Gamma \tag{11.37}$$

we can organize the weak formulation as

$$\int_{\Gamma_N} \tilde{\mathbf{h}} \cdot \mathbf{v} \, \mathrm{d}\Gamma_N - \int_{\Omega} \sigma : \nabla \mathbf{v} \, \mathrm{d}\Omega - \int_{\Omega} \rho (\mathbf{u} \cdot \nabla \mathbf{u}) \cdot \mathbf{v} \, \mathrm{d}\Omega = 0 \tag{11.38}$$

Based on Newtonian fluid, substituting $\sigma = -p\mathbf{I} + 2\mu\mathbf{D}$:

$$\int_{\Gamma_N} \tilde{\mathbf{h}} \cdot \mathbf{v} \, \mathrm{d}\Gamma_N - \int_{\Omega} (-pI + 2\mu\mathbf{D}) : \nabla \mathbf{v} \, \mathrm{d}\Omega - \int_{\Omega} \rho (\mathbf{u} \cdot \nabla \mathbf{u}) \cdot \mathbf{v} \, \mathrm{d}\Omega = 0 \tag{11.39}$$

Finally, the weak form reads: Find $u \in V_g = \{u \in H^1(\Omega), u|_{\Gamma_D} = \tilde{u}\}$ and $p \in P = \{p | p \in H^1(\Omega)\}$ such that

$$\int_{\Omega} (-pI + 2\mu\mathbf{D}) : \nabla \mathbf{v} \, \mathrm{d}\Omega + \int_{\Omega} \rho (\mathbf{u} \cdot \nabla \mathbf{u}) \cdot \mathbf{v} \, \mathrm{d}\Omega = \int_{\Gamma_N} \tilde{\mathbf{h}} \cdot \mathbf{v} \, \mathrm{d}\Gamma_N \tag{11.40}$$

$$\int_{\Omega} (\nabla \cdot \mathbf{u}) \, \mathbf{q} \, \mathrm{d}\Omega = 0 \tag{11.41}$$

The weak form for the Brinkman equation reads: Find $u \in V_g = \{u \in H^1(\Omega), u|_{\Gamma_D} = \tilde{u}\}$ and $p \in P = \{p | p \in H^1(\Omega)\}$ such that

$$\int_\Omega \varepsilon(-pI+2\frac{\mu}{\varepsilon}\mathbf{D}) : \nabla\mathbf{v}\,\mathrm{d}\Omega+\int_\Omega (\frac{\varepsilon\mu}{K}\mathbf{u})\cdot\mathbf{v}\,\mathrm{d}\Omega+\int_\Omega \rho(\mathbf{u}\cdot\nabla\frac{\mathbf{u}}{\varepsilon})\cdot\mathbf{v}\,\mathrm{d}\Omega=\int_{\Gamma_N}\varepsilon\tilde{\mathbf{h}}\cdot\mathbf{v}\,\mathrm{d}\Gamma_N \tag{11.42}$$

$$\int_\Omega (\nabla\cdot\mathbf{u})\,\mathbf{q}\,\mathrm{d}\Omega=0 \tag{11.43}$$

Finally, the weak form for Convection-Diffusion equation reads: $Find\ c\ \in\ C=\left\{c\ \in\ \mathbf{H}^1(\Omega)\right\}\ such\ that$

$$\int_\Omega \frac{\partial c}{\partial t}\mathbf{v}\,\mathrm{d}\Omega-\int_\Omega (\nabla\cdot(\mathbf{u}c)\,\mathbf{v}\,\mathrm{d}\Omega+\int_\Omega (D\nabla c)\cdot\nabla\mathbf{v}\,\mathrm{d}\Omega=\int_{\Gamma_N}(D\nabla c\cdot\mathbf{n})\cdot\mathbf{v}\,\mathrm{d}\Gamma_N \tag{11.44}$$

Discretization

Approximating the variable fields with

$$\mathbf{u}(\mathbf{x})\approx\mathbf{u}^h(\mathbf{x})=\sum_{A=1}^{nu}N_u^A(\mathbf{x})\,\mathbf{u}_A \tag{11.45}$$

$$\mathbf{u}^h(\mathbf{x})\ \in\mathbf{U}^h\ \subset\ \mathbf{U} \tag{11.46}$$

where $\mathbf{U}=\left\{\mathbf{u}\,|\,\mathbf{u}\ \in\ \mathbf{H}^1,\ \mathbf{u}=\mathbf{u}_D\ in\ \Gamma_D\right\}$.

$$p(\mathbf{x})\approx p^h(\mathbf{x})=\sum_{I=1}^{np}N_p^I(\mathbf{x})\,p_I \tag{11.47}$$

$$p^h(\mathbf{x})\ \in P^h\ \subset\ \mathbf{P} \tag{11.48}$$

where $\mathbf{P}=\left\{p\,|\,p\ \in\mathbf{H}^1\right\}$. Approximating the test functions of the velocities:

$$v(x)\approx v^h(x)=\sum_{B=1}^{nu}N_u^B(x)\delta v_B \tag{11.49}$$

$$v^h(x)\in\mathbf{V}^h\subset\mathbf{V} \tag{11.50}$$

Approximating the test functions of the pressure:

$$q(x)\approx q^h(x)=\sum_{J=1}^{nu}N_p^J(x)\delta q_J \tag{11.51}$$

$$q^h(x) \in \mathbf{Q}^h \subset \mathbf{Q} \tag{11.52}$$

The discrete form of the weak form equations can be written as algebraic equations:

$$\mathbf{K}\mathbf{u}_A + \mathbf{Q}^T\mathbf{p}_I + \mathbf{N}(\mathbf{u}_A)\mathbf{u}_A = \mathbf{F} \tag{11.53}$$

$$\mathbf{Q}\mathbf{u}_A = \mathbf{0} \tag{11.54}$$

where the convection matrix $N$ is:

$$\mathbf{N}(\mathbf{u}_A) = \sum_{e=1}^{n_{el}} \mathbf{n}^e(\mathbf{u}_A) \tag{11.55}$$

with

$$\mathbf{n}^e = \begin{bmatrix} n(\mathbf{u}_A)^{11}\mathbf{I}_{ndim} & \cdots & n(\mathbf{u}_A)^{1n_u}\mathbf{I}_{ndim} \\ \vdots & \ddots & \vdots \\ n(\mathbf{u}_A)^{nu\,1}\mathbf{I}_{ndim} & \cdots & n(\mathbf{u}_A)^{nu\,nu}\mathbf{I}_{ndim} \end{bmatrix} \tag{11.56}$$

and the coefficients $n(\mathbf{u}_A)^{\alpha\beta}$ can be obtained as follows:

$$n(\mathbf{u}_A)^{\alpha\beta} = \rho_f \int_{\Omega_e} N_u^\alpha \mathbf{u}^h \cdot \nabla N_u^\beta \mathrm{d}\Omega_e \quad (\alpha, \beta = 1, \ldots, n_u) \tag{11.57}$$

The viscosity matrix $\mathbf{K}$ is:

$$\mathbf{K} = \sum_{e=1}^{n_{el}} \mathbf{k}^e \tag{11.58}$$

with

$$\mathbf{k}^e = \begin{bmatrix} k^{11}\mathbf{I}_{ndim} + \mathbf{k}^{11} & \cdots & k^{1n_u}\mathbf{I}_{ndim} + \mathbf{k}^{1n_u} \\ \vdots & \ddots & \vdots \\ k^{n_u 1}\mathbf{I}_{ndim} + \mathbf{k}^{n_u 1} & \cdots & k^{n_u n_u}\mathbf{I}_{ndim} + \mathbf{k}^{n_u n_u} \end{bmatrix} \tag{11.59}$$

and the coefficients $k^{\alpha\beta}$can be obtained by:

$$k^{\alpha\beta} = \mu \int \nabla N_u^\alpha \cdot \nabla N_u^\beta \mathrm{d}\Omega_e \quad (\alpha, \beta = 1, \ldots, n_u) \tag{11.60}$$

and the matrices $k^{\alpha\beta}$ are:

$$k^{\alpha\beta} = \begin{bmatrix} k_{11}^{\alpha\beta} & \cdots & k_{1ndim}^{\alpha\beta} \\ \vdots & \ddots & \vdots \\ k_{ndim}^{\alpha\beta} & \cdots & k_{ndim\,ndim}^{\alpha\beta} \end{bmatrix} \tag{11.61}$$

with the elements $k_{rs}^{\alpha\beta}$:

$$k_{rs}^{\alpha\beta} = \mu \int_{\Omega_e} N_{u,s}^{\alpha} \cdot N_{u,r}^{\beta} \mathrm{d}\Omega \quad (\alpha, \beta = 1, \ldots, n_u) \quad (r, s = 1, \ldots, n_{dim}) \tag{11.62}$$

Matrix of pressure and incompressibility is:

$$\mathbf{Q} = \sum_{e=1}^{n_{el}} q^e \tag{11.63}$$

with

$$q^e = \begin{bmatrix} \varrho^{11^T} & \cdots & \varrho^{1n_u^T} \\ \vdots & \ddots & \vdots \\ \varrho^{np1^T} & \cdots & \varrho^{np\,nu^T} \end{bmatrix} \tag{11.64}$$

where the vectors $\varrho^{\gamma\beta^T}$ are:

$$\varrho^{\gamma\beta^T} = \left[ \varrho_1^{\gamma\beta}, \ldots, \varrho_{ndim}^{\gamma\beta} \right] \tag{11.65}$$

and

$$\varrho_r^{\gamma\beta} = -\int_{\Omega_e} N_p^{\gamma} N_{u,r}^{\beta} \mathrm{d}\Omega_e \quad (\gamma = 1, \ldots, n_p) \quad (\beta = 1, \ldots, n_u) \quad (r = 1, \ldots, n_{dim}) \tag{11.66}$$

The forcing vector $F$ is:

$$\mathbf{F} = \sum_{e=1}^{n_{el}} f_e \tag{11.67}$$

where

$$f^e = \begin{bmatrix} \zeta^1 \\ \vdots \\ \zeta^{nu} \end{bmatrix} \tag{11.68}$$

The vectors $\zeta^{\alpha^T}$ are:

$$\zeta^{\alpha^T} = \left[\zeta_1^{\alpha}, \cdots, \zeta_{ndim}^{\alpha}\right] \tag{11.69}$$

and

$$\zeta_r^{\alpha} = \int_{\Gamma_n} N_p^{\alpha} h_r \mathrm{d}\Gamma_n \quad (\alpha = 1, \ldots, n_p) \quad (r = 1, \ldots, n_{dim}) \tag{11.70}$$

Assumptions and Boundary Conditions

Due to the complex interactions of all the physical and chemical processes taking place, it is necessary to consider some simplifications and assumptions in order to computationally solve the problem. The model simplifications and assumptions are as follows:

1. the wall is considered rigid,
2. chemical interactions and the influence of the electric charge of the cells are neglected,
3. the cells are considered solid spheres,
4. Magnus effect are considered negligible (does not consider particle rotational effects),
5. the domains are saturated by the moving fluid, so that there are no capillarity effects,
6. and assume the model relies purely on fluid-particle interactions, so any particle-particle interaction is currently neglected.

Figure 11.1 depicts the geometry that consists of an in vitro cell culture system (hydrogel) with the objective of quantifying the major factors that affect the cell migration process at the macro-scale. This three-dimensional geometry emulates a simplified vascularized tumor system with the hydrogel acting as the tumor tissue and a microchannel acting as a vessel. This simple system was chosen for conducting the simulations because it will be easily developed during experimental tests in future work. The hydrogel was considered as a homogeneous porous media for this case. The objective of this study case is to understand the pressure effects, distribution of nutrients, drag interactions, and viscous shear stress exertions on cell motion at the macro-scale. A finite element method was implemented to solve the mathematical model. Tetrahedral elements were used to mesh the three-dimensional computational domain and mesh sensitivity analysis was carried out by varying the number of mesh elements in the domain.

The boundary conditions specify that there is no slip at the wall, upstream flow varies in a parabolic fashion, and there is free flow at the outlet. The tube is long enough to generate developed axial velocity profiles.

The parameters used in the simulation, in Table 11.1, consist of both estimated and experimental values. The velocity inlet was 5.45 mm/s, which was calculated based on the volume flow rate of $Q = 0.130$ mL/min.

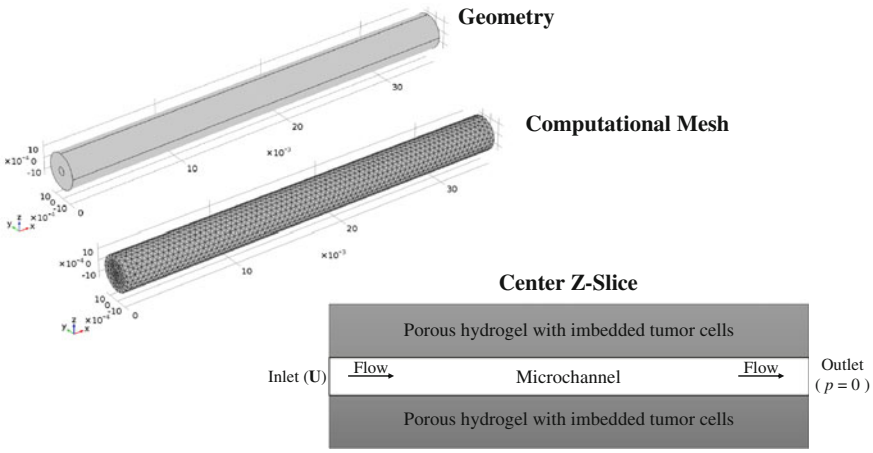


**Fig. 11.1** Geometry of the hydrogel at the macro-scale

**Table 11.1** Macro-scale simulation parameters

| Parameter | Value (hydrogel) | Value (microchannel) |
|---|---|---|
| Nutrient attraction (M) [J m$^3$/mol] | $5 \times 10^{-4}$ | $5 \times 10^{-4}$ |
| Force from hydrogel (K) [N s/m] | $1 \times 10^{-4}$ | $1 \times 10^{-4}$ |
| Dynamic viscosity ($\mu$) [Pa s] | 1.3 | $7.8 \times 10^{-4}$ |
| Permeability ($k$) [m$^2$] | 1 | 1 |
| Porosity ($\varepsilon$) | 0.9 | 1 |
| Density ($\rho$) [kg/m$^3$] | 3,000 | 1,000 |

Nanoparticles can be used to passively target tumor tissue through leaky blood vessels. Nanoparticles with less than 200 nm diameters easily pass through these leaky vessel walls; thus they are capable of targeting tumors [28]. This simulation, therefore, includes nanoparticles that are smaller than 200 nm. Although the hydrogel has a three-dimensional porous structure, this first approach was simplified in 2D as shown in Fig 11.2.

### 11.3.1.2 Macro-scale Results

Although the flow in the human circulatory system is unsteady in response to pulsatile pressure, steady flow models, like the model introduced in this section, provide useful information about the aspects of fluid flow. This case was considered steady flow. A parabolic fluid flow was introduced at the inlet and nutrients were introduced into the same inlet as fluid flow into the microchannel and hydrogel. Particles imbedded in the hydrogel migrated in response to their attraction to the nutrients.

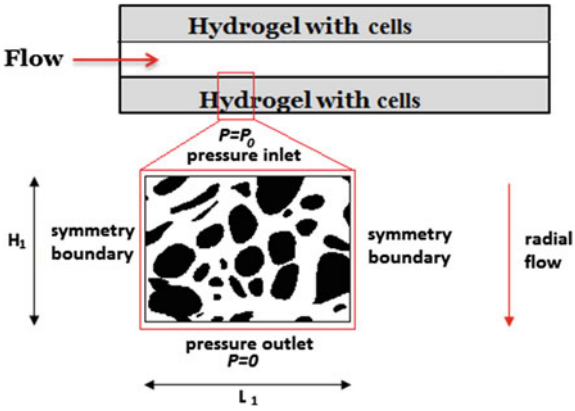


**Fig. 11.2** Network of the hydrogel

The simulation results of Fig. 11.3 describe the movement of the cells due to advection and diffusion at macro-scale and only displays cells that have a velocity greater than 0.1 mm/s. Advection involves the movement of the cells through the microchannel and hydrogel at the rate of movement of the fluid carrier. Diffusion is caused by the motion of the cells from zones of high concentration to zones of lower concentration. The accuracy of the simulation results was improved by employing a finer mesh that contains one cell per element.

#### 11.3.1.3 Micro-scale Results

The velocity magnitude is higher in the narrowest pores and tends to decrease where the pore channel size increases. However, there is a considerable zone with low flow velocity levels where the permeability would be affected possibly by the increase of the pore path (tortuosity). This may imply that this area would be susceptible to cell attachment and deposition.

Simulation cases with differing pressure gradients at steady state were conducted with the results indicating that the distribution of the velocities, pressure, and shear stress were similar for three cases inside the wall of the hydrogel. Different Reynolds numbers and shear stresses, in Table 11.2, were obtained in the three cases.

Figure 11.4 displays the transport phenomena related to advection and diffusion inside the hydrogel, the mechanical dispersion, and the mixing of the cells due to changes in fluid velocities along the streamlines. These variations are associated with three phenomena: pore size, pore friction, and path length. Figure 11.4a depicts how some particles gain inertia in the narrowest pores. Figure 11.4b shows stagnant zones where some cells might interact with other cells and the wall.

Figure 11.4c shows deposition points close enough to the wall, where the cells might be attracted due to the weak forces known as van der Waal's (assuming absence of electrical charge of the cells) [29]. The trapped particles might act like an extension

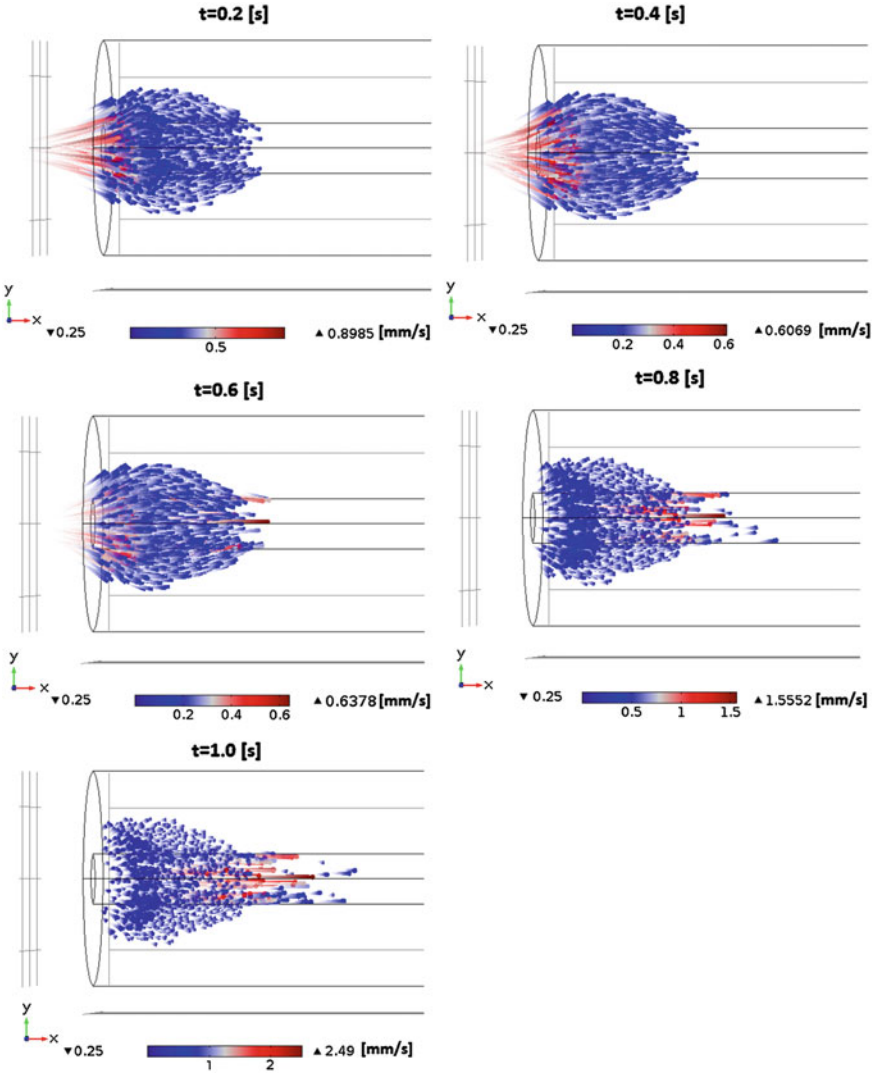


**Fig. 11.3** Time evolution of cell transport (only cells with velocity greater than 0.1 mm/s)

of the wall and trap other particles or block pores at various sites. The fast moving particles with higher inertia may not become trapped. Figure 11.4d and e shows zones of bad irrigation of nutrients and recirculation, where the lack of nutrients might affect the cells viability and consequently promote mechanical stimulus into biochemical reactions near to the wall (mechanotransduction).

**Table 11.2** Reynolds average and maximum values of shear stress considering a blood density at 37 °C = 1,060 [kg/m$^3$] and blood dynamic viscosity = 0.005 [Pa s]

| Pressure gradient [Pa] | Reynolds average | Max Shear stress [dynes/cm$^2$] |
|---|---|---|
| 0.10 | 1.21 | 0.23 |
| 1.00 | 9.32 | 1.99 |
| 10.0 | 57.9 | 12.4 |

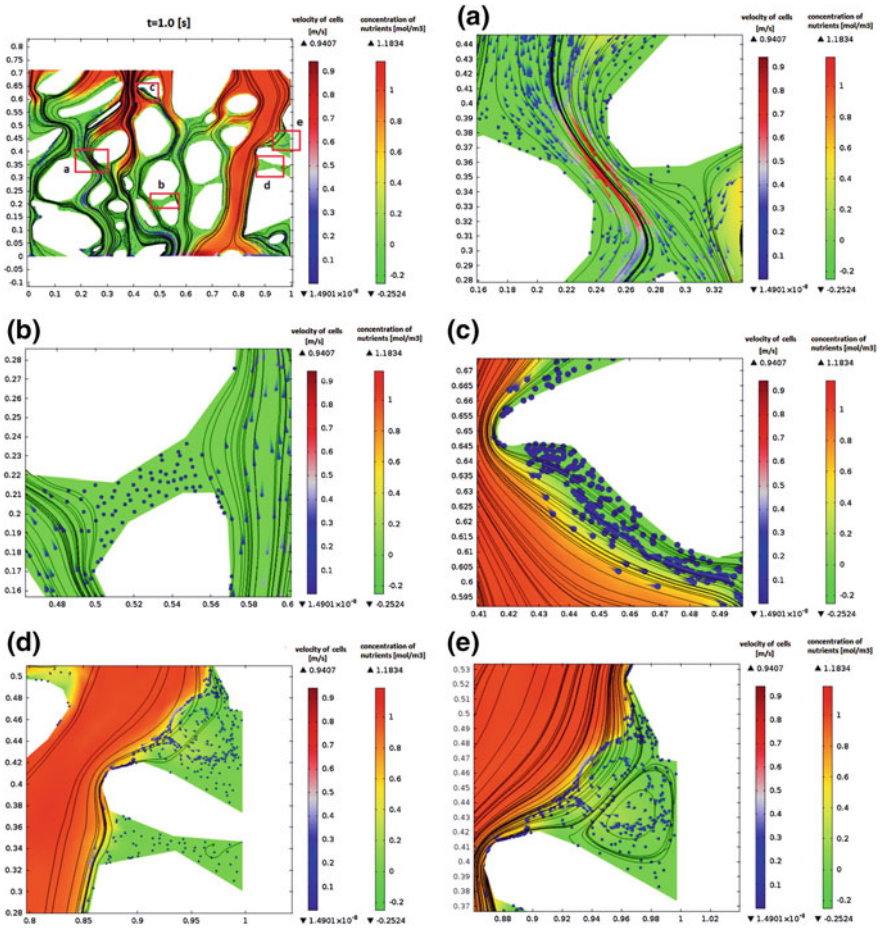


**Fig. 11.4** Different phenomena of dispersion over the particles inside the wall: **a** effect of a narrow pore channel; **b** stagnation points; **c** deposition; **d** bad irrigation; **e** recirculation zones

### 11.3.2 Bone Remodeling and Wound Healing

In general, mixture theory provides a comprehensive framework [30] that allows multiple species to be included under the abstract notion of a continuous media. In this framework, biological tissue can be considered as a multi-phasic system with different species, including solid tissue, body fluids, cells, extracellular matrix (ECM), nutrients, etc. The species (or constituents) are denoted by $\phi_\alpha (\alpha = 1, 2, \ldots, \kappa)$, where $\kappa$ is the number of species in the mixture. The nominal densities of each constituent is denoted by $\rho^\alpha$ and the true densities are denoted by $\rho^{\alpha R}$.

To introduce a formal characterization of the volume fraction, a domain occupying the control space $B_S$ is defined with the boundary $\partial B_S$, in which all the constituents $\phi_\alpha$ occupy the volume fractions $\eta_\alpha$, which satisfy the constraint

$$\sum_{\alpha=1}^{\kappa} \eta^\alpha (\mathbf{x}, t) = \sum_{\alpha=1}^{\kappa} \frac{\rho^\alpha}{\rho^{\alpha R}} = 1, \tag{11.71}$$

where $\mathbf{x}$ is the position vector of the actual placement and $t$ denotes the time.

Two frames of reference are used to describe the governing principles of continuum mechanics. The Lagrangian frame of reference is often used in solid mechanics, while the Eulerian frame of reference is used in fluid mechanics. The Lagrangian description is usually suitable to establish mathematical models for stress-induced growth, such as bone remodeling and wound healing (e.g., [31]), while the Eulerian description is often used for developing mass transfer driven tumor growth models [32–35] with a few exceptions when tumors undergo large deformations [36].

To develop mathematical models for each application, the governing equations are provided by the conservation laws, and the constitutive relations are usually developed through empirical relationships subject to constraints such as frame invariance condition and consistency with thermodynamics, to name a few. Specifically, the governing equations can be obtained from conservations of mass, momentum, and energy for each species as well as the mixture. When the free energy of the system is given as a function of dependent field variables, such as strain and temperature, the second law of thermodynamics (the Clausius-Duhem inequality) provides a means for determining forms of some constitutive equations via the well-known method of Coleman and Noll [37].

Predictive medicine is emerging as a research field as well as a potential medical tool for designing optimal treatment options by advancing deeper understanding of biological and biomedical processes and providing patient-specific prognosis and therapies. Characterizing a biological system involves studies of complex phenomena at various spatial and temporal scales. At a macro-level, continuum mechanics can be employed to investigate tissue behavior. In particular, both mixture theory and porous media theory can be used to model both hard and soft tissues in terms of growth, particle flow, bioheat transfer, etc. Mixture theory can be introduced for modeling both hard and soft tissues.

In continuum mixture theory, an arbitrary point in a continuous medium can be occupied simultaneously by many different constituents differentiated only through their volume fractions. The advantage of this mathematical representation of tissues is that it permits direct reconstruction of patient-specific geometry from medical imaging; inclusion of species from different scales as long as they can be characterized by either density or volume fraction functions; and automatically provides for interactions among species included in the mixture without the need of front tracking or complex interaction condition. Furthermore, the mathematical models based on the notion of mixture can be derived from the first principles (conservation laws and the second law of thermodynamics).

The applications considered here include bone remodeling, wound healing, and tumor growth. Models of the cardiovascular system can also be included within the mixture framework if soft tissues such as heart and vessels are treated as separate species different than fluid (blood) and the extracellular matrix.

Bone remodeling is a natural biological process that occurs during the course of maturity or after injuries, which can be characterized by a reconfiguration of the density of bone tissue due to mechanical forces or other biological stimuli. Wound healing (or cicatrization), on the other hand, mainly involves skin or other soft organ tissues that repair themselves after the protective layer and/or tissues are broken and damaged. In particular, wound healing in fasciated muscle occurs due to the presence of traction forces that accelerate the healing process. Both bone remodeling and wound healing can be investigated under the general framework of continuum mixture theory at the tissue level. Another important application is tumor growth modeling, which is relevant to cancer biology, treatment planning, and outcome prediction. The mixture theory framework can provide a convenient vehicle to simulate growth (or shrinking) phenomena under various biological conditions.

Considering the conservation of mass for each species $\phi^\alpha$ in a control volume, the mass production and fluxes across the boundary of the control volume are required to be equal:

$$\frac{\partial \rho^\alpha}{\partial t} + \nabla \cdot \left(\rho^\alpha \mathbf{v}\right) = \hat{\rho}^\alpha. \tag{11.72}$$

In Eq. (11.72), the velocity of the constituent is denoted by $\mathbf{v}$ and the mass supplies between the phases are denoted by $\hat{\rho}^\alpha$. From a mechanical point of view, the processes of bone remodeling and wound healing are mainly induced by traction forces. For simplicity, we choose a triphasic system comprised of solid, liquid, and nutrients to illustrate the modeling process [31]. The mass exchange terms are subject to the constraint

$$\sum_{\alpha=1}^{\kappa} \hat{\rho}^\alpha = 0 \quad \text{or} \quad \hat{\rho}^S + \hat{\rho}^N + \hat{\rho}^L = 0. \tag{11.73}$$

Moreover, if the liquid phase is not involved in the mass transition, then,

$$\hat{\rho}^S = -\hat{\rho}^N \quad \text{and} \quad \hat{\rho}^L = 0. \tag{11.74}$$

Next, the momentum of the constituent $\phi_\alpha$ is defined by

$$\mathbf{m}^\alpha = \int_{B_\alpha} \rho^\alpha \mathbf{v}_\alpha dv. \tag{11.75}$$

By including $\mathbf{m}^\alpha$ in the total change of linear momentum in $B_\alpha$ and denoting the interaction of the momentum of the constituents $\phi_\alpha$ by $\hat{\mathbf{p}}^\alpha$, the standard momentum equation (Cauchy equation of motion) for each constituent becomes

$$\nabla \cdot \mathbf{T}^\alpha + \rho^\alpha (\mathbf{b} - \mathbf{a}_\alpha) + \hat{\mathbf{p}}^\alpha - \hat{\rho}^\alpha \mathbf{v}_\alpha = \mathbf{0}, \tag{11.76}$$

where the expression $\hat{\rho}^\alpha \mathbf{v}_\alpha$ represents the exchange of linear momentum through the density supply $\hat{\rho}^\alpha$. The term $\mathbf{T}^\alpha$ denotes the partial Cauchy stress tensor, $\rho^\alpha \mathbf{b}$ specifies the volume force. In addition, the terms $\hat{\mathbf{p}}^\alpha$, where $\alpha = S, L, N$, are required to satisfy the constraint condition

$$\hat{\mathbf{p}}^S + \hat{\mathbf{p}}^L + \hat{\mathbf{p}}^N = \mathbf{0}. \tag{11.77}$$

In the case of either bone remodeling or wound healing, the velocity field is nearly in steady state. Thus, the acceleration can be neglected by setting $\mathbf{a}_\alpha = 0$. The resulting system of equations can then be written

$$\nabla \cdot \mathbf{T}^\alpha + \rho^\alpha \mathbf{b} + \hat{\mathbf{p}}^\alpha = \hat{\rho}^\alpha \mathbf{v}_\alpha. \tag{11.78}$$

The second law of thermodynamics (entropy inequality) provides expressions for the stresses in the solid and fluid phases that are dependent on the displacements and the seepage velocity, respectively. The seepage velocity is a relative velocity between the liquid and solid phases, which are often obtained from explicit Darcy velocity expressions for flow through a porous medium (solid phase). Various types of material behavior can be described in terms of principal invariants of the structural tensor $\mathbf{M}$ and the right Cauchy-Green Tensor $\mathbf{C_S}$, where

$$\mathbf{M} = \mathbf{A} \otimes \mathbf{A} \quad \text{and} \quad \mathbf{C_S} = \mathbf{F_S^T F_S}, \tag{11.79}$$

and $\mathbf{A}$ is the preferred direction inside the material and $\mathbf{F_S}$ is the deformation gradient for a solid undergoing finite deformations. The expressions for the stress in the solid are dependent on the deformation gradient and consequently the displacements of the solid. Summation of the momentum conservation equations provides the equation for the solid displacements. Mass conservation equations, with incorporation of the saturation condition, provide the equation for interstitial pressure. In addition, the mass conservation equations for each species provide the equations for the evolution of volume fractions.

Assuming the fluid phase ($F$) is comprised of the liquid ($L$) and the nutrient phases ($N$) we obtain ($F = L + N$)

$$\nabla \cdot \sum_{\alpha}^{S,L,N} \mathbf{T}^{\alpha} + \mathbf{b} \sum_{\alpha}^{S,L,N} \rho^{\alpha} + \sum_{\alpha}^{S,L,N} \hat{\mathbf{p}}^{\alpha} - \hat{\rho}^{S}\mathbf{v}_{S} - \hat{\rho}^{F}\mathbf{v}_{F} = 0. \tag{11.80}$$

Since $\hat{\rho}^{F} = -\hat{\rho}^{S}$, and $\hat{\mathbf{p}}^{S} + \hat{\mathbf{p}}^{N} + \hat{\mathbf{p}}^{F} = 0$, we obtain

$$\nabla \cdot \sum_{\alpha}^{S,L,N} \mathbf{T}^{\alpha} + \mathbf{b} \sum_{\alpha}^{S,L,N} \rho^{\alpha} + \hat{\rho}^{S}\left(\mathbf{v_F} - \mathbf{v_S}\right) = 0. \tag{11.81}$$

The definition of the seepage velocity $\mathbf{w}_{FS}$ provides the following equation

$$\nabla \cdot \sum_{\alpha}^{S,F} \mathbf{T}^{\alpha} + \mathbf{b} \sum_{\alpha}^{S,F} \rho^{\alpha} + \hat{\rho}^{S}\left(\mathbf{w}_{FS}\right) = 0. \tag{11.82}$$

The strong form for the pressure equation can be written as follows

$$\nabla \cdot \left(\eta^{F}\mathbf{w}_{FS}\right) + \mathbf{I} : \mathbf{D}_{S} - \hat{\rho}^{S}\left(\frac{1}{\rho^{SR}} - \frac{1}{\rho^{NR}}\right) = 0. \tag{11.83}$$

The strong form of mass conservation equation for the solid phase is

$$\frac{D^{S}(\eta^{S})}{Dt} + \eta^{S}\mathbf{I} : \mathbf{D}_{S} = \frac{\hat{\rho}^{S}}{\rho^{SR}}. \tag{11.84}$$

Finally, the balance of mass for the nutrient phase can be described as

$$\frac{D^{S}(\eta^{N})}{Dt} - \frac{\hat{\rho}^{N}}{\rho^{NR}} + \eta^{N}\mathbf{I} : \mathbf{D}_{S} + \nabla \cdot \left(\eta^{N}\mathbf{w}_{FS}\right) = 0. \tag{11.85}$$

In the above, $\mathbf{w_{FS}}$ is the seepage velocity, $\mathbf{D_S}$ denotes the symmetric part of the spatial velocity gradient, and $\frac{D^{S}()}{Dt}$ denotes the total derivative of quantities with respect to the solid phase. The seepage velocity is obtained from

$$\mathbf{w_{FS}} = \frac{1}{\mathbf{S_F}}\left[\lambda \nabla \eta^{F} - \hat{\mathbf{p}}^{\mathbf{F}}\right], \tag{11.86}$$

Here, $\mathbf{S_F}$ is the permeability tensor, $\lambda$ denotes the pressure, and $\eta^{F}$ is the volume fraction of the fluid. Equations 11.78–11.85 are required to be solved for the bone remodeling problem with the mixture theory. The primary dependent variables are $\{\mathbf{u_S}, \lambda, n_S, n_N\}$, the solid displacements, interstitial pressure, and the solid and nutrient volume fractions.

Bone remodeling is an important biological application that can be studied within the aegis of the above mathematical framework. The process of bone remodeling involves three types of cells namely osteoblasts, osteocytes, and osteoclasts. The remodeling process is a continuous process and annually around 10 % of the bone is replaced. It is driven by the requirement of calcium in the extracellular fluid, and can also occur in response to mechanical stresses on the bone tissue. The above framework presented studies the bone reconfiguration due to external stress. One example of bone remodeling is a femur under traction loadings, which drives the process so that the bone density is redistributed. Based on the stress distribution, the bone usually becomes stiffer in the areas of higher stresses.

The same set of equations can also be used to study the process of wound healing. It is obvious, however, that the initial and boundary conditions are specified differently. It is worth noting that traction forces inside the wound can facilitate the closure of the wound. From the computational point of view, the specification of solid and liquid volume fractions as well as pressure are required on all interior and exterior boundaries of the computational domain. The interior boundary is assumed to be inside surface exposed due to the wounding of the tissue.

The interior boundary (inner face) of the wound can be assumed to possess a sufficiently large quantity of the solid and liquid volume fractions, which is modeled biologically with sufficient nutrient supply at this face. On the other hand, the opening of the wound can be prescribed with natural boundary conditions with seepage velocity.

### *11.3.3 Modeling Tumor Growth*

Attempts at developing computational mechanics models of tumor growth date back over half a century (see, e.g., [38]). Various models have been proposed based on ordinary differential equations (ODE) e.g., ([39–42]), extensions of ODE's to partial differential equations [33, 43] or continuum mechanics based descriptions that study both vascular and avascular tumor growth. Continuum mechanics-based formulations consider either a Lagrangian [31] or an Eulerian description of the medium [33]. Various considerations such as modifications of the ordinary differential equations (ODE's) to include effects of therapies [41], studying cell concentrations in capillaries during vascularization with and without inhibitors, multiscale modeling [2, 4, 44–46], and cell transport equations in the extracellular matrix (ECM) [34] have been included.

Modeling tumor growth can also be formulated under the framework of mixture theory with a multi-constituent description of the medium. It is convenient to use an Eulerian frame of reference. Other descriptions have considered the tumor phase with diffused interface [35]. Consider, the volume fraction of cells denoted by ($\xi$), extracellular liquid ($l$), and extracellular matrix ($m$) [33]. The governing equations are derived from conservation laws for each constituent of the individual phases.

The cells can be further classified as tumor cells, epithelial cells, fibroblasts, etc. denoted by subscript, $\alpha = 1, 2, \ldots, N$. Similarly, we can distinguish different components of the extra-cellular matrix (ECM) namely, collagen, elastin, fibronectin, vitronectin, etc. [47] denoted by subscript $\beta = 1, 2, \ldots, M$. The ECM component velocities are assumed to be the same, based on the constrained submixture assumption [34]. The concentrations of chemicals within the liquid are of interest in the extracellular liquid. The above assumptions lead to the mass conservation equations for the constituents as ($\xi$, $m$, and $l$),

$$\begin{aligned} \frac{\partial \xi_\alpha}{\partial t} + \nabla \cdot (\xi_\alpha v_{\xi_\alpha}) &= \Gamma_{\xi_\alpha}, \\ \frac{\partial m_\beta}{\partial t} + \nabla \cdot (m_\beta v_m) &= \Gamma_{m_\beta}. \end{aligned} \tag{11.87}$$

In the equations above $v_{\xi_\alpha}$ and $v_m$ denote the velocities of the respective phases. Note that no subscript on $v_m$ (constrained submixture assumption). Mass balance equation expressed as concentrations in the liquid phase are expressed as

$$\frac{\partial c}{\partial t} = \nabla \cdot (D \nabla c) + G. \tag{11.88}$$

Here, $D$ denotes the effective diffusivity tensor in the mixture, $G$ contains the production/source terms and degradation/uptake terms relative to the entire mixture. The system of equations requires the velocities of each component to obtain the closure. The motion of the volume fraction of the cells are governed by the momentum equations

$$\rho \xi \left( \frac{\partial v_\xi}{\partial t} + v_\xi \cdot \nabla v_\xi \right) = \nabla \cdot \tilde{T}_\xi + \rho \xi \mathbf{b} + \tilde{m_\xi}. \tag{11.89}$$

Similar expressions hold for the extracellular matrix and the liquid phases. The presence of the saturation constraint requires one to introduce a Lagrange multiplier into the Clauius-Durhem inequality and provides expressions for the excess stress $\tilde{T_\xi}$ and excess interaction force $m_\xi$. The Lagrange multiplier is classically identified with the interstitial pressure $P$. Body forces, $\mathbf{b}$ are ignored for the equations for the ECM and the excess stress tensor in the extracellular liquid is assumed to be negligible in accordance with the low viscous forces in porous media flow studies. With these assumptions, we obtain the following equations

$$\begin{aligned} -\xi_\alpha \nabla P + \nabla \cdot (\xi_\alpha T_{\xi_\alpha}) + m_{\xi_\alpha} + \rho \xi_\alpha b_\alpha &= 0, \\ -m \nabla P + \nabla \cdot (m T_m) + m_m &= 0, \\ -l \nabla P + m_l &= 0. \end{aligned} \tag{11.90}$$

These equations provide the governing differential equations required to solve tumor growth problems. The primary variables to be solved are $\{\xi_\alpha, m_\beta, P\}$.

The governing equations can be solved with suitable boundary conditions of specified volume fractions of the cells, extracellular liquid, and pressures. Fluxes of these variables across the boundaries also need to be specified for a complete description of the problem.

Other approaches in modeling tumor growth involve tracking the moving interface of the growing tumor. Among them is the phase field approach. The derivation of the basic governing equations is given in Wise [32]. From the continuum advection-reaction-diffusion equations, the volume fractions of the tissue components obey

$$\frac{\partial \phi}{\partial t} + \nabla \cdot (\mathbf{u}\phi) = -\nabla \cdot \mathbf{J} + S. \tag{11.91}$$

Here, $\phi$ denotes the volume fraction, $\mathbf{J}$ denotes the fluxes that account for the mechanical interactions among the different species, and the source term $S$ accounts for the inter-component mass exchange as well as gains due to proliferation and loss due to cell death.

The above Eq. (11.91) is interpreted as the evolution equation for $\phi$ which characterizes the phase of the system. This approach modifies the equation for the interface to provide both for convection of the interface along with an appropriate diminishing of the total energy of the system. The free energy of a system of two immiscible fluids consists of mixing, bulk distortion, and anchoring energy. For simple two-phase flows, only mixing energy is retained, which results in a rather simple expression for the free energy $\phi$

$$F(\phi, \nabla\phi, T) = \int \left( \frac{1}{2}\epsilon^2 |\nabla\phi|^2 + f(\phi, T) \right) \mathrm{d}V = \int f_{\mathrm{tot}} \mathrm{d}V. \tag{11.92}$$

Physical processes involve those in which the total energy is minimized. The following equation describes evolution of the phase field parameter:

$$\frac{\partial \phi}{\partial t} + \mathbf{u}\nabla\phi = \nabla \cdot \gamma \nabla \left( \frac{\partial f_{\mathrm{tot}}}{\partial \phi} - \nabla \cdot \frac{\partial f_{\mathrm{tot}}}{\partial \nabla \phi} \right) \tag{11.93}$$

where, $f_{\mathrm{tot}}$ is the total free energy of the system. Equation (11.93) seeks to minimize the total free energy of the system with a relaxation time controlled by the mobility $\gamma$. With some further approximations, the partial differential equation governing the phase field variable is obtained as the Cahn-Hillard equation,

$$\frac{\partial \phi}{\partial t} + \mathbf{u}\nabla\phi = \nabla \cdot \gamma \nabla G, \tag{11.94}$$

where $G$ is the chemical potential. The mobility ($\gamma$) determines the timescale of the Cahn-Hillard diffusion and must be large enough to retain a constant interfacial thickness but small enough so that the convective terms are not overly damped.

The mobility is defined as a function of the interface thickness as $\gamma = \chi\epsilon^2$. The chemical potential is provided by

$$G = \lambda\left[-\nabla^2\phi + \frac{\phi(\phi^2-1)}{\epsilon^2}\right]. \tag{11.95}$$

The Cahn-Hillard equation forces $\phi$ to take values of $-1$ or $+1$ except in a very thin region on the fluid-fluid interface. The above equation is of fourth order and poses a formidable challenge to solve. The solutions are characterized by nearly constant states, with complex morphologies, separated by evolving narrow transition layers that describe diffuse interfaces between tumor and host tissues.

The presence of the fourth-order term poses stringent restrictions on the time step. The step size for time integration of the above equation is constrained by $h^4$ where $h$ is the spatial grid size. To remove this restriction one ca use a Crank-Nicholson-like time integration method, which results in non-linear equations at the implicit time level. Multilevel nonlinear *full approximation storage* (FAS) multi-grid method is adopted to solve the discrete system, with respect to time and space. When taking the finite difference approach for the spatial discretization of the Cahn-Hillard equation one starts with a central difference approximation of the derivative in space along with a backward difference approximation of the time derivative. Alternatively, Crank-Nicholson approximation scheme can be implemented for time discretization, with an appropriate treatment of the advection term. Higher order approximation of the divergence and the gradient operators are obtained from the appropriate Taylor series terms in constructing the discrete forms. The advection terms need special treatment to avoid numerical oscillations at the tumor-host interface.

In the finite difference framework various schemes have been proposed to discretize the advective flux. In specific for the phase field approach the advection operator appears as a shock term which needs to be stabilized. Classical discretization methods, such as the central difference approximation, have the disadvantage of causing non-physical oscillations across or in the near vicinity of discontinuities known as the Gibbs phenomenon. To suppress the Gibbs phenomenon, Harten [48] proposed an essentially non-oscillatory scheme (ENO) scheme based on the Godunov upwind scheme, which achieves an accuracy of arbitrary high order. Efforts toward improving the ENO scheme have resulted in the development of weighted non-oscillatory scheme or the WENO scheme [49].

Finite element analysis of Cahn-Hillard equation have also been accomplished [50–52]. Error bounds of the Cahn-Hillard equation with degenerate mobility were examined in Barrett [50]. Both convergence and well-posed finite element approximation were examined in addition to determining the stability bounds of the approximation. The existence of the Lyapunov energy functional was found to be of primary importance in the error analysis [51]. Backward difference in time was utilized and optimal error bounds were established. Usage of multi-grid methods for solving Cahn-Hillard equation without the presence of the advection term have been presented in Kay [52]. Implicit backward Euler stepping in time in conjugation with continuous piecewise linear basis functions in space were found to provide

faithful results. Conservation of the total energy of the Lyapunov energy functional provided further confirmation of the accuracy of the simulation. A multi-grid scheme was proposed to solve the problem in opposition to Gauss-Seidel variants as solvers for the discrete system.

The introduction of the phase field interface allows the fourth-order Cahn-Hillard equation to be written as a set of two second order PDEs

$$\frac{\partial \phi}{\partial t} + \mathbf{u} \cdot \nabla \phi = \nabla \cdot \frac{\gamma \lambda}{\epsilon^2} \nabla \psi, \tag{11.96}$$

$$\psi = -\nabla \cdot \epsilon^2 \nabla \phi + (\phi^2 - 1)\phi. \tag{11.97}$$

The above equation is the simplest phase field model, and is known as model A in the terminology of phase field transitions [4, 35, 53]. Phase field approaches have been applied for solving the tumor growth and multiphase descriptions of an evolving tumor have been obtained with each phase having its own interface and a characteristic front of the moving interface obtained with suitable approximations.

When specific applications of the phase field approach to tumor growth are considered, the proliferative and non-proliferative cells are described by the phase field parameter $\phi$. The relevant equations in the context of tumor growth are provided by the following [35, 54]

$$\frac{\partial \phi}{\partial t} = M \nabla^2 \left[ -\phi + \phi^3 - \epsilon \nabla^2 \phi \right] + \alpha_p(T) \phi \Theta(\phi). \tag{11.98}$$

Here, $M$ denotes the mobility coefficient, $T$ stands for the concentration of hypoxic cell produced angiogenic factor, and $\Theta(\phi)$ denotes the Heaviside function which takes a value of 1 when its argument is positive. The proliferation rate is denoted by $\alpha_p(T)$ and as usual $\epsilon$ denotes the width of the capillary wall. The above equation is solved with the governing equation for the angiogenic factor $T$. The angiogenic factor diffuses randomly from the hypoxic tumor area where it is produced and obeys the following equation

$$\frac{\partial T_i}{\partial t} = \nabla \cdot (D \nabla T) - \alpha_T T \phi \Theta(\phi). \tag{11.99}$$

In the equation above $D$ denotes the diffusion coefficient of the factor in the tissue and $\alpha_T$ denotes the rate of consumption by the endothelial cells.

## 11.4 Open Questions

Multiscale methods have been used in a wide range of applications: materials and nanomaterials science [55, 56], elasticity and plasticity analysis [57], computational biomechanics [58], drug development [59], vascular tumor growth [44], coarse-grain

peptide and protein folding modeling [60–62], mutation and immune competition of cancer cells [63], organ level analysis [64], computational physiology [65], and genetic regulatory networks [66]. The common goal of all these applications is to create a predictive multiscale mathematical model to simulate a complex system.

The open question that spans each application of multiscale modeling is how to validate and calibrate the model with experimental data. Although still a useful tool, a mathematical model does not become a predictive tool until it has been validated and calibrated with experimental data [56]. Another limitation and open question of current multiscale methods is how to easily extend the analysis to three dimensions. Most of the methods described in this chapter are useful only in one or two dimensions [1]. Currently available multiscale methods have tremendous challenge in dealing with nonlinear problems [67].

Moreover, a consistent difficulty in multiscale mathematical modeling is how to bridge spatial and temporal scales in a systematic and seamless fashion. In many biological phenomena, such as protein folding and cell proliferation, events at small scales occur much quicker than events at larger scales. In some cases, multiscale methods provide the tools to handle the different spatial scales, but not the temporal scales [1, 5, 6, 8, 10–12, 14, 15].

The future direction of multiscale modeling calls for developing mathematical methods to apply in three dimensions with the ability to simultaneously bridge spatial and temporal scales. These additional capabilities will allow for development of more biologically relevant and useful predictive models.

**Acknowledgments** The authors would like to express our sincere gratitude to J. Cliff Zhou for his early involvement in this work, and Dr. M.N. Rylander and her group for providing information regarding the 3D in vitro cell culture system. The funding from NSF/CREST program ♯0932339 is highly appreciated and acknowledged.

## References

1. W.K. Liu, E.G. Karpov, H.S. Park, Nano mechanics and materials: theory, multiscale methods and applications (Wiley, 2006).
2. T.S. Deisboeck, G.S. Stamatakos, Multiscale cancer modeling, vol. 34 (CRC PressI Llc, 2010).
3. S. Schnell, R. Grima, P. Maini, Am. Sci 95(2), 134 (2007).
4. V. Cristini, J. Lowengrub, Multiscale modeling of cancer: an integrated experimental and mathematical modeling approach (Cambridge University Press, 2010).
5. S. Xiao, T. Belytschko, Computer methods in applied mechanics and engineering 193(17), 1645 (2004).
6. S. Zhang, R. Khare, Q. Lu, T. Belytschko, International Journal for Numerical Methods in Engineering 70(8), 913 (2007).
7. R. Sunyk, P. Steinmann, International Journal of Solids and Structures 40(24), 6877 (2003).
8. E.B. Tadmor, M. Ortiz, R. Phillips, Philosophical Magazine A 73(6), 1529 (1996).
9. J. Oden, T. Strouboulis, P. Devloo, Computer Methods in Applied Mechanics and Engineering 59(3), 327 (1986).
10. W.A. Curtin, R.E. Miller, Modelling and simulation in materials science and engineering 11(3), R33 (2003).

11. L. Shilkrot, R. Miller, W. Curtin, Physical review letters 89(2), 025501 (2002).
12. L. Shilkrot, R.E. Miller, W.A. Curtin, Journal of the Mechanics and Physics of Solids 52(4), 755 (2004).
13. E. Van der Giessen, A. Needleman, Modelling and Simulation in Materials Science and Engineering 3(5), 689 (1995).
14. F.F. Abraham, J.Q. Broughton, N. Bernstein, E. Kaxiras, EPL (Europhysics Letters) 44(6), 783 (1998).
15. R.E. Rudd, J.Q. Broughton, Physical Review B 58(10), R5893 (1998).
16. N.V. Mantzaris, S. Webb, H.G. Othmer, Journal of mathematical biology 49(2), 111 (2004).
17. M.A. Chaplain, S.R. McDougall, A. Anderson, Annu. Rev. Biomed. Eng. 8, 233 (2006).
18. A.R. Anderson, Mathematical Medicine and Biology 22(2), 163 (2005).
19. J. Berthier, P. Silberzan, Microfluidics for biotechnology. Second Edition. (Artech House, 2010).
20. B.M. OConnell, M.T. Walsh, Annals of biomedical Engineering 38(4), 1354 (2010).
21. K. Vafai, Porous media: Application in biological systems and biotechnology (CRC Press, 2011).
22. B. Verleye, M. Klitz, R. Croce, D. Roose, S. Lomov, I. Verpoest, Computation of the Permeability of Textiles (SFB 611, 2006).
23. C.C. Wong, Modelling the effects of textile preform architecture on permeability. Ph.D. thesis, The University of Nottingham (2006).
24. A.F.S. Rahul Vallabh, Pamela Banks-Lee, Journal of Engineered Fibers and Fabrics 5(3), 7 (2010).
25. K.B. Chandran, A.P. Yoganathan, S.E. Rittgers, Biofluid mechanics: the human circulation (CRC Press, 2012).
26. M.H. Kroll, The Journal of The American Society of Hematology 88, No. 5 (September 1), 1525 (1996).
27. R.L. Fournier, Basic Transport Phenoma in Biomedical Engineering (Taylor and Francis Group, 2007).
28. K. Lee, H. Lee, K.H. Bae, T.G. Park, Biomaterials 31(25), 6530 (2010).
29. K. Sutherland, Filters and filtration Handbook (Elsevier, 2008).
30. R. Atkin, R. Craine, The Quarterly Journal of Mechanics and Applied Mathematics 29(2), 209 (1976).
31. T. Ricken, A. Schwarz, J. Bluhm, Computational materials science 39(1), 124 (2007).
32. S. Wise, J. Lowengrub, H. Frieboes, V. Cristini, Journal of theoretical biology 253(3), 524 (2008).
33. D. Ambrosi, L. Preziosi, Mathematical Models and Methods in Applied Sciences 12(05), 737 (2002).
34. L. Preziosi. Cancer modeling and simulation. mathematical and computational biology (2003).
35. J.T. Oden, A. Hawkins, S. Prudhomme, Mathematical Models and Methods in Applied Sciences 20(03), 477 (2010).
36. D. Ambrosi, F. Mollica, International Journal of Engineering Science 40(12), 1297 (2002).
37. B.D. Coleman, W. Noll, Archive for Rational Mechanics and Analysis 13(1), 167 (1963).
38. P. Armitage, R. Doll, British journal of cancer 8(1), 1 (1954).
39. J.P. Ward, J. King, Mathematical Medicine and Biology 14(1), 39 (1997).
40. D. Grecu, A. Carstea, A. Grecu, A. Visinescu, Romanian Reports in Physics 59(2), 447 (2007).
41. J.P. Tian, K. Stone, T.J. Wallin, DYNAMICAL SYSTEMS pp. 771–779 (2009).
42. B.A. Lloyd, D. Szczerba, G. Székely, in Medical Image Computing and Computer-Assisted Intervention-MICCAI 2007 (Springer, 2007), pp. 874–881.
43. T. Roose, S.J. Chapman, P.K. Maini, Siam Review 49(2), 179 (2007).
44. P. Macklin, S. McDougall, A.R. Anderson, M.A. Chaplain, V. Cristini, J. Lowengrub, Journal of mathematical biology 58(4–5), 765 (2009).
45. W.Y. Tan, Handbook of cancer models with applications, vol. 9 (World Scientific, 2008).
46. D. Wodarz, N.L. Komarova, Computational biology of cancer: lecture notes and mathematical modeling (World Scientific Publishing Company, 2005).

47. S. Astanin, L. Preziosi, in Selected Topics in Cancer Modeling (Springer, 2008), pp. 1–31.
48. A. Harten, B. Engquist, S. Osher, S.R. Chakravarthy, Journal of Computational Physics 71(2), 231 (1987).
49. G.S. Jiang, C.W. Shu, Efficient implementation of weighted eno schemes. Tech. rep., DTIC Document (1995).
50. J.W. Barrett, J.F. Blowey, H. Garcke, SIAM Journal on Numerical Analysis 37(1), 286 (1999).
51. C.M. Elliott, S. Larsson, Mathematics of Computation 58(198), 603 (1992).
52. D. Kay, R. Welford, Journal of Computational Physics 212(1), 288 (2006).
53. R.D. Travasso, M. Castro, J.C. Oliveira, Philosophical Magazine 91(1), 183 (2011).
54. R.D. Travasso, E.C. Poiré, M. Castro, J.C. Rodrguez-Manzaneque, A. Hernández-Machado, PloS one 6(5), e19989 (2011).
55. T. Belytschko, S. Loehnert, J.H. Song, International Journal for Numerical Methods in Engineering 73(6), 869 (2008).
56. S. Zhang, S.L. Mielke, R. Khare, D. Troya, R.S. Ruoff, G.C. Schatz, T. Belytschko, Physical Review B 71(11), 115403 (2005).
57. W.K. Liu, S. Hao, T. Belytschko, S. Li, C.T. Chang, International Journal for Numerical Methods in Engineering 47(7), 1343 (2000).
58. M. Tawhai, J. Bischoff, D. Einstein, A. Erdemir, T. Guess, J. Reinbolt, Engineering in Medicine and Biology Magazine, IEEE 28(3), 41 (2009).
59. D.A. Nordsletten, B. Yankama, R. Umeton, V. Ayyadurai, C. Dewey, Biomedical Engineering, IEEE Transactions on 58(12), 3508 (2011).
60. J. Zhou, I.F. Thorpe, S. Izvekov, G.A. Voth, Biophysical journal 92(12), 4289 (2007).
61. S.C. Flores, J. Bernauer, S. Shin, R. Zhou, X. Huang, Briefings in bioinformatics 13(4), 395 (2012).
62. S. Kmiecik, M. Jamroz, A. Kolinski, in Multiscale Approaches to Protein Modeling (Springer, 2011), pp. 281–293.
63. N. Bellomo, M. Delitala, Physics of Life Reviews 5(4), 183 (2008).
64. P. Hunter, P. Nielsen, Physiology 20(5), 316 (2005).
65. P.J. Hunter, E.J. Crampin, P.M. Nielsen, Briefings in bioinformatics 9(4), 333 (2008).
66. H. De Jong, Journal of computational biology 9(1), 67 (2002).
67. W.K. Liu, E. Karpov, S. Zhang, H. Park, Computer Methods in Applied Mechanics and Engineering 193(17), 1529 (2004).